Perspectives on Ocean Ridge Basalts from the Segment to the Global Scale

Dissertation Advisor: Professor Charles H. Langmuir Allison Gale

Perspectives on Ocean Ridge Basalts from the Segment to the Global Scale

Abstract

This study addresses the influences on ridge basalt chemistry, through analysis of their major and trace element and isotopic composition at scales ranging from individual ridge segments to the entire length of the ridge system. Local-scale studies of basalts along the Mid-Atlantic Ridge shed light on crustal accretion at slow-spreading ridges, and on the nature of plume-ridge interaction in this region. We show that segments must have multiple supplies of magma delivered along their length, but with preferential delivery of magma to segment centers. Plume-ridge interaction near the Azores is not simple two-component mixing between "plume" mantle and "depleted" mantle as previously argued. The elevated highly incompatible trace element ratios possessed by basalts well south of the plume are the definitive sign of a low-degree melt, which can fractionate highly incompatible element ratios. We show that a low-degree melt of plume mantle acts to metasomatize ambient depleted mantle, creating a mixed source that melts to produce the enriched basalts south of the Azores. This metasomatized source is the enriched mixing component that produces the observed geochemical gradient, rather than bulk plume mantle.

The latter half of this study is global in scope, involving a carefully compiled ridge basalt geochemical database. This database is unparalleled in size and coverage – including data from portions of the Gakkel and Southwest Indian Ridges and Lau basin that were unavailable in prior data compilations. It includes a catalog of 771 global ridge segments, enabling the calculation of mean MORB by averaging the "segment means", including weighting on segment length and spreading rate and a quantitative treatment of errors. We show that the mean composition of ocean ridge basalts is more enriched than previously suggested, and argue for a re-definition of "normal MORB". Segment basalt compositions are individually corrected for crystal fractionation, arriving at

parental magma compositions that can be interpreted in terms of mantle processes. The fractionation-corrected mean segment compositions correlate with ridge depth, and with each other, in a manner that is consistent with control by mantle temperature variations. Mantle compositional heterogeneity is also seen, but appears to be a second-order effect.

Contents

List of Figures

List of Tables

Acknowledgements

Neither of my parents are scientists, so a part of me has always felt that I "found my own way" to science, and geology in particular. That said, I have benefited from the support, wisdom, guidance, tough love and inspiration of my parents and so many while on my scientific journey. I am deeply grateful.

In the fall of 2001, I enrolled in Geology 100 to fulfill a "core" requirement. I thank John Merck for igniting in me a love of geology that has persisted through the years. I also wish to thank the many professors at the University of Maryland, College Park who taught me the fundamentals of geology while making it fun. These professors include: Roberta Rudnick, Bill McDonough, Tom Holtz, and, of course, my igneous petrology professor Rich Walker. Thanks to Paul Tomascak for letting me make filaments for him in the summer of 2002 (my first science job), and for willingly bringing me back rocks from fieldwork in Maine. I am sincerely appreciative of Bill Minarik for getting me involved in a project on ultramafic rocks in Maryland. I didn't know then just how much I would value from "hard rock" research experience. I am proud to be a Terp.

I thank Marilyn Fogel of the Carnegie Institution of Washington for selecting me as a summer intern in 2003. My experience at Carnegie was truly eye opening, being surrounded by so many excellent scientists who treated each undergraduate as if they were a colleague.

A significant step along my journey was my time at the Smithsonian Institution, working for Tim McCoy. Tim treated me with kindness and respect and taught me a lot about meteorites and life. "When you go to grad school", he said, "always remember that more important than the number of hours worked is the quality of hours worked." I tried to remember this, and continue to admire Tim for his work-life balance. Also during this time I had the privilege of working for Leslie Hale. I admired Leslie's work ethic deeply and I am pleased to call her a friend. Paul Pohwat also became a mentor and friend, as we share a love of minerals.

I enrolled in graduate school when Charles H. Langmuir accepted me as his student. Charlie took me from student to scientist, teaching me to think rather than memorize. He challenged me at every turn, always pushing for more. I suspect that the constant challenging was because he deemed me capable, and it made me stronger. I appreciate that Charlie demanded excellence. Stéphane Escrig, a research scientist in the Langmuir lab, taught me everything from how to pipette to how to set up a spreadsheet in Excel to how to measure isotopes. Without Stéphane's guidance, I would have floundered. I am indebted to him. Muriel Laubier came in January of 2007, just in time. We soon found ourselves working on a project together, a 'FAMOUS' project in fact. The rest is history. Muriel is one of the most genuine people I have ever known. I thank her for her patience, guidance and support for the duration of my PhD. I'm so glad that we shared our time at Harvard together. Sincere thanks to Colleen Dalton, the queen of Matlab scripting. She deserves credit for the endless patience she showed as we developed our geochemical database, never seeming annoyed by my phone calls. I learned so much from her. Stephen Turner is forever my geochemical brother, the other 'Langmuir graduate student'. Steve and I have wildly different personalities, but found common ground through humor. Steve, I thank you for sending me amusing internet links when I needed them most, and for being such a loyal teammate. Zhongxing Chen, the Langmuir laboratory manager, never failed to patiently help me when I needed it. To Rady Rogers and Olga Kolas, thank you for being so supportive. You deserve more credit than you receive. And thanks to Javier Escartin, for supporting me from afar, to Jeff Standish, for constant optimism, and to Carolina Rodriguez, my wonderful officemate.

I thank my committee members, Richard O'Connell and Sujoy Mukhopadhyay, for their support. Rick, I especially appreciated our chats about jazz records. The "fourth floor" of Hoffman is loaded with incredible people. I am deeply thankful for Chenoweth Moffatt, who would drop everything if I needed her and never make it seem like an inconvenience. Thank you for so many helpful conversations. Thanks also to Sarah Colgan for her consistent support and welcomed presence on graduate student field trips. And thank you to the department for enabling me to visit Iceland, Hawaii, Chile,

Wyoming and California while a graduate student. Never in my life have I felt so lucky. Miaki Ishii was a valuable mentor to me, willing to offer guidance and insight whenever it was needed. Special thanks also to Hiromi, who provided me countless delicious home-cooked meals when I needed them most. You epitomize goodness.

I wish to thank Cin-Ty Lee for taking me to collect xenoliths with him in the Sierras one weekend in the summer of 2010. Scientific discussions during that weekend taught me to think more deeply, and made a lasting impression on me. Cin-Ty's genuine and thoughtful approach to science (and students) I greatly admire.

Then there are my dear graduate student friends, those who consistently brightened the long journey. To Rita Parai for making time for tea and reassurance and sanity-checks, to Eileen Evans, for being the most dedicated lunch friend imaginable, to Bess Sturges Corbitt for lunches filled with validation, to John Crowley for consistently helpful conversations. To Ben Kotrc for reminding me that even if I failed math I'd still be a good person, to JC for our shared interest in teaching, and to Moeko Yoshitomi and Nancy Martinez, my dear friends.

To Frances Mansfield for being my first new friend in Cambridge, and to Su Gao, a former undergraduate and friend who always found a way to make me feel better. To Raquel Alonso-Perez and her wonderful children. And to Sasha Breus, who came late in my journey but at the time I most needed her. Thank you for your honesty and insights.

Sincere thanks to my colleagues at the Derek Bok Center for Teaching and Learning, especially John Girash and Virginia Maurer. And to Hillary Jenkins for giving me the opportunity to hone my teaching skills as the Department Teaching Fellow, and for the countless laughs. Heartfelt thanks to Susanna Gallor and Sara Kimmel.

To my family: Mom, Dad, and older sisters Jennifer, Beth and Erin, and to my brother-in-laws and dear nieces and nephews, thank you for your love and support. I consider myself among the lucky ones because I had parents who encouraged me to find my own interests, supporting without pressuring. Mom, thank you for never making a face when your little girl wanted to play the drums or study geology. I am who I am because of the time you spent nurturing and teaching me, and I hope I've made you

proud of the person I am. You'll never receive the accolades you deserve for being a great mother, but please know that I owe this degree to you. Thank you for the unconditional love. And Dad, thank you for instilling in me a love of nature, a strong work ethic, and the refusal to do anything less than my best. To my oldest sister Jenn, you'll never know how much your constant unconditional love and support through the years has meant to me. I respect and admire you so very much. To Beth, for trailblazing the road to the PhD and for supporting me in just the right ways. To Erin, for believing in me and for our shared sense of humor. To my nieces and nephews, thanks for keeping things in perspective. To my "other" family: Pam, Howard, Rebeccah, Allison and Lisa, thank you. Reba, you especially paved the way toward a science PhD, always showing me the next move. Pam and Howard, I continue to appreciate your earnest interest in all things science! And to my lovebirds, the late George, and the current Rowan and Sydney, you are my family. Thanks for sitting on my shoulders day in and day out.

And, last but not least, to my dear Sarah L. Waterworth. You are my inspiration, my love, and my best friend. Thank you for sharing this journey with me since the earliest days, from Maryland to Massachusetts. Thank you for listening patiently to whatever absurdities had crept up that day, for providing hugs (and cupcakes) at just the right time, and for always believing in me. Your quiet and unwavering support sustained me through countless dark days, and I simply could not have done this without you. I can't wait until our next chapter.

Dedication

To my mom, Jo Ann Schwab Gale, for making sure I had the opportunities she never had, for unwavering support and love, and for allowing and encouraging me to be myself

And to my Sarah Lynn Waterworth, for going on more geology trips than any non-geologist should ever have to, for untiring patience, for genuine kindness, and for loving me

Chapter 1

Introduction

Oceanic spreading centers extend for more than 64,000 km across the globe, accounting for more than 80% of annual volcanic activity. The relative simplicity of their eruption environment, away from overriding continental crust, coupled with the availability of fresh basaltic glasses, make ridges a prime location for assessing the petrogenesis of basaltic lavas. Petrogenetic insights can then shed light on the mantle being melted – in terms of both composition and process.

Over four decades of study on ridges have led to immense strides in our understanding. It has been shown, for example, that geochemical indicators of extent of melting relate to the crustal thickness of ridges in a fairly straightforward way. As ocean crust is the product of mantle melting, thicker crust indicates larger extents of melting. This thicker crust will also be at higher elevations (shallower depth) due to isostatic compensation. Incompatible elements in the mantle such as Na or Ti decrease in concentration as the extent of melting increases. Taken together, the first-order prediction is that shallow regions of the ridge system (thicker crust) will have lower Na and Ti concentrations (after correction for the effects of crystal fractionation) than deeper regions of the ridge system. Observations largely agree with these predictions; quantitative models of variable mantle temperature (Klein and Langmuir, 1987; Langmuir et al., 1992) have been able to successfully account for the composition and thickness of the ocean crust, and for the observed variation in ridge depths.

This model has been seriously challenged (Shen and Forsyth, 1995; Niu and O'Hara, 2008; Kimura and Sano, 2012) on various grounds. These challenges stem from the

recognition that there are many other factors that could affect the relationship between crustal thickness and basalt geochemistry, including variable melt extraction processes, mantle source heterogeneity, and the impact of volatiles on the melting process. One aim of this thesis is to assess these various hypotheses in the context of the vastly increased global data that is now available.

Other developments in our description of ocean ridges are the extensive studies of ridge segmentation. Ridges are known to be segmented on a variety of length scales – from 'first-order' transform faults, to 'second-order' non-transform offsets, to even 'fourth-order' discontinuities where there is a discrete change in chemistry with very small offsets in the ridge axis (Macdonald et al., 1991; Langmuir et al., 1986). At times large transform faults appear to be boundaries between discrete mantle compositional domains (Schilling et al., 1982; Langmuir and Bender, 1984), perhaps most strikingly at the Australian-Antarctic Discordance (Klein et al., 1988).

The existence of transform offsets at the edges of many ridge segments juxtaposes cold, millions-of-years old lithosphere up against the zero-age spreading axis. This cold, old lithosphere cools and thickens the young lithosphere at the end of ridge segments, with probable effects on the petrogenesis of basalt lavas. One effect is that lavas erupted near transform faults tend to be more differentiated (Thompson and Melson, 1972; Schilling and Sigurdsson, 1979; Natland and Melson, 1980; Lawson et al., 1996). Some have suggested that the thicker lithosphere at segment ends shortens the melting column, resulting in lower extents of melting caused by the "transform fault effect" (Bender et al., 1984; Langmuir and Bender, 1984; Morgan and Forsyth, 1988; Ghose et al., 1996). Still others have suggested that the thicker lithosphere at segment edges acts as an impermeable, sloping boundary along which melts can be focused toward the center of the segments (Sparks and Parmentier, 1991; Spiegelman, 1993; Magde and Sparks, 1997). Greater extents of melting at segment centers or enhanced melt focusing, or both, help to explain another first-order observable of the structure of slower-spreading ridge segments: crustal thickness increases toward the center of segments (Kuo and Forsyth, 1988).

Uncertainty remains about the mode of crustal accretion, especially at slow-spreading ridges. Some authors, based on observations of eruptions at Iceland and Hawaii, suggest that ridge segments erupt magma from a central pipe, with subsequent lateral diking to the edges to generate the ocean crust (e.g., Parfitt, 1991; Gudmundsson, 1998). Still others argue, on the basis of geochemistry, that ridge segments cannot be solely centrally fed and instead contain discrete sources of magma erupting along the length of the segments (Langmuir et al., 1977; Langmuir et al., 1986; Niu and Batiza, 1994).

Adding more complexity to considerations of crustal accretion and ridge dynamics is the existence of mantle plumes with varying proximity to ridges. Such regions of plume-ridge interaction, such as Iceland, the Azores and Galapagos have been studied in detail by Jean-Guy Schilling and coauthors (e.g., Schilling, 1975; Schilling et al., 1983; Schilling, 1985). They showed that ridge depth, concentrations of highly incompatible elements and radiogenic isotopic ratios often change progressively along the ridge with distance from the plume. This led to the suggestion of "plume" mantle and "depleted" mantle mixing in various proportions to generate the geochemical gradient seen along ridges near plumes.

The suggestion of geochemical gradients near plumes ties nicely into questions of crustal accretion (at least at slow-spreading rates), as there are differing predictions for magma compositions along segments near plumes if they are centrally or multiply supplied. A centrally supplied segment, even within a plume-ridge geochemical gradient, should erupt fairly homogeneous magmas that show no progressive change with distance along the segment. Instead, a segment that has multiple sites of magma delivery would likely show progressive geochemical enrichment in the direction of the enriched plume.

While these are readily testable predictions, early studies were largely reconnaissance studies with only one or two dredge locations per ridge segment. There were simply not enough samples per segment to properly test if observable compositional gradients existed in erupted basalts from a given segment. We aim to rectify this in Chapters 2 and 3, which present the results of detailed analyses of many samples from four segments directly south of the Azores plume: Menez Gwen, Lucky Strike, North Famous and FAMOUS.

Chapter 2 focuses on Menez Gwen and Lucky Strike, the segments closest to the

Azores. We find that all basalts from the southerly Lucky Strike and northerly Menez Gwen segments (37-38.2°N Mid-Atlantic Ridge) are enriched relative to depleted MORB, consistent with the influence of the Azores hot spot, but there is much complexity in detail. Each segment contains two groups of chemically distinct basalts. Moderately enriched basalts are found throughout the segments. At the segment centers, highly enriched basalts with high concentrations of the incompatible elements and an enriched isotopic signature predominate, although less enriched basalts are also present. The highly enriched basalts from both segments have similar major element and highly incompatible element concentrations and ratios. Remarkably, incompatible element ratios (e.g. K2O/TiO2, Ba/La, Nb/Zr) of these basalts can be higher than basalts from the center of the Azores platform, while their isotopic values are less enriched.

This dichotomy between trace element ratios and isotopes of the highly enriched samples is explained with a model that adds a low-degree melt in the garnet field of an Azores source to a mantle depleted by previous melt removal. Subsequent melting of this recently 'metasomatized' mantle, without garnet in the residue, produces lavas that match quantitatively the composition of the enriched samples in major elements, trace elements and isotopes.

Apart from the highly enriched basalts, a regional gradient towards the Azores is reflected in moderately incompatible element ratios (e.g. Zr/Y), incompatible element concentrations and isotopes, as Menez Gwen samples are all more enriched than those from Lucky Strike. Highly incompatible element ratios at Lucky Strike, however, can be more enriched than Menez Gwen, even though Menez Gwen is closer to the Azores. This may result because these Lucky Strike samples possess more of the "low-F" signature. Our results show that the Azores gradient is not simple two-component mixing, but reflects an important contribution from a low degree melt transfer process likely occurring as mantle plume material melts and flows southward along the ridge.

With respect to segmentation models, central supply is supported by a step function in Pb isotopes across the offset between the two segments. Moderately incompatible element ratios, however, show a within-segment gradient for the less enriched basalts.

The enhanced crustal thickness and volcanic constructions at the segment centers require physical delivery of most of the magma to the center of the segment.

In Chapter 3, we report in detail on the North Famous and FAMOUS segments to the south of Lucky Strike and Menez Gwen. The FAMOUS segment was one of the first sites of ocean ridge research in the early-1970's and is one of the best-sampled (and studied) ridge segments in the world. Most studies, however, took place prior to the advent of modern ICP-MS technology, and did not encompass samples from both the French and American collections. A comprehensive investigation of samples along the entire length of the FAMOUS segment, coupled with a recent extensive melt inclusion study by Laubier et al. (2012), shows enormous trace element diversity within a single segment. We confirm multiple supply of magmas along the length of the segment and the ability of melting processes to deliver highly diverse melts over short distances and times.

The origin of the diversity observed at FAMOUS involves mantle heterogeneity, different extents of melting, magma mixing and crustal interaction. The mantle heterogeneity can be modeled as mixtures between enriched and depleted sources, but the enriched end member has a composition distinct from the Azores plume. For the segments investigated, nearly all basalts have highly incompatible trace element ratios (e.g., Th/La, Nb/La) as high or higher than the most plume-influenced MORB near the Azores hotspot, despite being over 300 km farther south and much less enriched isotopically. Mixing between plume and depleted mantle sources does not produce these characteristics. To account for the elevated highly incompatible trace element ratios of these lavas, a metasomatic component formed by adding deep, low-degree melts of Azores plume material to a depleted mantle is required. This metasomatized source is the same that produces the highly enriched basalts seen further north at Menez Gwen and Lucky Strike.

The regional gradient in geochemistry is also not systematic with distance from the Azores, as N. Famous lavas are geographically closer to the Azores and yet are more depleted in trace elements and isotopes than FAMOUS lavas. This suggests that the delivery of the enriched component to individual segments is influenced by other factors such as segment size and offset in addition to distance from the plume.

As seen in Chapters 2 and 3, certain questions require a very detailed, local-scale perspective. Still others, however, require just the opposite – a broad global view. Such questions, including whether mantle temperature or composition exerts the dominant influence on erupted basalt compositions, whether there are systematic compositional differences among ridges from different spreading rates or from different ocean basins, or the extent to which crystal fractionation or melt-rock reaction modify the observed basalt compositions, require knowledge of the mean composition of global ridge basalts. Chapters 4 and 5 address the composition of ocean ridge basalts from a global perspective.

Chapter 4 presents the mean composition of ocean ridge basalts using a scrupulously compiled dataset of major and trace elements and isotopes. This dataset combines new and literature data, and is released in the electronic appendix. A global catalog of 771 ridge segments including mean depth, length and spreading rate enables calculation of "segment values" for each segment. Segment values counteract the effects of uneven sampling and allow means to be weighted by segment length and spreading rate. A bootstrapping statistical technique provides rigorous error estimates for the new mean compositions. Based on the characteristics of the data we propose a new classification of MORB, with All-MORB reflecting the total composition of the crust, N-MORB the most likely basalt composition encountered along the ridge >500 km from hot spots, and D-MORB the depleted end member. All-MORB and N-MORB are substantially more enriched than early estimates of normal ridge basalts.

We show that important differences among ocean basins exist, including the effect of enriched/plume material on Atlantic compared to Pacific MORB. The back-arc mean requires higher extents of melting and greater concentrations of fluid-mobile elements, reflecting the influence of water on back-arc petrogenesis. The global MORB averages also shed light on fundamental questions including the K/U and Sm/Nd ratios of the upper mantle. The K/U ratio reported in Chapter 4 is lower than the recent estimate of Arevalo and McDonough (2010), with implications for Earth's heat budget. In addition, the low Sm/Nd and 143Nd/144Nd ratio of All-MORB poses serious difficulties for the suggestions that Earth has a non-chondritic primitive mantle (e.g., Jackson and Carlson,

2011).

In Chapter 5, we present major element data that have been carefully corrected for crystal fractionation. This enables the assessment of global variations in magma compositions that are independent of crystallization and instead relate to extent of melting differences, mantle compositional differences and/or differences in crustal processing. We show, in keeping with the earlier results of Klein and Langmuir (1987) and Langmuir et al. (1992), that the corrected "8" values vary systematically with ridge depth, and with each other. This study expands the scope of the earlier studies by correcting Al, Ca and Si for the effects of fractionation in addition to Fe and Na. The observed variations are consistent with mantle temperature (extent of melting) differences being the dominant influence on global MORB major element compositions.

Important second-order processes can also be seen in the data, including source heterogeneity and lithospheric effects. Ridges near plumes, for example, have elevated Na relative to the predicted Na based on the global correlation between Na8 and ridge depth. This is likely caused by an enriched mantle source near plumes. We also show that ultra-slow spreading ridges are offset to lower Si and Ca, and higher Na and Al, relative to ridges from faster spreading rates. These effects are probably related to the thicker 'lithospheric lid' at ultra-slow spreading ridges, which can lead changes in the melting process and crystallization sequence.

The combination of our detailed segment-scale perspective in Chapters 2 and 3 with the global-scale perspective in Chapters 4 and 5 provides a new perspective on ridge basalts. In detail, mantle source and melting effects, coupled with the effects of crustal processing, are all shown to affect basalt compositions on a scale of ~40 km. We also show that plume-ridge interaction, at least near the Azores, leads to an intricate series of melting and metasomatic processes that give rise to the observed ridge basalt compositions. In remarkable contrast, at the global scale the complicated systematics observed at the local scale diminish, with rather straightforward systematics (in major element compositions) emerging.

References

Arevalo, R., and W. F. McDonough (2010), Chemical variations and regional diversity observed in MORB, Chemical Geology, 271(1-2), 70-85.

Bender, J. F., C. H. Langmuir, and G. N. Hanson (1984), Petrogenesis of basalt glasses from the Tamayo Region, East Pacific Rise, Journal of Petrology 25(1), 213-254.

Ghose, I., M. Cannat, and M. Seyler (1996), Transform fault effect on mantle melting in the MARK area (Mid-Atlantic Ridge south of the Kane transform), Geology, 24(12), 1139-1142.

Gudmundsson, A. (1998), Magma chambers modeled as cavities explain the formation of rift zone central volcanoes and their eruption and intrusion statistics, Journal of Geophysical Research-Solid Earth, 103(B4), 7401-7412.

Jackson, M. G., and R. W. Carlson (2011), An ancient recipe for flood-basalt genesis, Nature, 476(7360), 316-U377.

Kimura, J.-I., and S. Sano (2012), Reactive Melt Flow as the Origin of Residual Mantle Lithologies and Basalt Chemistries in Mid-Ocean Ridges: Implications from the Red Hills Peridotite, New Zealand, Journal of Petrology.

Klein, E. M., and C. H. Langmuir (1987), Global correlations of ocean ridge basalt chemistry with axial depth and crustal thickness, Journal of Geophysical Research 92(B8), 8089-8115.

Klein, E. M., C. H. Langmuir, A. Zindler, H. Staudigel, and B. Hamelin (1988), Isotope evidence of a mantle convection boundary at the Australian-Antarctic Discordance, Nature, 333(6174), 623-629.

Kuo, B.-Y., and D. W. Forsyth (1988), Gravity anomalies of the ridge-transform system in the South Atlantic between 31 and 34.5°S: upwelling centers and variations in crustal thickness, MGR 10, 205-232.

Langmuir, C. H., and J. F. Bender (1984), The geochemistry of oceanic basalts in the vicinity of transform faults : observations and implications, Earth and Planetary Science Letters 69, 107-127.

Langmuir, C. H., J. F. Bender, and R. Batiza (1986), Petrological and tectonic segmentation of the East Pacific Rise, 5-degrees 30-minutes — 14-degrees 30-minutes North, Nature, 322(6078), 422-429.

Langmuir, C. H., E. M. Klein, and T. Plank (1992), Petrological systematics of midocean ridge basalts - Constraints on melt generation beneath ocean ridges, in Mantle Flow and Melt Generation at Mid-Ocean Ridges, edited by J. P. Morgan, pp. 183-280.

Langmuir, C. H., J. F. Bender, A. E. Bence, G. N. Hanson, and S. R. Taylor (1977), Petrogenesis of Basalts from the FAMOUS Area - Mid-Alantic Ridge, Earth and Planetary Science Letters, 36(1), 133-156.

Laubier, M., A. Gale, and C. H. Langmuir (2012), Melting and Crustal Processes at the FAMOUS Segment (Mid-Atlantic Ridge): New Insights from Olivine-hosted Melt Inclusions from Multiple Samples, Journal of Petrology, 53(4), 665-698.

Lawson, K., R. C. Searle, J. A. Pearce, P. Browning, and P. Kempton (1996), Detailed volcanic geology of the MARNOK area, Mid-Atlantic Ridge north of Kane transform, in Tectonic, magmatic, hydrothermal and biological segmentation of mid-ocean ridges edited by C. J. MacLeod, P. Tyler and C. L. Walker, pp. 61-102, Geological Society Special Publication.

Macdonald, K. C., D. S. Scheirer, and S. M. Carbotte (1991), Midocean ridges - discontinuities, segments and giant cracks, Science, 253(5023), 986-994.

Magde, L. S., and D. W. Sparks (1997), Three-dimensional mantle upwelling, melt generation, and melt migration beneath segment slow spreading ridges, Journal of Geophysical Research-Solid Earth, 102(B9), 20571-20583.

Morgan, J. P., and D. W. Forsyth (1988), 3-dimensional flow and temperature perturbations due to a transform offset - effects on oceanic crustal and upper mantle structure, Journal of Geophysical Research-Solid Earth and Planets, 93(B4), 2955-2966.

Natland, J. H., and W. G. Melson (1980), Composition of basaltic glasses from the east Pacific Rise and Siqueiros Fracture Zone near 9° N, In Rep DSDP 54, 705-723.

Niu, Y., and R. Batiza (1994), Magmatic processes at a slow-spreading ridge segment: 26S Mid-Atlantic Ridge, Journal of Geophysical Research

Niu, Y. L., and M. J. O'Hara (2008), Global correlations of ocean ridge basalt chemistry with axial depth: A new perspective, Journal of Petrology, 49(4), 633-664.

Parfitt, E. A. (1991), The role of rift-zone storage in controlling the site and timing of eruptions and intrusions of Kilauea volcano, Hawaii, Journal of Geophysical Research-Solid Earth and Planets, 96(B6), 10101-10112.

Schilling, J. G. (1975), Azores mantle blob - rare-Earth evidence, Earth and Planetary Science Letters, 25(2), 103-115.

Schilling, J. G. (1985), Upper mantle heterogeneities and dynamics, Nature, 314(6006), 62-67.

Schilling, J. G., and H. Sigurdsson (1979), Thermal Minima Along the Axis of the Mid-Atlantic Ridge, Nature, 282(5737), 370-375.

Schilling, J. G., R. H. Kingsley, and J. D. Devine (1982), Galapagos Hot Spot-spreading Center System .1. Spatial Petrological and Geochemical Variations (83-degrees-w-101-degrees-w), Journal of Geophysical Research, 87(NB7), 5593-5610.

Schilling, J. G., M. Zajac, R. Evans, T. Johnston, W. White, J. D. Devine, and R. Kingsley (1983), Petrologic and geochemical variations along the Mid-Atlantic Ridge from 29-degrees-N to 73-degrees-N, Am. J. Sci., 283(6), 510-586.

Shen, Y., and D. W. Forsyth (1995), Geochemical constraints on initial and final depths of melting beneath midocean ridges, Journal of Geophysical Research-Solid Earth, 100(B2), 2211-2237.

Sparks, D. W., and E. M. Parmentier (1991), Melt Extraction from the Mantle Beneath Spreading Centers, Earth and Planetary Science Letters, 105(4), 368-377.

Spiegelman, M. (1993), Physics of melt extraction - theory, implications and applications, Philosophical Transactions of the Royal Society of London Series a-Mathematical Physical and Engineering Sciences, 342(1663), 23-41.

Thompson, G., and W. G. Melson (1972), The petrology of oceanic crust across fracture zones in the Atlantic Ocean: evidence of a new kind of sea-floor spreading, The Journal of Geology, 80, 526-538.

Chapter 2

Enriched Basalts at Segment Centers: The Lucky Strike (37° 17' N) and Menez Gwen (37° 50' N) Segments of the Mid-Atlantic Ridge

2.1. Introduction

Classical work by Schilling (1975) established a gradient in ridge depth and chemical compositions of basalts extending southwards from the Azores hot spot. Basalts near the hot spot were more enriched in highly incompatible elements and $^{87}Sr/^{86}Sr$ (White and Schilling, 1978), and this enrichment lessened southwards until depleted MORB were encountered south of the Hayes fracture zone near 34°N.

As maps of ocean ridges grew more detailed, it became clear that the concept of "gradient" needed refinement. Ocean ridges consist of a series of ridge segments defined by transform faults and other offsets (Macdonald et al., 1991). Segments tend to be shallow in their central regions and deeper at their ends, so the "regional gradient" in depth south of the Azores consists of a series of undulations at various scales (see Detrick et al. (1995)). The question then arises how the "regional gradient" in geochemistry is influenced by segmentation. Is the gradient regular, or is it undulating like the depth, or does it have other characteristics? In order to fully grasp the mechanisms involved in the creation of ocean crust and the distribution of mantle plume influence, the effects of segmentation on regional gradients need to be better understood.

The gradients around plumes also provide a natural laboratory to explore the relationships between ridge segmentation and magma supply. Two end-member models

An amended version of this chapter was published with Stéphane Escrig, Elizabeth J. Gier, Charles H. Langmuir and Steven L. Goldstein in Geophysics, Geochemistry, Geosystems, vol. 12, 26 pp., 2011.

for the formation of segments are “multiple supply” and “central supply.” Multiple supply (e.g., Bender et al., 1984; Langmuir et al., 1986; Langmuir et al., 1977) calls on vertical upwelling of magma from the mantle to the crust, with volcanic eruptions sourced along the entire length of a ridge segment. Melt compositions then reflect the composition of the mantle and the extent of melting as it varies (or not) along the segment. Central supply (e.g., Schouten et al., 1985) equates ridge segments with central volcanoes, akin to Hawaii, with a single central pipe as the source of dike-fed eruptions that fill the entire segment. The “multiple supply” model also allows for greater extents of volcanism at segment centers compared to segment ends, but nonetheless calls upon distributed magmatism along the length of the segment rather than a point source injection.

These two views of ocean ridge magmatism have a long history. Central injection is supported by detailed studies of volcanoes on rift zones of Hawaii and Iceland (Parfitt, 1991; Gudmundsson, 1998), by the recent evidence for lengthy dike propagation on the Juan de Fuca ridge (Embley et al., 1995; Fox et al., 1995) and by the ubiquity of dikes as a fundamental feature of the ocean crust (Curewitz and Karson, 1998). Michael et al. (1989) noted geochemical distributions along strike that suggested lateral injection of magma from central segment highs toward segment edges along the Explorer Ridge. Central injection has also been inferred from recent seismic studies (Hooft, 2000; Magde et al., 2000), from geophysical modeling (Magde and Sparks, 1997), and from systematic variations in magma temperature with distance from segment centers (Thompson and Melson, 1972; Schilling and Sigurdsson, 1979; Natland and Melson, 1980; Lawson et al., 1996). The common occurrence of mantle Bouguer anomaly (MBA) lows at the centers of ridge segments implies greater crustal thickness and hence preferential emplacement of magma to the segment center (e.g., Kuo and Forsyth, 1988).

Multiple injection also has convincing evidence. Geochemical studies of basalts from the FAMOUS area (Langmuir et al., 1977; White and Bryan, 1977; LeRoex et al., 1981) showed that individual cones in the middle of the rift valley represent discrete melts from the mantle. Bender et al. (1984) suggested a “transform fault effect” of lower extents of melting at segment ends as compared to segment centers, subsequently supported

by modeling of mantle flow (Phipps Morgan and Forsyth, 1988). Variations in degree of melting systematically distributed within a segment require multiple supply. A study by Niu and Batiza (1994) supported the inference of systematic segment scale changes in extent of melting, requiring vertical transport of different melts to crustal levels. In their study of basalts from the MARK area south of the Kane fracture zone, Reynolds and Langmuir (1997) argued that melts from the segment edges are independent of those from the segment center. These lines of evidence support multiple supply of magma along strike, which in turn requires limited focusing. Of course it is likely that no single model applies to all segments. Some may be centrally and others multiply supplied, and these characteristics may vary with time.

Segmentation within a regional gradient provides opportunities to address these models. Multiple supply would be necessary if geochemical gradients were present within the segments. Central supply would be implicated by more homogeneous parental magmas within segments, and a step function in chemistry between segments. Variable magmas could still exist in a centrally supplied segment, but the variation would not be systematically distributed along-strike.

In this paper we address these issues with a detailed petrological study of the Lucky Strike and Menez Gwen segments on the Mid-Atlantic Ridge (MAR; Figure 2.1). These segments are within the geochemical and bathymetric gradient just south of the main Azores platform and have been well sampled along most of their length. Several active seismic and refraction studies at Lucky Strike provide important physical constraints (e.g., Singh et al., 2006; Combier, 2007; Seher et al., 2010). To better place the data in the context of the regional gradient in composition, we also report data for samples from the nearby 'plume' segments KP-2 and 3 on the Azores platform that had limited existing ICP-MS trace element data (see Figure 2.1; segment nomenclature from Detrick et al. (1995)).

2.2. Regional Setting

The Menez Gwen (KP-5) and Lucky Strike (PO-1) segments are the second and third segments south of the bathymetric summit that occurs adjacent to the Azores islands

near 39°N (Figure 2.1). The segments are separated by the Pico transform fault.

The Lucky Strike segment (Figure 2.1) is 65 km long and rectangular (11-12 km wide) with a mean depth of ~2580m. One of the largest seamounts along the MAR is found in the center of the segment, rising to 1660m depth. Several ridges extend from the seamount toward the north and south (Langmuir et al., 1997; Parson, 2000), suggesting dike-fed fissure systems. The seamount summit is filled by young lava flows that overlie older lavas that make up the main edifice (Fouquet et al., 1995), and is the site of the Lucky Strike hydrothermal field (Langmuir et al., 1997). A large negative MBA near the central part of the segment (Detrick et al., 1995) is consistent with thicker crust at the segment center (~6 km) than the segment ends (~4 km). An axial magma chamber (AMC) has been seismically detected 3.4 km beneath the central volcano, extending for

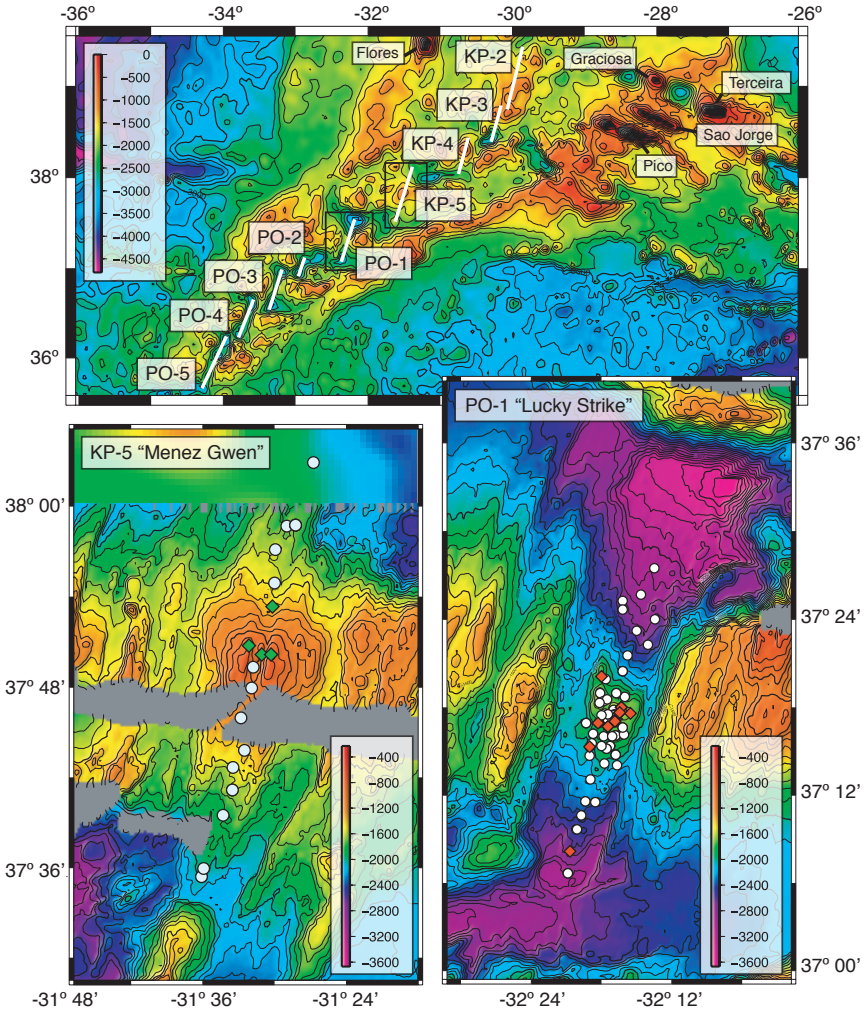

Figure 2.1: Bathymetric map of the northern Mid-Atlantic Ridge, with detailed maps of the Lucky Strike (PO-1) and Menez Gwen (KP-5) segments showing the location of samples in this study. Labeled segments (indicated by white lines in regional map) follow the nomenclature of Detrick et al. (1995). Note that in both segments nearly all enriched samples (shown in diamonds) are near the central volcanic edifice. A multibeam bathymetry grid (300m spacing) (Cannat et al., 1999; Escartin et al., 2001) was used for the detailed maps. Global multi-resolution bathymetry as compiled by Ryan et al. (2009) was used for the regional map (bathymetry in meters).

~6 km along-axis (Singh et al., 2006; Combier, 2007). Recent microseismic experiments indicate that the brittle lithosphere thickens from ~6.5 km at the segment center to more than 10 km at the segment ends (Dusunur et al., 2009).

The Menez Gwen segment, just north of Lucky Strike (Figure 2.1), has a length of 64 km with a central bathymetric high that also hosts high-temperature hydrothermal activity (Fouquet et al., 1995). It is shallower than Lucky Strike overall (mean depth of ~1620m), with a large volcanic edifice that occupies most of the segment length (Ondreas et al., 1997). These characteristics are consistent with its closer proximity to the main Azores platform. Young lava flows have been seen during dives within the graben at the volcanic summit (Ondreas et al., 1997).

2.3. Sampling and Analytical Techniques

The samples were collected by dredges, wax-rock cores and by the submersible Alvin during cruises AII127, AII129-6 and K145-19. In both segments, the highest density sampling occurred near the central region containing the hydrothermal vent (Figure 2.1). Nearly all of the samples studied were basaltic glass, but aphyric rocks were analyzed when glass was unavailable. Unaltered pieces of rock and glass chips for chemical analyses were hand-picked under a microscope and cleaned ultrasonically in methanol for 20 minutes.

Major elements were measured using a Cameca SX100 electron microprobe (EMP) at the American Museum of Natural History. A defocused beam resulting in an 8-10μm spot size was used. The samples were analyzed at 15kV using two different running conditions. First, to minimize volatilization of K_2O and Na_2O, a low beam current of 5nA with an 80 second (s) count time was used. The beam current was then increased to 20nA with a 30s count time for SiO_2, CaO, MgO, FeO and a 60s count time for Al_2O_3, TiO2, MnO, and P_2O_5. Each probe mount disk included an internal monitor standard, JDF-D2. This internal glass standard was analyzed (5 analytical spots) after every 25 analytical spots to monitor instrumental drift over time. Individual analyses reported in the Appendix are averages of 5 analytical spots normalized to JDF-D2, for which values are also reported. Analytical uncertainties were obtained from replicate measurements of JDF-D2. The precision (2σ

RSD) for SiO_2, TiO_2, Al_2O_3, MgO, FeO and CaO is better than 2%. The precision for K_2O and Na_2O is ~6%, and for MnO and P_2O_5 ~10%.

Trace elements were measured by solution nebulized and laser ablation inductively coupled mass spectrometry (SN-ICP-MS and LA-ICP-MS) at Lamont-Doherty Earth Observatory (LDEO) and by SN-ICP-MS at Harvard University (Selected results in Table 2.1; full results in Appendix). Due to detection limits, different sets of elements are reported for each method and institution. For SN-ICP-MS, 50mg of hand-picked rock or glass chips were digested in an HF:HNO_3 mixture. Two dilutions were run (1:2K and 1:10K) at LDEO and one dilution was run at Harvard (1:5K) using a matrix solution of 0.2N HNO_3 with Ge (10 ppb), In (3 ppb), Tm (3ppb) and Bi (3ppb) as internal standards for drift correction. Measurements were obtained on a VG Plasma Quad2+ at LDEO and on a Thermo X-series quadripole at Harvard. Standard powders BHVO-2, DNC-1, JB-2 and W-2 as well as two in-house standards (powdered MAR and hand-picked glass chips of VE-32) were used to generate calibration curves (standard values in the Appendix). To ensure consistency between laboratories, certain samples were analyzed at both LDEO and Harvard (duplicates shown in Table 2.1).

LA-ICP-MS analyses were performed on the same mounts used for the electron microprobe analyses using a Merchantech EXCIMER LASER (193nm wavelength) connected to the VG Plasma Quad2+. This technique was useful for samples with limited glass or rock available. A 90-100μm spot size was used with settings of 23-25kv, resulting in energies of ~100mJ. The ablation cell was flushed with a helium carrier gas using a flow rate of ~0.8 l/min. The precision for trace elements measured in this study is better than 5% for all elements except for U, Th and Pb measured at LDEO (both LA and SN) with precisions of 10% or better (2σ).

For isotopes, the hand-picked rock and glass chips were leached for 20 minutes with 8N HNO_3 and then rinsed with quartz-distilled water. Samples were digested using a HF:HNO_3 mixture in Teflon beakers. The Sr, Nd and Pb isotopes were measured from a single digestion that was run through progressive columns to isolate the element of interest. For samples with limited material, Sr and Nd or only Sr isotopes were determined. The isotopes

Table 2.1: Representative ICP-MS Analyses of Trace Element Concentrations of Glassy Basalts From Segments KP-3,5 and PO-1[a]

Detrick Segment	Sample Name	Group Name	Latitude	Longitude	TE Ref	Li	Be	Sc	Ti	V	Cr	Mn	Co	Ni	Cu	Zn	Ga
KP-5	AII0127-1-017-005	Enriched	37.836	-31.518	Harvard	3.9	0.60	44.5	1.30	256	390	0.15	41.5	112	90	65.5	15.2
KP-5	AII0127-1-017-003(A)	Enriched	37.836	-31.518	Harvard	3.7	0.65	39.9	1.30	237	346	0.14	38.4	100	86	62.0	14.9
KP-5	AII0127-1-R048	Enriched	37.889	-31.503	Harvard	3.9	0.65	39.5	1.30	240	374	0.15	38.6	100	84	63.3	14.9
KP-5	AII0127-1-R046	Transitional	37.711	-31.558	Harvard	5.8	0.49	42.0	1.33	303	56	0.19	44.2	43	79	91.3	16.9
KP-5	AII0127-1-018-001	Transitional	37.979	-31.471	Harvard	4.2	0.35	47.2	0.95	254	109	0.17	45.6	72	100	68.8	14.8
KP-5	AII0127-2-034-002	Transitional	37.590	-31.602	Harvard	5.3	0.46	43.1	1.16	287	66	0.17	43.2	51	82	77.6	15.7
KP-5	AII0127-2-033-002	Transitional	38.048	-31.446	Harvard	5.4	0.43	41.8	1.13	273	65	0.18	45.0	52	97	80.8	15.9
PO-1	AII0129-6 2604-3	Enriched	37.296	-32.272	LDEO			42.4		249	430			118	87	63.0	
PO-1	AII0127-1-R041	Enriched	37.284	-32.281	Harvard	4.6	0.54	42.8	1.34	258	491	0.16	41.3	95	83	71.0	15.4
PO-1	AII0127-2-R116-002	Enriched	37.278	-32.291	Harvard	4.2	0.56	42.4	1.22	235	848	0.15	40.2	114	90	70.2	14.9
PO-1	AII0129-6-002-001	Transitional	37.285	-32.281	Harvard	4.8	0.36	42.3	1.07	273	77	0.18	46.2	63	77	80.0	15.8
PO-1	AII0127-2-R108-001	Transitional	37.316	-32.279	Harvard	4.4	0.31	42.9	0.95	258	100	0.16	45.4	68	88	71.5	15.1
PO-1	AII0127-1-015-001	Transitional	37.291	-32.283	Harvard	4.8	0.35	39.8	0.99	253	74	0.17	44.0	60	73	75.0	15.1
PO-1	AII0127-2-037	Transitional	37.256	-32.300	Harvard	4.3	0.34	42.1	0.94	238	284	0.16	43.2	89	88	66.9	14.6
KP-3	AII0127-1-021-003	n/a	38.491	-30.265	Harvard	6.1	1.40	28.5	2.08	258	75		33.6	48	72	88.8	18.3
	AII0127-1-021-003 Duplicate	n/a	38.491	-30.265	LDEO												
KP-5	AII0127-1-017-005	Enriched	37.836	-31.518	Harvard	3.9	0.60	44.5	1.30	256	390		41.5	112	90	65.5	15.2
	AII0127-1-017-005 Duplicate	Enriched	37.836	-31.518	LDEO								42.0	110	92	65.1	
PO-1	AII0127-2-036-020	Transitional	37.256	-32.288	Harvard	4.8	0.41	38.9	1.08	250	38		44.6	53	75	76.3	15.7
	AII0127-2-036-020 Duplicate	Transitional	37.256	-32.288	LDEO	4.5											

Table 2.1 (Continued)

Sample Name	Rb	Sr	Y	Zr	Nb	Mo	Sn	Cs	Ba	La	Ce	Pr	Nd	Sm	Eu	Gd	Tb	Dy	Ho	Er
AII0127-1-017-005	17.23	263	21.6	90.6	25.73	0.99	0.74	0.21	213.5	14.37	28.62	3.54	14.64	3.39	1.13	3.83	0.61	3.73	0.74	2.08
AII0127-1-017-003(A)	19.78	283	20.6	94.5	28.26	1.17	0.78	0.25	241.7	15.66	30.86	3.78	15.82	3.46	1.20	3.83	0.61	3.65	0.74	2.03
AII0127-1-R048	17.70	265	20.8	93.0	25.67	1.06	0.76	0.22	211.8	14.63	28.91	3.59	15.14	3.38	1.16	3.79	0.61	3.64	0.75	2.05
AII0127-1-R046	6.31	133	28.3	84.4	12.80	0.57	0.77	0.07	74.6	8.14	17.91	2.45	11.15	3.12	1.08	4.15	0.71	4.67	1.00	2.83
AII0127-1-018-001	5.37	141	21.4	60.6	9.95	0.42	0.52	0.06	65.8	6.14	13.34	1.80	8.25	2.29	0.83	3.07	0.53	3.50	0.74	2.13
AII0127-2-034-002	5.53	134	25.6	72.0	10.86	0.49	0.64	0.06	66.9	6.93	15.15	2.09	9.67	2.71	0.97	3.66	0.63	4.16	0.91	2.54
AII0127-2-033-002	5.12	123	24.7	68.5	9.89	0.49	0.64	0.05	61.8	6.19	13.71	1.90	8.89	2.56	0.93	3.48	0.61	4.05	0.88	2.48
AII0129-6 2604-3	16.27	291	22.9	88.6	34.28				282.3	17.40	32.90	3.84	15.28	3.40	1.18	3.64	0.60	3.61	0.78	2.09
AII0127-1-R041	11.22	196	24.8	86.8	20.30	0.85	0.77	0.13	143.6	10.78	22.09	2.84	12.20	3.13	1.06	3.90	0.65	4.22	0.86	2.43
AII0127-2-R116-002	12.21	217	21.8	81.5	20.85	1.00	0.70	0.14	160.1	11.46	23.11	2.91	12.21	3.02	1.01	3.56	0.59	3.74	0.75	2.11
AII0129-6-002-001	4.70	108	24.6	57.7	8.62	0.44	0.56	0.05	58.0	5.06	11.28	1.59	7.69	2.36	0.86	3.37	0.59	4.05	0.87	2.45
AII0127-2-R108-001	3.46	105	21.6	47.8	6.51	0.33	0.47	0.03	43.3	3.95	9.05	1.30	6.47	2.06	0.77	2.97	0.52	3.56	0.76	2.13
AII0127-1-015-001	4.54	100	23.4	56.4	8.11	0.43	0.52	0.05	56.5	4.91	10.84	1.53	7.45	2.26	0.84	3.22	0.57	3.82	0.83	2.36
AII0127-2-037	4.15	106	22.2	55.0	7.60	0.40	0.53	0.04	50.2	4.58	10.34	1.47	7.21	2.16	0.80	3.06	0.54	3.64	0.79	2.25
AII0127-1-021-003	23.76	373	28.2	191.3	36.76	1.54	1.50	0.24	263.6	23.30	49.12	6.08	25.45	5.50	1.76	5.76	0.90	5.12	1.01	2.70
AII0127-1-021-003 Duplicate	23.32	381	29.1	193.8	35.72	1.51		0.25	257.9	23.73	47.62	6.17	25.23	5.49	1.81	5.94	0.92	5.16	0.99	2.68
AII0127-1-017-005	17.23	263	21.6	90.6	25.73	0.99	0.74	0.21	213.5	14.37	28.62	3.54	14.64	3.39	1.13	3.83	0.61	3.73	0.74	2.08
AII0127-1-017-005 Duplicate	16.41	260	21.4	86.4	25.15			0.20	205.4	14.28	28.54	3.46	14.44	3.32	1.15	3.69	0.59	3.62	0.75	2.03
AII0127-2-036-020	4.87	115	22.6	61.3	9.09	0.47	0.62	0.05	60.4	5.35	11.98	1.69	8.03	2.39	0.88	3.28	0.57	3.75	0.80	2.26
AII0127-2-036-020 Duplicate	4.74	123	23.0	63.3	9.18	0.52			61.8	5.49	12.19	1.71	8.21	2.45	0.91	3.33	0.58	3.86	0.84	2.33

Table 2.1 (Continued)

Sample Name	Yb	Lu	Hf	Ta	W	Tl	Pb	Th	U
AII0127-1-017-005	1.94	0.31	2.17	1.42	0.37	0.016	0.80	1.81	0.51
AII0127-1-017-003(A)	1.92	0.29	2.23	1.53	0.40	0.018	0.88	1.95	0.56
AII0127-1-R048	1.94	0.30	2.21	1.41	0.36	0.018	0.85	1.76	0.51
AII0127-1-R046	2.78	0.44	2.17	0.92	0.17	0.010	0.57	0.85	0.27
AII0127-1-018-001	2.09	0.33	1.55	0.57	0.16	0.008	0.41	0.68	0.23
AII0127-2-034-002	2.54	0.39	1.85	0.69	0.15	0.011	0.44	0.74	0.35
AII0127-2-033-002	2.46	0.39	1.80	0.57	0.14	0.010	0.47	0.66	0.21
AII0129-6 2604-3	2.04	0.31	2.04	1.73				2.21	0.55
AII0127-1-R041	2.34	0.37	2.16	1.12	0.27	0.012	0.63	1.32	0.38
AII0127-2-R116-002	2.00	0.32	2.01	1.10	0.26	0.017	0.67	1.39	0.41
AII0129-6-002-001	2.45	0.38	1.59	0.50	0.12	0.006	0.39	0.55	0.16
AII0127-2-R108-001	2.11	0.33	1.35	0.38	0.10	0.005	0.32	0.42	0.12
AII0127-1-015-001	2.36	0.37	1.55	0.47	0.12	0.006	0.39	0.54	0.16
AII0127-2-037	2.25	0.35	1.49	0.44	0.15	0.006		0.49	0.17
AII0127-1-021-003	2.46	0.38	4.27	2.09	0.44	0.036	1.94	2.43	0.77
AII0127-1-021-003 Duplicate	2.49	0.40	4.31	2.08				2.52	0.73
AII0127-1-017-005	1.94	0.31	2.17	1.42	0.37	0.016	0.80	1.81	0.51
AII0127-1-017-005 Duplicate	1.95	0.29	2.05	1.36			0.85	1.68	0.47
AII0127-2-036-020	2.21	0.34	1.65	0.53	0.13	0.007	0.42	0.58	0.18
AII0127-2-036-020 Duplicate	2.25	0.34	1.69	0.56				0.60	0.18

[a]Concentrations in ppm except for Ti and Mn which are in wt. %.

were measured by TIMS on a VG Sector 54 multicollector at LDEO (Results in Table 2.2). Sr and Nd isotopes were measured in dynamic mode. Sr isotopic values were corrected to an $^{87}Sr/^{86}Sr$ value of 0.710235 for NBS 987. Our measured value for NBS 987 $^{87}Sr/^{86}Sr$ was 0.710255 (2×10^{-5} 2σ). The Nd analyses were corrected using the JNDi standard ($^{143}Nd/^{144}Nd = 0.512115$). The average measured value was 0.512096 (2.1×10^{-5} 2σ). The Pb isotope data were collected in static mode using a double spike method for calibration. Both the samples and the NBS-981 standard were spiked with a ^{204}Pb and ^{207}Pb mixture. The double spike corrected values for NBS 981 were $^{206}Pb/^{204}Pb = 16.937$ (3.5×10^{-3} 2σ), $^{207}Pb/^{204}Pb = 15.490$ (4.7×10^{-3} 2σ), and $^{208}Pb/^{204}Pb = 36.691$ (1.4×10^{-2} 2σ). The measured values were then corrected to the values reported by Todt (1996).

2.4. Results

We report 110 new major element analyses, 79 new trace element analyses and 27 new isotope analyses in this study (representative trace element analyses in Table 2.1; isotope analyses in Table 2.2; all analyses reported in the Appendix). 'New' analyses were mostly on new samples, but in certain cases were re-analyses (or supplementary analyses where only limited published trace element data existed) of previously measured samples. We

Table 2.2: Sr, Nd, and Pb Isotope Ratios of Samples from Lucky Strike Segment (PO-1)

Sample Name	Group Name	Latitude	Longitude	$^{87}Sr/^{86}Sr$	$^{143}Nd/^{144}Nd$	$^{206}Pb/^{204}Pb$	$^{207}Pb/^{204}Pb$	$^{208}Pb/^{204}Pb$
AII0129-6-R016	Transitional	37.161	-32.335	0.702892	0.513120	18.837	15.530	38.434
AII0127-1-015-001	Transitional	37.291	-32.283	0.702915	0.513126	18.856	15.530	38.430
AII0129-6-R005	Transitional	37.309	-32.292	0.702932	0.513115	18.929	15.538	38.501
AII0127-2-R105	Transitional	37.291	-32.300	0.702967	0.513129	18.946	15.549	38.551
AII0127-2-R107	Transitional	37.312	-32.267	0.702941	0.513113	18.812	15.533	38.419
AII0129-6 2602-3	Enriched	37.294	-32.274	0.703066	0.513022	19.224	15.569	38.757
AII0127-2-R108-001	Transitional	37.316	-32.279	0.702935	0.513127	18.967	15.549	38.567
AII0127-1-R041	Enriched	37.284	-32.281	0.703083	0.513081	19.243	15.574	38.784
AII0127-1-R040	Transitional	37.218	-32.316	0.702937	0.513112	18.975	15.581	38.585
AII0127-2-R103-001	Transitional	37.253	-32.293	0.702964	0.513140	18.878	15.539	38.479
AII0127-2-R113-001	Transitional	37.411	-32.270	0.702874	0.513172	18.807	15.528	38.409
AII0127-2-R110	Transitional	37.359	-32.263	0.703020	0.513122	18.910	15.539	38.492
AII0127-1-016-001	Transitional	37.458	-32.225	0.702925	0.513116	18.896	15.538	38.467
AII0127-2-R116-002	Enriched	37.278	-32.291	0.703098	0.513031	19.254	15.571	38.779
AII0127-2-R104	Transitional	37.267	-32.285	0.702910	0.513106			
AII0129-6 2604-3	Enriched	37.296	-32.272	0.703125	0.513021			
AII0127-2-038-004	Transitional	37.111	-32.348	0.702925	0.513118			
AII0127-2-036-020	Transitional	37.256	-32.288	0.702925	0.513131			
AII0129-6-003	Transitional	37.335	-32.289	0.703023	0.513141			
AII0127-2-R117-001	Transitional	37.236	-32.296	0.702888	0.513121			
AII0127-2-R112-001	Transitional	37.400	-32.224	0.703045	0.513139			
AII0127-2-035	Transitional	37.421	-32.270	0.702915	0.513117			
AII0127-2-R111-001	Transitional	37.371	-32.234	0.702989	0.513082			
AII0127-2-R109-001	Transitional	37.341	-32.270	0.702972	0.513126			
AII0129-6-002-001	Transitional	37.285	-32.281	0.702932				
AII0129-6 2602-5b	Enriched	37.300	-32.272	0.703145				
AII0127-1-R039	Enriched	37.136	-32.345	0.702941				

*Note: these isotopic data are from the thesis of Elizabeth Gier, published with permission in Gale et al. (2011).

report 65 new major element analyses complemented by 46 trace element analyses on samples from Lucky Strike. A selected subset (n=27) of samples was also analyzed for Sr, Nd and/or Pb isotopes. For the Menez Gwen segment we report 23 new major element analyses and 17 new trace element analyses. We also present 22 new major element analyses and 16 new trace element analyses from segments KP-2,3 on the Azores platform for comparative purposes. Isotopic data from Dosso et al. (1999) on many of the same Menez Gwen and KP-2,3 samples for which we have new major and trace element data supplement our isotopic analyses from Lucky Strike.

2.4.1. Major Elements

At the outset it is necessary to be clear about terminology for describing MORB compositions. The terms "enriched" and "depleted" have become common parlance in ocean ridge studies. Depleted MORB (N-MORB) have $La/Sm_N<1$, $K_2O/TiO_2<0.11$ and isotopic compositions reflecting long-term depletion in the more incompatible element (e.g., high $^{143}Nd/^{144}Nd$, low $^{87}Sr/^{86}Sr$, low $^{206}Pb/^{204}Pb$). Enriched MORB (E-MORB) are enriched in the highly incompatible elements (e.g., $La/Sm_N>2$, $K_2O/TiO_2>0.2$) and their isotope ratios also reveal less long-term depletion of the more incompatible element (e.g., low $^{143}Nd/^{144}Nd$, high $^{87}Sr/^{86}Sr$, high $^{206}Pb/^{204}Pb$). Transitional MORB (T-MORB) are intermediate between the two. Ultimately there is a continuity of compositions, so such names are arbitrary. In comparing samples, terms such as "more enriched" and "less enriched" are clear.

Chemical compositions of basalt samples from Lucky Strike and Menez Gwen are all enriched relative to N-MORB, but separate into two distinct groups in major elements (Figure 2.2). Both Lucky Strike and Menez Gwen contain a T-MORB group (hereafter referred to as "transitional") characterized by K_2O contents between 0.12-0.23 wt.%, TiO_2 from 0.89-1.01 wt.%, FeO between 8.74-9.31 wt.%, Al_2O_3 from 14.84-15.09 wt.% and SiO_2 ranging from 50.72-51.7 wt.% for MgO between 8.72-8.04 wt.%. These major element characteristics are very similar to most samples from the well-studied FAMOUS segment ~70km to the south (e.g., Bryan and Moore, 1977; Bryan, 1979; Melson et al., 2002). In contrast, Lucky Strike and Menez Gwen also contain a true E-MORB group (called "enriched"), distinguished by distinctly higher K_2O (0.58-0.67 wt.%), higher TiO_2 (1.22-

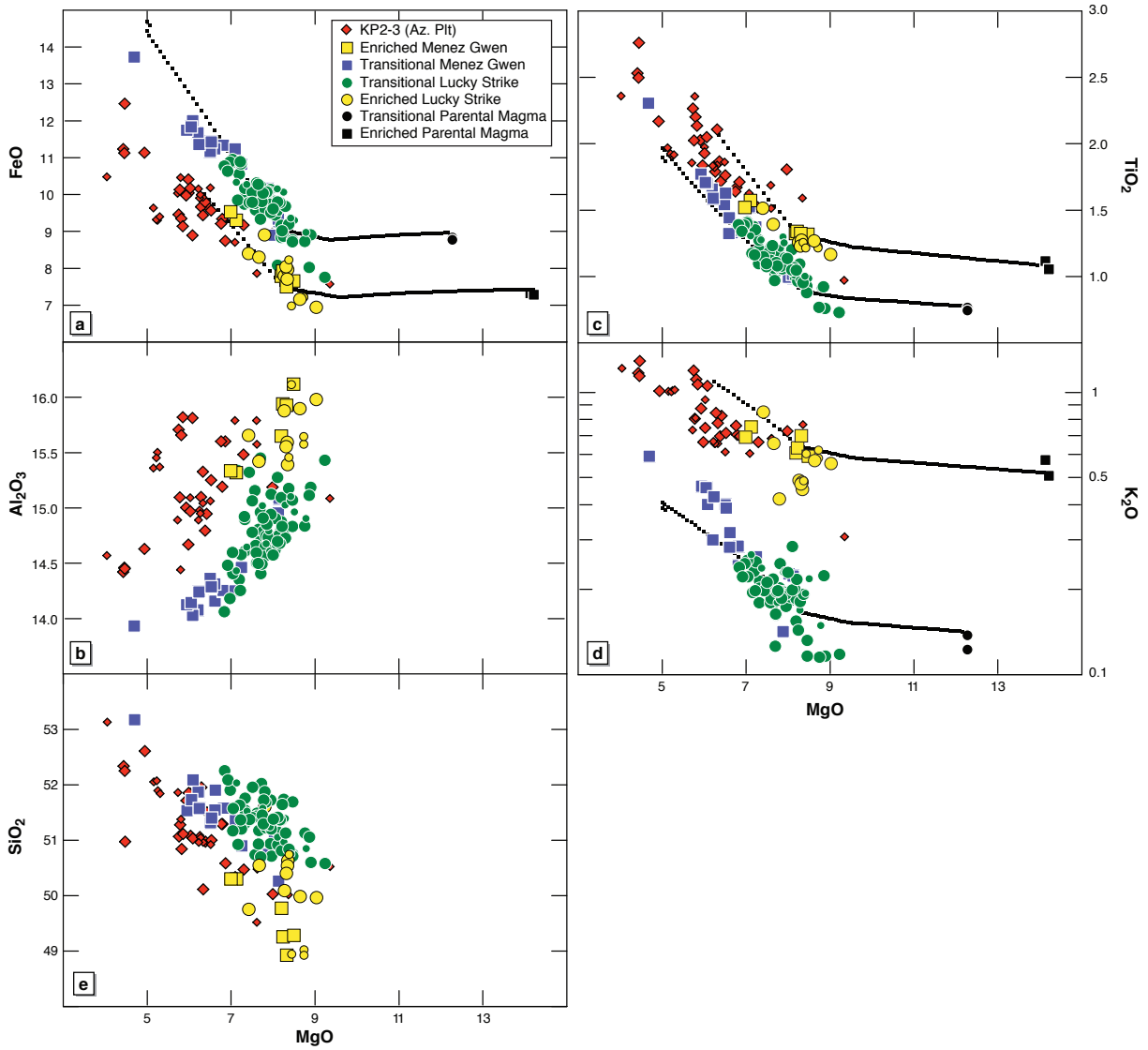

Figure 2.2: (a-e) FeO, Al_2O_3, TiO_2, K_2O and SiO_2 vs. MgO. Smaller symbols indicate data already published (Langmuir et al., 1997; Cooper et al., 2004). At both Menez Gwen and Lucky Strike, there are two distinct groups in major elements, an enriched group and a transitional group. Multiple parental magmas are required to explain the variability observed at a given MgO content (represented by the black squares (showing extent of melting (F) of 6.5 and 7.5%) and circles (F of 7.2 and 8.7%)). The variability within the groups, however, shows a large effect of low-pressure fractionation (representative LLDs from Bezos et al., in prep; no LLDs shown for SiO_2 and Al_2O_3 because they are not included in our major element model). Also shown for comparison are samples from segments KP2-3 on the Azores platform (data from this study and smaller symbols from Sigurdsson (1981) and Melson et al. (2002)). The enriched groups from both segments are quite similar to the Azores platform lavas.

1.35 wt.%), lower FeO (6.99-7.95 wt.%), higher Al_2O_3 (15.58-16.12 wt.%) and lower SiO_2 (48.93-50 wt.%) for the same MgO range. These samples are also more vesicular than the transitional samples, indicative of higher initial volatile contents.

Chemical variation within the groups is also evident. Low-pressure crystal fractionation has played an important role in diversifying the lava compositions (Figure 2.2; calculated liquid lines of descent from hBasalt; Bezos et al., in prep), but there are also differences within each group that cannot be attributed to fractionation. For example, $K_{8.0}$, the concentration of K_2O corrected for fractionation to 8% MgO, varies from 0.12 to 0.29 for Lucky Strike transitional samples, and these variations correlate positively with $Ti_{8.0}$. The variations within each group are small, however, relative to the contrast between the transitional and enriched groups.

There are other important aspects to note in the major element data. The MgO contents of transitional samples decrease northwards, with very few samples from Menez Gwen having as high MgO as the average sample from Lucky Strike. The average $Si_{8.0}$ (SiO_2 corrected to 8% MgO) of transitional lavas also decreases northwards from 51.24 at Lucky Strike to 50.85 at Menez Gwen. The enriched samples from Menez Gwen and Lucky Strike are virtually identical in their major element composition and have higher MgO, and much higher Mg# (defined as (Mg/(Mg+Fe*)) x 100; Fe expressed as total Fe), than the average transitional sample from the same segment. Their major element characteristics are more similar to (but less fractionated than) those of Azores platform lavas (Figure 2.2).

To be consistent with the gradient in enrichment south of the Azores, Menez Gwen samples would be more enriched than those from Lucky Strike, since Menez Gwen is closer to the Azores. Indeed, the transitional lavas exhibit such a 'regional gradient', with Menez Gwen having a higher average K_2O/TiO_2 ratio than Lucky Strike (see Figure 2.7a), although there is substantial variability within each segment. A more striking aspect of the data, however, is that the enriched groups of both segments have samples with higher K_2O/TiO_2 ratios than the Azores platform lavas and their extreme values are very similar (Figure 2.7a). This suggests that the processes giving rise to the enriched groups may be alike at both segments.

2.4.2. Trace Elements

Trace elements confirm and expand the observations from the major elements. The more enriched groups in both segments have strongly elevated concentrations of the

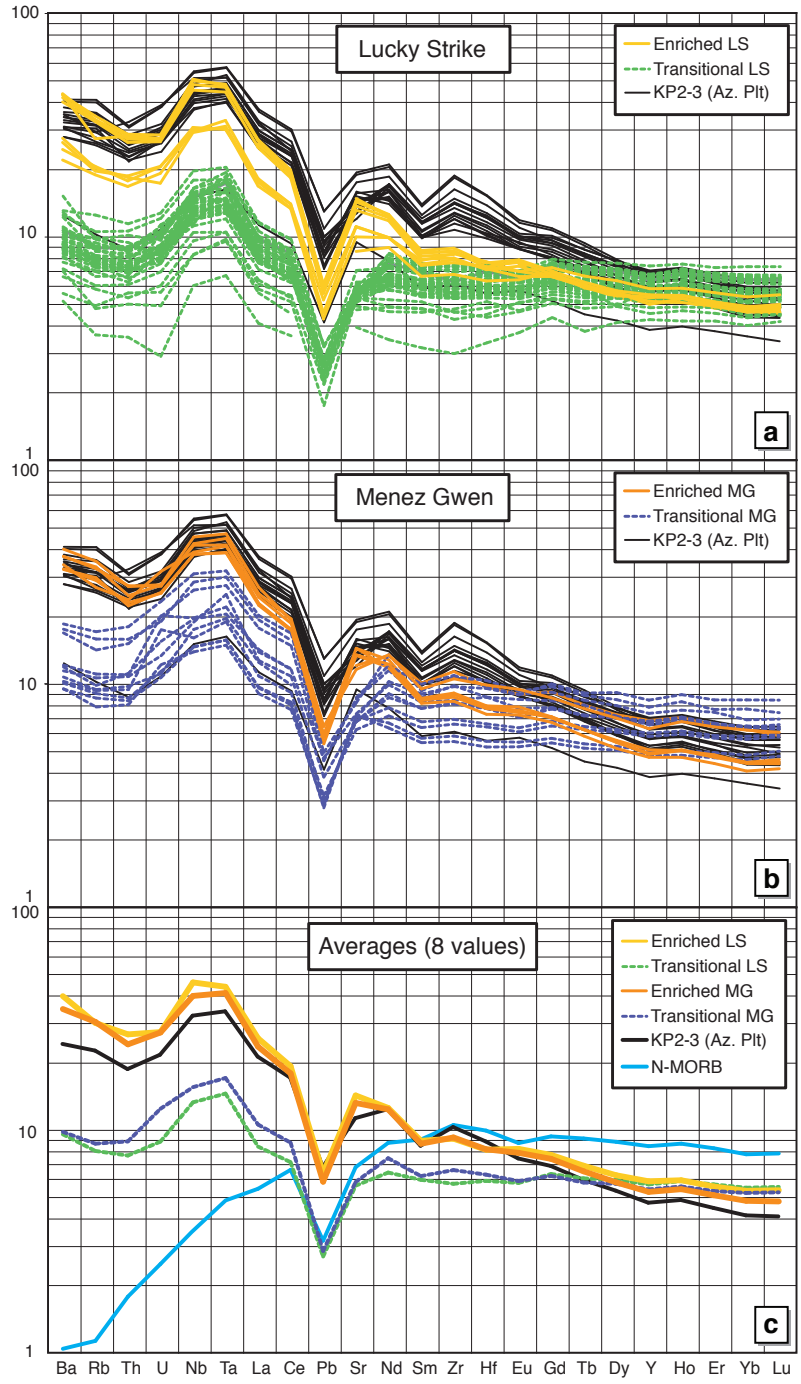

highly incompatible trace elements such as Ba, Rb, Th, Nb and U (Figures 2.3a,b). On a pyrolite-normalized spidergram (values from McDonough and Sun (1995)), the enriched samples show a steeply sloping pattern extending to the heavy rare earth elements (HREE) that crosses over the somewhat flatter pattern in the transitional samples. The enriched samples also have normalized patterns that are more concave upward through the light rare earth elements (LREE), evident when comparing their average $(La/Sm)_N$ (2.78) to that of the transitional samples (1.56).

Figure 2.3: (a-b) Pyrolite-normalized spidergrams (McDonough and Sun, 1995) showing the trace element patterns of enriched and transitional samples from both segments, with lavas from KP2-3 for comparison. Note the strong enrichment in highly-incompatible elements associated with the enriched groups, and the crossing patterns of the enriched and transitional groups in the REE. (c) Average trace element patterns of the enriched and transitional groups at each segment compared to an N-MORB from the MAR (Donnelly et al., 2004) and the average of samples from KP2-3 (concentrations corrected to 8 wt.% MgO; details on correction given in appendix). All samples from Menez Gwen and Lucky Strike are enriched relative to N-MORB in the highly incompatible elements, but the enriched groups are more extremely enriched, with concentrations nearly identical to the Azores platform lavas.

Average trace element compositions of the enriched and transitional samples from each segment are also shown in a pyrolite-normalized diagram (Figure 2.3c), along with the average composition of Azores platform lavas and an N-MORB from the MAR (Donnelly et al., 2004) for comparison. The trace element concentrations of all samples were corrected to 8 wt.% MgO prior to averaging to eliminate the effects of crystal fractionation (details on the correction given in the Appendix). Key observations include: (1) all samples are enriched relative to N-MORB in the highly incompatible elements due to the influence of the Azores hot spot (Schilling et al., 1983; Schilling, 1975); (2) the enriched groups are significantly more enriched and their trace element concentrations and patterns are similar to the Azores platform samples; (3) the Menez Gwen transitional group has elevated concentrations relative to the Lucky Strike transitional group in the highly- to moderately-incompatible elements; (4) the M- to HREE concentrations of all groups are lower than those of the N-MORB.

The enriched basalts in the Lucky Strike, Menez Gwen and Azores platform segments have important differences. For example, enriched basalts at Menez Gwen and Lucky Strike have higher ratios of highly incompatible to moderately incompatible elements (e.g. Nb/Zr, Th/Sm, Ba/La, Rb/Hf) than the Azores segments (Figure 2.4a), but lower moderately incompatible element ratios (e.g. Zr/Y, Sm/Yb). The trace element data also show a subtle distinction between the Menez Gwen and Lucky Strike enriched lavas, as the average Zr/Y and Sm/Yb increase from Lucky Strike to Menez Gwen.

To sum up, both major and trace elements define two different groups of lavas, with enriched (E-MORB) and transitional (T-MORB) groups in each segment with distinctive compositions. The enriched samples from both segments have very similar major elements, and highly incompatible to moderately incompatible element ratios that exceed those of the Azores platform lavas. Both groups also show gradients toward the Azores. The transitional samples show decreasing $Si_{8.0}$ and increasing incompatible element concentrations and moderately incompatible element ratios from Lucky Strike to Menez Gwen. The enriched samples show gradients in moderately incompatible element ratios. Both the existence of the distinct groups within each segment and their gradients need to

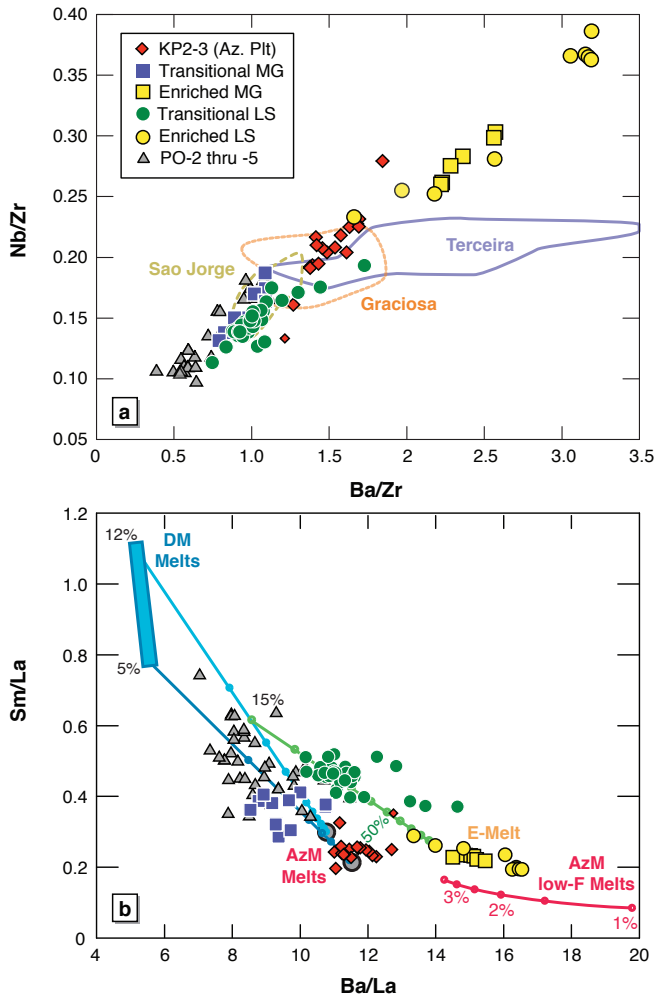

Figure 2.4: (a) Nb/Zr vs. Ba/Zr for samples from Lucky Strike, Menez Gwen, KP2-3 and other segments farther south (segments PO-2 through PO-5). ICP-MS data from PO-2 through 5 taken from Yi et al. (2000), Nishio et al. (2007), Chauvel and Blichert-Toft (2001), Cooper et al. (2004) and Gale unpublished data. Seven complete ICP-MS analyses have been published on KP2-3, Menez Gwen and Lucky Strike; five of them are from Yi et al. (2000) and Cooper et al. (2004) and are from samples we also analyzed. As our analyses agree very well, we show only our data for these samples. The two remaining analyses from Chauvel and Blichert-Toft (2001) and Cooper et al. (2004) appear in the figures (smaller symbols). Fields are also shown for the islands of Terceira, Sao Jorge and Graciosa (data taken from GeoROC). The enriched samples are much higher than the Azores platform and island lavas in the highly-incompatible trace element ratios. (b) Sm/La vs. Ba/La. All Lucky Strike samples plot off the main trend between the N-MORB and the Azores platform (AzM) toward a higher Ba/La ratio. The enriched samples have the most extreme Ba/La ratios - higher than the Azores platform lavas despite their similar Sm/La ratios. Also shown are three curves: the dark and light blue curves show the 'regional gradient' between DM and AzM (dots are 10% increments) melted 5 and 12% respectively, the green curve shows a mix between a 'regional melt' with 15% Azores in the source and an enriched melt (E-Melt), and the red curve shows the field for low-F Azores melts in the garnet field between 1 and 3.5% (dots are 0.5% increments).the average of samples from KP2-3 (concentrations corrected to 8 wt.% MgO; details on correction given in appendix). All samples from Menez Gwen and Lucky Strike are enriched relative to N-MORB in the highly incompatible elements, but the enriched groups are more extremely enriched, with concentrations nearly identical to the Azores platform lavas.

be explained.

2.4.3. Isotopes

This study combines new isotopic measurements for Lucky Strike with literature data from Menez Gwen and the Azores. All lavas from Menez Gwen and Lucky Strike are isotopically intermediate between depleted MORB mantle (DM) and the fields of the Azores islands (Figure 2.5). The regional gradient is reflected in the more enriched (e.g., higher $^{87}Sr/^{86}Sr$ and $^{206}Pb/^{204}Pb$, lower $^{143}Nd/^{144}Nd$) isotopic ratios of transitional Menez Gwen basalts compared to transitional Lucky Strike basalts. In

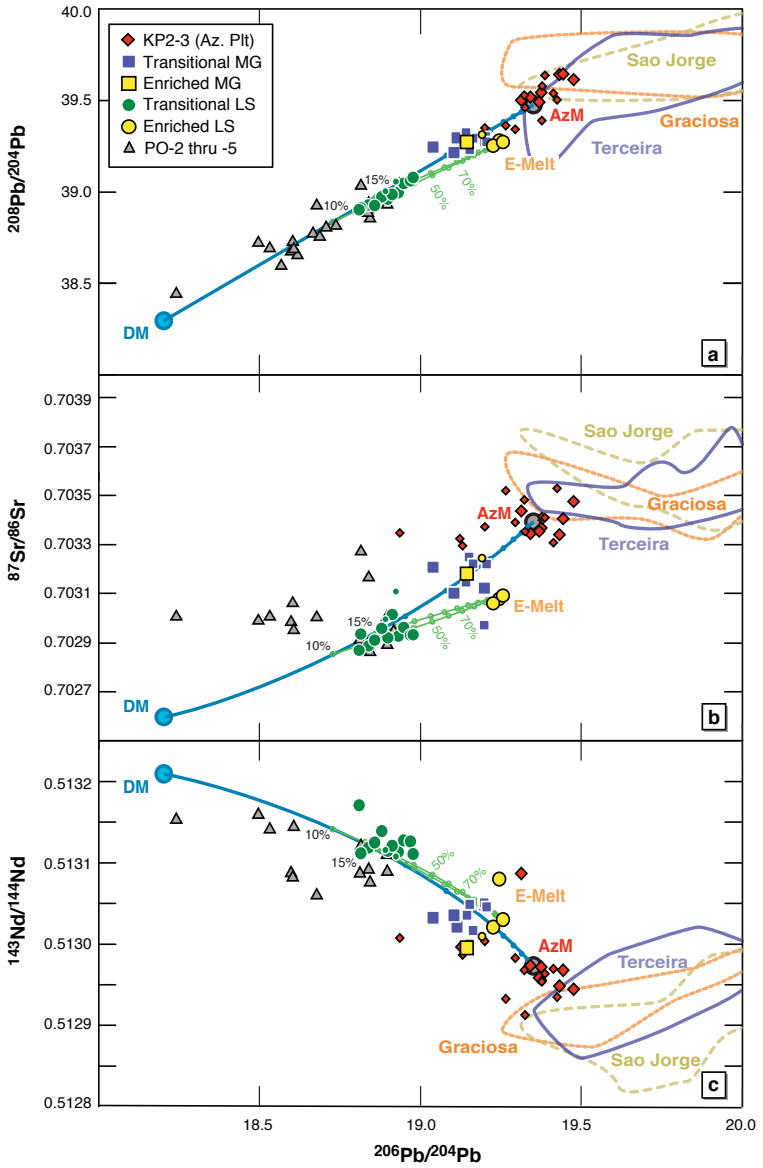

the $^{208}Pb/^{204}Pb$ vs. $^{206}Pb/^{204}Pb$ diagram, samples from Lucky Strike and Menez Gwen form a linear trend pointing toward the KP-2,3 lavas and certain Azores islands, implying that the source of isotopic enrichment is the Azores plume (Figure 2.5a).

There are several notable features in the isotopic ratios of enriched samples. First, the isotopic ratios of the enriched Lucky Strike samples are more enriched than the transitional Lucky Strike samples. There is no clear isotopic difference between the measured Menez Gwen enriched sample and the transitional Menez Gwen lavas, but this was one analysis

Figure 2.5: (a-c) $^{208}Pb/^{204}Pb$, $^{87}Sr/^{86}Sr$ and $^{143}Nd/^{144}Nd$ vs. $^{206}Pb/^{204}Pb$. Data from this study and others (Dosso et al., 1999; Yu et al., 1997; Chauvel and Blichert-Toft, 2001; Agranier et al., 2005; Ito et al., 1987; Frey et al., 1993; Nishio et al., 2007). Fields are also shown for the islands of Terceira, Sao Jorge and Graciosa (data taken from GeoROC). Isotope data from before 1985 is not shown in the figures. For consistency, all data was renormalized according to the normalization scheme given in Section 2.3. For Lucky Strike, smaller symbols indicate isotope data from Dosso et al. (1999). For Menez Gwen and KP2-3, smaller symbols indicate that we do not report ICP-MS data on the sample. All Lucky Strike samples form a linear trend pointing toward the Azores (AzM) in $^{208}Pb/^{204}Pb$ vs. $^{206}Pb/^{204}Pb$. Within this general enrichment, however, enriched Lucky Strike samples are even more enriched isotopically than the transitional samples. The enriched Lucky Strike samples are also more similar in $^{208}Pb/^{204}Pb$ than in $^{87}Sr/^{86}Sr$ to the AzM, evidence for the low-F metasomatization of their mantle source. Menez Gwen samples are isotopically intermediate between Lucky Strike and AzM. Shown are the 'regional gradient' (mixing curve for DM and AzM) and two green curves indicating the mixing between a regional melt with 10-15% Azores and E-Melt, consistent with the trace element modeling for the transitional Lucky Strike samples.

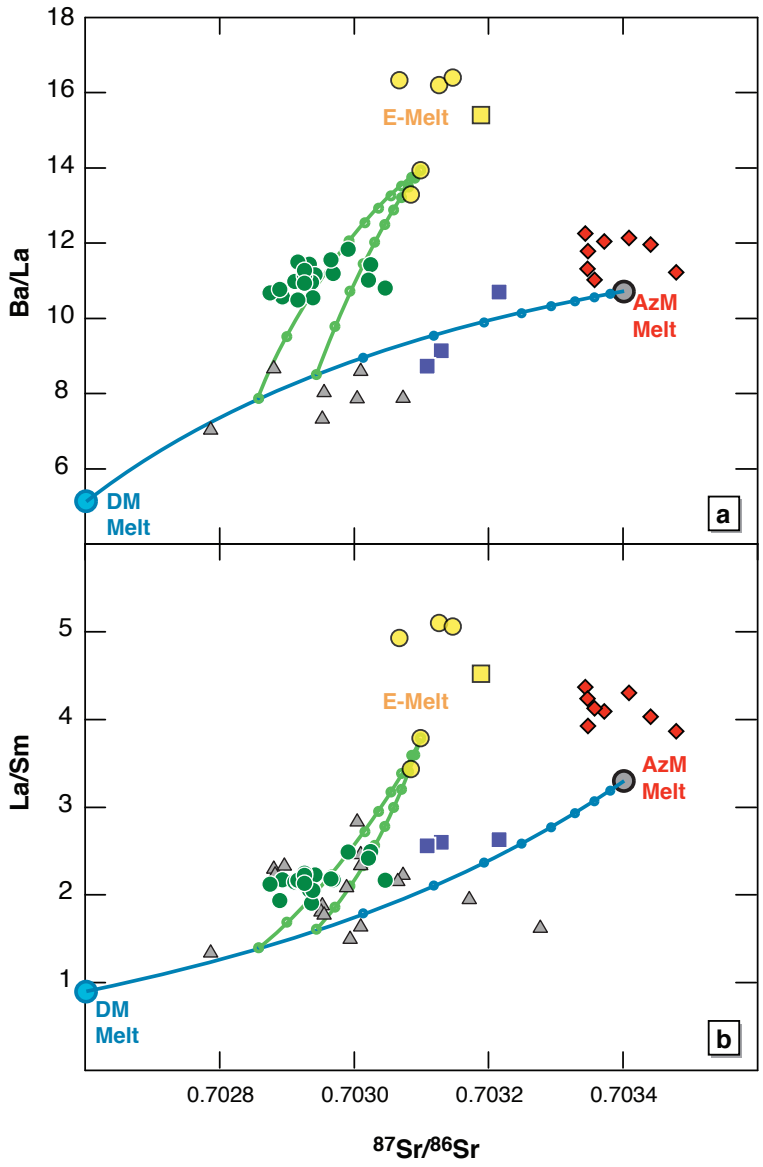

Figure 2.6: (a-b) Ba/La and La/Sm vs. $^{87}Sr/^{86}Sr$. Symbols as in previous figures. For southern segments PO-2 thru 5 for which no ICP-MS data was available on samples with measured isotopes, we show non-ICP-MS trace element data (same data sources as above). The enriched samples from both segments have as high or higher La/Sm and Ba/La than KP2-3 lavas while having lower $^{87}Sr/^{86}Sr$ values. Again, the 'regional' gradient and the mixing curves between a regional melt and E-Melt are shown; transitional Menez Gwen samples are on the regional gradient whereas transitional Lucky Strike lavas show a deflection toward the E-Melt.

on a whole rock so we hesitate to infer too much from this result. Second, the enriched Lucky Strike lavas are lower than Menez Gwen samples in $^{87}Sr/^{86}Sr$, but are actually higher in $^{206}Pb/^{204}Pb$. This peculiarity of Pb isotopes showing more extreme enrichment than the Sr isotopes of the enriched samples will provide constraints on the process involved. Third, the isotopes of enriched Lucky Strike and Menez Gwen samples are still less enriched than those of the Azores. This central feature of enriched samples with higher incompatible trace element ratios (e.g., Ba/La and La/Sm) than the Azores platform samples despite lower isotopic ratios (Figure 2.6) is a core observation that must be explained.

2.4.4. Enriched Samples Occur at Segment Centers

In both segments the enriched samples occur near the center of the segment. In Figures 2.7 and 2.8, these "central spikes" are clearly visible in major element, trace element and isotopic ratios vs. latitude

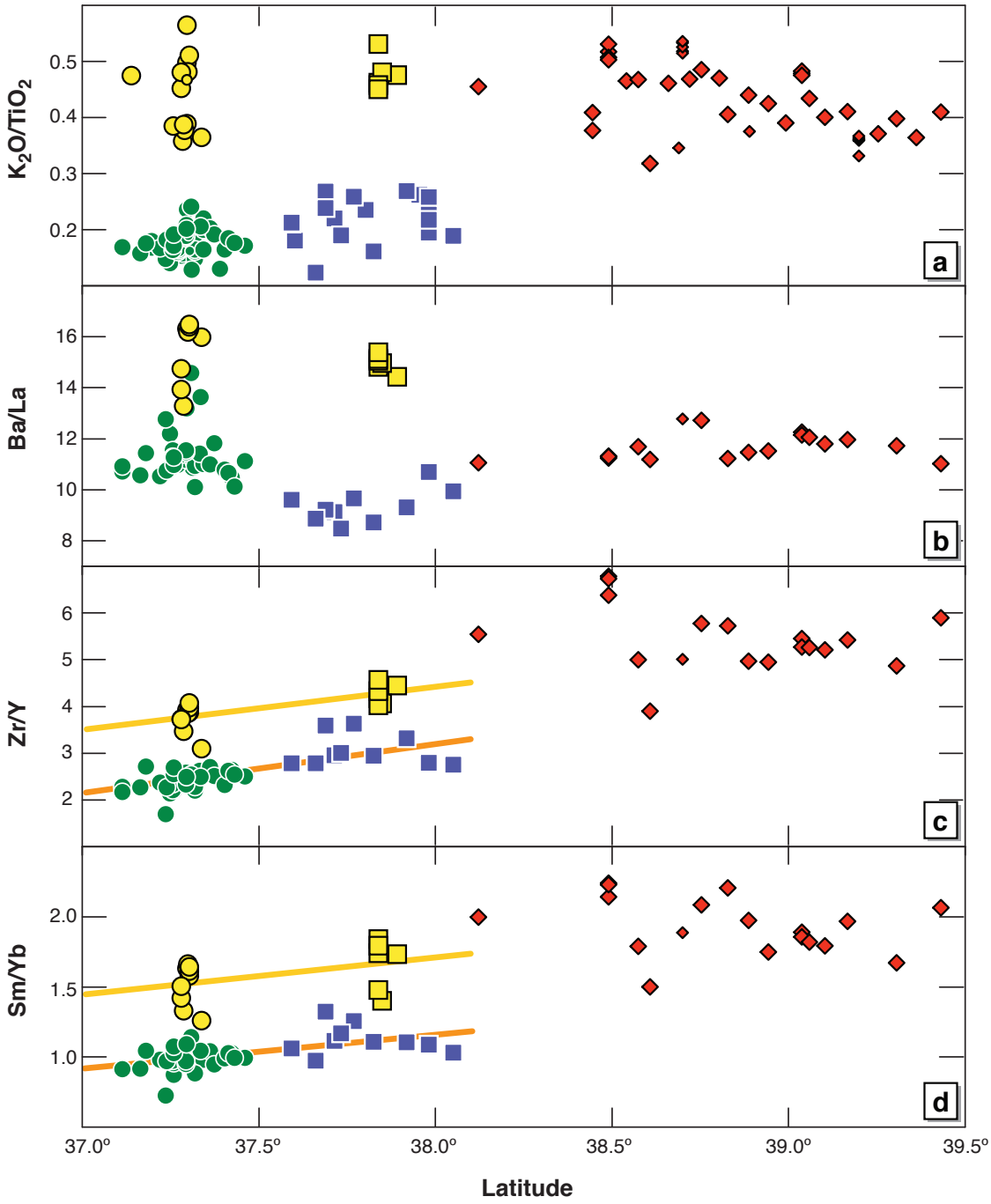

Figure 2.7: (a-d) K_2O/TiO_2, Ba/La, Zr/Y and Sm/Yb vs. Latitude for the Lucky Strike, Menez Gwen and KP2-3 segments. Symbols as in previous figures; errors on the ratios are smaller than the symbols. "Central spikes" are clearly visible in major and trace element ratios at Menez Gwen and Lucky Strike, with the enriched samples offset to higher values at the segment centers. Surprisingly, the average Ba/La of the transitional Lucky Strike samples is higher than that of Menez Gwen, while their average Zr/Y and Sm/Yb are lower. This highlights an amplified "low-F" signature at Lucky Strike, while the bulk Azores enrichment reflected in moderately incompatible elements is stronger at Menez Gwen. Zr/Y and Sm/Yb increase from Lucky Strike to Menez Gwen in the enriched samples and they appear to increase continuously from southern Lucky Strike to northern Menez Gwen in the transitional group samples (calculated lines of best fit shown).

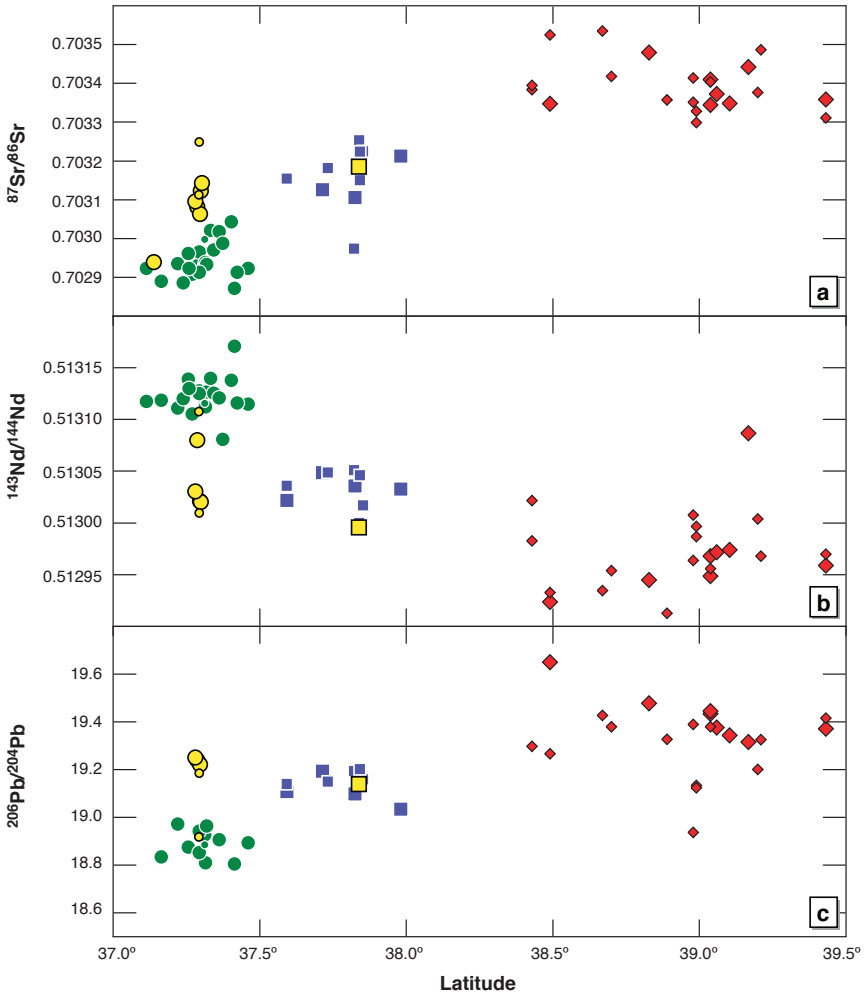

Figure 2.8: (a-c) $^{87}Sr/^{86}Sr$, $^{143}Nd/^{144}Nd$ and $^{206}Pb/^{204}Pb$ vs. Latitude for Lucky Strike, Menez Gwen and KP-2,3 segments. Errors are smaller than the symbol size. "Central spikes" are also visible in isotopic ratios at Lucky Strike. Rather than the more gradual increase seen within segments in the moderately incompatible element ratios, there is a sharp jump in isotopic signature between the northernmost end of Lucky Strike and the southernmost end of Menez Gwen and no clear within-segment gradients (calculated lines of best fit shown).

plots. There also appear to be more intermediate samples at Lucky Strike, whereas at Menez Gwen the two groups remain quite distinct.

2.4.5. Complexities of the Regional Gradient

The new data show that the regional gradient is not smooth. First, the enriched samples have higher highly-incompatible trace element ratios than Azores platform samples. Second, transitional Lucky Strike samples have higher highly-incompatible element ratios (e.g., Ba/La, Rb/La, Nb/La) relativeto transitional Menez Gwen samples but lower moderately-incompatible element ratios (e.g., K_2O/TiO_2, Zr/Y) and less radiogenic isotopic signatures (see Figures 2.5 and 2.7). These characteristics cause the Lucky Strike basalts to deviate from the smooth trend of enrichment between N-MORB and the Azores platform lavas exhibited by other segments south of the Azores (see Figure 2.4b). Finally, while the moderately incompatible element ratios of transitional samples show within-segment gradients of continuous increase from the southern end of Lucky

Strike toward the northern end of Menez Gwen (Figure 2.7c,d), isotopes show no such gradient. Instead, there is a discrete step change from the isotopes of transitional Lucky Strike samples to the isotopes of transitional Menez Gwen samples (see Figure 2.8).

2.5. Discussion

The absence of a simple regional gradient complicates discussion of issues of central and multiple supply and their relationship to segmentation. Before addressing the magma supply questions, the two distinct geochemical groups in each segment and the complexities of the regional gradient need to be understood.

2.5.1. Origin of the Enriched Samples from Segment Centers: General Framework

There are two pieces of critical evidence for the origin of the enriched samples: (1) the dichotomy between the isotope and trace element systematics; (2) the higher highly incompatible element ratios in the enriched samples compared to the Azores platform lavas.

Highly incompatible element ratios can be fractionated only by very low extents of melting, suggesting involvement of a “low-F” melt akin to what was proposed by Donnelly et al. (2004). A low-degree (low-F) melt contribution from a garnet-bearing enriched “Azores source” (more details on Azores source below) could lead to the elevated incompatible element ratios of the enriched lavas. Such a low-F melt has (1) strongly enriched highly-incompatible trace element abundances with very low HREE contents, (2) fractionated highly-incompatible trace element ratios that are higher than the original Azores source and (3) an Azores isotopic signature. When this low-F melt is mixed with a more depleted component, the characteristics required by the enriched samples can be accounted for, including a negligible effect on the HREE and a very modest effect on moderately incompatible elements.

Quantitative assessment of this process requires an estimate of the trace element content of the enriched Azores source. We must first consider whether the Azores islands or platform lavas (or both) are representative of a “true” Azores plume composition. The Azores plume has long been known to be chemically heterogeneous, in particular with

regard to the island of Sao Miguel (e.g., White et al., 1979; Beier et al., 2007; Widom et al., 1997; Turner et al., 1997 and references therein). Samples from the island of Terceira contain the most primitive He isotope ratios measured at the Azores ($^4He/^3He$ ~64,000) but a similar helium isotopic signature was found in KP-2,3 MORB (Moreira and Allegre, 2002; Moreira et al., 1999). Lavas from the Azores islands of Terceira, Sao Jorge and Graciosa also overlap the most enriched basalts from the KP-2,3 segments in other isotopic and trace element ratios (shown on Figures 2.4a and 2.5). These lines of evidence suggest that the KP-2,3 lavas are representative of a 'Regional Azores plume component' (Turner et al., 1997). The observed differences in major and trace elements between the Azores MORB (KP-2,3) and isotopically similar Azores island basalts largely reflect lower extents of melting in the islands (2-5%) relative to the MORB (10-15%) caused by the thick lithosphere beneath the islands (Beier et al., 2010; Turner et al., 1997; White et al., 1979). An Azores mantle source composition was calculated by Gier (2005) using a representative Azores platform sample (AII0127-1-R064) with high-quality ICP-MS trace element data. Given that KP-2,3 lavas can be considered to represent "plume" material, we will use this source in our modeling (composition given in Table 2.3).

2.5.1.1. The Mechanism of Low-F Melt Addition

Two mechanisms of low-F melt addition must be considered. The first is mixing the low-F Azores melt directly with transitional group melts from each segment. This scenario is ruled out because enriched samples have higher Al_2O_3 contents than transitional samples (see Figure 2.2b). Melts with garnet in the residue are characteristically low in Al_2O_3 (e.g., Walter, 1998), so the proposed low-F melt with garnet in the residue (required by the very low HREE abundances of the enriched samples), would have low Al_2O_3. Mixing a low-Al_2O_3 low-F melt with transitional melts would not create the higher Al_2O_3 contents of the enriched samples. In a recent study of the Azores islands, Beier et al. (2008) call for such low-F (1-2%) melts in the garnet field to generate Sao Miguel (Azores) lavas. The estimated primitive Al_2O_3 contents of these magmas (10.8%) are lower than those of other Azores islands due to increased amounts of residual garnet.

The second alternative is to add the low-F melt to a depleted mantle source, creating

Table 2.3: K_ds, Mantle Source Compositions and Melting Reactions Used in the Modeling

	K_d Olivine/ Melt	K_d Opx/Melt	K_d Cpx/Melt	K_d Gt/melt	Mantle Source 1	Mantle Source 2	Azores (AzM)	DM (S&S, 2004)	Average Metaso-matized Mantle Source
Rb	0.000045	0.00045	0.0006	0.00001	0.0003		1.804	0.088	1.140
Sr	0.008	0.009	0.096	0.003	1.814		41.718	9.800	20.407
Y	0.007	0.025	0.421	2.8	1.606		4.885	4.070	2.053
Zr	0.0013	0.013	0.128	0.27	1.203		17.756	7.940	6.662
Nb	0.000041	0.0001	0.007	0.0042	0.002		3.054	0.211	1.867
Ba	0.000043	0.00004	0.00068	0.00001	0.001		25.100	1.200	15.601
La	0.00005	0.00005	0.042	0.001	0.012		2.024	0.234	1.033
Ce	0.00006	0.003	0.09	0.007	0.074		4.448	0.772	2.084
Nd	0.0002	0.007	0.19	0.06	0.147		2.582	0.713	1.108
Sm	0.0006	0.01	0.28	0.115	0.080		0.642	0.270	0.268
Eu	0.00015	0.013	0.355	0.5	0.037		0.237	0.107	0.098
Gd	0.00099	0.016	0.37	0.8	0.147		0.819	0.395	0.319
Tb	0.002	0.021	0.382	1	0.031		0.131	0.075	0.053
Dy	0.004	0.025	0.402	1.4	0.234		0.804	0.531	0.337
Ho	0.006	0.029	0.41	2	0.056		0.174	0.122	0.072
Er	0.0087	0.041	0.422	3.2	0.182		0.485	0.371	0.210
Yb	0.017	0.047	0.432	4.18	0.205		0.471	0.401	0.213
Lu	0.02	0.052	0.439	4.5	0.034		0.070	0.063	0.034
Hf	0.005	0.013	0.23	0.115	0.053		0.460	0.199	0.171
Pb	0.0003	0.0021	0.086	0.0003	0.003		0.180	0.023	0.059
Th	0.00005	0.00005	0.003	0.0015	0.00004		0.207	0.014	0.125
U	0.00005	0.00005	0.0052	0.027	0.00003		0.061	0.005	0.033
$^{87}Sr/^{86}Sr$							0.703400	0.702600	
$^{143}Nd/^{144}Nd$							0.512974	0.513210	
$^{206}Pb/^{204}Pb$							19.350	18.200	
$^{207}Pb/^{204}Pb$							15.610	15.507	
$^{208}Pb/^{204}Pb$							38.980	37.800	
MgO						36.70			39.00
FeO						8.30			6.34
Na_2O						0.21			0.21
TiO_2						0.10			0.12
K_2O						0.01			0.04
H_2O						0.02			0.03
	Source mineralogy		*Melting reactions, cpx residual*						
	Azores	Metaso-matized & Regional Mantles	Azores	Metaso-matized & Regional Mantles					
Ol	0.604	0.52	0.08	-0.1					
Opx	0.189	0.38	-0.19	0.35					
Cpx	0.15	0.1	0.81	0.75					
Gt	0.057	0	0.3						

a mixed source that is subsequently melted. Low extents of mantle melting with garnet in the residue generate melts with strongly enriched highly-incompatible trace element abundances and very low HREE contents. Adding even a small amount (< 3%) of this low-F melt to a depleted source is enough to dominate its trace element signature (e.g., steeply sloping REE pattern). So this mixed source, upon being melted, will generate melts with trace element characteristics that show evidence of residual garnet even if none is present during the second melt stage. This is consistent with the high Al_2O_3 contents of the enriched lavas, which preclude garnet in the source during the second melting event. So the proposed model is two-stage: first a low-F melt of a garnet-bearing Azores mantle source is generated. This melt is then added to a depleted mantle, creating a mixed source that is later melted without garnet in the residue. This model reconciles the seeming contradiction of a 'garnet signature' in the trace elements and a 'garnet-free signature' in the major elements.

It is important to be clear about the phrase "depleted mantle source" used in this context. For example, extraction of a 2% mantle melt has very little effect on the major element composition of the residue, but can drastically deplete the incompatible element contents. For an incompatible element with a D of 0.001 (typical for Rb, Ba, Th, U), 2% melting can lead to 95% depletion of the residue, while if the melt contains 15% Al_2O_3 and the source 4% Al_2O_3, Al_2O_3 is very modestly diminished by less than 10%. And in an exactly analogous way, addition of this low-F melt to another source can greatly enrich the highly incompatible elements and have negligible effect on the major elements. While many now consider "enriched" and "depleted" to refer to an eclogite vein on the one hand, and a depleted harzburgite on the other, this is not the way we are using the terms. For the region under study, and indeed for much of the mantle heterogeneity signal, we (and others (e.g., Donnelly et al., 2004; Cooper et al., 2004; Schilling et al., 1980)) suggest that movement of low-degree melts is central. This movement can cause drastic changes in trace element compositions while preserving a mantle lherzolite. "Depleted" in this context refers largely to incompatible elements, not major elements. Below we argue for less than 5% melt removal to create our depleted mantle source, significantly depleting

trace elements while only modestly depleting major elements.

To further develop the model, we turn to geophysical constraints. Yang et al. (2006), in a seismic tomography study near the Azores, show evidence that plume material upwelling near the island of Terceira is deflected to the southwest (the direction of regional upper mantle shear flow) toward the islands of Pico, Faial and Sao Jorge. They postulate that plume material then feeds perpendicular to the ridge system (to segments KP-2,3) along a sloping rheological boundary layer. Their tomographic model supports many previous geochemical and bathymetric studies showing extensive Azores plume influence south of the MAR and little influence to the north (e.g., Schilling, 1975; White and Schilling, 1978; Goslin and Triatnord Sci, 1999). Donnelly et al. (2004) proposed that low-F partial melting that metasomatizes the surrounding mantle could occur in the 'margins of plumes'. Given these previous studies, we propose that low-F melting in the garnet field is taking place in the southwestern margin of the Azores plume. These melts then get injected into surrounding depleted lithospheric mantle, creating a metasomatized source that flows southwestward, eventually melting to form the enriched samples seen at Menez Gwen and Lucky Strike.

2.5.1.2. Major Element Systematics

The proposed two-stage process is consistent with the major elements. Recall that low FeO, high K_2O and low SiO_2 distinguish the enriched samples in major element diagrams. It is difficult to generate parental magmas with simultaneously low FeO and low SiO_2, as both are sensitive to pressure of melting and have opposite behaviors, i.e. high pressure melts are low-SiO_2 and high-FeO (e.g., Jaques and Green, 1980). Melting a mantle with a higher Mg# lowers FeO contents (Langmuir and Hanson, 1980), but this effect is not pronounced enough to generate a suitable parental magma for the enriched magmas. Moreover, a more refractory mantle would not likely melt at deep enough pressures to create low enough SiO_2, and it certainly would not have high enough K_2O or TiO_2 contents. The addition of low-F melts to a moderately refractory source (Mg #91), however, resolves this problem by significantly increasing the concentration of water and alkalis in the source. This increase in water and alkalis acts to (1) increase the mantle olivine Kd's, lowering the

FeO in the melts (Roeder, 1974), (2) increase the K_2O contents to levels that are consistent with the enriched magmas at Lucky Strike and Menez Gwen, (3) depress the solidus so that melting can take place at higher pressures, compatible with the observed low SiO_2.

In our major element model we calculate a mantle source composition and the extent(s) of melting required to generate parental magmas for the enriched samples. We estimated parental melt compositions by taking the seven most primitive enriched lavas (MgO>8.2 wt.%) and adding incremental equilibrium olivine until the liquids were in equilibrium with Mg#91 olivine (moderately refractory mantle). We then calculated a mantle source by fixing its Mg# to 91 and optimizing the concentrations of major element oxides (allowing them to vary within a reasonable range) until appropriate parental melt(s) could be generated using the parameterization of Langmuir et al. (1992). We find that pooled fractional melts with an integrated F of 6.5-7.5% generate suitable parental melts for the enriched basalts at Lucky Strike and Menez Gwen (see Figure 2.2; two parental melts representing 6.5 and 7.5% melting are shown. Note that the parameterization of Langmuir et al. (1992) does not include Al_2O_3 or SiO_2, which is why no parental magmas are shown on Figures 2.2b and 2.2e). The composition of the source is given in Table 2.3 ("Metasomatized Mantle"). Note that our estimates of K_2O in this source agree with the amount of low-F melt added to the source (2-2.6%) indicated by the trace element modeling detailed below.

The fairly low (6.5-7.5%) melting extent is reasonable considering the moderately refractory mantle source which likely limits melt productivity. An important question, however, is why the Al_2O_3 contents of enriched samples are higher than transitional samples if they are melts from a moderately refractory mantle. While we do not constrain Al_2O_3 in our melting model, based on the observed relationship between MgO and Al_2O_3 in mantle peridotites (McDonough and Sun, 1995 and data from GeoROC), we estimate that our mantle source has ~2.8% Al_2O_3. Adding ~2.6% of the low-F component (as suggested by the trace element modeling below) with ~10.8% Al_2O_3 (the Al_2O_3 contents of Sao Miguel low-F melts in the garnet field) brings the source to 3.1% Al_2O_3. This is lower than bulk DM estimates (4% Al_2O_3; (Workman and Hart, 2005)), but still much higher than harzburgites with Al_2O_3 contents typically <1%. The lower extents of melting (6.5-

7.5%) relative to normal MORB without garnet in the residue could then lead to higher Al_2O_3 enriched lavas, as Al_2O_3 tends to increase as extent of melting decreases.

2.5.1.3. Trace Element Modeling

Incompatible trace element ratios and concentrations further refine the model by constraining the extent of melting of the low-F melt and the relative amount that must be added to the depleted source to generate appropriate metasomatized sources. Full details of the trace element modeling are provided in the Appendix; here we outline the concepts. A primary magma can be inverted for the trace element composition of its mantle source if F is known. We calculated primary incompatible trace element compositions of the seven enriched lavas from Menez Gwen and Lucky Strike by applying a dilution factor based on how much olivine was added to be in equilibrium with Mg#91 mantle (following the major element modeling above). We then inverted these primary magmas using a non-modal batch melting equation and the constraints on F from the major element modeling to estimate the trace element composition of the metasomatized sources (see average "metasomatized" source composition, source mineralogy, D values and melting reactions in Table 2.3; the seven individual sources are provided in the Appendix). The metasomatized sources are shown in Figure 2.9.

The modeling assumes that the metasomatized sources consist of a single depleted source with variable amounts of low-F addition. This is reasonable given that the concentrations of HREE, elements largely unaffected by the low-F addition, are nearly constant in the enriched lavas (see Figure 2.3). We therefore use the HREE contents of the metasomatized sources to estimate the composition of the depleted mantle prior to the low-F addition. The HREE contents of the inverted sources (e.g. 0.034 ppm Lu) are lower than published values for depleted MORB mantle (e.g., Workman and Hart, 2005; Salters and Stracke, 2004), thus requiring a slightly more depleted 'depleted source'. This is not surprising given the moderately refractory source required to reconcile the low FeO contents of the enriched lavas. We calculated the composition of this depleted source (pre-low-F addition) by extracting a 4.7% batch melt from the average MORB mantle reported in Workman and Hart (2005) so that the HREE contents matched the contents of the inverted sources.

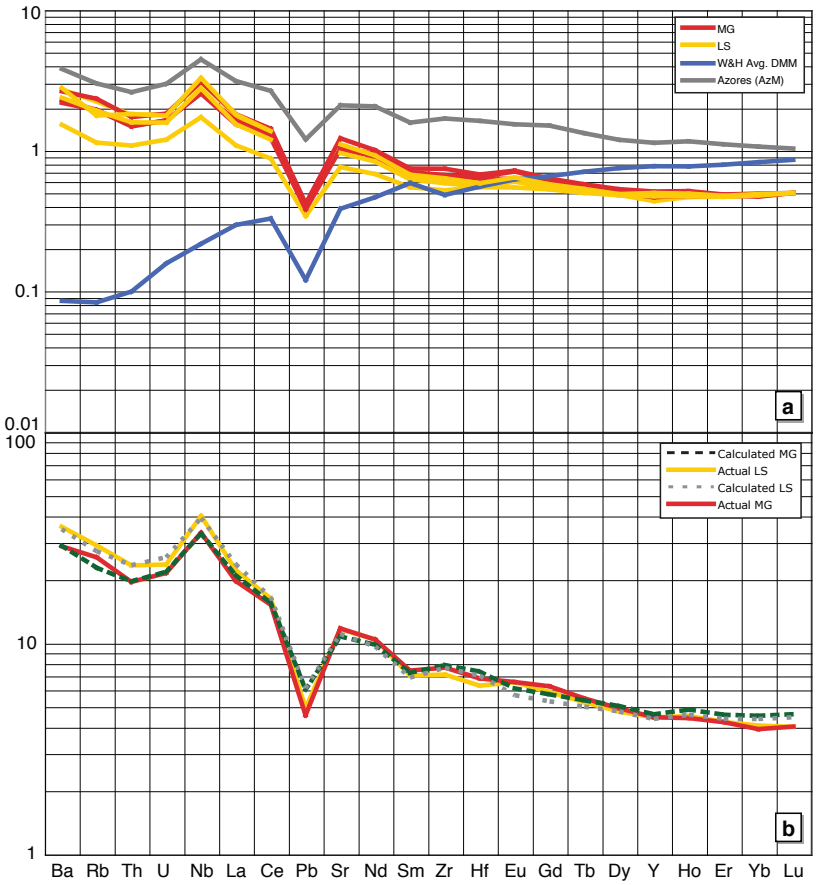

Figure 2.9: (a) Trace element patterns of the inverted metasomatized sources of seven primitive enriched samples from Menez Gwen and Lucky Strike, with the Azores source and the average DM from Workman and Hart (2005) for comparison. The nearly constant HREE in the metasomatized sources reflect the depleted source composition whereas the large variability in the highly incompatible elements reflects the variable low-F addition. (b) Trace element patterns of representative enriched samples from Menez Gwen and Lucky Strike ("actual") compared to our best-fit model output ("calculated").

The source composition is given in Table 2.3 ("Mantle Source 1"). As noted above, this level of melt removal is enough to significantly deplete the trace elements with more moderate effects on major elements.

We then minimized differences between the inverted sources and a source created by mixing low-F Azores melt with our Mantle Source 1, including absolute concentrations and key trace element ratios (e.g., La/Sm, Ba/La, Zr/Nb). We also minimized differences between subsequent batch melts of our mixed sources and the primary enriched lava compositions. We allowed three parameters to vary: (1) the F of the low-F of Azores mantle; (2) the quantity of that low-F added to Mantle Source 1; (3) the F of the metasomatized source. The non-modal batch melting of the Azores source (the low-F event) took place with garnet in the source; the melting reactions and mineral modes are given in Table 2.3. Note that 5.7% garnet in our source is consistent with the ~4-10% range of garnet in the source of Azores islands estimated by Bourdon et al. (2005).

The fit was performed for each of the seven samples, and the results of the optimization

can be found in the Appendix. The metasomatized sources can be fit by this model with an average low-F of the Azores source of 3.8% (range 2.9-4.8%) and an average addition of 2.2% (range 1.9-2.6%) of that low-F to Mantle Source 1. Subsequent batch melting of these metasomatized sources between 6 and 7.7% (average of 7.2%) without garnet in the source beneath the ridge segments produces lavas equivalent to the observed enriched lavas. Shown in Figure 2.9b are trace element patterns of representative enriched lavas from Lucky Strike and Menez Gwen and the corresponding "best-fit" model melts. Also see Figure 2.4 for the compositional field spanned by the low-F melts.

2.5.1.4. Isotope Systematics

Our model also accounts well for the isotopic data (Figure 2.5). The low concentrations of incompatible elements in our depleted source enable even a small quantity of low-F addition to strongly influence the isotopic ratio of the metasomatized source. For example, of the metasomatized source Pb concentrations (average of 0.75 ppm), 95% of this Pb comes from the low-F melt addition. A melt of this source will then have isotopic ratios very similar to (but still lower than) Azores lavas. The low-F addition also reconciles another peculiar feature exhibited by the enriched Lucky Strike samples: they are more similar to the Azores lavas in Pb isotopes than they are in Sr isotopes. This again relates to the extent of depletion of the depleted source, and the amount that the low-F contributes to the overall trace element budget. The low-F (with Azores isotopic signature) contributes 95% of the Pb but only 90% of the Sr to the depleted source. As such, the low-F melts affect the source slightly more in Pb than in Sr, explaining why the enriched Lucky Strike samples nearly match the Azores in Pb isotopic ratios but are not as close in Sr isotopic ratios.

2.5.2. Origin of the Transitional Samples

2.5.2.1. Major Element Systematics

The major element characteristics of the transitional basalts from Menez Gwen and Lucky Strike are similar enough to be considered here as one group. The differences in their $Si_{8.0}$ and $K_{8.0}$ are not large enough to affect our major element modeling, though they are

consistent with a slightly more enriched source and deeper onset of melting moving northwards toward the Azores. We estimated appropriate parental melt compositions for the transitional lavas by taking four of the most primitive samples (MgO>8.9 wt.%) and adding incremental equilibrium olivine until the liquids were in equilibrium with Mg#89 olivine. Note that Mg#89 was used instead of Mg#91 because, as noted above, the average Mg# of transitional lavas is much lower than that of enriched lavas. Next, we estimated a mantle source by fixing its Mg# equal to 89 and optimizing the concentrations of the major element oxides until appropriate parental melt(s) could be generated using the parameterization of Langmuir et al. (1992). Reasonable parental melts for the transitional basalts at Lucky Strike and Menez Gwen can be generated by pooling fractional melts with an integrated F of 7.2-8.7% (see Figure 2.2 – parental melts are shown representing 7.2 and 8.7% melting; Mantle Source 2 given in Table 2.3). Our major element modeling of one mantle source with variable F is an approximation, as obvious evidence in trace element and isotopic ratios exists for source heterogeneity between Menez Gwen and Lucky Strike. This source variation, however, seems to have minimal effects on most major elements.

2.5.2.2. Trace Element Systematics

Clear differences in the trace element concentrations and isotopic ratios of transitional samples from Menez Gwen and Lucky Strike imply that their mantle sources contain different proportions of Azores mantle. We can use trace elements to estimate a “regional” mantle source (mixture of depleted mantle and Azores mantle) for Lucky Strike and Menez Gwen transitional samples. We first approximate a regional gradient by mixing in 10% increments the DM from Salters and Stracke (2004) with the Azores source (AzM) given in Table 2.3. We then melt this range of compositions 5% and 12% (see mineral proportions for “regional mantles” in Table 2.3) to generate a spectrum of regional melts to compare with our transitional samples from Menez Gwen and Lucky Strike (see Figures 2.4, 2.5 and 2.6 for regional gradient). We simplify our regional gradient modeling by assuming no garnet in the source, as neither the Menez Gwen nor the Lucky Strike transitional samples show evidence of a garnet-bearing source (see trace element patterns, Figure

2.3).

These 'regional melts' can then be used to estimate the regional mantle sources of transitional Menez Gwen and Lucky Strike lavas. This is straightforward for the transitional Menez Gwen basalts because they fall near the calculated regional gradient (Figure 2.4b). Their regional mantle source contains between 25 and 55% AzM. Much of the trace element variability seen in the transitional Menez Gwen samples, therefore, can be attributed to source variation. The transitional Lucky Strike samples deviate from the regional gradient toward higher highly incompatible element ratios, so estimating their regional mantle source(s) is not so straightforward. We approximate their regional mantle composition by fitting a curve to the transitional Lucky Strike lavas in the Sm/La vs. Ba/La plot; the intersection of this curve with the modeled regional gradient is taken as an estimate of the Lucky Strike regional mantle. An appropriate regional mantle contains 10-15% AzM and 90-85% DM. For simplicity, the trace element modeling below (and shown in Figure 2.4) assumes 15% AzM in the Lucky Strike regional mantle source.

The relative enrichment of transitional Lucky Strike samples compared to the calculated regional gradient requires explanation. Note that their trend is between the regional mantle melts and the field for both the enriched samples and the low-F of AzM (see Figure 2.4b). This apparent mixing curve could be produced either through the variable addition of enriched melts to regional melts, through the addition of a low-F melt itself to either the regional mantle source or melts, or through mixing between the enriched (metasomatized) and regional mantle sources. As mentioned above, however, the similarities between the enriched Menez Gwen and Lucky Strike samples imply that the low-F process giving rise to these samples is not segment-specific. We argue that the low-F of AzM is being generated at the edge of the Azores plume and not beneath individual ridge segments. This leads us to the conclusion that the transitional Lucky Strike samples reflect mixing between either enriched and regional melts or enriched (metasomatized) and regional mantle sources, rather than direct contribution from the Azores plume low-F melt. Mixing with the enriched melt (or metasomatized mantle source) imparts a bit of the low-F signature to the transitional Lucky Strike melts, which explains their anomalously

high Ba/La compared to Menez Gwen transitional lavas (see Figures 2.4b and 2.7). We cannot distinguish between the two possibilities (source vs. melt mixing) for generating Lucky Strike transitional lavas, but to demonstrate the concept we model melt mixing. We find that mixing a regional melt with between 10 and 60% of a representative enriched melt (AII0127-2-R116-002) accounts well for the transitional Lucky Strike samples.

2.5.2.3. Isotope Systematics

We now consider the models for generating Lucky Strike and Menez Gwen transitional samples in light of isotopic constraints. The more enriched isotopic ratios of Menez Gwen samples compared to those of Lucky Strike are consistent with a larger proportion of AzM in their mantle source. In detail, a gap can be seen between transitional Lucky Strike and Menez Gwen samples in the $^{208}Pb/^{204}Pb$ vs. $^{206}Pb/^{204}Pb$ diagram (Figure 2.5a). This gap agrees with our estimated difference between the amount of AzM in the regional mantle at Lucky Strike (~10-15%) and at Menez Gwen (~25-55%). The Pico transform fault between Menez Gwen and Lucky Strike may be somewhat limiting to the southern flow of AzM. With regard to Menez Gwen specifically, there are only three transitional samples with both isotopic and ICP-MS trace element data. It is thus difficult to test whether the samples that we propose have more AzM in their source using trace elements are more enriched isotopically.

At Lucky Strike, our model must account for the clear isotopic variation within the transitional samples. Basalts with more enriched melt contribution indicated by trace elements should be more enriched isotopically, and this indeed turns out to be the case (Figure 2.5). Our calculated mixing curves between a regional mantle with 10-15% AzM and the enriched samples cover the range of isotopic variation in the transitional samples (Figures 2.5 and 2.6). Also importantly, the absolute proportions of enriched melt added to the regional melt inferred from trace elements remain appropriate for the isotopic data. The isotopic composition of DM and AzM are given in Table 2.3.

2.5.3. Constraints on Crustal Accretion Processes

We now consider the implications of our dataset for the melt delivery styles along this

portion of the MAR. Here our focus will be on Lucky Strike, as there are far more geophysical studies that, together with our new geochemical data, provide valuable constraints on the nature of the melt delivery process. The key observations from geophysical and seismic studies are: (1) the presence of a magma chamber 3.4 km beneath the central volcanic region, extending ~6km along axis (Singh et al., 2006), (2) the systematic thickening of the lithosphere from ~6.5 km at the segment center to 10 km at the segment edges (Dusunur et al., 2009; Cannat, 1996), and (3) evidence for a recent dike intrusion (Dziak, 2004). These three features, combined with the presence of a robust central volcano, all suggest a significant role of focused, central delivery of melts to the Lucky Strike segment with at least some lateral diking. This process is similar to the one proposed by Singh et al. (2006). Indeed, Dusunur et al. (2009) argue that the lithospheric geometry implied by their seismic observations promotes overall flow "upslope" to the center of the segment, further supporting the idea of focused melt delivery at Lucky Strike. Clear evidence exists for a component of "central supply", but it does not preclude that modest amounts of magma are emplaced throughout the segment rather than exclusively at the segment center.

The stratigraphy of lava flows at Lucky Strike implies temporal geochemical variation. According to Langmuir et al. (1997), the highly vesicular, enriched lavas that comprise the main flanks of the central volcano are moderately altered and underlie the eruptions of fresh, glassy transitional lavas in the summit basin that appear to have erupted recently. This provides clear evidence that: (1) the enriched lavas are older magmas and (2) recent lavas (and likely the magma chamber beneath) are made up of transitional magma. This evidence for discrete eruptions is consistent with the observations of Dziak (2004), who suggests that volcanic activity at Lucky Strike may be caused by highly focused magma bodies that create "sporadic intrusions" into the shallow ocean crust.

The geologic evidence implies that the coexistence of transitional and enriched groups at the segment center reflects temporal variability, and that the magma chamber must be short-lived. The enriched melts represent an earlier, distinct volcanic eruption at the center of the segment. The absence of enriched lavas at segment edges suggests that if a magma chamber were involved, there was no dike propagation toward the segment

edges. Then, more recently, regional melts have been variably mixed with enriched melts within the melting regime to produce the transitional lavas. A significant proportion of the transitional melts must be focused toward the segment center, as they are found in the current central lava lake and are likely in the magma chamber below (Singh et al., 2006).

Two possibilities remain for the generation of the transitional ocean crust at the most distal segment edges. One possibility is that lateral diking of these variably mixed transitional melts from the magma chamber creates the crust at the segment edges (see Figures 2.10b,c). An alternative idea is that melt travels vertically from the edges of the melting regime through the thicker lithosphere to erupt on the ocean floor (see Figure 2.10d). Both lateral diking (central supply) and vertical transport through the lithosphere (multiple supply) could account for why the MgO contents decrease in the transitional samples toward the edges of the segment (see Figure 2.11). Cooling and fractionation (decreasing the MgO) of the lavas could occur either through extensive vertical travel through the thicker lithosphere at segment edges or through long lateral travel away from the segment center.

There are issues with both possibilities. For the pure central supply model, a question is whether or not diking for 30km (from segment center to edge) is reasonable. Diking may instead be confined to the central $\pm$15km of segment. For the "hybrid supply" model which combines melt focusing to the center with vertical transport of melts to the edges, melt focusing cannot be as efficient as it was for the enriched lavas, where all magma was centrally injected. Exactly what would cause melt focusing to be more or less efficient through time is not clear.

A test of these ideas is whether there is a within-segment gradient in chemical composition. Given all the complexities involving enriched and transitional magmas, temporal variability and two distinct processes of mixing in Azores components, such a test is conceptually simple, but in practice complex to interpret. Isotopes are strongly influenced by the mixing systematics, as are highly incompatible trace elements. It is perhaps in the moderately incompatible elements, less influenced by the low-F melts but

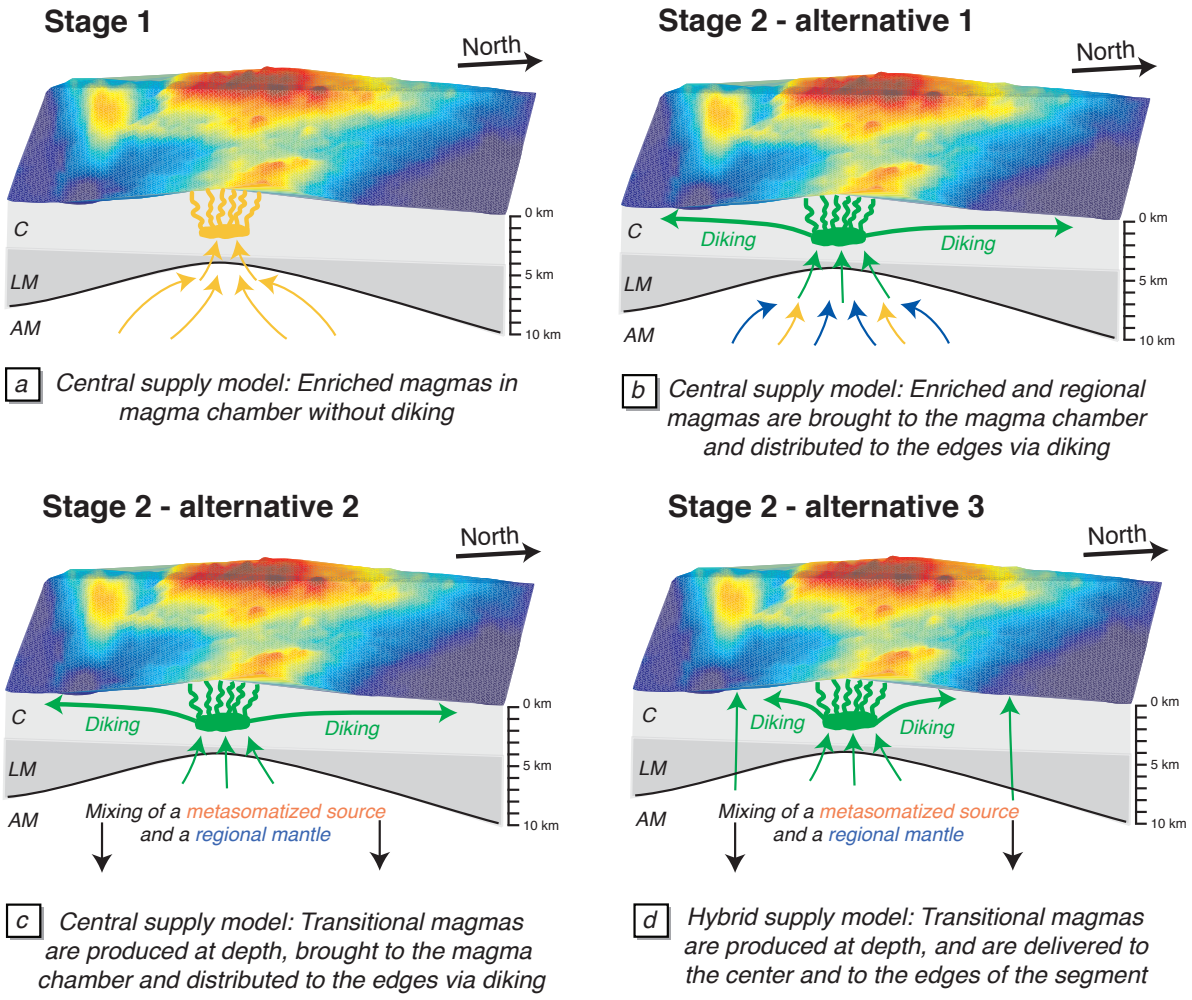

Figure 2.10: Cartoon showing the possible models to explain the data at Lucky Strike. During Stage 1, enriched samples are erupted at the center of the segment. During Stage 2, regional mantle melts mix with enriched melts and either (i) are injected at the segment center with diking to the edges or (ii) are partially focused to the segment center, with some independent eruptions occurring at the segment edges. Crustal (C), lithospheric mantle (LM) and asthenospheric mantle (AM) layers and the location of the magma chamber are consistent with the geophysical constraints.

still influenced by the regional gradient, that within-segment variations could be observed. There does appear to be a gradual increase northward in Zr/Y and Sm/Yb within Lucky Strike and Menez Gwen (Figure 2.7c,d), and this variation would be consistent with a within-segment gradient that could be produced only by multiple supply.

We are then left with a conflicting assessment of segmentation models. In support of central supply is the step function in isotopes, the existence of maximum chemical variability in the center of the segment and the robust central volcano. These results could suggest that diverse magmas appear at the center of the segment, and are homogenized and

cooled as they propagate to the segment ends. In this case, however, why would not all the magmas have propagated to the segment ends, producing equal variability at all segment positions? Multiple supply also has support and hurdles to overcome. The gradients in moderately incompatible element ratios suggest within-segment variations. It would be more conclusive, however, if the gradients were present in all incompatible element and isotope ratios. Multiple supply would also require melting and transport models that would lead to more variable magmas delivered to the segment center, and a physical mechanism for preferential delivery of enriched magmas to segment centers. Ultimately these models would be best tested by more complete sampling of the segment ends, capture of an eruption in process that shows the extent of diking, or possibly an eruption at a segment end not associated with seismicity and volcanism at the segment center. At this point the data seem to suggest a hybrid supply model where aspects of both central and multiple supply contribute to the segment scale variations.

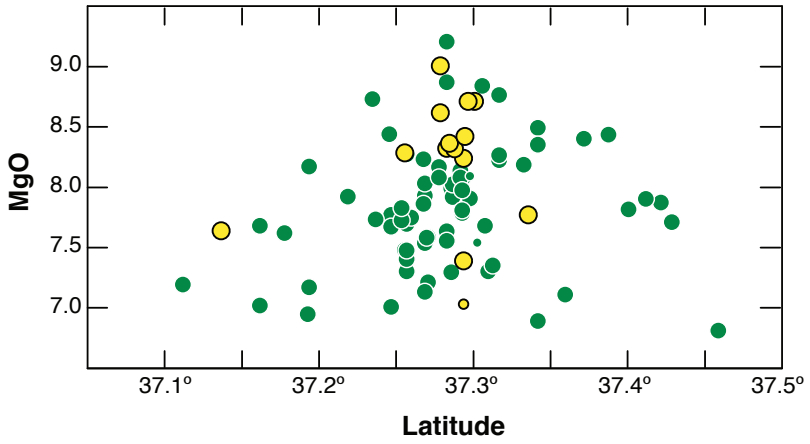

Figure 2.11: MgO vs. Latitude for samples from the Lucky Strike segment. There is a nearly symmetrical decrease in MgO content away from segment center, consistent with more pronounced cooling and crystallization in magmas at the edges of the segment.

2.6. Conclusions

The main results of our study can be summarized as follows:

(1) The regional gradient south of the Azores is complex in detail. Mean compositions of transitional samples are more enriched in isotopic ratios and most incompatible trace elements at Menez Gwen than Lucky Strike, consistent with the gradient. However, enriched samples, with even higher

incompatible element ratios than the Azores platform, occur near the center of both segments.

(2) There is clear evidence for low-F melt involvement in the generation of enriched samples from Menez Gwen and Lucky Strike not seen in samples from the Azores platform. The low-F of Azores mantle acts to metasomatize a depleted mantle source prior to the main melting event.

(3) There is an enhanced low-F signature in the transitional lavas at Lucky Strike. Transitional basalts from Lucky Strike do not lie on the regional gradient and are offset to higher highly-incompatible trace element ratios; they are formed through variable mixing of the regional melts (or mantle source) with the enriched melts (or mantle source).

(4) The geochemical and geophysical evidence are not conclusive with respect to the multiple supply and central supply models. A “hybrid supply” model, incorporating aspects of both multiple and central supply, is most consistent with all of the data. The generality of this model remains to be determined by studies of many segments with diverse geological characteristics.

References

Agranier, A., J. Blichert-Toft, D. Graham, V. Debaille, P. Schiano, and F. Albarede (2005), The spectra of isotopic heterogeneities along the mid-Atlantic Ridge, Earth and Planetary Science Letters, 238(1-2), 96-109.

Beier, C., A. Stracke, and K. M. Haase (2007), The peculiar geochemical signatures of Sao Miguel (Azores) lavas: Metasomatised or recycled mantle sources?, Earth and Planetary Science Letters, 259(1-2), 186-199.

Beier, C., S. Turner, T. Plank, and W. White (2010), A preliminary assessment of the symmetry of source composition and melting dynamics across the Azores plume, Geochemistry Geophysics Geosystems, 11.

Beier, C., K. M. Haase, W. Abouchami, M. S. Krienitz, and F. Hauff (2008), Magma genesis by rifting of oceanic lithosphere above anomalous mantle: Terceira Rift, Azores, Geochemistry Geophysics Geosystems, 9, 26.

Bender, J. F., C. H. Langmuir, and G. N. Hanson (1984), Petrogenesis of basalt glasses from the Tamayo Region, East Pacific Rise, Journal of Petrology 25(1), 213-254.

Bourdon, B., S. P. Turner, and N. M. Ribe (2005), Partial melting and upwelling rates beneath the Azores from a U-series isotope perspective, Earth and Planetary Science Letters, 239(1-2), 42-56.

Bryan, W. B. (1979), Regional variation and petrogenesis of basalt glasses from the FAMOUS area, Mid-Atlantic Ridge, Journal of Petrology 20(2), 293-325.

Bryan, W. B., and J. G. Moore (1977), Compositional variations of young basalts in the Mid-Atlantic Ridge rift valley near lat 36°49'N, GSAB 88, 556-570.

Cannat, M. (1996), How thick is the magmatic crust at slow spreading oceanic ridges?, Journal of Geophysical Research-Solid Earth, 101(B2), 2847-2857.

Cannat, M., et al. (1999), Mid-Atlantic Ridge-Azores hotspot interactions: along-axis migration of a hotspot-derived event of enhanced magmatism 10 to 3 Ma ago, Earth and Planetary Science Letters, 173(3), 257-269.

Chauvel, C., and J. Blichert-Toft (2001), A hafnium isotope and trace element perspective on melting of the depleted mantle, Earth and Planetary Science Letters, 190(3-4), 137-151.

Combier, V. (2007), Mid-ocean ridge processes: Insights from 3D reflection seismics at the 9°N OSC on the East Pacific Rise, and the Lucky Strike Volcano on the Mid-Atlantic Ridge, Ph.D. thesis, Inst. de Phys. du Globe de Paris, Paris.

Cooper, K. M., J. M. Eller, P. D. Asimow, and C. H. Langmuir (2004), Oxygen isotope evidence for the origin of enriched mantle beneath the mid-Atlantic ridge, Earth and Planetary Science Letters, 220(3-4), 297-316.

Curewitz, D., and J. A. Karson (1998), Geological Consequences of Dike Intrusion at Mid-Ocean Ridge Spreading Centers, in Faulting and Magmatism at Mid-Ocean Ridges, edited by W. R. Buck, P. T. Delaney, J. A. Karson and Y. Lagabrielle, American Geophysical Union.

Detrick, R., H. Needham, and V. Renard (1995), Gravity anomalies and crustal thickness variations along the Mid-Atlantic Ridge between 33° N and 40° N, Journal of Geophysical Research 100(B3), 3767-3787.

Donnelly, K. E., S. L. Goldstein, C. H. Langmuir, and M. Spiegelman (2004), Origin of enriched ocean ridge basalts and implications for mantle dynamics, Earth and Planetary

Science Letters, 226(3-4), 347-366.

Dosso, L., H. Bougault, C. Langmuir, C. Bollinger, O. Bonnier, and J. Etoubleau (1999), The age and distribution of mantle heterogeneity along the Mid-Atlantic Ridge (31-41 degrees N), Earth and Planetary Science Letters, 170(3), 269-286.

Dusunur, D., J. Escartin, V. Combier, T. Seher, W. Crawford, M. Cannat, S. C. Singh, L. M. Matias, and J. M. Miranda (2009), Seismological constraints on the thermal structure along the Lucky Strike segment (Mid-Atlantic Ridge) and interaction of tectonic and magmatic processes around the magma chamber, Mar. Geophys. Res., 30(2), 105-120.

Dziak, R. P. (2004), Evidence of a recent magma dike intrusion at the slow spreading Lucky Strike segment, Mid-Atlantic Ridge, Journal of Geophysical Research, 109.

Embley, R. W., W. W. Chadwick, I. R. Jonasson, D. A. Butterfield, and E. T. Baker (1995), Initial results of the rapid response to the 1993 coaxial event - relationships between hydrothermal and volcanic processes, Geophysical Research Letters, 22(2), 143-146.

Escartin, J., M. Cannat, G. Pouliquen, A. Rabain, and J. Lin (2001), Crustal thickness of V-shaped ridges south of the Azores: Interaction of the Mid-Atlantic Ridge (36 degrees-39 degrees N) and the Azores hot spot, Journal of Geophysical Research-Solid Earth, 106(B10), 21719-21735.

Fouquet, Y., H. Ondreas, J.-L. Charlou, J.-P. Donval, J. Radford-Knoery, I. Coasta, N. Lourenco, and M. K. Tivey (1995), Atlantic lava lakes and hot vents, Nature 377, 201.

Fox, C. G., W. E. Radford, R. P. Dziak, T. K. Lau, H. Matsumoto, and A. E. Schreiner (1995), Acoustic detection of a sea-floor spreading episode on the Juan-de-Fuca Ridge using military hydrophone arrays, Geophysical Research Letters, 22(2), 131-134.

Frey, F. A., N. Walker, D. Stakes, S. R. Hart, and R. Nielson (1993), Geochemical characteristics of basalt glasses from the AMAR and FAMOUS axial valleys, Mid-Atlantic Ridge (36°-37°N): petrogenic implications, Earth and Planetary Science Letters 115, 117-136.

Goslin, J., and P. Triatnord Sci (1999), Extent of Azores plume influence on the Mid-Atlantic Ridge north of the hotspot, Geology, 27(11), 991-994.

Gudmundsson, A. (1998), Magma chambers modeled as cavities explain the formation of rift zone central volcanoes and their eruption and intrusion statistics, Journal of Geophysical Research-Solid Earth, 103(B4), 7401-7412.

Hart, S. R., Schillin.Jg, and J. L. Powell (1973), Basalts from Iceland and along Reykjanes Ridge- Sr Isotope Geochemistry, Nature-Physical Science, 246(155), 104-107.

Hooft, E. E. E., R.S. Detrick, D.R. Toomey, J.A. Collins, J. Lin (2000), Crustal thickness and structure along three contrasting spreading segments of the Mid-Atlantic Ridge, 33.5°-35°N, Journal of Geophysical Research 105(B4 8205-8226).

Ito, E., W. M. White, and C. Goepel (1987), The O, Sr, Nd and Pb isotope geochemistry of MORB, Chemical Geology 62, 157-176.

Jaques, A. L., and D. H. Green (1980), Anhydrous melting of peridotite at 0-15 kb pressure and genesis of tholeiitic basalts, Contributions to Mineralogy and Petrology 73, 287-310.

Kuo, B.-Y., and D.W. Forsyth (1988), Gravity anomalies of the ridge-transform system in the South Atlantic between 31 and 34.5ºS: Upwelling centers and variations in crustal thickness, Mar. Geophys. Res., 10, 205-232.

Langmuir, C.H. and G. Hanson (1980), An evaluation of major element heterogeneity in the mantle sources of basalts, Philosophical Transactions of the Royal Society of London,

A297, 383-407.

Langmuir, C. H., J. F. Bender, and R. Batiza (1986), Petrological and tectonic segmentation of the East Pacific Rise, 5-degrees 30-minutes — 14-degrees 30-minutes North, Nature, 322(6078), 422-429.

Langmuir, C. H., E. M. Klein, and T. Plank (1992), Petrological systematics of Mid-Ocean ridge basalts : Constraints on melt generation beneath ocean ridges, American Geophysical Union Geophysical Monograph 71 183-280.

Langmuir, C. H., J. F. Bender, A. E. Bence, G. N. Hanson, and S. R. Taylor (1977), Petrogenesis of Basalts from the FAMOUS Area - Mid-Alantic Ridge, Earth and Planetary Science Letters, 36(1), 133-156.

Langmuir, C. H., et al. (1997), Hydrothermal vents near a mantle hot spot: the Lucky Strike vent field at 37°N on the Mid-Atlantic Ridge, Earth and Planetary Science Letters, 148, 69-91.

Lawson, K., R. C. Searle, J. A. Pearce, P. Browning, and P. Kempton (1996), Detailed volcanic geology of the MARNOK area, Mid-Atlantic Ridge north of Kane transform, in Tectonic, magmatic, hydrothermal and biological segmentation of mid-ocean ridges edited by C. J. MacLeod, P. Tyler and C. L. Walker, pp. 61-102, Geological Society Special Publication.

LeRoex, A. P., A. J. Erlank, and H. D. Needham (1981), Geochemical and Mineralogical evidence for the occurrence of at least three distinct magma types in the 'Famous' Region, Contributions to Mineralogy and Petrology 77, 24-37.

Macdonald, K. C., J. M. Sinton, S. M. Smaglik, and J. J. Mahoney (1991), Magmatic processes at superfast spreading mid ocean ridges: glass compositional variations along the east Pacific rise 13° - 23° S, Journal of Geophysical Research 96(B4), 6133-6155.

Magde, L. S., and D. W. Sparks (1997), Three-dimensional mantle upwelling, melt generation, and melt migration beneath segment slow spreading ridges, American Geophysical Union 20,571-520,583.

Magde, L. S., A. H. Barclay, D. R. Toomey, R. S. Detrick, and J. A. Collins (2000), Crustal magma plumbing within a segment of the Mid-Atlantic Ridger, 35°N, Earth and Planetary Science Letters 175, 55-67.

McDonough, W. F., and S. Sun (1995), The composition of the Earth, Chemical Geology 120, 223-253.

Melson, W. G., T. O'Hearn, and E. Jarosewich (2002), A data brief on the Smithsonian Abyssal Volcanic Glass Data File, Geochemistry Geophysics Geosystems, 3, 11.

Michael, P. J., R. L. Chase, and J. F. Allan (1989), Petrologic and geologic variations along the Southern Explorer Ridge, northeast Pacific Ocean, Journal of Geophysical Research 94(B10), 13,895 - 813,918.

Moreira, M., and C. J. Allegre (2002), Rare gas systematics on Mid Atlantic Ridge (37-40 degrees N), Earth and Planetary Science Letters, 198(3-4), 401-416.

Moreira, M., R. Doucelance, M. D. Kurz, B. Dupre, and C. J. Allegre (1999), Helium and lead isotope geochemistry of the Azores Archipelago, Earth and Planetary Science Letters, 169(1-2), 189-205.

Morgan, J. P., and D. W. Forsyth (1988), 3-dimensional flow and temperature perturbations due to a transform offset - effects on oceanic crustal and upper mantle structure, Journal of Geophysical Research-Solid Earth and Planets, 93(B4), 2955-2966.

Natland, J. H., and W. G. Melson (1980), Composition of basaltic glasses from the east Pacific Rise and Siqueiros Fracture Zone near 9° N, In Rep DSDP 54, 705-723.

Nishio, Y., S. Nakai, T. Ishii, and Y. Sano (2007), Isotope systematics of Li, Sr, Nd, and volatiles in Indian Ocean MORBs of the Rodrigues Triple Junction: Constraints on the origin of the DUPAL anomaly, Geochim. Cosmochim. Acta, 71(3), 745-759.

Niu, Y. L., and R. Batiza (1994), Magmatic processes at a slow-spreading ridge segment - 26-degrees-S, Mid-Atlantic Ridge, Journal of Geophysical Research-Solid Earth, 99(B10), 19719-19740.

Ondreas, H., Y. Fouquet, M. Voisset, and J. Radford-Knoery (1997), Detailed Study of Three Contiguous Segments of the Mid-Atlantic Ridge, south of the Azores (37° N to 38°30' N), Using Acoustic Imaging Coupled with Submersible Observations, Mar. Geophys. Res 19, 231-255.

Parfitt, E. A. (1991), The role of rift-zone storage in controlling the site and timing of eruptions and intrusions of Kilauea volcano, Hawaii, Journal of Geophysical Research-Solid Earth and Planets, 96(B6), 10101-10112.

Parson, L., E. Gracia, D. Coller, C. German, D. Needham (2000), Second order segmentation: the relationship between volcanism and tectonism at the MAR, 38°N-35°40'N, Earth and Planetary Science Letters 178, 231-251.

Reynolds, J., and C. Langmuir (1997), Petrological systematics of the Mid-Atlantic Ridge south of Kane: Implications for ocean crust formation, Journal of Geophysical Research 102(B7), 14,915-914,946.

Roeder, P. L. (1974), Activity of Iron and Olivine Solubility in Basaltic Liquids, Earth and Planetary Science Letters, 23(3), 397-410.

Ryan, W. B. F., et al. (2009), Global Multi-Resolution Topography synthesis, Geochemistry Geophysics Geosystems, 10.

Salters, V. J. M., and A. Stracke (2004), Composition of the depleted mantle, Geochemistry Geophysics Geosystems , 5(5), 27.

Schilling, J. G. (1975), Azores mantle blob - rare-Earth evidence, Earth and Planetary Science Letters, 25(2), 103-115.

Schilling, J. G., and H. Sigurdsson (1979), Thermal minima along the axis of the Mid-Atlantic ridge, Nature 282, 370-375.

Schilling, J. G., M. B. Bergeron, and R. Evans (1980), Halogens in the Mantle beneath the North-Atlantic, Philosophical Transactions of the Royal Society of London Series a Mathematical Physical and Engineering Sciences, 297(1431), 147-178.

Schilling, J. G., R. Kingsley, D. Fontignie, R. Poreda, and S. Xue (1999), Dispersion of the Jan Mayen and Iceland mantle plumes in the Arctic: A He-Pb-Nd-Sr isotope tracer study of basalts from the Kolbeinsey, Mohns, and Knipovich Ridges, Journal of Geophysical Research-Solid Earth, 104(B5), 10543-10569.

Schilling, J. G., M. Zajac, R. Evans, T. Johnston, W. White, J. D. Devine, and R. Kingsley (1983), Petrologic and geochemical variations along the Mid-Atlantic Ridge from 29-degrees-N to 73-degrees-N, Am. J. Sci., 283(6), 510-586.

Schouten, H., K. D. Klitgord, and J. A. Whitehead (1985), Segmentation of mid-ocean ridges, Nature 317, 225-229.

Seher, T., W. C. Crawford, S. C. Singh, and M. Cannat (2010), Seismic layer 2A variations in the Lucky Strike segment at the Mid-Atlantic Ridge from reflection measurements,

Journal of Geophysical Research-Solid Earth, 115, 20.

Sigurdsson, H. (1981), First-order major element variation in basalt glasses from the Mid-Atlantic ridge: 29° N to 73° N, Journal of Geophysical Research 86(B10), 9483-9502.

Singh, S. C., W. C. Crawford, H. Carton, T. Seher, V. Combier, M. Cannat, J. P. Canales, D. Dusunur, J. Escartin, and J. M. Miranda (2006), Discovery of a magma chamber and faults beneath a Mid-Atlantic Ridge hydrothermal field, Nature, 442(7106), 1029-1032.

Thompson, G., and W. G. Melson (1972), The petrology of oceanic crust across fracture zones in the atlantic ocean: evidence of a new kind of sea-floor spreading, Journal of Geology 80, 526-538.

Todt, W., R. A. Cliff, A. Hanser, and A. W. Hofmann (1996), Evaluation of a 202Pb–205Pb double spike for high-precision lead isotope analysis, in Earth Processes: Reading the Isotopic Code, Geophys. Monogr. Ser., edited, pp. 429–437, AGU, Washington, D. C.

Turner, S., C. Hawkesworth, N. Rogers, and P. King (1997), U-Th isotope disequilibria and ocean island basalt generation in the Azores, Chemical Geology, 139(1-4), 145-164.

Walter, M. J. (1998), Melting of garnet peridotite and the origin of komatiite and depleted lithosphere, Journal of Petrology, 39(1), 29-60.

White, W. M., and W. B. Bryan (1977), Sr-isotope, K, Rb, Cs, Sr, Ba, and rare earth geochemistry of basalts from the FAMOUS area, GSAB 88, 571-576.

White, W. M., and J. G. Schilling (1978), The nature and origin of geochemical variation in Mid-Atlantic Ridge basalts from central North Atlantic, Geochim Cosmochim Acta 42, 1501-1516.

White, W. M., M. D. M. Tapia, and J. G. Schilling (1979), Petrology and Geochemistry of the Azores Islands, Contributions to Mineralogy and Petrology, 69(3), 201-213.

Widom, E., R. W. Carlson, J. B. Gill, and H. U. Schmincke (1997), Th-Sr-Nd-Pb isotope and trace element evidence for the origin of the Sao Miguel, Azores, enriched mantle source, Chemical Geology, 140(1-2), 49-68.

Workman, R. K., and S. B. Hart (2005), Major and trace element composition of the depleted MORB mantle (DMM), Earth and Planetary Science Letters, 231, 53-72.

Yang, T., Y. Shen, S. van der Lee, S. C. Solomon, and S. H. Hung (2006), Upper mantle structure beneath the Azores hotspot from finite-frequency seismic tomography, Earth and Planetary Science Letters, 250(1-2), 11-26.

Yi, W., A. N. Halliday, J. C. Alt, D. C. Lee, M. Rehkamper, M. O. Garcia, and Y. J. Su (2000), Cadmium, indium, tin, tellurium, and sulfur in oceanic basalts: Implications for chalcophile element fractionation in the Earth, Journal of Geophysical Research-Solid Earth, 105(B8), 18927-18948.

Yu, D., D. Fontignie, and J.-G. Schilling (1997), Mantle plume-ridge interactions in the Central North Atlantic: A Nd isotope study of Mid-Atlantic Ridge basalts from 30 degrees N to 50 degrees N, Earth and Planetary Science Letters 146, 259-272.

Chapter 3

Constraints on Melting Processes and Plume-Ridge Interaction from Comprehensive Study of the FAMOUS and North Famous Segments, Mid-Atlantic Ridge

3.1. Introduction

The famous ("French American Mid-Ocean Undersea Study") segment of the Mid-Atlantic Ridge (MAR) was the first site of focused work on an ocean ridge. Initial cruises focused on the 'famous area', an area a few km^2 just north of the segment center, and later another small region at the segment center, called 'Narrowgate' because of the narrow rift valley that occurs there.

As a result of such early and extensive sampling, the petrogenesis of these lavas has been studied in detail (e.g., Bougault and Hékinian, 1974; Bougault et al., 1984; Bryan, 1979; Bryan and Moore, 1977; Frey et al., 1993; Kamenetsky, 1996; Langmuir et al., 1977; Laubier et al., 2012; Laubier et al., 2007; le Roex et al., 1981; le Roex et al., 1996; Shimizu, 1998; Stakes et al., 1984; White and Bryan, 1977). Bryan and Moore (1977), using major element chemistry, suggested that famous area basalts were derived from a single magma chamber. Langmuir et al. (1977) showed that trace element (TE) variations were too large to be explained by magma chamber processes. They argued instead that dynamic partial melting of a homogeneous source region, which produces both low and high degree melts, better accounted for the data, and that large magma chambers did not exist. Stakes et al. (1984) used petrographic observations and major element compositions of "Narrowgate" lavas farther to the south to suggest that shallow

An amended version of this chapter, in collaboration with Muriel Laubier, Stéphane Escrig, and Charles H. Langmuir was submitted to the journal Earth and Planetary Science Letters in December, 2011.

magma chamber processes could account for their compositional diversity. Frey et al. (1993) later demonstrated that crustal processes could not account for the TE chemistry (e.g., highly variable La/Yb ratios) of the Narrowgate lavas, and instead proposed more complex partial melting processes to explain the data.

These early studies assumed a homogeneous mantle source based on isotopic data that showed little resolvable variation (e.g., Frey et al., 1993; White and Bryan 1977). Three isotopic measurements of Narrowgate samples by le Roex et al. (1996), however, showed isotopic differences that they interpreted to reflect a temporal change in the composition of mantle beneath the segment. Within each temporal group, however, they argued for dynamic melting processes to account for the data array.

Nearly all of these studies took place prior to the advent of modern ICP-MS techniques for collecting TE data and did not encompass samples from the entire French and American collections, which include many dredge locations outside the restricted FAMOUS and Narrowgate areas. The present study offers a comprehensive view of the entire ridge segment by including samples from over 110 unique locations from the French and American collections, and by reporting new major element, ICP-MS TE and Sr, Nd, Pb isotopic analyses on basaltic glasses. A parallel major and TE study of over 300 olivine-hosted melt inclusions from multiple samples from the FAMOUS segment (Laubier et al., 2012) provides additional insights into mantle melting and crustal processes occurring along the segment. The sheer number of samples analyzed with consistent laboratory techniques, and the ability to compare results with such a comprehensive melt inclusion study, make this the single largest study of its kind of a MAR segment.

A dataset of this magnitude permits exploration of fundamental questions regarding the accretion of ocean crust at slow-spreading segments. For example, how much chemical diversity exists within on-axis lavas erupted along a single segment? Do lava compositions change systematically with position in the segment? What are the relative roles of mantle heterogeneity, partial melting and crustal processing in determining lava compositions? How do major and TE variations in the lavas compare with similar data on melt inclusions from the same segment? How are melt inclusions related to the lavas?

Another interesting aspect stems from the location of the FAMOUS segment within the geochemical and bathymetric gradient south of the Azores (Dosso et al., 1999; Schilling, 1975; White and Schilling, 1978). Basalt compositions from ridge segments near the Azores hotspot are enriched in isotopes and highly incompatible elements, and this enrichment lessens southward. Our new data, coupled with recent data published by Gale et al. (2011) on the next two segments north (Lucky Strike "LS" (PO-1) and Menez Gwen "MG" (KP-5); Fig. 3.1), constrain the origin of the 'regional gradient' associated with plume-ridge interaction in this region. In particular, Gale et al. (2011) showed that the geochemical gradient south of the Azores to LS is not caused by simple

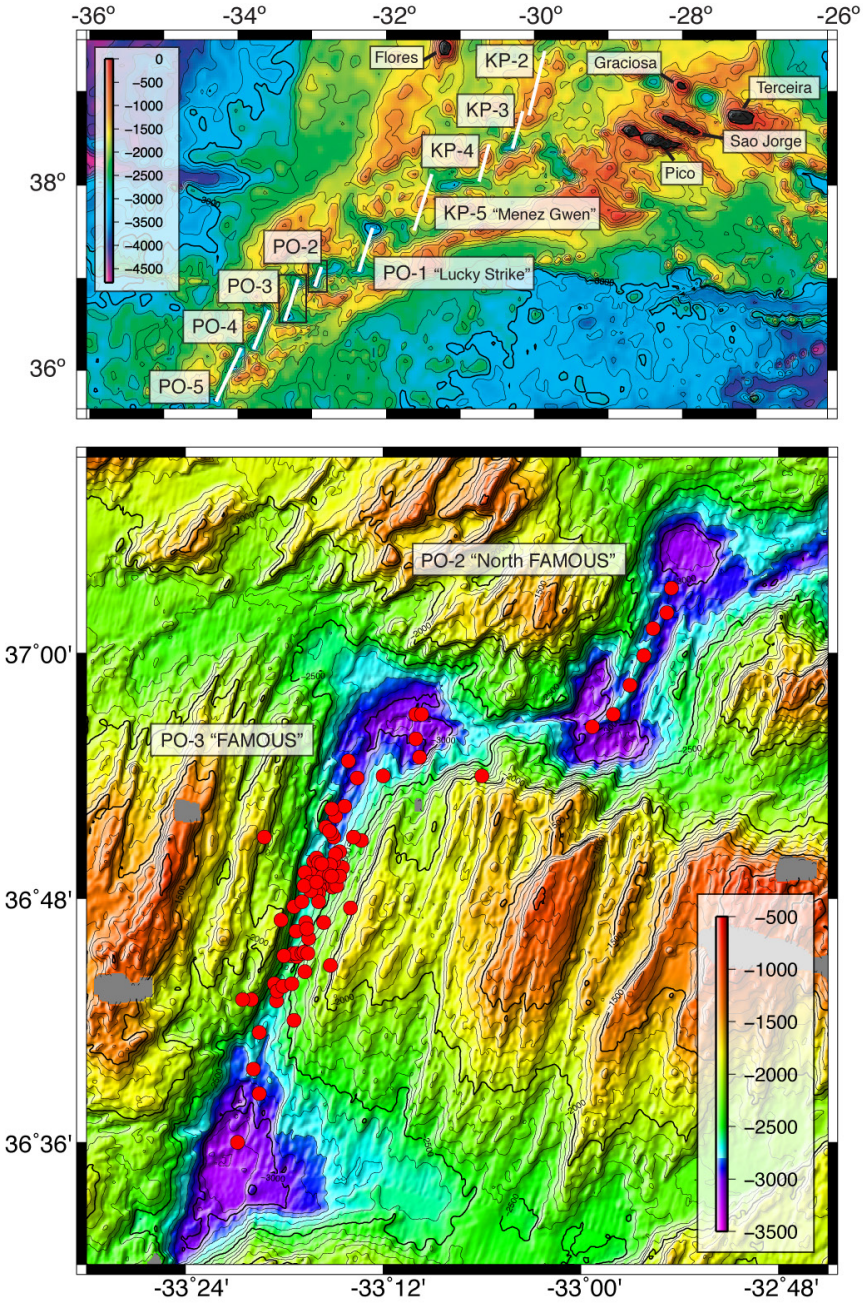

Figure 3.1: Bathymetric map of the northern Mid-Atlantic Ridge, with detailed maps of the FAMOUS (PO-3) and North Famous (PO-2) segments showing the location of samples in this study. Labeled segments (indicated by white lines in regional map) follow the nomenclature of Detrick et al. (1995). Note the extensive sampling of the FAMOUS segment. A multibeam bathymetry grid (300m spacing; Cannat et al., 1999; Escartin et al., 2001) was used for the detailed maps. Global multi-resolution bathymetry as compiled by Ryan et al. (2009) was used for the regional map (bathymetry in meters).

mixing between 'plume' mantle and 'depleted' mantle. An outstanding question, then, is how the geochemical characteristics observed by Gale et al. (2011) in lavas from LS and MG compare to those farther south from N. Famous and FAMOUS.

3.2. Regional Setting

A bathymetric gradient is observed on the MAR near the Azores, with shallow segments nearest the Azores platform and deepening segments toward the south. The shallowest of these, and the most "plume-influenced" isotopically, are the KP-2 and -3 segments near 39°N (Fig. 3.1). Just to the south are the MG and LS segments with robust axial volcanoes (Langmuir et al., 1997; Ondreas et al., 1997) recently studied by Gale et al. (2011). The primary focus of the present study, the N. Famous (PO-2) and FAMOUS (PO-3) segments, are directly south of the LS segment (Fig. 3.1).

The FAMOUS segment (containing the small FAMOUS area) is 45 km long, bounded by 25 km offsets from the adjacent AMAR and N. Famous segments to south and north. The segment varies from 2500m depth at its shallowest point to >3000 m at each end. Based on its mantle Bouguer anomaly, (Detrick et al., 1995) suggest 3 km thicker crust at the segment center than segment ends. The FAMOUS segment (Fig. 3.1) is marked by individual, small volcanic centers on the rift valley floor, and no clearly defined axial volcanic ridge (Ballard et al., 1975). The individual cones are separate volcanic edifices with distinct chemical compositions (Langmuir et al., 1977).

The N. Famous segment (Fig. 3.1) is the shortest (<18 km) segment from this portion of the North Atlantic (Detrick et al., 1995). It also has a regular depth gradient from 2700m at segment center to 3100m at segment ends, and 3 km crustal thickness variations estimated from gravity (Detrick et al., 1995). Note that the mean depth of N. Famous (2880 m) is greater than FAMOUS (2670 m). This breaks the trend of shallowing segments as the Azores platform is approached. In contrast to the FAMOUS segment, N. Famous has a well-developed axial volcanic ridge extending three quarters of the segment length.

3.3. Results

We report 105 new major element analyses, 145 new TE analyses and 43 new isotope analyses from the FAMOUS and N. Famous segments (all analyses reported in Tables B1-B3 in Appendix B). Full analytical details can be found in Appendix B. "New" analyses are either on new samples or are reanalyses of previously measured samples. For this study, we carried out a systematic study to determine interlaboratory bias factors so the abundant major element data from the Smithsonian (Melson et al., 2002) could be readily included (see Appendix B for details).

To be clear about terminology, we define enriched MORB (E-MORB) as samples with $La/Sm_N>2$, $K/Ti> 0.2$, with isotopes revealing less long-term depletion in the more incompatible element (e.g., low $^{143}Nd/^{144}Nd$, high $^{87}Sr/^{86}Sr$, high $^{206}Pb/^{204}Pb$). In contrast, normal MORB (N-MORB) are characterized by more depleted compositions (e.g., $La/Sm_N<1$, $K/Ti<0.11$), with isotopes showing long-term depletion in the incompatible elements (e.g., high $^{143}Nd/^{144}Nd$, low $^{87}Sr/^{86}Sr$, low $^{206}Pb/^{204}Pb$). Transitional MORB (T-MORB) are intermediate in composition.

3.3.1. Major Elements

The major element data from the FAMOUS segment are remarkably diverse (Fig. 3.2). Three major element groups are noteworthy.

(1) The "high-Al_2O_3, low SiO_2 group" (hereafter referred to as "HiAl-LoSi") has unusually high Al_2O_3 (15.75-17 wt.%) and MgO (9-11 wt.%), low SiO_2 (48-50 wt.%) and low K_2O contents (<0.11 wt.%). These basalts have characteristics similar to the high-Al_2O_3 basalts found along the Galapagos spreading center (Eason and Sinton, 2006).

(2) The dominant group of the FAMOUS segment (hereafter referred to as "Main") has TiO_2 between 1 and 1.3 wt.%, Al_2O_3 from 14.5 to 15.3 wt.%, FeO between 9 and 10.1 wt.% and SiO_2 from 50.3 to 52 wt.% for MgO between 7.75 and 8.25 wt.%. This group has characteristics markedly similar to the T-MORB seen at the nearby LS segment (Gale et al., 2011).

(3) The "high TiO_2" group ("HiTi"), has a narrow MgO range (7.8-8.8 wt.%) with higher

TiO_2 (1.42-1.52 wt. %) than the Main group. They are also noticeably higher in FeO (10.2-10.8 wt.%) and lower in CaO relative to the Main lavas.

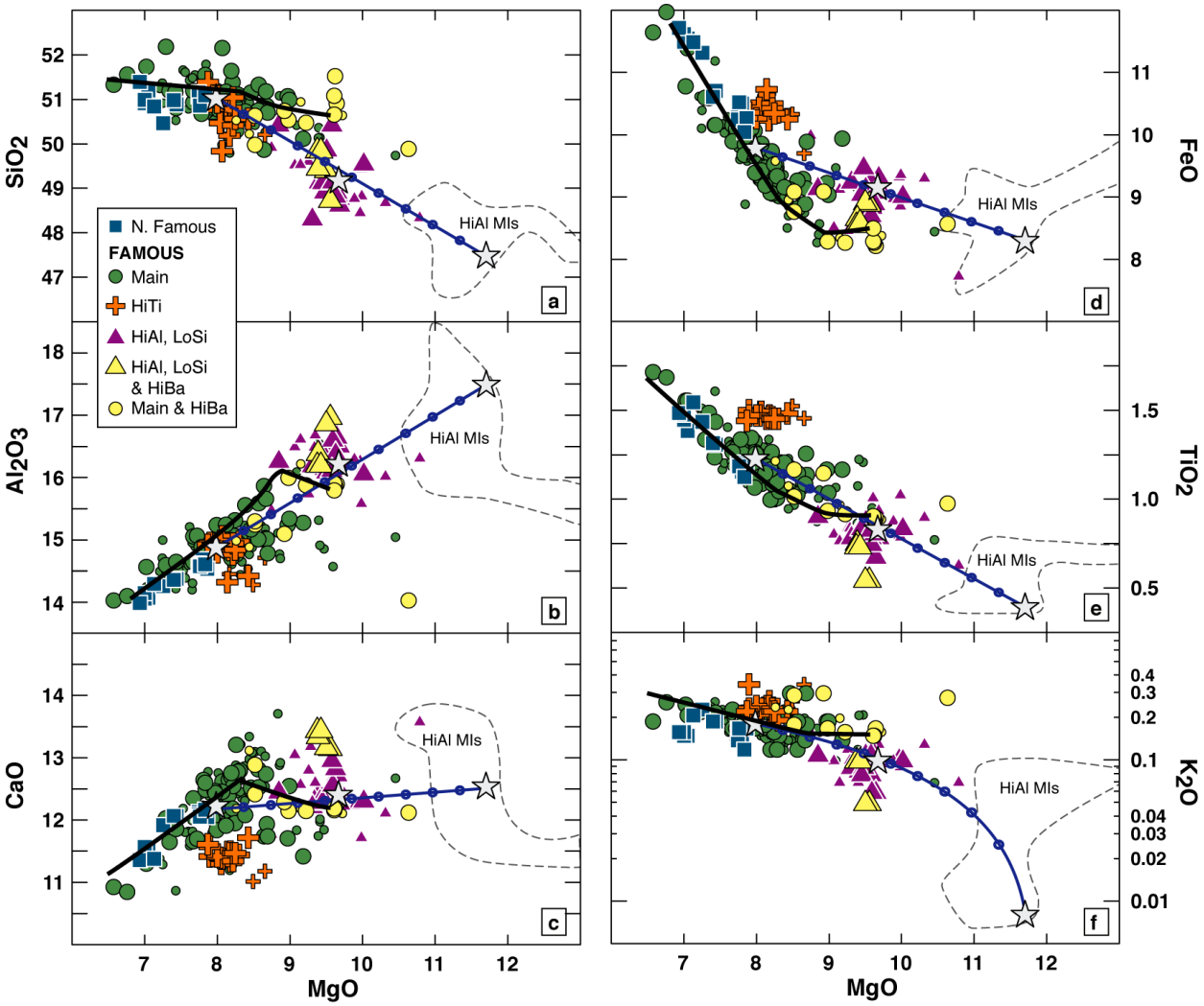

Figure 3.2: (a-f) SiO_2, Al_2O_3, CaO, FeO, TiO_2 and K_2O versus MgO. Smaller symbols indicate data already published (Bryan, 1979; Bryan and Moore, 1977; Kamenetsky, 1996; Melson et al., 2002; Sigurdsson, 1981; Stakes et al., 1984). N. Famous has one major element group, and its basalts are noticeably more fractionated than those from FAMOUS. In the FAMOUS segment there are three major element groups: Main, HiAl-LoSi and HiTi. The HiBa samples are a subgroup characterized by high Ba/La ratios, found in both the Main and HiAl-LoSi groups (see text). There is a remarkable diversity of major element compositions seen in basalts from the FAMOUS segment. Of particular note is the preponderance of primitive (>9 wt. % MgO) samples. More than one parental magma is required to explain the chemical variation seen at a given MgO content, but crystal fractionation has also been important in diversifying the compositions (see black line indicating a representative liquid line of descent from Bezos et al., in preparation). Also shown are fields for HiAl melt inclusions from the FAMOUS segment (Laubier et al., 2012). Mixing a representative HiAl melt inclusion and the average Main lava in 50:50 proportions accounts well for the major (and trace) element characteristics of the average HiAl-LoSi basalt (see dark blue curve with dots indicating 10% mixing increments, gray stars indicate the composition of the representative HiAl melt inclusion, the average HiAl-LoSi basalt and the average Main lava).

The N. Famous segment has only one major element group. The N. Famous lavas are all quite fractionated, with no lava having more than 7.9 wt.% MgO. This contrasts sharply with the FAMOUS segment, where there is an unusually large population of primitive MORB.

Variation within the groups is also important. Crystal fractionation has played a role in diversifying the lava compositions, especially for N. Famous and the Main group at FAMOUS (Fig. 3.2; calculated liquid lines of descent from hBasalt (Bezos et al., in preparation). There are also differences within the groups that cannot be attributed to crystal fractionation. For example, K_{90}, the concentration of K_2O corrected for fractionation to be in equilibrium with Fo_{90} olivine (details of fractionation correction in Appendix B), varies from 0.1 to 0.25 in the Main group at FAMOUS and Ti_{90} varies as well. To sum up, we see three major compositional groups at FAMOUS and one at N. Famous, but clear chemical variations also exist within the groups suggesting important roles for multiple parental magmas and crystal fractionation.

3.3.2. Trace Elements

Trace elements show even more distinctions among the groups than were apparent in major elements. The HiAl-LoSi lavas are the most depleted in the FAMOUS segment with low TE concentrations (e.g., Nb_{90}, Ti_{90}) and ratios (e.g., La/Sm). A notable TE feature is that all HiAl-LoSi lavas have unusually low Dy/Yb ratios (Dy/Yb <1.5). Even lower Dy/Yb ratios are seen in HiAl olivine-hosted melt inclusions from FAMOUS (see Fig. 3.3; Laubier et al., 2012). This low Dy/Yb signature is evident in the downward-sloping pattern from Lu to Sm of the HiAl-LoSi lavas in a primitive mantle-normalized spidergram (values from Sun and McDonough (1989)). Importantly, however, this more 'residual' signature in the heavy rare earth elements (HREE) does not remain in the more incompatible TE such as Ba, Rb, Th, Nb and U. In contrast to the N-MORB from the MAR farther south, even these low Dy/Yb, HiAl-LoSi lavas are enriched in the most incompatible elements (Fig. 3.3b). This feature of middle to heavy REE depletion coupled with enrichment in the most incompatible elements is fundamental to these lavas and provides constraints on their petrogenesis, as originally noted by Langmuir et al. (1977).

The Main lavas are all either flat or sloping upward from Lu to Sm, in some cases crossing over the patterns of the HiAl-LoSi samples (Fig. 3.3). They exhibit a similar pattern to the HiAl-LoSi samples in the elements Rb through Ba, but offset to higher absolute concentrations. The most enriched samples in the FAMOUS segment, including true E-MORB, are in the Main group. The highly incompatible TE ratios of the Main samples, such as Th/La, Nb/La and Ba/La ratios, are as high or higher than those of the most Azores plume-influenced ridge segments (KP-2 and-3), while their moderately incompatible element ratios (e.g., Zr/Y, Sm/Yb) are much lower.

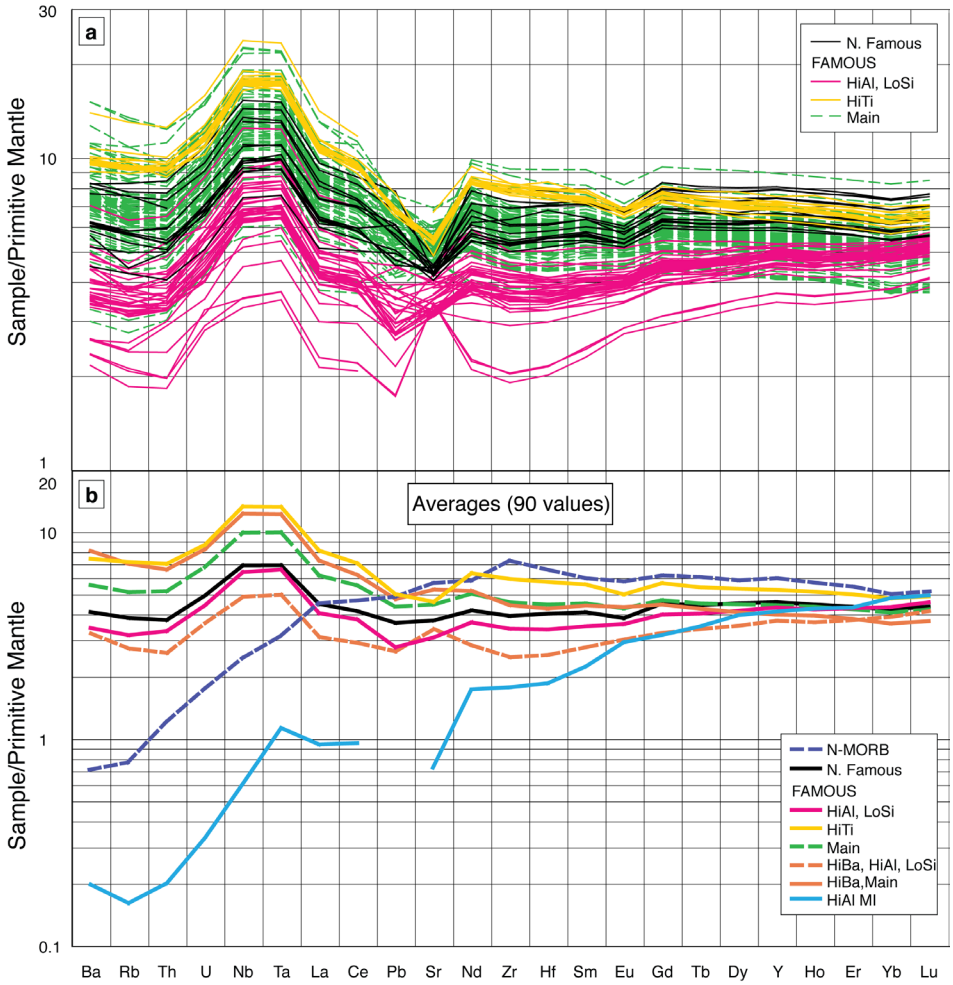

Figure 3.3: (a) Primitive mantle-normalized spidergrams (Sun and McDonough, 1989) showing the trace element patterns of the main compositional groups from both segments. Note the downward sloping patterns from Lu to Sm of the HiAl-LoSi group that cross over the patterns from the Main group. HiTi lavas have elevated TE concentrations. Three HiAl-LoSi lavas from near the northern fracture zone at FAMOUS are significantly more depleted and have positive Sr anomalies (see text). (b): Average trace element patterns of the compositional groups at each segment compared to a HiAl melt inclusion from FAMOUS (Laubier et al., 2012) and an N-MORB from the MAR (Donnelly et al., 2004; concentrations corrected to equilibrium with Fo_{90}, details on correction given in Appendix B). Notice that all lava groups are enriched (and roughly symmetrical) in the highly incompatible elements, while the HiAl melt inclusion is much more depleted. The HiBa groups show the positive Ba spike.

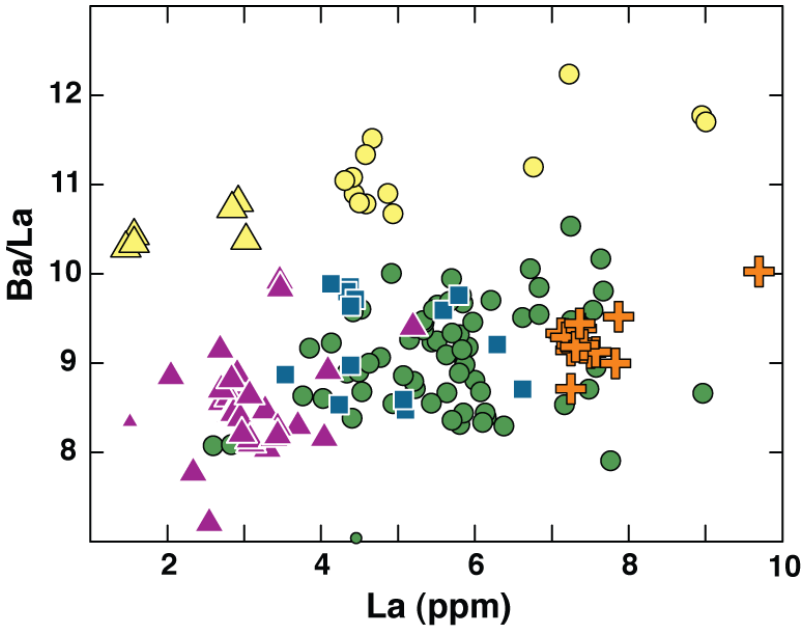

Figure 3.4: Ba/La vs. La. Symbols as in Fig. 3.2 (smaller symbols indicate published values from Chauvel and Blichert-Toft, 2001, and Nishio et al., 2007). Notice that the HiBa samples are offset to a higher Ba/La for a given La, and that the samples span the entire compositional range in La. while the HiAl melt inclusion is much more depleted. The HiBa groups show the positive Ba spike.

One other "high Ba/La" (HiBa) group emerges from the data, apparent in the spidergrams with a distinct Ba spike (Fig. 3.3b). This group contains basalts from both the HiAl-LoSi and Main major element groups, and spans the entire range of La concentrations (Fig. 3.4). The HiBa samples from the HiAl-LoSi group have the low Dy/Yb ratios characteristic of a residue despite having Ba/La (and Th/La) ratios on par with the highly enriched KP-2 and-3 segments.

The HiTi basalts at FAMOUS, for a given incompatible TE ratio (e.g., Zr/Nb), are offset to higher TE concentrations (e.g., Ta_{90}, Th_{90}). The HiTi lavas also have the highest 90-value concentrations for moderately incompatible elements such as the MREE and HREE (see Fig. 3.3b).

The N. Famous samples are some of the most depleted lavas in the dataset. They have lower moderately incompatible ratios than the Main FAMOUS lavas (e.g., Zr/Y), but with nearly identical highly incompatible TE ratios (e.g., Th/La). So while they are more depleted in both concentrations and moderately incompatible TE ratios, their highly incompatible TE ratios are also as high as KP-2 and-3. The N. Famous lavas extend to La/Sm ratios as low as the depleted HiAl-LoSi FAMOUS samples, but they have 90-value concentrations higher than the HiAl-LoSi lavas and do not possess the anomalous low Dy/Yb ratios.

Emerging from nearly all the TE groups is a common feature that must be

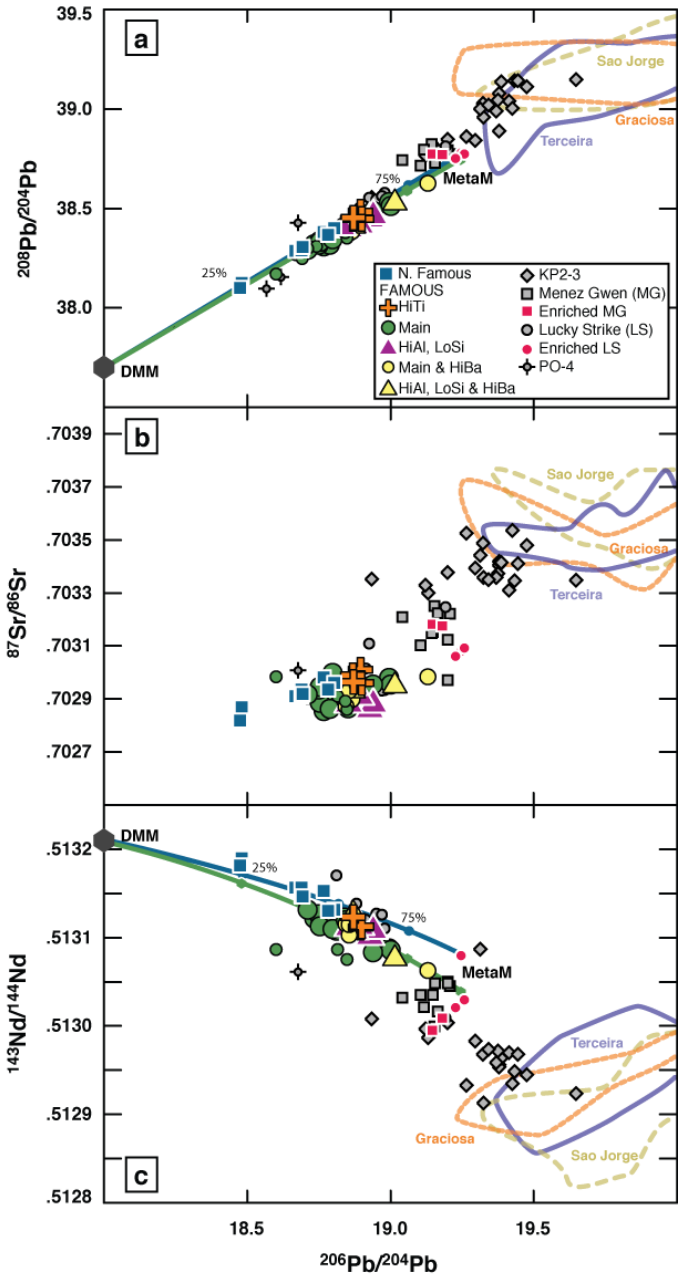

explained: a dichotomy between highly incompatible element ratios higher than the plume segments, coupled with lower moderately incompatible element ratios.

3.3.3. Isotopes

The new isotope data show clear mantle heterogeneity in this region, in agreement with le Roex et al. (1996). All lavas from FAMOUS and N. Famous are isotopically intermediate between a representative depleted MORB mantle (DMM) and the fields of the Azores islands (Fig. 3.5). The N. Famous samples, despite being geographically situated between the FAMOUS and LS segments, are not intermediate isotopically but instead extend the depleted end of the FAMOUS array in the $^{208}Pb/^{204}Pb$ vs. $^{206}Pb/^{204}Pb$ diagram to less

Figure 3.5: (a-c) $^{208}Pb/^{204}Pb$, $^{87}Sr/^{86}Sr$ and $^{143}Nd/^{144}Nd$ vs. $^{206}Pb/^{204}Pb$. Data from this study and others (Agranier et al., 2005; Chauvel and Blichert-Toft, 2001; Dosso et al., 1999; Frey et al., 1993; Gale et al., 2011; Ito et al., 1987; Yu et al., 1997). Fields are also shown for the islands of Terceira, Sao Jorge and Graciosa (data taken from GeoROC). Isotope data from before 1985 is not shown in the figures. For consistency, all data was renormalized according to the normalization scheme given in Appendix B. For FAMOUS, smaller symbols indicate published data. All FAMOUS and N. Famous samples are intermediate in composition between depleted mantle (DMM) and the Azores. Within this general enrichment, however, N. Famous samples are on the depleted end of the array. This is unexpected given that N. Famous is geographically closer to the Azores. Note also the complete overlap between transitional LS samples and Main FAMOUS samples. There is a strong correlation between $^{143}Nd/^{144}Nd$ and $^{206}Pb/^{204}Pb$, but only weak correlation in the FAMOUS $^{87}Sr/^{86}Sr$ with $^{206}Pb/^{204}Pb$. Shown are mixing curves between DMM and MetaM (the metasomatized mantle source, Appendix B) for FAMOUS (green line) and N. Famous (blue line).

radiogenic compositions. There is isotopic variation seen at the N. Famous segment despite the small number of sample locations and its short length.

Even with all the major and TE variability, the samples from FAMOUS and N. Famous form a crisp linear trend in the Pb-Pb diagram pointing towards lavas from the Azores ridge segments (KP-2 and -3) and islands (Fig. 3.5a), suggesting the source of isotopic enrichment is related to the Azores plume. The subtle slope difference between the FAMOUS and N. Famous trends, however, could indicate a small difference in the isotopic composition of the enriched end member. This is not surprising given the extensive isotopic variability seen in Azores plume basalts.

The Main group of basalts encompasses the full isotopic range at FAMOUS. The most enriched, HiBa E-MORB sample is more enriched isotopically than many samples seen at the LS segment farther north. The HiAl-LoSi group occupies the middle of the FAMOUS array and is not distinct isotopically. The HiTi lavas are also clustered in the middle of the array. While samples from all chemical groups at FAMOUS and N. Famous are less enriched isotopically than KP-2 and -3 (Azores MORB) samples, they have as high or higher highly incompatible TE ratios. This characteristic is similar to (but less extreme than) the feature displayed by the E-MORB seen at the nearby LS and MG segments (Gale et al., 2011).

The Nd and Pb isotopic data correlate well with each other, while the $^{87}Sr/^{86}Sr$ data from FAMOUS do not correlate well with either $^{143}Nd/^{144}Nd$ or $^{206}Pb/^{204}Pb$. This raises the question of whether the $^{87}Sr/^{86}Sr$ has been influenced by seawater. Fresh, unaltered glasses were handpicked and leached carefully prior to dissolution, making it unlikely that the seawater signal is a surface diagenetic feature. Instead, a seawater effect could be produced by direct interaction with the magma or assimilation of some altered material (e.g., Michael et al., 1989; Schiffman et al., 2010). This possibility could be explored in future work with chemical proxies for seawater such as Cl. Due to the uncertainties associated with the $^{87}Sr/^{86}Sr$ data, interpretation for the remainder of this paper will be based upon Nd and Pb isotopes only.

3.3.4. Complexities of the Regional Gradient

The data shed light on the detailed characteristics of the regional gradient in enrichment toward the Azores platform. For consistency with the gradient, N. Famous lavas would be more enriched than the FAMOUS lavas, as N. Famous is closer to the Azores. Yet the N. Famous samples are less enriched in their TE and isotopic signature than FAMOUS samples. Additionally, nearly all of the samples from these two segments have highly incompatible TE ratios equal to or higher than those from KP-2 and -3 despite lower moderately incompatible TE ratios and less enriched isotopic signatures. Excluding N. Famous, there is a regional gradient in Pb isotopes, but not in Th/La, and with intermediate complexity for La/

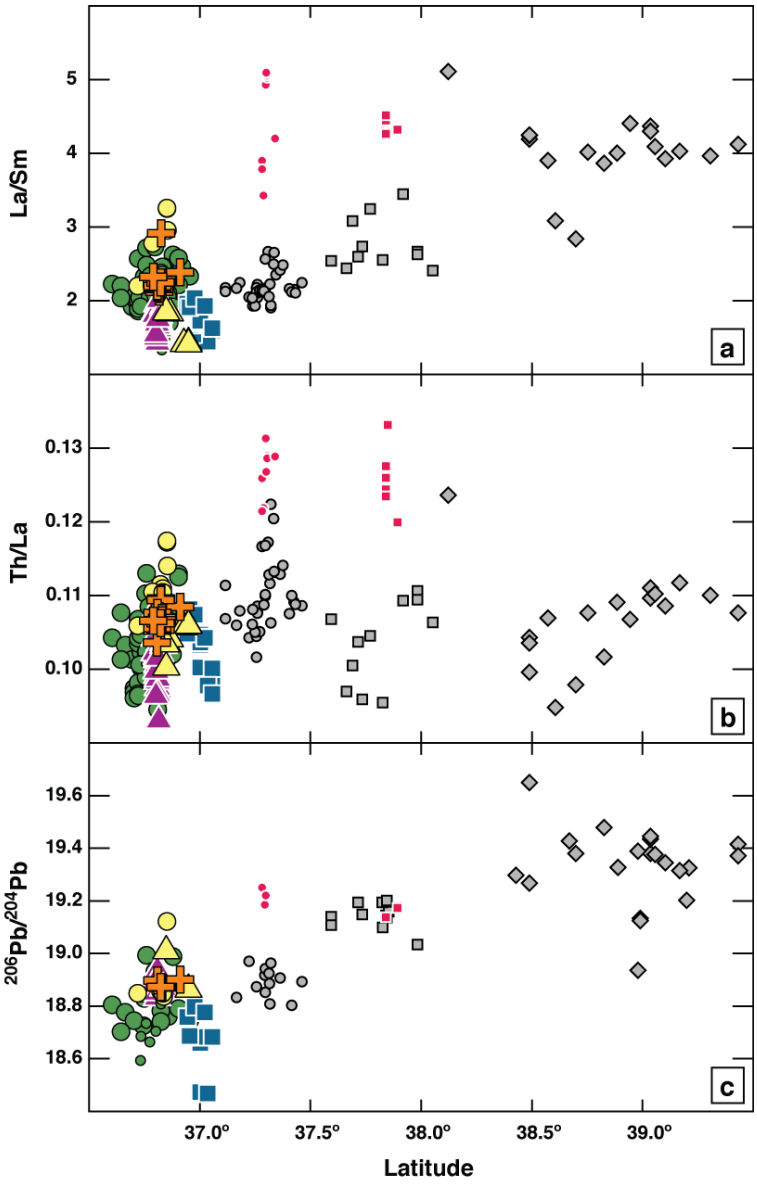

Figure 3.6: (a-c) La/Sm, Th/La and $^{206}Pb/^{204}Pb$ vs. Latitude for a portion of the MAR south of the Azores. Data from this study and other sources previously cited. Symbols are as in Fig. 3.5; errors on the ratios are smaller than the symbols. Note the rich complexity of the geochemical gradient. Pb isotopes show the most systematic decrease with latitude, but N. Famous is more depleted than expected. Note also that while the baseline La/Sm tends to decrease with latitude, Th/La shows almost no change (or even increases) from the Azores platform lavas south to FAMOUS. N. Famous in particular has anomalously high Th/La ratios given such low La/Sm and $^{206}Pb/^{204}Pb$ values. This feature of the data is strongly suggestive of the metasomatized source as the enriched mixing component giving rise to the gradient. The metasomatized source strongly influences highly incompatible trace element ratios (see the highly enriched E-Melts from LS and MG) without a large effect on isotopes and moderately incompatible element ratios.

Sm (Fig. 3.6). Clearly, the regional gradient is not smooth and continuous, but has complexities that provide constraints on its origin (see also Gale et al., 2011).

3.4. Discussion

3.4.1. Evidence for magma mixing: the origin of HiAl-LoSi lavas at famous

The HiAl-LoSi lavas, with their diagnostic low Dy/Yb signature, are unique to the famous segment in this region of the MAR. Olivine-hosted melt inclusions with similar but even more extreme signatures have been found at famous (Laubier et al., 2012). These HiAl melt inclusions have SiO_2 contents as low as 46.6%, Al_2O_3 as high as 18.4 wt.%, a strong depletion in the most incompatible elements and distinctively low MREE/HREE ratios (see melt inclusion compositions on Figs. 3.2-3.3). As Laubier et al. (2012) argue, to generate such ultra-depleted melt inclusion compositions, a mantle source depleted by previous melt removal is required. If this melt removal occurs in the spinel stability field, however, the anomalously low Dy/Yb ratios cannot be attained. Instead, melt removal must be happening in the garnet stability field, as garnet is a phase that preferentially retains Yb relative to Dy. Melt removed from a mantle source with garnet in the residue has high Dy/Yb, leaving the residue with low Dy/Yb. Subsequent melting of this residue without garnet present would generate depleted, low Dy/Yb melts similar in composition to melt inclusions analyzed by Laubier et al. (2012). As there is clear evidence for melting in the garnet field seen in some lavas at LS and MG (Gale et al., 2011), it is possible that the famous segment is seeing re-melting of the residue formed when such melts are extracted. Rather than direct evidence of melting in the presence of garnet then, the low Dy/Yb, HiAl-LoSi famous melt inclusions and lavas show evidence of “ghost garnet”.

While the low Dy/Yb links these melt inclusions and lavas, they also have clear differences. For example, in the TE patterns in Fig. 3.3b the HiAl-LoSi melt inclusions and lavas are nearly subparallel in the elements Gd through Lu. In the elements more incompatible than Gd, however, the HiAl-LoSi lavas are much more enriched, with a nearly identical pattern to the Main lavas in Ba through Gd. This feature of HiAl-LoSi lavas tracking the HiAl melt inclusions in the M- to HREE and tracking the Main lavas in the most incompatible elements must be explained. The HiAl-LoSi lavas are also

intermediate in major and trace elements (e.g., avg. SiO_2 49 wt.%, Al_2O_3 16.2 wt.%, La 3.1 ppm) between Main lavas (51%, 14.9%, 5.8 ppm) and HiAl melt inclusions (~47%, ~17.5%, 0.59 ppm).

The fact that the HiAl-LoSi lavas are (1) intermediate between the HiAl melt inclusions and the Main lavas in element concentrations and (2) possess TE ratios with characteristics of both groups (e.g., Dy/Yb like HiAl melt inclusions and Nb/La like Main lavas) strongly suggests melt mixing for their origin. Indeed, we find that mixing a representative depleted HiAl melt inclusion with the average Main lava in a 50:50 proportion can fit every major and TE in the average HiAl-LoSi basalt to better than 6%, with P the only exception (fit to 12%; details given in Appendix B; see mixing curves on Fig. 3.2). The HiAl-LoSi lavas receive their "depleted" low Dy/Yb signature from the HiAl melt inclusions, and their "enriched" incompatible element signature from the Main lavas.

There are three other lines of evidence confirming that HiAl-LoSi lavas are derived from mixing instead of from a distinct mantle source. First, recall that the HiBa signature is present in some HiAl-LoSi lavas. While this HiBa signature coupled with low Dy/Yb is initially counterintuitive (conflicting enriched and depleted signatures), it can be understood through melt mixing. Because we have both HiBa and non-HiBa Main lavas, if they are a mixing component one would expect to see both HiBa and non-HiBa in the resulting HiAl-LoSi lavas. Second, the HiAl-LoSi lavas have an isotope signature coherent with other lavas (Fig. 3.5a), but are noticeably offset from the correlations seen in those lavas between ratios such as La/Sm, Zr/Y and $^{206}Pb/^{204}Pb$ (Fig. 3.7). This suggests a recent TE perturbation rather than a distinct mantle source. Third, olivines within the HiAl-LoSi lavas trapped melts of both HiAl and more "Main" compositional types, consistent with both melts being present (and mixing) to form the HiAl-LoSi lavas (Laubier et al., 2012).

Our observations also highlight important relationships between melt inclusions and erupted lavas. The lavas, which likely represent pooled melts from within the melting regime, are all enriched in the highly incompatible elements relative to N-MORB. Yet the

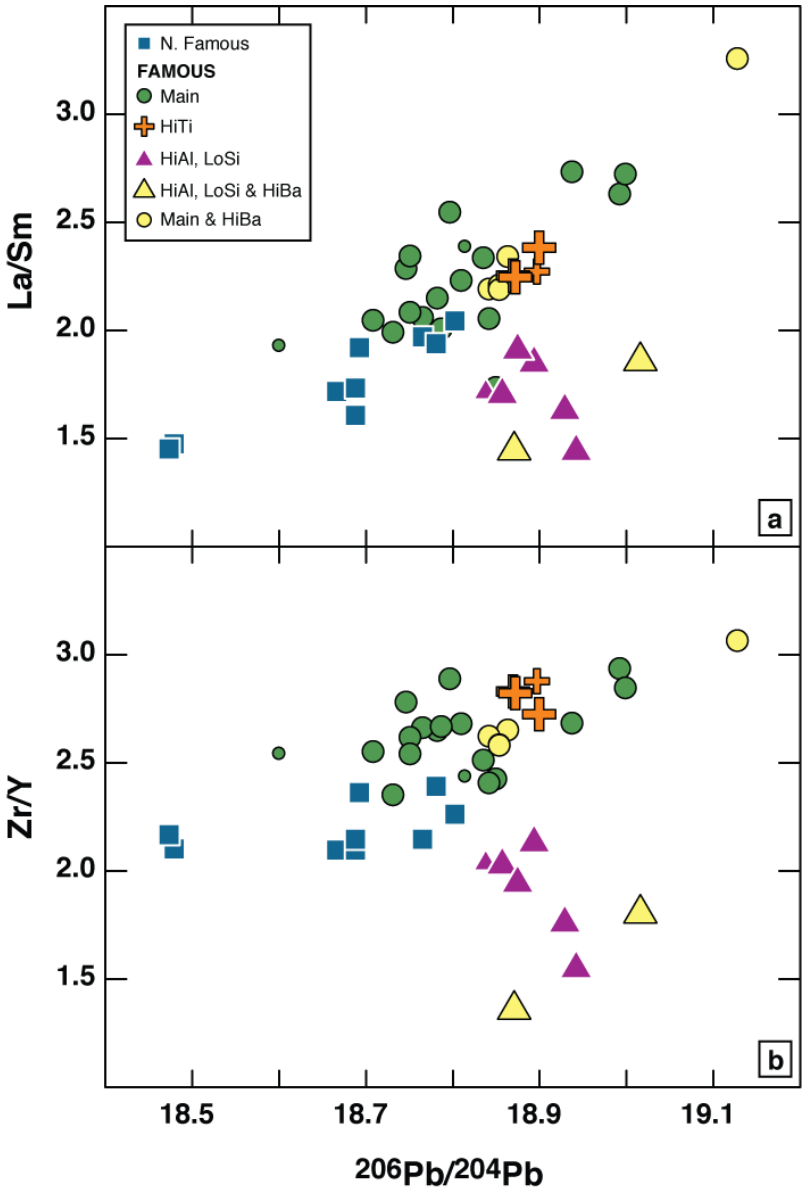

Figure 3.7: (a-b) La/Sm and Zr/Y vs. $^{206}Pb/^{204}Pb$ for N. Famous and FAMOUS basalts. Smaller symbols indicate published data (sources as in previous figures). Note the remarkably coherent relationship between incompatible TE ratios and $^{206}Pb/^{204}Pb$ seen in all but the HiAl-LoSi group from FAMOUS. Their pronounced offset is evidence that a recent melting process has disrupted their trace element composition.

melt inclusion compositions can be even more depleted than N-MORB (Fig. 3.3b; Laubier et al., 2012). Melt inclusions thus provide critical evidence of specific compositions within the melting regime that are overprinted during the pooling of melts to form lavas. Such mixing of melts gives rise to HiAl-LoSi lavas, with characteristics of the most depleted melt inclusions and the most enriched lavas.

Three HiAl-LoSi glasses found near the northern fracture zone (ARP74-14-31,32,33) have unique characteristics, including Sr anomalies ($Sr/Sr^* = (Sr_N/sqrt(Ce_N*Nd_N))$) of 1.5-1.61, high Ba/La and the most depleted compositions of any lavas from the FAMOUS segment (Fig. 3.3). Positive Sr anomalies have also been found in certain HiAl melt inclusions from FAMOUS (Laubier et al., 2012), and were used as evidence for assimilation of plagioclase-rich cumulates in the crust. Such assimilation is a mechanism for generating the high Sr and high Ba seen in these melts. The coupling of depleted TE signatures with Sr anomalies has been emphasized in the literature (e.g., Danyushevsky

et al., 2004; Danyushevsky et al., 2003; Gurenko and Sobolev, 2006; Kamenetsky and Crawford, 1998; Slater et al., 2001; Sobolev et al., 2000), but largely with regard to melt inclusions. It is therefore important to recognize that the FAMOUS segment shows such compositions in both melt inclusions and lavas.

3.4.2. HETEROGENEOUS MANTLE SOURCES WITH METASOMATIZED MANTLE AS THE ENRICHED COMPONENT: ORIGIN OF OTHER LAVAS FROM FAMOUS AND N. FAMOUS

Here we address the primary observation of FAMOUS and N. Famous basalts with highly incompatible TE ratios as high or higher than the basalts from the plume segments KP-2 and -3, while moderately incompatible TE ratios are much lower. In plots of Th/La and Nb/La vs. Sm/La (Fig. 3.8), all lavas from FAMOUS and N. Famous form a nearly linear trend. As mixing is linear in this figure, this trend could indicate mixing between two mantle sources (or melts) which give rise to the data array. Notably, the basalts are mixing toward a composition similar to the highly enriched melts

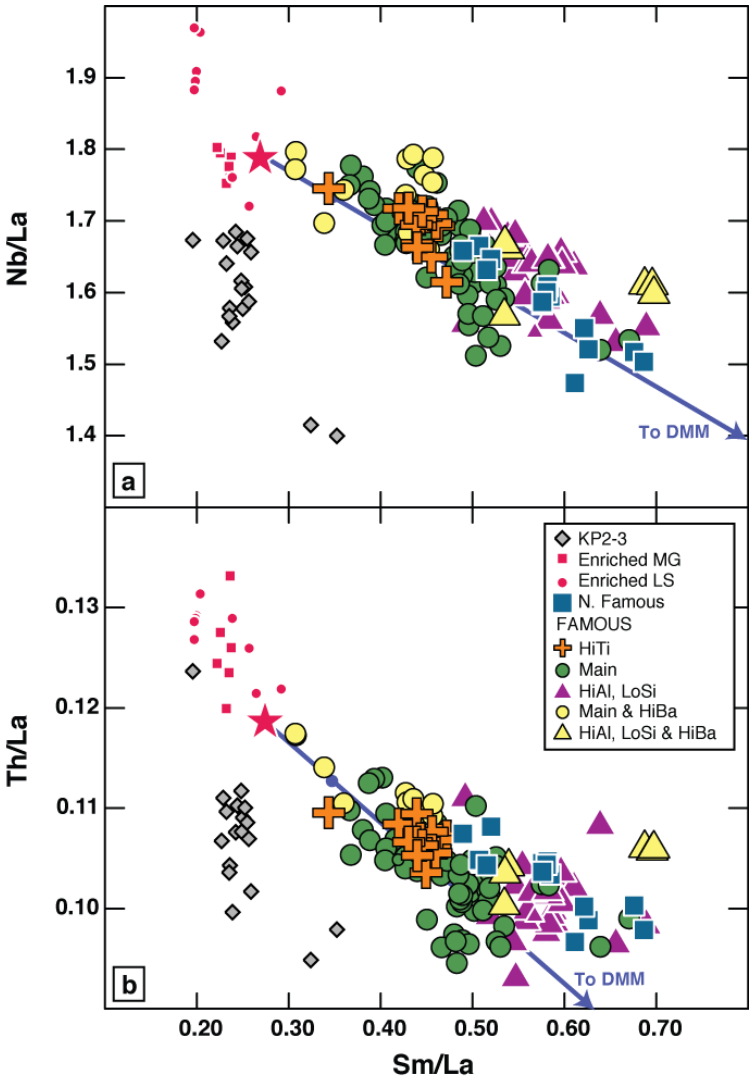

Figure 3.8: (a-b) Nb/La and Th/La vs. Sm/La of basalts from N. Famous, FAMOUS, KP2-3 and E-Melts from Lucky Strike (LS) and Menez Gwen (MG). E-Melts from LS and MG have much higher highly incompatible TE ratios than Azores platform lavas (KP2-3) for a given Sm/La. All samples from FAMOUS and N. Famous appear to be mixing toward this E-Melt type component (indicated by the red star) rather than toward the more "plume-like" component represented by the KP2-3 Azores platform lavas. This explains how the FAMOUS and N. Famous samples could have Th/La and Nb/La similar to the Azores platform lavas while being much less enriched in incompatible TE concentrations and isotopes (see Fig. 3.5). Shown are mixing curves between the metasomatized source and DMM, melted 10%.

(E-Melts) seen at nearby segment LS (red star on figures), rather than the enriched melts from the Azores platform (KP-2 and -3). As emphasized by Gale et al. (2011), these E-Melts at LS are distinctive in that their highly incompatible TE ratios are much higher than the Azores platform segments for a given Sm/La, and require a low degree melt component of the Azores plume source that serves as a metasomatic agent for the sources farther to the south. Similarly (but less extremely) elevated TE ratios at FAMOUS and N. Famous imply that this E-Melt type component, rather than a pure Azores plume component, is required by the data.

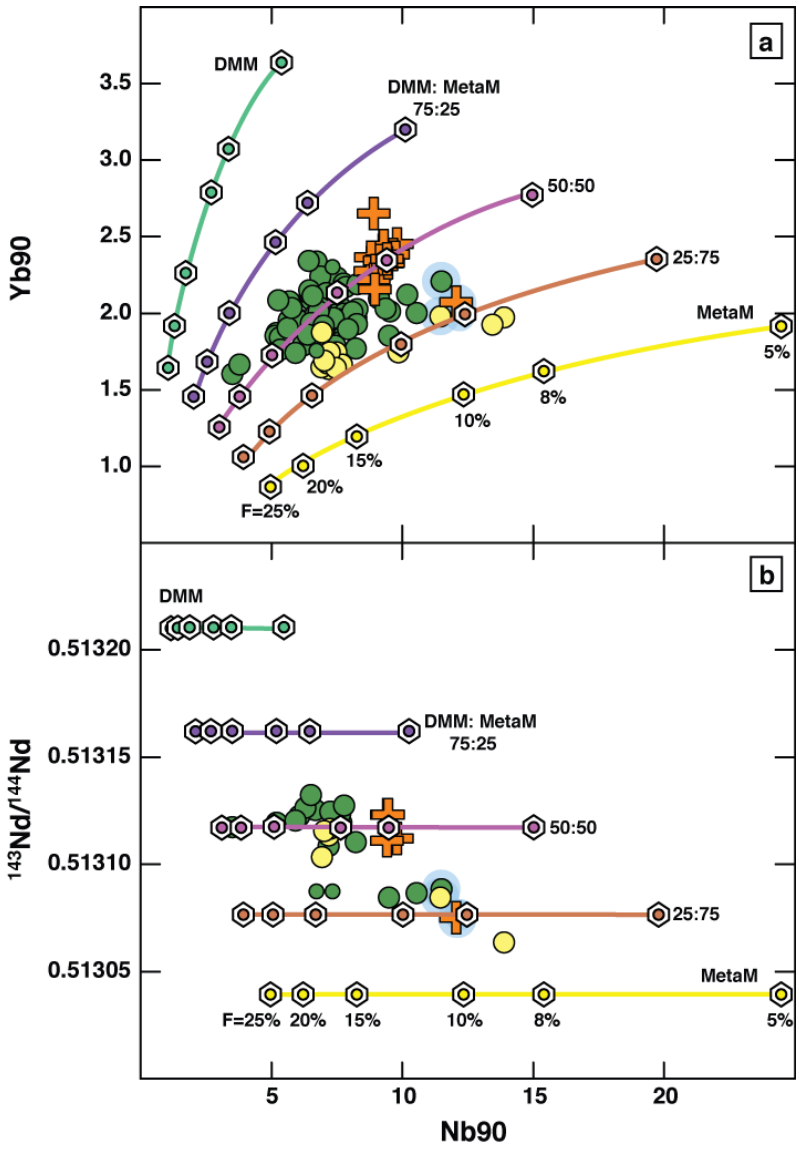

Figure 3.9: (a-b) Yb_{90} and $^{143}Nd/^{144}Nd$ vs. Nb_{90} of FAMOUS lavas (not including the HiAl-LoSi samples which have a separate petrogenesis - see text). Symbols as in previous figures. Five sources that are mixtures between a metasomatized enriched source (Gale et al., 2011) and a DMM (Salters and Stracke, 2004) are shown (different colored lines). These sources are then melted to various extents (5-25%, demarcated by hexagons). The grid shows the combined effects of F and source composition on lava compositions. Our model is able to account well for the TE and isotopic variability of FAMOUS basalts through a combination of F and source variation. The combination that works for a given sample in TE diagrams also holds when considering isotopic compositions (see highlighted samples).

Mixing alone cannot account entirely for the data array, however, as shown by a plot of Yb_{90} vs. Nb_{90} (Fig. 3.9a). Mixing in this figure would also create linear arrays, unlike that seen in the data. Yb, only a moderately incompatible element, is less sensitive to source variability and more sensitive to extent of

melting (F) variations. Nb, a highly incompatible element, is more sensitive to source variations. This figure, then, strongly suggests that both F and mantle source variation are important. The importance of F variations has been emphasized in earlier studies of FAMOUS lavas (Frey et al., 1993; Langmuir et al., 1977; le Roex et al., 1996). The variation in Yb_{90} shows the F effect, and the deviation toward higher Nb_{90} shows the source effect.

The data imply that a model to explain the range of chemical variation in the lavas from FAMOUS and N. Famous must include both mantle source and F variation. Full details of the TE and isotope modeling are given in Appendix B; here we outline the concepts. We focused on the 33 samples from FAMOUS and N. Famous that have both TE and isotopic measurements to ensure that the model could explain both. The first step was to correct the raw TE data back to equilibrium with Fo_{90} olivine to have "primary" melts with which to compare our model output. To quantify both the "source effect" and the "F effect" on the data, the model: (a) mixes two mantle sources (depleted and enriched) in varying proportions and then (b) melts that mixed source.

Appropriate enriched and depleted mantle sources are required for the modeling. There is strong evidence in highly incompatible TE ratios (Fig. 3.8) that the enriched mantle source has characteristics similar to the one giving rise to the E-Melts from LS. The mantle source of the E-Melts at LS is a 'metasomatized' source made by adding a low-F melt of Azores plume material to a depleted source (Gale et al., 2011); it is also a suitable enriched isotopic end member (Fig. 3.5). We thus selected a representative metasomatized source from LS (Gale et al., 2011) to use as our enriched mantle component. A subtle but important point is that the E-Melts from LS (and their metasomatized sources) are too high in Ba/La (and slightly too high in Rb/La, Cs/La) to be an appropriate mixing endmember for FAMOUS or N. Famous lavas. We therefore reduced the Ba concentration of the metasomatized source by 20%. The fact that Ba/La, Rb/La and Cs/La (and not Th/La or Nb/La) are strongly elevated at LS suggests that modest amounts of phlogopite in the mantle source might be influencing the behavior of these elements, as Ba, Rb and Cs are known to be compatible in phlogopite

(e.g., Green et al., 2000). Our depleted source is the DMM published by Salters and Stracke (2004), with slight adjustments to Y, Zr, Nb and Pb within their reported error (see Appendix B). Note that this mixing between a metasomatized source and a depleted source is very similar to the model of Gale et al. (2011) for the transitional LS basalts. Transitional LS basalts are remarkably alike in both isotopic composition and TE composition to Main FAMOUS lavas (see for example, Fig. 3.5).

Because of the subtle offset of N. Famous lavas in $^{208}Pb/^{204}Pb$ vs. $^{206}Pb/^{204}Pb$, we use different Pb and Nd isotopic compositions for the metasomatized sources at N. Famous and FAMOUS (Appendix B). This is reasonable given that isotopic variability exists within the E-Melts from LS and MG (Gale et al., 2011). The isotopic composition of the DMM endmember is estimated to be at the convergence of the FAMOUS and N. Famous trends.

For each sample included in the model (n=33), we minimized differences between the model output and the primary magma compositions, including TE and isotopes, by varying both (1) the proportion of metasomatized mantle in the source and (2) the extent of melting (F). The melting of the mixed sources was modeled as non-modal batch melting without garnet in the residue (see Appendix B for mantle source compositions, partition coefficient (D) values, mineral modes and melting reactions). Despite the simplicity of this model, all incompatible TE contents (20 elements modeled) are fit to better than 10% with few exceptions (Pb worse in 8 cases: avg. misfit in these cases is 13.5%, max. misfit of 19.6%; U worse in 7 cases: avg. misfit in these cases is 13.6%, max misfit of 16.7%). Also, all $^{143}Nd/^{144}Nd$ and $^{207}Pb/^{204}Pb$ and most $^{206}Pb/^{204}Pb$ and $^{208}Pb/^{204}Pb$ compositions were fit within typical analytical error, with only 10 samples slightly worse in $^{206}Pb/^{204}Pb$. The proportion of metasomatized mantle in the source of FAMOUS lavas varies between 43 and 82%, with an average of 55%, and F varies from 7.6 to 13.4% with an average of 10.3%. At N. Famous, the proportion of metasomatized mantle in the source ranges from 25 to 47%, with a mean of 37%, and F ranges from 10.4 to 13.9 with an average of 12.6%.

Several important aspects emerge from the model. First, the disparate groups seen at the FAMOUS segment, including HiBa, Main and HiTi, are all explained. In

particular, samples with unusually high Ba/La (HiBa), including the most enriched sample measured, contain high quantities of metasomatized mantle in their source (Fig. 3.9). This leads to their elevated highly incompatible TE ratios and more enriched isotopic signatures. The HiTi group, which based on major elements alone required a different parental magma, can be explained through lower extents of melting of a moderately enriched source. Lower-degree melts will be elevated in the incompatible elements while still possessing similar isotopic characteristics to the higher-degree melts, as observed in the HiTi lavas. This is also consistent with their low CaO contents, as CaO contents in primary magmas decrease as extent of melting decreases when clinopyroxene is present in the residue (e.g., Jaques and Green, 1980; Longhi, 2002).

Another intriguing outcome of the model is a correlation between extent of melting and quantity of metasomatized source (Fig. 3.10). Perhaps counterintuitively, the modeled F decreases as the quantity of enriched, metasomatized source increases. The metasomatized source has 300 ppm water (Gale et al., 2011), so one question is whether such an effect could be related to hydrous melting. Asimow and Langmuir (2003) emphasized a decrease in mean F coupled with increased mantle water contents, but their models considered constant mantle source water contents within an entire melting regime, not two different mantle components with different water contents within a single melting

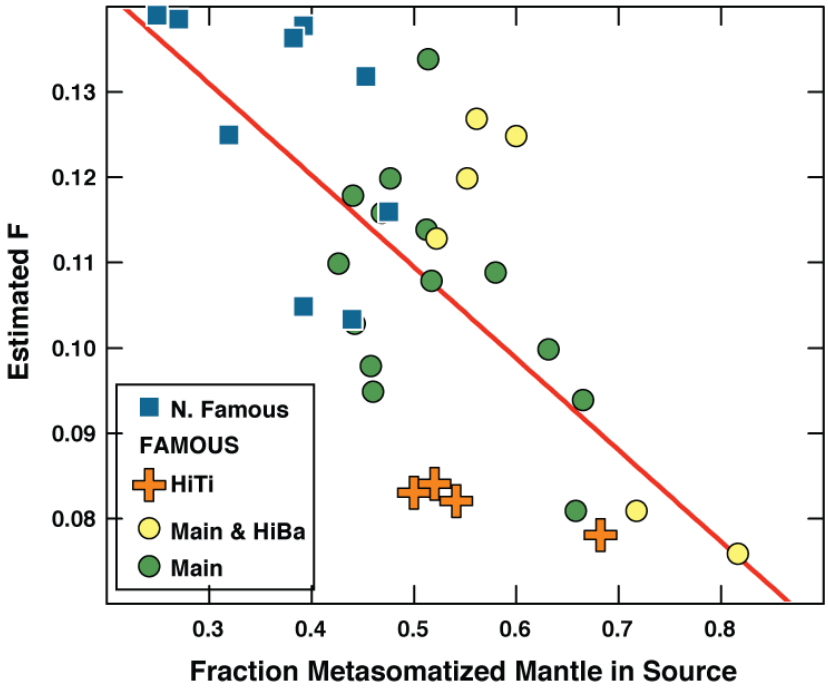

Figure 3.10: Estimated F vs. fraction metasomatized mantle in source for modeled lavas from N. Famous and FAMOUS. Shown is a least-squares regression through the data. To the first order, there is a negative correlation between the fraction of metasomatized mantle in the source and the extent of melting.

regime. As such, their modeling is not directly applicable here. Still, an important aspect does apply: a more hydrous mantle can begin melting before a dry mantle. A possible explanation, then, emerges by considering the geometry of the melting regime, based on the melting triangle and "residual mantle column" (RMC) concepts presented by Langmuir et al. (1992). At the edges of the melting regime, where extents of melting are small, the more hydrous (likely to melt) component is the dominant component. So lower extents of melting of enriched sources are found in the "wings" of the melting regime, and may rise and flow along high-porosity channels to erupt at the top of the melting regime (e.g., Hebert and Montési, 2010; Katz, 2008; Sparks and Parmentier, 1991). This would provide a mechanism for low degree melts of an enriched component to be one end member of the F vs. source correlation. Another contributing factor to the relationship of F and source may be the more refractory nature of the metasomatized source in terms of major element composition (higher Mg#; Gale et al., 2011), which would limit its total fusibility.

N. Famous is both more depleted and has a higher mean extent of melting than FAMOUS. One possible explanation would be that the N. Famous segment is so short that it is does not effectively sample the wings of the melting regime that deliver the enriched component. This would lead to a higher mean extent of melting and a less enriched source composition.

It should be emphasized that the correlation between extent of melting and source depends on the metasomatized source composition modeled by Gale et al. (2011) for LS E-Melts. Specific major element characteristics of these E-Melts (e.g., high Al, low Si) led the authors to the conclusion that they are ~7% melts. Gale et al. (2011) inverted for the source TE composition of these E-Melts assuming an F of 7%. The modeled source composition, then, is dependent upon this choice of F. Despite these uncertainties, however, there is strong evidence for the F choice made by Gale et al. (2011) for the LS E-Melts. The observed relationship between F and quantity of metasomatized source then appears justified, but involves a significant chain of reasoning.

3.4.3. Implications for the Regional Gradient near the Azores Plume

Two main classes of models have been proposed to explain the origin of along-axis geochemical gradients. The classical model for gradients around plumes involves mixing between DMM and a plume source, with plume mantle getting progressively diluted as it disperses along the ridge axis (e.g., Dosso et al., 1999; Schilling, 1975; Schilling et al., 1983). A more recent model considers the mantle a mixture of depleted and enriched components, with no compositional difference between plumes and ambient upper mantle (Ingle et al., 2010; Ito and Mahoney, 2005a; Ito and Mahoney, 2005b). These different components can melt at different depths depending on their fusibility, so changes in mantle flow can lead to variations in the rate at which these components melt. These authors argue that the most pronounced signature of the enriched components is in lavas nearest the plume where deep mantle flow is the strongest. Fast mantle flow at depth, where the enriched veins begin melting, enables a larger contribution of the enriched component. The geochemical gradient is created by variable mantle flow with distance from the plume, rather than variable mantle composition.

Neither of these models can account for the data from the ridge segments south of the Azores. Both models predict that highly incompatible TE ratios and radiogenic isotopes should decrease systematically with distance from the most plume-influenced segments. This is not the case for segments south of the Azores platform.

Instead the data require metasomatism from melts of the Azores plume to produce the geochemical observations. This metasomatized source is “plume-like” in that it has very similar isotopic characteristics to the Azores, but it has somewhat reduced TE concentrations and elevated highly incompatible TE ratios. The necessity for a metasomatic component instead of bulk plume material is made especially clear by the geochemistry of lavas from N. Famous. These basalts have TE ratios such as Nb/La and Th/La as high as the Azores platform lavas, despite much less enriched La/Sm, TE concentrations and isotopic signatures (Fig. 3.6). There must be a means to drive up the highly incompatible TE ratios in the N. Famous lavas without over-enriching their La/Sm and TE concentrations. This mechanism is the addition of the

metasomatized source.

The challenge then is to frame a physical model that is consistent with the geochemical constraints. Implicit to our model is the need to generate a metasomatized source through a mixture of a slightly refractory DMM (~4% melt removed) and a low-degree melt of the Azores plume (Gale et al., 2011). How might these two components combine? Yang et al. (2006) show that plume material upwelling near the island of Terceira is deflected to the southwest (the direction of upper mantle shear flow; see Fig. 3.11 for location of Terceira). Meanwhile, mantle melting at the nearby spreading ridges creates a slightly refractory mantle, which flows eastward (and westward), perpendicular to segment axes. Such shallow, eastward-flowing, slightly refractory mantle inevitably intersects and overlies the southwestward flowing plume material. Low-degree melts of the plume could then be injected into this depleted lithospheric mantle, creating the metasomatized source. The proximity of depleted lithospheric mantle to (presumably) hot plume material, coupled with the addition of water from the low-F melt, might act to remobilize the lithospheric mantle by decreasing its viscosity. Water especially has been shown to strongly affect mantle viscosity (Hirth and Kohlstedt, 1996). It would then flow southward as part of the asthenosphere toward MG, LS, N. Famous and FAMOUS, where it mixes with ambient DMM and gives rise to the geochemistry of the lavas.

A question is whether our model of low-F melts creating the geochemical gradient seen in MORB south of the Azores applies to other plumes. In recent data from the Galapagos spreading center (Ingle et al., 2010), E-MORB with higher highly incompatible TE ratios than the plume MORB are not found. Still, TE ratios like Nb/La and Ba/La remain as high as the isotopically enriched plume MORB for more than 200 km, whereas more moderately incompatible TE ratios like Zr/Y and Sm/Yb decrease immediately (within 50 km) away from the plume. Elevated highly incompatible TE ratios coupled with lower moderately incompatible element TE ratios, seen in the Galapagos, are the very characteristics possessed by the T-MORB near the Azores. This motivates further study of the Galapagos MORB in light of the new view of the Azores. Future numerical modeling will also provide important constraints on the physical behavior of plumes and the extent to which our model is more globally applicable.

Finally, it is noteworthy that the N. Famous segment requires its own explanation in all of these models. While lying geographically between FAMOUS and Lucky Strike, the N. Famous basalts are more depleted than either adjoining segment, violating any progressive gradient extending southwards from the Azores. We suggest the very short length of the segment influences its ability to sample the entire melting regime. If the enriched melts of the Lucky Strike and FAMOUS segments are strongly influenced by low degree melts from the "wings" of the melting regime, N. Famous may be preferentially sampling only the center of the melting regime, and hence tapping a source that appears less enriched.

3.5. Conclusions

The main conclusions of this study can be summarized as follows:

1. FAMOUS lavas show significant diversity within a single segment, indicating multiple supply of magmas along the length of the segment, and the ability of melting processes to deliver highly diverse melts over short distances and times.
2. A remarkably successful model for FAMOUS and N. Famous basalts involves variable degrees of melting of a two-component source. HiAl-LoSi lavas are an exception to this model, and are generated by mixing between Main FAMOUS lavas and a highly depleted composition present in some melt inclusions from this region (Laubier et al., 2012).
3. The enrichment signal in this region is not simply created by mixing with an Azores plume source. Instead, the enriched source is generated by adding deep, low-degree melts of Azores plume material to a mantle depleted by a small amount of previous melt removal (Gale et al., 2011). Our model involving mixing between this metasomatized mantle and a depleted mantle applies to multiple segments in this region.
4. The regional gradient in geochemistry is not systematic with distance from the Azores. N. Famous lavas are closer to the Azores and yet are more depleted in TE and isotopes than FAMOUS lavas. This suggests that the delivery of the enriched component to individual segments is more complicated than previously known.

References

Agranier, A. et al., 2005. The spectra of isotopic heterogeneities along the mid-Atlantic Ridge. Earth Planet. Sci. Lett., 238(1-2): 96-109.

Asimow, P.D. and Langmuir, C.H., 2003. The importance of water to oceanic mantle melting regimes. Nature, 421: 815-820.

Ballard, R.D. et al., 1975. Manned Submersible Observations In Famous Area - Mid-Atlantic Ridge. Science, 190(4210): 103-108.

Bougault, H. and Hékinian, R., 1974. Rift Valley in the Atlantic Ocean near 36˚50'N: Petrology and geochemistry of basaltic rocks. Earth Planet. Sci. Lett., 24: 249-261.

Bougault, H. et al., 1984. Basalts From The Atlantic Crust West Of The Barbados Ridge (Site-543, Leg-78a) - Geochemistry And Mineralogy. Initial Reports Of The Deep Sea Drilling Project, 78(AUG): 401-408.

Bryan, W.B., 1979. Regional Variation and Petrgenesis of Basalt Glasses from the FAMOUS Area, Mid-Atlantic Ridge. J. Petrol., 20(2): 293-325.

Bryan, W.B. and Moore, J.G., 1977. Compositional variations of young basalts in mid-Atlantic Ridge rift valley near Lat 36˚49'N. Geological Society Of America Bulletin, 88(4): 556-570.

Cannat, M. et al., 1999. Mid-Atlantic Ridge-Azores hotspot interactions: along-axis migration of a hotspt-derived event of enhanced magmatism 10 to 4 Ma ago. Earth Planet. Sci. Lett., 173: 257-269.

Chauvel, C. and Blichert-Toft, J., 2001. A hafnium isotope and trace element perspective on melting of the depleted mantle. Earth Planet. Sci. Lett., 190(3-4): 137-151.

Danyushevsky, L.V., Leslie, R.A.J., Crawford, A.J. and Durance, P., 2004. Melt inclusions in primitive olivine phenocrysts: the role of localized reaction processes in the origin of anomalous compositions. J. Petrol., 45: 2531-2553.

Danyushevsky, L.V., Perfit, M.R., Eggins, S.M. and Falloon, T.J., 2003. Crustal origin for coupled 'ultra-depleted' and 'plagioclase' signatures in MORB olivine-hosted melt inclusions: evidence from the Siqueiros Transform Fault, East Pacific Rise. Contrib. Mineral. Petrol., 144(5): 619-637.

Detrick, R.S., Needham, H.D. and Renard, V., 1995. Gravity-Anomalies And Crustal Thickness Variations Along The Mid-Atlantic-Ridge Between 33˚N And 40˚N. J. Geophys. Res., 100(B3): 3767-3787.

Donnelly, K.E., Goldstein, S.L., Langmuir, C.H. and Spiegelman, M., 2004. Origin of enriched ocean ridge basalts and implications for mantle dynamics. Earth Planet. Sci. Lett., 226(3-4): 347-366.

Dosso, L. et al., 1999. The age and distribution of mantle heterogeneity along the Mid-Atlantic Ridge (31-41°N). Earth Planet. Sci. Lett., 170: 269-286.

Eason, D. and Sinton, J., 2006. Origin of high-Al N-MORB by fractional crystallization in the upper mantle beneath the Galapagos Spreading Center. Earth Planet. Sci. Lett., 252: 423-436.

Escartin, J., Cannat, M., Pouliquen, G., Rabain, A. and Lin, J., 2001. Crustal thickness of V-shaped ridges south of the Azores: Interaction of the Mid-Atlantic Ridge (36˚-39˚N) and the Azores hot spot. J. Geophys. Res, 106(B10): 21719-21735.

Frey, F.A., Walker, N., Stakes, D., Hart, S.R. and Nielsen, R., 1993. Geochemical characteristics of basaltic glasses from the AMAR and FAMOUS axial valleys, Mid-Atlantic Ridge (36-37°N): Petrogenetic implications. Earth Planet. Sci. Lett., 115: 117-136.

Gale, A., Escrig, S., Gier, E.J., Langmuir, C.H. and Goldstein, S.L., 2011. Enriched basalts at segment centers: The Lucky Strike (37°17ºN) and Menez Gwen (37°50ºN) segments of the Mid-Atlantic Ridge. Geochem. Geophys. Geosys., 12(Q06016).

Green, T.H., Blundy, J.D., Adam, J. and Yaxley, G.M., 2000. SIMS determination of trace element partition coefficients between garnet, clinopyroxene and hydrous basaltic liquids at 2-7.5 GPa and 1080-1200 ˚C. Lithos, 53(3-4): 165-187.

Gurenko, A.A. and Sobolev, A.V., 2006. Crust-primitive magma interaction beneath neovolcanic rift zone of Iceland recorded in gabbro xenoliths from Midfell, SW Iceland. Contrib. Min. Petrol., 151: 495-520.

Hebert, L.B. and Montési, L.G.J., 2010. Generation of permeability barriers during melt extraction at mid-ocean ridges. Geochem. Geophys. Geosys., 11: Q12008.

Hirth, G. and Kohlstedt, D.L., 1996. Water in the oceanic upper mantle: Implications for rheology, melt extraction and the evolution of the lithosphere. Earth Planet. Sci. Lett., 144(1-2): 93-108.

Ingle, S. et al., 2010. Mechanisms of geochemical and geophysical variations along the western Galapagos Spreading Center. Geochem. Geophys. Geosys., 11.

Ito, E., White, W.M. and Gopel, C., 1987. The O, Sr, Nd and Pb isotope geochemistry of MORB. Chem. Geol., 62(3-4): 157-176.

Ito, G. and Mahoney, J.J., 2005a. Flow and melting of a heterogeneous mantle: 1. Method and importance to the geochemistry of ocean island and mid-ocean ridge basalts. Earth and Planetary Science Letters, 230(1-2): 29-46.

Ito, G. and Mahoney, J.J., 2005b. Flow and melting of a heterogeneous mantle: 2. Implications for a chemically nonlayered mantle. Earth and Planetary Science Letters, 230(1-2): 47-63.

Jaques, A.L. and Green, D.H., 1980. Anhydrous melting of periodotite at 0-15 Kb pressure and the genesis of tholeiitic basalts. Contrib. Mineral. Petrol., 73(3): 287-310.

Kamenetsky, V., 1996. Methodology for the study of melt inclusions in Cr-spinel, and implications for parental melts of MORB from FAMOUS area. Earth Planet. Sci. Lett., 142: 479-486.

Kamenetsky, V. and Crawford, A.J., 1998. Melt-peridotite reaction recorded in the chemistry of spinel and melt inclusions in basalt from 43°N, Mid-Atlantic Ridge. Earth Planet. Sci. Lett., 164: 345-352.

Katz, R.F., 2008. Magma dynamics with the enthalpy method: Benchmark solutions and magmatic focusing at MORs. J. Petrol., 49(12): 2099-2121.

Langmuir, C. et al., 1997. Hydrothermal vents near a mantle hot spot: The Lucky Strike vent field at 37˚N on the Mid-Atlantic Ridge. Earth Planet. Sci. Lett., 148(1-2): 69-91.

Langmuir, C.H., Bender, J.F., Bence, A.E., Hanson, G.N. and Taylor, S.R., 1977. Petrogenesis of basalts from the FAMOUS area: Mid-Atlantic Ridge. Earth Planet. Sci. Lett., 36: 133-156.

Langmuir, C.H., Klein, E.M. and Plank, T., 1992. Petrological systematics of mid-ocean ridge basalts: constraints on melt generation beneath ocean ridges. In: J. Phipps Morgan, Blackman, D.K. & Sinton, J.M. (Editor), Mantle Flow and Melt Generation at Mid-Ocean Ridges. Geophysical Monograph. Am. Geophys. Union, Washington, DC, pp. 183-280.

Laubier, M., Gale, A. and Langmuir, C.H., 2012. Melting and crustal processes at the FAMOUS segment (mid-Atlantic Ridge): new insights from olivine-hosted melt inclusions from multiple samples. J. Petrol., 53 (4): 665-698.

Laubier, M., Schiano, P., Doucelance, R., Ottolini, L. and Laporte, D., 2007. Olivine-hosted melt inclusions and melting processes beneath the FAMOUS zone (Mid-Atlantic Ridge). Chemical Geology, 240(1-2): 129.

le Roex, A.P., Erlank, A.J. and Needham, H.D., 1981. Geochemical and mineralogical evidence for the occurrence of at least three distinct magma types in the 'Famous' region. Contrib. Mineral. Petrol., 77: 24-37.

le Roex, A.P., Frey, F.A. and Richardson, S.H., 1996. Petrogenesis of lavas from the AMAR Valley and Narrowgate region of the FAMOUS Valley, 36˚-37˚N on the Mid-Atlantic Ridge. Contrib. Mineral. Petrol., 124(2): 167-184.

Longhi, J., 2002. Some phase equilibrium systematics of lherzolite melting: I. Geochem. Geophys. Geosys., 3.

Melson, W.G., O'Hearn, T. and Jarosewich, E., 2002. A data brief on the Smithsonian Abyssal Volcanic Glass Data File. Geochem. Geophys. Geosys., 3(4).

Michael, P.J., Chase, R.L. and Allan, J.F., 1989. Petrologic and geologic variations along the Southern Explorer Ridge, Northeast Pacific Ocean. J. Geophys. Res, 94: 13895-13919.

Nishio, Y., Nakai, S., Ishii, T. and Sano, Y., 2007. Isotope systematics of Li, Sr, Nd, and volatiles in Indian Ocean MORBs of the Rodrigues Triple Junction: Constraints on the origin of the DUPAL anomaly. Geochim. Cosmochim. Acta, 71(3): 745-759.

Ondreas, H., Fouquet, Y., Voisset, M. and RadfordKnoery, J., 1997. Detailed study of three contiguous segments of the Mid-Atlantic Ridge, South of the Azores (37˚N to 38˚30' N), using acoustic imaging coupled with submersible observations. Marine Geophysical Researches, 19(3): 231-255.

Ryan, W.B.F. et al., 2009. Global Multi-Resolution Topography synthesis. Geochem. Geophys. Geosys., 10.

Salters, V.J. and Stracke, A., 2004. Composition of the depleted mantle. Geochem. Geophys. Geosys., 5(Q05B07).

Schiffman, P., Zierenberg, R., Chadwick, W.W., Clague, D.A. and Lowenstern, J., 2010. Contamination of basaltic lava by seawater: Evidence found in a lava pillar from

Axial Seamount, Juan de Fuca Ridge. Geochem. Geophys. Geosys., 11.

Schilling, J.-G., 1975. Azores mantle blob: rare earth evidence. Earth Planet. Sci. Lett., 25: 103-115.

Schilling, J.G. et al., 1983. Petrologic and geochemical variations along the mid-Atlantic Ridge from 29˚N to 73˚N. American Journal of Science, 283(6): 510-586.

Shimizu, N., 1998. The geochemistry of olivine-hosted melt inclusions in a FAMOUS basalt ALV519-4-1. Phys. Earth Planet. Int., 107: 183-201.

Sigurdsson, H., 1981. 1st-order major element variation in basalt glasses from the mid-Atlantic Ridge - 29˚N to 73˚N. J. Geophys. Res, 86: 9483-9502.

Slater, L., McKenzie, D., Grönvold, K. and Shimizu, N., 2001. Melt generation and movement beneath Theistareykir, NE Iceland. J. Petrol., 42: 321-354.

Sobolev, A.V., Hofmann, A.W. and Nikogosian, I.K., 2000. Recycled oceanic crust observed in 'ghost plagioclase' within the source of Mauna Loa lavas. Nature, 404: 986-989.

Sparks, D.W. and Parmentier, E.M., 1991. Melt extraction from the mantle beneath spreading centers. Earth Planet. Sci. Lett., 105: 368-377.

Stakes, D.S., Shervais, J.W. and Hopson, C.A., 1984. The Volcanic-Tectonic Cycle Of The Famous And Amar Valleys, Mid-Atlantic Ridge (36˚47'N) - Evidence From Basalt Glass And Phenocryst Compositional Variations For A Steady-State Magma Chamber Beneath The Valley Midsections, Amar-3. J. Geophys. Res., 89(NB8): 6995-7028.

Sun, S.-s. and McDonough, W.F., 1989. Chemical and isotopic systematics of oceanic basalts: implications for mantle composition and processes. In: A.D.N. Saunders, M.J. (Editor), Magmatism in the ocean basins. Geological Society Special Publication, pp. 313-345.

White, W.M. and Bryan, W.B., 1977. Sr-isotope, K, Rb, Cs, Sr, Ba, and rare-earth geochemistry of basalts from the FAMOUS area. Geol. Soc. Am. Bull., 88: 571-576.

White, W.M. and Schilling, J.-G., 1978. The nature and origin geochemical variation in Mid-Atlantic Ridge basalts from the Central North Atlantic. Geochim. Cosmochim. Acta, 42: 1501-1516.

Yang, T., Shen, Y., van der Lee, S., Solomon, S.C. and Hung, S.H., 2006. Upper mantle structure beneath the Azores hotspot from finite-frequency seismic tomography. Earth Planet. Sci. Lett., 250(1-2): 11-26.

Yu, D.M., Fontignie, D. and Schilling, J.G., 1997. Mantle plume-ridge interactions in the Central North Atlantic: A Nd isotope study of Mid-Atlantic Ridge basalts from 30˚N to 50˚N. Earth Planet. Sci. Lett., 146(1-2): 259-272.

Chapter 4

The Mean Composition of Ocean Ridge Basalts

4.1. Introduction

The global ocean ridge system stretches over 60,000 km, randomly sampling the mantle while producing over 80% of Earth's volcanism. The mean composition of mid-ocean ridge basalts (MORB), therefore, provides one of the best available constraints on the composition of the upper mantle. Comparisons of the mean compositions of ocean basins, back-arc basins or plume-influenced regions may also shed light on the different processes that affect MORB compositions, including fractionation, melting differences, fluid addition and mantle source heterogeneity. Four decades of study on MORB have provided important insights on all of these processes, and yet first-order questions requiring a global perspective remain. Such questions include the relative roles of mantle temperature, mantle heterogeneity and spreading rate on erupted MORB compositions, and the importance of spreading rate to both melting and fractionation.

Global average compositions of MORB have traditionally been calculated on a small number of carefully chosen samples (e.g., Hofmann, 1988; Sun and McDonough, 1989). More recently, multiple groups have calculated averages using a more extensive set of basalt compositions (Salters and Stracke, 2004; Rubin and Sinton, 2007; Arevalo and McDonough, 2010, hereafter referred to as AM (2010)). These global studies, however, either: (1) simply averaged samples to estimate a global mean (AM (2010)), a method prone to biasing the result toward better-sampled regions, or (2) averaged basalts over "ridge sections" of hundreds of kilometers containing multiple tectonic segments (Rubin

An amended version of this chapter, in collaboration with Colleen A. Dalton, Charles H. Langmuir, Yongjun Su and Jean-Guy Schilling was submitted to the journal Geochemistry, Geophysics, Geosystems in July, 2012.

and Sinton, 2007). In case (2), the mean ridge section values were released in the supplement without the original dataset from which the average numbers were derived, limiting the future utility of the database.

Su (2002), in a pioneering attempt to characterize the ocean ridge system at the segment scale, defined a global set of individual ridge segments and carefully compiled the highest-quality geochemical data possible. Still, his study was somewhat hampered by the lack of a software program such as GeoMapApp that provides access to the best-available global bathymetry and a ready means for digitizing the segment catalog. Like Rubin and Sinton (2007), Su (2002) released average segment values but not the individual analyses from which those segment averages were derived. Furthermore, during the decade since his study there has been a dramatic increase in the availability of ICP-MS trace element data, including over 1000 analyses from the Schilling (Kelley, Kingsley and Schilling, in prep) and Langmuir laboratories (this study).

The present conditions are ideal for the creation of a comprehensive, global database of the ridge system at the segment scale, in the spirit of Su (2002) but with an improved digital catalog of ridge segments and an unparalleled major and trace element dataset. Toward this end, we: (1) define 771 individual ridge segments that constitute the global mid-ocean ridge system, including segments at back-arc spreading centers; (2) assign each sample to its proper ridge segment; (3) perform a series of systematic and careful checks for data quality; (4) calculate a mean composition for each ridge segment; (5) calculate global and regional mean compositions. Along with this study, we are releasing both our segment average values and the individual sample analyses in our compilation so that others may readily use the database for their own scientific pursuits. Over 700 unpublished high-quality ICP-MS analyses from around the globe are published here, with a particular highlight being a comprehensive dataset from the remote Gakkel ridge in the Arctic. In the following text, we address the creation of the database, the calculation of averages, and the implications of these findings. Perhaps most significantly, however, we release the carefully compiled database itself - a contribution with a reach far beyond this paper.

4.2. Creating a Global MORB Database at the Segment Scale

4.2.1. Defining Ridge Segments

First, we identified the global system of ridge segments. Ridges are segmented on a variety of length scales, from first-order segmentation due to active transform faults to second- and third-order segmentation caused by non-transform offsets, overlapping spreading centers and even "deviations from axial linearity" (Macdonald, 1982; Langmuir et al., 1986). Identifying ridge segments globally is not straightforward, both because of the various types of ridge segmentation and because of variable-quality bathymetry. In regions where many cruises have taken place, high-resolution bathymetry is available and identifying ridge segments is simple (see Figure 4.1a).

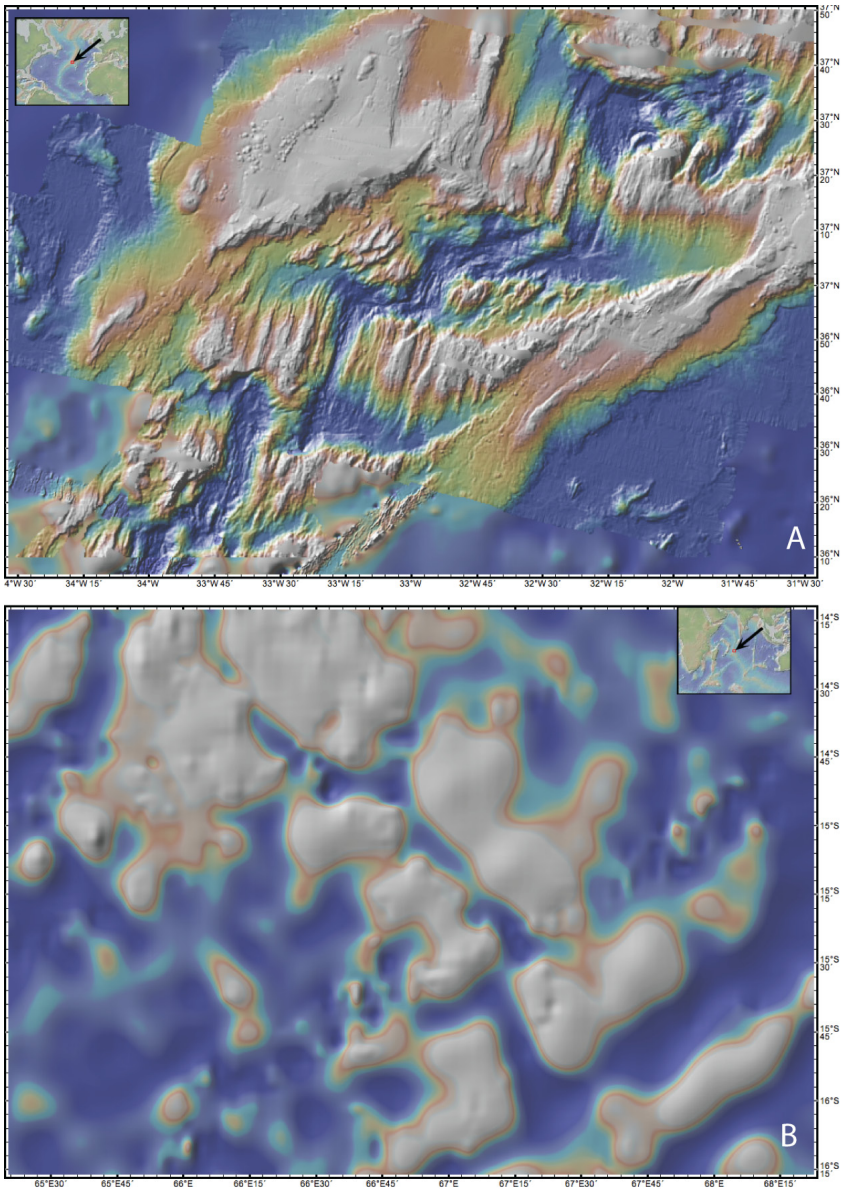

Figure 4.1: Sample bathymetry available from the software GeoMapApp. (a) a region of the Mid-Atlantic Ridge (36°-37°N) with high-quality, multi-beam bathymetry (Cannat et al., 1999; Escartin et al., 2001). (b): a region of the Central Indian Ridge (14°-16°S) for which only satellite bathymetry is publicly available. Both regions are shown at approximately the same scale. Segment selection is easier along sections of the ridge with high-quality bathymetry available.

For other regions, we must rely on satellite bathymetry and the detailed ridge architecture

is lost, making such identifications much more challenging (Figure 4.1b). Details of our ridge segment selection process will be discussed elsewhere (Langmuir et al., in prep).

In short, we used the software GeoMapApp to aid us in manually defining 771 individual ridge segments globally (extending a length of 60,864 km), including back-arcs. These ridge segments (lines along the spreading axis) were saved as ASCII text files. The ASCII files output by GeoMapApp consist of tables with evenly spaced points along the given line segment, including latitude, longitude and elevation information. The spacing of the points depends on the quality of the bathymetry in the region. Importantly, the ASCII files provide all the necessary information to precisely calculate length and mean depth for every segment. The length of individual segments ranges from 6.6 to 375.8 km, with a median length of 66.7 km, and the mean depth spans from 5382 m below sea level along the Mid-Cayman spreading center to 1025 m above sea level at Iceland.

Once the ASCII files were read into Matlab, we defined a rectangular polygon with a width of 10 km on either side of the segment axis around each segment. The 20-km polygon width was chosen to include as many samples as possible while excluding samples located too far from the ridge axis. We also developed a naming scheme consisting of 4 letters followed by numbers to identify the individual segments. For example, SWIR12 indicates that the segment is the 12^{th} segment in our sequence of polygons along the Southwest Indian Ridge. The full catalog of ridge segments is provided in the Appendix.

For 692 of the 771 ridge segments in our global database, spreading rate was calculated at the midpoint of each segment using the rotation poles and angular velocities from NUVEL-1A (DeMets et al., 1994) and the equations for relative motion on a plate boundary (e.g., Fowler, 2008). Spreading rates for back-arc spreading centers, and for the Juan de Fuca ridge were calculated from NR-MORVEL56 (Argus et al., 2011), which includes the plate motions of 31 additional small plates defined by Bird (2003).

4.2.2. Major Elements

Our approach to assembling the dataset of major element compositions was to compile all available analyses from several sources, including PetDB (Lehnert et al., 2000), GeoROC (for subaerial Iceland sample data) and unpublished data, and to retain only high-quality analyses of samples located on-axis by implementing several selection criteria. To avoid potentially excluding basalt samples that are misclassified in PetDB, data were downloaded on March 15, 2010 with the only requirement that at least one major element oxide be reported. Samples with compositions far outside the basaltic range were removed at a later stage through filters applied to the major elements, as described below. This resulted in an initial database size of 36,734 glass and whole rock samples. From this compilation we immediately eliminated Deep Sea Drilling Project (DSDP) and Ocean Drilling Program (ODP) off-axis samples, and samples from land outcrops (e.g., data on the Palisades are included in PetDB). We then added 1560 unpublished data and 5512 data for Iceland from GeoRoc. This updated compilation contained 33,695 samples.

We excluded any sample not located within a segment polygon, an efficient means of eliminating samples significantly off-axis. Before making these cuts, however, we visually inspected the points outside of polygons on a global map. In the case where samples were clearly mislocated (e.g., in Mexico), we looked up the references and fixed the latitude/longitude issue manually (usually a sign issue or a decimal to minutes conversion issue). On the rare occasion that a sample fit in more than one polygon (occasionally our polygons overlap on the edges), we checked the sample location on the map to determine the appropriate polygon. This usually required a slight narrowing of polygon width to avoid the overlap and force the sample into the more appropriate polygon (polygon widths are reported in the segment catalog).

The ability to link each sample to an individual ridge segment is a unique and important aspect of the current study. Our approach provides the ability to choose the scale of consideration, whether the local segment scale or a more regional scale by stringing segments together. The segment-scale approach has also proven invaluable for calculating the global average compositions, as it allows for weighting by factors such as segment length or spreading rate, discussed further below.

For the major element data, we required each sample to have Fe (as FeO and/or Fe_2O_3), SiO_2, Al_2O_3, MgO, TiO_2, Na_2O, CaO and K_2O. Removing off-axis samples located outside a segment polygon and/or missing major element oxides reduced our database by nearly half. We then checked for and eliminated duplicates, which were defined as having identical latitude, longitude, SiO_2, Al_2O_3, MgO, TiO_2, Na_2O, CaO, and K_2O. Duplicates were most often encountered with electron microprobe data collected at the Smithsonian; there is often overlap in PetDB between data in Ph.D. theses and the Smithsonian glass file (Melson et al., 2002).

After these selection criteria were applied, the database contained 16,964 samples. We calculated the total FeO content (FeO_T) for all samples in the database according to a systematic procedure. If FeO_T was reported, we used it. If FeO was reported and Fe_2O_3 was not, we used FeO for FeO_T. If FeO was not reported and Fe_2O_{3T} was, we used $0.9*Fe_2O_{3T}$ to calculate FeO_T. If both FeO and Fe_2O_3 were reported, we used FeO + $0.9*Fe_2O_3$. If neither FeO nor Fe_2O_{3T} were reported and Fe_2O_3 was, we used $0.9*Fe_2O_3$.

With all oxides in the appropriate form, we then applied, where possible, “interlaboratory bias correction factors” to each analysis, using the laboratory information reported by PetDB for each reference. Different laboratories calibrate their analyses to different standards, which often leads to a significant and systematic offset between analyses from different labs. Because these interlab differences can be large, it is important to apply corrections to the data in order to make them consistent with one another. Our interlab bias corrections are primarily derived from the extensive work of Su (2002), who used multiple approaches to estimate interlab bias correction factors, including: 1) Analyzing a geo-standard used by other laboratories as an unknown, calibrated to the Langmuir laboratory standard; 2) Comparing different analyses on the same samples; 3) Comparing regional averages for groups of samples; 4) Comparing regional correlations for analogous elements; 5) Comparing geo-standard values. The latter three were used only when the first two methods were not applicable, and in some cases several methods were combined to give more robust results.

Of over 12,000 glass analyses in our final database (described below), nearly half

come from either the Smithsonian (W. Melson) or the laboratory of C.H. Langmuir. We therefore focused particular attention on assessing the interlab bias factors between the Smithsonian and the Langmuir lab, updating the values in Su (2002). To do this, we analyzed VG-2, the Smithsonian glass standard, 195 times (in different sessions) as an unknown, normalizing it to the Langmuir lab in-house standard VE-32 (details of our microprobe method are given in Gale et al., 2012, in review). We then calculated the offset between our value of VG-2 and the Smithsonian value of VG-2 to estimate interlab bias factors to apply to the Smithsonian dataset. To confirm our factors, we also reanalyzed a subset of the samples that Melson et al. (2002) analyzed, using the same exact probe mounts (Figure 4.2a). When comparing these analyses, and also analyses from both laboratories on samples from a given region (Figure 4.2b,c), it is clear that our interlab bias factors are appropriate and make the datasets consistent with each other. Estimated interlab bias correction factors for major elements for the Smithsonian and

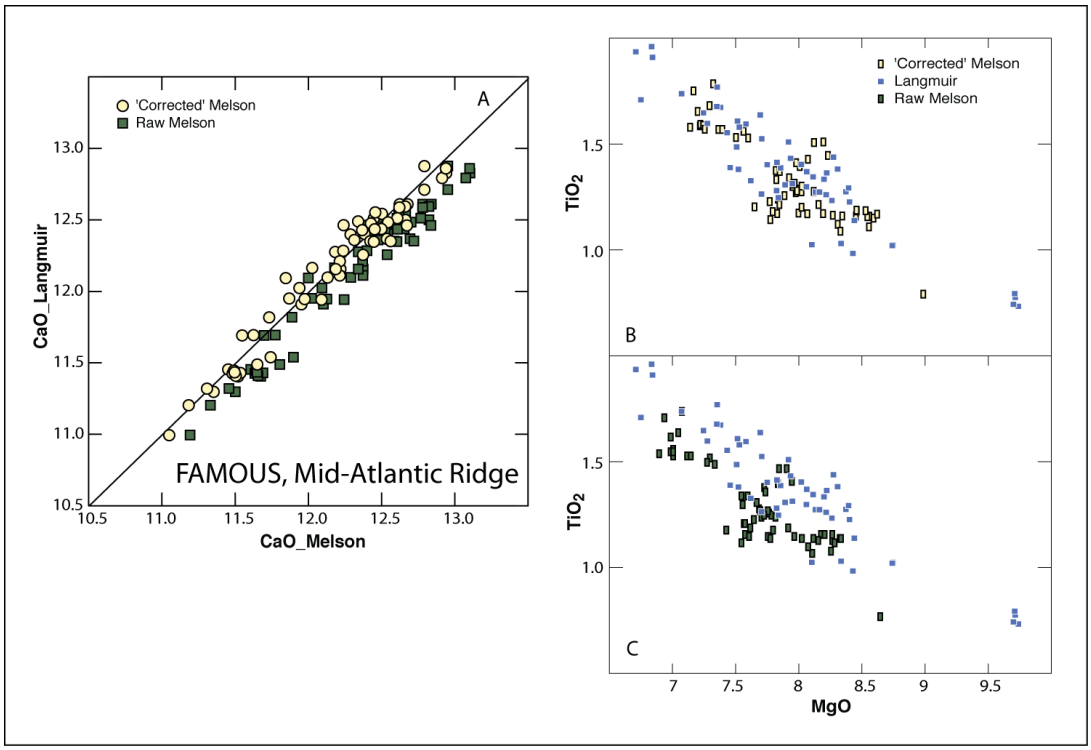

Figure 4.2: (a) Measurements of CaO (wt. %) from both the Langmuir and Smithsonian laboratories on identical samples from the FAMOUS segment, with a 1:1 line for reference. (b,c): TiO_2 (wt. %) versus MgO (wt. %) data from the Smithsonian and Langmuir laboratories on samples from a selected region of the Central Indian Ridge. The offset between laboratories is eliminated once proper interlaboratory bias corrections are applied. Without the application of such factors, apparent chemical differences in lavas, caused simply by analytical procedures, could be erroneously interpreted as true differences.

other major laboratories producing data on ridge basalts are provided in the Appendix. For methods where data quality limited an accurate assessment of a bias factor, a correction factor of 1 was assigned (i.e., no correction). More than 92% of the glasses in our database have been assigned interlab bias factors.

Once interlab bias factors were applied to the major element data, we employed a broad filter to exclude samples with major element contents far outside of the basaltic range (e.g., palagonite analyses were present in the original dataset). We required: SiO_2: 45-77 wt.%, Al_2O_3: 10-19 wt.%, MgO: <12 wt.%, TiO_2: 0.5-5 wt.%, FeO_T: 3-20 wt.%, CaO: <14 wt.%, K_2O <3 wt.%, and Na_2O <6 wt.%. A sample with any oxide outside of this range was eliminated from the database. Particular attention was paid to FeO_T at this stage, as we were wary of erroneously high values of FeO_T that could result from our calculation of $FeO_T = FeO + 0.9*Fe_2O_3$ for cases where the reported FeO was in fact the total FeO (and therefore FeO_T = FeO). For 124 samples with FeO_T >17 wt.%, we manually checked their Fe data. Of these, 21 samples were found to have erroneously high Fe contents due to the misreporting of the data in PetDB (i.e., FeO was actually FeO_T), and we adjusted the Fe contents of those samples accordingly.

The final step in the data selection process for major elements involved a check on the total oxide content, as poor sums can indicate poor data quality. The sum was defined as: $FeO_T + SiO_2 + Al_2O_3 + MgO + TiO_2 + Na_2O + CaO + K_2O + MnO + P_2O_5$. Since MnO and P_2O_5 are not analyzed by all laboratories (a notable example being the lack of MnO data from the Smithsonian), care was needed to avoid erroneously eliminating data for low sums caused by missing MnO or P_2O_5. To address this, if a sample was lacking data for either MnO or P_2O_5, we calculated placeholder values strictly for the sum calculations. If no MnO was reported, we estimated $MnO = FeO_T/54$. If no P_2O_5 was reported, we estimated it using a polynomial best-fit equation based on K_2O contents. The sum was then calculated as defined above, and any analyses with sums <98.5 wt. % or >101 wt. % were eliminated.

It is also important to account for variable H_2O contents, especially given that we include back-arc basins in our compilation. We therefore calculated an estimated H_2O

value: H_2O_{est} = 1.5*K_2O for open-ocean ridge basalts. For back-arcs, we customized the H_2O formulas based on observed data, ranging from 14.1* K_2O in the Lau basin to 2* K_2O for most of the segments in Scotia. Our estimated H_2O formulas for back-arcs are provided in the Appendix. For some high-K_2O samples, H_2O_{est} is larger than expected from the solubility of H_2O in basaltic magmas. Solubility has a large dependence on pressure of eruption, so we estimated a maximum H_2O (H_2O_{max}) for each sample based on its eruption depth (Dixon et al., 1995; Newman and Lowenstern, 2002). In the rare cases where H_2O_{est} was larger than H_2O_{max}, we set H_2O_{est} = H_2O_{max} (~200 glasses and 50 whole rocks; noted in the tables in the Electronic Appendix).

In the final version of the major element dataset, the measured oxide contents were re-normalized to a customized sum of 99.8 wt.% - H_2O_{est} for each sample. The selection of 99.8 wt.% instead of 100 accounts for the trace elements (e.g., Ni, V, Cr) not included in the sum formula. This final major element dataset was then separated into two files, one containing the glass samples and one containing the whole rocks. Both the re-normalized and the raw data are provided in the Electronic Appendix.

Over 1800 new major element analyses are being published with this study. The major elements were collected by either DCP (direct current plasma) or EMP (electron microprobe) in the Langmuir laboratories at Lamont-Doherty Earth Observatory and Harvard University. DCP protocol followed that described by Klein et al. (1991), and EMP techniques are described in Gale et al. (2011).

4.2.3. Trace Elements

The above procedures provided interlab-bias corrected, filtered, renormalized major element data, with each sample assigned to a given ridge segment (polygon). The next step was to add trace element data to our database. On January 11, 2011, we downloaded a file from PetDB containing 23,713 samples with at least one trace element measured. As with the major elements, we did not want to potentially exclude data by requiring a basalt classification in PetDB. We then had to carefully merge this published trace element data from PetDB with extensive unpublished ICP-MS trace element data from Schilling (Kelley, Kingsley and Schilling, in prep), Langmuir's laboratory, and two Ph.D.

theses (Bézos, 2003; Standish, 2005), as well as analyses on Iceland samples from Georoc. We also became aware of important published trace element datasets that had been omitted from PetDB, such as the Sun et al. (2003) and Sun et al. (2008) datasets used extensively in AM (2010); we manually added these data to our main dataset.

From this compilation, we eliminated off-axis samples (not within a segment polygon). Next, we excluded any sample with the PetDB "Rock" classification of plutonic, metamorphic and/or ultramafic. We also removed any samples that did not have at least one of the following elements: Ba, Be, Ce, Co, Cr, Cs, Cu, Dy, Er, Eu, Ga, Gd, Hf, Ho, La, Li, Lu, Mn, Mo, Nb, Nd, Ni, Pb, Pr, Rb, Sc, Sm, Sn, Sr, Ta, Tb, Th, Ti, Tl, U, V, W, Y, Yb, Zn, Zr.

Merging the published and unpublished trace element data was a massive task, largely because we wanted to avoid having duplicate analyses (including glass/whole rock duplicates) in our dataset. For example, much of the Schilling (Kelley, Kingsley and Schilling, in prep) and Langmuir unpublished ICP-MS data are on samples for which non-ICP-MS data have already been published in PetDB. A critical first step to allow us to detect such duplicates was to convert all the sample names in our various unpublished data spreadsheets to the appropriate "PetDB" format (e.g., EN026 16D-1 in Schilling's file became END0026-016-001). We then checked for name matches (same Sample ID and material) within the compiled file, and if one sample had ICP-MS data and the other did not, we eliminated the sample with non-ICP-MS data. If both samples had ICP-MS data, or neither one had it, we flagged both analyses for manual inspection. In total, 575 samples were manually checked, and we used the following criteria to handle these duplicates: (1) for samples with the same Sample ID and material with different trace elements analyzed, we manually merged the analyses and marked the Sample ID with "Merged" in the Notes column; (2) for samples with the same Sample ID and material and identical elements analyzed, we selected one analysis using a hierarchy similar to that in PetDB (if it was Langmuir unpublished data, we kept it; otherwise the most recent data were kept); (3) in rare cases with same Sample ID and material reported from the same laboratory, we kept both analyses.

We also encountered duplicates having the same Sample ID but different materials: one analysis was done on a whole rock and the other on glass. This was the case for 1516 samples (758 duplicate pairs). For 261 such pairs, the whole rock trace element data were redundant, so we deleted the whole rock analysis and kept the glass analysis. We manually checked the other 497 whole rock-glass duplicate pairs by comparing their major and trace elements. If the analyses on elements in common were within 5%, we merged the whole rock and glass trace element analyses, and indicated the merge in the Notes column. In the case where the major or trace elements indicated differences too large to justify merging the analyses into one, we kept the highest-quality trace element analysis and deleted the other analysis.

With our trace element database compiled and duplicate-free, the next step was to match our trace element analyses with their interlab-bias corrected, re-normalized major element analyses. We did this through matching Sample ID and material. In the case where a sample with a trace element analysis does not have a corresponding major element analysis, we kept it and assigned it to the proper ridge segment using its geographic location. For samples that previously had their major element analysis cut for being "out of the basaltic range" (see our filters above; e.g., SiO_2 between 45 and 77%), we excluded their trace element analyses for consistency.

After eliminating off-axis samples, non-basaltic samples and duplicates, 7078 samples remained in the database. Given the variable precision associated with different measurement techniques, we opted to high-grade our database to include only samples with trace elements measured by ICP-MS, LA-ICP-MS, MC-ICP-MS, ID, ICP-AES, and DCP. This was in large part possible due to the enormous quantity of high-quality unpublished trace element data we had access to from the Schilling (Kelley, Kingsley and Schilling, in prep) and Langmuir laboratories, as well as two unpublished Ph.D. theses. In particular, ICP-MS trace element data from the Gakkel Ridge, the Lau back-arc basin, the Afar region and portions of the Central and Southwest Indian Ridges have not been available for any prior compilation of global MORB data. Indeed, of the 3971 trace element analyses in our high-graded file, 1567 (or over 39%) are unpublished. To put that in perspective, the recent MORB compilation of AM (2010) contained 792

analyses in total, of which 79 were previously unpublished. We include more than 792 just considering our access to unpublished solution ICP-MS analyses, the vast majority of which are released here or in a forthcoming paper (Kelley, Kingsley and Schilling, in prep). The unpublished solution ICP-MS trace element data released in this study were collected over a period of years in the Langmuir laboratories at the Lamont-Doherty Earth Observatory and Harvard University. The analytical techniques and accuracy are documented in Gale et al. (2011).

Figure 4.3 is a global map showing the location of samples with trace element data in this study (red circles) compared with the location of samples with trace element data in the recent AM (2010) study (yellow circles). Note in the AM (2010) compilation the paucity of data from the Reykanes and Kolbeinsey sections of the Mid-Atlantic

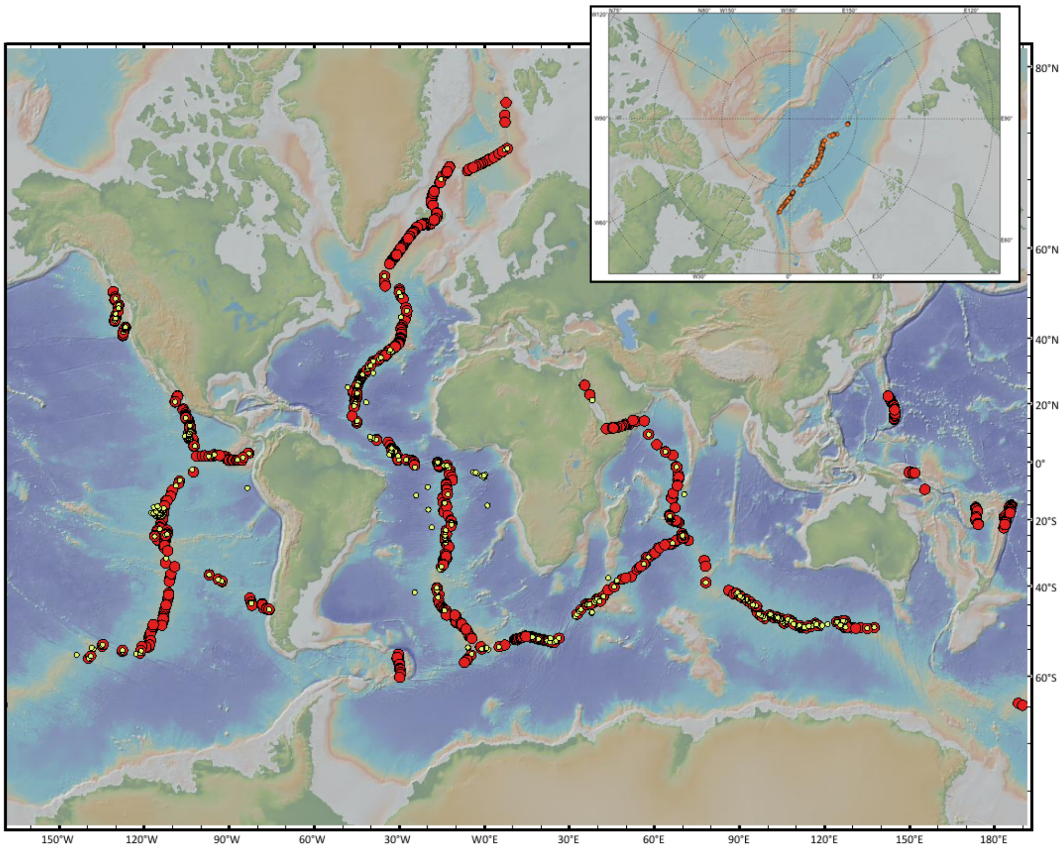

Figure 4.3: Comparison of the locations of samples with trace element data used in this study (larger red circles) and those used in Arevalo and McDonough (2010) (smaller yellow circles). Note that the samples used in this study are on-axis, include back-arc basins, and cover regions of the ridge system not included in the AM (2010) study, including near Iceland, Afar, portions of the Central Indian Ridge and the Gakkel Ridge. Bathymetry from GeoMapApp (Ryan et al., 2009).

Ridge, the Central Indian Ridge, Pacific-Antarctic Ridge, Afar, and Gakkel ridge. Note also that they included many off-axis samples in their study, but excluded back-arcs. Our dataset is far more comprehensive - not just in total number of samples but also in the global distribution of those samples.

As a sidenote, Jenner and O'Neill (2012) released 600 LA-ICP-MS trace element analyses on basaltic glasses from the Smithsonian collection, well after we had compiled our final data set and removed duplicate samples. Because their dataset was so extensive, however, we felt it important to consider their data. Of their 600 analyses, 253 are located in our segment polygons, and we augmented our database with analyses from ridge segments that otherwise had no trace element data (n=116). The remaining samples (n=137) were not included, as we already had excellent coverage for those segments.

To finalize our dataset of ~4,000 high-grade trace element analyses, we screened for quality by manually checking several 'canonical' trace element ratios (for non-back arc samples only) to identify possible problem elements. In particular, we flagged samples with: Th/U<1.5; Nb/U<25, or >70; Ba/Rb>18 or <7; Pr/Pb<1.6; Ce/Pb<11; Nb/Th>23; Li/Yb>2.5 or <1; Ta/Th>1.5; Nb/Ta<12.3 or >18.9; Ba/Cs<600; and Mo/Ce>0.05. If a particular ratio was out of range for a sample, we considered other ratios to identify the problem element. For example, if Th/U was off, Nb/U was off and Nb/Th was fine, we eliminated the U value. The Nb/Th ratio was often plagued by low Th issues (likely an intercept problem on the calibration curve for very depleted samples). The Ta/Th ratio was useful in identifying bad Ta values. In the case where the Ba/Rb ratio was out of range, we deleted both Ba and Rb. In out-of-range ratios involving Pb, we deleted Pb as it is prone to contamination. We used the Li/Yb ratio to search for bad Li values. For any samples with a Mo/Ce ratio >0.05, their Mo value was deleted. We also manually checked analog elements, such as Zr-Sm, Hf-Nd, and Y-Ho to identify outliers. In each case of an elemental value being deleted, it has been indicated in the Notes column.

4.2.4. Isotopes

A final step was to add isotope analyses to our high-graded trace element database. We added any Sr, Nd, Pb or Hf isotopic data that existed for samples in our trace element

database, including both published data available on PetDB and values from the Schilling unpublished file (Kelley, Kingsley and Schilling, in prep.). A spot check was performed to remove any obvious outliers, but nearly all data were kept.

4.3. Calculating Meaningful Average Compositions

The goal of calculating an "average" composition of ocean ridge basalts is complicated by issues such as uneven sampling, whether or not to include hotspot-influenced or back-arc basalts, and skewed distributions. Here we address the various challenges associated with arriving at an average.

Issue 1: Uneven sampling

Certain regions of the ridge system have been much more extensively sampled than other regions. The better-sampled regions exist partly due to logistics (i.e., it is easier to get to/work in some regions of the world than others), and partly due to the greater interest in areas erupting unusual basalt compositions, such as hotspot-influenced ridge segments. Simply averaging all individual samples skews the result toward areas of the ridge that happen to have more samples. Most studies (e.g., AM (2010), Hofmann, 1988) used individual samples to arrive at their reported averages. Owing to our much more comprehensive data coverage, and our global segment catalog, we are able to adopt a more robust approach and calculate "segment values" for each of our ridge segments with data. Since each sample is already assigned to a particular ridge segment, we can readily average the samples within each ridge segment to calculate a segment value. This approach is similar to that used by Su (2002).

Calculating major element segment values

For major elements, it is necessary to be especially wary of uneven sampling. Quite often a particular dredge or rock core location will be sub-sampled with 10, 15 or even 30 glass chips analyzed from that one location. As an example, 16 glass chips from sample AII0092-2-005 were analyzed by Melson et al. (2002), all of which were given an identical "magma batch code". Melson et al. (2002) developed the magma batch coding system "to attempt to identify a magma type (magma batch)"; otherwise,

as they note, “average values for oceans or regions might be distorted by inclusion of such identical analyses.” To avoid such distortion in our dataset, we calculate segment average values for major elements by first averaging the samples from one location, and then averaging these location averages within each segment. In the best-sampled case of the 9ºN segment of the EPR (EPRR29 in our ridge segment catalog), 641 unique sample locations are used to arrive at a segment mean. For other segments, there is just one sample location used. By: (1) calculating major element segment means by averaging the sample location averages and (2) calculating a global mean by averaging the segment averages, our approach reduces the effects of uneven sampling on the mean. Note that we only use glasses (not whole rocks) for our major element averages.

Calculating trace element segment values

For trace elements, other aspects prove challenging. While multiple analyses of the same rock or flow are less of a concern, there is the issue of different elements being analyzed on different samples. For example, within a single segment, there may be Ba data on six samples and Cs data on only three of those samples. And if the three samples lacking Cs data were chemically distinct, then the mean Cs would not be as representative as the mean Ba, possibly resulting in a segment Ba/Cs ratio that deviates from those in natural samples. This concern is lessened by the use of mostly ICP-MS data in our compilation, where chemical analyses are much more complete, but data gaps do exist.

When faced with this unavoidable situation, there are two options. One option is to estimate the missing Cs data using analog element relationships and then calculate a segment average that includes the estimated Cs values. This option may result in more reasonable trace element ratios for each segment, but requires assumptions about analog elements and the creation of synthetic data. A second option, and the one used in this study, is to accept the data gaps and calculate a trace element segment average using any available samples that contain data for a particular element. The appeal of this approach is that no synthetic data are created and no assumptions are required. As will be shown below, we have confidence that the data gaps do not strongly affect the global and regional mean compositions (in terms of concentration) we report. It must

be noted, however, that a consequence of option 2 is that our individual segment trace element values cannot necessarily be used directly for considering trace element ratio variations.

As with the major elements, our trace element segment averages provide a means of reducing the bias in global mean values that may be introduced by uneven sampling. A single chemical value is assigned to every segment possible, from the heavily sampled 9°N EPR segment that contains 147 samples with trace element data to those segments that contain only one sample. This ensures that our mean value is not calculated with 9°N on the EPR having 147 times the relative weighting compared to other less sampled segments.

Calculating isotopic ratio segment values

To arrive at meaningful isotopic ratios for each segment, we weighted the isotopic ratio of each sample by its elemental concentration. For example, for all samples with $^{143}Nd/^{144}Nd$ values from a given segment, we multiplied the $^{143}Nd/^{144}Nd$ ratio by the Nd concentration for that sample. We then summed the weighted Nd ratios and divided by the total Nd concentration (of samples with isotopic data), to arrive at the segment $^{143}Nd/^{144}Nd$ value. Our segment average values for major (n= 465), trace elements (n= 455) and isotopic ratios (n=308) are provided in the Electronic Appendix.

Issue 2: Skewed distributions and the meaning of "mean"

Assuming our segment values are robust, there is another issue to consider with regard to the distributions of those segment values. The distributions of highly-incompatible trace elements such as Ba, Th, U, Nb, etc., in ocean ridge basalts can span many orders of magnitude and are positively skewed. This is certainly the case for our segment means, as a small number of segments are highly enriched (Figure 4.4a). The skewness lessens considerably for the more moderately incompatible elements, but still remains (Figure 4.4b). As pointed out by AM (2010), it is well known that positively skewed distributions can be converted to more normal, or Gaussian distributions, by taking the logarithm of the variable in question. This is referred to as a "log-normal" distribution.

It is important to recognize that the mean of the original distribution (arithmetic mean), and the mean of the log-normal distribution (geometric mean) are not the same value. The log-normal mean values of a highly-incompatible element more closely approximate the median value of the distribution, being much less affected by the long positive tail in the original distribution. AM (2010) use log-normal mean values to arrive at their proposed chemical composition of global MORB (c.f., Table 2, AM (2010)). We emphasize that both the true mean and the log-normal mean of the distributions provide important information for addressing questions about the composition of global MORB. Below we explore the utility of the log-normal mean but argue that the true mean provides the actual composition of the global ocean crust. The confusion lies in what is meant by "average ocean crust".

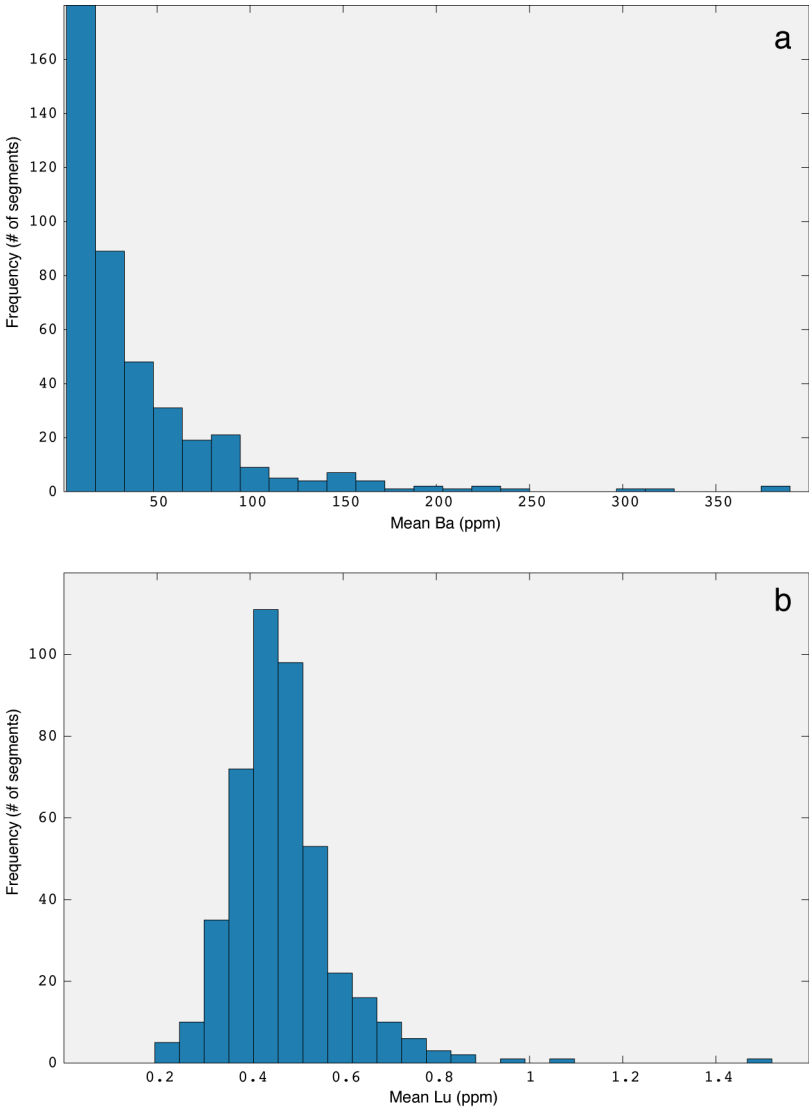

Figure 4.4: Comparison of the frequency distribution of the concentration of Ba (a), a highly incompatible element, to that of moderately incompatible element Lu (b) in global ridge segments. Note that both distributions are positively skewed, but the skewness is much more pronounced in highly incompatible elements than in moderately incompatible elements because highly-incompatible element concentrations span many more orders of magnitude (e.g., factor of 260 change in Ba versus a factor of 8 change in Lu). The non-Gaussian distribution of the ridge segment trace element data results in two distinct means: the log-normal (geometric) and true (arithmetic) mean, both of which provide insights on the composition of ridge basalts. See text for more details.

True mean

The true mean of the population is meaningful, even with skewed distributions, when the question is "What is the concentration of a given element in the ocean crust reservoir?" In this case, the skewness of a distribution matters not. In an extreme example, if 98% of the ocean crust had 5 ppm Ba and 2% of the ocean crust had 1000 ppm Ba, that 2% is extremely important when considering the concentration of Ba in the total ocean crust.

Calculating an accurate true mean

An important aspect to our calculation of means is that we have information about segment length and spreading rate in addition to chemical composition. For calculation of total ocean crust composition, segment length and spreading rate need to be taken into account. The contribution of a long, fast-spreading ridge segment to the total ocean crust budget is larger than the contribution of a short, ultra-slow spreading segment. In particular, on a per-volume basis, the ocean crust reservoir is currently pulled toward the EPR composition, because the annual production of EPR-type crust is 10x more than that of, say, Gakkel-type crust. As such, when calculating the average composition of the ocean crust (in terms of the mean concentration of each element residing in the crustal reservoir), we weight the segment values by both spreading rate and length. The ability to weight by spreading rate and length is another advantage of our "segment means" approach, as such weighting is impossible when considering individual samples.

An accurate true mean for isotopic ratios requires an additional step. As mentioned, each segment isotopic value has already been weighted by concentration. For the global averages of isotopic ratios, then, each segment must be weighted by concentration in addition to spreading rate and length. There is a small complexity that arises with regard to weighting the segment isotopic ratios by segment concentrations. Quite often the average segment concentration of, for example, Nd is calculated from many more samples than have measured Nd isotopic ratios. If the average Nd concentration of the samples with measured isotopes differs from the average Nd concentration of all the

samples, then weighting using the segment concentrations may be invalid. To check this, we calculated the true mean of each isotopic ratio in two ways: (1) weighting the segment isotopic ratio by the segment element concentration (and spreading rate and length); (2) weighting the segment isotopic ratio by the average element concentration of only those samples with measured isotopic ratios (and spreading rate and length). We find that there is no significant difference between the two methods (e.g., global average $^{143}Nd/^{144}Nd$ is 0.513074 vs. 0.513073), increasing confidence in the isotopic ratios we report.

Log-normal mean

The log-normal mean addresses the different question: "What is the typical concentration of a given element in ridge basalts?" The true mean of highly incompatible element distributions is not useful for answering this question, as the positive skew distorts the true mean higher than typical values. Instead, the log-normal mean gives a better sense of the 'central tendency' of the data. As the log-normal distribution is also Gaussian, the 2-sigma standard deviation can be used to estimate 95% confidence (meaningful only with normal distributions, see below) on the typical concentration of a given element in ridge basalts. The log-normal mean can be interpreted as the most likely basalt composition encountered while sampling the length of the ridge system.

Calculating an accurate log-normal mean

In calculating the typical composition of basalts erupted along the ridge system, spreading rate is not important. Spreading rate would only be important for an estimate of the typical basalt composition of the entire ocean basin. Segment length still matters, however, as one is obviously more likely to encounter the basalt compositions erupting at longer segments than at shorter segments. Therefore, we weight our log-normal mean by segment length to arrive at our "typical" basalt composition.

In order to estimate a 95% confidence interval on the distribution of a particular element while taking into account segment length, we calculated the trace element content of each km of ridge (for which data exist) using the segment means and segment length. For example, if a segment is 150 km long with a mean Ba content of 14.2 ppm,

this would lead to 150 Ba values of 14.2 (each km of that segment is assigned the mean Ba content of the segment). We repeated this process for every segment and then calculated the log-normal mean and two-sigma standard deviation (95% confidence interval) to characterize the range of Ba along the length of the ridge system (36,302 km with Ba data). In doing this, one can see both the typical (log-normal mean) value, and how variable the data for a given element are around that value.

Issue 3: Physical interpretation of standard deviations

Standard deviations are often reported along with averages and used for estimating confidence intervals. For example, the oft-used 'empirical rule' states that 95% of observations are within two standard deviations of the mean. Implicit to this empirical rule, however, is the assumption that the data distribution is Gaussian. As shown above, the distributions of geochemical data – especially data on highly-incompatible trace elements - are highly skewed. Therefore, calculated standard deviations cannot be used for estimating confidence intervals. This is exemplified by the standard deviations reported on the recent global MORB compositions estimated by Su (2002) and AM (2010). Su (2002) reports an average MORB Ba of 36.2 ppm, with a (1 sigma) standard deviation of 42.4. Similarly, AM (2010) report a global MORB average Ba of 34.2 ppm, with a standard deviation of 49. One standard deviation below the mean in both cases leads to negative Ba concentrations; this is the case for many other trace elements as well. Clearly, negative Ba concentrations are non-physical, so standard deviations on skewed distributions have little physical meaning. To estimate a confidence interval on the data distribution, the standard deviation of the log-normal distribution (which is Gaussian) can be used instead, as discussed in the preceding section.

Perhaps more important than a confidence interval on the spread of data, however, is a confidence interval on the calculated mean. For example, there is much debate currently regarding whether the silicate Earth is chondritic or not (e.g., Jackson and Carlson, 2012 and references therein). The mean composition of the ocean crust can provide critical insight on this issue, but only if one can be confident about reported mean values (and the uncertainties on those mean values). For this, the standard

deviation of the mean (defined as the standard deviation/√n) is applicable, even for skewed distributions (e.g., Devore and Peck, 2005).

An approach to estimating the standard deviation of the mean that provides flexible use of weighting factors is the statistical bootstrapping technique. Recall that the means are weighted differently depending on whether we are considering the true mean or the log-normal mean. The bootstrapping approach is to resample the entire population randomly, allowing some data (segments) to be counted more than once and some not at all. For example, there are 428 segments in our database with Ba data. The bootstrapping technique randomly selects a new combination of 428 segments with replacement (allowing repeats). In the most extreme case, one segment would be picked 428 times. Each random selection of 428 segments is counted as 1 trial, and the mean of those randomly picked segments is calculated. The appeal of bootstrapping is its simplicity, as it only requires the assumption that the distribution of the true population is reasonably approximated by the distribution of the subsample (i.e., that the histogram shape of the 428 segments with data is similar to that of all 771 segments). It does not matter whether the distribution is Gaussian or not. Given that we have chemical data on ridge segments from the full range of spreading rates and ridge depths, and from plume-influenced and non-plume-influenced regions, it is reasonable to assume that the distribution of our subsample approximates that of the true population.

We perform 1000 bootstrapping trials for each element and calculate 1000 means. The distribution of those means then provides a quantifiable sense of how much uncertainty there is on the mean value we report (Figure 4.5). The reporting of uncertainties on our estimated mean composition represents a marked change from previous studies. Table 4.1 provides the average composition and typical (log-normal) compositions, the 95% confidence on those values (i.e., errors on the mean), and the 95% confidence interval on the range of the data. This allows us to make the clear distinction between the following three statements, all of which are true: (1) At the 95% confidence level, the mean composition of Ba in the ocean crust is 29.2 ppm +/- 3.8; (2) At the 95% confidence level, the typical value of Ba in ocean crust is 23.1 ppm +/- 3.7; (3) 95% of all ocean crust at ridges has between 3.9 and 160.3 ppm Ba. Notice that the 95% envelope in (3) is

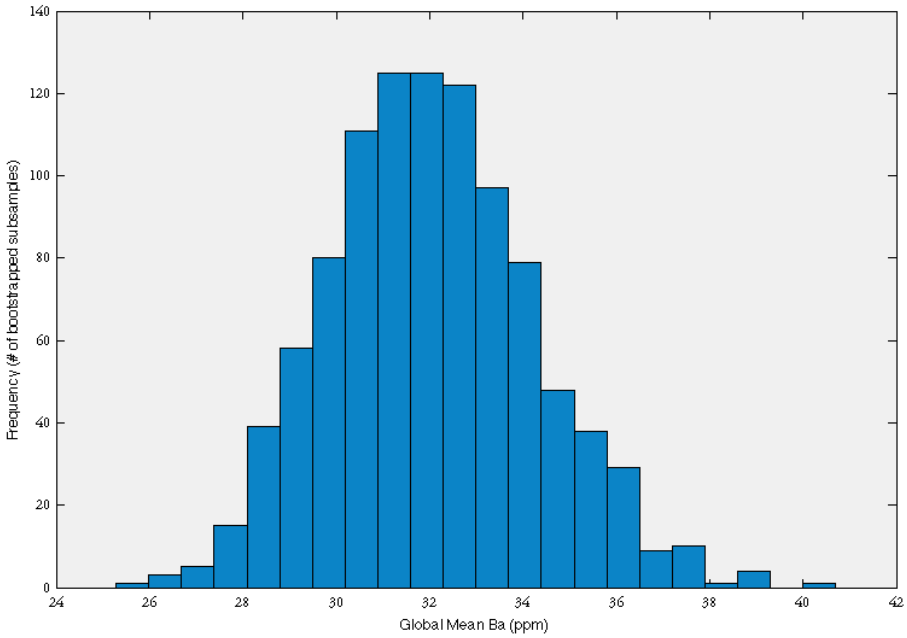

Figure 4.5: The distribution of the mean Ba content for 1000 bootstrapped trials. Each bootstrapped trial is the mean Ba of a random resample of the initial global segment population, with replacement. The distribution of mean values enables the calculation of a 95% confidence interval on the mean value we report. Note that the distribution of means is Gaussian, even though the initial population is decidedly non-Gaussian (Figure 4.4a).

highly asymmetric around the mean. This demonstrates why the percentile approach, instead of the standard deviation approach, is required to characterize highly skewed distributions.

Issue 4: Trace element data gaps

The issue of segment trace element data gaps must also be addressed. Because certain trace elements are harder to measure or have only been measured recently (e.g., Sn, Be, Cs), we do not have the same number of segments with Be data as we do with, for example, Nd data. Indeed, Nd is our best element in terms of data coverage with 454 segments with data, whereas Be is our worst element with only 154 segments with data. So there is the large-scale issue of a maximum of 454 segments with trace element data out of 771, and the small-scale issue of uneven numbers of segments with data on the various trace elements. One could ask whether the mean composition calculated for Be, on 154 segments, is reliable. Put differently, if we had 454 segments with Be data would our reported mean change significantly? Ultimately, we cannot fully address

Table 4.1: Global MORB average trace element and isotope compositions

	n	**All Segments Mean[1]**	± (95% conf)	**All Segments Log-Norm Mean[2]**	±	Upper bound	Lower bound
Ba	428	32.0	4.4	24.1	2.7	160.3	3.9
Be	154	0.73	0.06	0.62	0.05	1.22	0.25
Ce	446	14.65	1.19	12.89	0.69	33.18	5.15
Co	385	42.5	0.7	42.5	0.5	53.0	33.7
Cr	405	244	11	244	11	403	76
Cs	307	0.045	0.010	0.032	0.004	0.198	0.007
Cu	393	75	2	75	2	122	55
Dy	446	5.97	0.29	5.35	0.17	8.83	3.52
Er	445	3.72	0.17	3.32	0.10	5.71	2.08
Eu	447	1.34	0.05	1.24	0.03	2.02	0.79
Ga	336	17.3	0.2	17.0	0.2	20.0	14.1
Gd	421	4.91	0.21	4.45	0.13	7.56	2.85
Hf	434	2.73	0.15	2.40	0.10	4.44	1.09
Ho	440	1.26	0.05	1.14	0.03	1.85	0.75
La	448	5.17	0.50	4.49	0.29	16.32	1.50
Li	272	6.5	0.3	6.0	0.2	9.1	3.9
Lu	446	0.52	0.02	0.47	0.01	0.83	0.31
Mn	71	0.19	0.01	0.18	0.01	0.26	0.15
Mo	198	0.45	0.05	0.41	0.03	1.24	0.15
Nb	438	5.07	0.57	3.96	0.37	22.81	0.92
Nd	454	11.85	0.71	10.71	0.39	22.55	5.40
Ni	401	90	5	96	4	183	44
Pb	406	0.61	0.04	0.55	0.03	1.54	0.20
Pr	425	2.22	0.12	2.03	0.08	4.15	0.92
Rb	416	3.16	0.47	2.25	0.26	13.87	0.38
Sc	373	39.5	0.8	38.6	0.5	48.8	29.5
Sm	453	3.76	0.16	3.44	0.10	6.17	2.03
Sn	213	0.89	0.06	0.78	0.05	1.59	0.28
Sr	449	132	5	132	4	271	70
Ta	388	0.32	0.04	0.26	0.02	1.35	0.06
Tb	433	0.88	0.04	0.81	0.02	1.31	0.53
Th	430	0.407	0.072	0.297	0.030	2.135	0.059
Ti	246	1.49	0.07	1.40	0.05	2.38	0.82
Tl	219	0.023	0.003	0.019	0.001	0.070	0.006
U	409	0.123	0.013	0.097	0.009	0.495	0.022
V	368	307	12	285	7	393	194
W	222	0.12	0.02	0.10	0.01	0.40	0.02
Y	446	36.1	1.8	32.1	1.0	53.6	20.8
Yb	447	3.57	0.18	3.19	0.10	5.80	1.97
Zn	363	90.5	3.0	86.3	1.9	119.5	59.5
Zr	448	114.1	7.8	98.8	4.1	220.0	49.7
$^{87}Sr/^{86}Sr$	295	0.702845	0.000067				
$^{143}Nd/^{144}Nd$	295	0.513074	0.000017				
$^{206}Pb/^{204}Pb$	268	18.415	0.078				
$^{207}Pb/^{204}Pb$	268	15.515	0.008				
$^{208}Pb/^{204}Pb$	268	38.103	0.085				
$^{176}Hf/^{177}Hf$	138	0.283	0.000				
Sm/Nd	452	0.324	0.004				
Zr/Hf	434	40.43	0.88				
Ba/Th	411	78.86	9.72				
Nb/U	401	41.54	2.26				
Ce/Pb	400	22.72	1.42				
Nb/Ta	388	15.21	0.60				
Th/U	407	3.11	0.10				
Ba/Rb	412	10.79	0.48				
Ba/Cs	300	756	60				
Rb/Cs	301	68.21	5.36				
K/U	375	12885	905				
Y/Ho	429	28.08	0.40				
Zr/Sm	446	29.63	0.62				
Hf/Nd	434	0.236	0.006				
Y/Yb	444	10.10	0.10				

Table 4.1 (Continued)

	n	**Global Mean[1*] No BAB**	± (95% conf)	**Global Log-Norm Mean[2] No BAB**	±	Upper bound	Lower bound
Ba	392	29.2	3.8	23.1	2.7	160.3	3.9
Be	139	0.76	0.05	0.64	0.05	1.22	0.25
Ce	410	14.86	1.26	12.99	0.70	33.18	5.09
Co	350	43.0	0.7	42.9	0.5	53.0	35.9
Cr	369	249	12	251	11	406	81
Cs	272	0.034	0.006	0.029	0.004	0.175	0.006
Cu	357	74	2	75	2	122	57
Dy	411	6.08	0.30	5.43	0.17	8.83	3.66
Er	410	3.79	0.17	3.37	0.10	5.71	2.28
Eu	411	1.36	0.05	1.25	0.03	2.02	0.81
Ga	300	17.5	0.2	17.1	0.2	20.0	14.6
Gd	386	4.99	0.23	4.51	0.14	7.56	2.98
Hf	398	2.79	0.15	2.44	0.10	4.51	1.26
Ho	404	1.28	0.05	1.16	0.03	1.85	0.78
La	412	5.21	0.53	4.51	0.30	16.32	1.43
Li	255	6.5	0.3	6.0	0.2	9.1	3.7
Lu	410	0.53	0.02	0.48	0.01	0.83	0.32
Mn	62	0.19	0.01	0.18	0.01	0.26	0.15
Mo	185	0.46	0.05	0.41	0.04	1.24	0.16
Nb	402	5.24	0.59	4.11	0.38	24.50	1.01
Nd	418	12.03	0.78	10.81	0.45	22.55	5.40
Ni	365	92	5	97	4	183	44
Pb	370	0.57	0.03	0.53	0.03	1.31	0.20
Pr	390	2.24	0.12	2.05	0.09	4.15	0.92
Rb	380	2.88	0.44	2.15	0.27	13.87	0.37
Sc	338	39.8	0.8	38.8	0.6	49.2	29.5
Sm	417	3.82	0.15	3.49	0.10	6.17	2.06
Sn	200	0.92	0.06	0.79	0.05	1.63	0.28
Sr	413	129	4	129	5	246	70
Ta	352	0.34	0.04	0.27	0.03	1.44	0.07
Tb	397	0.90	0.04	0.82	0.02	1.31	0.53
Th	395	0.404	0.081	0.292	0.033	2.135	0.059
Ti	237	1.53	0.07	1.42	0.05	2.38	0.87
Tl	200	0.020	0.001	0.019	0.001	0.041	0.006
U	374	0.119	0.013	0.095	0.009	0.495	0.022
V	337	309	13	287	7	396	194
W	209	0.12	0.02	0.10	0.01	0.40	0.01
Y	410	36.8	1.9	32.6	1.0	53.6	21.5
Yb	411	3.63	0.18	3.23	0.10	5.80	2.15
Zn	338	91.3	3.1	86.6	1.9	119.5	59.9
Zr	412	116.9	8.4	100.7	4.4	220.0	49.9
$^{87}Sr/^{86}Sr$	272	0.702819	0.000067				
$^{143}Nd/^{144}Nd$	272	0.513074	0.000017				
$^{206}Pb/^{204}Pb$	245	18.412	0.090				
$^{207}Pb/^{204}Pb$	245	15.515	0.010				
$^{208}Pb/^{204}Pb$	245	38.100	0.091				
$^{176}Hf/^{177}Hf$	138	0.283	0.000				
Sm/Nd	416	0.325	0.005				
Zr/Hf	398	40.64	0.95				
Ba/Th	376	71.93	8.32				
Nb/U	366	44.37	1.99				
Ce/Pb	364	24.85	1.07				
Nb/Ta	352	15.19	0.62				
Th/U	372	3.16	0.11				
Ba/Rb	376	10.87	0.52				
Ba/Cs	265	876	35				
Rb/Cs	266	77.56	3.08				
K/U	347	12344	812				
Y/Ho	393	28.09	0.44				
Zr/Sm	410	29.83	0.66				
Hf/Nd	398	0.237	0.006				
Y/Yb	408	10.12	0.11				

Table 4.1 (Continued)

	n	**Normal Segs[3] Mean[1]**	± (95% conf)	**Normal Segs[3] Log-Norm Mean[2]**	±	Upper bound	Lower bound
Ba	310	25.0	3.6	19.6	2.4	127.0	3.9
Be	115	0.76	0.05	0.64	0.06	1.22	0.21
Ce	323	14.22	1.45	12.42	0.72	32.09	4.95
Co	272	42.7	0.8	42.3	0.5	49.5	35.0
Cr	289	254	13	263	12	396	90
Cs	199	0.027	0.005	0.024	0.004	0.135	0.005
Cu	277	73	2	73	2	110	56
Dy	324	6.10	0.33	5.50	0.18	9.92	3.74
Er	323	3.80	0.18	3.42	0.11	6.29	2.38
Eu	324	1.35	0.06	1.26	0.04	2.02	0.82
Ga	224	17.4	0.3	17.0	0.2	19.5	14.7
Gd	299	4.99	0.25	4.55	0.15	7.19	3.08
Hf	313	2.76	0.15	2.46	0.10	4.44	1.34
Ho	319	1.28	0.06	1.18	0.04	1.86	0.78
La	326	4.86	0.60	4.19	0.29	14.80	1.42
Li	192	6.6	0.3	6.1	0.2	8.9	3.9
Lu	323	0.53	0.02	0.48	0.01	0.77	0.34
Mn	52	0.19	0.02	0.18	0.01	0.26	0.15
Mo	128	0.41	0.05	0.36	0.04	1.06	0.16
Nb	318	4.56	0.56	3.62	0.36	19.26	0.92
Nd	331	11.82	0.84	10.66	0.45	20.71	5.40
Ni	285	93	6	100	5	179	44
Pb	291	0.55	0.03	0.51	0.03	1.15	0.20
Pr	306	2.16	0.11	1.98	0.09	3.79	0.91
Rb	299	2.55	0.46	1.84	0.25	11.34	0.35
Sc	259	39.5	1.1	38.4	0.6	49.4	29.5
Sm	330	3.78	0.18	3.48	0.12	5.41	2.13
Sn	142	0.91	0.07	0.80	0.06	1.51	0.31
Sr	328	127	4	128	5	242	69
Ta	280	0.30	0.04	0.24	0.02	1.32	0.07
Tb	312	0.90	0.04	0.82	0.03	1.30	0.57
Th	311	0.353	0.090	0.252	0.029	1.742	0.057
Ti	174	1.51	0.08	1.40	0.05	2.24	0.95
Tl	143	0.019	0.001	0.017	0.001	0.036	0.006
U	292	0.102	0.011	0.083	0.008	0.454	0.021
V	257	303	16	280	9	393	178
W	150	0.10	0.01	0.08	0.01	0.30	0.01
Y	323	37.1	2.1	33.2	1.2	62.2	22.6
Yb	324	3.65	0.21	3.28	0.11	5.88	2.25
Zn	261	90.1	3.3	85.3	2.3	121.0	59.9
Zr	325	116.5	9.3	101.9	4.8	220.0	52.1
$^{87}Sr/^{86}Sr$	213	0.702807	0.000078				
$^{143}Nd/^{144}Nd$	213	0.513083	0.000020				
$^{206}Pb/^{204}Pb$	190	18.298	0.082				
$^{207}Pb/^{204}Pb$	190	15.505	0.009				
$^{208}Pb/^{204}Pb$	190	37.992	0.086				
$^{176}Hf/^{177}Hf$	97	0.283	0.000				
Sm/Nd	329	0.329	0.005				
Zr/Hf	313	40.58	1.15				
Ba/Th	297	69.43	10.93				
Nb/U	286	44.04	2.48				
Ce/Pb	285	24.30	1.07	1 = mean weighted by spreading rate and length			
Nb/Ta	280	15.13	0.83	2 = log-normal mean, weighted by length only			
Th/U	291	3.09	0.13	3 = "normal" segments exclude BAB and any segment closer than			
Ba/Rb	295	10.63	0.72	500km to a hotspot			
Ba/Cs	195	855	49	* = our preferred All MORB composition			
Rb/Cs	196	76.90	3.67	Note: PARR2 was omitted when calculating the global Sm/Nd, Ce/Pb, Zr/Sm and Y/Ho ratios. CHIL27 was omitted during the calculation of the Rb/Cs ratio. MARR251, EPRR30, FIJI3, FIJI6, SWIR 66, GALA15 and EPRR22 were omitted during calculation of global the Y/Ho ratio.			
K/U	269	13207	999				
Y/Ho	309	28.22	0.53				
Zr/Sm	323	29.89	0.74				
Hf/Nd	313	0.241	0.006				
Y/Yb	321	10.14	0.13				

this issue because we do not know the “true” Be distribution of the MORB population. One way to explore the issue, however, is to test whether the means calculated for elements with good coverage (>400 segments with data) are captured within the mean ± uncertainty estimates when the means for those same elements are instead calculated using only 154 segments. In other words, how are the mean values affected when we force the sampling for other elements to be as limited as it is for Be?

To address this question we carried out the following procedure. For the 18 trace elements with data from more than 427 segments, we created an analog for the Be data coverage by randomly selecting 154 segments with data. We then used the bootstrapping technique on those 154 randomly selected segments, as if we only had data from those 154 segments. Not surprisingly, the uncertainties on the means for the elements increase when bootstrapping from a smaller sample size. For all 18 elements, however, the original mean (calculated on 400+ segments) was captured within the mean +/- 2-sigma calculated by bootstrapping with only 154 segments. We therefore posit that while our reported mean for Be is almost certainly not the true population mean, we have reason to believe that the true mean is captured within the 95% confidence interval.

It bears mentioning again that because our reported Be average is calculated using 154 segments and our Nd average is calculated using 454 segments, the Be/Nd ratio of our mean concentrations is not necessarily the Be/Nd ratio seen in natural lavas. Calculating ratios using our segment averages requires propogating the errors on the individual elements to be sure to encompass the true ratio, resulting in large uncertainties. A more careful treatment of ratios, described below, can narrow these errors considerably.

Issue 5: Calculating meaningful trace element ratios

Many petrogenetic questions require not only a reliable estimate of the mean concentration of a certain element in the ocean crust, but also an estimate of the uncertainty on particular trace element ratios. As discussed above, simply using the mean trace element concentration numbers reported in our table and dividing

one by another will not necessarily result in the most accurate ratios, because each concentration has been calculated on a different number of segments. Of course a ratio can be calculated in this manner, but as we show below the errors estimated on the ratios by taking the ratio of the mean concentrations and propagating the reported uncertainties are overestimated because many of the errors on trace elements are correlated.

To determine more accurate trace element ratios, we only consider segments that have data on both of the elements in the ratio of interest. As an example, there are 302 segments with data on both Rb and Cs – fewer than the number of segments with Rb (416) and Cs (307). To calculate the Rb/Cs ratio, we bootstrap the 302 segments, calculating the mean Rb and mean Cs for each bootstrapped trial, and then dividing the means to get a ratio. We then calculate the mean and uncertainty of the 1000 bootstrapped Rb/Cs ratios, enabling us to report the confidence on that trace element ratio. In the case of Rb/Cs, our % error on the ratio is less than the % error on the mean Cs concentration. This holds true for many other calculated ratios. The fact that the error is smaller on the ratio than on the concentration demonstrates that accurate errors on the ratio cannot be propagated directly from the errors on the individual trace element concentrations. The number of segments used in the ratio calculations is provided with each reported ratio.

Issue 6: To include hotspots and back-arcs, or not

There exists a fundamental question (perhaps a divide) with regard to what "counts" as "MORB". For calculating the average composition of the ocean crust, we consider all crust produced at spreading ridges to be important. Therefore, one of our calculated average MORB compositions casts the widest net by including back-arcs and regions influenced by hotspots such as the Galapagos and Iceland ("All Segments"). Some workers in the field, however, prefer to exclude back-arcs or hotspot-influenced areas when calculating average compositions. To address these issues, we report an average MORB composition excluding all back-arcs ("No BAB"). To then systematically exclude hotspot-influenced regions, we calculated an average MORB composition (excluding

back-arcs) using only segments >500 km from the hotspots compiled by Courtillot et al. (2003) ("Normal Segments"). In this way, the readers can select whichever global MORB composition they consider most useful for the question at hand.

4.4. Presentation of Global Average MORB Compositions

The unprecedented global data coverage in this study, coupled with the ability to weight by segment length and spreading rate, result in the need for a new vocabulary for MORB compositions that accurately reflects the global systematics.

We suggest the term "All MORB" as the true mean composition of the ocean crust. This true mean, which represents the concentration of elements in the zero age ocean crust reservoir, is the best proxy for the total composition of the upper mantle. To accommodate the diverse points of view of our colleagues, we present values calculated with and without back-arc and plume-influenced segments. Our preference is for the value calculated with plumes and without back-arcs (No BAB), since plumes contribute to the upper mantle composition, and back-arcs may simply be a "pass through" of subduction zone components.

The term "N-MORB" has traditionally been used for a highly depleted composition, considered to be "normal." As we show in this work, normal MORB is not highly depleted. We suggest the term N-MORB should reflect the word "normal" and be used to refer to the most likely basalt composition encountered along the global ridge system distant from hot spots. Such a composition is represented by the log-normal mean of segments more than 500 km from plumes (332/419 segments, excluding back-arcs).

A term is also needed for the most highly depleted MORB (D-MORB), though they are not representative of the ocean crust or upper mantle composition, nor are they the common MORB encountered away from hot spots. We propose D-MORB to have the composition of the log-normal mean of segments with $La/Sm_N<0.8$ (normalized to primitive mantle; Sun and McDonough 1989), excluding back-arcs (225/419 segments).

It is also useful to have a clear definition of E-MORB. We define it as the log-normal mean of segments with $La/Sm_N>1.5$ (38/419 segments, excluding back-arcs).

In the following section we present our new All MORB, N-MORB, D-MORB and E-MORB compositions and compare them to previous literature values. The specific compositions are presented in Tables 4.1 and 4.2.

4.4.1. The "All MORB" averages

First we consider the "All MORB" compositions, calculated as the true mean composition of the ocean crust with and without back-arc and plume segments ("All Segments", "No BAB", and "Normal Segments"). The compositions are remarkably similar. Indeed, the average compositions overlap within the 95% confidence interval for all trace elements except Cs. In the case of Cs, the All Segments average is distinctly higher than the Normal Segments average.

Within the shape of the trace element patterns of the mean concentrations, however, distinct features are apparent (Figure 4.6). First, for all trace elements more compatible than Pr, there is no difference between the three different All MORB compositions. It is clear that the average concentration of the moderately incompatible elements in ocean crust can be estimated with great confidence. For elements more incompatible than Pr (Pb, Ce, La, Ta, Nb, U, Th, Ba, Rb and Cs), the Normal Segments average is ~15% lower in concentration than the No BAB Segment average, but with a very similar pattern. This indicates that the plume influence acts to enrich only the most incompatible elements. The All Segments pattern is nearly identical to the No BAB pattern except for four key elements: Pb, Ba, Rb and Cs. These are known to be fluid-mobile elements enriched in many BAB relative to open-ocean MORB. The increase in fluid-mobile elements seen in the All Segments average manifests in lower Ce/Pb, Rb/Cs and Ba/Cs ratios. Interestingly, Ba/Rb shows no difference between All Segments and No BAB, perhaps suggesting a uniform contribution to Ba and Rb from the BAB signal.

As our approach to calculating a global average MORB composition contrasts with all previous approaches, it is important to compare our new MORB averages and earlier estimates (Figure 4.6b). Some of the original calculations of average MORB composition, by Hofmann (1988) and Sun and McDonough (1989), are far more depleted in highly-incompatible elements than our All MORB averages. Indeed, these early N-MORB

Table 4.2: N-, D-, and E-MORB average compositions

	n	**N-MORB[1]**	± (95% conf)	n	**D-MORB[2]**	± (95% conf)	n	**E-MORB[3]**	± (95% conf)
Ba	310	19.6	2.4	207	11.4	0.9	38	125.5	18.8
Be	115	0.64	0.06	90	0.60	0.06	8	0.56	0.23
Ce	323	12.42	0.72	224	10.01	0.57	37	25.52	3.73
Co	272	42.3	0.5	193	43.6	0.5	34	41.7	1.6
Cr	289	263	12	202	269	15	34	216	33
Cs	199	0.024	0.004	142	0.015	0.002	28	0.124	0.024
Cu	277	73	2	194	75	2	34	74	8
Dy	324	5.50	0.18	224	5.48	0.18	37	4.62	0.21
Er	323	3.42	0.11	223	3.46	0.11	37	2.75	0.12
Eu	324	1.26	0.04	224	1.21	0.04	37	1.29	0.08
Ga	224	17.0	0.2	177	16.9	0.2	27	17.3	0.7
Gd	299	4.55	0.15	213	4.43	0.16	37	4.26	0.26
Hf	313	2.46	0.10	218	2.31	0.14	37	2.54	0.26
Ho	319	1.18	0.04	221	1.19	0.04	35	0.96	0.05
La	326	4.19	0.29	225	3.12	0.19	38	12.02	1.66
Li	192	6.1	0.2	153	6.1	0.2	22	5.3	0.6
Lu	323	0.48	0.01	224	0.50	0.02	37	0.38	0.02
Mn	52	0.18	0.01	38	0.18	0.01	6	0.18	0.02
Mo	128	0.36	0.04	97	0.30	0.03	21	0.76	0.21
Nb	318	3.62	0.36	218	2.40	0.19	38	17.07	2.83
Nd	331	10.66	0.45	225	9.46	0.45	38	14.86	1.33
Ni	285	100	5	199	100	6	34	97	10
Pb	291	0.51	0.03	204	0.43	0.02	35	0.98	0.14
Pr	306	1.98	0.09	214	1.71	0.09	35	3.28	0.42
Rb	299	1.84	0.25	195	1.05	0.10	38	10.56	1.47
Sc	259	38.4	0.6	180	39.5	0.7	35	35.7	1.2
Sm	330	3.48	0.12	225	3.32	0.13	38	3.72	0.28
Sn	142	0.80	0.06	107	0.73	0.07	24	0.87	0.14
Sr	328	128	5	223	111	3	37	207	22
Ta	280	0.24	0.02	196	0.17	0.01	32	1.09	0.18
Tb	312	0.82	0.03	217	0.82	0.03	35	0.73	0.04
Th	311	0.252	0.029	213	0.156	0.013	36	1.367	0.232
Ti	174	1.40	0.05	137	1.35	0.06	27	1.50	0.11
Tl	143	0.017	0.001	112	0.015	0.001	21	0.031	0.005
Tm*		0.52			0.52			0.41	
U	292	0.083	0.008	203	0.055	0.005	36	0.386	0.061
V	257	280	9	187	298	9	35	265	10
W	150	0.08	0.01	117	0.07	0.01	23	0.31	0.07
Y	323	33.2	1.2	222	33.2	1.1	37	26.6	1.1
Yb	324	3.28	0.11	224	3.31	0.11	37	2.59	0.10
Zn	261	85.3	2.3	189	88.1	2.5	29	82.4	6.1
Zr	325	101.9	4.8	223	92.6	4.8	37	110.1	12.0
MgO	304	7.76	0.09	200	7.82	0.11	35	7.45	0.28
SiO_2	304	50.42	0.08	200	50.39	0.08	35	50.45	0.28
FeO	304	9.81	0.15	200	10.15	0.18	35	9.44	0.37
CaO	304	11.35	0.07	200	11.49	0.09	35	11.22	0.30
Na_2O	304	2.83	0.05	200	2.71	0.05	35	2.74	0.22
Al_2O_3	304	15.13	0.12	200	14.93	0.12	35	15.12	0.25
TiO_2	304	1.53	0.04	200	1.51	0.05	35	1.51	0.13
K_2O	305	0.14	0.01	206	0.10	0.007	36	0.50	0.075
P_2O_5	298	0.16	0.01	194	0.15	0.009	35	0.24	0.069
MnO	272	0.17	0.004	171	0.178	0.006	34	0.16	0.01

1= N-MORB calculated as the log-normal mean of segments > 500 km from a plume, excluding back-arcs, weighted by length
2= D-MORB calculated as the log-normal mean of segments with $La/Sm_N<0.8$, excluding back-arcs, weighted by length
3= E-MORB calculated as the log-normal mean of segments with $La/Sm_N>1.5$, excluding back-arcs, weighted by length
*Tm value extrapolated from the Er and Yb values

estimates better reflect depleted MORB than "normal MORB", as discussed further below. For elements more compatible than Sr, however, the Hofmann (1988) estimate does track our new estimate.

Su (2002), in a segment scale study similar to ours, showed for the first time a much more enriched value for average MORB in the highly-incompatible elements. AM (2010) report a global MORB true average that matches Su

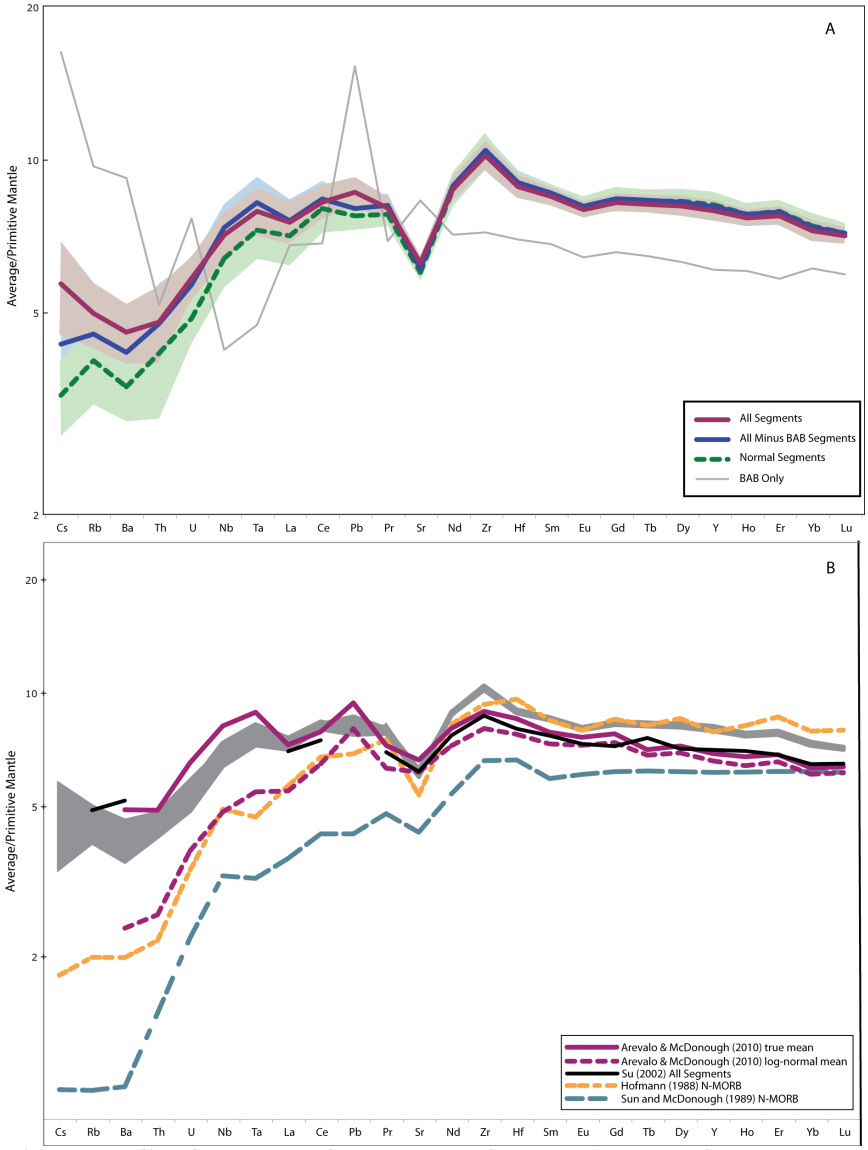

Figure 4.6: (a) Primitive mantle-normalized (Sun and McDonough, 1989) trace element patterns of the three global MORB ("All MORB") compositions calculated in this study (All Segments, No BAB, Normal Segments), shown with shading indicating the 95% confidence interval on each mean composition. Note that the compositions are indistinguishable from eachother in all elements more compatible than Pr. The All Segments pattern is similar to the No BAB pattern except for pronounced peaks in the elements Cs, Rb, Ba and Pb. These elements are fluid-mobile elements that are enhanced in back-arc basin basalts, as evidenced by the trace element pattern of BAB Only. The Normal Segments composition, calculated on segments more than 500 km away from hotspots (Courtillot et al., 2003), is ~15% depleted in the highly incompatible elements relative to the No BAB pattern. This shows the enriching effect of plumes on the highly-incompatible element composition of nearby ridge basalts. (b) Comparison of our All MORB averages (shown in gray shading) to other estimates in the literature. Note the similarity between the All Segments average of Su (2002) and the global MORB true mean estimate of AM (2010). These two average estimates are the most similar to the new All MORB compositions reported here, although slightly more enriched in highly-incompatible elements and more depleted in moderately incompatible elements. The N-MORB estimates of Hofmann (1988) and Sun and McDonough (1989), and the log-normal estimate of AM (2010) are far more depleted than the All MORB compositions estimated in this study.

(2002) to better than 8% in all elements except Nb, which differs by 16%. In contrast, the log-normal mean estimate of AM (2010), their preferred estimate, is more depleted in the highly-incompatible elements and more closely tracks the estimate by Hofmann (1988). The statement by AM (2010) that their log-normal mean composition of global MORB is "more incompatible element enriched than previously suggested by earlier geochemical models" requires modification; Su (2002) provides a more enriched average MORB composition based on "All Segments" than the log-normal estimate of AM (2010). The "All Segments" average by Su (2002) was overlooked by AM (2010), who only report his "Normal Segments" and "Depleted Samples" averages.

Nevertheless, the "All Segments" average of Su (2002), the true average of AM (2010) and the new averages calculated here are remarkably similar, differing by an average of only 13%. Our newest All-MORB averages are slightly less enriched in highly-incompatible elements and more enriched in moderately incompatible elements, reflecting the spreading rate weighting. Our average is pulled toward the composition of Pacific MORB, which is slightly more fractionated and less plume-influenced than the other ocean basins, resulting in lower concentrations of highly-incompatible elements and higher concentrations of moderately incompatible elements (see section 5.1, below). Still, the similarities of the values suggest that average MORB is now well known to be more enriched than the traditional concept of "N-MORB". Our methodology here, with segment length and spreading rate weighting factors, and real confidence estimates on the mean values, provides the most reliable estimate of average MORB ("All MORB") to date.

4.4.2. Normal MORB vs. Depleted MORB

Our new N-MORB composition, calculated as the log-normal mean (typical value) of segments more than 500 km from plumes, is more enriched than earlier N-MORB estimates which were calculated using chemical, rather than distance-from-hotspot, definitions (Hofmann, 1988; Sun and McDonough, 1989; AM (2010)). Indeed for the highly incompatible elements, our N-MORB is a factor of 3 more enriched than the most depleted N-MORB estimate by Sun and McDonough (1989) (Figure 4.7). The N-MORB

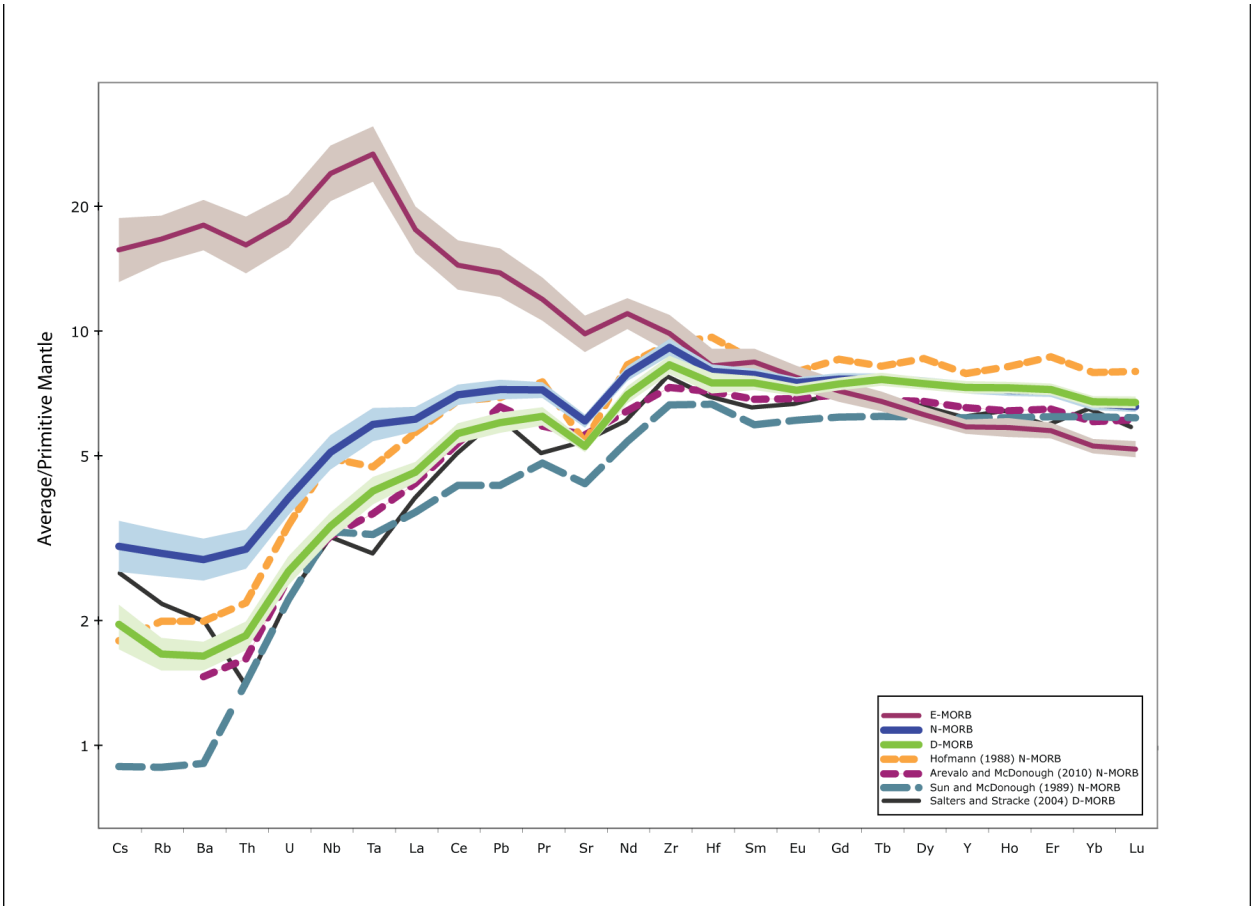

Figure 4.7: Trace element patterns of the E-MORB, N-MORB and D-MORB (enriched, normal, and depleted MORB) compositions reported in this study, compared with earlier estimates. The E-MORB pattern is characterized by a strong enrichment in the highly-incompatible elements and a depletion in the middle to heavy REE, crossing over the REE patterns of the N- and D-MORB. Our N-MORB, calculated as the log-normal mean (most typical value) of segments more than 500 km from a plume, is more enriched than previously suggested; other published values for N-MORB better approximate D-MORB. Note that the N-MORB of Sun and McDonough (1989), however, is even more depleted than the estimate for D-MORB in this study.

estimate from Hofmann (1988) is the most similar to our new N-MORB composition, but is still too depleted in the most highly-incompatible elements and too enriched in the middle-to-heavy REE relative to our values.

The previous literature values for N-MORB better represent the depleted end of the MORB compositional spectrum, or D-MORB (Figure 4.7). This was first shown by Salters and Stracke (2004), as their estimate of D-MORB is similar to (and slightly more enriched than) the N-MORB of Sun and McDonough (1989). Our new D-MORB composition is even more enriched than the N-MORB value of Sun and McDonough (1989), demonstrating the extreme depletion in this early N-MORB estimate. Our D-MORB composition is very

similar to the N-MORB composition of AM (2010).

In view of this, it must be stressed that the N-MORB compositions entrenched in the literature are too depleted to accurately represent “normal MORB”. The normal MORB composition calculated here is the most typical basalt composition erupted far from hotspots, truly ‘normal’. The N-MORB estimates in earlier studies more closely reflect D-MORB, or depleted MORB. Even our D-MORB estimate, using a chemical definition similar to those in the earlier classifications of N-MORB, is more enriched than some previous N-MORB estimates. Normal MORB are simply not as depleted as usually assumed.

4.4.3. Plume-influenced MORB vs. E-MORB

That our N-MORB composition is more enriched than previous estimates, even when plume segments have been eliminated, is indicative of a fundamental characteristic of the ridge system: enriched MORB are not necessarily near plumes.

Classical work by Schilling and co-authors (e.g., White and Schilling, 1978; Schilling et al., 1983) documented observable geochemical gradients along many ridge transects near plumes, with basalts nearest the hotspot the most enriched in highly-incompatible trace elements and radiogenic isotopes. This led to the broad model of mixing between enriched, “plume-source” mantle, perhaps from the deep mantle, and more depleted “MORB-source” mantle to account for the observed enrichment. While E-MORB often arise near plumes, many authors have documented the occurrence of E-MORB far from any known hotspots (e.g., Donnelly et al., 2004; Langmuir et al., 1986; Cousens et al., 1995; Niu et al., 1999). Given this, it is interesting to consider the differences that arise (spatially and chemically) when classifying “enriched MORB” using a distance-from-hotspot scheme vs. solely on the traditional La/Sm basis (Sun et al., 1979).

E-MORB are generally considered to occur near plume centers. Farther from the plume there can still be a “plume influence” but it is moderated and so produces “transitional MORB”, compositions somewhere between E-MORB and D-MORB. To test the correspondence of high plume influence with E-MORB we define “plume segments”

as those with geochemical data that are within 200 km of a plume identified by Courtillot et al. (2003). The only plumes near segments that meet this rather stringent criterion are: Jan Mayen, Iceland, Azores, Ascension and Juan de Fuca/Cobb.

There is remarkable diversity among the five hotspots in terms of the plume expression along the ridge (Figure 4.8a). For example, E-MORB segments are found much more than 200 km away from Jan Mayen and the Azores, with the plume influence seeming to extend well past the "plume segments". In stark contrast, none of the plume segments associated with Ascension and Juan de Fuca/Cobb are E-MORB segments. And near Iceland, the most robust hotspot, only one of the six plume segments is also an E-MORB segment. There are clear intricacies associated with the enriched expression of a plume (or not) along a ridge. An additional complexity is the large number of E-MORB segments that do not have such close proximity to plumes, especially along the MAR and SWIR. This observation becomes even more robust when one considers individual samples with $La/Sm_N>1.5$ (Figure 4.8b), as E-MORB then appear in greater number along the EPR and SEIR. It is clear, then, that while most plumes are enriched and produce a recognizable signal on nearby ridge segments, there is not a simple and universal relationship between plume segments and enriched segments, and vice versa.

The lack of clear correspondence between plume-influenced segments and E-MORB segments leads to a notable difference between their mean chemistry. In the Appendix is a table showing the estimated log-normal mean composition of E-MORB, defined using a La/Sm_N classification scheme or defined by proximity to a hotspot. Given that plumes do not always lead to enriched ridge segments, it is no surprise that plume segments are much less enriched (e.g., Ba=56 ppm) relative to true E-MORB segments with $La/Sm_N>1.5$ (Ba=125 ppm). We suggest that since enriched segments are not necessarily plume segments, E-MORB should be defined using the chemical definition, of $La/Sm_N>1.5$.

4.5. Regional Comparisons

4.5.1. Comparison of the Pacific, Atlantic and Indian Ocean Basins

In this study, "Pacific MORB" includes segments from the Juan de Fuca Ridge (JUAN),

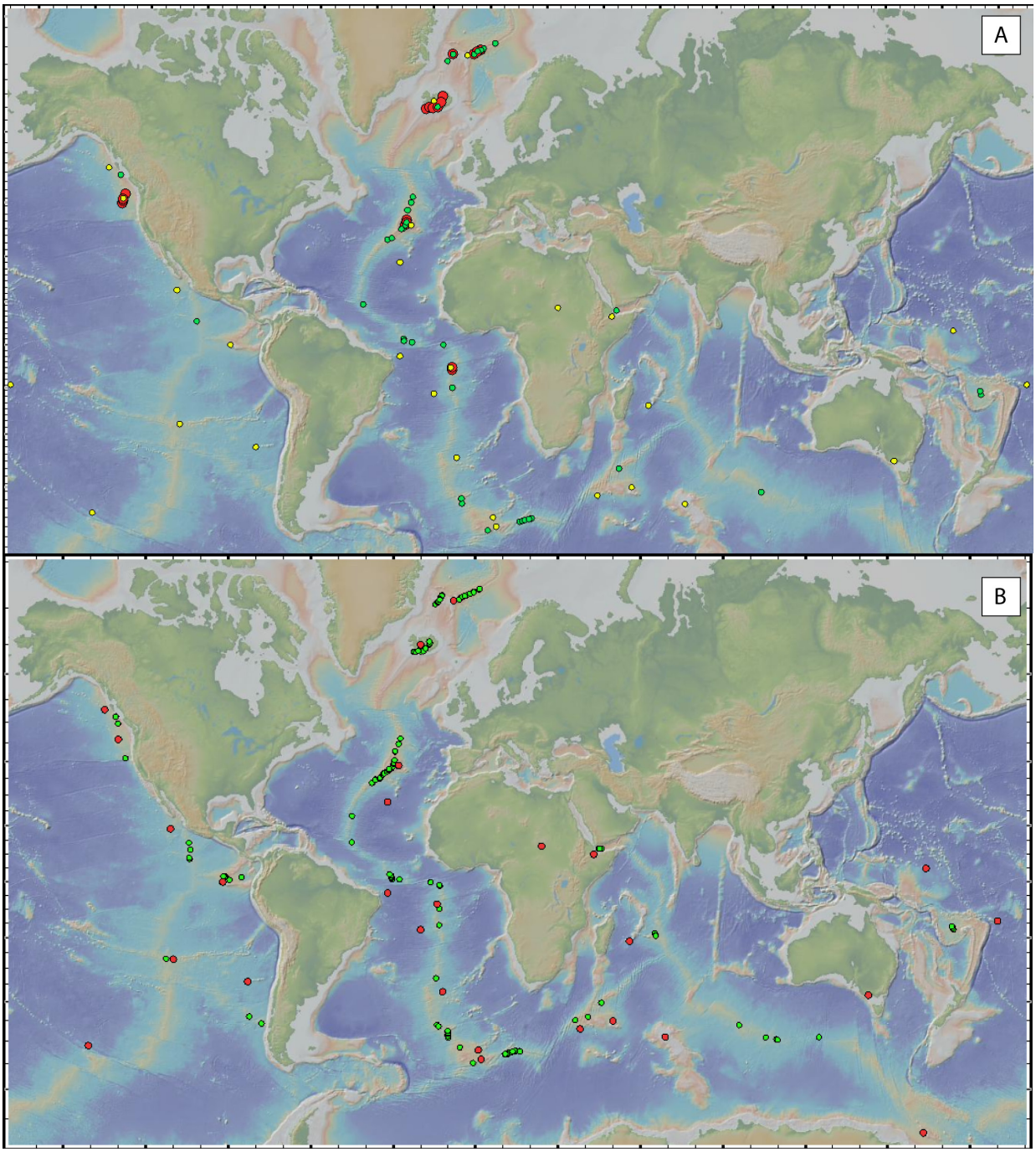

Figure 4.8: (a) Map showing the location of hotspots near ridges (Courtillot et al., 2003) in yellow circles, the location of E-MORB segments (defined by having La/Sm_N >1.5) in green circles, and plume segments (within 200 km of a hotspot) in red circles. There are five hotspots within 200 km of a ridge: Jan Mayen, Iceland, Azores, Ascension and Juan de Fuca/Cobb. Note that the expression of each plume along the ridge is highly variable. At Iceland, only one of the plume segments is an E-MORB segment. In contrast, there are E-MORB segments extending more than 200 km away from the Azores. Plume segments are not necessarily enriched segments, and vice versa. (b) Map showing the location of E-MORB (individual sample locations) in green circles, with near-ridge hotspots shown for reference in red circles. Note how many E-MORB occur far from any known hotspot locations, especially along the SEIR and portions of the EPR and MAR.

East Pacific Rise (EPRR), Chile Rise (CHIL), Pacific Antarctic Ridge (PARR), Galapagos Ridge (GALA), and two Fiji Ridge (FIJI) segments. “Atlantic MORB” includes segments from the Gakkel Ridge (GAKK), Mid-Atlantic Ridge (MARR) and the American-Antarctic Ridge (AARR). “Indian MORB” includes segments from the Afar Ridge (AFAR), Central Indian Ridge (CIRR) and the Southwest and Southeast Indian Ridges (SWIR and SEIR).

4.5.1.1. Major Elements

With regard to major elements, two important effects on the mean compositions can be seen: crystallization and melting. Pacific MORB have slightly lower mean MgO contents (7.4 wt.%) compared to Atlantic and Indian MORB (7.7 wt.%) (Table 4.3). This lower MgO content, indicative of greater extents of fractional crystallization (beyond plagioclase saturation), also explains the highest mean FeO, TiO_2 and MnO, lowest mean Al_2O_3, and the larger negative Sr and Eu anomalies seen in Pacific MORB relative to the other ocean basins. More differentiated magmas are often associated with higher melt supply at faster spreading ridges (Rubin and Sinton, 2007), consistent with our observations in the Pacific. The Atlantic and Pacific MORB segments have approximately the same mean Na_2O and mean depth (~2.75 and 2980 m and 2800 respectively). This is consistent with both ocean basins being generated, on a very coarse average, from approximately the same mean extent of melting (Klein and Langmuir, 1987). The distinguishing characteristics of Pacific MORB, then, seem driven largely by greater extents of fractional crystallization.

Table 4.3: Average major element compositions of global and regional MORB

	n	All Segments Mean[1]	± (95% conf)	n	Pacific Mean[1]	± (95% conf)	n	Atlantic Mean[1]	± (95% conf)	n	Indian Mean[1]	± (95% conf)	n	BAB Mean[1]	± (95% conf)
MgO	465	7.51	0.12	117	7.42	0.18	212	7.71	0.17	124	7.74	0.10	35	6.68	0.49
SiO_2	465	50.54	0.09	117	50.45	0.13	212	50.72	0.15	124	50.43	0.15	35	51.67	0.72
FeO	465	10.39	0.21	117	10.90	0.28	212	10.20	0.28	124	9.57	0.26	35	9.88	0.66
CaO	465	11.35	0.10	117	11.39	0.15	212	11.33	0.13	124	11.40	0.10	35	10.85	0.53
Na_2O	465	2.79	0.03	117	2.76	0.04	212	2.75	0.06	124	2.94	0.06	35	2.82	0.16
Al_2O_3	465	14.73	0.12	117	14.35	0.15	212	14.72	0.21	124	15.40	0.18	35	15.17	0.34
TiO_2	465	1.66	0.05	117	1.78	0.07	212	1.55	0.06	124	1.55	0.08	35	1.37	0.15
K_2O	465	0.165	0.015	117	0.143	0.018	212	0.175	0.025	124	0.173	0.022	35	0.236	0.049
P_2O_5	444	0.184	0.011	103	0.186	0.013	200	0.204	0.034	120	0.157	0.012	35	0.179	0.026
MnO	409	0.184	0.005	103	0.196	0.005	177	0.176	0.006	112	0.159	0.013	30	0.190	0.015

1 = mean weighted by spreading rate and length

There are indications that melting differences are also important, especially between Indian MORB and the other ocean basins. A ready comparison can be made between Indian and Atlantic MORB, as both have identical mean MgO (7.7 wt.%) and therefore any apparent differences cannot be attributed to crystallization. Indian MORB compared to Atlantic MORB are characterized by: lower FeO and distinctly higher Na_2O and Al_2O_3. These characteristics are all consistent with a lower mean extent of melting for Indian MORB, also supported by an increased mean depth (3400m; Klein and Langmuir, 1987). This notion is further evidenced by the constant mean K_2O contents between Atlantic and Indian MORB; as K_2O is highly influenced by mantle source differences, similar mean K_2O contents suggest that melting, rather than source, is driving their differences. The question remains, however, why the mean TiO_2 of Indian MORB is the same as that of Atlantic MORB, since TiO_2 is expected to be higher in MORB generated by lower extents of melting. The anomalous behavior of TiO_2 in Indian MORB has been documented previously and remains to be explained (Langmuir et al., 1992).

4.5.1.2. Trace Elements

The trace element patterns (Figure 4.9a) reveal even more differences among the ocean basins. Pacific MORB are the most depleted in highly-incompatible elements, but the most enriched in the moderately incompatible elements (Table 4.4). The difference in the mean middle-to-heavy REE concentrations between Pacific MORB and the other ocean basins is too large to be caused solely by fractional crystallization (25% difference; fractional crystallization of plag+ol±cpx could only account for 7%). There is another effect at play on the trace elements - the plume effect.

Mantle sources associated with plumes are enriched and often begin melting in the garnet field, enriching the highly-incompatible elements and buffering the middle-to-heavy REE during melting. Therefore, relative enrichments in highly incompatible elements coupled with relative depletions in moderately incompatible elements are signs of plume-influenced MORB – exactly those apparent in the plume-rich Atlantic. The opposite signal, depletion in highly incompatible elements with enrichment in moderately incompatible elements, as noted here and previously in Pacific MORB (AM

(2010)), is consistent with the relative lack of plumes in the Pacific.

A test of the hypothesis that plume influence is driving the difference in trace elements between the plume-poor Pacific and the plume-rich Atlantic involves a comparison of average D-MORB (La/Sm_N<0.8) from the Atlantic vs. average D-MORB from the Pacific. A telling feature of the patterns is that the Pacific D-MORB pattern is nearly the same as the total Pacific MORB pattern, while the Atlantic D-MORB pattern is markedly different than the total Atlantic pattern, flatter in the middle to heavy REE and far more depleted in the highly-incompatible elements. This shows the important influence of enriched sources on the mean composition of Atlantic MORB. Considering just the D-MORB, mean Atlantic D-MORB have a MgO content of 8.14 wt.%, while mean Pacific D-MORB have 7.37 wt.% MgO. Fractional crystallization (plag+ol±cpx) can account for more than 95% of the concentration difference between Pacific and

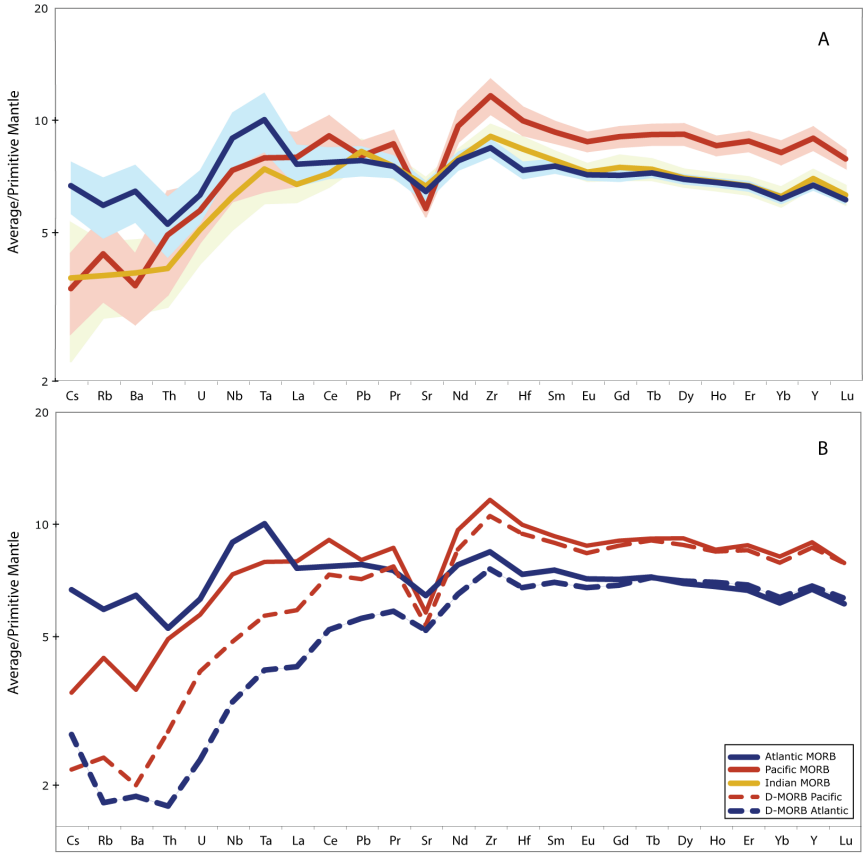

Figure 4.9: (a) Primitive mantle-normalized trace element patterns of mean Atlantic, Pacific and Indian MORB, with shaded regions indicating the 95% confidence interval. Atlantic MORB are the most enriched in highly-incompatible elements. Pacific MORB have the highest concentrations of moderately-incompatible elements, and low concentrations of highly-incompatible elements. Indian MORB are intermediate in composition. The differences between Pacific and Atlantic MORB are too large to be accounted for by fractional crystallization, and instead seem related to a more enriched Atlantic mantle source. (b) To eliminate highly-enriched segments, mean Atlantic and Pacific D-MORB (La/Sm_N<0.8) are compared (D-MORB compositions provided in the Appendix). Note that the pattern of Pacific MORB is similar in shape to Pacific D-MORB, whereas the pattern of Atlantic MORB deviates from Atlantic D-MORB in the highly-incompatible trace elements. The more extensive plume-influence in the Atlantic compared to the Pacific acts to enrich the Atlantic MORB.

Table 4.4: Regional MORB average trace element and isotope compositions

	n	**Pacific Mean[1]**	± (95% conf)	n	**Atlantic Mean[1]**	±	n	**Indian Mean[1]**	±
Ba	95	25.1	5.3	177	44.9	8.0	120	27.1	6.1
Be	38	0.83	0.07	66	0.60	0.04	35	0.69	0.09
Ce	97	16.07	2.07	186	13.63	1.34	127	12.73	0.99
Co	75	43.6	1.1	167	43.7	0.6	108	41.1	0.6
Cr	87	222	17	171	287	12	111	284	17
Cs	61	0.028	0.007	157	0.053	0.008	54	0.030	0.012
Cu	77	75	3	170	76	3	110	70	3
Dy	98	6.74	0.43	186	5.10	0.17	127	5.15	0.27
Er	97	4.20	0.25	186	3.18	0.11	127	3.19	0.17
Eu	98	1.47	0.08	186	1.19	0.04	127	1.22	0.06
Ga	65	17.9	0.3	175	16.9	0.2	60	16.9	0.6
Gd	97	5.37	0.33	186	4.23	0.17	103	4.44	0.34
Hf	88	3.07	0.26	184	2.26	0.12	126	2.58	0.19
Ho	95	1.40	0.08	182	1.11	0.03	127	1.12	0.06
La	97	5.45	0.88	186	5.22	0.67	129	4.61	0.48
Li	55	6.9	0.5	153	5.8	0.2	47	6.2	0.5
Lu	97	0.58	0.03	186	0.45	0.01	127	0.47	0.03
Mn	11	0.22	0.02	35	0.18	0.01	16	0.17	0.01
Mo	28	0.45	0.08	141	0.48	0.05	16	0.40	0.12
Nb	94	5.22	0.91	181	6.36	1.09	127	4.43	0.81
Nd	103	13.02	1.23	186	10.50	0.63	129	10.65	0.61
Ni	83	80	8	171	115	6	111	101	8
Pb	83	0.57	0.05	176	0.55	0.05	111	0.58	0.04
Pr	89	2.38	0.20	182	2.07	0.15	119	2.07	0.15
Rb	84	2.78	0.70	176	3.75	0.70	120	2.42	0.55
Sc	69	41.7	1.2	168	39.2	0.7	101	36.8	0.9
Sm	102	4.11	0.27	186	3.34	0.16	129	3.45	0.20
Sn	32	1.00	0.11	138	0.83	0.06	30	0.84	0.13
Sr	103	122	6	182	136	9	128	140	7
Ta	79	0.32	0.06	175	0.41	0.07	98	0.30	0.06
Tb	89	0.99	0.06	182	0.78	0.02	126	0.80	0.05
Th	88	0.417	0.129	182	0.446	0.083	125	0.340	0.072
Ti	40	1.64	0.12	160	1.43	0.05	37	1.34	0.15
Tl	29	0.021	0.003	144	0.021	0.002	27	0.015	0.004
U	83	0.120	0.021	180	0.132	0.022	111	0.107	0.020
V	75	329	20	176	280	6	86	275	18
W	36	0.11	0.02	148	0.14	0.02	25	0.11	0.07
Y	100	40.6	2.8	185	30.4	1.0	125	31.6	1.8
Yb	98	4.03	0.28	186	3.03	0.10	127	3.07	0.18
Zn	76	97.5	4.6	167	86.2	1.8	95	80.4	4.3
Zr	100	129.7	13.6	185	94.2	5.5	127	101.1	7.5
$^{87}Sr/^{86}Sr$	60	0.702637	0.000074	129	0.702904	0.000138	83	0.703060	0.000107
$^{143}Nd/^{144}Nd$	59	0.513110	0.000021	133	0.513041	0.000034	80	0.513018	0.000022
$^{206}Pb/^{204}Pb$	47	18.551	0.132	125	18.520	0.124	73	18.120	0.126
$^{207}Pb/^{204}Pb$	47	15.525	0.018	125	15.526	0.012	73	15.490	0.009
$^{208}Pb/^{204}Pb$	47	38.114	0.171	125	38.242	0.102	73	37.973	0.122
$^{176}Hf/^{177}Hf$	20	0.283	0.000	7	0.283	0.000	7	0.283	0.000
Sm/Nd	101	0.327	0.007	186	0.318	0.008	129	0.324	0.007
Zr/Hf	88	40.90	1.51	184	41.65	0.99	126	39.21	1.08
Ba/Th	85	59.31	9.63	175	96.35	5.77	116	80.99	5.51
Nb/U	80	43.25	3.59	177	47.95	1.85	109	43.39	1.98
Ce/Pb	79	26.12	1.67	176	24.90	1.12	109	22.09	1.50
Nb/Ta	79	15.28	1.05	175	15.19	0.76	98	14.97	1.06
Th/U	83	3.04	0.16	179	3.39	0.11	110	3.23	0.23
Ba/Rb	81	10.10	0.87	176	12.01	0.38	119	11.23	0.49
Ba/Cs	59	852	47	155	915	61	51	849	101
Rb/Cs	59	77.84	5.18	155	75.58	4.31	52	81.78	7.08
K/U	81	11284	1105	163	13360	833	103	14217	1289
Y/Ho	89	28.30	0.64	180	27.16	0.22	124	28.20	0.62
Zr/Sm	98	30.34	0.95	185	28.20	0.49	127	29.56	0.74
Hf/Nd	88	0.241	0.009	184	0.215	0.007	126	0.244	0.008
Y/Yb	98	10.10	0.16	185	10.04	0.07	125	10.28	0.13

Table 4.4 (Continued)

	n	**BAB Mean**[1]	± (95% conf)
Ba	36	64.3	21.0
Be	15	0.45	0.08
Ce	36	12.14	1.99
Co	35	37.6	1.6
Cr	36	189	30
Cs	35	0.129	0.049
Cu	36	81	7
Dy	35	4.64	0.68
Er	35	2.90	0.45
Eu	36	1.08	0.11
Ga	36	15.5	0.6
Gd	35	3.92	0.52
Hf	36	2.15	0.38
Ho	36	1.00	0.15
La	36	4.66	1.01
Li	17	6.4	0.9
Lu	36	0.44	0.07
Mn	9	0.17	0.01
Mo	13	0.33	0.08
Nb	36	3.01	1.08
Nd	36	9.64	1.28
Ni	36	76	11
Pb	36	1.08	0.26
Pr	35	1.91	0.30
Rb	36	6.16	2.08
Sc	35	36.3	1.9
Sm	36	3.03	0.41
Sn	13	0.55	0.09
Sr	36	175	26
Ta	36	0.19	0.06
Tb	36	0.70	0.10
Th	35	0.440	0.132
Ti	9	0.87	0.21
Tl	19	0.044	0.016
U	35	0.161	0.040
V	31	285	18
W	13	0.08	0.04
Y	36	27.8	4.0
Yb	36	2.87	0.44
Zn	25	79.5	6.1
Zr	36	80.6	14.5
$^{87}Sr/^{86}Sr$	23	0.703131	0.000161
$^{143}Nd/^{144}Nd$	23	0.513073	0.000012
$^{206}Pb/^{204}Pb$	23	18.438	0.174
$^{207}Pb/^{204}Pb$	23	15.519	0.014
$^{208}Pb/^{204}Pb$	23	38.119	0.161
$^{176}Hf/^{177}Hf$	7	0.283	0.000
Sm/Nd	36	0.314	0.016
Zr/Hf	36	37.44	1.37
Ba/Th	35	149.75	35.39
Nb/U	35	18.97	5.37
Ce/Pb	36	11.20	2.29
Nb/Ta	36	15.53	0.89
Th/U	35	2.74	0.37
Ba/Rb	36	10.44	1.24
Ba/Cs	35	512	64
Rb/Cs	35	49.02	6.54
K/U	28	19693	4294
Y/Ho	36	27.92	0.72
Zr/Sm	36	26.60	1.54
Hf/Nd	36	0.223	0.019
Y/Yb	36	9.67	0.18

1= mean weighted by spreading rate and length
Note: the same segments omitted for the calculation of global TE ratios were omitted for regional TE ratios

Atlantic D-MORB in moderately incompatible elements. Hence, the difference between mean Atlantic and mean Pacific compositions, inclusive of all segments, can be attributed to the effect of plumes, as the difference disappears (with fractionation taken into account) once plume-influenced segments are excluded.

Indian MORB are intermediate in composition between Atlantic and Pacific MORB. That the Indian MORB are less enriched in highly incompatible elements relative to Atlantic MORB lends support to the previous claim that the high Na_2O and Al_2O_3 contents of Indian MORB are not due simply to a more enriched source.

Trace Element Ratios

There are perceptible differences in trace element ratios in MORB from the different ocean basins. Atlantic MORB possess certain features that correspond broadly with E-MORB features, such as lower Sm/Nd, Y/Ho and Hf/Nd and higher Zr/Hf, Th/U and Nb/U, all consistent with a more enriched source and/or a more pronounced signature from melting in the garnet field. It has been suggested previously that the correlated Sm/Nd, Zr/Hf ratios in MORB track source enrichment (Weyer et al., 2003). Y/Ho, a “canonical” ratio that is difficult to fractionate during petrogenetic processes (Langmuir et al., 1992; AM (2010)), is noticeably lower in Atlantic MORB (27.3) relative

to any of our other average MORB estimates, global or regional (range: 28-28.3). Lower Y/Ho is likely indicative of a more pronounced garnet signature in the mean Atlantic trace element composition. Further evidence supporting a garnet signature comes from the Th/U and Nb/U ratios in the Atlantic. It has been documented previously that the Atlantic has a distinctly higher Th/U ratio compared to Pacific MORB, although the absolute ratios reported here are higher than those reported in earlier studies by Salters and Stracke (2004) and AM (2010) (Pacific Th/U ~3 in this study compared to ~2.6, Atlantic Th/U of 3.4 compared to ~2.9). U is preferentially held in garnet relative to Th or Nb during mantle melting, so we posit that the elevated Th/U and Nb/U observed in Atlantic MORB is related to melting in the garnet field. Atlantic MORB also have distinctly high Ba/Th and Ba/Rb ratios relative to the other regions; the Atlantic basin seems to be a “high Ba province”.

Indian MORB are perhaps best known for their anomalous isotopic signature relative to Atlantic and Pacific MORB (discussed below). Earlier work on the trace element composition of Indian MORB showed evidence for lower Ce/Pb ratios (Sims and DePaolo, 1997; AM (2010)) and elevated K/U and K/Nb ratios relative to Atlantic and Pacific MORB (Rehkamper and Hofman, 1997). In broad agreement with earlier studies, we observe a distinctly lower Ce/Pb ratio in Indian MORB, but our value (22) is less extreme than earlier reported (range 15-20.9). Indian MORB also possess elevated K/U and K/Nb ratios relative to the Pacific and Atlantic, seeming to indicate a K enrichment in the Indian mantle source (Rehkamper and Hofmann, 1997). The Ba/Th ratio of Indian MORB is intermediate, but distinct, between the high value in the Atlantic and the low value in the Pacific. Also intriguingly, the Zr/Hf value is markedly lower in Indian MORB relative to Atlantic MORB (and global MORB). As Zr/Hf is thought to represent the mantle source at degrees of melting typical of MORB (Westrenen et al., 2001; Weyer et al., 2003), the low Zr/Hf ratio could indicate a slightly depleted mantle source (in certain trace elements) of Indian MORB, an idea further hinted at by higher Sm/Nd in Indian MORB relative to the more enriched Atlantic MORB. This depletion does not extend to all elements, with noteworthy exceptions being K and Pb.

Pacific MORB show trace-element ratios that are consistent with more depletion (less plume influence), such as low Th/U, Ba/Rb and Ba/Th. One interesting feature of Pacific MORB is its low K/U relative to Atlantic or Indian MORB. Perhaps the Pacific K/U is not low so much as the Atlantic and Indian MORB K/U is 'high' due to either the influence of garnet melting (Atlantic) or K enrichment relative to other highly incompatible elements (Indian; Rehkamper and Hofmann, 1997).

4.5.1.3. Isotopic Ratios

Any comparison of ocean basin isotopic ratios must begin by noting that a southern hemisphere isotopic anomaly has been suggested (Hart, 1984), encompassing portions of the Southern Mid-Atlantic Ridge and much of the Indian basin. More recently, a 'southern hemisphere' isotopic signal was detected in Gakkel Ridge basalts (Goldstein et al., 2008). A broad isotopic average of ocean basins, then, including basalts from the southern and northern reaches of each basin, may subdue the stark differences that have been previously noted with regard to Atlantic, Pacific and Indian MORB. Nevertheless, it is clear that Pacific MORB are characterized by the least radiogenic Sr and Nd isotopic ratios, consistent with an overall less enriched source. While Atlantic and Indian MORB overlap within error in Sr and Nd isotopic space (perhaps the result of binning southern and northern hemisphere Atlantic basalts together), the Indian MORB are slightly higher in $^{87}Sr/^{86}Sr$ and lower in $^{143}Nd/^{144}Nd$ than the Atlantic. They also have distinctly low $^{206}Pb/^{204}Pb$ relative to the other ocean basins. These observed $^{87}Sr/^{86}Sr$, $^{143}Nd/^{144}Nd$ and $^{206}Pb/^{204}Pb$ characteristics of Indian MORB have been documented previously (e.g., Dupre and Allegre, 1983; Hamelin et al., 1986). The $^{207}Pb/^{204}Pb$ ratio of Indian MORB is also distinctly lower than the Pacific and Atlantic, while its $^{208}Pb/^{204}Pb$ ratio is lower than the Atlantic but overlaps the Pacific. In terms of $^{176}Hf/^{177}Hf$, within the relatively limited dataset there is no difference between the mean compositions of the ocean basins.

4.5.2. Back-arc Basins

Our back-arc basin (BAB) average includes data from the Lau (including an extensive

suite of high-quality ICP-MS data released with this study), Manus, Marianas, Scotia and Woodlark basins (Tables 4.3 and 4.4). BAB represent an intermediate environment between mid-ocean ridges and island arcs. Especially pertinent here, BAB are more hydrous magmas than open-ocean MORB. Water can affect the extent of melting (e.g., Burnham and Davis, 1974; Hirth and Kohlstedt, 1996; Gaetani and Grove, 1998), the saturation of phases during fractionation, and the delivery of fluid-mobile incompatible elements (Asimow et al., 2004). Many of these effects are apparent in our average BAB major and trace element composition.

BAB Major Elements

In comparison with the All MORB averages, BAB have distinctly lower MgO and TiO_2 and higher SiO_2 and K_2O. They also have slightly lower FeO and CaO and higher Al_2O_3 contents, although these values overlap All MORB within the 95% confidence interval. These characteristics, in particular low MgO, TiO_2 and FeO coupled with high SiO_2 and Al_2O_3 of BAB basalts relative to open-ocean MORB have been documented previously (e.g., Sinton and Fryer, 1987; Langmuir et al., 2006 and references therein). The lower FeO and TiO_2 with higher Al_2O_3 are particularly noteworthy, because if plagioclase + olivine are crystallizing, FeO and TiO_2 increase and Al_2O_3 decreases. With such a low mean MgO content (6.67) relative to global MORB, then, TiO_2 and FeO contents would be expected to be higher in BAB, with Al_2O_3 contents lower. Recall that this is the case for the lower-MgO Pacific MORB.

The onset of plagioclase crystallization is delayed in hydrous conditions, which could account partially for the higher Al_2O_3 and lower FeO and TiO_2 contents in BAB (Asimow et al., 2004). Langmuir et al. (2006) showed, however, that the low FeO and TiO_2 persist in BAB data even when the delayed plagioclase effect is taken into account. Instead, the low FeO, high SiO_2 and low TiO_2 possessed by average BAB can be explained by greater extents of melting at low pressures caused by the higher water contents (Langmuir et al., 2006). Therein lies a fundamental distinction between BAB and open-ocean MORB: the relationship between H_2O and extent of melting (F). In the mid-ocean ridge environment, water acts to decrease F; in BAB, water increases F

(Langmuir et al., 2006). As we show below, the trace elements are also consistent with the interpretation that BAB have been derived by higher F.

BAB Trace Elements

There are two main features of the trace element composition of average BAB to note: (1) the distinctly low concentrations of moderately incompatible trace elements, and (2) the pronounced peaks in certain trace elements, deviating sharply from the global MORB trend (Figure 4.6). The 20% lower concentrations of moderately incompatible trace elements in BAB compared to global MORB are especially remarkable because BAB are more fractionated than MORB, which would tend to increase trace element concentrations. As with TiO_2, the ~20% lower concentrations of moderately incompatible trace elements are consistent with higher average extents of melting at BAB. There are also pronounced peaks in Cs, Rb, Ba, U, Pb and Sr in the BAB pattern. Cs, Rb, Ba, U, and Pb are all fluid-mobile elements, delivered to the BAB source region along with water. The strongly elevated Sr contents in BAB are likely related to the combined effects of fluid delivery and the delayed appearance of plagioclase.

Not surprisingly, the marked differences in trace element concentrations manifest in many distinct trace element ratios in BAB relative to global MORB. The peaks in fluid-mobile elements create high Ba/Th and low Nb/U, Ce/Pb, and Th/U. There is interesting structure even within the fluid mobile elements; Ba/Cs and Rb/Cs are low, but Ba/Rb is indistinguishable from global MORB. We therefore posit that Cs is delivered preferentially by the fluid component affecting BAB, and that Ba and Rb have similar fluid mobility. Using similar reasoning, the high K/U in BAB indicates that K is more fluid-mobile than U. This first-order estimate of the relative proportion of elements delivered by the fluid component is remarkably similar to that in the “wet component” calculated independently by Bézos et al. (2009) for the Lau basin. As a final note, while the largest driver of the observed major and moderately incompatible trace element concentrations in BAB is F instead of source, source depletion is observed in some BAB (Langmuir et al., 2006). Such source depletion may be the cause of the low Zr/Sm and Zr/Hf ratios in BAB relative to MORB. Y/Yb is also low in BAB relative to open-ocean

MORB, consistent with higher extents of melting and a more depleted source.

4.6. Geochemical Implications

4.6.1. K/U Ratio

The K/U ratio has fundamental implications for the heat budget of the planet. As such, multiple studies have addressed the K/U of the silicate earth (Lassiter, 2004; Albarede, 1998; Davies, 1999; Jochum et al., 1983). A reliable estimate of the average K/U of MORB constrains these models by providing insight on the K/U of the upper mantle, as K and U behave similarly during partial melting and crystal fractionation and therefore the K/U of MORB reflects the K/U of the upper mantle (e.g., Hofmann et al., 1986). Arevalo and McDonough (2009) recently released an estimate for the K/U of the "composite MORB source", or DMM, of 19000 ± 2600. As noted in Table 4.1, our best estimate for the K/U of MORB is 12340 ± 810 (back-arcs excluded). These two estimates are considerably different, and below we explore why this newest estimate of K/U differs so markedly from the Arevalo and McDonough (2009) estimate.

Contrast 1: Data selection/coverage

Arevalo and McDonough (2009) (hereafter referred to as AM (2009)) utilize 87 samples for assessing the K/U of MORB. In contrast, our database comprises 2320 samples with both K and U measured. Of the 87 samples included by AM (2009), 43 were excluded in our study for being more than 10 km off-axis or located in a fracture zone. For example, DSDP034-0320-003-001/101 (among other DSDP samples) was included in the AM (2009) study despite being classified in PetDB as "OLD_OCEANIC_CRUST". Our database includes many more samples and also ensures that those samples are relatively fresh, on-axis samples.

Contrast 2: Method for K measurements

A strength of the AM (2009) study is that the K measurements are made using a high-precision LA-ICP-MS technique. In contrast, our database includes K data from a variety of methods including DCP, EMP, x-ray fluorescence (XRF), etc. The majority of the K data in our database is EMP data, not considered a high-precision measurement

technique for K on depleted MORB samples with K ~0.1 wt.%. It is therefore necessary to validate the use of EMP K data for an assessment of the K/U ratio of MORB.

To do this, we carefully compiled a dataset of 373 Langmuir laboratory analyses with K measured by both high-precision (either DCP or solution ICP-MS) and lower-precision (EMP) techniques to compare the results. Our compiled analyses include suites of data from several regions including the EPR, Gakkel, and MAR. Figure 4.10 demonstrates that EMP and DCP/ICP K are coherent (with the exception of 4 NHOCHEPR analyses). Moreover, regional trends in K vs. U are captured whether using DCP K or EMP K (Figure 4.11). As another check, it is necessary to be certain that individual segment average K values are approximately the same whether using DCP or EMP K data, as ultimately our average calculations are pinned to the segment averages. For the 23 segments compiled with sample K measured by both DCP/ICP and EMP, the DCP/ICP and EMP-based K segment averages agree to better than 9% in all but 4 cases (at worst is a 27% offset for a highly-depleted segment with ICP K of 0.08 wt.% and EMP K of 0.1 wt. %; Figure 4.12). We therefore have reason to believe that our master database, while consisting primarily of K data measured by EMP, is reliable for assessing the K/U of global MORB.

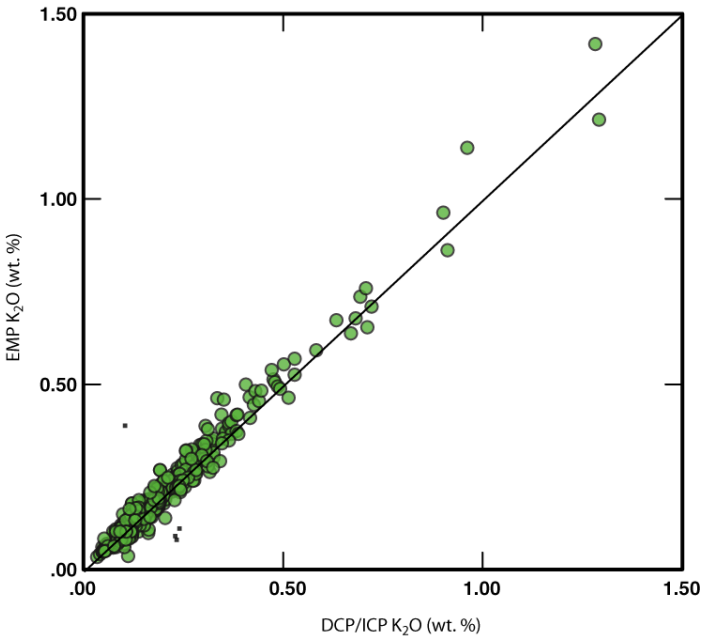

Figure 4.10: Comparison of K_2O measured by EMP to K_2O measured by higher-precision techniques including DCP and ICP-MS in the Langmuir laboratory. Note that over a wide range of K_2O contents, the measured values are remarkably coherent (with the exception of 4 samples that likely have suffered a sample switch and are shown as small black squares). A 1:1 line is shown for reference.

Of course, EMP is not the most precise technique for measuring K in highly-depleted basalts; there are often large errors associated with the K/U ratio of an individual depleted basalt with K measured by EMP. As will be stressed below, however, our approach to calculating an average MORB K/U ratio does not involve the use of individual sample ratios (as was the case for AM (2009)). Instead,

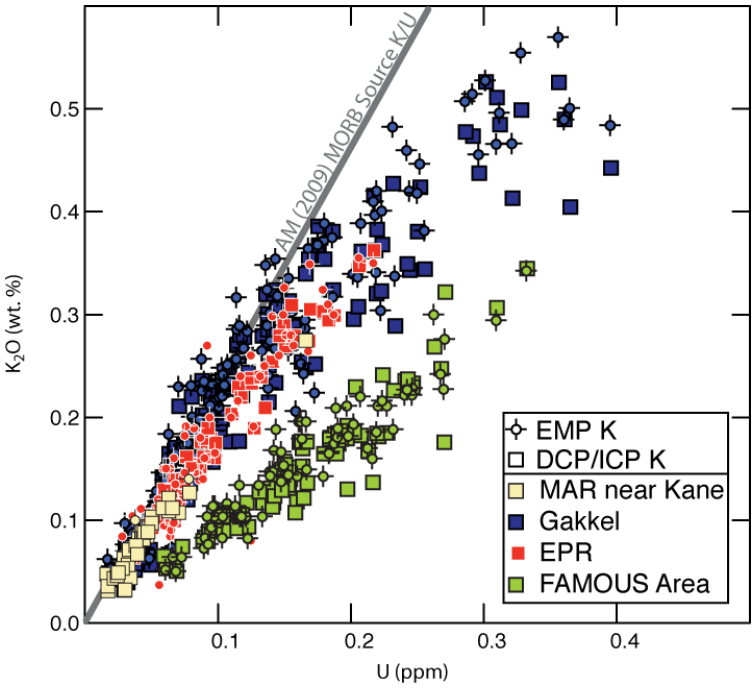

Figure 4.11: K_2O (measured by EMP and DCP/ICP) versus U for samples from a wide range of locations measured in the Langmuir laboratory. Note that regional differences in K/U are captured whether K_2O is measured by EMP or DCP-ICP. For reference, the K/U ratio estimated by AM (2009) for the "MORB Source" is shown. Note that the AM (2009) ratio is at the most depleted end of the MORB spectrum, and is not representative of the mean MORB source.

we use the average K content of the MORB reservoir, divided by its average U content, to arrive at an estimate for the global K/U ratio. Thus, occasionally errant K/U ratios on depleted basalts due to imprecise K EMP data are immaterial to our approach. Moreover, in our averaging scheme a segment with 0.3 wt.% K is 15 times more important than a segment with 0.02 wt.% K, reducing the concern for excellent K precision at the most depleted end of the basaltic spectrum.

Contrast 3: Data treatment

As the previous discussion shows, measurement precision is not a factor in the discrepancy between our result and AM (2009). Instead, the extent of the difference between the AM (2009) K/U ratio and the new K/U ratio reported here ultimately hinges on two key issues: (1) how to calculate a meaningful average ratio, and (2) decisions regarding the proportion of the "E-MORB source" vs. the proportion of the "N-MORB source" comprising the "composite MORB source".

Calculating the Average K/U Ratio

As discussed above, it is necessary to pose clear questions when engaging in an effort to calculate an "average" composition. If the question is: "What is the average K/U of basalts erupting at ridges?", then simple averaging of the K/U of every sample in a database is appropriate. If, however, the question is "what is the K/U of the MORB reservoir?", then averaging of ratios is not appropriate. This is because simply averaging

ratios does not account for the fact that a sample with the same K/U but a higher overall concentration will have a larger effect on the MORB reservoir K/U ratio. While the study by AM (2009) clearly aims to address the question of the average K/U ratio of the MORB reservoir, the technique used is a simple averaging of individual sample ratios. As a result, sample VG6387, with a K content of 450 ppm and a K/U ratio of 22517 has approximately the same effect on the AM (2009) calculated global MORB K/U ratio as sample VG 5259, with 227 ppm K and a K/U of 22130. The sample K/U ratios are weighted by the uncertainty in the analytical measurements, but not by concentration.

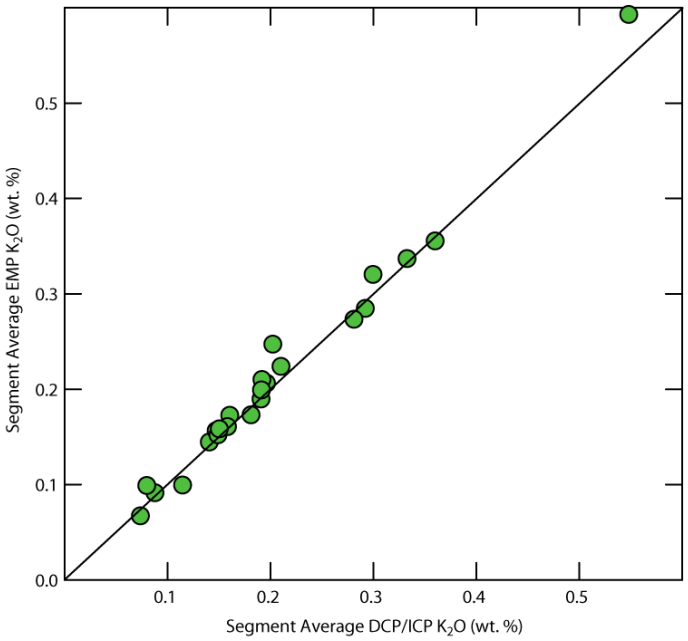

Figure 4.12: Comparison of mean K_2O calculated using EMP data vs. mean K_2O calculated using DCP/ICP data for 23 ridge segments containing samples with K_2O measured by both techniques in the Langmuir laboratory. Also shown is a 1:1 line for reference. Note how coherent the calculated mean K_2O values are using both techniques, with 19 of the 23 segment values agreeing to better than 9%.

An approach more suited to the question of reservoir K/U is described in the section on calculating trace element ratios, above. In brief, our approach involves calculating the global average K concentration using segment K values weighted by spreading rate and length, separately calculating the average U concentration using the same method, and then dividing the averages. Instead of average(K/U), as was the method employed in AM (2009), we calculate average(K)/average(U), for 1000 bootstrapped segment subsamples. The distribution of the 1000 K/U ratios provides a means of estimating the uncertainty on our reported global MORB K/U ratio. This method properly accounts for the effects of variable segment concentrations on the global ratios, and eliminates the need for extremely precise K/U ratios on depleted samples, further justifying our use of EMP K data.

The ultimate goal of estimating the K/U ratio of the MORB reservoir is to estimate

the K/U ratio of the MORB mantle, so weighting by concentration must be carefully considered. Our method of calculating averages is the most appropriate if the K or U contents of segments are largely driven by source variations. In this case, a more enriched mantle source leads to more enriched basalt compositions, and therefore weighting the enriched basalts is essentially weighting the more enriched mantle. Of course, the K or U concentration of a segment is not just related to the enrichment of the mantle source but also to the extent of melting. For example, if two segments are sampling the same mantle source, but one has 400 ppm K and the other 200 ppm K due to melting differences, then for purposes of estimating a mantle K/U ratio both segments should be weighted equally.

K and U are both highly incompatible elements, varying as approximately 1/F. Mean extent of melting differences likely differ by a factor of 2-3 (e.g., Klein and Langmuir, 1987), which will lead to at most a factor of 3 difference in K and U concentrations at segments related to melting effects. We observe a factor of 100 variation in the mean K contents of segments, and a factor of 200 variation in the U contents of segments. Melting effects on K and U clearly pale in comparison to source effects, and therefore our weighting by concentration is justified.

It must be stressed that the difference in approach between averaging ratios and calculating a ratio of averages is not trivial. Indeed, using the AM (2009) dataset, their estimated E-MORB ratio changes from 15700 to 13040 if the average ratio is calculated using the method (average(K)/average(U)) instead of average(K/U). This one change, with all else the same, then would move the AM (2009) DMM K/U ratio from 19000 to 17,800. The fact that the estimated E-MORB ratio changes when concentration is weighted suggests a change in K/U ratio with concentration. Indeed, considering the AM (2009) E-MORB samples, there appears to be a logarithmic decline in K/U ratio as U concentration increases. Interestingly, data from Jochum et al. (1983) shows no such variation with concentration, instead hovering at ratios similar to the AM (2009) samples with the highest U content (Figure 4.13).

Global proportions of 'N-MORB' and 'E-MORB'

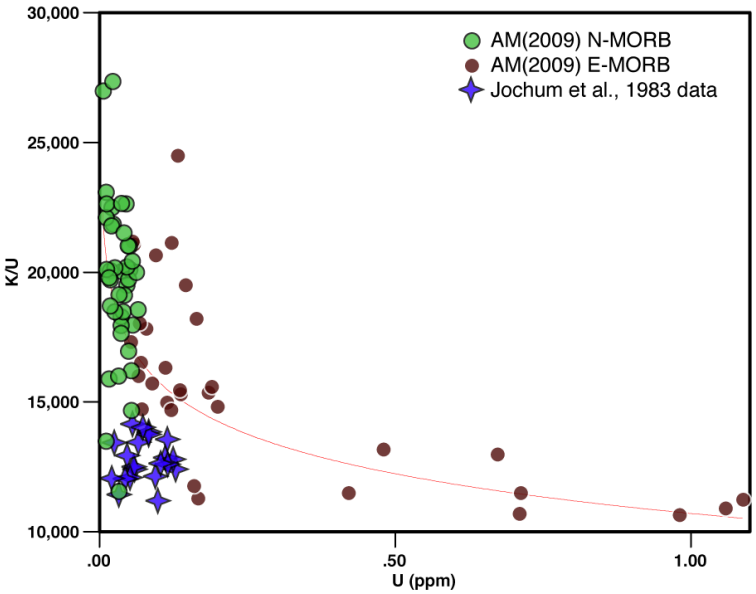

Figure 4.13: K/U versus U in the AM (2009) dataset (circles) compared to those measured by Jochum et al. (1983). Note that the AM (2009) data show a change in K/U with concentration, with higher U samples possessing a lower K/U ratio. Interestingly, the K/U ratios of the enriched samples measured by AM (2009) are similar to those of the Jochum et al. (1983) samples. That K/U changes with concentration suggests that higher concentration samples should be weighted more strongly when estimating the MORB source K/U ratio. Averaging sample K/U ratios to estimate the MORB source ratio, the method of AM (2009), does not account for the change in K/U with concentration apparent in their dataset.

The other difference between the results of the two studies is caused by the specific binning of N-MORB and E-MORB by AM (2009). They assign a K/U ratio to an N-MORB bin with a 95% mass contribution, and to an E-MORB bin with a 5% mass contribution, also allowing for a 6x enrichment weighting factor on the E-MORB bin (here allowing concentration to matter when calculating the global ratio). When it comes to creating the bin cutoffs, however, AM (2009) use La/Sm (un-normalized) of 1. This means that the E-MORB bin contains samples with normalized La/Sm ($(La/Sm)_{N)}$ ranging from 0.63 to 3.2. The issue is not in the definition of E-MORB or N-MORB, as that is ultimately arbitrary, but rather in the proportions assigned to each.

The mass contribution assumed for the N-MORB bin (no matter how N-MORB is defined) must correspond with observed distributions of basalt chemical data. Considering a histogram of La/Sm segment values in our database, note that only 32% of the segments, not 95%, have La/Sm<1 (Figure 4.14a). Narrowing the view to the segment scale, even in the canonical "N-MORB" MARK segment (MARR121) only 40% of the 47 measured samples have La/Sm <1 (Figure 4.14b). Considering both our global segment database and a classic N-MORB locality, it is clear that assigning a 95% contribution to an N-MORB bin defined by La/Sm < 1 is unjustified. At most it should be assigned a ~40% contribution to the MORB reservoir (with E-MORB then

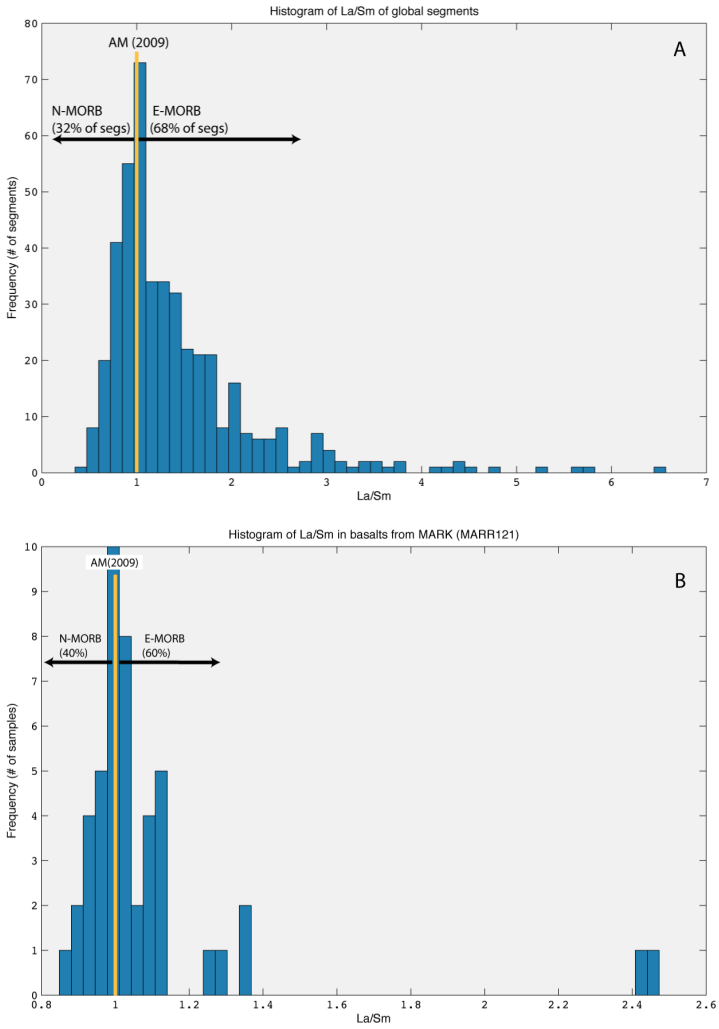

Figure 4.14: (a) Frequency distribution of the La/Sm (unnormalized) of segments in our global database. Using the definition of AM (2009) for E-MORB and N-MORB, 68% of segments would be "E-MORB segments" and 32% of segments would be "N-MORB segments." (b) Frequency distribution of the La/Sm of individual samples from the MARK segment (MARR121 in our segment catalog), a canonical "N-MORB" segment. Note that even in this depleted segment, only 40% of basalts have La/Sm<1. This demonstrates that the 95% mass contribution of N-MORB assumed in the modeling of AM (2009) requires modification.

contributing 60%).

AM (2009) pin their estimated proportions to the estimate by Donnelly et al., (2004) of an E-MORB contribution of ~3% (similar to their 5% value) based on the frequency of E-MORB erupting at the MARK segment. The Donnelly et al. (2004) estimate, however, was based on a definition of E-MORB of La/Sm > 2.4. If Donnelly et al. (2004) had defined E-MORB in the way AM (2009) do (La/Sm>1), their estimated E-MORB contribution would have increased to 60%. In short, any definition of E-MORB and N-MORB can be used to estimate the MORB source K/U ratio using the AM (2009) method as long as the proportional contributions are adjusted in line with the definition chosen. The invalid assignment of 95% mass contribution to a highly-depleted MORB subset leads to an AM (2009) composite MORB K/U ratio on the most depleted end of the basalt spectrum (Figure 4.11).

A true comparison of AM (2009) and this study thus requires determining average K and U for their E-MORB and N-MORB samples to weight the results by concentration, and using a proportion of E-MORB and N-MORB that corresponds with the global data set. Toward this end, if the mass contribution of the AM (2009) N-MORB bin is adjusted from 95% to 40%, and each bin is assigned a ratio based on average(K)/average(U) instead of average (K/U), the AM (2009) Mean MORB mantle K/U ratio is 13660. This result is insensitive to the definition of N- and E-MORB provided the proportions used reflect the global data distribution. For example, if instead the cutoff is La/Sm_N =1, the N-MORB bin contribution would increase to 72.5%, but the resulting reservoir K/U ratio is a very similar 13753. Given a reported uncertainty on the order of ± 2600, this new estimate for the mean MORB mantle ratio calculated using the AM (2009) dataset overlaps our reported ratio within error. The MORB K/U ratio, then, can be reliably estimated at ~13000. The high K/U of 19,000 for the MORB mantle reported in AM (2009) is not an accurate reservoir value.

4.6.2. Sm/Nd Ratio

In recent years, numerous studies have demonstrated that terrestrial silicate rocks have a $^{142}Nd/^{144}Nd$ excess relative to chondrites (e.g., Boyet and Carlson, 2005; Boyet and Carlson, 2006; Caro and Bourdon, 2010). There are two general possibilities to explain this difference: (1) the ^{142}Nd excess is caused by the decay of the short-lived isotope ^{146}Sm, or (2) the ^{142}Nd excess is caused by nucleosynthetic anomalies. Ranen and Jacobsen (2006) suggested that the difference between chondrites and terrestrial rocks is related to incomplete mixing in the solar nebula, and not to the decay of ^{146}Sm. Still others have challenged this position (Andreasen and Sharma, 2006, 2007; Carlson et al., 2007; Qin et al., 2011), and assert that the ^{142}Nd excess is most likely related to the decay of ^{146}Sm.

If indeed the ^{142}Nd anomaly is caused by the decay of ^{146}Sm, then either (1) the Earth had a non-chondritic Sm/Nd ratio from the beginning; or, (2) the Earth underwent an early differentiation event that created a high Sm/Nd “Early Depleted Reservoir (EDR)” and a low Sm/Nd “Early Enriched Reservoir” (Boyet and Carlson, 2008). For

the discussion here, whether the “accessible” mantle had a non-chondritic Sm/Nd ratio from the start, or attained it due to a differentiation event is immaterial. We wish to address the suggestion that the ‘predecessor to all modern terrestrial mantle reservoirs’ is the EDR (to account for the elevated $^{142}Nd/^{144}Nd$ relative to chondrites in terrestrial rocks), and that the EDR can be considered (non-chondritic) “primitive mantle” (Jackson and Carlson, 2011). To account for the ~18 ppm excess in terrestrial lavas relative to chondrites in ^{142}Nd, the Sm/Nd ratio of the EDR/non-chondritic primitive mantle is estimated to be 4.2-7.3% higher than chondrites (Jackson and Carlson, 2011), with uncertainties due to the 5 ppm error on the 18 ppm excess. Of course, ^{146}Sm is not the only radioactive isotope of Sm; ^{147}Sm also decays to ^{143}Nd. The estimated increase in the EDR Sm/Nd ratio, then, results in a predicted $^{143}Nd/^{144}Nd$ for the “primitive mantle” of 0.5130±0.0001 (Jackson and Carlson, 2012).

There are two concrete predictions about the EDR that we can compare to our global MORB study: the Sm/Nd ratio and the $^{143}Nd/^{144}Nd$ ratio. As MORB provide a random and global sampling of the upper mantle, their mean composition can shed light on models for the mantle composition. Note that the average Sm/Nd and $^{143}Nd/^{144}Nd$ MORB ratios utilized for the following comparison have not been weighted by spreading rate. We consider the mean mantle composition to be the average composition sampled along the length of the ridge system, with the composition of mantle sampled independent of spreading rate. For example, if the East Pacific Rise slowed in spreading rate by a factor of two, it would still be sampling the same mantle, and have the same source Sm/Nd and $^{143}Nd/^{144}Nd$.

We explore first the constraints from the Sm/Nd ratio of global MORB, excluding back-arcs and both including and excluding hotspot-influenced segments. A complexity in comparing the Sm/Nd ratio in MORB to the estimated Sm/Nd ratio for the EDR is caused by the fractionation of the Sm/Nd ratio during mantle melting. To address this, we inverted for a mantle source Sm/Nd, assuming non-modal batch melting (similar results to pooled fractional melting) using the mineralogy, p- and d-values in Gale et al. (2011) (regional mantle source) for a reasonably large F range between 8 and

15%. By 15% melting, the MORB Sm/Nd ratio matches the source ratio. Considering a global MORB Sm/Nd (excluding back-arcs) of 0.319±.005, we find that the mantle source for global MORB, at the highest end (F=8%) would have a Sm/Nd ratio of 0.331-0.341. As F increases to 15%, the mantle source Sm/Nd ratio inferred for global MORB decreases. Remarkably, the estimates for the Sm/Nd ratio of the EDR "primitive" mantle are between 0.342 and 0.352 (4.2-7.3% higher than chondrites), slightly more depleted than our global MORB estimated mantle source ratio.

If just considering "normal segments" more than 500 km from any known mantle plume, the estimated mantle source Sm/Nd ratio for normal MORB (Sm/Nd ratio = 0.325±0.0046), at its highest (F of 8%), ranges from 0.338-0.347. It is worth pointing out that our average MORB Sm/Nd ratios are not unusually enriched; the Sm/Nd ratio of global MORB in Su (2002) is 0.328, and the global mean and log-normal mean Sm/Nd ratios in the recent study by AM (2010) are 0.32 and 0.332, respectively. All studies suggest that the current MORB mantle source in terms of Sm/Nd ratio overlaps the estimate for the EDR, or non-chondritic primitive mantle.

This can be even more directly explored using the mean MORB $^{143}Nd/^{144}Nd$, as it does not depend on an inversion for mantle source and therefore provides a direct comparison between MORB mantle and the estimated $^{143}Nd/^{144}Nd$ for the EDR. Jackson and Carlson (2012) predict the isotopic range for "primitive mantle" to be between 0.51290 and 0.5131. Both our mean $^{143}Nd/^{144}Nd$ for all segments (excluding back-arcs, 0.513057±0.000017) and normal segments (0.513072±0.000018) fall within this range. Interestingly, the "All MORB" $^{143}Nd/^{144}Nd$ of 0.5131 estimated by Salters and Stracke (2004), with filters to exclude most plume-influenced segments, is also within the range of "primitive mantle". The $\varepsilon^{143}Nd$ values of MORB in this study (8-9), even excluding plume-influenced segments, are more enriched than has been previously assumed ($\varepsilon^{143}Nd$ +10; Carlson and Boyet, 2008). Even the D-MORB segments in this study, with $La/Sm_N<0.8$, have mean $\varepsilon^{143}Nd$ = +9. Associating an $\varepsilon^{143}Nd$ of +10 with the MORB source is simply unsubstantiated by the data.

The conclusion, then, is that the current MORB-source mantle overlaps the composition of the estimated EDR or non-chondritic primitive mantle. We suggest

here that if MORB can be considered a representative sample of the upper mantle (often referred to as "DMM"), then DMM=EDR. In this case there is no possibility of a complementary relationship between continental crust and oceanic upper mantle. The entire relationship between depleted upper mantle and continental crust would need to be revisited. A far more likely conclusion is that the accessible Earth is chondritic in composition. The data from the global ocean basins suggest that the non-chondritic primitive mantle hypothesis is problematic and unlikely.

4.7. Conclusions

The key points of this study are:

(1) We have created the most comprehensive MORB database to date, including a detailed catalog of 771 global ridge segments, a major element database that has been carefully interlab-bias corrected and re-normalized, and a predominantly ICP-MS trace element database manually checked for data quality and including more than 40% unpublished data, over 800 of which are published here.

(2) The segment catalog enables the calculation of "segment values" with average chemistry for all segments with basalt data. Unlike earlier studies, the segment-value approach enables a weighting by both segment length and spreading rate to calculate the mean global MORB composition. It also provides a method to deal with uneven sampling, as segments with 100 samples or 10 samples are each assigned one chemical value per element.

(3) To provide meaningful uncertainties on the calculated weighted averages, we use the bootstrapping statistical technique to resample our segment population and generate 1000 means from these 1000 bootstrapped subsamples. The distribution of the 1000 means enables us to provide a 95% confidence interval on each mean value (both element and element ratio) we report.

(4) These approaches provide the most reliable and quantitative estimates of the mean composition of the ocean crust, and a new definition of MORB. All MORB reflects the true mean composition of the zero age ocean crust. N-MORB is the

most likely composition encountered away from hot spots and back-arc basins. D-MORB is the depleted end member of the MORB population. The concept of a highly depleted "normal ocean crust" should be abandoned.

(5) E-MORB cannot be defined as segments close to plumes, since some of these segments are not enriched, but can be defined as the mean of all segments with $(La/Sm)_N > 1.5$.

(6) Pacific MORB are slightly more fractionated than Indian or Atlantic MORB. Indian MORB show signs of a lower mean extent of melting in major elements, with the exception of TiO_2, which remains to be explained. With regard to trace elements, Atlantic MORB are the most enriched in highly incompatible elements and depleted in moderately incompatible elements, explained by the extensive plume influence in the Atlantic. Indian MORB show lower Ce/Pb and anomalous $^{206}Pb/^{204}Pb$, as had been suggested previously (Rehkamper and Hofmann, 1997 and references therein).

(7) Back-arc basin basalts show pronounced peaks in Cs, Rb, Ba, U, Pb, and Sr, evidence of the "wet" arc component that delivers these fluid-mobile elements. They also possess noticeably lower mean concentrations of the moderately incompatible elements, demonstrating that the increased water at BAB also leads to higher extents of melting (Langmuir et al., 2006).

(8) The K/U ratio of MORB, and by extension MORB-source mantle, is ~13,000. The recent estimate of 19,000 by Arevalo and McDonough (2009) is unsubstantiated by the current study, and we obtain the same value within error of our value using their data with a more appropriate methodology.

(9) The Sm/Nd ratio estimated for the MORB-source mantle and the mean $^{143}Nd/^{144}Nd$ of MORB (even when excluding segments within 500 km of hotspots) overlap those estimated for the "non-chondritic primitive mantle" (e.g., Jackson and Carlson, 2012). If MORB source mantle is equivalent to the non-chondritic primitive mantle, this could create serious mass-balance issues for the silicate Earth, making a non-chondritic primitive mantle unlikely.

References

Albarede, F. (1998), Time-dependent models of U-Th-He and K-Ar evolution and the layering of mantle convection, Chemical Geology, 145(3-4), 413-429.

Andreasen, R., and M. Sharma (2006), Solar nebula heterogeneity in p-process samarium and neodymium isotopes, Science, 314(5800), 806-809.

Andreasen, R., and M. Sharma (2007), Mixing and homogenization in the early solar system: Clues from Sr, Ba, Nd, and Sm isotopes in meteorites, Astrophysical Journal, 665(1), 874-883.

Arevalo, R., Jr., and W. F. McDonough (2010), Chemical variations and regional diversity observed in MORB, Chemical Geology, 271(1-2), 70-85.

Arevalo, R., Jr., W. F. McDonough, and M. Luong (2009), The K/U ratio of the silicate Earth: Insights into mantle composition, structure and thermal evolution, Earth and Planetary Science Letters, 278(3-4), 361-369.

Argus, D. F., R. G. Gordon, and C. DeMets (2011), Geologically current motion of 56 plates relative to the no-net-rotation reference frame, Geochemistry Geophysics Geosystems, 12.

Asimow, P. D., J. E. Dixon, and C. H. Langmuir (2004), A hydrous melting and fractionation model for mid-ocean ridge basalts: Application to the Mid-Atlantic Ridge near the Azores, Geochemistry Geophysics Geosystems, 5.

Bézos, A., S. Escrig, C. Langmuir, P. J. Michael, and P. D. Asimow (2009), Origins of chemical diversity of back-arc basin basalts: a segment-scale study of the Eastern Lau Spreading Center, Journal of Geophysical Research, 114, 1-25.

Bézos, A. (2003), Study of lithophile and siderophile elements (Ir, Ru, Pt and Pd) in mid-oceanic ridge basalts.

Bird, P. (2003), An updated digital model of plate boundaries, Geochemistry Geophysics Geosystems, 4.

Boyet, M., and R.W. Carlson (2005), 142Nd Evidence for Early (>4.53 Ga) Global Differentiation of the Silicate Earth, Science, 309, 576-581.

Boyet, M., and R.W. Carlson (2006), A new geochemical model for the Earth's mantle inferred from 146Sm-142Nd systematics, Earth and Planetary Science Letters, 250, 254-268.

Burnham, C. W., and N. F. Davis (1974), Role of H2O in silicate melts .2. Thermodynamic and phase relations in system NaAlSi3O8-H2O to 10 kilobars, 700°C to 1100°C, Am. J. Sci., 274(8), 902-940.

Cannat, M., et al. (1999), Mid-Atlantic Ridge-Azores hotspot interactions: along-axis migration of a hotspot-derived event of enhanced magmatism 10 to 3 Ma ago, Earth and Planetary Science Letters, 173(3), 257-269.

Carlson, R. W., and M. Boyet (2008), Composition of the Earth's interior: the importance of early events, Philosophical Transactions of the Royal Society a-Mathematical Physical and Engineering Sciences, 366(1883), 4077-4103.

Carlson, R. W., M. Boyet, and M. Horan (2007), Chondrite barium, neodymium, and

samarium isotopic heterogeneity and early earth differentiation, Science, 316(5828), 1175-1178.

Caro, G., and B. Bourdon (2010), Non-chondritic Sm/Nd ratio in the terrestrial planets: Consequences for the geochemical evolution of the mantle crust system, Geochim. Cosmochim. Acta, 74(11), 3333-3349.

Courtillot, V., A. Davaille, J. Besse, and J. Stock (2003), Three distinct types of hotspots in the Earth's mantle, Earth and Planetary Science Letters, 205(3-4), 295-308.

Cousens, B. L., J. F. Allan, M. I. Leybourne, R. L. Chase, and N. Vanwagoner (1995), Mixing of magmas from enriched and depleted mantle sources: the Northeast Pacific – West-Valley segment, Juan de Fuca Ridge, Contributions to Mineralogy and Petrology, 120(3-4), 337-357.

Davies, G. F. (1999), Geophysically constrained mantle mass flows and the (40)Ar budget: a degassed lower mantle?, Earth and Planetary Science Letters, 166(3-4), 149-162.

Demets, C., R. G. Gordon, D. F. Argus, and S. Stein (1994), Effect of recent revisions to the geomagnetic reversal time-scale on estimates of current plate motions, Geophysical Research Letters, 21(20), 2191-2194.

Devore, J., and R. Peck (2005), Statistics: The Exploration and Analysis of Data, Fifth ed., Brooks/Cole.

Dixon, J. E., E. M. Stolper, and J. R. Holloway (1995), An experimental study of water and carbon dioxide solubilities in mid ocean ridge basaltic liquids .1. Calibration and solubility models, Journal of Petrology, 36(6), 1607-1631.

Donnelly, K. E., S. L. Goldstein, C. H. Langmuir, and M. Spiegelman (2004), Origin of enriched ocean ridge basalts and implications for mantle dynamics, Earth and Planetary Science Letters, 226(3-4), 347-366.

Dupre, B., and C. J. Allegre (1983), Pb-Sr Isotope Variation in Indian-Ocean Basalts and Mixing Phenomena, Nature, 303(5913), 142-146.

Escartin, J., M. Cannat, G. Pouliquen, A. Rabain, and J. Lin (2001), Crustal thickness of V-shaped ridges south of the Azores: Interaction of the Mid-Atlantic Ridge (36 degrees-39 degrees N) and the Azores hot spot, Journal of Geophysical Research-Solid Earth, 106(B10), 21719-21735.

Fowler, C. M. R. (2005), The Solid Earth: An Introduction to Global Geophysics, Cambridge University Press.

Gaetani, G. A., and T. L. Grove (1998), The influence of water on melting of mantle peridotite, Contributions to Mineralogy and Petrology, 131(4), 323-346.

Gale, A., S. Escrig, E. J. Gier, C. H. Langmuir, and S. L. Goldstein (2011), Enriched basalts at segment centers: The Lucky Strike (37 degrees 17 ' N) and Menez Gwen (37 degrees 50 ' N) segments of the Mid-Atlantic Ridge, Geochemistry Geophysics Geosystems, 12.

Goldstein, S. L., G. Soffer, C. H. Langmuir, K. A. Lehnert, D. W. Graham, and P. J. Michael (2008), Origin of a 'Southern Hemisphere' geochemical signature in the Arctic upper mantle, Nature, 453(7191), 89-+.

Hamelin, B., B. Dupre, and C. J. Allegre (1986), Pb-Sr-Nd Isotopic Data of Indian-Ocean Ridges - New Evidence of Large-Scale Mapping of Mantle Heterogeneities, Earth and Planetary Science Letters, 76(3-4), 288-298.

Hart, S. R. (1984), A large-scale isotope anomaly in the southern-hemisphere mantle, Nature, 309(5971), 753-757.

Hirth, G., and D. L. Kohlstedt (1996), Water in the oceanic upper mantle: Implications for rheology, melt extraction and the evolution of the lithosphere, Earth and Planetary Science Letters, 144(1-2), 93-108.

Hofmann, A. W. (1988), Chemical differentiation of the Earth: the relationship between mantle, continental crust, and oceanic crust, Earth and Planetary Science Letters, 90, 297-314.

Hofmann, A. W., K. P. Jochum, M. Seufert, and W. M. White (1986), Nb and Pb in oceanic basalts: new constraints on mantle evolution, Earth and Planetary Science Letters, 79, 33-45.

Jackson, M. G., and R. W. Carlson (2011), An ancient recipe for flood-basalt genesis, Nature, 476(7360), 316-U377.

Jackson, M. G., and R. W. Carlson (2012), Homogeneous superchondritic $^{142}Nd/^{144}Nd$ in the mid-ocean ridge basalt and ocean island basalt mantle, Geochemistry Geophysics Geosystems, 13(Q01011), 10.

Jenner, F. E., and H. S. C. O'Neill (2012), Analysis of 60 elements in 616 ocean floor basaltic glasses, Geochemistry Geophysics Geosystems, 13.

Jochum, K. P., A. W. Hofmann, E. Ito, H. M. Seufert, and W. M. White (1983), K, U and Th in mid-ocean ridge basalt glasses and heat-production, K/U and K/Rb in the mantle, Nature, 306(5942), 431-436.

Klein, E. M., and C. H. Langmuir (1987), Global correlations of ocean ridge basalt chemistry with axial depth and crustal thickness, JGR 92(B8), 8089-8115.

Klein, E. M., C. H. Langmuir, and H. Staudigel (1991), Geochemistry of basalts from the Southeast Indian Ridge, 115°E-138°-E, Journal of Geophysical Research-Solid Earth and Planets, 96(B2), 2089-2107.

Langmuir, C. H., J. F. Bender, and R. Batiza (1986), Petrological and tectonic segmentation of the East Pacific Rise, 5-degrees-30'-14-degrees-30'-N, Nature, 322(6078), 422-429.

Langmuir, C. H., E. M. Klein, and T. Plank (1992), Petrological systematics of mid-ocean ridge basalts – constraints on melt generation beneath ocean ridges, in Mantle Flow and Melt Generation at Mid-Ocean Ridges, edited by J. P. Morgan, pp. 183-280.

Langmuir, C. H., Bezos, A., Escrig, S. and Parman, S.W. (2006), Chemical Systematics and Hydrous Melting of the Mantle in Back-Arc Basins, in Back-Arc Spreading Systems: Geological, Biological, Chemical and Physical Interactions, edited, American Geophysical Union: Geophysical Monograph Series 166.

Lassiter, J. C. (2004), Role of recycled oceanic crust in the potassium and argon budget of the Earth: Toward a resolution of the "missing argon" problem, Geochemistry Geophysics Geosystems, 5.

Lehnert, K., Y. Su, C. H. Langmuir, B. Sarbas, and U. Nohl (2000), A global geochemical database structure for rocks, Geochemistry Geophysics Geosystems, 1.

Macdonald, K. C. (1982), Mid-Ocean Ridges: Fine scale Tectonic, volcanic and hydrothermal processes within the plate boundary zone, Annual Review of Earth and

Planetary Sciences, 10, 155-190.

Melson, W. G., T. O'Hearn, and E. Jarosewich (2002), A data brief on the Smithsonian Abyssal Volcanic Glass Data File, Geochemistry Geophysics Geosystems, 3, 11.

Newman, S., and J. B. Lowenstern (2002), VOLATILECALC: a silicate melt-H2O-CO2 solution model written in Visual Basic for excel, Computers & Geosciences, 28(5), 597-604.

Niu, Y. L., K. D. Collerson, R. Batiza, J. I. Wendt, and M. Regelous (1999), Origin of enriched-type mid-ocean ridge basalt at ridges far from mantle plumes: The East Pacific Rise at 11 degrees 20 ' N, Journal of Geophysical Research-Solid Earth, 104(B4), 7067-7087.

Qin, L., R. W. Carlson, and C. M. O. D. Alexander (2011), Correlated nucleosynthetic isotopic variability in Cr, Sr, Ba, Sm, Nd and Hf in Murchison and QUE 97008, Geochim. Cosmochim. Acta, 75(24), 7806-7828.

Ranen, M. C., and S.B. Jacobsen (2006), Barium Isotopes in Chondritic Meteorites: Implications for Planetary Reservoir Models, Science, 314, 809-812.

Rehkamper, M., and A. W. Hofmann (1997), Recycled ocean crust and sediment in Indian Ocean MORB, Earth and Planetary Science Letters, 147(1-4), 93-106.

Rubin, K. H., and J. M. Sinton (2007), Inferences on mid-ocean ridge thermal and magmatic structure from MORB compositions, Earth and Planetary Science Letters, 260(1-2), 257-276.

Ryan, W. B. F., et al. (2009), Global Multi-Resolution Topography synthesis, Geochemistry Geophysics Geosystems, 10.

Salters, V. J. M., and A. Stracke (2004), Composition of the depleted mantle, Geochemistry Geophysics Geosystems, 5(5), 27.

Schilling, J. G., M. Zajac, R. Evans, T. Johnston, W. White, J. D. Devine, and R. Kingsley (1983), Petrologic and geochemical variations along the Mid-Atlantic Ridge from 29-degrees-N to 73-degrees-N, Am. J. Sci., 283(6), 510-586.

Sims, K. W. W., and D. J. DePaolo (1997), Inferences about mantle magma sources from incompatible element concentration ratios in oceanic basalts, Geochim. Cosmochim. Acta, 61(4), 765-784.

Sinton, J. M., and P. Fryer (1987), Mariana trough lavas from 18°N - Implications for the origin of back-arc basin basalts, Journal of Geophysical Research-Solid Earth and Planets, 92(B12), 12782-12802.

Standish, J. (2005), The Influence of Ridge Geometry on Lithospheric Accretion at Ultraslow-Spreading Rates between 9°-25°E on the Southwest Indian Ridge: Basalt Composition Sensitivity to Local Tectonomagmatic Processes, Massachusetts Institute of Technology.

Su, Y. (2002), Mid-Ocean Ridge Basalt Trace Element Systematics: Constraints from database management, ICP-MS analyses, global data compilation, and petrologic modeling, Columbia University.

Sun, S. s., and W. F. McDonough (1989), Chemical and isotopic systematics of oceanic basalts: implications for mantle composition and processes, Geological Society, London, Special Publications, 42(1), 313-345.

Sun, S. S., R. W. Nesbitt, and A. Y. Sharaskin (1979), Geochemical characteristics of mid-ocean ridge basalts, Earth and Planetary Science Letters, 44, 119-138.

Sun, W., Y. Hu, V. S. Kamenetsky, S. M. Eggins, M. Chen, and R. J. Arculus (2008), Constancy of Nb/U in the mantle revisited, Geochim. Cosmochim. Acta, 72(14), 3542-3549.

Sun, W. D., V. C. Bennett, S. M. Eggins, R. J. Arculus, and M. R. Perfit (2003), Rhenium systematics in submarine MORB and back-arc basin glasses: laser ablation ICP-MS results, Chemical Geology, 196(1-4), 259-281.

van Westrenen, W., J. D. Blundy, and B. J. Wood (2001), High field strength element/rare earth element fractionation during partial melting in the presence of garnet: Implications for identification of mantle heterogeneities, Geochemistry Geophysics Geosystems, 2.

Weyer, S., C. Munker, and K. Mezger (2003), Nb/Ta, Zr/Hf and REE in the depleted mantle: implications for the differentiation history of the crust-mantle system, Earth and Planetary Science Letters, 205(3-4), 309-324.

White, W. M., and J. G. Schilling (1978), The nature and origin of geochemical variation in Mid-Atlantic Ridge basalts from central North Atlantic, Geochim Cosmochim Acta 42, 1501-1516.

Chapter 5

The Global Systematics of Ocean Ridge Basalts: Tests of Mantle Temperature and Mantle Composition Hypotheses

5.1. Introduction

The temperature and composition of the upper mantle are critical to our understanding of solid Earth processes. Temperature and compositional variations have implications for convection, volcanism and crustal uplift and subsidence. The petrology of ocean ridge basalts provides a means to investigate these variations, as ridge basalts are a product of mantle melting and occur globally.

The potential temperature of the mantle exerts a primary influence on its overall extent of melting. Hotter mantle intersects the solidus deeper, melting to a larger overall extent and producing a thicker basaltic crust. Using the principles of isostasy, thicker crust should be situated at higher elevations than thinner crust. The concentration of many incompatible elements, like Na and Ti, vary approximately inversely with the extent of melting. Taken together, these arguments suggest that, for an approximately homogeneous source, areas of the ridge with shallow depths will have low concentrations of incompatible elements. This was shown to be the case by Klein and Langmuir (1987), who interpreted global chemical basalt systematics in terms of mantle temperature variations of ~220ºC.

This interpretation is not accepted by all, however. Some argue that the temperature of the mantle is roughly uniform beneath ridges, either warm (e.g., Green et al., 2001) or cool (Shen and Forsyth, 1995; Presnall et al., 2002). Others have asserted that compositional, rather than temperature, variations are the dominant influence on variations in the chemical compositions of erupted basalts (e.g., Niu and O'Hara, 2008).

Still others contend that melt-rock reaction can explain the global variations in ocean ridge basalts (Kimura and Sano, 2012).

There is thus a fundamental and persistent debate in the literature with regard to which variable – composition, temperature or crustal processing – exerts the most important influence on ocean ridge basalt compositions. Adding to the complexity is the issue that erupted basalt compositions have cooled (fractionated) since their generation as primary mantle melts. This fractionation leads to changes in the chemical composition of basalts that are unrelated to mantle melting or reaction processes. Therefore, answers to the large-scale mantle questions require that basalt compositions be carefully corrected for the effects of crystal fractionation to arrive at parental magma compositions that can be more readily interpreted.

In this study, we take advantage of an unparalleled major element database in terms of size and quality, and use an improved approach to fractionation correction to arrive at parental magma estimates for over 240 global ridge segments. These magma compositions can then be explored for global variations that may be interpreted in the light of the competing hypotheses for their origin.

5.2. Calculating Segment "8-" and "90-"values

The recently submitted manuscript by Gale et al. (2012) includes a carefully compiled database of inter-laboratory bias-corrected, filtered, renormalized major element data for whole rocks and glasses. Each sample with a major element analysis is also assigned to a ridge segment (catalog of ridge segments provided in Gale et al. (2012), submitted). This database is perfectly suited for a systematic global correction for the effects of low-pressure crystal fractionation, to allow for an assessment of the chemical systematics derived from mantle processes.

Through the years various fractionation correction techniques have been applied, including the 'constant slope' technique using MgO (Klein and Langmuir (1987)) and more complex polynomial equations using Mg/(Mg+Fe) (Mg#; Niu and O'Hara, 2008, hereafter referred to as NO (2008)). In contrast to previous approaches, in this study

we customize the fractionation correction scheme for each individual segment, feasible because of the segment-scale approach to compiling the major element database in Gale et al. (2012), submitted. Customizing the fractionation approach for each segment is a unique and important aspect of this study, as crystallization sequences and slopes can vary considerably from place to place.

To carry out fractionation correction in a systematic manner on such a large dataset, a basic set of guidelines was established. One involved how many samples a given segment needed in order to qualify for fractionation correction, given the competing priorities of including as many segments as possible for global coverage, and excluding segments that would lead to very poorly constrained values. To be included, a segment needed to have interlab bias-corrected major element data on glasses available from a minimum of three locations. The location requirement stems from the fact that 15-20 glass chips are often analyzed from a given dredge location and we wanted to avoid basing our fractionation-corrected mean estimates on one dredge location.

This requirement led to 182 qualified segments, out of 771 total segments, and 465 segments with at least some data. To put our knowledge of the global ridge system in perspective, this result shows that less than 25% of global ridge segments have published major element data on glasses from even three locations (albeit with interlab bias factors). To increase the global coverage in some poorly sampled regions such as the Southwest Indian Ridge (SWIR), Pacific-Antarctic Ridge (PAR), and some regions of the Mid-Atlantic Ridge (MAR), we merged individual segments into longer ones (e.g., 'SWIR47SWIR48'). In the case of merged segments, we reduced the location requirement from three to two with glass data and interlab bias factors. In certain instances it was also appropriate to allow whole rock data to satisfy the criteria, as certain authors (notably J.G. Schilling) worked with carefully prepared aphyric whole rocks (WR). By merging segments and allowing for WR in certain circumstances, we increased the number of segments qualified for fractionation correction to 241. Note that the following discussion pertains to *glasses with interlab bias correction factors*. Any exceptional cases where WR were used, or interlab bias correction factors were not required, are noted in the Appendix.

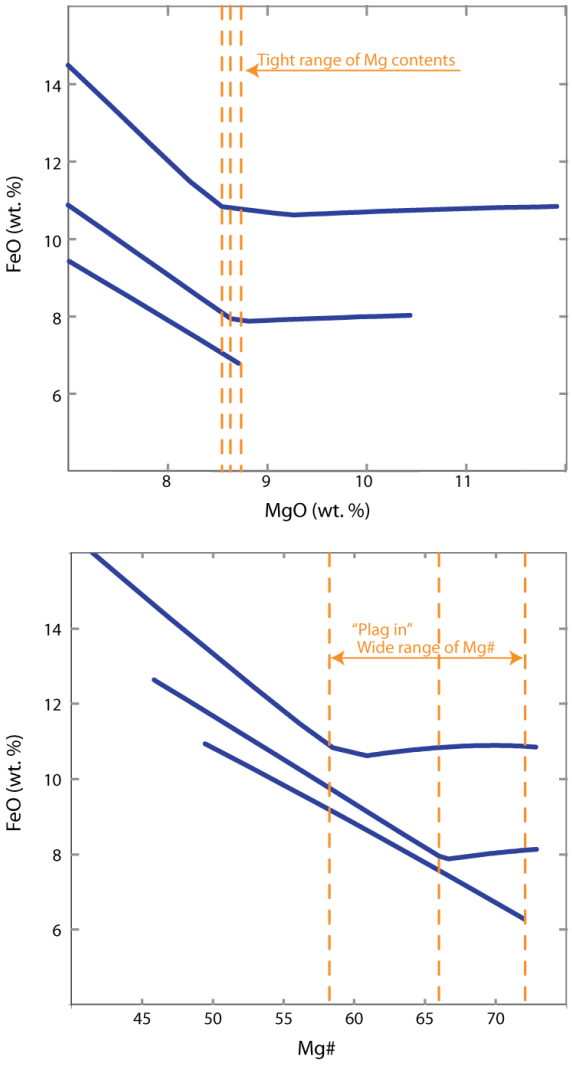

Figure 5.1: Diagrams showing liquid lines of descent (dark blue lines; calculated using hBasalt, Bézos et al., in prep) from high FeO, medium FeO and low FeO parental magmas. Note that all three magmas begin crystallizing plagioclase (indicated by dashed orange line) at a narrow MgO interval near 8.5 wt. %. In contrast, the three magmas begin crystallizing plagioclase at a wide range of Mg#. This demonstrates the motivation for fractionation correction based on MgO, which is applicable to a wide compositional range, as opposed to the Mg# approach.

For each of these 241 segments, we examined individual variation diagrams (including SiO_2, FeO_T, Al_2O_3, CaO, Na_2O, TiO_2 and K_2O versus MgO, and P_2O_5 vs. K_2O and TiO_2 vs. Na_2O) to manually determine the appropriate fractionation correction method. We first established the straightforward protocol that there would be two slopes used for fractionation correction: one for the "olivine-only" slope when only olivine is crystallizing (slopes provided in Appendix), and one for the "custom slope" when plagioclase ± clinopyroxene (cpx) have joined the liquidus. The use of a hinge point is essential to avoid erroneously high values in high MgO samples.

For simplicity, we assume that the hinge point between the two slopes occurs at 8.5 wt.% MgO, in keeping with experimental data and calculated liquid lines of descent that show typical plagioclase saturation in ocean ridge basalts just higher than 8 wt.% MgO. Indeed, over a wide range of initial parental magma FeO contents of 7-11 wt. %, plagioclase saturates very near to 8.5 wt.% MgO (Figure 5.1; liquids lines of descent from hBasalt, Bézos et al., in prep). It occurs at slightly lower MgO contents as FeO contents increase, as FeO is

not a component of plagioclase. Thus increasing FeO stabilizes olivine and destabilizes plagioclase. The relative uniformity of MgO content where ocean ridge basalts saturate with plagioclase is in stark contrast to the Mg/(Mg+Fe) where plagioclase saturates. Plagioclase saturation occurs over a wide Mg# range, with the highest FeO magmas requiring a much lower Mg# in order to stabilize plagioclase as a crystallizing phase. This important difference between MgO and Mg# must be recognized when carrying out fractionation correction, especially if using a Mg#-based approach. Note that occasionally the data required that the hinge point be adjusted, as described further below.

For a decision on the "custom slope", we examined the major element variations for each segment and then chose the most appropriate slope using one of three possible methods, designated by "method codes". A method code was assigned to SiO_2, FeO_T, Al_2O_3, CaO, Na_2O and TiO_2 for each segment. K_2O and P_2O_5 were handled differently, as discussed below. The three options for calculating the custom slope were: (1) use the slope defined by the individual data between 5 and 8.5 wt.% MgO, preferable when a large amount of data provided a well determined slope; (2) use the slope defined by the "location averages" (details below); (3), canonical slopes, using the values in Langmuir et al. (1992) - this was optimal, for example, when a small number of samples with considerable dispersion were present. For case (2), there were at least 3 unique sample locations used for each segment, and only samples between 5 and 8.5 wt.% MgO were considered. The mean value for each location was calculated (could be from one or multiple samples), and the best-fitting line was calculated through these 'location means'. Thus, the best-fitting line in method 2 was determined from at least three points, and usually many more. The three slopes were shown on each variation diagram to aid our selection of the most appropriate custom slope. Note that the estimated regressions for methods (1) and (2) are orthogonal regressions, which minimize the perpendicular distance from each point to the line. Most line-fitting techniques minimize the vertical distance (y-axis) from point to line, which assumes that all of the error is in the vertical direction. Our approach assigns the error to both the x- and y-variables.

In certain segments there are dozens of samples with MgO contents near 8 wt.% MgO, in which cases we adopted a fourth method. Method 4 calculated the average

of samples with MgO between 7.5 and 8.5 wt.% for each oxide, and then moved that mean oxide content to 8 wt.% MgO along the canonical slopes from method 3. The rationale behind method 4 is that when large quantities of data exist, a robust 8-value calculation is possible with minimal fractionation correction.

All the variation diagrams are available in the on-line appendix as well as the method code selection, the slope used, and the average and standard deviation of the segment 8-values. We also provide a separate file including the individual glass samples with their major elements corrected to 8 wt. % MgO that were included in the calculation of the 8-values, and their original data for comparison. Figure 5.2 shows sample correction schemes for three different segments from different ocean basins. Note how the slopes for FeO or Na_2O vary slightly from segment to segment, an important feature

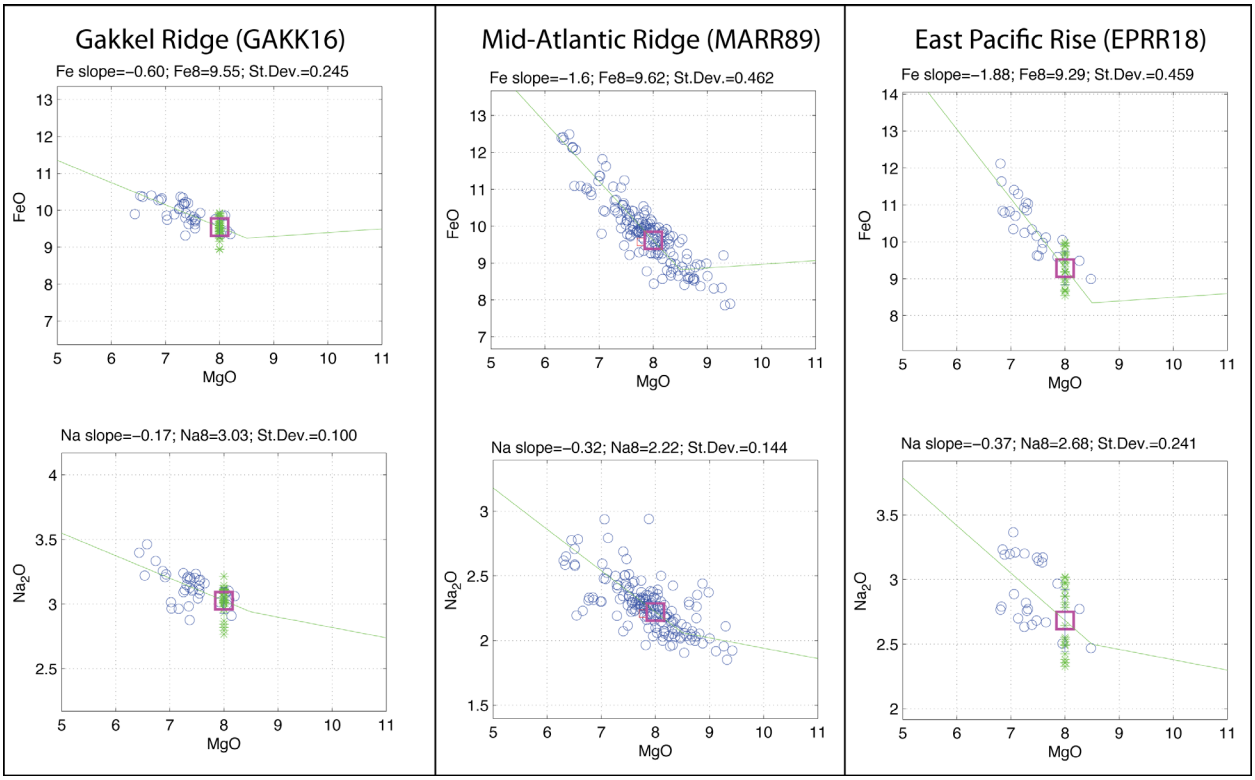

Figure 5.2: Example variation diagrams (FeO versus MgO and Na_2O versus MgO) for three segments from our global catalog. Open blue circles indicate the sample data, green lines show the slopes (olivine only and custom) used for correction to 8 wt.% MgO, green asterisks show the location of the corrected samples at 8 wt.% MgO, and the pink box indicates the calculated mean segment '8-value'. Also shown at the top of each diagram are the custom slope value, the mean segment 8-value, and the standard deviation of the sample 8-values. Note that from region to region there are variable, but well constrained, fractionation slopes. Our method accounts for this variation by allowing the data to define the slope for fractionation correction, as opposed to the 'constant-slope' and polynomial corrections found in the literature.

to account for when calculating 8-values.

K_2O and P_2O_5 were treated differently because, unlike the other major element oxides, they behave as incompatible trace elements during low-pressure fractionation. We did not customize with a method code and instead used one slope for the custom slope and one slope for olivine-only, using the log of the abundance (see Langmuir et al. (1992)).

Customizing the correction to suit each individual ridge segment being considered, rather than blindly applying a formula to the entire dataset, is a part of our approach that distinguishes it from all previous studies. It also ensures that the "8-values" correspond with the data distribution in each segment.

5.2.1. Calculating Segment 8-values

With the custom slopes assigned, to arrive at a final segment 8-value we moved all samples with >5.5 and <8.5 wt. % MgO to 8 along the custom slope specified for each oxide. Any samples with >8.5 wt. % MgO were moved first to 8.5 wt.% along the olivine-only slope and then to 8 along the custom slope. Samples with <5.5 wt. % MgO were considered too far away from 8 to give reliable values and therefore were excluded from the 8-value calculations. With each sample moved to its estimated composition at MgO=8 (see green asterisks in Figure 5.2), we then calculated the average for each oxide at 8 (the segment "8-value") and the standard deviation.

Data from some segments did not fit into the correction scheme presented above. The discrepancies are of several different types. (1) There is a particular magma type erupted periodically around the global system of ridges which is a "HiAl" magma, characterized by exceptionally high Al_2O_3 contents, high MgO, low SiO_2 (e.g., 48% SiO_2) and often very low TiO_2. Such samples do not occupy an entire segment, but occur sporadically in certain segments, particularly on the margins of hot spots (e.g., Eason and Sinton, 2006; Gale et al., 2012 in press). These compositions were not included in the segment averages, as they reflect a unique sample type and petrogenesis. (2) Occasionally the plagioclase-in hinge point was at higher values than 8.5% MgO. In this case using olivine only slopes for the higher MgO samples would lead to erroneous data points. This led to the occasional application of a "MgMax" screen to eliminate the high MgO

samples. (3) There was also occasionally a kink in the liquid line of descent at about 6% MgO. Rather than including yet another slope in correcting the data, we simply set a "MgMin" parameter to eliminate the low MgO samples from the calculation of the segment average. (4) For a few segments, the hinge point for plagioclase-in is at lower MgO. For segments with a lower MgO hinge point, the MgO content of the plagioclase-in slope was adjusted. All of the above corrections generally make little difference to the mean calculated "8-values", though they do reduce the errors somewhat. All segments for which these restrictions were emplaced are identified in the Appendix. Readers are invited to examine the individual segment plots to make their own evaluation.

As mentioned, in order to increase the global coverage we included some WR data where glass major element data were not available, especially in regions of the ridge system where J.G. Schilling worked. Along the PAR, Hamelin et al. (2010) recently released data on WR. While the data is on WR and lacking interlab bias correction factors, the PAR is so under sampled that we decided to use the major element data for 8-value calculations. Segment 8-values based on WR data are noted in the Appendix.

The data quantity and quality and the amount of "geological noise" in various ridge segments is quite variable. Some segments have abundant data and clear and tight liquid lines of descent. Others have little data and substantial scatter. Based on the data appearance, we assigned a "confidence number" to the data from each segment, from 1 to 3. These estimates are qualitative. Examples of segments corresponding to each confidence interval are shown in the Appendix. Notably, it turns out that the main results are the same whether considering only all segments or only the highest-confidence segments (see Appendix).

Fractionation correction is necessary—segments can vary by more than 4 wt. % in mean MgO content (not even including back-arc segments). Considering Fe and Na correction slopes of ~1.6 and ~0.32 this would lead to variations of ~6 and ~1.3 in mean segment Fe and Na compositions, about the same as the global range observed in Fe_8 and Na_8. Our approach to fractionation correction includes a certain amount of human judgment. An alternative approach is to apply a single algorithm to all segments (e.g.,

Klein and Langmuir, 1987; NO (2008)). This has the advantage of being completely unbiased, but it also introduces unnecessary errors, particularly if non-petrologically based polynomial correction is used (e.g. NO (2008), see below). Spreading centers fractionate at different pressures, can have different extents of magma mixing along liquid lines of descent, and may have other complex fractionation processes. These are all revealed in the spectrum of erupted lava compositions. By actually examining the data from each segment and evaluating them, it is possible to assure that the corrected values accurately reflect the actual magma compositions within the segment.

It also raises the question, however, of whether a particular correction procedure might be cherry-picked on a segment basis to conform to biases. In fact, this is a minor issue, because the corrected data generally have small errors (see online Appendix) and in most cases span 8% MgO where no correction is applied. In order to assure ourselves and others, however, that the calculated "8-values" are as free from bias as possible, we carried out all the fractionation correction *prior* to any plotting of the global segment chemical data or comparison with physical parameters such as ridge depth. All corrections were chosen and applied though an independent evaluation of each segment to try to obtain the most accurate representation of the data from that segment. After those choices were made, no changes were made. We considered this approach preferable to a single quantitative correction scheme, because of the variable and sometimes unique data characteristics of ridge segments. In order for these choices to be fully transparent and to allow for assessment by others, all diagrams and chosen regressions are available in the online Appendix for independent appraisal by interested readers.

5.2.2. Calculating 90-values

A criticism of the 8-value approach has been that the resulting compositions are not in equilibrium with mantle olivine (NO (2008)). Klein and Langmuir (1987) and Langmuir et al. (1992) never claimed that 8-values were in equilibrium with mantle olivine; rather, they selected 8 wt.% MgO because it is in the field of observed basalt compositions. Therefore nearly all mean segment 8-values are pinned to real data near 8 wt.% MgO that require

little or no correction. To directly compare 8-values with mantle melting models, mantle melts were fractionated to 8% MgO. Taking mantle melts and fractionating them to 8% MgO, or taking 8% MgO values and back-correcting them to forsterite-90 (Fo_{90}) lead to identical results. Therefore the 8-value approach is sufficient, provided any mantle calculations are appropriately fractionated to be comparable, as done in Langmuir et al. (1992). Nonetheless, there have been concerns raised in the literature and in personal communications over the 8-value approach (e.g., NO (2008)). To address any concerns over its validity, we also calculated Fo_{90} compositions ("90-values"; sample compositions in equilibrium with Fo_{90} olivine) for every sample with an 8-value in our database. The 90-values can then be simply compared with calculations of primitive mantle melts.

To calculate 90-values, we first corrected every sample (with <8.5 wt % MgO) to its value at 8.5 wt.% MgO following the exact method outlined above for 8-values. For example, whichever custom slopes were chosen for estimating 8-values for a particular segment, the same slopes were used when calculating the 8.5 values. Recall that 8.5 wt.% MgO is the normal "hinge-point" where the slope changes to olivine-only. Samples with >8.5 wt.% MgO are already on the olivine-only slope and so their data required no correction. We then ran a code in Matlab which calculates the Mg# (defined as (Mg/(Mg + Fe*)) x 100; Fe expressed as total Fe) of each sample at 8.5% MgO. If the sample Mg# is in equilibrium with Fo_{90} olivine, no correction is applied. If it is in equilibrium with an olivine Mg# lower than Fo_{90}, equilibrium olivine is added in 0.1% increments until the sample oxides are in equilibrium with Fo_{90} olivine. We used a $K_D (C^{FeO}{}_{ol}/C^{FeO}{}_{L})/(C^{MgO}{}_{ol}/C^{MgO}{}_{L}) = 0.3$. For all elements other than SiO_2, FeO and MgO (the oxides that constitute olivine), the addition of olivine leads to a simple dilution. Once all sample compositions had been corrected to equilibrium with Fo_{90} olivine, we averaged those samples to estimate a segment 90-value for each segment with 8-values.

5.3. Results

The fractionation and averaging methods presented above permit calculation of corrected values for each of the 241 segments, which span all the ocean basins, the

total range of axial depth from +1000 to -5400 meters, and a range of spreading rates from less than 10 mm per year in the Gakkel Ridge to the super-fast spreading East Pacific Rise at 150 mm per year (Figure 5.3). This coverage compares, for example, to the 84 data points that were used in the original Klein and Langmuir (1987) study. The new dataset with triple the data coverage, more precise fractionation correction, far better geographic constraints, and correction for inter-laboratory bias permits a rigorous and comprehensive reevaluation of the global relationships of ocean ridge basalts.

5.3.1. Systematics at MgO = 8.0 wt. %

Many of the chemical "8" parameters show good correlations among each other and with the average depth of the ridge segment (Figures 5.4 and 5.5). Na_8 correlates strongly (negatively) with ridge depth, one of the most compelling correlations in the dataset. Al_8 also correlates negatively with mean ridge depth, and a notable offset to higher Na and Al (or shallower depths) is apparent for the shallowest ridge segments near and on Iceland. Si_8 also shows a negative trend with depth. With the exception of back-arc basins, which are low in Ti_8, and Iceland segments, which are high in Ti_8, there is also a crude negative correlation between Ti_8 and depth. Fe_8 and Ca_8 correlate positively with depth. Segments on and near Iceland are notably offset in the Ca_8-depth trend to lower Ca_8. In general terms, shallow ridge segments are characterized by

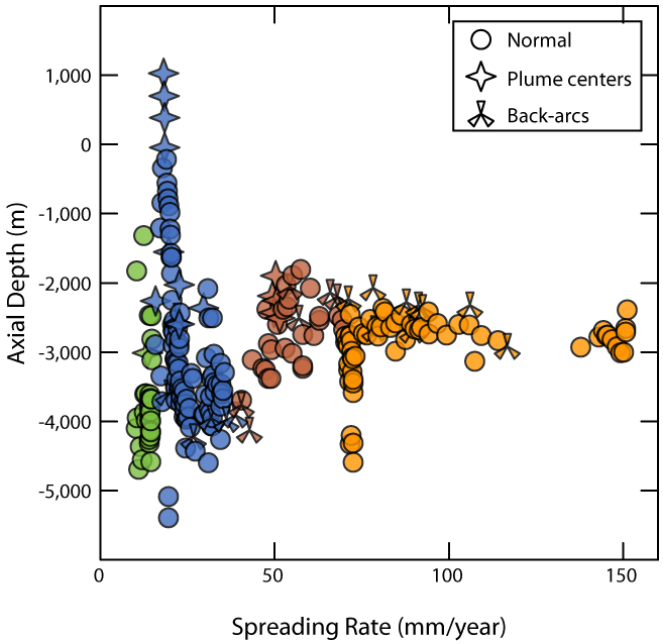

Figure 5.3: Axial depth versus spreading rate for the 241 ridge segments considered in this study. Color coding relates to spreading rate (orange: spreading rate > 70 mm per year, brown: spreading between 40 and 70 mm per year, blue: spreading between 15 and 40 mm per year, green: spreading at less than 15 mm per year. Note that our study has fractionation-corrected values from the full range of axial depths (+1000 to -5000) and spreading rates found along the length of the ridge system.

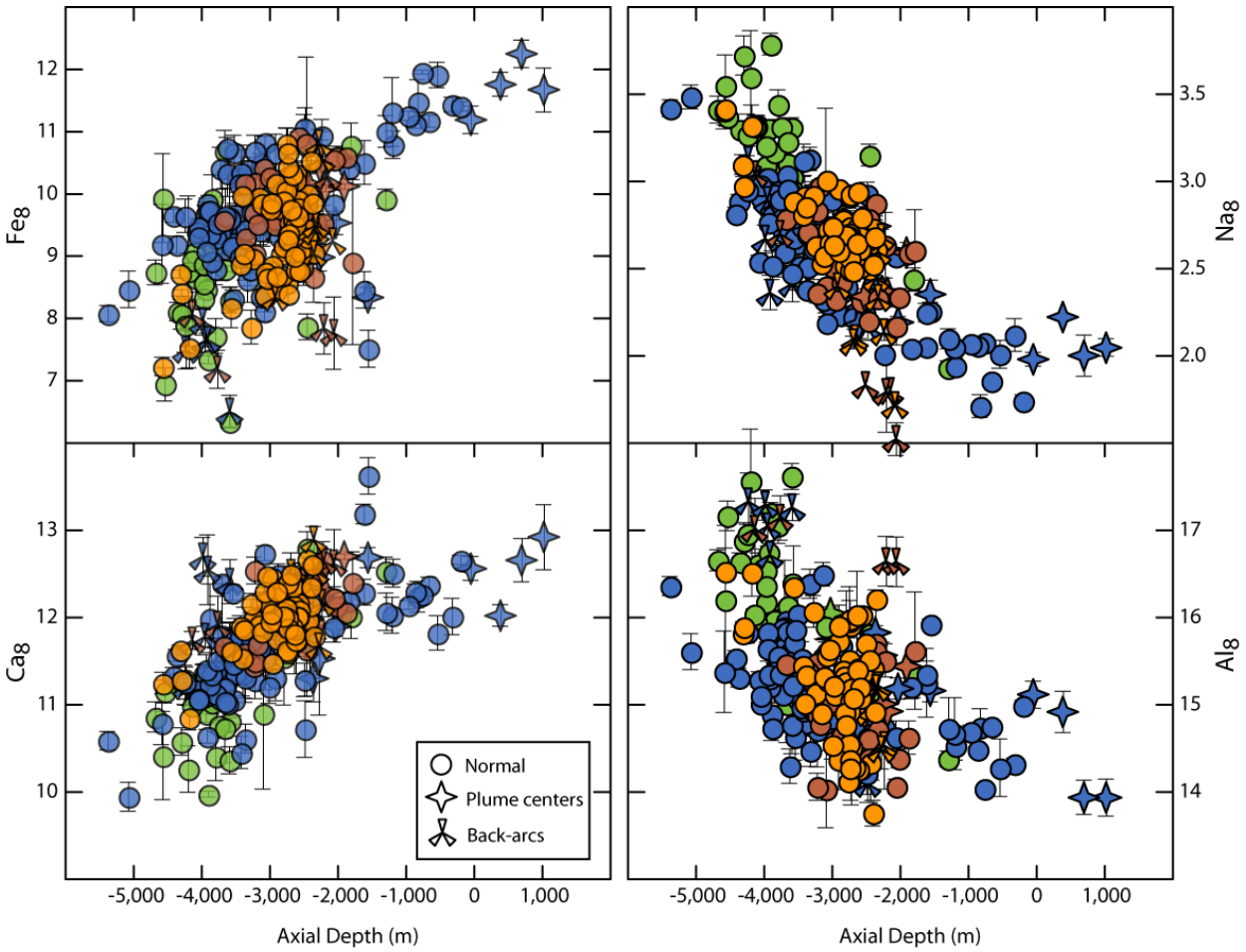

Figure 5.4: Fe_8, Ca_8, Na_8 and Al_8 versus axial depth. Colors indicate spreading rate, as in previous figure. Error bars are calculated as two standard deviations of the mean. Fe and Ca correlate positively with axial depth, while Al and Na correlate negatively. Note the kink in the Na_8-depth trend associated with plume segments on and near Iceland, which are offset to higher Na_8. These segments also possess low Ca_8. Back-arc basin basalts (BAB) have low Fe_8 and high Al_8.

low Na, low Al, high Fe, low Si, low Ti and high Ca, and deep ridge segments are the opposite. These are the same systematics identified by Klein and Langmuir (1987) and Langmuir et al. (1992).

There are also relationships among the major element oxides. Na_8 correlates well (negatively) with Ca_8/Al_8 (Figure 5.5), owing to a positive correlation with Al_8 and negative correlation with Ca_8. There is also a striking and strong negative correlation between Fe_8 and Al_8 (Figure 5.5). A negative correlation also exists between Na_8 and Fe_8, but here the systematics are obscured somewhat by the back-arc basins substantially offset to low Fe_8, and by the low Fe_8 of many segments along the MAR near the Azores plume. The co-variation between Na_8 and Ti_8 is complex. BAB have been shown to be offset to low

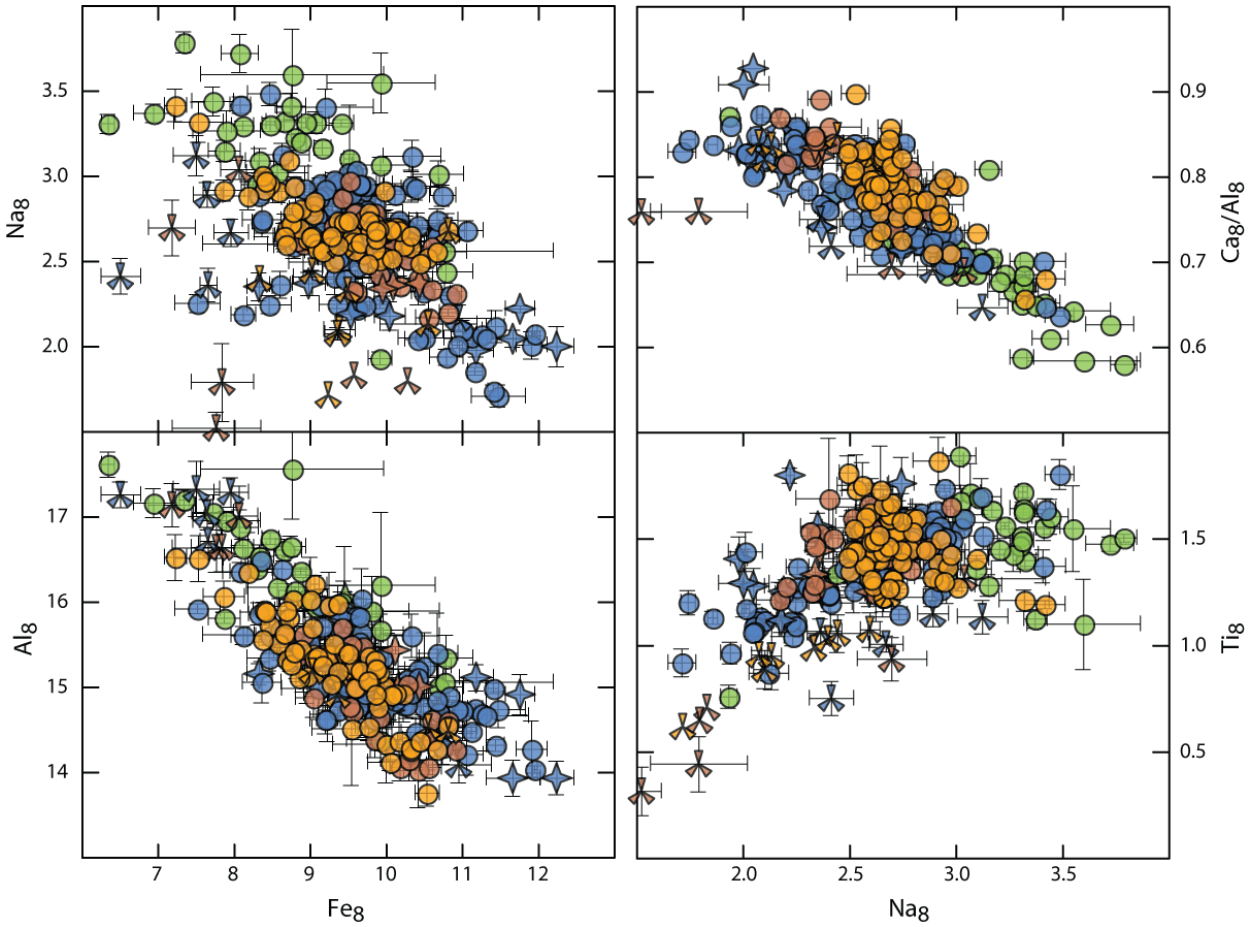

Figure 5.5: Na_8 and Al_8 versus Fe_8, and Ca_8/Al_8 and Ti_8 versus Na_8. Symbols as in previous figures. Na_8 shows a negative correlation with Fe_8, with the exception of BAB and certain segments near the Azores, which are offset to low Fe_8. There are robust correlations between Al_8 and Fe_8 and Ca_8/Al_8 with Na_8, again showing that BAB are offset to high Al_8. A crude correlation exists between Ti_8 and Na_8, with some complexities. BAB are offset to low Ti_8, forming a nearly subparallel array beneath the open-ocean ridge basalts. Super-slow spreading segments (green circles) possess low Ti_8 for their Na_8.

Ti_8 (e.g., Langmuir et al., 2006), clearly evident in this new compilation. The back-arc basins as a group have a positive correlation. For open-ocean ridges there is a group with high Na_8 at the same Ti_8 as other ridges.

Shown on the figures are the error bars for the data points calculated as two standard deviations of the mean for each segment. While occasionally the errors can be large relative to the size of the data points, it is clear that errors on segment averages are not the cause of the scatter and complex trends on the various diagrams. Instead, there are real variations that need to be accounted for, and deserve investigation in greater detail. No single process can account for the data distribution.

5.3.2. Comparison to the early global studies

One of the purposes of the present compilation is to test whether the results of Klein and Langmuir (1987) and Langmuir et al. (1992), now over twenty years old, remain valid given the advances in data coverage and treatment. The tripling of data includes many regions of the ridge system that were not included in the early studies (e.g., Gakkel, most of SWIR, the PAR, most of SEIR) and the new approach to fractionation correction and inter-laboratory corrections used in this study could change the earlier values as well. Despite this, the earlier studies and the present work overlap almost exactly in Na_8 vs. ridge depth (Figure 5.6). Indeed, the range in Na_8 from approximately 3.5 at 5000 m depth to 1.75 at 0 m depth is nearly identical in the two studies. A difference in the current treatment is our inclusion of subaerial Iceland data, which does not extend the original correlation, but forms a kink towards higher Na_8 contents. The present study also extends the global range to higher Na_8, seen in four segments from the SWIR, and to lower Na_8, seen in five BAB segments from the Lau Basin.

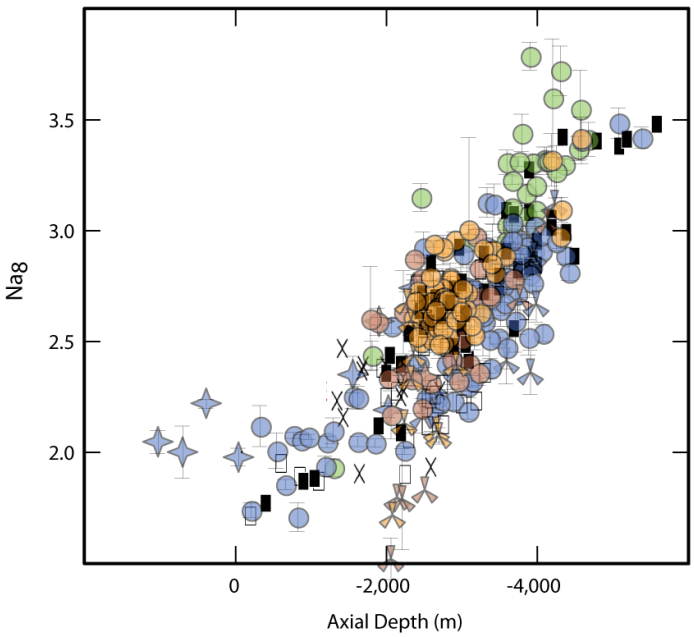

Figure 5.6: Na_8 versus axial depth from this study (symbols as before) compared to that of Langmuir et al. (1992) (rectangles and crosses). Note the remarkable correspondence between the data from this study and that in Langmuir et al. (1992). The present study extends the range in axial depth by including subaerial Iceland segments. The range in Na_8 is also expanded through the inclusion of segments from SWIR (high Na_8) and certain Lau back-arc segments (low Na_8) that were unavailable in previous compilations. Even with a vast increase in data, and the improved fractionation correction procedure carried out here, the original Langmuir et al. Na_8-axial depth correlation remains robust.

The relationship between Fe_8 and depth is also very similar between the present and older studies, albeit with some noteworthy differences. First among them is the large increase in segment Fe_8 values of ~8.5 at a depth of 3000 m, largely from the SEIR. In the earlier studies that

region was circled as perhaps a low-Fe_8 zone related to BAB, but our study shows that many normal ridge segments also possess the "low" Fe_8 relative to axial depth. Another difference lies in the data for the Cayman trough. Klein and Langmuir (1987) estimated Fe_8 values of ~7.15 for Cayman, whereas our new estimates suggest a higher Fe_8 of between 8 and 8.5 for the Cayman segments. Other ridge segments at slightly shallower depths have low Fe_8 contents, however, so the overall trend is little affected.

In Ti_8 versus Na_8 we see many of the same features that were pointed out in Langmuir et al. (1992), including the lower Ti_8 of BAB, the characteristically high Ti_8 of Iceland segments, and the low Ti_8 of Indian ocean MORB for a given Na_8. New to the present study, however, is the observation that some Gakkel segments also possess low Ti_8 for their Na_8, quite similar to the Indian Ocean signal. Our results extend the lower range of observed Ti_8 values (Ti_8 as low as 0.31) with data on certain segments from the Lau basin.

Important additions in the present study involve the inclusion of Na_8, Ca_8, Si_8 and P_8 for all of the ridge segments, a quantitative and reproducible approach to segment depth, the quantification of errors, and the inclusion of spreading rate for each segment, permitting exploration of variations with spreading rate. These additions reveal relationships that were not known previously, as will be developed below.

5.3.3. Comparison of MgO=8, and Fo_{90} values.

An important issue to address is whether correction to a constant MgO content or constant Mg/Fe ratio makes a difference to the data systematics. Figure 5.7 compares "8-values" and "Fo90-values" for the global ridge segments. Note that there are very tight correlations between the two sets of corrected values for most elements. The correlations are not one to one, however. As noted above, generally segments with high Fe_8 have low Al_8, low Na_8, low Ti_8, low Si_8 and high Ca_8. The extent of the correction to Fo_{90} depends on the Fe_8 value. High Fe_8 values lead to large corrections in order to arrive at a composition in equilibrium with Fo_{90}, while low Fe_8 values lead to negligible corrections. Adding olivine to arrive at a composition in equilibrium with Fo_{90} does not change Fe much, but increases MgO, while decreasing the elements that are not

incorporated in olivine—Al, Na, Ti and Ca. Si is also lowered because olivine has lower SiO_2 than ocean ridge magmas. Therefore high Fe_8 magmas, which already have low Na_8, Ti_8, Al_8 and Si_8, have even lower 90-values. Correction to Fo_{90} then amplifies the

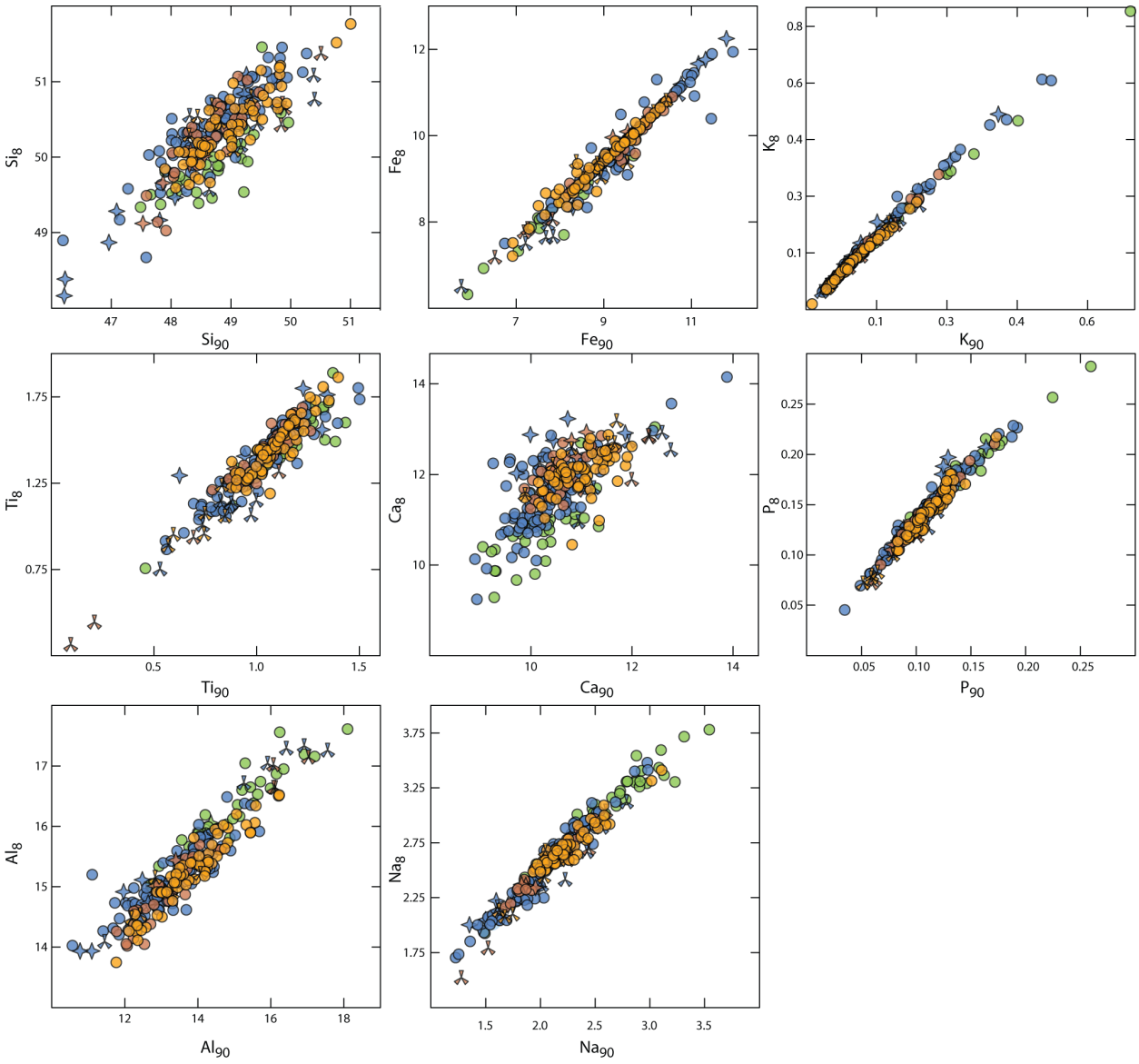

Figure 5.7: Segment 8-values versus segment 90-values for the major oxides Si, Ti, Al, Fe, Ca, Na, K and P. Symbols as in previous figures. Note that there are very tight correlations between the two sets of corrected values for most elements. The correlations are not one to one, however. The elements Al, Na, Ti and Si have a larger range in 90-values than they do in 8-values, related to their negative correlations with Fe_8. Samples with high Fe_8 tend to have low Al_8, Na_8, Ti_8 and Si_8 and also require the greatest quantity of olivine addition to be in equilibrium with Fo_{90} olivine. Therefore, the already-low Al, Na, Ti and Si-8's get even lower during correction to Fo_{90}. Ca is more complicated, as it correlates positively with Fe_8. Therefore high Ca_8 samples are lowered more during correction, and low Ca_8 samples are lowered less during correction, precluding a crisp correlation between Ca_8 and Ca_{90}.

observed variations in these elements, because high Fe_8 segments have low values of all these parameters, and the values are further lowered by the extensive olivine addition.

Ca does not exhibit this behavior. CaO is more complex than the other elements because most elements have uni-directional changes with extent of melting. In contrast, at constant pressure, CaO first increases with extent of melting, and then decreases once cpx is exhausted from the residue. This leads to a smaller relative range of variation than the other elements (with the exception of SiO_2). High Fe_8 magmas have a large decrease in Ca to get to Ca_{90}, while low Fe_8 magmas have little correction. Since the range of Ca_8 is already limited, and olivine correction is orthogonal to the variations in the 8-values, the trends for Ca_{90} are lessened relative to the trends for 8-values.

These factors then lead to an expansion of the range of Al_{90}, Na_{90}, Si_{90} and Ti_{90} relative to Al_8, Na_8, Si_8 and Ti_8, and excellent correlations for these elements between 8-values and 90-values. The contrasting behavior of Ca leads to a less good correlation between Ca_8 and Ca_{90}. The important aspect, of course, will be the comparison of the data with models of mantle melting and mantle composition, and not the existence of a correlation or not, as discussed below.

Not surprisingly, it thus turns out that the data systematics for 8-values and 90-values are remarkably similar. The same correlations exist with depth, with the exception of Ca_{90}. The inter-element correlations are generally tighter in the 90-values, in part because of the mutual "stretching" of the data discussed above. Correlations among Fe_{90}-Al_{90}-Na_{90} are particularly pronounced, and there is also a good correlation between Si_{90}-Fe_{90} and a much better correlation between Ti_{90}-Na_{90} (Figure 5.8).

There have been recent claims that the global 8-value correlations disappear if using 'proper' mantle melts in equilibrium with mantle olivine (NO (2008)). While we discuss this paper in some detail below, it is evident from the above presentation that this claim completely contrasts with the results presented here. With the exception of Ca_8 and Ca_{90}, we show a very close correspondence between the segment 90-values and segment 8-values, especially for the most-questioned Fe_8 relative to Fe_{90} (Figure 5.7). Furthermore, as demonstrated above, inter-element variations are if anything

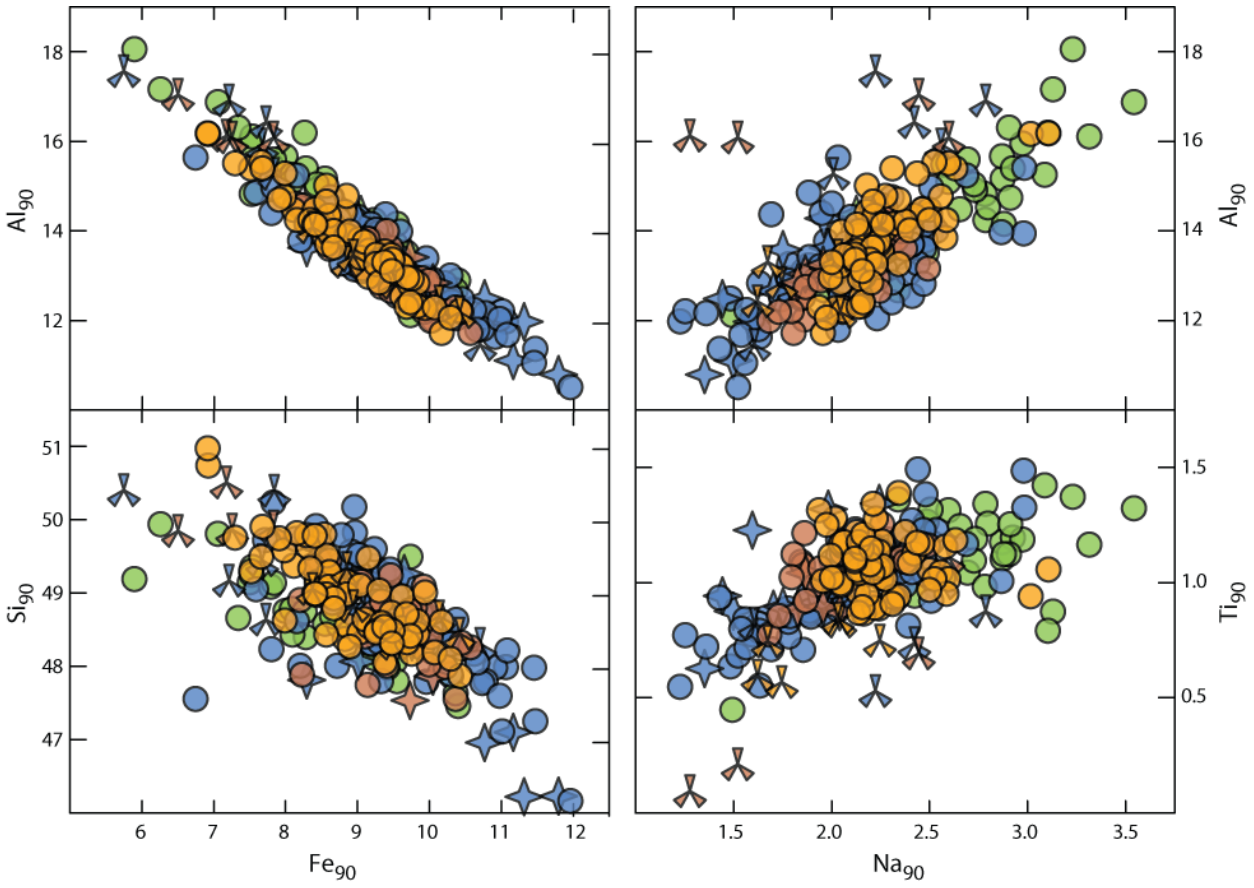

Figure 5.8: Al_{90} and Si_{90} versus Fe_{90}, and Al_{90} and Ti_{90} versus Na_{90}. Symbols as in previous figures. Note the strong correlations, especially in Al_{90} versus Fe_{90}. Most of the correlations observed among the segment 8-values persist in the 90-values, in many cases becoming even more pronounced.

enhanced by correction to Fo_{90} rather than 8% MgO. To sum up, corrections to Fo_{90} or 8% MgO are both legitimate approaches to fractionation correction, provided output from models is considered under the same conditions, that is, corrected to 8% MgO or Fo_{90}.

5.3.4. Fine Structure within the Global Correlations

As noted above there is much more variation within the data than can be accounted for by a single uniform process. A full exploration of all the detailed structure of the data would require work on a finer scale than segment averages, that would be able to concentrate on highly sampled regions in depth. Here we point out some of the most notable aspects of the data.

(1) Super-slow spreading ridges

Super-slow spreading ridges are represented by the SWIR and the Gakkel Ridge, both spreading at less than 15 mm per year, as well as two segments from the Red Sea. Segments from Gakkel and SWIR are preponderant at the greatest depths and highest Na contents of the global dataset, though SWIR segments can be as shallow as 2400 m. Fortunately, the Australian-Antarctic Discordance, which is intermediate spreading, occupies the same depth range; it is therefore possible to separate variables and identify which aspects of the data are unique to the super-slow spreading ridges.

When plotted versus Fe_{90}, the super-slow ridges are offset to lower Si_{90} and Ca_{90}, and higher Na_{90} and Al_{90} compared to faster spreading ridges, forming fields that only slightly overlap (Figure 5.9). While there are a few exceptional segments, these offsets seem to exist across the entire depth range. Clearly there is some additional effect, presumably associated with lithospheric cooling, that is causing these offsets relative to other ridges.

(2) Ridges near hotspots

A second effect has to do with segments that are located in the vicinity of hot spots. There are multiple aspects to this effect. One is that at hot spot centers there is an elevation of Na relative to what would be expected from the Na_8-depth correlation observed elsewhere (see the kink in the Na_8-depth trend in Iceland segments in Figure 5.4). In order to demonstrate this, we have calculated the Na_8 anomaly relative to the "expected" Na_8 using the Na_8-depth relationship of open-ocean segments far from hot spots. This anomaly can then be plotted versus latitude for a series of segments that traverse a hot spot. Figure 5.10 shows the elevation of Na at the centers of the Azores and Iceland hot spots. Importantly, the positive Na anomaly over plume centers is also associated with elevated K_{90} and $^{87}Sr/^{86}Sr$ (Figure 5.10). Mean isotopic ratios for each segment are taken from Gale et al. (2012), submitted. The co-variations among Na anomalies and K_{90} with isotopes suggest that source enrichment is affecting the segments directly adjacent to hot spots.

(3) Back-arcs

The third set of distinctive ridges is associated with back-arcs. Here the contrast

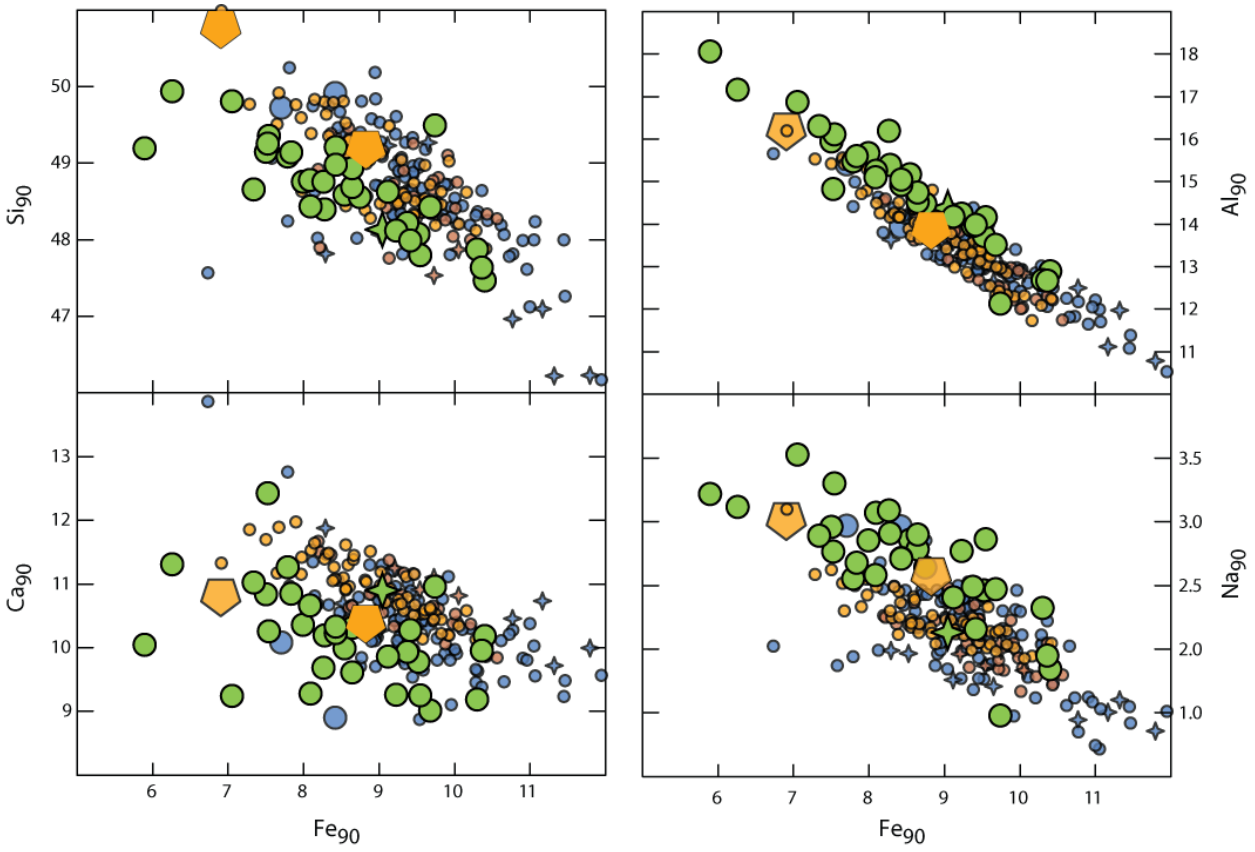

Figure 5.9: Si_{90}, Ca_{90}, Al_{90} and Na_{90} versus Fe_{90}, highlighting the systematics in super-slow spreading ridge segments. Symbols as in previous figures, although data from faster-spreading segments have been reduced by 50% to aid visualization. Two segments from the AAD are shown in orange hexagons as a point of comparison, as these segments are in the depth range of most super-slow spreading segments but are intermediate-spreading. Differences between the AAD and super-slow spreading segments are likely related to a spreading rate effect. The very deep segments from the Cayman trough are also shown in large blue circles. Note that super-slow spreading segments, with few exceptions, are offset to low Si_{90} and Ca_{90}, and high Al_{90} and Na_{90} relative to faster-spreading segments. This is likely caused by the cold lithospheric cap present at super-slow spreading segments.

with the global population of ridges is most pronounced. Back-arcs have exceptionally low Ti and Fe, and high Si and Al. They form almost completely separated fields on many diagrams (c.f., Figure 5.5). Part of this major element signal may be due to the higher water contents in back-arc basin magmas, which tend to suppress the crystallization of plagioclase. Delayed plagioclase could lead to higher Fe and lower Al values at MgO =8.

5.4. Discussion

5.4.1. Comparison between this study and NO (2008)

NO (2008) present results that are in stark contrast to the present study. They suggest

that corrections to MgO=8 “are equivalent to fractionation-uncorrected raw data”, and that if corrections are made instead to a constant Mg/(Mg+Fe) in the melt, which is equivalent to correcting to a liquid in equilibrium with a particular olivine composition, then the systematics of the data change completely. On this basis, they challenge the conclusions of Klein and Langmuir (1987) and Langmuir et al. (1992) that a principal influence on basalt compositions is mantle temperature. The critical difference between

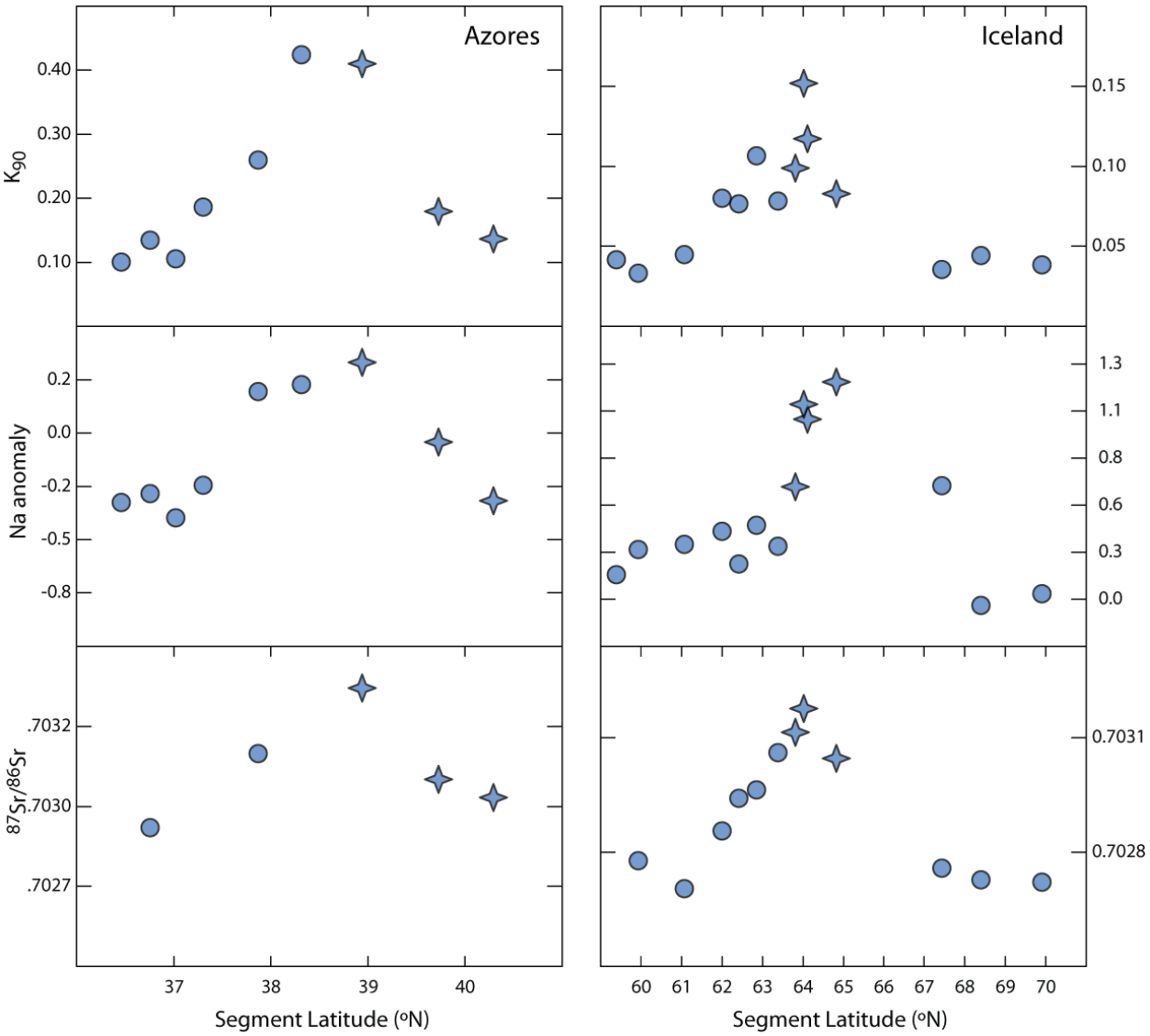

Figure 5.10: K_{90}, ‘Na anomaly’ and $^{87}Sr/^{86}Sr$ versus segment latitude for transects near the Azores and Iceland plumes. Data on $^{87}Sr/^{86}Sr$ is from Gale et al. (2012), submitted, symbols as in previous figures. Na anomaly calculated as the difference between the observed and “predicted” Na based on the correlation between Na_8 and ridge depth apparent in open-ocean ridges away from plumes. Notice the pronounced increase in Na, K and $^{87}Sr/^{86}Sr$ near the plume. The observed enrichment is likely related to a localized influence of source heterogeneity. Axes are scaled differently for the two plumes.

NO (2008) and the results of this study is that NO (2008) show a change of only 1 wt.% Fe with axial depth in contrast to the original Klein and Langmuir (1987) results that show a change of 5 wt.% Fe with axial depth. NO (2008) suggest the correction to 8% MgO is the source of the discrepancy. Yet the mean Fe_{90} values presented here, equivalent to the Mg#72 values of NO (2008), confirm the global range of over 5 wt.% Fe, and the data correlate inversely with axial depth, Na_{90} and Al_{90}. The two studies disagree.

This difference is a matter of data—what are the real data systematics of ocean ridge basalts? The first issue must be—what do the data show? Following that, various interpretations can follow and hypotheses can be tested. It is necessary therefore to understand in detail differences between the results of the two studies. *The difference in the two studies is not associated with a change from correcting to 8% MgO to* $Fo_{90,}$ as is evident from our reporting of 8-values and Fo_{90}-values that are consistent with one another. Instead, it relates to unsound methodology in many aspects of the NO (2008) study. In the following section we explain the reasons for the differences between this study and NO (2008), and show the features of their methodology that lead them to erroneous conclusions.

Contrast 1: Data selection/coverage

The major element dataset released by Gale et al. (2012), submitted and used in this study was meticulously compiled. It includes large quantities of previously unavailable data from regions such as the PAR, Gakkel and Central Indian Ridges. Duplicate analyses were checked for and eliminated, samples more than 10 km off-axis were excluded, and sum requirements (sum between 98.5 and 101) were implemented to ensure a high-quality database. Perhaps most importantly, Gale et al. (2012), submitted, carefully applied interlab bias correction factors to as much of their data as possible (over 92%). As shown in earlier work (e.g., Langmuir et al., 1992; Langmuir et al., 2006), interlab bias issues can lead to important and systematic offsets between analyses from different laboratories solely related to their normalization procedure. Not taking these differences into account can obscure data trends. As a final step, Gale et al. (2012), submitted, renormalized the data in their dataset to make sure the analyses were comparable. The full dataset, including both raw and corrected data, is available in the supplement of Gale

et al. (2012), submitted. The compilation effort of Gale et al. (2012), submitted differs markedly from the approach of NO (2008), who simply downloaded raw data from PetDB and eliminated samples erupted shallower than 400 m, with SiO_2>53 wt.% or MgO<7 wt.%, or without water depth information. No apparent effort was made to eliminate duplicates, deal with interlaboratory bias issues, or to eliminate off-axis samples. Even more, the reader does not have access to the "9130 samples on a global scale" that were included in the study, thereby precluding any knowledge of the geographic locations of the samples or the major element composition of the samples used in their calculations. Their calculations are therefore not testable and reproducible independently.

Contrast 2: How to calculate the mean ridge axial depth

The mean depth of each segment in the Gale et al. (2012), submitted, catalog is precisely calculated using the digital ASCII file output from GeoMapApp, which consists of evenly spaced points with depth information along the length of each segment. NO (2008) argue that axial depths for each segment "are arbitrary", and that instead the actual sample eruption depths should be used. They therefore bin, irrespective of geographic location, all samples from specific depth intervals (such as 3000-3250 m). Some of these samples may be far from their eruption depth, for example if they are from rift valley walls. All geological information and insight is thereby eliminated from their approach.

Binning by sample recovery depth is an improper approach. The goal of a global study is to assess the effect of large-scale variables such as mantle temperature on the composition of erupted basalts. Because of the rapid diffusion of heat, mantle potential temperature varies on scales of ~100 km, not over 1 or 10 km. For example, using a thermal diffusivity of $8*10^{-7}m^2/sec$ (Katsura, 1995), temperature homogenizes over 20 km in only 20 Ma, a fraction of the opening time of an ocean basin. Therefore, "regional depth" reflecting the mean depth of the region is the appropriate parameter to use when exploring variables such as mantle temperature. Indeed within a given ridge segment, particularly at slower spreading rates, tectonic processes can lead to >1000m of depth variation over distances of km that have nothing to do with the temperature of the mantle (Figure 5.11). NO (2008) bin basalts that may have erupted within a few km of each other, perhaps from the rift valley floor and rift valley walls, into different depth bins. These

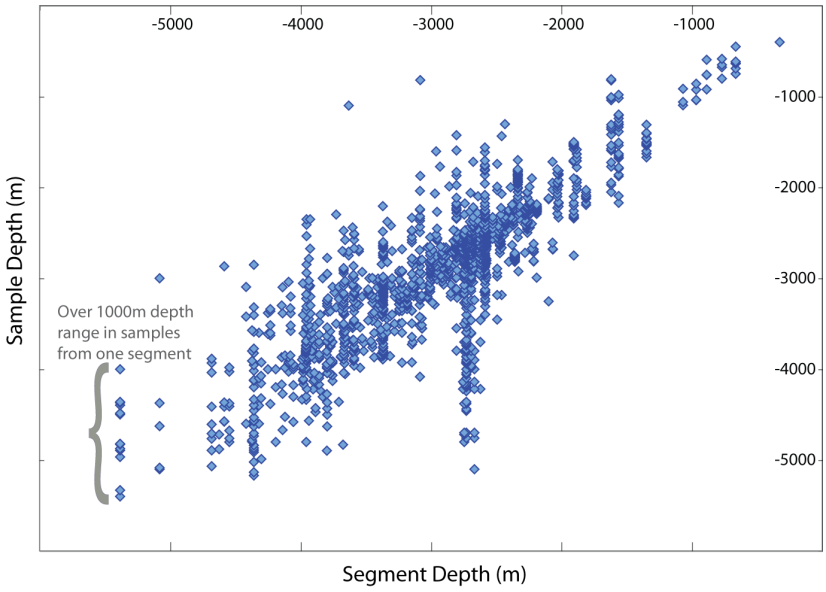

Figure 5.11: Sample recovery depth versus mean segment depth for basalts in this study. Note that, from a given segment, sample recovery depths can vary by 1000 m or more. This variation is primarily related to the structural characteristics of ridge segments; for example, samples can be recovered from the rift valley and its walls. Using sample recovery depth when addressing large-scale variables such as mantle temperature is inappropriate, as any extreme depth variations on a segment scale cannot be related to large-scale variables (i.e., the mantle cannot change temperature over scales of 1 km).

samples nonetheless must be derived from mantle with the same potential temperature. And basalts erupting from ridges located at opposite sides of the globe could be placed in the same depth bin, ruling out any possibility of evaluation of regional variations. Indeed, if we apply the method of NO (2008) and bin our global data by sample eruption depth, the 1500-1750 m bin contains samples from more than five different ridges (Figure 5.12), some of which have regional depths far from these values. Of course this leads to "smearing" of the global data, because samples from segments of very different mean depths are averaged with one another, leading all depth intervals to become closer to the mean.

Therein lies the strength of the mean segment depth technique; it smoothes out the depth variations related to tectonic effects, is a parameter that is sensitive to mantle potential temperature rather than local tectonics, and enables a global comparison based on geography, spreading rate, or other parameters.

In order to investigate the consequences of the binning approach, using our dataset we created bins with the same depth intervals (250 m) used in NO (2008), and eliminated samples with eruption depths less than 400 m for consistency with their study. Figure 5.13 shows that the observed relationship between Fe_{90} and axial depth remains even when binning by sample depth. The smearing effect reduces the total variation from 5

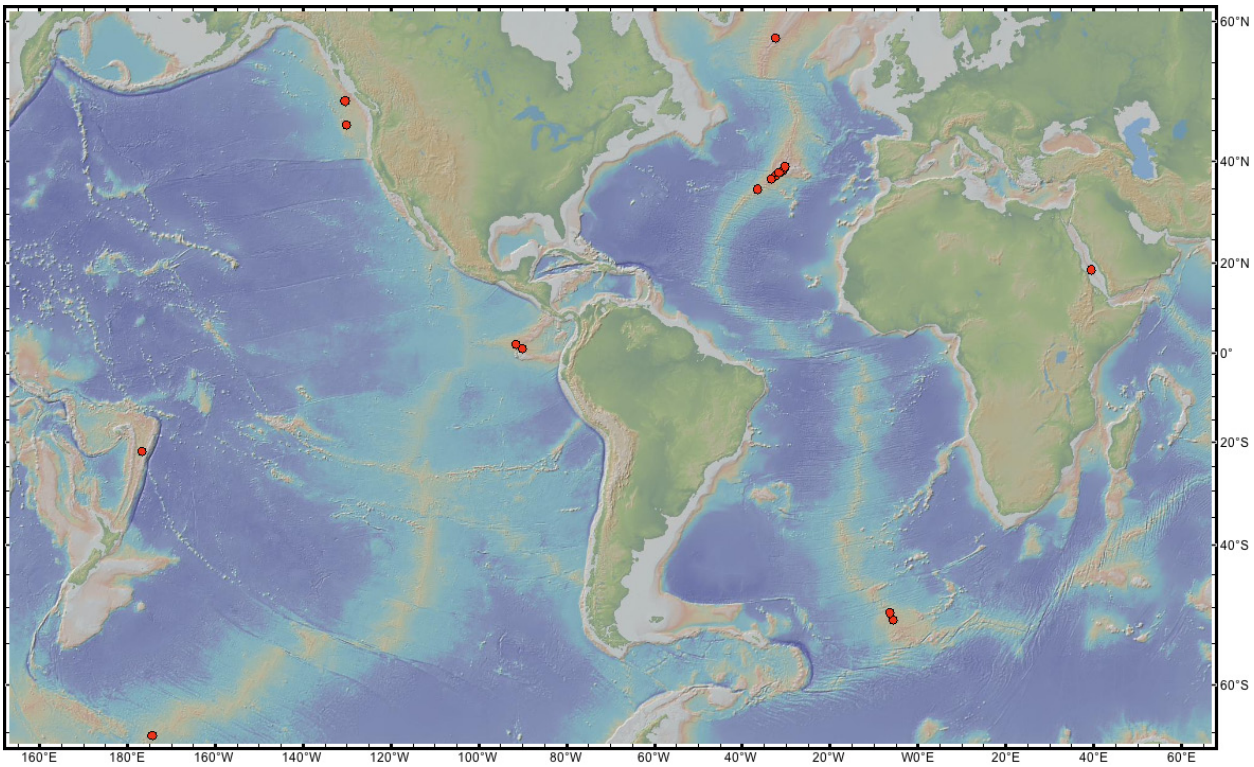

Figure 5.12: Map showing the location of samples with recovery depths between 1500-1750 m in this study. Following the procedure in NO (2008), these samples, from more than five different ridge segments, would all be binned together and assigned one mean '90-value' for each major element. Global multi-resolution bathymetry as compiled by Ryan et al. (2009) was used for the map.

wt.% Fe to ~3.5 wt.%, yet there is still far more Fe variation than the 1 wt.% variation claimed by NO (2008) (c.f., Figure 10 in NO (2008)). While binning by sample depth is an inappropriate method and lessens real variations among ridge segments, it is not the only reason for the discrepancies between the two studies.

Contrast 3: Method of Fractionation Correction

The other important difference between the two studies is the method of fractionation correction. In this and previous studies we have made fractionation correction on the basis of liquid lines of descent that are calibrated to experimental data and expressed in basalt compositions. These corrections are made in the light of the exact data from each segment, as described above. NO (2008) instead follow the approach in Niu et al. (1999), where data from a limited region, largely the East Pacific Rise, was fit with a sixth-order polynomial. NO (2008) updated the MgO and FeO calibration using a second-order polynomial fit to their global dataset. They then apply these polynomials with no

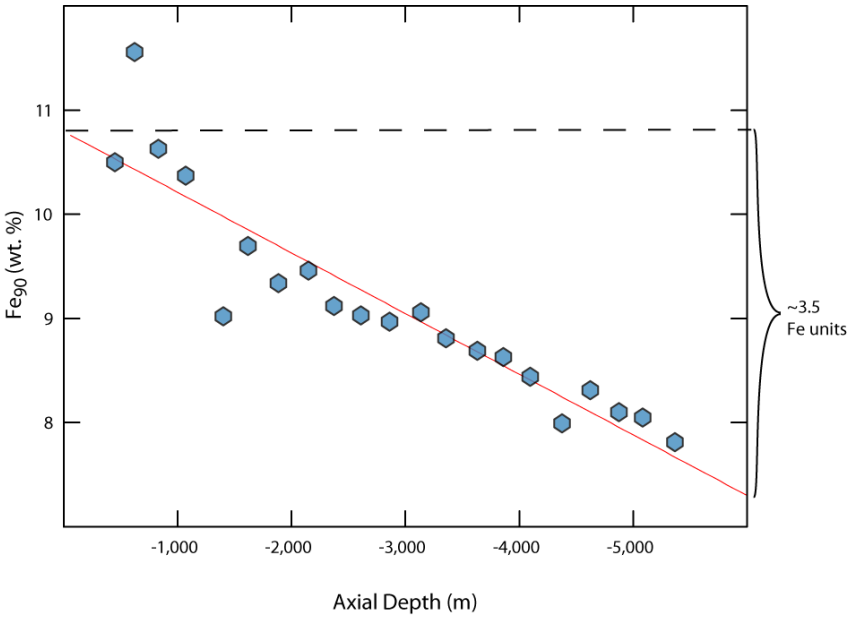

Figure 5.13: Fe_{90} versus axial depth, calculated using the depth-binning technique advocated by NO (2008). We used our sample 90-values and binned them by sample recovery depth following the protocol in NO (2008) precisely, including the exclusion of samples recovered from shallower than 400 m. This technique reduces the global variation in Fe_{90} from ~5 wt.% to 3.5 wt.% as a result of the "smearing" effect of including samples from diverse ridges in one depth bin (see text). Still, the overall trend of decreasing Fe_{90} with deepening ridges remains.

discrimination to the entire dataset they assembled from PetDB to arrive at Mg#72 compositions. The second-order polynomial fit for MgO and FeO leads to odd discrepancies in the data—a sample corrected to a given Mg# using their polynomial possesses MgO and FeO contents that do not have the Mg# to which they were corrected.

Liquid lines of descent are not polynomial functions. They are generally quasi-linear line segments with abrupt kinks where a new phase appears on the liquidus. For many elements (e.g. MgO, Na_2O, FeO) the change in concentration is unidirectional with decreasing temperature (for MORB >5% MgO). There is no change in the sign of the slope, and as long as a particular phase assemblage is crystallizing the slopes on variation diagrams are close to linear. There is no thermodynamic or other justification for a polynomial correction scheme, which inherently has changes in the sign of the slope, and no regions of constant slope. These functional characteristics are not those of liquid lines of descent. These drawbacks are illustrated in Figure 5.14, which shows the polynomial expressions for MgO and FeO used for fractionation correction. Note that MgO first decreases and then increases with decreasing Mg#. NO (2008) try to avoid this problem by limiting the dataset to >7% MgO, but at higher Mg# their correction scheme never goes below 7% MgO, thereby in principle allowing a reversal in slope of FeO versus MgO.

In the range of 8 – 9% FeO where NO (2008) calibrated their polynomial, the errors imposed by their approach are small. The polynomial has a shallow slope around MgO = 9, where olivine crystallizes alone, and then it steepens between 8.5 and 7% MgO, where plagioclase (and possibly cpx) are also crystallizing. Where the errors become extreme is when the same polynomial is used to correct samples with higher or lower FeO contents (Figure 5.14). The procedure takes the same polynomial from their calibration region and translates it along a line of constant slope (with Mg/(Mg+0.9Fe)) = 0.72) on an Fe-Mg diagram. High FeO samples will be corrected necessarily to higher MgO, in order to preserve constant Mg#. But in this case the form of the polynomial is incorrect, because at high MgO plagioclase does not crystallize. At low MgO the form

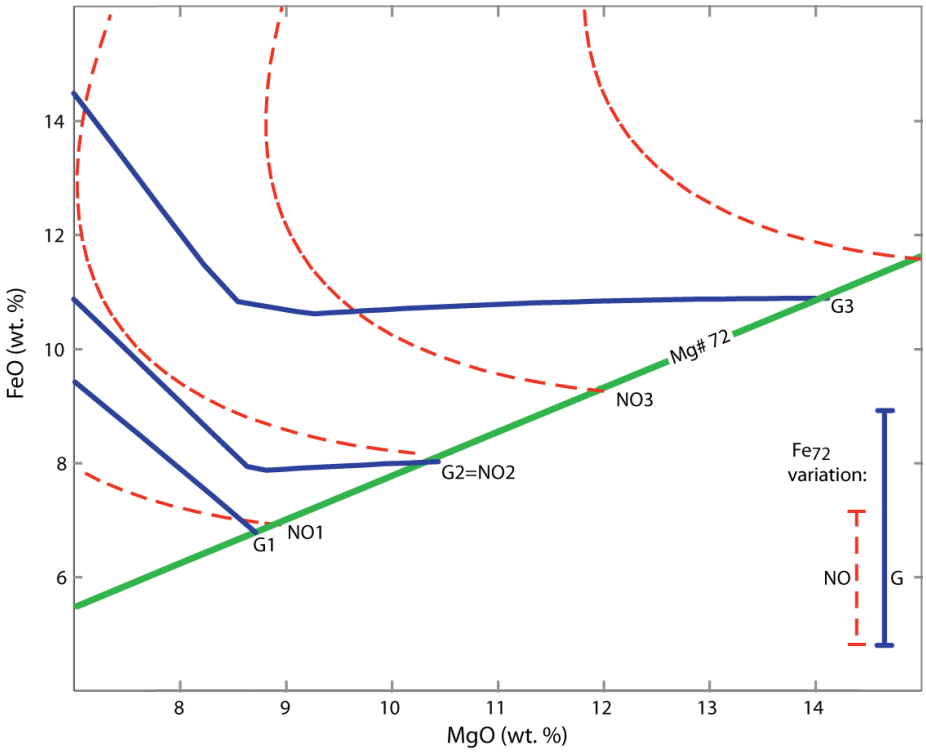

Figure 5.14: FeO versus MgO comparing liquid lines of descent from this study (blue lines; hBasalt, Bézos et al., in prep), analogues for those used for fractionation correction, to the polynomials used by NO (2008) (dashed red lines) to correct for fractionation back to Mg#72 (equilibrium with mantle olivine). Green line indicates Mg#72. Note that liquid lines of descent calibrated to experimental data show a nearly flat slope while olivine only is crystallizing, and then a steep slope once plagioclase has joined the liquidus (consistently around 8.5 wt. % MgO). At moderate Fe contents between 9 and 10 wt.%, in the chemical range where the NO (2008) polynomial was calibrated, the differences between the two correction approaches are relatively modest. At higher Fe contents, however, the NO (2008) polynomials have a steep slope similar to the "plag in" slope at unreasonably high MgO, where plagioclase cannot be stable. This over-steepened slope at high MgO contents results in an artificial and erroneous correction of high-Fe magmas to low Fe values at Mg#72 (see the difference between the Fe_{72} estimated here (G3) and that using the polynomial of NO (2008) (NO3)). This effect leads to a collapsing of the range of global Fe_{72} variation using the NO (2008) method relative to the method presented here (bars indicate the difference in the Fe_{72} range inferred from the same magmas, using the two different methods of fractionation correction).

is also incorrect, because there olivine never crystallizes alone. The consequence is that high FeO samples are over-corrected, and low FeO samples are under-corrected, thus compressing (erroneously) the range of Fe_{72}.

Put another way, the NO (2008) approach corrects higher Fe magmas along a slope corresponding to "plagioclase in" at high MgO contents where no plagioclase is stable. In fact, magmas with high Fe_{90} also have low Na_{90} and Al_{90} (see Figure 5.8), so that high FeO parental magmas crystallize plagioclase at slightly lower MgO than low FeO magmas. The high FeO stabilizes olivine relative to plagioclase. This is shown in Figure 5.14, where liquid lines of descent are shown for high and low Fe magmas and compared to the NO (2008) polynomials. The polynomial approximates data well with Fe_{72} of 8-9. It produces incorrect slopes for higher and lower Fe samples. Therefore, the NO (2008) correction scheme cannot be extrapolated outside the range of calibration because it is based on a non-physical polynomial fit rather than the known phase equilibria of MORB.

The implications of these correction problems are quite striking. In order to arrive at an Fe_{72} value of 11%, for example, the polynomial fit would require a lava to have 20% Fe at 8 wt. % MgO. No terrestrial lava has such a composition, but mantle melts with 11% FeO are evident both in natural samples and in experimental data. The correction scheme is simply inapplicable to high Fe samples. It artificially and erroneously lowers the corrected Fe contents.

To demonstrate this, we selected individual samples from five ridge segments in our dataset that span a range of axial depths and Fe contents. To be consistent with the approach of NO (2008), we excluded samples with MgO< 7%. We then corrected each sample to equilibrium with mantle olivine using the polynomial approach. The 90-values for each segment resulting from the two correction methods, calculated using identical samples, can then be readily compared. Figure 5.15 highlights the large discrepancy between the Fe_{90} values for high-Fe segments estimated using the NO (2008) polynomial versus our method. As pointed out, the higher the Fe contents in the original magmas, the larger the invalid lowering of the Fe_{90} content by the polynomial. This explains why real global variations in Fe_{90} of multiple wt. % are reduced to almost nothing in the

NO (2008) work. Note that the errors so evident in Fe are less important for Na, as our segment means are relatively comparable (Figure 5.15). For Na the change in slope when plagioclase appears relative to olivine is smaller, so the correction errors are not as large.

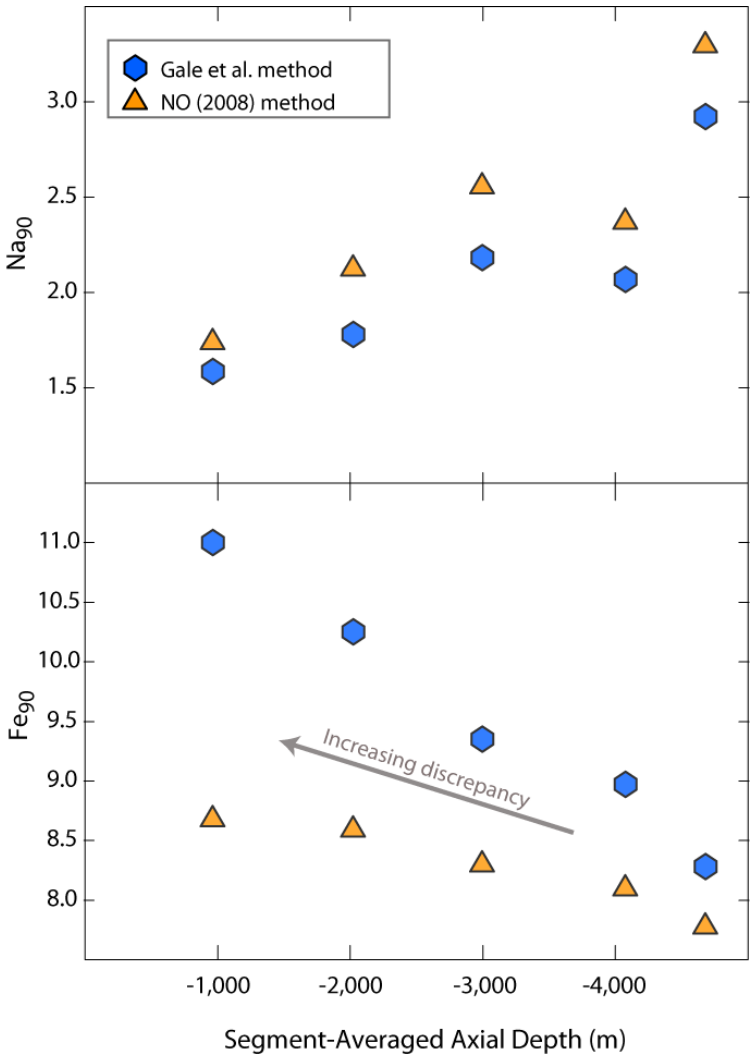

Figure 5.15: Na_{90} and Fe_{90} versus axial depth calculated for five segments over a large range of axial depths and chemical contents, comparing the different fractionation correction techniques in this study and NO (2008). The axial depth shown is segment-averaged axial depth. Note that the mistaken lowering of the high Fe contents when using the NO (2008) polynomial causes increasing disparity of up to almost 2.5 wt. % in the calculated Fe_{90} values. Because Na is an incompatible element much less sensitive to the exact crystallization sequence, the two studies track each other much more closely in Na_{90}.

The bottom line of this analysis is that the NO (2008) correction scheme should not be used for fractionation correction. It is immaterial whether corrections are made to a constant MgO content, or a constant Mg#, or to equilibrium with some forsterite content. All of these are equivalent provided care is taken with the phase equilibria and liquid lines of descent. For this reason one sees similar ranges and systematics in the "8's" and "Fo90's" published in this paper. Polynomials are an incorrect functional form, and extrapolation of a polynomial function outside its exact region of calibration leads to serious errors.

We therefore conclude that the systematics of MORB data that we present at both 8% MgO and Fo_{90} reflect real variations in the lavas and parental magmas that comprise

the ocean crust. The next step is then to consider various hypotheses for the origin of these variations, and see to what extent these can be rigorously evaluated.

5.4.2. Hypotheses for the Origin of the Global Systematics of MORB

The trends apparent in our global 90-values can be compared with mantle melts over a range of temperatures and source compositions to explore whether the two effects can be distinguished from one another, and whether one better accounts for the observations. This was done rigorously by Langmuir et al. (1992) for the elements Na, Mg and Fe, but not for the elements Al, Ca and Si. They demonstrated that mantle temperature best explains the observed data arrays, and suggested that mantle heterogeneity predicts trends in Na_8-Fe_8 that are orthogonal to the observed data. Here we aim to test this assertion by including calculations from the thermodynamic program pMELTS (Ghiorso et al., 2002) and modern experimental data, and by expanding the consideration to the elements Al, Ca and Si. We should state at the outset that pMELTS does not provide reliable data for several elements, particularly Na and Si, and has a melting function that does not correspond with experimental data. Nonetheless, in terms of the overall trends produced by temperature and compositional variations, pMELTS provides reliable indications. So the trends from pMELTS are important, the exact values less so.

To make use of pMELTS, we carried out the following calculations. In the first case we calculated the pooled melt compositions obtained from varying mantle potential temperature from 1250º-1500ºC using a fixed mantle starting composition (Workman and Hart, 2004). Second, we calculated pooled melt compositions using a variable starting composition and fixed mantle temperature of 1350ºC. We varied the source to include residual compositions from Baker and Stolper (1994), thereby showing the effects of a progressively depleted source, and created more enriched sources akin to different proportions of recycled crust by mixing N-MORB (Gale et al., 2012, submitted) in various proportions to the starting mantle composition of Baker and Stolper (1994). The results of these calculations are highlighted in Figure 5.16.

Many of the original observations of Langmuir et al. (1992) remain in these new calculations. For example, it is clear that the trend of the pooled melts generated by

variable mantle temperature in Na_{90} versus Fe_{90} are far more consistent with the data, and that the melts generated from mantle heterogeneity form an array opposite to the observations. While the precise slope in Na versus Fe in the pooled melts formed by

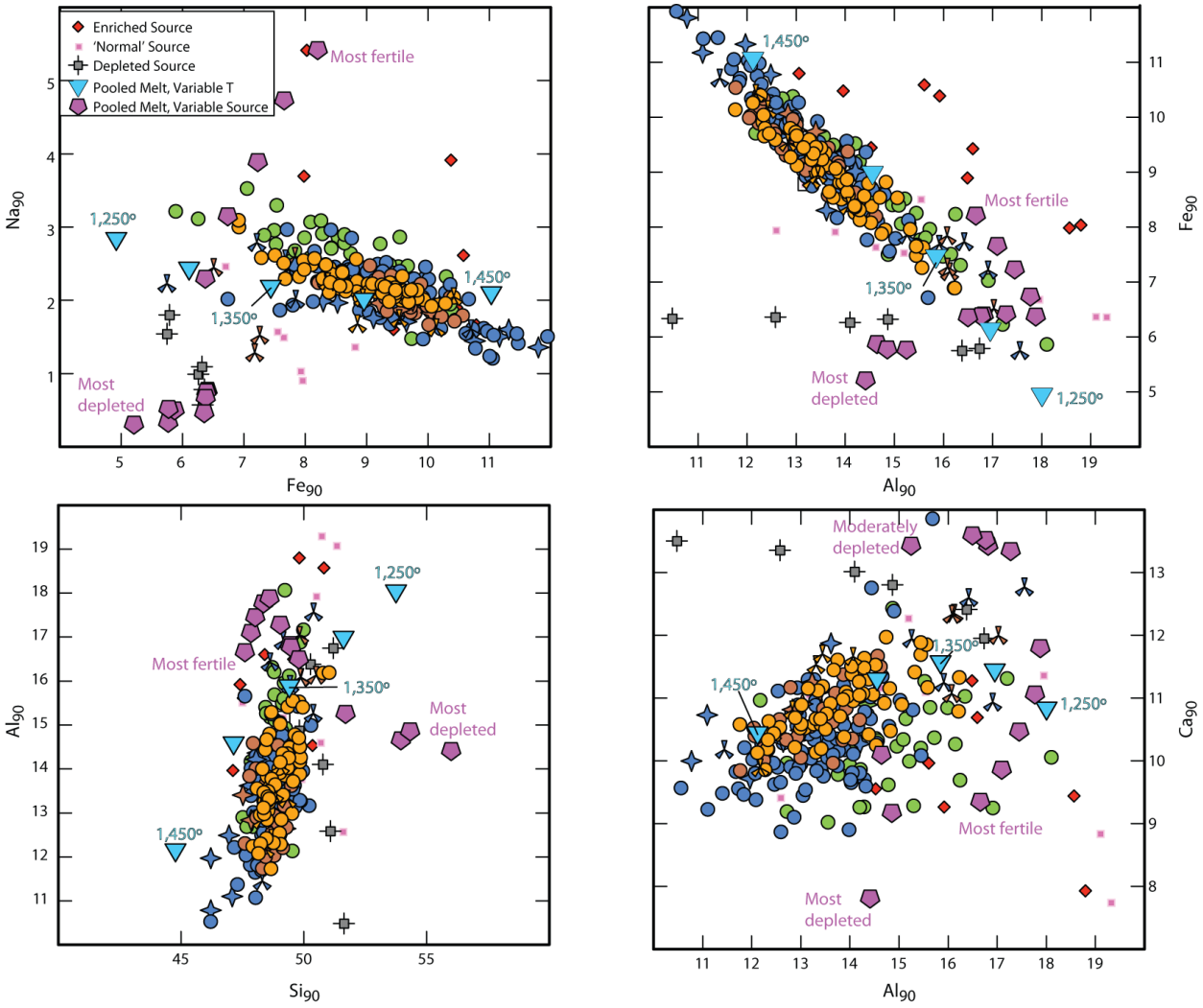

Figure 5.16: Na_{90} and Al_{90} versus Si_{90}, and Fe_{90} and Ca_{90} versus Al_{90}, showing the global data compared to experimental melts (red diamonds, enriched source (Hirose and Kushiro, 1993); small pink squares, 'normal source' (Hirose and Kushiro, 1993); small gray symbols, depleted source (Schwab and Johnston, 2001)) and pooled melt calculations from the thermodynamic program pMELTS (Ghiorso et al., 2002). The pentagons show pooled melts of a range of mantle source compositions from residual to fertile (see text), at 1350°C. The blue triangles show melts of a fixed source composition (Workman and Hart, 2004), melted at variable potential temperatures. It is apparent that while the pMELTS outputs are not perfect (with slight discrepancies in Na, and Si, for example), the trends associated with variable mantle temperature account for the global correlations far better than the vector associated with mantle heterogeneity. In many cases the mantle heterogeneity trend is orthogonal to the data array, and also does not lead to the requisite range of variation. Further evidence comes from the experimental data, where it can be seen that changing from one source to another results in a vector perpendicular to the global array. Mantle temperature variations on the order of 200°C can account for the broad-scale features apparent in the global major element data.

varying mantle temperature differs slightly, this is a detail, as it is clear that the mantle temperature trend is far more consistent than the mantle heterogeneity trend. The difference in slope occurs because the pMELTS output underestimates the magnitude of Na variations (Figure 5.17).

The quantitative results of Langmuir et al. (1992) and the pMELTS results can be understood as follows. More fertile sources have higher Fe contents, and also have a lower solidus temperature, which deepens the initial pressure of melting. As shown by Langmuir and Hanson (1980), a higher Fe source leads to higher Fe melts for the same pressure and extent of melting. In addition, higher-pressure melts also have higher Fe contents, so the two effects of heterogeneity amplify Fe contents. For Na, however, things are a bit more complicated. More enriched sources have more Na, which increases the Na concentration in melts, but they also melt more, which dilutes the Na concentration. Importantly, however, the increase in Na per unit source enrichment outweighs the dilution effect, so Na contents increase as source fertility increases. This leads to the prediction that more Na-rich sources produce melts with higher Na contents, and hence source heterogeneity creates a positive correlation between Na and Fe, as calculated by Langmuir et al. (1992), seen in the output from pMELTS, and apparent in experimental data on sources of varying fertility (Figure 5.16).

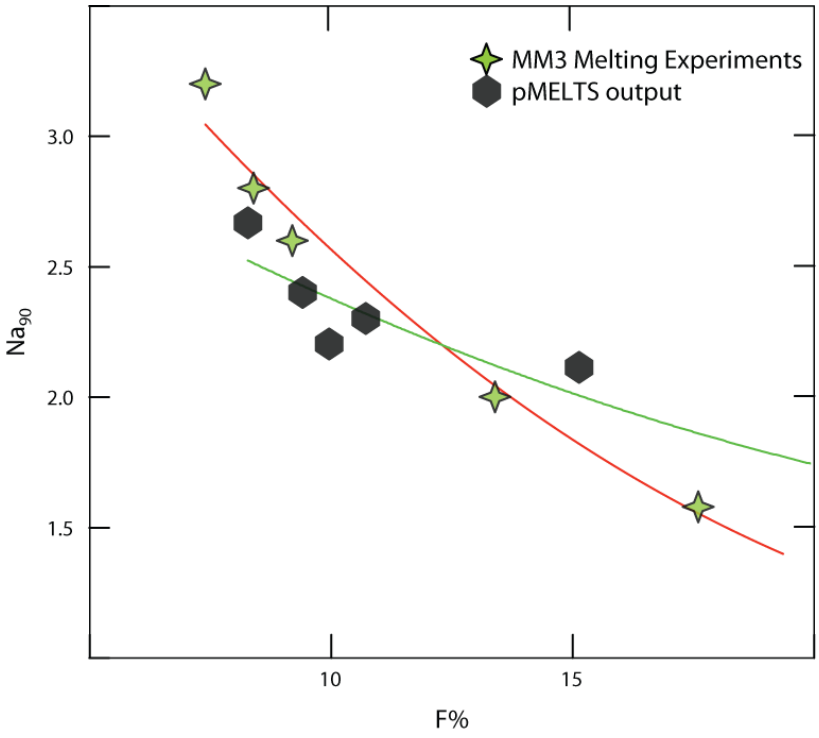

Figure 5.17: Na_{90} versus F% for experiments on mantle composition MM3 (Baker and Stolper, 1994; Hirschmann et al., 1998) compared with the output from pMELTS. Lines are best-fit polynomials. The Na_{90} in the pMELTS output is slightly too low at low extents of melting, and much too high at higher extents of melting relative to the experiments, leading to a diminished range of predicted Na contents.

One of the most compelling correlations in

our dataset exists between Fe_{90} and Al_{90}. This new correlation then permits a convincing test of the mantle temperature model. Melting a homogeneous source to varying extents resulting from variable mantle temperature accounts successfully for the Fe_{90}-Al_{90} observations, whereas variable mantle composition generates neither the proper slope nor the necessary range (Figure 5.16). The same holds true for Si_{90}-Al_{90}, and Si_{90}-Mg_{90}, although here an issue in the pMELTS output for Si becomes obvious. For example, comparing the trend of the Si-Al output by pMELTS to the experimental data, it is clear that the trend in pMELTS is incorrect. Si rises too steeply per unit Al increase in the pMELTS output, explaining why the array seen in our dataset more closely tracks the trends of experimental melts of a given source than the pMELTS calculations.

Recall that Ca is an element with a limited range of variation, and with variable behavior during melting depending on whether cpx is present. This leads to some "noisy" trends in Ca_{90}. Nevertheless, the figure of Ca_{90} vs. Al_{90} shows that the trajectory is, while not perfect, much more consistent with the effect produced by variable mantle temperature than by variable mantle sources.

These considerations then lead us to the conclusion, in agreement with Langmuir et al. (1992), that the primary influence on ocean ridge basalt chemistry is mantle temperature, which appears to vary over ~150-200°C based on the calculations here. Other factors certainly *contribute* to the observations, however. The width of the observed correlations is likely related to source heterogeneity and complex fractionation processes.

Mantle heterogeneity is of course obvious and necessary once one considers the more highly incompatible elements. The range in K_{90}, for example, of a factor of 50 is far more than can be accounted for by melting variations, and instead relates to source heterogeneity. This is further supported by the fact that K_{90} correlates with radiogenic isotopes (Figure 5.18). As also noted, there is a pronounced deviation in predicted Na concentration as a function of depth when hotspots are approached. Hotspots have higher Na_8 or Na_{90} than they "should", which is readily explained by source enrichment. The anomalously low Fe_{90} of the segments near the Azores plume has also been explained

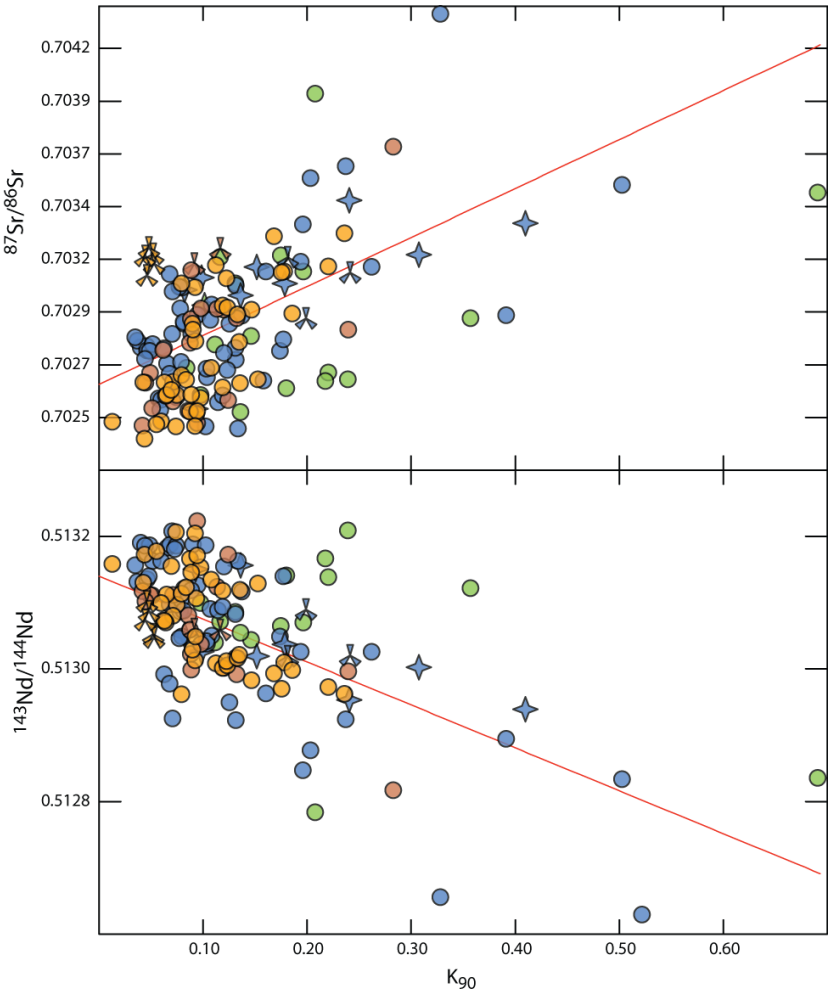

Figure 5.18: $^{87}Sr/^{86}Sr$ and $^{143}Nd/^{144}Nd$ versus K_{90}. Isotopic data on segments from Gale et al. (2012), submitted. Red lines indicate a least-squares regression through the data. To the first order, radiogenic isotopes correlate with K_{90}, suggesting that mantle heterogeneity has the dominant influence on the K contents of ocean ridge basalts. The mantle heterogeneity signal contributes to the global array.

in terms of major element heterogeneity associated with the plume (Langmuir and Hanson, 1980; Schilling, 1980). There is little doubt that mantle heterogeneity has a secondary effect on basalt major element compositions.

Is it reasonable that major element compositions show relatively little variation, while incompatible elements like K show large variations? It is if the origin of mantle heterogeneity is very low degree melts (e.g., McKenzie and O'Nions, 1995; Halliday et al., 1995, Donnelly et al., 2004; Gale et al., 2011). Low-degree melts have a large influence on trace elements, but little effect on major elements. For example, at deep pressures where low-F melts are generated, the partition coefficient (D) for Na is slightly higher than usual due to the increased jadeite component in residual cpx, about 0.1. Elements such as Th, Ba, U and K, however, have D-values of about 0.001. Deep, low-F melts can then be enriched by a factor of 100 in highly incompatible trace elements, but by only a factor of 10 in Na. With a typical source concentration of ~1 ppm Ba and 0.3 wt.% Na (Salters and Stracke, 2004; Langmuir et al., 1992), a low F melt might have 100 ppm Ba and 3 wt.% Na. Adding 2% of this melt to a depleted mantle then triples the source Ba content

(from 1 to 3), but only increases the source Na by 18%. This is an "enriched" mantle in trace elements, but the major elements would show little effect.

The same logic holds true for the depletion of the mantle; extraction of a 2-3% mantle melt severely depletes the incompatible element concentrations of the source with minimal impact on the major elements. For an incompatible element with a D of 0.001, for example, the residue can be depleted 95% by the extraction of a 2% melt, while major elements are diminished by less than 10% (Gale et al., 2011). These results reconcile the apparent conflicting signatures between trace elements and major elements, and support the existence of mantle temperature variations beneath ridges.

Lithospheric effects also likely add to the offset in major element compositions apparent in the super-slow spreading ridge segments, where there is a substantially increased lid of cold lithosphere. Thicker lithosphere can lead to early fractionation of pressure-sensitive cpx, and to lower concentrations of pressure-sensitive Si. These effects are qualitatively consistent with the observed low Si and Ca in the ultraslow spreading segments, although they must be more fully investigated. There are indications that the pressure of crystallization may vary inversely with spreading rate (Michael and Cornell, 1998). Langmuir et al. (2006b) suggested in a study of the super-slow spreading Gakkel ridge that lithospheric variations play a minor role in influencing the global array.

5.5. Conclusions

The main points of this study are:

(1) We have corrected a global catalog of ridge basalt major element data for fractionation to their values at 8 wt.% MgO, and to equlibrium with Fo_{90} olivine, using a custom correction scheme for each of over 240 ridge segments. The data include ridge segments from the full range of axial depths (+1000 to -5000 m), and from all spreading rates.

(2) These corrections provide parental magma compositions for each of the segments that can be compared with each other, and with variables such as ridge depth or spreading rate, to explore the global chemical systematics.

(3) In contrast to claims made in the literature, “8-values” and “90-values”, are in close agreement. The one exception is Ca. Ca_{90} shows little change with other chemical parameters, while Ca_8 correlates well with Na_8, for example. Of particular importance, Fe_8 and Fe_{90} show a similar range of variation, in conflict with the conclusions of Niu and O’Hara (2008).

(4) We demonstrate that, in agreement with the results of Langmuir et al. (1992), the 8- and 90-values show coherent global correlations with each other and with ridge depth. There is no correlation between the chemical parameters and spreading rate. The range of depths and chemical variations increases as spreading rate decreases.

(5) These data can be used to test the main competing hypotheses for the principal origin of the compositional variations of ocean ridge basalts, mantle temperature or mantle compositional heterogeneity. The correlations are best explained by a range of mantle temperature of ~200°C. Mantle source heterogeneity produces major element trends that are orthogonal to those apparent in the global dataset. The dominant influence on ridge depth and chemical composition is mantle temperature.

(6) Mantle heterogeneity also contributes to the chemical systematics, evident in the higher Na contents of ridge segments near plumes relative to their “predicted” contents using the global relationship between Na_8 and ridge depth. K, the most incompatible major element, shows broad correlations with radiogenic isotopes and a factor of 50 variation, also requiring a role for source heterogeneity. The relative homogeneity of major elements and heterogeneity in highly incompatible elements suggests that addition and removal of low degree melts, not large scale changes in mantle composition, are responsible for magmatic variations at ocean ridges.

(7) Super-slow spreading ridge segments are offset to low Ca and Si, and high Al and Na, relative to faster-spreading ridge segments. These offsets are likely due to the increased lithospheric lid at super-slow spreading ridges, which would cause truncation of the melting regime at greater depths and crystallization of clinopyroxene at higher pressures.

References

Baker, M. B., and E. M. Stolper (1994), Determining the composition of high-pressure mantle melts using diamond aggregates, Geochemica et Cosmochimica Acta 58(13), 2811-2827.

Donnelly, K. E., S. L. Goldstein, C. H. Langmuir, and M. Spiegelman (2004), Origin of enriched ocean ridge basalts and implications for mantle dynamics, Earth and Planetary Science Letters, 226(3-4), 347-366.

Eason, D., and J. Sinton (2006), Origin of high-Al N-MORB by fractional crystallization in the upper mantle beneath the Galapagos Spreading Center, Earth and Planetary Science Letters, 252(3-4), 423-436.

Gale, A., S. Escrig, E. J. Gier, C. H. Langmuir, and S. L. Goldstein (2011), Enriched basalts at segment centers: The Lucky Strike (37 degrees 17 ‘ N) and Menez Gwen (37 degrees 50 ‘ N) segments of the Mid-Atlantic Ridge, Geochemistry Geophysics Geosystems, 12.

Ghiorso, M. S., M. M. Hirschmann, P. W. Reiners, and V. C. Kress (2002), The pMELTS: A revision of MELTS for improved calculation of phase relations and major element partitioning related to partial melting of the mantle to 3 GPa, Geochemistry Geophysics Geosystems, 3.

Green, D. H., T. J. Falloon, S. M. Eggins, and G. M. Yaxley (2001), Primary magmas and mantle temperatures, Eur. J. Mineral., 13(3), 437-451.

Halliday, A. N., D. C. Lee, S. Tommasini, G. R. Davies, C. R. Paslick, J. G. Fitton, and D. E. James (1995), Incompatible trace elements in OIB and MORB and source enrichment in the sub-oceanic mantle, Earth and Planetary Science Letters, 133(3-4), 379-395.

Hamelin, C., L. Dosso, B. Hanan, J. A. Barrat, and H. Ondreas (2010), Sr-Nd-Hf isotopes along the Pacific Antarctic Ridge from 41 to 53 degrees S, Geophysical Research Letters, 37.

Hirose, K., and I. Kushiro (1993), Partial melting of dry peridotites at high pressures: determination of compositions of melts segregated from peridotite using aggregates of diamond, Earth and Planetary Science Letters, 114, 477-489.

Hirschmann, M. M., M. B. Baker, and E. M. Stolper (1998), The effect of alkalis on the silica content of mantle-derived melts, Geochim. Cosmochim. Acta, 62(5), 883-902.

Katsura, T. (1995), Thermal-diffusivity of olivine under upper-mantle conditions, Geophysical Journal International, 122(1), 63-69.

Kimura, J.-I., and S. Sano (2012), Reactive Melt Flow as the Origin of Residual Mantle Lithologies and Basalt Chemistries in Mid-Ocean Ridges: Implications from the Red Hills Peridotite, New Zealand, Journal of Petrology.

Klein, E. M., and C. H. Langmuir (1987), Global correlations of ocean ridge basalt chemistry with axial depth and crustal thickness, Journal of Geophysical Research 92(B8), 8089-8115.

Langmuir, C. H., and G. N. Hanson (1980), An evaluation of major element heterogeneity in the mantle sources of basalts, Philosophical Transactions of the Royal Society of London Series a-Mathematical Physical and Engineering Sciences, 297(1431), 383-

407.

Langmuir, C. H., E. M. Klein, and T. Plank (1992), Petrological systematics of midocean ridge basalts - Constraints on melt generation beneath ocean ridges, in Mantle Flow and Melt Generation at Mid-Ocean Ridges, edited by J. P. Morgan, B. D. K. and S. J. M., pp. 183-280.

Langmuir, C. H., Bezos, A., Escrig, S. and Parman, S.W. (2006), Chemical Systematics and Hydrous Melting of the Mantle in Back-Arc Basins, in Back-Arc Spreading Systems: Geological, Biological, Chemical and Physical Interactions, edited, American Geophysical Union: Geophysical Monograph Series 166.

Langmuir, C.H., Standish, J., Michael, P. and Goldstein, S. (2006b), Constraints on ocean ridge basalt generation from Gakkel Ridge basalts. Eos, Transactions, American Geophysical Union 87(52), Fall Meeting Supplement, Abstract V12c-01.

McKenzie, D., and R. K. Onions (1995), The source regions of ocean island basalts, Journal of Petrology, 36(1), 133-159.

Michael, P. J., and W. C. Cornell (1998), Influence of spreading rate and magma supply on crystallization and assimilation beneath mid-ocean ridges: Evidence from chlorine and major element chemistry of mid-ocean ridge basalts, Journal Of Geophysical Research-Solid Earth, 103(B8), 18325-18356.

Niu, Y. L., and M. J. O'Hara (2008), Global correlations of ocean ridge basalt chemistry with axial depth: A new perspective, Journal of Petrology, 49(4), 633-664.

Niu, Y. L., K. D. Collerson, R. Batiza, J. I. Wendt, and M. Regelous (1999), Origin of enriched-type mid-ocean ridge basalt at ridges far from mantle plumes: The East Pacific Rise at 11 degrees 20 ' N, Journal of Geophysical Research-Solid Earth, 104(B4), 7067-7087.

Presnall, D. C., G. H. Gudfinnsson, and M. J. Walter (2002), Generation of mid-ocean ridge basalts at pressures from 1 to 7 GPa, Geochim. Cosmochim. Acta, 66(12), 2073-2090.

Ryan, W. B. F., et al. (2009), Global Multi-Resolution Topography synthesis, Geochemistry Geophysics Geosystems, 10.

Salters, V. J. M., and A. Stracke (2004), Composition of the depleted mantle, Geophysics, Geochemistry, Geosystems 5(5), 27.

Schilling, J. G., M. B. Bergeron, and R. Evans (1980), Halogens in the Mantle beneath the North-Atlantic, Philosophical Transactions of the Royal Society of London Series a-Mathematical Physical and Engineering Sciences, 297(1431), 147-178.

Schwab, B. E., and A. D. Johnston (2001), Melting systematics of modally variable, compositionally intermediate peridotites and the effects of mineral fertility, Journal of Petrology, 42(10), 1789-1811.

Shen, Y., and D. W. Forsyth (1995), Geochemical constraints on initial and final depths of melting beneath midocean ridges, Journal of Geophysical Research-Solid Earth, 100(B2), 2211-2237.

Workman, R. K., and S. B. Hart (2005), Major and trace element composition of the depleted MORB mantle (DMM), Earth and Planetary Science Letters, 231, 53-72.

Appendix A

Supplementary Material for Chapter 2

A1. Method for Correcting Incompatible Trace Elements to Their Values at MgO = 8 wt. %:

Following the approach of Langmuir et al., 1992, we use the formula:

$\log(X_{8.0}) = \log(X) - 0.11*(8\text{-MgO})$

Here, X represents the concentration of an incompatible element (Ba, Rb, Th, U, Nb, Ta, La, Ce, Pb); $X_{8.0}$ indicates the concentration at 8 wt.% MgO. This formula can be applied to a sample with any MgO content <8.5, as it is appropriate for any crystallizing assemblage for the elements considered.

To account for the slightly more compatible nature of the M to HREE, we use the formula:

$\log(X_{8.0}) = \log(X) - 0.10*(8\text{-MgO})$ for the elements Nd, Sm, Zr, Hf, Eu, Gd, Tb

AND

$\log(X_{8.0}) = \log(X) - 0.09*(8\text{-MgO})$ for the elements Dy, Y, Ho, Er, Yb, Lu

A2. Trace Element Modeling of the Enriched Samples:

1. Step 1 in the trace element modeling required estimating the TE concentrations of 'primary' enriched magma(s). For this, we selected seven primitive samples that showed evidence of having only crystallized olivine. We then added step-wise increments (0.1% per step) of equilibrium olivine to each of the seven magma compositions until they were in equilibrium with Mg# 91 olivine. We used a K_D $(C^{FeO}{}_{ol}/C^{FeO}{}_{L})/(C^{MgO}{}_{ol}/C^{MgO}{}_{L}) = 0.3$. Next, we used the ratio of K_2O in the calculated primary lava to the K_2O in the original lava to get a "dilution factor." We multiplied all the incompatible trace elements by this dilution factor to estimate their

concentrations in the primary lavas.

2. Step 2 in the trace element modeling involved inverting the seven primary magmas for their metasomatized sources, using the F constraints from the major elements. Direct inversion is possible with a known F and the batch melting equation (details of mineral modes and melting reactions in Table 3), but the major element modeling is not detailed enough to give a specific F for each sample.

   To get an F for each sample, we utilized Lu contents. Our model assumes one depleted mantle source (DM) to which the low-F of the Azores is added. The Lu content of the DM is essentially unaffected by the low-F addition because (1) the low-F (in the garnet field) contains minimal Lu and (2) Lu is only moderately incompatible and so is not too depleted in the DM (making its concentration less susceptible to change with low-F addition). We assume that, to the first order, the concentration of Lu is the same in the DM and all the metasomatized sources.

   As such, we fixed the concentration of Lu in the sources so that the average enriched primary magma would be generated by the average F from the major element modeling (F=7%). Knowing the Lu content of the sources, we calculate an F for each of the seven lavas, and use this F to invert for the entire trace element composition of the metasomatized sources. Importantly, the calculated Fs for the seven samples stayed within the narrow range of 6.5-7.5%, consistent with the major element modeling.

3. We then needed an estimate of the trace element composition of the DM pre-low-F addition. The estimated Lu content in the sources was lower than published values for DM, so we calculated a DM (Mantle Source 1). We did this by extracting a batch melt (4.7%) from the average DMM reported by *Workman and Hart* (2005) so that the Lu content matched those of our inverted sources (details about mineral modes and melting reactions in main text).

4. We minimized differences between the inverted sources and a source created by mixing low-F Azores melt with our Mantle Source 1, including absolute concentrations and key trace element ratios (e.g., La/Sm, Ba/La, Zr/Nb). We allowed two parameters to vary: (1) the F of the low-F of Azores mantle; (2) the quantity of that low-F added to Mantle Source 1. The non-modal batch melting of the Azores source (the low-F event) took place with garnet in the source; the melting reactions and mineral modes are given in Table 3.

5. As a final check for consistency, we allowed the F of our calculated metasomatized sources to vary in order to “best-fit” the seven actual primary enriched lavas (this time without garnet in the source – see Table 3). All seven lavas were best-fit with an F that ranged between 6 and 7.7% (very close to our range of 6.5-7.5% estimated with major element modeling). Details of our model output can be found in Table A3.

Table A1: Major Element Contents (in wt. %) of Glasses from KP-2,3,5 and PO-1

Detrick Segment	Sample Name	Sample Group	Latitude	Longitude	Depth	ME method	SiO_2	TiO_2	Al_2O_3	FeO_T	MnO	MgO	CaO	Na_2O	K_2O	P_2O_5	Sum
KP-2	AII0127-1-022-006(B)	n/a	39.038	-30.025		probe	51.50	1.72	14.95	9.69	0.19	6.42	11.12	2.49	0.83	0.28	99.18
KP-2	AII0127-1-022-007	n/a	39.038	-30.025	1386	probe	51.95	1.79	15.10	9.66	0.13	6.29	10.92	2.74	0.85	0.30	99.73
KP-2	AII0127-1-R064	n/a	38.887	-30.072	1190	probe	50.47	1.52	15.48	9.16	0.15	7.30	11.84	2.65	0.67	0.27	99.51
KP-2	AII0127-1-R065	n/a	38.944	-30.059	1300	probe	51.29	1.67	15.19	9.34	0.18	6.80	11.65	2.60	0.71	0.28	99.69
KP-2	AII0127-1-R066	n/a	39.059	-30.027	1279	probe	51.71	2.02	15.00	9.97	0.19	5.93	10.50	2.88	0.88	0.35	99.44
KP-2	AII0127-2-R086	n/a	39.363	-29.938	1735	probe	51.85	1.83	14.67	10.41	0.19	5.99	10.34	2.76	0.67	0.29	99.00
KP-2	AII0127-2-R088	n/a	39.255	-29.963	1661	probe	50.11	2.10	15.33	9.44	0.16	6.34	11.34	2.85	0.78	0.36	98.81
KP-2	AII0127-2-R089	n/a	39.168	-29.981	1523	probe	50.58	1.71	15.60	8.74	0.17	6.87	11.60	2.76	0.70	0.28	99.00
KP-2	AII0127-2-R090	n/a	39.104	-30.020	1210	probe	51.27	2.02	15.09	10.13	0.18	5.78	10.15	3.08	0.81	0.34	98.87
KP-2	AII0127-2-R091	n/a	38.993	-30.039	1338	probe	51.07	1.93	14.97	10.17	0.19	6.04	10.77	3.00	0.75	0.31	99.18
KP-3	AII0127-1-021-001(A)	n/a	38.491	-30.265	2095	probe	51.03	2.05	15.81	8.89	0.17	6.09	10.88	3.29	1.06	0.36	99.62
KP-3	AII0127-1-021-003	n/a	38.491	-30.265		probe	50.84	2.20	15.66	9.34	0.19	5.82	10.61	3.34	1.11	0.39	99.50
KP-3	AII0127-1-021-004	n/a	38.491	-30.265	2095	probe	51.06	2.26	15.71	9.45	0.16	5.75	10.53	3.47	1.20	0.42	100.02
KP-3	AII0127-1-021-005	n/a	38.491	-30.265	2095	probe	51.11	2.13	15.82	9.13	0.16	5.85	10.67	3.38	1.07	0.40	99.74
KP-3	AII0127-1-R057	n/a	38.445	-30.275	2170	probe	50.97	1.86	14.79	9.79	0.18	6.38	10.78	2.90	0.70	0.31	98.67
KP-3	AII0127-1-R057	n/a	38.445	-30.275	2170	probe	51.00	1.76	15.25	9.57	0.19	6.53	11.32	2.74	0.72	0.28	99.35
KP-3	AII0127-1-R058	n/a	38.541	-30.249	1944	probe	52.33	2.52	14.42	11.23	0.20	4.43	8.53	3.50	1.17	0.44	98.78
KP-3	AII0127-1-R060	n/a	38.661	-30.193	1170	probe	52.25	2.49	14.46	11.12	0.19	4.47	8.51	3.48	1.15	0.44	98.56
KP-3	AII0127-1-R061	n/a	38.721	-30.169	1222	probe	52.61	2.17	14.63	11.13	0.19	4.94	9.01	3.55	1.01	0.42	99.66

Table A1 (Continued)

KP-3	AII0127-1-R062-A	n/a	38.804	-30.137	1352	probe	50.97	2.75	14.45	12.46	0.23	4.47	8.79	3.91	1.29	0.55	99.88
KP-3	AII0127-1-R063	n/a	38.828	-30.087	1240	probe	50.03	1.80	15.19	8.94	0.17	7.99	11.94	2.66	0.73	0.27	99.72
KP-3	AII0127-2-R093-001	n/a	38.575	-30.226	1792	probe	51.29	1.64	15.60	9.20	0.17	6.77	11.00	2.88	0.77	0.26	99.57
KP-5	AII0127-1-017-002	En-riched	37.836	-31.518	1009	probe	49.30	1.32	16.13	7.67	0.13	8.47	13.65	2.28	0.60	0.23	99.77
KP-5	AII0127-1-017-003	En-riched	37.836	-31.518	1009	probe	48.94	1.33	15.93	7.52	0.16	8.30	13.53	2.17	0.71	0.27	98.87
KP-5	AII0127-1-017-005	n/a	37.836	-31.518	1009	probe	49.79	1.33	15.66	7.81	0.14	8.18	13.76	2.28	0.62	0.24	99.80
KP-5	AII0127-1-018-001	Normal	37.979	-31.471	1725	probe	51.09	1.00	14.92	8.92	0.18	8.01	13.16	2.08	0.23	0.11	99.69
KP-5	AII0127-1-018-002	Normal	37.979	-31.471		probe	50.28	1.03	14.96	9.35	0.19	8.11	13.35	2.17	0.22	0.14	99.80
KP-5	AII0127-1-018-004	n/a	37.979	-31.471	1725	probe	50.86	1.00	15.09	9.29	0.15	8.13	13.32	2.10	0.20	0.10	100.22
KP-5	AII0127-1-R045	En-riched	37.599	-31.599	1971	probe	51.89	1.66	14.08	11.69	0.23	6.19	10.62	2.86	0.30	0.19	99.73
KP-5	AII0127-1-R046	Normal	37.711	-31.558	1421	probe	51.92	1.45	14.16	11.27	0.20	6.60	11.09	2.52	0.32	0.20	99.74
KP-5	AII0127-1-R047	Normal	37.799	-31.532	1018	probe	52.10	1.71	14.04	12.02	0.23	6.07	10.14	2.76	0.40	0.24	99.71
KP-5	AII0127-1-R048	En-riched	37.889	-31.503	1365	probe	49.27	1.35	15.95	7.95	0.16	8.22	13.78	2.35	0.64	0.23	99.89
KP-5	AII0127-1-R049	Normal	37.952	-31.499	1581	probe	51.55	1.78	14.13	11.77	0.25	5.93	10.55	2.87	0.47	0.22	99.50
KP-5	AII0127-2-034-002(A)	Normal	37.590	-31.602	1950	probe	51.59	1.35	14.26	11.36	0.20	6.80	11.32	2.55	0.29	0.18	99.89
KP-5	AII0127-2-034-GL	Normal	37.590	-31.602	1950	probe	51.56	1.33	14.32	11.26	0.20	6.59	11.15	2.50	0.29		99.20
KP-5	AII0127-2-R094-001	Normal	37.978	-31.483	1713	probe	53.19	2.31	13.94	13.75	0.26	4.68	8.89	2.64	0.60	0.30	100.56
KP-5	AII0127-2-R095	Normal	37.915	-31.500	1537	probe	51.74	1.71	14.15	11.86	0.20	6.03	10.40	2.76	0.46	0.21	99.52
KP-5	AII0127-2-R096-002	En-riched	37.846	-31.536	823	probe	50.31	1.58	15.33	9.33	0.17	7.11	12.06	2.83	0.76	0.26	99.74
KP-5	AII0127-2-R097-002	En-riched	37.836	-31.505	811	probe	50.31	1.52	15.34	9.55	0.18	6.97	11.83	2.77	0.70	0.25	99.43

Table A1 (Continued)

KP-5	AII0127-2-R098	Normal	37.822	-31.530	1042	probe	51.37	1.53	14.26	11.26	0.21	7.08	11.19	2.53	0.25	0.18	99.86
KP-5	AII0127-2-R099	Normal	37.766	-31.547	1312	probe	51.33	1.55	14.37	11.18	0.21	6.49	11.18	2.55	0.40	0.18	99.44
KP-5	AII0127-2-R100	Normal	37.730	-31.542	1338	probe	50.91	1.38	14.47	10.84	0.21	7.23	11.91	2.41	0.26	0.16	99.79
KP-5	AII0127-2-R101-001	Normal	37.686	-31.559	1594	probe	51.59	1.59	14.25	11.37	0.20	6.22	10.97	2.68	0.43	0.21	99.51
KP-5	AII0127-2-R101-003	Normal	37.686	-31.559	1594	probe	51.41	1.63	14.29	11.45	0.22	6.51	11.10	2.56	0.39	0.21	99.78
KP-5	AII0127-2-R102-003	Normal	37.658	-31.572	1773	probe	50.76	1.14	14.69	10.17	0.18	7.87	12.52	2.22	0.14	0.11	99.80
PO-1	AII0127-1-015-001	Normal	37.291	-32.283	1706	probe	51.38	1.07	14.69	9.80	0.18	8.14	12.08	2.17	0.20	0.14	99.86
PO-1	AII0127-1-015-002	Normal	37.291	-32.283	1706	probe	51.42	1.06	14.71	9.82	0.17	8.09	12.06	2.20	0.20	0.14	99.87
PO-1	AII0127-1-016-001	Normal	37.458	-32.225	2952	probe	52.27	1.40	14.07	10.80	0.19	6.82	11.33	2.41	0.24	0.16	99.68
PO-1	AII0127-1-R039	En-riched	37.136	-32.345	2663	probe	50.56	1.40	15.43	8.33	0.15	7.65	12.88	2.48	0.67	0.27	99.81
PO-1	AII0127-1-R040	Normal	37.218	-32.316	2176	probe	51.22	1.15	14.95	9.53	0.19	7.93	12.12	2.26	0.19	0.15	99.69
PO-1	AII0127-1-R044	Normal	37.387	-32.250	2570	probe	50.72	0.89	15.08	8.74	0.16	8.44	13.33	2.09	0.12	0.10	99.66
PO-1	AII0127-2-036-011	Normal	37.256	-32.288	1959	probe	51.39	1.15	15.33	9.80	0.16	7.41	12.09	2.45	0.20	0.14	100.13
PO-1	AII0127-2-036-012	Normal	37.256	-32.288	2274	probe	51.77	1.21	14.90	9.95	0.16	7.31	11.94	2.47	0.22	0.15	100.08
PO-1	AII0127-2-036-020	Normal	37.256	-32.288	1959	probe	51.97	1.10	15.07	9.81	0.16	7.49	11.81	2.35	0.21	0.15	100.13
PO-1	AII0127-2-036-024	Normal	37.256	-32.288	2274	probe	52.04	1.06	14.72	9.86	0.17	7.70	12.13	2.29	0.16	0.14	100.27
PO-1	AII0127-2-038-004	Normal	37.111	-32.348	2930	probe	51.38	1.17	14.26	10.91	0.19	7.20	11.91	2.44	0.20	0.15	99.82
PO-1	AII0127-2-R103-002	Normal	37.253	-32.293	1864	probe	51.30	1.08	14.86	10.09	0.19	7.84	11.88	2.33	0.19	0.11	99.86
PO-1	AII0127-2-R108-003	Normal	37.316	-32.279	1801	probe	51.14	1.10	14.73	9.70	0.18	8.27	12.07	2.25	0.18	0.14	99.77
PO-1	AII0127-2-R109-001	Normal	37.341	-32.270	2125	probe	52.10	1.35	14.49	10.65	0.16	6.90	11.26	2.46	0.22	0.14	99.73

Table A1 (Continued)

PO-1	AII0127-2-R109-002	Normal	37.341	-32.270	2125	probe	50.85	0.96	15.18	9.22	0.16	8.36	12.73	2.08	0.19	0.11	99.85
PO-1	AII0127-2-R114-001	Normal	37.428	-32.244	2836	probe	51.47	1.11	14.50	9.83	0.19	7.72	12.30	2.26	0.20	0.15	99.73
PO-1	AII0127-2-R116-001	En-riched	37.278	-32.291	1755	probe	50.00	1.27	15.91	7.18	0.14	8.63	13.85	2.23	0.58	0.24	100.01
PO-1	AII0127-2-R116-002	En-riched	37.278	-32.291	1755	probe	49.98	1.17	15.99	6.96	0.14	9.02	13.66	2.29	0.57	0.25	100.01
PO-1	AII0127-2-R117-001	Normal	37.236	-32.296	2083	probe	51.31	1.09	14.92	10.06	0.19	7.74	11.78	2.32	0.20	0.13	99.72
PO-1	AII0127-2-R118-001	Normal	37.177	-32.329	2466	probe	50.94	1.24	14.50	10.30	0.21	7.63	12.23	2.31	0.22	0.16	99.73
PO-1	AII0129-6 2608 1-1S	En-riched	37.293	-32.275		probe	50.10	1.26	15.88	7.81	0.15	8.25	13.27	2.27	0.49	0.22	99.71
PO-1	AII0129-6-001-3	Normal	37.297	-32.283		probe	50.95	1.08	14.75	9.85	0.17	7.92	12.01	2.17	0.18	0.11	99.20
PO-1	AII0129-6-002-001	Normal	37.285	-32.281		probe	51.27	1.08	14.65	9.84	0.17	8.00	12.02	2.19	0.18	0.11	99.51
PO-1	AII0129-6-002-B	Normal	37.285	-32.281		probe	51.31	1.10	14.93	9.76	0.17	7.30	12.24	2.20	0.18	0.11	99.31
PO-1	AII0129-6-004 SED	Normal	37.282	-32.322		probe	50.61	0.77	15.19	8.93	0.16	8.88	13.34	2.05	0.12	0.07	100.12
PO-1	AII0129-6-004 SEDB	Normal	37.282	-32.322		probe	50.59	0.74	15.44	7.78	0.13	9.22	14.21	1.79	0.12	0.08	100.07
PO-1	AII0129-6-004 SEDG	Normal	37.282	-32.322		probe	51.19	1.08	14.81	9.78	0.17	7.64	12.10	2.19	0.18	0.11	99.25
PO-1	AII0129-6-FF1	En-riched	37.293	-32.259		probe	49.76	1.52	15.66	8.42	0.15	7.40	12.50	2.74	0.86	0.31	99.33
PO-1	AII0129-6-FF2	En-riched	37.282	-32.305		probe	50.65	1.27	15.40	7.98	0.14	8.33	13.09	2.23	0.46	0.20	99.75
PO-1	AII0129-6-FF3	Normal	37.286	-32.279		probe	51.74	1.10	14.59	10.15	0.18	7.93	11.69	2.30	0.19	0.11	99.98
PO-1	AII0129-6-FF4	En-riched	37.287	-32.279		probe	50.55	1.28	15.60	7.72	0.13	8.32	13.33	2.27	0.49	0.20	99.90
PO-1	AII0129-6-R002	Normal	37.286	-32.291		probe	51.37	1.08	14.63	9.72	0.17	8.03	11.97	2.19	0.18	0.12	99.46
PO-1	AII0129-6-R004	Normal	37.293	-32.295		probe	50.93	1.21	15.28	8.10	0.14	8.09	12.98	2.11	0.29	0.14	99.27
PO-1	AII0129-6-R005	Normal	37.309	-32.292		probe	51.55	1.28	14.62	10.18	0.18	7.31	11.53	2.36	0.20	0.14	99.35

Table A1 (Continued)

PO-1	AII0129-6-R006	Normal	37.277	-32.270		probe	51.38	1.00	14.88	8.86	0.16	8.18	12.55	2.10	0.16	0.10	99.37
PO-1	AII0129-6-R007	Normal	37.282	-32.304		probe	51.44	1.13	14.67	9.60	0.16	7.56	12.22	2.24	0.18	0.11	99.33
PO-1	AII0129-6-R008	Transi-tional	37.305	-32.303		probe	51.07	0.93	15.12	8.04	0.15	8.85	13.77	1.90	0.23	0.11	100.18
PO-1	AII0129-6-R009	Normal	37.316	-32.302		probe	51.75	0.97	14.78	8.89	0.15	8.23	12.88	2.09	0.15	0.09	99.99
PO-1	AII0129-6-R010 SED	Transi-tional	37.332	-32.294		probe	51.66	1.05	14.84	9.04	0.16	8.19	12.62	2.15	0.22	0.12	100.05
PO-1	AII0129-6-R011	Normal	37.292	-32.291		probe	51.70	1.19	14.66	9.61	0.17	7.79	12.16	2.29	0.25	0.14	99.95
PO-1	AII0129-6-R011 SED	Transi-tional	37.292	-32.291		probe	51.39	1.14	14.58	9.64	0.16	7.98	12.41	2.21	0.23	0.13	99.88
PO-1	AII0129-6-R012	En-riched	37.335	-32.300		probe	51.62	1.15	14.85	8.93	0.15	7.78	12.53	2.20	0.42	0.18	99.82
PO-1	AII0129-6-R013	Normal	37.245	-32.317	2160	probe	51.70	0.94	14.84	8.79	0.15	8.45	12.96	2.04	0.13	0.09	100.07
PO-1	AII0129-6-R014	Normal	37.234	-32.278		probe	51.14	0.78	14.84	8.75	0.16	8.74	13.77	1.88	0.12	0.07	100.25
PO-1	AII0129-6-R015	Normal	37.193	-32.323		probe	51.65	1.38	14.36	10.57	0.18	7.18	11.71	2.30	0.23	0.15	99.71
PO-1	AII0129-6-R016	Normal	37.161	-32.335		probe	51.59	1.42	14.41	10.90	0.19	7.03	11.30	2.39	0.22	0.14	99.59
PO-1	AII0129-6-R017	Normal	37.161	-32.336		probe	51.47	1.03	14.41	10.15	0.18	7.69	12.49	2.29	0.16	0.10	99.96
PO-1	AII0129-6-R018	Normal	37.270	-32.312		probe	51.50	1.23	14.51	10.34	0.18	7.60	11.56	2.31	0.21	0.14	99.57
PO-1	AII0129-6-R018 SED	Normal	37.270	-32.312		probe	51.21	1.36	14.59	10.85	0.19	7.22	11.43	2.38	0.25	0.18	99.65
PO-1	AII0129-6-R019	Normal	37.246	-32.280		probe	51.89	1.20	14.57	9.91	0.16	7.78	11.80	2.25	0.21	0.13	99.90
PO-1	AII0129-6-R019A	Normal	37.246	-32.280		probe	51.43	1.07	14.97	10.10	0.18	7.68	11.79	2.27	0.19	0.12	99.78
PO-1	AII0129-6-R019B	Normal	37.246	-32.280		probe	51.18	1.41	14.60	10.97	0.19	7.02	11.34	2.39	0.26	0.19	99.55
PO-1	AII0129-6-R020	Normal	37.259	-32.314		probe	51.74	1.10	14.80	10.08	0.17	7.76	11.69	2.30	0.18	0.11	99.93
PO-1	AII0129-6-R023	Normal	37.192	-32.309		probe	51.92	1.39	14.19	10.90	0.18	6.96	11.61	2.35	0.25	0.15	99.89

Table A1 (Continued)

PO-1	KNO145-19-005-A	Normal	37.268	-32.280		probe	50.94	1.18	15.35	9.87	0.18	7.14	12.11	2.36	0.20	0.12	99.44
PO-1	KNO145-19-005-B	Normal	37.268	-32.280		probe	50.76	1.19	15.16	9.78	0.17	7.55	12.06	2.33	0.19	0.12	99.32
PO-1	KNO145-19-005-C	Normal	37.268	-32.280		probe	50.73	1.09	15.13	9.52	0.17	7.94	12.28	2.16	0.18	0.12	99.31
PO-1	KNO145-19-005-D	Normal	37.268	-32.280		probe	51.19	1.09	14.91	9.46	0.17	8.04	12.32	2.17	0.19	0.13	99.68
PO-1	KNO145-19-R004	Normal	37.292	-32.282		probe	51.23	1.07	14.76	9.89	0.19	7.82	12.23	2.24	0.19	0.12	99.73
PO-1	KNO145-19-R005	Normal	37.269	-32.268		probe	51.44	1.13	14.60	9.95	0.18	7.59	11.97	2.44	0.19	0.13	99.61
PO-1	KNO145-19-R006	Normal	37.267	-32.297		probe	51.34	1.06	14.74	10.10	0.18	7.87	11.74	2.35	0.20	0.12	99.70
PO-1	KNO145-19-R007	Normal	37.193	-32.323		probe	50.82	1.03	15.10	9.19	0.17	8.18	12.70	2.21	0.19	0.12	99.71
PO-1	KNO145-19-R013	Normal	37.307	-32.297		probe	50.71	0.98	15.46	9.35	0.16	7.69	12.71	2.23	0.13	0.09	99.50
PO-1	KNO145-19-R019	Normal	37.255	-32.317		probe	51.42	1.08	14.79	10.08	0.18	7.49	11.80	2.30	0.21	0.13	99.47
PO-1	KNO145-19-R019VES	En-riched	37.255	-32.317		probe	50.41	1.24	15.56	8.06	0.15	8.29	13.09	2.25	0.48	0.21	99.74
	Standard JDF-D2						50.8	1.89	13.8	12.17	0.22	6.83	10.8	2.77	0.22	0.23	

*Note: Data from cruises AII0129-6 and KNO145 are from the thesis of Elizabeth Gier and published with permission in Gale et al. (2011)

Table A2: Trace Element Concentrations of Glassy Basalts From Segments KP-2,3,5 and PO-1[a]

Sample Name	AII0127-1-022-005(A)	AII0127-1-022-006(B)	AII0127-1-R066	AII0127-2-029	AII0127-2-R087
Detrick Segment	KP-2	KP-2	KP-2	KP-2	KP-2
Sample Group	n/a	n/a	n/a	n/a	n/a
Latitude	39.038	39.038	39.059	39.432	39.307
Longitude	-30.025	-30.025	-30.027	-29.846	-29.949
Depth			1279	1860	1662
TE Ref	Harvard	Harvard	Harvard	Harvard	Harvard
TE Method	ICP-MS	ICP-MS	ICP-MS	ICP-MS	ICP-MS
Li	5.7	5.3	5.9	14.0	6.2
Be	0.98	0.88	0.97	0.83	0.95
Sc	33.5	33.9	34.1	34.3	34.2
Ti	1.86	1.67	1.91	1.66	1.82
V	304	279	310	243	297
Cr	60	84	84	298	104
Mn	0.17	0.17	0.17	0.15	0.18
Co	38.5	37.2	38.2	37.6	37.3
Ni	41	47	45	93	48
Cu	58	66	62	71	56
Zn	89.8	80.5	92.3	73.4	90.6
Ga	17.7	16.6	17.9	16.1	18.0
Rb	21.35	19.43	19.75	15.58	18.87
Sr	272	259	271	287	237
Y	26.9	25.3	27.9	21.9	30.1
Zr	146.6	133.4	146.7	129.4	146.5
Nb	33.91	30.33	31.99	28.01	29.88
Mo	1.21	1.08	1.17	1.07	1.12
Sn	1.16	1.09	1.20	1.04	1.18
Cs	0.21	0.20	0.20	0.17	0.20
Ba	248.5	224.4	231.4	183.2	217.8
La	20.28	18.49	19.22	16.63	18.59
Ce	42.26	38.37	40.43	34.55	39.18
Pr	5.24	4.76	5.08	4.37	4.94
Nd	21.30	19.73	21.03	18.32	20.78
Sm	4.64	4.30	4.70	4.03	4.69
Eu	1.50	1.42	1.53	1.35	1.53
Gd	5.05	4.73	5.20	4.34	5.34
Tb	0.80	0.75	0.83	0.68	0.86
Dy	4.72	4.47	4.94	3.97	5.21
Ho	0.96	0.91	1.00	0.79	1.08
Er	2.60	2.49	2.68	2.13	2.95
Yb	2.46	2.32	2.59	1.96	2.81
Lu	0.38	0.36	0.39	0.30	0.43
Hf	3.41	3.16	3.40	2.97	3.50
Ta	1.89	1.70	1.79	1.60	1.70
W	0.39	0.36	0.37	0.34	0.36
Tl	0.028	0.026	0.028	0.021	0.026
Pb	1.48	1.35	1.42	1.07	1.42
Th	2.25	2.03	2.12	1.79	2.04
U	0.64	0.58	0.61	0.54	0.59

Table A2 (Continued)

	AII0127-2-R089	AII0127-2-R090	AII0127-1-021-003	AII0127-1-021-005	AII0127-1-R063	AII0127-2-030
	KP-2	KP-2	KP-3	KP-3	KP-3	KP-3
	n/a	n/a	n/a	n/a	n/a	n/a
	39.168	39.104	38.491	38.491	38.828	38.754
	-29.981	-30.020	-30.265	-30.265	-30.087	-30.096
	1523	1210		2095	1240	980
	Harvard	Harvard	Harvard	Harvard	Harvard	Harvard
	ICP-MS	ICP-MS	ICP-MS	ICP-MS	ICP-MS	ICP-MS
Li	4.9	5.9	6.1	6.3	4.8	4.1
Be	0.89	0.99	1.40	1.47	0.85	0.95
Sc	35.5	31.4	28.5	29.6	34.6	36.6
Ti	1.70	1.98	2.08	2.13	1.78	1.53
V	266	308	258	264	253	231
Cr	234	97	75	74	409	504
Mn	0.15	0.17	0.16	0.16	0.16	0.15
Co	36.5	36.2	33.6	34.1	42.2	41.5
Ni	77	44	48	48	138	178
Cu	74	64	72	73	77	79
Zn	82.2	96.9	88.8	89.1	82.5	66.3
Ga	16.7	17.9	18.3	18.6	16.8	14.6
Rb	17.40	18.79	23.76	24.39	16.49	18.19
Sr	291	251	373	383	309	315
Y	24.4	29.7	28.2	29.0	24.5	21.7
Zr	132.4	154.3	191.3	195.4	140.1	125.3
Nb	27.56	31.99	36.76	37.36	29.42	25.54
Mo	1.04	1.18	1.54	1.55	1.04	1.17
Sn	1.05	1.26	1.50	1.61	1.21	1.02
Cs	0.18	0.18	0.24	0.25	0.17	0.20
Ba	203.9	225.0	263.6	269.2	199.2	202.1
La	17.06	19.10	23.30	23.86	17.76	15.91
Ce	35.75	40.74	49.12	50.18	38.12	32.72
Pr	4.51	5.13	6.08	6.26	4.85	4.15
Nd	18.62	21.31	25.45	26.15	20.12	17.95
Sm	4.24	4.87	5.50	5.62	4.60	3.97
Eu	1.38	1.58	1.76	1.81	1.48	1.35
Gd	4.62	5.45	5.76	5.90	4.93	4.30
Tb	0.73	0.86	0.90	0.92	0.77	0.68
Dy	4.32	5.22	5.12	5.28	4.50	3.94
Ho	0.85	1.06	1.01	1.03	0.87	0.77
Er	2.32	2.86	2.70	2.77	2.33	2.09
Yb	2.16	2.72	2.46	2.52	2.09	1.91
Lu	0.33	0.42	0.38	0.39	0.32	0.29
Hf	3.08	3.58	4.27	4.31	3.26	2.87
Ta	1.56	1.78	2.09	2.11	1.66	1.46
W	0.34	0.37	0.44	0.44	0.33	0.34
Tl	0.026	0.027	0.036	0.039	0.024	0.028
Pb	1.38	1.50	1.94	1.93	1.27	1.22
Th	1.91	2.07	2.43	2.47	1.81	1.71
U	0.54	0.60	0.77	0.77	0.54	0.54

Table A2 (Continued)

	AII0127-1-019-001A	AII0127-1-017-002	AII0127-1-017-003	AII0127-1-017-005	AII0127-1-018-001
	KP-4	KP-5	KP-5	KP-5	KP-5
	n/a	Enriched	Enriched	n/a	Normal
	38.123	37.836	37.836	37.836	37.979
	-30.728	-31.518	-31.518	-31.518	-31.471
	1877	1009	1009	1009	1725
	Harvard	Harvard	Harvard	Harvard	Harvard
	ICP-MS	ICP-MS	ICP-MS	ICP-MS	ICP-MS
Li	4.4	3.6	3.7	3.9	4.2
Be	0.78	0.63	0.65	0.60	0.35
Sc	35.1	39.7	39.9	44.5	47.2
Ti	1.45	1.24	1.30	1.30	0.95
V	239	229	237	256	254
Cr	228	330	346	390	109
Mn	0.15	0.14	0.14	0.15	0.17
Co	36.7	37.3	38.4	41.5	45.6
Ni	82	102	100	112	72
Cu	86	74	86	90	100
Zn	66.8	57.8	62.0	65.5	68.8
Ga	15.2	14.6	14.9	15.2	14.8
Rb	17.48	16.01	19.78	17.23	5.37
Sr	288	284	283	263	141
Y	22.6	19.9	20.6	21.6	21.4
Zr	124.9	86.7	94.5	90.6	60.6
Nb	34.86	26.33	28.26	25.73	9.95
Mo	1.41	1.00	1.17	0.99	0.42
Sn	0.97	0.82	0.78	0.74	0.52
Cs	0.22	0.19	0.25	0.21	0.06
Ba	230.5	222.4	241.7	213.5	65.8
La	20.85	14.66	15.66	14.37	6.14
Ce	40.17	28.92	30.86	28.62	13.34
Pr	4.80	3.56	3.78	3.54	1.80
Nd	19.65	14.53	15.82	14.64	8.25
Sm	4.08	3.29	3.46	3.39	2.29
Eu	1.34	1.10	1.20	1.13	0.83
Gd	4.37	3.62	3.83	3.83	3.07
Tb	0.69	0.57	0.61	0.61	0.53
Dy	4.00	3.43	3.65	3.73	3.50
Ho	0.81	0.69	0.74	0.74	0.74
Er	2.20	1.91	2.03	2.08	2.13
Yb	2.05	1.78	1.92	1.94	2.09
Lu	0.31	0.28	0.29	0.31	0.33
Hf	2.83	2.05	2.23	2.17	1.55
Ta	1.89	1.51	1.53	1.42	0.57
W	0.49	0.37	0.40	0.37	0.16
Tl	0.021	0.029	0.018	0.016	0.008
Pb	1.11		0.88	0.80	0.41
Th	2.58	1.87	1.95	1.81	0.68
U	0.78	0.64	0.56	0.51	0.23

Table A2 (Continued)

	AII0127-1-018-002	AII0127-1-R046	AII0127-1-R048	AII0127-2-033-002	AII0127-2-034-002(A)	AII0127-1-015-001
	KP-5	KP-5	KP-5	KP-5	KP-5	PO-1
	Normal	Normal	Enriched	Normal	Normal	Normal
	37.979	37.711	37.889	38.048	37.590	37.291
	-31.471	-31.558	-31.503	-31.446	-31.602	-32.283
		1421	1365	2050	1950	1706
	Harvard	Harvard	Harvard	Harvard	Harvard	Harvard
	ICP-MS	ICP-MS	ICP-MS	ICP-MS	ICP-MS	ICP-MS
Li	3.5	5.8	3.9	5.4	5.3	4.8
Be	0.37	0.49	0.65	0.43	0.46	0.35
Sc	45.8	42.0	39.5	41.8	43.1	39.8
Ti	0.91	1.33	1.30	1.13	1.16	0.99
V	245	303	240	273	287	253
Cr	115	56	374	65	66	74
Mn	0.16	0.19	0.15	0.18	0.17	0.17
Co	44.4	44.2	38.6	45.0	43.2	44.0
Ni	76	43	100	52	51	60
Cu	100	79	84	97	82	73
Zn	65.0	91.3	63.3	80.8	77.6	75.0
Ga	14.7	16.9	14.9	15.9	15.7	15.1
Rb	4.67	6.31	17.70	5.12	5.53	4.54
Sr	142	133	265	123	134	100
Y	20.3	28.3	20.8	24.7	25.6	23.4
Zr	57.3	84.4	93.0	68.5	72.0	56.4
Nb	9.42	12.80	25.67	9.89	10.86	8.11
Mo	0.56	0.57	1.06	0.49	0.49	0.43
Sn	0.67	0.77	0.76	0.64	0.64	0.52
Cs	0.07	0.07	0.22	0.05	0.06	0.05
Ba	62.1	74.6	211.8	61.8	66.9	56.5
La	5.79	8.14	14.63	6.19	6.93	4.91
Ce	12.67	17.91	28.91	13.71	15.15	10.84
Pr	1.72	2.45	3.59	1.90	2.09	1.53
Nd	7.85	11.15	15.14	8.89	9.67	7.45
Sm	2.19	3.12	3.38	2.56	2.71	2.26
Eu	0.80	1.08	1.16	0.93	0.97	0.84
Gd	2.93	4.15	3.79	3.48	3.66	3.22
Tb	0.50	0.71	0.61	0.61	0.63	0.57
Dy	3.36	4.67	3.64	4.05	4.16	3.82
Ho	0.71	1.00	0.75	0.88	0.91	0.83
Er	2.02	2.83	2.05	2.48	2.54	2.36
Yb	2.00	2.78	1.94	2.46	2.54	2.36
Lu	0.32	0.44	0.30	0.39	0.39	0.37
Hf	1.46	2.17	2.21	1.80	1.85	1.55
Ta	0.54	0.92	1.41	0.57	0.69	0.47
W		0.17	0.36	0.14	0.15	0.12
Tl		0.010	0.018	0.010	0.011	0.006
Pb	0.42	0.57	0.85	0.47	0.44	0.39
Th	0.63	0.85	1.76	0.66	0.74	0.54
U	0.24	0.27	0.51	0.21	0.35	0.16

Table A2 (Continued)

	AII0127-1-015-002	AII0127-1-R041	AII0127-2-035	AII0127-2-036-011	AII0127-2-036-020	AII0127-2-037
	PO-1	PO-1	PO-1	PO-1	PO-1	PO-1
	Normal	Enriched	Normal	Normal	Normal	Normal
	37.291	37.284	37.421	37.256	37.256	37.256
	-32.283	-32.281	-32.270	-32.288	-32.288	-32.300
	1706	1561	2728	1959	1959	1959
	Harvard	Harvard	Harvard	Harvard	Harvard	Harvard
	ICP-MS	ICP-MS	ICP-MS	ICP-MS	ICP-MS	ICP-MS
Li	4.9	4.6	5.4	5.0	4.8	4.3
Be	0.36	0.54	0.51	0.42	0.41	0.34
Sc	40.6	42.8	40.9	39.5	38.9	42.1
Ti	1.05	1.34	1.30	1.13	1.08	0.94
V	263	258	279	249	250	238
Cr	77	491	285	92	38	284
Mn	0.18	0.16	0.17	0.17	0.17	0.16
Co	45.6	41.3	43.2	43.0	44.6	43.2
Ni	62	95	84	60	53	89
Cu	77	83	74	76	75	88
Zn	76.7	71.0	83.1	75.8	76.3	66.9
Ga	15.6	15.4	16.1	15.8	15.7	14.6
Rb	4.69	11.22	5.82	4.81	4.87	4.15
Sr	104	196	109	109	115	106
Y	24.3	24.8	28.8	24.6	22.6	22.2
Zr	57.1	86.8	76.7	63.2	61.3	55.0
Nb	8.46	20.30	10.73	8.81	9.09	7.60
Mo	0.42	0.85	0.53	0.46	0.47	0.40
Sn	0.56	0.77	0.72	0.65	0.62	0.53
Cs	0.05	0.13	0.06	0.05	0.05	0.04
Ba	57.6	143.6	66.8	58.0	60.4	50.2
La	4.98	10.78	6.35	5.27	5.35	4.58
Ce	11.13	22.09	14.36	11.84	11.98	10.34
Pr	1.58	2.84	2.05	1.68	1.69	1.47
Nd	7.64	12.20	9.92	8.16	8.03	7.21
Sm	2.34	3.13	2.93	2.48	2.39	2.16
Eu	0.86	1.06	1.03	0.91	0.88	0.80
Gd	3.31	3.90	4.08	3.47	3.28	3.06
Tb	0.59	0.65	0.71	0.61	0.57	0.54
Dy	3.94	4.22	4.75	4.03	3.75	3.64
Ho	0.86	0.86	1.02	0.87	0.80	0.79
Er	2.44	2.43	2.87	2.44	2.26	2.25
Yb	2.40	2.34	2.83	2.39	2.21	2.25
Lu	0.38	0.37	0.44	0.37	0.34	0.35
Hf	1.59	2.16	2.08	1.71	1.65	1.49
Ta	0.48	1.12	0.64	0.50	0.53	0.44
W	0.13	0.27	0.16	0.13	0.13	0.15
Tl	0.006	0.012	0.008	0.006	0.007	0.006
Pb	0.41	0.63	0.48	0.42	0.42	
Th	0.55	1.32	0.69	0.57	0.58	0.49
U	0.16	0.38	0.22	0.17	0.18	0.17

Table A2 (Continued)

	AII0127-2-R108-001	AII0127-2-R113-001	AII0127-2-R116-002	AII0129-6-002-001	AII0129-6-003
	PO-1	PO-1	PO-1	PO-1	PO-1
	Normal	Normal	Enriched	Normal	Normal
	37.316	37.411	37.278	37.285	37.335
	-32.279	-32.270	-32.291	-32.281	-32.289
	1801	2658	1755		
	Harvard	Harvard	Harvard	Harvard	Harvard
	ICP-MS	ICP-MS	ICP-MS	ICP-MS	ICP-MS
Li	4.4	5.3	4.2	4.8	5.5
Be	0.31	0.47	0.56	0.36	0.45
Sc	42.9	40.6	42.4	42.3	40.7
Ti	0.95	1.26	1.22	1.07	1.30
V	258	278	235	273	283
Cr	100	465	848	77	154
Mn	0.16	0.17	0.15	0.18	0.17
Co	45.4	42.8	40.2	46.2	43.0
Ni	68	88	114	63	71
Cu	88	83	90	77	70
Zn	71.5	83.0	70.2	80.0	83.5
Ga	15.1	15.9	14.9	15.8	16.3
Rb	3.46	5.58	12.21	4.70	7.43
Sr	105	107	217	108	117
Y	21.6	28.1	21.8	24.6	28.8
Zr	47.8	74.2	81.5	57.7	76.1
Nb	6.51	10.34	20.85	8.62	13.35
Mo	0.33	0.52	1.00	0.44	0.59
Sn	0.47	0.74	0.70	0.56	0.72
Cs	0.03	0.06	0.14	0.05	0.08
Ba	43.3	65.4	160.1	58.0	85.6
La	3.95	6.11	11.46	5.06	7.47
Ce	9.05	13.85	23.11	11.28	16.19
Pr	1.30	1.97	2.91	1.59	2.22
Nd	6.47	9.56	12.21	7.69	10.24
Sm	2.06	2.87	3.02	2.36	2.98
Eu	0.77	1.00	1.01	0.86	1.02
Gd	2.97	3.96	3.56	3.37	4.07
Tb	0.52	0.70	0.59	0.59	0.70
Dy	3.56	4.58	3.74	4.05	4.73
Ho	0.76	0.99	0.75	0.87	1.01
Er	2.13	2.79	2.11	2.45	2.84
Yb	2.11	2.77	2.00	2.45	2.82
Lu	0.33	0.43	0.32	0.38	0.44
Hf	1.35	2.03	2.01	1.59	2.04
Ta	0.38	0.59	1.10	0.50	0.75
W	0.10	0.15	0.26	0.12	0.19
Tl	0.005	0.008	0.017	0.006	0.011
Pb	0.32		0.67	0.39	0.48
Th	0.42	0.67	1.39	0.55	0.90
U	0.12	0.20	0.41	0.16	0.26

Table A2 (Continued)

	AII0129-6-R005	AII0127-1-R064	AII0127-1-R065	AII0127-1-021-001(A)	AII0127-2-R093-001	AII0127-2-R095
	PO-1	KP-2	KP-2	KP-3	KP-3	KP-5
	Normal	n/a	n/a	n/a	n/a	Normal
	37.309	38.887	38.944	38.491	38.575	37.915
	-32.292	-30.072	-30.059	-30.265	-30.226	-31.500
		1190	1300	2095	1792	1537
	Harvard	LDEO	LDEO	LDEO	LDEO	LDEO
	ICP-MS	ICP-MS	ICP-MS	ICP-MS	ICP-MS	ICP-MS
Li	5.5	4.7	5.0			7.0
Be	0.41	1.11	1.08			0.98
Sc	41.7	36.0		28.3	34.9	
Ti	1.25	1.49	1.64			1.63
V	290	267	291	260	289	323
Cr	157	64	120	83	176	57
Mn	0.18					
Co	44.2	41.0	41.0	32.1	38.0	42.0
Ni	64	52	54	46	69	29
Cu	74	68	70	62	58	72
Zn	85.3	74.0	75.3	85.9	86.5	99.1
Ga	16.9	16.6	16.9			18.5
Rb	5.22	15.24	15.80	21.08	18.66	10.14
Sr	113	300	268	346	283	162
Y	28.1	22.6	24.1	26.7	29.7	33.4
Zr	68.6	111.9	119.3	169.9	148.4	111.8
Nb	9.75	25.18	26.87	32.85	28.88	21.02
Mo	0.48	1.01	0.96			0.91
Sn	0.68	0.90				1.06
Cs	0.06	0.15	0.18			0.12
Ba	62.2	182.9	201.8	236.9	212.7	121.0
La	5.70	15.97	17.54	21.09	18.20	12.95
Ce	13.01	33.21	35.46	44.24	38.02	27.84
Pr	1.86	4.12	4.48	5.53	4.76	3.68
Nd	8.96	17.35	18.79	23.04	19.81	16.69
Sm	2.76	3.99	3.99	5.04	4.67	3.74
Eu	0.99	1.34	1.44	1.68	1.54	1.41
Gd	3.90	4.27	4.48	5.19	5.07	5.23
Tb	0.68	0.67	0.70	0.81	0.83	0.87
Dy	4.60	3.92	4.21	4.89	4.99	5.66
Ho	0.99	0.82	0.87	0.95	1.03	1.23
Er	2.81	2.18	2.37	2.52	2.78	3.32
Yb	2.78	2.03	2.28	2.35	2.61	3.37
Lu	0.44	0.29	0.33	0.35	0.40	0.50
Hf	1.90	2.75	2.90	3.88	3.45	2.90
Ta	0.65	1.48	1.52	1.94	1.60	1.17
W	0.15					
Tl	0.007					
Pb	0.48	1.28	1.20	1.62		0.73
Th	0.64	1.74	1.87	2.10	1.95	1.42
U	0.18	0.48	0.53	0.62	0.56	0.47

Table A2 (Continued)

	AII0127-2-R096-002	AII0127-2-R097-002	AII0127-2-R098	AII0127-2-R099	AII0127-2-R100	AII0127-2-R101-003
	KP-5	KP-5	KP-5	KP-5	KP-5	KP-5
	Enriched	Enriched	Normal	Normal	Normal	Normal
	37.846	37.836	37.822	37.766	37.730	37.686
	-31.536	-31.505	-31.530	-31.547	-31.542	-31.559
	823	811	1042	1312	1338	1594
	LDEO	LDEO	LDEO	LDEO	LDEO	LDEO
	ICP-MS	LA-ICP-MS	LA-ICP-MS	ICP-MS	ICP-MS	LA-ICP-MS
Li	5.3			5.4	5.6	
Be	0.98			0.80	0.74	
Sc	33.8			35.5	39.0	
Ti	1.49			1.48	1.39	
V	283			310	309	
Cr	24			13	31	
Mn						
Co	42.6			42.4	46.9	
Ni	44			29	44	
Cu	106			79	107	
Zn	77.3			87.1	89.7	
Ga	17.3			17.0	17.3	
Rb	19.39	20.95	5.59	8.41	5.83	9.40
Sr	228	238	133	169	144	171
Y	26.8	29.2	28.9	27.9	29.0	31.3
Zr	109.4	117.9	85.5	101.9	87.7	113.2
Nb	28.69	30.75	11.87	17.81	13.22	19.30
Mo	1.22			0.69	0.62	
Sn						
Cs	0.25			0.09	0.06	
Ba	243.2	261.1	70.0	110.4	77.6	114.6
La	16.21	17.30	8.00	11.37	9.12	12.38
Ce	32.35	31.86	16.37	24.53	19.15	25.91
Pr	3.99	4.04	2.33	3.13	2.62	3.43
Nd	16.64	16.57	10.73	14.21	12.23	14.94
Sm	3.81	4.04	3.12	3.49	3.32	4.00
Eu	1.44	1.37	1.08	1.30	1.18	1.36
Gd	4.66	4.95	4.21	4.52	4.22	4.94
Tb	0.76	0.79	0.70	0.79	0.71	0.83
Dy	4.68	4.84	4.72	4.78	4.71	5.33
Ho	1.00	1.04	1.05	1.01	1.03	1.12
Er	2.78	2.82	2.89	2.85	2.80	3.23
Yb	2.71	2.73	2.80	2.77	2.82	3.01
Lu	0.40	0.39	0.42	0.42	0.43	0.46
Hf	2.77	2.71	2.22	2.44	2.44	2.70
Ta	1.64	1.71	0.72	1.01	0.75	1.10
W						
Tl						
Pb	0.96			0.67	0.69	
Th	2.16	2.14	0.77	1.19	0.88	1.25
U	0.55	0.56	0.22	0.40	0.31	0.38

Table A2 (Continued)

	AII0127-2-R102-003	AII0127-1-016-001	AII0127-1-R040	AII0127-2-036-012	AII0127-2-036-024	AII0127-2-038-002
	KP-5	PO-1	PO-1	PO-1	PO-1	PO-1
	Normal	Normal	Normal	Normal	Normal	Normal
	37.658	37.458	37.218	37.256	37.256	37.111
	-31.572	-32.225	-32.316	-32.288	-32.288	-32.348
	1773	2952	2176	2274	2274	2930
	LDEO	LDEO	LDEO	LDEO	LDEO	LDEO
	LA-ICP-MS	ICP-MS	ICP-MS	ICP-MS	ICP-MS	ICP-MS
Li		5.0	5.0			
Be		0.55	0.53			
Sc						
Ti						
V						260
Cr						
Mn						
Co						
Ni						
Cu						
Zn						
Ga						
Rb	6.56	5.82	3.95	4.84	4.58	4.81
Sr	139	112	106	118	103	111
Y	35.9	26.1	23.9	25.8	26.7	28.7
Zr	100.8	65.8	57.1	63.7	58.8	66.0
Nb	13.34	9.83	7.74	9.02	8.54	9.56
Mo		0.47	0.40			
Sn						
Cs						
Ba	79.1	69.7	53.5	59.8	55.4	61.3
La	8.88	6.24	5.06	5.37	4.90	5.70
Ce	19.34	13.82	11.38	12.48	11.43	12.36
Pr	2.77	1.92	1.64	1.75	1.61	1.76
Nd	12.65	9.23	7.96	8.23	7.53	8.45
Sm	3.62	2.77	2.45	2.55	2.38	2.61
Eu	1.36	0.96	0.86	0.96	0.90	1.04
Gd	5.37	3.94	3.60	3.60	3.50	3.93
Tb	0.89	0.69	0.63	0.62	0.62	0.68
Dy	6.08	4.58	4.26	4.27	4.35	4.50
Ho	1.32	1.00	0.92	0.91	0.94	1.03
Er	3.67	2.84	2.60	2.62	2.74	2.94
Yb	3.69	2.76	2.48	2.48	2.71	2.85
Lu	0.56	0.42	0.39	0.38	0.41	0.44
Hf	2.67	1.87	1.65			1.72
Ta	0.81	0.69	0.60	0.54	0.51	0.55
W						
Tl						
Pb						
Th	0.86	0.68	0.53			0.61
U	0.41	0.21	0.21			0.17

Table A2 (Continued)

	AII0127-2-038-004	AII0127-2-R103-001	AII0127-2-R103-002	AII0127-2-R104	AII0127-2-R105	AII0127-2-R106-001
	PO-1	PO-1	PO-1	PO-1	PO-1	PO-1
	Normal	Normal	Normal	Normal	Normal	Normal
	37.111	37.253	37.253	37.267	37.291	37.277
	-32.348	-32.293	-32.293	-32.285	-32.300	-32.270
	2930	1864	1864	1804	1770	1707
	LDEO	LDEO	LDEO	LDEO	LDEO	LDEO
	ICP-MS	ICP-MS	LA-ICP-MS	ICP-MS	ICP-MS	LA-ICP-MS
Li	5.1	5.3		5.2	4.4	
Be	0.45	0.50		0.54	0.45	
Sc	36.9					
Ti	1.04					
V	264					
Cr	79					
Mn						
Co	56.0					
Ni	75					
Cu	171					
Zn	145.4					
Ga	16.3					
Rb	4.32	4.61	4.45	4.72	4.36	3.59
Sr	108	117	115	116	113	93
Y	25.1	24.7	24.7	24.7	23.2	19.3
Zr	55.0	55.3	58.3	63.2	60.3	48.0
Nb	8.37	9.06	8.31	8.90	8.39	7.10
Mo	0.39	0.41		0.39	0.38	
Sn	0.57					
Cs	0.05					
Ba	54.8	60.2	57.0	61.0	58.7	47.0
La	5.00	5.20	5.03	5.54	5.23	4.11
Ce	11.15	11.64	10.58	12.43	11.69	8.81
Pr	1.53	1.63	1.57	1.76	1.65	1.30
Nd	7.46	7.84	7.51	8.50	7.97	5.99
Sm	2.34	2.38	2.36	2.57	2.39	1.91
Eu	0.92	0.90	0.89	0.95	0.91	0.70
Gd	3.39	3.32	3.42	3.64	3.37	2.71
Tb	0.60	0.59	0.61	0.64	0.59	0.47
Dy	4.04	3.94	3.89	4.23	3.98	3.25
Ho	0.90	0.86	0.88	0.92	0.86	0.69
Er	2.55	2.41	2.52	2.54	2.40	1.97
Yb	2.54	2.41	2.41	2.50	2.36	1.90
Lu	0.39	0.37	0.37	0.38	0.36	0.30
Hf	1.57	1.51		1.79	1.67	1.22
Ta	0.49	0.51		0.51	0.47	0.38
W						
Tl						
Pb	0.33	0.36				
Th	0.56	0.54	0.51	0.58	0.58	0.48
U	0.18	0.16	0.15	0.17	0.17	0.14

Table A2 (Continued)

	AII0127-2-R107	AII0127-2-R108-003	AII0127-2-R109-003	AII0127-2-R110	AII0127-2-R111-001	AII0127-2-R112-001
	PO-1	PO-1	PO-1	PO-1	PO-1	PO-1
	Normal	Normal	Normal	Normal	Normal	Normal
	37.312	37.316	37.341	37.359	37.371	37.400
	-32.267	-32.279	-32.270	-32.263	-32.234	-32.224
	1808	1801	2125	2207	2558	2617
	LDEO	LDEO	LDEO	LDEO	LDEO	LDEO
	ICP-MS	LA-ICP-MS	LA-ICP-MS	ICP-MS	ICP-MS	ICP-MS
Li	5.5			5.6	4.3	6.0
Be	0.61			0.59	0.46	0.58
Sc						
Ti						
V						
Cr						
Mn						
Co						
Ni						
Cu						
Zn						
Ga						
Rb	5.40	2.92	4.48	6.26	5.33	4.90
Sr	111	97	114	108	107	106
Y	27.5	21.4	22.7	28.4	24.0	27.3
Zr	66.7	49.3	58.7	77.4	60.9	63.8
Nb	10.41	5.62	8.66	12.16	10.06	9.95
Mo	0.48			0.51	0.44	0.43
Sn						
Cs						
Ba	71.3	36.5	57.9	81.7	72.4	64.0
La	6.38	3.60	5.24	7.40	6.10	5.91
Ce	14.27	7.50	10.32	16.12	13.24	13.31
Pr	2.00	1.18	1.52	2.23	1.80	1.88
Nd	9.58	5.71	7.12	10.44	8.44	9.08
Sm	2.85	1.84	2.21	3.05	2.44	2.71
Eu	1.00	0.71	0.82	1.04	0.87	0.96
Gd	4.10	2.86	3.22	4.13	3.43	3.80
Tb	0.71	0.50	0.55	0.72	0.60	0.67
Dy	4.79	3.54	3.68	4.80	4.06	4.46
Ho	1.04	0.77	0.82	1.06	0.90	0.97
Er	2.93	2.22	2.36	2.96	2.57	2.74
Yb	2.86	2.07	2.24	2.91	2.56	2.72
Lu	0.44	0.30	0.35	0.44	0.39	0.41
Hf	2.00	1.44	1.60	2.10	1.64	1.82
Ta	0.65	0.35	0.51	0.66	0.54	0.52
W						
Tl						
Pb						0.37
Th	0.71	0.44	0.59	0.84	0.70	0.64
U	0.21	0.11	0.18	0.24	0.20	0.18

Table A2 (Continued)

	AII0127-2-R114-001	AII0127-2-R116-001	AII0127-2-R117-001	AII0127-2-R118-001	AII0129-6 2602-3
	PO-1	PO-1	PO-1	PO-1	PO-1
	Normal	Enriched	Normal	Normal	Enriched
	37.428	37.278	37.236	37.177	37.294
	-32.244	-32.291	-32.296	-32.329	-32.274
	2836	1755	2083	2466	
	LDEO	LDEO	LDEO	LDEO	LDEO
	ICP-MS	ICP-MS	ICP-MS	LA-ICP-MS	ICP-MS
Li			6.1		
Be			0.58		
Sc		34.5			43.0
Ti					
V		213			246
Cr		357			407
Mn					
Co					
Ni		96			111
Cu		92			100
Zn		60.0			64.3
Ga					
Rb	4.18	11.65	4.69	5.27	20.55
Sr	111	218	108	117	285
Y	24.7	21.1	28.9	23.6	23.3
Zr	63.4	79.2	66.4	64.5	92.0
Nb	8.04	20.04	9.26	9.66	33.72
Mo			0.41		
Sn					
Cs					
Ba	52.6	172.1	60.5	64.3	280.6
La	5.18	11.64	5.60	5.60	17.16
Ce	10.69	23.13	12.88	13.11	32.75
Pr	1.58	2.90	1.84	1.79	3.89
Nd	7.69	12.22	9.14	8.22	15.53
Sm	2.44	2.98	2.88	2.48	3.47
Eu	0.90	1.06	1.03	0.95	1.20
Gd	3.51	3.55	4.05	3.38	3.77
Tb	0.63	0.59	0.71	0.58	0.61
Dy	4.14	3.75	4.81	3.89	3.80
Ho	0.91	0.78	1.05	0.85	0.80
Er	2.57	2.16	2.99	2.46	2.20
Yb	2.45	2.08	2.95	2.36	2.12
Lu	0.37	0.32	0.45	0.35	0.33
Hf	1.69	2.05	1.95	1.64	2.13
Ta	0.47	1.21	0.53	0.53	1.76
W					
Tl					
Pb		0.77			0.91
Th	0.56	1.47	0.61	0.61	2.26
U	0.15	0.41	0.23	0.22	0.57

Table A2 (Continued)

	AII0129-6 2602-5a	AII0129-6 2602-5b	AII0129-6 2602-5c	AII0129-6 2604-3	AII0129-6-R008	AII0129-6-R010 SED
	PO-1	PO-1	PO-1	PO-1	PO-1	PO-1
	Enriched	Enriched	Enriched	Enriched	Transitional	Transitional
	37.300	37.300	37.300	37.296	37.305	37.332
	-32.272	-32.272	-32.272	-32.272	-32.303	-32.294
	LDEO	LDEO	LDEO	LDEO	LDEO	LDEO
	ICP-MS	ICP-MS	ICP-MS	ICP-MS	LA-ICP-MS	ICP-MS
Li		3.6	3.6			
Be		0.86	0.86			
Sc	36.4	36.4		42.4		
Ti						
V	225	225		249		
Cr	416	416		430		
Mn						
Co						
Ni	107	107		118		
Cu	86	86		87		
Zn	57.8	57.8		63.0	70.7	70.1
Ga						
Rb	19.41	19.61	19.81	16.27	5.79	5.11
Sr	258	269	281	291	139	123
Y	21.3	21.6	21.8	22.9	22.6	22.2
Zr	83.2	86.2	89.3	88.6	57.8	55.6
Nb	30.60	31.54	32.47	34.28	11.21	9.79
Mo		1.24	1.24			
Sn						
Cs						
Ba	261.6	273.1	284.5	282.3	99.5	79.9
La	16.02	16.62	17.23	17.40	6.81	5.85
Ce	30.35	31.35	32.36	32.90	14.43	12.58
Pr	3.63	3.73	3.84	3.84	1.93	1.69
Nd	14.53	14.99	15.45	15.28	8.99	7.88
Sm	3.18	3.28	3.38	3.40	2.54	2.19
Eu	1.12	1.14	1.17	1.18	0.95	0.84
Gd	3.56	3.65	3.74	3.64	3.52	3.16
Tb	0.58	0.59	0.60	0.60	0.59	0.53
Dy	3.57	3.63	3.69	3.61	3.89	3.62
Ho	0.75	0.76	0.77	0.78	0.87	0.78
Er	2.07	2.08	2.09	2.09	2.43	2.26
Yb	2.00	2.02	2.05	2.04	2.21	2.08
Lu	0.30	0.30	0.31	0.31	0.36	0.32
Hf	1.99	2.03	2.08	2.04	1.68	1.55
Ta	1.62	1.66	1.70	1.73	0.71	0.58
W						
Tl						
Pb	0.82	0.86	0.89		0.41	0.34
Th	2.07	2.14	2.22	2.21	0.80	0.66
U	0.53	0.54	0.55	0.55	0.19	0.17

Table A2 (Continued)

	AII0129-6-R011 SED	AII0129-6-R012	AII0129-6-R013	AII0129-6-R014	AII0129-6-R016
	PO-1	PO-1	PO-1	PO-1	PO-1
	Transitional	Enriched	Normal	Normal	Normal
	37.292	37.335	37.245	37.234	37.161
	-32.291	-32.300	-32.317	-32.278	-32.335
			2160		
	LDEO	LDEO	LDEO	LDEO	LDEO
	ICP-MS	ICP-MS	LA-ICP-MS	ICP-MS	ICP-MS
Li					6.6
Be					0.60
Sc					
Ti					
V					
Cr					
Mn					
Co					
Ni					
Cu					
Zn	69.4	71.2	66.1	47.1	
Ga					
Rb	5.90	12.03	2.83	2.16	5.34
Sr	121	169	105	77	103
Y	25.8	22.6	20.5	18.1	31.5
Zr	64.8	70.2	44.3	31.2	72.2
Nb	11.14	19.77	5.65	4.09	10.65
Mo					0.52
Sn					
Cs					
Ba	83.9	179.8	45.7	33.6	68.4
La	6.34	11.22	3.74	2.63	6.46
Ce	13.44	22.20	8.49	5.97	14.51
Pr	1.78	2.62	1.24	0.84	2.06
Nd	8.11	11.03	6.02	4.27	9.84
Sm	2.46	2.66	1.92	1.28	2.96
Eu	0.87	0.97	0.78	0.57	1.07
Gd	3.48	3.73	2.83	2.34	4.27
Tb	0.57	0.58	0.49	0.37	0.75
Dy		3.68	3.34	2.76	5.09
Ho	0.84	0.80	0.72	0.62	1.11
Er	2.42	2.20	2.09	1.82	3.16
Yb	2.24	2.11	1.95	1.75	3.21
Lu	0.37	0.33	0.30	0.28	0.49
Hf	1.66	1.77	1.26	0.94	2.00
Ta	0.66	1.14	0.36	0.25	0.61
Pb	0.36		0.26		
Th	0.74	1.45	0.39	0.28	0.69
U	0.17	0.35	0.10	0.06	0.21

Table A2 (Continued) **Standard Values Used for Calibration Curves**

	BHVO-2	DNC-1	W-2	JB-2	MAR
Li	4.6	5.1	9.3	8.25	5.6
Be	1.22	0.224	0.74	0.32	0.403
Sc	30.8	31	35	54.4	39.3
Ti	2.73	0.48	1.06	1.19	1.24
V	299	148	262	578	261
Cr	288	285	93	25	320
Mn	0.1722	0.149	0.163	0.219	0.1808
Co	44	57	44	36	54.12
Ni	112	251	70	13.7	150.9
Cu	131	96	103	227	73.7
Zn	108	64	77	109	78.4
Ga	21	14	17.5	17	15
Rb	9.76	3.65	20	6.2	0.9
Sr	388	144.5	196.5	178	92
Y	27.00	18.00	22.20	24.50	31.90
Zr	180	38	93.5	48.3	78
Nb	19.8	1.66	7.9	0.57	1.534
Mo	3.740	0.150	0.472	0.959	0.215
Sn	1.707	1.308	1.678	0.590	0.733
Cs	0.0965	0.21	0.9	0.79	0.03
Ba	129	103	172	218	6.6
La	15	3.56	10.7	2.4	2.023
Ce	36.8	8.3	23.4	6.64	6.94
Pr	5.29	1.12	3.02	1.15	1.31
Nd	24.2	4.98	12.91	6.7	7.6
Sm	5.92	1.43	3.24	2.25	2.715
Eu	1.94	0.57	1.1	0.855	1.069
Gd	6.32	2.11	3.732	3.3	4.105
Tb	0.95	0.4	0.624	0.58	0.76
Dy	5.34	2.76	3.831	3.93	5.113
Ho	0.984	0.62	0.801	0.863	1.14
Er	2.46	1.869	2.168	2.5	3.266
Yb	2.02	1.98	2.05	2.52	3.203
Lu	0.296	0.314	0.314	0.4	0.494
Hf	4.45	0.991	2.48	1.4	2.08
Ta	1.19	0.098	0.5	0.046	0.2
W	0.2299	0.0592	0.2765	0.3221	
Tl	0.0194	0.0207	0.0919	0.0339	0.0133
Pb	1.66	6.3	7.8	5.31	0.31
Th	1.19	0.24	2.1	0.26	0.0962
U	0.412	0.05	0.49	0.15	0.075

*Note: Trace elements from LDEO are from the thesis of Elizabeth Gier, published with permission in Gale et al. (2011)

[a]Concentrations are in ppm except for Ti and Mn which are in wt. %

Table A3: Trace element contents (ppm) of the inverted metasomatized sources

Detrick Segment	Sample Name	Ba	Rb	Th	U	Nb	La	Ce	Pb	Sr	Nd	Sm	Zr	Hf	Eu	Gd	Tb	Dy	Y	Ho	Er	Yb	Lu
KP-5	AII0127-1-017-005	14.4	1.17	0.12	0.03	1.75	1.00	2.06	0.06	20.5	1.13	0.28	7.0	0.18	0.10	0.33	0.05	0.35	2.0	0.07	0.21	0.21	0.034
KP-5	AII0127-1-017-003	17.5	1.40	0.14	0.04	2.12	1.17	2.40	0.06	24.3	1.26	0.30	7.8	0.19	0.11	0.34	0.06	0.36	2.2	0.08	0.21	0.22	0.034
KP-5	AII0127-1-R048	15.1	1.17	0.12	0.03	1.76	1.06	2.13		21.2	1.18	0.29	7.0	0.18	0.11	0.34	0.06	0.34	2.0	0.07	0.21	0.21	0.034
PO-1	AII0127-2-R116-001	10.1	0.68	0.09	0.02	1.18	0.71	1.47	0.05	15.2	0.85	0.22	5.5	0.16	0.08	0.29	0.05	0.33	1.9	0.07	0.21	0.21	0.034
PO-1	AII0129-6 2602-5b	18.0	1.34	0.14	0.04	2.11	1.13	2.22	0.06	20.4	1.14	0.26	6.5	0.17	0.10	0.31	0.05	0.34	2.1	0.07	0.21	0.22	0.034
PO-1	AII0129-6 2602-3	15.7	1.15	0.13	0.03	1.90	1.00	2.00		19.1	1.05	0.25	6.1	0.16	0.09	0.30	0.05	0.32	2.0	0.07	0.21	0.21	0.034
PO-1	AII0129-6 2604-3	18.5	1.07	0.14	0.04	2.25	1.17	2.30		22.1	1.15	0.27	6.7	0.17	0.10	0.31	0.05	0.33	2.1	0.07	0.21	0.22	0.034

Trace Element Modeling Results		F_Azores	X_Azores	F_Metasomatized
KP-5	AII0127-1-017-005	4.23%	2.39%	7.40%
KP-5	AII0127-1-017-003	3.89%	2.63%	7.71%
KP-5	AII0127-1-R048	4.36%	2.58%	7.73%
PO-1	AII0127-2-R116-001	4.85%	1.90%	6.46%
PO-1	AII0129-6 2602-5b	2.87%	1.98%	7.53%
PO-1	AII0129-6 2602-3	3.16%	1.90%	6.05%
PO-1	AII0129-6 2604-3	3.00%	2.10%	7.25%

F_Azores = extent of melting of Azores source

X_Azores= proportion of "low-F" added to Mantle Source 1, creating "metasomatized" sources

F_Metasomatized= extent of melting of metasomatized source, creating "enriched" samples

Appendix B

Supplementary Material for Chapter 3

B1. Sampling and Analytical Techniques

This study comprises samples collected over a period of 20 years on various cruises, including AII127, AII73, AII77, ARP73, ARP74, CH31, CYA74, GIL103, KN42, NR, TR119 and many Alvin dives. The famous segment is one of the best-sampled ridge segments in the world. Through our access to the French collections, we are able to publish a modern, high-quality dataset encompassing both the American and French samples from over 110 distinct sample locations. N. Famous by comparison is far less sampled, but we report data from every sampling location (n=7). The samples analyzed were fresh basaltic glass with the exception of three aphyric whole rocks (marked with an * in tables). The glass was handpicked under a microscope to exclude any alteration products and then cleaned ultrasonically in distilled water.

Major elements were measured using a Cameca SX-100 electron microprobe (EMP) at Rensselaer Polytechnic Institute (RPI) and a Cameca SX-50 at the University of Massachusetts, Amherst. The procedure involved: an accelerating voltage of 15 kV, a sample current of 10 nA for Na (20 s), Fe (50 s), Si (20s), Al (30 s) and Ca (50 s), and 50 nA for Mg (50 s), Ti (50 s), K (60 s), Mn (100s), P (100 s) and a defocused beam of 10 μm. Each probe mount included an internal monitor standard (VE-32), and the USGS basaltic glass standard VG-2. This internal glass standard and VG-2 were analyzed (2 spots each) after every 15 analytical spots to monitor instrumental drift over time. Individual analyses reported in Table B1 are averages of 5 analytical spots normalized to VE-32, for which values are also reported. Analytical uncertainties were obtained from replicate measurements of VE-32 and VG-2. The precision (2σ RSD) for SiO2, TiO2, Al2O3, MgO, FeO and CaO is better than 3%. The precision for K2O and Na2O is ~6% and for MnO and P2O5 ~10%.

We are also publishing previously collected major elements that were analyzed on the

microprobe at the American Museum of Natural History, New York (samples from cruise A127) following the procedure described in Gale et al. (2011). Three sample powders were analyzed by direct current plasma (DCP) emission spectrometry following the procedure of Klein et al. (1991). We applied small correction factors to the DCP data following the approach of Su (2002), to account for the effects of microphenocrysts in the powders (values given in Table B1). Our new probe analyses, the Lamont probe analyses and the DCP analyses all used the same internal standard to ensure close calibration of our data.

Trace elements (TE) were measured by solution nebulized ICP-MS and laser ablation ICP-MS (SN-ICP-MS and LA-ICP-MS) at Harvard University (full results in Table B2). Due to detection limits, different sets of elements are reported for each method. The SN-ICP-MS procedure is as described in Gale et al. (2011). For LA-ICP-MS, analyses were performed on the same mounts used for electron microprobe analyses using a pulsed 213 nm ArF EXCIMER LASER (New Wave/Merchantek) connected to the Thermo X series quadripole. A spot size ranging from 80-110 μm was used with a repetition rate between 10-20mHz. The ablation cell was flushed with a helium carrier gas at a flow rate of 760ml/min. The dwell time per isotope was 10ms, and the total acquisition time was 180s with an ablation time of 60-80s, a starting 40s and an ending 80s count on the gas blank. Calcium, previously analyzed by electron microprobe with an error of 2.4 rel.% (2σ), is used as an internal standard element during the analysis to correct for signal fluctuation and drift. Natural glass standards BHVO-2, DNC-1, JB-2 and W-2 as well as two in-house glass standards (MAR and VE-32) were used to generate calibration curves (standard values in Table A2). The precision for TE measured in this study is better than 5% for most elements except for Pb measured by LA-ICP-MS with precisions of ~10% (2σ).

For isotopes, handpicked glass chips were leached for 20 min with 8N HNO_3 (results in Table B3). Samples were digested using a HF:HNO3 mixture in Teflon beakers. The Sr isotopes of FAMOUS samples were measured in static mode by TIMS on a GV Isoprobe-T multicollector at Harvard University. Our measured value for NBS 987 $^{87}Sr/^{86}Sr$ during this time was 0.710277 (± 0.0000145 2σ). Sr isotopes from N. Famous and all Nd and Pb isotopes were measured by the Thermo Neptune multicollector ICP-MS (MC-ICP-MS) at Woods Hole Oceanographic Institution (WHOI), Massachusetts. The Sr isotopic measurements were performed with typical ^{88}Sr beam

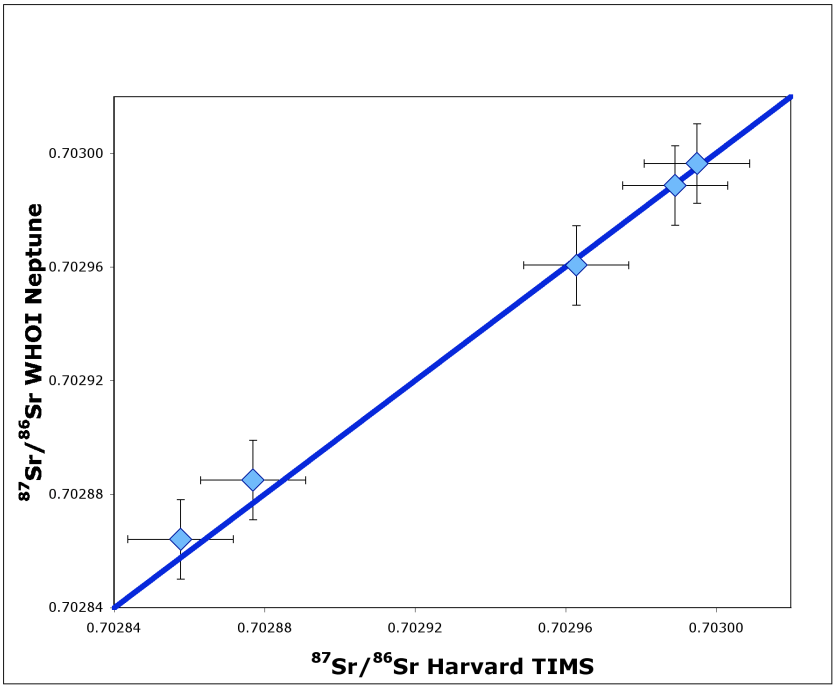

Figure B1. $^{87}Sr/^{86}Sr$ measured using the WHOI Neptune vs. the $^{87}Sr/^{86}Sr$ measured using the Harvard TIMS of 5 representative FAMOUS samples. Also shown is a 1:1 line. Error bars indicate the typical uncertainty of ±0.0000145 2σ. The measurements on the Neptune agree well with the measurements on the TIMS within our uncertainty.

intensities from 30 to 45 volts. $^{87}Sr/^{86}Sr$ ratios were Kr-corrected and normalized to $^{86}Sr/^{88}Sr$=0.1194. On TIMS and the MC-ICP-MS, NBS 987 was analyzed every few samples and used to correct the measured sample values to a value of $^{87}Sr/^{86}Sr$ = 0.710235 for NBS 987. To ensure consistency, we reanalyzed the $^{87}Sr/^{86}Sr$ of some FAMOUS samples on the MC-ICP-MS and the values agreed well with the TIMS data within the typical uncertainty (Figure B1).

NBS 987 measurements on the MC-ICP-MS averaged to 0.710272 with a daily external reproducibility of ±0.000011 2 σ. The Nd isotopic ratios were corrected using the JNDi standard ($^{143}Nd/^{144}Nd$ = 0.512115; Tanaka et al., 2000), which was analyzed repeatedly throughout the runs. Typical beam intensities for 144Nd were 2 to 3 volts, with isotopic ratios normalized to 146Nd/144Nd = 0.7219. The average measured value for JNDi during our data collection was 0.512094 (±0.000006 2σ). For Pb analyses, we correct for mass dependent isotopic fractionation using SRM997 (Tl) as an internal standard. SRM981 was analyzed every few samples and used to normalize the measured values to the values in Todt et al. (1996). The 2σ–standard deviation during our runs of SRM981 (N=23) is 116, 145, and 183 ppm, for $^{206}Pb/^{204}Pb$, $^{207}Pb/^{204}Pb$, and $^{208}Pb/^{204}Pb$ ratios, respectively.

B2. Comparison between our electron microprobe major element data and Smithsonian major element data

Different laboratories calibrate their electron microprobe analyses to different standards, which often leads to a significant and systematic offset between analyses from different laboratories. Because these interlaboratory differences can be large, it is important to apply corrections to the various data in order to make them consistent with one another.

Of interest here, W. Melson and colleagues at the Smithsonian report more than 170 microprobe analyses of FAMOUS glasses. In order to use the Smithsonian dataset we needed to estimate appropriate "interlaboratory" bias factors so that our new data would be comparable. To do this, we analyzed VG-2, the Smithsonian glass standard, 195 times (in different sessions) as an unknown, normalizing it to our in-house standard VE-32. We could then calculate the offset between our value of VG-2 and the Smithsonian value of VG-2, to estimate interlab bias factors that could be applied to the Smithsonian dataset. To confirm our factors, we also reanalyzed a subset of the samples that Melson et al. (2002) analyzed using the same probe mounts. When comparing the analyses directly, it is clear that our interlaboratory bias factors are appropriate and make the datasets consistent with eachother (Fig. B2).

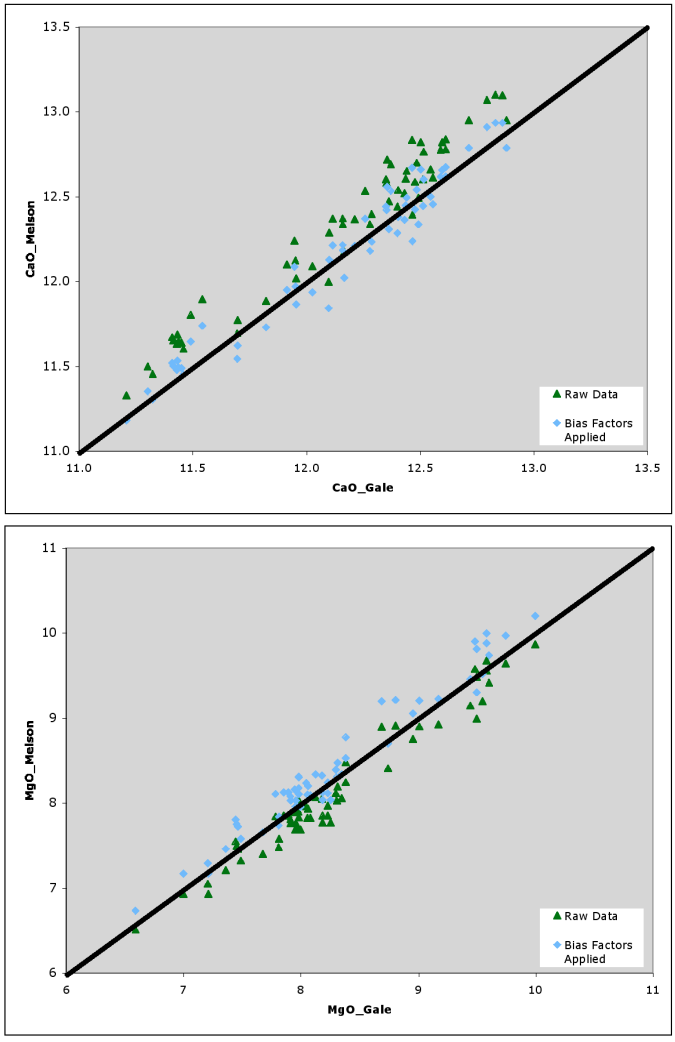

Figure B2. Microprobe data from the Smithsonian vs. our microprobe data on the same samples in the same probe mounts. Green symbols show raw data, blue symbols show the interlab-bias-corrected Smithsonian data. Also shown are 1:1 lines for reference. Note that once interlab bias factors have been applied to the Smithsonian data, there is a very good correspondence between data from the two laboratories.

B3. Correcting Incompatible Trace Elements to be in Equilibrium with Fo90 olivine

A. The first step in correcting trace element compositions to be in equilibrium with Fo90 olivine is

to get each lava composition to a point where there is "olivine only" on the liquidus. For the FAMOUS and N. Famous samples, we estimated based on liquid lines of descent, slope changes in variation diagrams and petrographic observations that the change from olivine only to olivine +plagioclase+clinopyroxene co-crystallizing occurred at 8.6 wt.% MgO.

B. Given this, we needed to correct the trace element compositions of all samples with <8.6 wt.% MgO to their values at 8.6 MgO. Following the approach of Langmuir et al. (1992), we use the formula:

$$\log(X_{8.6}) = \log(X) - 0.11*(8.6-MgO)$$

Here, X represents the concentration of an incompatible element (Ba, Rb, Th, U, Nb, Ta, La, Ce, Pb); $X_{8.6}$ indicates the concentration at 8.6 wt.% MgO. This formula can be applied to any sample with MgO content less than 8.6.

To account for the slightly more compatible nature of the M to HREE, we use the formula:

$$\log(X_{8.6}) = \log(X) - 0.10*(8.6-MgO)$$ for the elements Nd, Sm, Zr, Hf, Gd, Tb

and

$$\log(X_{8.6}) = \log(X) - 0.09*(8.6-MgO)$$ for the elements Dy, Y, Ho, Er, Yb, Lu

For samples with more than 8.6 wt.% MgO, their trace element composition remains unchanged.

C. With all samples now at 8.6 wt% MgO or higher, we then added step-wise increments (0.1% per step) of equilibrium olivine to each of the magma compositions until they were in equilibrium with Mg# 90 olivine. We used a K_D $(C^{FeO}{}_{ol}/C^{FeO}{}_{L})/(C^{MgO}{}_{ol}/C^{MgO}{}_{L})$ = 0.3. Next, we used the ratio of K_2O in the newly calculated primary lava to the K_2O in the "8.6" (or higher) lava to get a "dilution factor." We multiplied all the incompatible trace elements by this dilution factor to estimate their concentrations in the primary lavas, assuming they were perfectly incompatible in olivine.

B4. Modeling the HiAl-LoSi lavas

Our model involves mixing the average Main lava with a representative HiAl melt inclusion from Laubier et al. (2012) to generate the average HiAl-LoSi lava. To do this, we first calculated the average (in major and trace element compositions) Main and HiAl-LoSi lavas. These compositions are reported in Table B4.

We then minimized differences between the average HiAl-LoSi lava and a model melt created by mixing the average Main lava with the representative HiAl melt inclusion, based on

absolute element abundances. We simply allowed the proportions of the two components to vary. In doing this, we found that we could fit every major and trace element to better than 6% (except for P_2O_5) by mixing in 50:50 proportions. See Table B4 for the model melt composition.

B5. Trace element and isotopic modeling of N. Famous and Main famous Lavas

1. Using the method outlined in Step 3 above, we calculated "90-value" trace element compositions for the samples used in the modeling, in order to have "primary" magmas with which to directly compare our modeling output.
2. For our enriched and depleted sources, we used the DMM from Salters and Stracke (2004) and a metasomatized source published in Gale et al. (2011) with slight modifications. Source compositions given in Table B5.
3. We minimized differences between the primary magmas and model melts of a mixed source containing metasomatized source and DMM, using absolute concentrations and isotopic compositions. Our calculated "differences" were normalized to the range of variation for the given variable (e.g., for $^{206}Pb/^{204}Pb$ the range is 0.42, for Rb the range is 4.42) to be sure that the elemental and isotopic variations were weighted appropriately. We allowed two parameters to vary: (1) the proportion of metasomatized source; (2) the extent of melting (F). The melting of the mixed source was modeled as non-modal batch melting; the melting reactions and mineral modes used are given in Table B5.

References

Gale, A., Escrig, S., Gier, E.J., Langmuir, C.H. and Goldstein, S.L., 2011. Enriched basalts at segment centers: The Lucky Strike (37°17′N) and Menez Gwen (37°50′N) segments of the Mid-Atlantic Ridge. Geochem. Geophys. Geosys., 12(Q06016).

Klein, E.M., Langmuir, C.H. and Staudigel, H., 1991. Geochemistry of basalts from the Southeast Indian ridge, 115°E-138°E. J. Geophys. Res, 96(B2): 2089-2107.

Langmuir, C.H., Klein, E.M. and Plank, T., 1992. Petrological systematics of mid-ocean ridge basalts: constraints on melt generation beneath ocean ridges. In: J. Phipps Morgan, Blackman, D.K. & Sinton, J.M. (Editor), Mantle Flow and Melt Generation at Mid-Ocean Ridges. Geophysical Monograph. Am. Geophys. Union, Washington, DC, pp. 183-280.

Laubier, M., Gale, A. and Langmuir, C.H., 2012. Melting and crustal processes at the FAMOUS segment (mid-Atlantic Ridge): new insights from olivine-hosted melt inclusions from multiple samples. J. Petrol., 53 (4): 665-698.

Melson, W.G., O'Hearn, T. and Jarosewich, E., 2002. A data brief on the Smithsonian Abyssal Volcanic Glass Data File. Geochem. Geophys. Geosys., 3(4).

Salters, V.J. and Stracke, A., 2004. Composition of the depleted mantle. Geochem. Geophys. Geosys., 5(Q05B07).

Su, Y.J., 2002. Mid-ocean ridge basalt trace element systematics: constraints from database management, ICP-MS analyses, global data compilation and petrologic modeling. PhD thesis Thesis, Columbia University, 472 pp.

Tanaka, T. et al., 2000. JNdi-1: a neodymium isotopic reference in consistency with LaJolla neodymium. Chem. Geol., 168(3-4): 279-281.

Todt, W., Cliff, R.A., Hanser, A. and Hofmann, A.W., 1996. Evaluation of a 202Pb/205Pb double spike for high-precision lead isotope analysis. In: A. Basu and S. Hart (Editors), Earth Processes, Reading the Isotopic Code. AGU, Washington, D.C., pp. 429-437.

Table B1: Major Element Contents (in wt. %) of Glasses from PO-2 and -3.

Detrick Segment	Sample Name	Sample Group	Latitude	Longitude	Depth	ME method	SiO_2	TiO_2	Al_2O_3	FeO_T	MnO	MgO	CaO	Na_2O	K_2O	P_2O_5	Sum
PO-2	A127 DR13-1 avg.	N. Famous	36.998	-32.936		probe	51.22	1.39	14.08	11.56	0.21	7.04	11.53	2.41	0.15	0.15	99.73
PO-2	A127 DR13-14	N. Famous	36.998	-32.936		probe	51.06	1.16	14.70	10.52	0.20	7.79	12.06	2.28	0.14	0.12	100.11
PO-2	A127 DR13-3	N. Famous	36.998	-32.936		probe	51.17	1.21	14.63	10.33	0.16	7.73	12.14	2.20	0.14	0.13	99.69
PO-2	A127 DR13-4	N. Famous	36.998	-32.936		probe	51.09	1.20	14.61	10.26	0.20	7.73	12.10	2.24	0.17	0.12	99.71
PO-2	A127 DR13-6	N. Famous	36.998	-32.936		probe	51.12	1.19	14.55	10.28	0.18	7.85	12.06	2.18	0.17	0.13	99.70
PO-2	A127 DR13-8 avg.	N. Famous	36.998	-32.936		probe	50.88	1.19	14.59	10.54	0.20	7.75	12.07	2.20	0.17	0.12	99.72
PO-2	A127 DR14-1	N. Famous	37.053	-32.908		probe	50.93	1.45	14.07	11.63	0.24	6.99	11.56	2.60	0.15	0.14	99.76
PO-2	A127 DR14-2	N. Famous	37.053	-32.908		probe	51.01	1.48	14.16	11.51	0.19	6.99	11.58	2.51	0.16	0.15	99.73
PO-2	A127 DR14-3	N. Famous	37.053	-32.908		probe	51.41	1.49	14.00	11.73	0.18	6.92	11.37	2.45	0.16	0.18	99.89
PO-3	A127 RC 119	HiTi	36.912	-33.235		probe	50.68	1.45	14.32	10.73	0.21	8.14	11.48	2.33	0.24	0.19	99.76
PO-3	A127 RC 27	Main	36.600	-33.347		probe	50.89	1.20	14.56	9.83	0.18	7.80	12.66	2.20	0.22	0.15	99.69
PO-3	A127 RC 28	Main	36.660	-33.331		probe	50.98	1.28	14.98	9.28	0.17	8.07	12.29	2.30	0.21	0.15	99.70
PO-3	A127 RC 29	Main	36.690	-33.325		probe	50.32	1.07	14.78	9.44	0.20	8.25	13.22	2.17	0.13	0.12	99.70
PO-3	A127 RC 30	HiBa, Main	36.716	-33.308		probe	50.65	1.02	15.26	8.78	0.16	8.51	12.90	2.09	0.18	0.12	99.67
PO-3	A127 RC 31	Main	36.855	-33.254		probe	51.08	1.25	15.00	9.36	0.16	8.02	12.22	2.25	0.21	0.15	99.69
PO-3	A127 RC 31S	Main	36.855	-33.254		probe	51.19	1.15	15.26	9.20	0.18	8.11	11.92	2.37	0.18	0.14	99.69
PO-3	A127 RC 32	Main	36.875	-33.239		probe	50.87	1.26	15.03	9.15	0.19	8.67	11.95	2.12	0.30	0.17	99.69
PO-3	A127 RC 33S	Main	36.898	-33.226		probe	50.99	1.56	14.21	11.40	0.21	7.04	11.40	2.51	0.21	0.17	99.71
PO-2	A127 RC 34	N. Famous	36.940	-32.988		probe	50.48	1.44	14.27	11.33	0.22	7.24	11.93	2.44	0.23	0.16	99.74
PO-2	A127 RC 35 avg.	N. Famous	36.950	-32.967		probe	50.86	1.55	14.31	11.50	0.22	7.12	11.39	2.45	0.21	0.18	99.78
PO-2	A127 RC 36	N. Famous	36.974	-32.950		probe	50.91	1.31	14.39	10.72	0.19	7.43	12.08	2.33	0.19	0.16	99.72
PO-2	A127 RC 37	N. Famous	37.020	-32.927		probe	51.00	1.32	14.37	10.62	0.22	7.39	12.08	2.36	0.19	0.16	99.72
PO-2	A127 RC 38	N. Famous	37.033	-32.913		probe	51.11	1.13	14.62	10.06	0.19	7.82	12.18	2.37	0.12	0.13	99.71
PO-3	AII 73-10-DR2-1	Main	36.745	-33.253		probe	52.17	1.09	14.93	9.44	0.19	8.06	12.63	2.15	0.17	0.13	100.96
PO-3	AII 73-12-DR3-1	Main	36.740	-33.279		probe	50.89	1.16	14.96	9.19	0.18	8.15	12.66	2.09	0.16	0.13	99.58
PO-3	AII 73-14-DR4	Main	36.730	-33.310	-2519 to -2475	probe	51.17	1.19	14.96	9.73	0.19	8.14	12.40	2.22	0.15	0.13	100.28
PO-3	AII 73-14-DR4-1	Main	36.730	-33.310		probe	50.91	1.33	14.96	10.08	0.19	7.96	12.12	2.26	0.19	0.16	100.17
PO-3	AII 73-16-DR5-3	Main	36.700	-33.290	-2560	probe	51.06	1.35	14.91	10.11	0.19	7.92	12.04	2.18	0.19	0.16	100.14
PO-3	AII 73-16-DR5-5	Main	36.700	-33.290	-2560	probe	51.21	1.49	14.50	10.60	0.20	7.33	11.66	2.24	0.23	0.20	99.65
PO-3	AII 77-37-DR6-1	Main	36.717	-33.333	2437	probe	51.35	1.72	14.04	11.66	0.21	6.56	10.94	2.56	0.19	0.23	99.46
PO-3	AII 77-37-DR6-7	Main	36.717	-33.333	-2437	probe	50.88	1.01	15.02	9.06	0.18	8.27	12.77	2.09	0.13	0.10	99.51

Table B1 (Continued)

PO-3	AII 77-38-DR7-11	Main	36.717	-33.342	-2443	probe	51.04	1.27	15.03	9.40	0.18	7.97	12.45	2.16	0.21	0.18	99.88
PO-3	ALV 518-3-1	Main	36.821	-33.261		probe	50.95	1.29	15.07	10.17	0.18	7.66	11.67	2.47	0.17	0.14	99.76
PO-3	ALV 518-3-2	Main	36.821	-33.261		probe	51.18	1.29	15.08	10.11	0.18	7.71	11.71	2.40	0.17	0.14	99.98
PO-3	ALV 519-3-1	HiAl-LoSi	36.817	-33.263	-2709	probe	48.33	0.79	16.21	9.26	0.18	9.31	12.23	2.11	0.09	0.06	98.57
PO-3	ALV 520-1b	HiAl-LoSi	36.820	-33.260	-2689	probe	48.65	0.79	16.29	9.33	0.18	9.69	12.29	2.07	0.10	0.07	99.45
PO-3	ALV 522-1-2	HiAl-LoSi	36.813	-33.270		probe	49.16	0.79	16.43	9.26	0.18	9.58	12.49	2.02	0.08	0.07	100.06
PO-3	ALV 522-2	HiAl-LoSi	36.807	-33.270		probe	49.89	0.88	16.11	9.15	0.18	9.51	12.29	2.07	0.11	0.08	100.28
PO-3	ALV 523-1	Main	36.827	-33.253	-2726	probe	50.75	1.21	15.57	9.17	0.18	8.37	12.09	2.19	0.22	0.16	99.91
PO-3	ALV 523-2	HiTi	36.827	-33.252	-2743	probe	50.94	1.50	14.94	10.21	0.18	7.90	11.41	2.35	0.34	0.22	100.00
PO-3	ALV 523-3	HiTi	36.824	-33.244	-2540	probe	50.77	1.47	14.89	10.24	0.19	8.18	11.49	2.32	0.26	0.19	100.00
PO-3	ALV 523-3a	HiTi	36.824	-33.244		DCP	50.56	1.48	14.42	10.25	0.19	8.43	11.71	2.36	0.22	0.17	99.79
PO-3	ALV 523-4	HiTi	36.825	-33.241	-2532	probe	50.18	1.46	14.83	10.23	0.19	8.17	11.46	2.32	0.24	0.19	99.26
PO-3	ALV 524-2	Main	36.821	-33.279		probe	51.75	1.56	14.58	10.79	0.20	7.01	11.31	2.46	0.25	0.20	100.12
PO-3	ALV 525-2	Main	36.813	-33.273	-2715	probe	51.18	1.24	14.52	10.17	0.20	7.41	12.07	2.15	0.21	0.14	99.30
PO-3	ALV 525-4b	HiAl-LoSi	36.810	-33.268	-2750	probe	50.45	0.91	16.28	9.15	0.17	8.85	12.47	2.07	0.11	0.09	100.56
PO-3	ALV 526-2a	Main	36.819	-33.254		probe	49.89	1.10	15.88	9.30	0.17	8.63	11.75	2.40	0.14	0.12	99.37
PO-3	ALV 526-4	HiTi	36.818	-33.251	-2585	probe	50.62	1.45	14.97	10.36	0.19	8.30	11.44	2.34	0.19	0.18	100.04
PO-3	ALV 526-5	HiTi	36.818	-33.248	-2550	probe	50.48	1.49	14.90	10.47	0.19	8.06	11.29	2.38	0.23	0.19	99.69
PO-3	ALV 526-6	Main	36.818	-33.244	-2604	probe	51.10	1.00	14.72	9.21	0.18	8.18	12.71	2.02	0.12	0.11	99.36
PO-3	ALV 527-1	HiAl-LoSi	36.810	-33.262		probe	48.94	0.68	16.67	9.09	0.17	9.65	12.74	2.03	0.06	0.05	100.09
PO-3	ALV 527-4	HiTi	36.810	-33.252	-2584	probe	49.83	1.49	15.06	10.51	0.19	8.07	11.38	2.35	0.23	0.19	99.31
PO-3	ALV 527-5	HiTi	36.809	-33.251	-2512	probe	50.46	1.47	14.98	10.43	0.19	8.04	11.39	2.31	0.21	0.19	99.66
PO-3	ALV 527-6	HiTi	36.810	-33.247	-2565	probe	50.92	1.47	14.80	10.26	0.19	8.00	11.41	2.35	0.24	0.20	99.84
PO-3	ALV 527-6-3	HiTi	36.810	-33.247		DCP	50.41	1.46	14.76	10.50	0.18	8.22	11.34	2.42	0.23	0.17	99.69
PO-3	ALV 528-1	HiAl-LoSi	36.813	-33.267	-2680	probe	48.94	0.83	16.36	9.49	0.19	9.48	12.33	2.07	0.09	0.08	99.85
PO-3	ALV 528-2	HiAl-LoSi	36.812	-33.265	-2625	probe	49.57	0.84	16.08	9.03	0.17	10.02	12.32	2.02	0.10	0.07	100.23
PO-3	ALV 528-3-1	HiAl-LoSi	36.808	-33.264		probe	49.15	0.84	16.31	9.06	0.17	9.45	12.30	2.07	0.08	0.08	99.52
PO-3	ALV 528-4	HiAl-LoSi	36.804	-33.265	-2526	probe	49.17	0.75	16.62	8.85	0.17	9.59	12.58	2.04	0.06	0.06	99.90
PO-3	ALV 529-3-1	HiBa, Main	36.818	-33.265	-2705	probe	50.56	0.94	16.01	8.30	0.16	8.97	12.16	2.18	0.17	0.11	99.55
PO-3	ALV 529-4	Main	36.818	-33.261		probe	50.13	1.17	15.29	9.95	0.18	9.17	11.43	2.34	0.14	0.13	99.93
PO-3	ALV 530-2-1	Main	36.806	-33.273	-2663	probe	50.99	1.26	14.89	10.00	0.19	7.80	12.15	2.21	0.18	0.15	99.83
PO-3	ALV 821-2	Main	36.755	-33.288		probe	50.76	1.05	15.06	9.03	0.18	8.30	12.81	2.04	0.15	0.11	99.49
PO-3	ALV 821-8	Main	36.755	-33.282		probe	51.40	1.27	14.90	9.75	0.18	8.20	12.20	2.07	0.24	0.17	100.39
PO-3	ALV 821-9	Main	36.755	-33.282		probe	51.12	1.09	15.08	9.07	0.18	8.21	12.56	2.17	0.16	0.13	99.78
PO-3	ALV 832-2	Main	36.728	-33.301		probe	50.69	1.34	14.90	9.84	0.18	7.77	12.06	2.39	0.17	0.16	99.51

Table B1 (Continued)

PO-3	ARP 73-10-02	Main	36.836	-33.248		probe	51.58	1.69	14.11	11.99	0.22	6.75	10.86	2.54	0.26	0.21	100.21
PO-3	ARP 73-13-004	HiBa, Main	36.828	-33.267		probe	50.92	0.90	15.91	8.23	0.15	9.63	12.27	2.11	0.17	0.11	100.40
PO-3	ARP 73-7-001	HiBa, Main	36.828	-33.262		probe	50.68	0.91	15.81	8.51	0.15	9.60	12.20	2.14	0.15	0.10	100.24
PO-3	ARP 74-10-14	HiBa, Main	36.830	-33.270		probe	51.54	0.89	15.89	8.28	0.15	9.61	12.22	2.11	0.15	0.10	100.95
PO-3	ARP 74-11-17	Main	36.850	-33.250		probe	51.09	1.17	15.25	9.24	0.17	8.96	11.72	2.20	0.19	0.15	100.13
PO-3	ARP 74-11-18	Main	36.850	-33.250		probe	50.90	1.18	15.33	9.54	0.17	8.23	11.96	2.36	0.16	0.13	99.96
PO-3	ARP 74-12-19	Main	36.858	-33.258		probe	51.13	1.10	14.97	9.35	0.18	8.27	12.79	2.12	0.12	0.12	100.14
PO-3	ARP 74-14-31	HiBa, HiAl-LoSi	36.950	-33.167		probe	48.76	0.55	16.99	8.90	0.17	9.56	13.17	2.00	0.05	0.05	100.20
PO-3	ARP 74-14-33	HiBa, HiAl-LoSi	36.950	-33.167		probe	49.43	0.55	16.89	8.93	0.17	9.50	13.18	2.10	0.05	0.05	100.85
PO-3	ARP 74-16-36	Main	36.900	-33.200		probe	51.35	1.15	15.60	8.83	0.16	8.56	12.54	2.23	0.19	0.14	100.76
PO-3	ARP 74-16-37	Main	36.900	-33.200		probe	51.21	1.27	14.66	9.91	0.19	7.66	12.36	2.34	0.23	0.17	100.00
PO-3	ARP 74-7-5	HiTi	36.830	-33.250		probe	51.03	1.45	14.94	10.42	0.19	8.22	11.46	2.32	0.22	0.18	100.41
PO-3	ARP 74-7-6	HiTi	36.830	-33.250		probe	51.25	1.47	14.95	10.35	0.19	7.90	11.57	2.38	0.23	0.18	100.46
PO-3	ARP 74-9-12	HiBa, Main	36.830	-33.270		probe	51.10	0.90	15.92	8.30	0.15	9.60	12.17	2.10	0.15	0.11	100.51
PO-3	CH 31-D11-315	HiTi	36.825	-33.258		probe	50.56	1.45	14.84	10.34	0.18	8.25	11.46	2.34	0.22	0.17	99.82
PO-3	CH 31-D12	HiBa, HiAl-LoSi	36.867	-33.248		probe	49.48	0.76	16.41	8.67	0.17	9.39	13.36	1.83	0.10	0.07	100.25
PO-3	CH 31-D3-346	HiTi	36.792	-33.233		probe	51.38	1.44	14.92	10.26	0.19	7.87	11.61	2.35	0.22	0.17	100.42
PO-3	CH 31-D4	HiBa, Main	36.829	-33.265		probe	50.49	0.92	15.89	8.28	0.15	9.21	12.16	2.18	0.16	0.11	99.56
PO-3	CH 31-D5-304	Main	36.767	-33.275		probe	51.42	1.09	15.45	8.89	0.14	8.66	12.12	2.19	0.16	0.18	100.32
PO-3	CH 31-D8	HiAl-LoSi	36.838	-33.244		probe	48.85	0.81	16.40	8.91	0.16	9.63	12.84	1.87	0.11	0.08	99.66
PO-3	CH 31-D8-136	HiAl-LoSi	36.838	-33.244		probe	50.45	0.83	16.14	8.72	0.17	9.58	12.97	1.94	0.11	0.09	100.99
PO-3	CH 31-D9-344	Main	36.873	-33.252		probe	51.20	1.09	15.67	8.90	0.16	8.66	12.75	2.19	0.14	0.12	100.89
PO-3	CYA 74-29-31C	Main	36.900	-33.100		probe	50.72	1.14	14.80	9.90	0.18	8.68	11.75	2.19	0.18	0.14	99.68
PO-3	CYA 74-30-32	HiBa, HiAl-LoSi	36.850	-33.250		probe	49.88	0.74	16.22	8.56	0.17	9.38	13.46	1.81	0.10	0.08	100.41
PO-3	CYA 74-30-33	Main	36.853	-33.252		probe	51.21	1.26	15.25	9.78	0.18	7.98	11.85	2.38	0.18	0.15	100.21
PO-3	CYA 74-30-34	HiBa, HiAl-LoSi	36.850	-33.250		probe	49.87	0.74	16.22	8.61	0.16	9.43	13.46	1.92	0.10	0.07	100.58
PO-3	GIL 103-16-2	Main	36.780	-33.278		probe	51.05	1.19	14.89	9.86	0.19	7.83	12.50	2.30	0.17	0.13	100.11
PO-3	GIL 103-21-1	Main	36.775	-33.277		probe	51.66	1.17	15.01	9.08	0.18	8.18	12.77	2.23	0.19	0.14	100.60

Table B1 (Continued)

PO-3	GIL 103-24-19	Main	36.793	-33.290		probe	50.79	1.13	14.95	9.75	0.18	8.01	12.47	2.17	0.22	0.15	99.83
PO-3	GIL 103-32-13	Main	36.730	-33.292		probe	50.97	1.17	14.93	9.87	0.18	8.06	12.47	2.33	0.17	0.15	100.29
PO-3	GIL 103-33-42	Main	36.780	-33.260	-2674	probe	51.01	1.04	15.35	9.05	0.17	8.98	12.56	1.88	0.19	0.13	100.35
PO-3	KN 42-28-D4	Main	36.915	-33.163	-2889 to -2608	probe	52.20	1.34	14.61	10.61	0.20	7.28	12.04	2.28	0.23	0.17	100.95
PO-3	KN 42-86-D12	Main	36.640	-33.325	-2901 to -2740	probe	50.82	1.44	14.66	10.17	0.19	7.42	11.87	2.33	0.22	0.19	99.31
PO-3	KN 42-86-D12-78	Main	36.640	-33.325		probe	51.01	1.21	14.94	9.67	0.19	7.95	12.48	2.20	0.17	0.14	99.96
PO-3	KN 42-D23	Main	36.810	-33.280	-2250 to -2221	probe	51.17	1.07	14.83	9.79	0.19	7.96	12.45	2.11	0.17	0.13	99.87
PO-3	KN 42-ST88-3	Main	36.850	-33.320	-2271 to -1720	probe	51.57	1.15	14.87	9.69	0.19	7.82	12.61	2.24	0.17	0.14	100.45
PO-3	NR DR 3-4	HiBa, Main	36.847	-33.222		probe	50.76	1.15	15.11	9.10	0.17	8.91	12.30	2.08	0.30	0.17	100.05
PO-3	NR DR 3-7	HiBa, Main	36.847	-33.222		probe	50.00	1.17	15.31	9.10	0.17	8.51	12.43	2.14	0.29	0.17	99.30
PO-3	TR 119-4D-3A	HiBa, Main	36.850	-33.230		DCP	49.90	0.98	14.04	8.58	0.16	10.62	12.13	1.92	0.28	0.14	98.74
	Standard VE-32						50.88	1.86	14.13	11.6	0.21	6.7	10.86	2.97	0.27	0.21	
	DCP correction factors applied to account for microphenocrysts, from Su (2002):						1.01	1.04	0.97	1.00	1.00	1.00	1.00	1.00	1.00	1.00	

*Note: Data from cruise A127 were collected at Lamont.

Table B2: Trace Element Concentrations of Glassy Basalts From Segments PO-2 and -3[a]

Sample Name	A127 DR13-1	A127 DR13-14	A127 DR13-3	A127 DR13-4	A127 DR13-6	A127 DR13-8	A127 DR14-1
Detrick Segment	PO-2	PO-2	PO-2	PO-2	PO-2	PO-2	PO-2
Sample Group	N. Famous	N. Famous	N. Famous	N. Famous	N. Famous	N. Famous	N. Famous
Latitude	36.998	36.998	36.998	36.998	36.998	36.998	37.053
Longitude	-32.936	-32.936	-32.936	-32.936	-32.936	-32.936	-32.908
Depth							
TE Method	solution	solution	solution	solution	solution	solution	solution
Li	6.5	5.7	5.7	5.3	5.9	5.6	6.9
Be	0.42	0.38	0.38	0.27	0.34	0.38	0.45
Sc	43.2	40.6	41.1	39.9	42.3	42.6	45.1
Ti	1.25	1.13	1.12	1.01	1.12	1.12	1.41
V	306	286	286	268	287	281	321
Cr	81	130	132	128	130	130	103
Mn	0.20	0.18	0.18	0.17	0.18	0.18	0.20
Co	47.1	46.0	45.7	44.6	47.0	45.7	46.4
Ni	49	63	67	64	63	60	51
Cu	70	74	79	69	76	72	80
Zn	93.8	84.5	83.0	80.8	88.3	83.9	97.6
Ga	17.6	16.2	16.1	15.5	16.3	16.2	17.3
Rb	3.15	3.59	3.61	3.39	3.65	3.59	3.70
Sr	88	90	89	85	88	93	91
Y	33.7	28.6	28.3	26.6	28.8	28.4	36.0
Zr	71.0	59.3	58.3	55.9	60.8	59.8	77.1
Nb	6.41	6.95	6.85	6.62	7.10	6.93	7.74
Mo	0.35	0.38	0.34	0.35	0.35	0.38	0.40
Sn	0.68	0.61		0.58	0.61	0.59	0.76
Cs	0.04	0.04	0.04	0.04	0.04	0.04	0.04
Ba	36.1	43.0	42.4	40.7	43.1	42.1	43.1
La	4.22	4.36	4.32	4.11	4.43	4.37	5.08
Ce	10.55	10.35	10.32	9.75	10.52	10.57	12.42
Pr	1.62	1.54	1.53	1.47	1.57	1.55	1.89
Nd	8.39	7.74	7.59	7.35	7.95	7.72	9.67
Sm	2.85	2.54	2.48	2.39	2.57	2.51	3.18
Eu	1.01	0.89	0.89	0.87	0.92	0.89	1.13
Gd	4.36	3.75	3.71	3.54	3.79	3.74	4.74
Tb	0.78	0.66	0.66	0.63	0.68	0.66	0.85
Dy	5.35	4.56	4.49	4.30	4.61	4.51	5.73
Ho	1.18	1.01	1.00	0.94	1.01	0.99	1.26
Er	3.37	2.86	2.81	2.71	2.90	2.82	3.63
Yb	3.36	2.85	2.81	2.69	2.88	2.80	3.62
Lu	0.52	0.44	0.44	0.42	0.45	0.44	0.57
Hf	2.09	1.70	1.70	1.60	1.73	1.71	2.16
Ta	0.38	0.40	0.40	0.37	0.41	0.42	0.45
W	0.09	0.10	0.10			0.10	0.10
Tl	0.006	0.006	0.006	0.008	0.006	0.007	0.006
Pb	0.43	0.33	0.33	0.36	0.43	0.32	0.43
Th	0.42	0.45	0.45	0.43	0.46	0.45	0.50
U	0.14	0.15	0.14	0.15	0.14	0.14	0.17

Table B2 (Continued)

	A127 DR14-2	A127 DR14-3	A127 RC 119	A127 RC 27	A127 RC 28	A127 RC 29	A127 RC 30	A127 RC 31
	PO-2	PO-2	PO-3	PO-3	PO-3	PO-3	PO-3	PO-3
	N. Famous	N. Famous	HiTi	Main	Main	Main	HiBa, Main	Main
	37.053	37.053	36.912	36.600	36.660	36.690	36.716	36.855
	-32.908	-32.908	-33.235	-33.347	-33.331	-33.325	-33.308	-33.254
	solution	solution	solution	solution	solution	solution	solution	solution
Li	6.6	6.0	6.2	5.3	5.4	4.6	4.7	4.9
Be	0.48	0.35	0.51	0.44	0.42	0.35	0.31	0.43
Sc	45.2	43.3	40.3	42.3	40.1	45.7	40.5	37.2
Ti	1.38	1.15	1.34	1.12	1.21	0.96	0.98	1.11
V	322	283	305	284	274	265	247	245
Cr	108	208	311	161	318	225	319	423
Mn	0.20	0.18	0.18	0.17	0.16	0.17	0.16	0.16
Co	46.1	46.1	45.3	44.7	42.8	45.7	43.0	44.3
Ni	49	80	117	66	100	85	104	131
Cu	76	69	64	90	80	92	82	70
Zn	95.8	89.5	90.3	78.3	77.9	69.0	69.0	79.5
Ga	17.3	15.3	16.9	15.3	15.4	14.4	14.6	15.6
Rb	3.69	2.81	6.57	4.43	4.48	3.14	3.84	4.05
Sr	94	96	102	113	110	105	111	116
Y	35.8	30.2	33.0	25.4	26.5	23.8	22.0	24.1
Zr	77.2	63.9	89.9	68.2	70.3	56.4	57.0	64.2
Nb	7.85	6.45	13.51	9.98	9.92	7.11	8.07	8.71
Mo	0.40		0.66	0.47	0.44	0.35	0.43	0.42
Sn	0.77		0.85	0.68	0.67		0.54	0.59
Cs	0.04	0.03	0.07	0.05	0.05	0.03	0.04	0.04
Ba	43.5	39.3	74.9	52.7	54.2	38.4	53.0	47.7
La	5.06	4.37	7.87	5.85	5.90	4.32	4.86	5.14
Ce	12.29	10.35	17.59	13.48	13.58	10.25	11.14	11.94
Pr	1.89	1.62	2.48	1.93	1.95	1.51	1.59	1.74
Nd	9.64	8.23	11.59	9.14	9.41	7.37	7.67	8.38
Sm	3.13	2.67	3.31	2.62	2.74	2.23	2.19	2.49
Eu	1.12	0.97	1.10	0.93	0.97	0.82	0.81	0.89
Gd	4.71	3.95	4.58	3.57	3.78	3.18	3.06	3.42
Tb	0.84	0.71	0.79	0.62	0.66	0.57	0.54	0.60
Dy	5.72	4.84	5.31	4.15	4.34	3.84	3.58	3.98
Ho	1.26	1.07	1.16	0.90	0.93	0.84	0.78	0.85
Er	3.62	3.06	3.31	2.56	2.65	2.44	2.20	2.43
Yb	3.60	3.07	3.30	2.55	2.59	2.45	2.20	2.36
Lu	0.55	0.48	0.51	0.40	0.40	0.38	0.34	0.37
Hf	2.18	1.80	2.32	1.79	1.88	1.52	1.50	1.75
Ta	0.45	0.38	0.76	0.58	0.57	0.41	0.46	0.51
W			0.17	0.11	0.11	0.09	0.10	0.11
Tl	0.008		0.008	0.008	0.008		0.006	0.007
Pb	0.40		0.55	0.49	0.51		0.39	0.41
Th	0.51	0.42	0.85	0.61	0.61	0.44	0.52	0.53
U			0.27	0.21	0.20	0.14	0.16	0.19

Table B2 (Continued)

	A127 RC 32	A127 RC 34	A127 RC 35	A127 RC 36	A127 RC 37	A127 RC 38	AII 73-10-DR2-1	AII 73-12-DR3-1
	PO-3	PO-2	PO-2	PO-2	PO-2	PO-2	PO-3	PO-3
	Main	N. Famous	N. Famous	N. Famous	N. Famous	N. Famous	Main	Main
	36.875	36.940	36.950	36.974	37.020	37.033	36.745	36.740
	-33.239	-32.988	-32.967	-32.950	-32.927	-32.913	-33.253	-33.279
	solution	solution	solution	solution	solution	solution	solution	solution
Li	5.2	5.8	6.9	5.9	6.3	6.2	4.9	5.2
Be	0.44	0.44	0.47	0.45	0.46	0.33	0.43	0.39
Sc	38.8	42.1	42.0	41.8	42.1	42.2	42.0	40.4
Ti	1.19	1.24	1.46	1.21	1.37	1.08	1.07	1.06
V	271	285	311	297	306	265	277	262
Cr	463	248	134	138	181	260	178	434
Mn	0.16	0.18	0.19	0.19	0.19	0.17	0.17	0.16
Co	43.7	46.4	45.9	46.0	43.9	44.3	44.5	41.7
Ni	143	81	60	61	55	73	82	107
Cu	72	65	73	73	69	85	83	72
Zn	75.3	87.3	100.0	87.6	91.2	105.2	73.9	71.5
Ga	15.1	16.1	17.5	16.3	17.1	16.0	15.1	15.3
Rb	6.37	4.79	5.26	4.77	4.93	2.70	4.34	3.55
Sr	126	90	90	96	102	90	109	104
Y	26.1	31.3	36.7	30.1	33.8	27.1	24.3	24.7
Zr	76.8	67.5	86.9	68.4	81.0	59.0	61.2	58.3
Nb	13.45	9.29	10.88	9.59	10.25	5.30	9.95	7.68
Mo	0.63	0.40	0.51	0.44	0.48	0.32	0.45	0.39
Sn	0.72	0.62	0.86	0.67	0.78	0.59	0.56	0.54
Cs	0.07	0.05	0.06	0.06	0.06	0.03	0.05	0.04
Ba	77.6	53.5	57.6	56.4	57.8	31.3	53.9	43.2
La	7.62	5.57	6.60	5.77	6.27	3.52	5.78	4.76
Ce	16.84	12.92	15.39	13.10	14.59	8.92	13.11	11.17
Pr	2.30	1.81	2.26	1.89	2.15	1.39	1.83	1.61
Nd	10.68	8.78	11.19	9.20	10.59	7.29	8.53	7.79
Sm	2.89	2.82	3.42	2.82	3.22	2.41	2.47	2.38
Eu	0.97	0.95	1.15	0.99	1.13	0.89	0.88	0.86
Gd	3.79	4.09	4.96	4.08	4.65	3.62	3.38	3.37
Tb	0.65	0.74	0.87	0.72	0.81	0.65	0.60	0.60
Dy	4.29	4.91	5.91	4.86	5.46	4.37	3.97	4.01
Ho	0.93	1.07	1.29	1.07	1.19	0.96	0.87	0.88
Er	2.62	3.03	3.68	3.05	3.39	2.72	2.49	2.50
Yb	2.60	3.06	3.63	3.01	3.36	2.67	2.46	2.44
Lu	0.40	0.47	0.56	0.47	0.52	0.41	0.38	0.38
Hf	1.99	1.88	2.42	1.90	2.21	1.67	1.66	1.62
Ta	0.76	0.53	0.62	0.54	0.58	0.31	0.57	0.46
W	0.15	0.13						
Tl	0.009	0.007	0.009	0.007	0.008	0.005	0.007	0.008
Pb	0.51	0.40	0.55	0.42	0.48	0.35	0.39	0.33
Th	0.82	0.59	0.72	0.62	0.66	0.34	0.61	0.47
U	0.26		0.23	0.19	0.20	0.11	0.19	0.16

Table B2 (Continued)

	AII 73-14-DR4	AII 73-14-DR4-1	AII 73-16-DR5-1	AII 73-16-DR5-3	AII 73-16-DR5-5	AII 73-18-DR6-6	AII 77-37-DR6-1	AII 77-37-DR6-11	AII 77-37-DR6-7	AII 77-38-DR7-11
	PO-3	PO-3	PO-3	PO-3	PO-3	PO-3	PO-3	PO-3	PO-3	PO-3
	Main	Main	Main	Main	Main	Main	Main	Main	Main	Main
	36.730	36.730	36.700	36.700	36.700	36.717	36.717	36.717	36.717	36.717
	-33.310	-33.310	-33.290	-33.290	-33.290	-33.333	-33.333	-33.333	-33.333	-33.342
	-2519 to -2475			-2560	-2560	-2589	2437		-2437	-2443
	laser	solution	solution	laser	laser	laser	laser	solution	laser	laser
Li	5.4	5.7	5.7	5.6	6.3	5.2	7.6	4.9	4.9	5.3
Be		0.51	0.49					0.29		
Sc	42.9	41.3	40.9	42.5	42.5	43.7	44.3	39.3	41.9	41.1
Ti	1.17	1.29	1.31	1.28	1.46	1.12	1.72	0.90	0.97	1.21
V	286	295	297	288	309	276	368	249	273	279
Cr	240	238	262	256	208	176	128	406	431	305
Mn	0.17	0.18	0.18	0.17	0.18	0.17	0.20	0.15	0.16	0.16
Co	44.1	44.8	45.2	43.5	43.5	42.3	45.3	41.3	42.4	42.6
Ni	86	91	92	88	73	76	60	105	95	90
Cu	72	71	72	65	58	70	67	72	80	80
Zn	73.3	83.0	84.9	75.0	80.8	69.4	107.2	67.6	68.0	74.3
Ga	13.8	16.1	16.2	14.3	15.0	13.5	17.0	14.9	13.5	14.1
Rb	3.94	4.48	4.35	4.54	5.34	3.89	5.94	2.80	3.21	6.00
Sr	103	110	108	104	104	103	103	100	91	115
Y	26.9	29.2	29.1	29.9	31.9	27.9	40.5	22.0	22.8	26.0
Zr	66.2	73.9	76.5	79.0	87.5	67.8	103.1	48.6	50.9	75.5
Nb	8.50	9.85	10.13	10.34	12.12	8.38	12.69	6.11	6.56	12.62
Mo		0.48	0.50					0.34		
Sn		0.71	0.70					0.46		
Cs		0.05	0.05					0.03		
Ba	45.5	52.8	51.5	52.9	61.1	45.7	61.4	35.2	38.1	68.7
La	5.21	5.98	6.13	6.36	7.15	5.19	7.75	3.83	4.12	7.24
Ce	12.35	13.94	14.40	14.77	17.18	12.11	19.52	9.12	9.91	16.74
Pr	1.82	2.02	2.08	2.20	2.51	1.79	2.79	1.33	1.44	2.31
Nd	8.73	9.74	10.03	10.37	11.70	8.78	13.32	6.54	7.05	10.49
Sm	2.61	2.88	2.93	3.10	3.33	2.69	4.06	2.04	2.16	2.80
Eu	0.96	1.03	1.03	1.07	1.14	0.97	1.37	0.77	0.82	0.98
Gd	3.71	4.08	4.08	4.17	4.53	3.79	5.56	2.95	3.03	3.78
Tb	0.65	0.71	0.71	0.74	0.79	0.66	0.99	0.53	0.55	0.65
Dy	4.38	4.74	4.73	4.91	5.21	4.54	6.70	3.59	3.71	4.29
Ho	0.94	1.03	1.03	1.06	1.12	0.98	1.43	0.79	0.81	0.90
Er	2.69	2.94	2.94	2.99	3.16	2.81	4.07	2.25	2.31	2.56
Yb	2.68	2.90	2.90	3.01	3.24	2.75	4.06	2.22	2.26	2.61
Lu	0.42	0.45	0.45	0.46	0.48	0.43	0.63	0.35	0.35	0.39
Hf	1.78	2.01	2.07	2.09	2.27	1.84	2.83	1.36	1.36	2.01
Ta	0.48	0.57	0.59	0.58	0.67	0.48	0.70	0.36	0.37	0.71
W										
Tl		0.008	0.007					0.008		
Pb	0.38	0.44	0.50					0.29	0.29	0.41
Th	0.53	0.60	0.60	0.62	0.69	0.54	0.81	0.38	0.40	0.77
U	0.17	0.19	0.20	0.20	0.23	0.17		0.13	0.14	0.26

Table B2 (Continued)

	AII 77-38-DR7-9	ALV 518-1-1	ALV 518-2-2	ALV 518-2-3	ALV 518-3-1	ALV 518-3-2	ALV 518-3-3	ALV 518-3-4	ALV 519-2-1	ALV 519-2-3	ALV 519-3-1
	PO-3	PO-3	PO-3	PO-3	PO-3	PO-3	PO-3	PO-3	PO-3	PO-3	PO-3
	Main	Main	Main	Main	Main	Main	Main	Main	HiAl-LoSi	HiAl-LoSi	HiAl-LoSi
	36.717	36.819	36.820	36.820	36.821	36.821	36.821	36.821	36.818	36.818	36.817
	-33.342	-33.255	-33.257	-33.257	-33.261	-33.261	-33.261	-33.261	-33.263	-33.263	-33.263
	-2443			-2685				-2640			-2709
	laser	solution	solution	laser	solution	solution	solution	laser	solution	solution	laser
Li	4.9	4.5	3.8	4.0	5.3	5.4	5.3	5.3	4.1	4.1	4.2
Be		0.35	0.29		0.46	0.42	0.48		0.20	0.26	
Sc	43.7	35.7	32.2	33.9	37.6	38.3	37.5	40.8	42.6	42.1	40.2
Ti	0.99	0.94	0.77	0.87	1.19	1.22	1.14	1.29	0.72	0.70	0.76
V	280	216	184	201	258	264	257	261	208	207	216
Cr	336	469	521	699	314	308	309	308	486	543	441
Mn	0.17	0.16	0.15	0.15	0.17	0.17	0.17	0.17	0.17	0.16	0.16
Co	42.8	48.4	49.2	48.3	44.3	44.0	43.0	42.6	49.3	49.8	46.5
Ni	79	205	246	215	114	104	99	88	210	200	161
Cu	88	82	85	119	75	73	67	63	113	98	92
Zn	71.6	73.4	68.2	70.8	84.6	85.6	83.9	75.8	61.7	60.9	58.9
Ga	13.9	15.1	14.8	14.2	16.3	16.4	16.2	14.9	13.8	13.6	12.6
Rb	3.52	2.70	1.74	1.91	4.15	4.23	4.08	4.34	1.99	1.96	2.25
Sr	106	100	100	99	116	116	115	114	66	65	67
Y	23.5	22.2	18.7	18.8	26.1	26.6	25.7	27.4	22.2	21.9	20.9
Zr	56.0	54.0	42.7	43.0	69.8	70.9	69.0	72.8	39.4	38.7	38.8
Nb	7.01	6.05	3.96	4.28	9.11	9.28	8.98	9.30	4.46	4.41	4.84
Mo		0.31	0.29		0.46	0.45	0.43		0.23	0.24	
Sn		0.53			0.66	0.68	0.66		0.35	0.36	
Cs		0.03	0.02		0.04	0.05	0.04		0.02	0.02	
Ba	43.3	32.4	20.9	22.8	50.2	50.9	49.9	51.1	23.2	24.7	25.9
La	4.50	3.75	2.58	2.81	5.43	5.49	5.32	5.61	2.70	2.69	2.97
Ce	10.76	9.07	6.53	7.11	12.85	12.89	12.57	13.14	6.75	6.63	7.40
Pr	1.57	1.39	1.01	1.09	1.87	1.89	1.84	1.94	1.00	1.01	1.08
Nd	7.57	6.93	5.27	5.39	9.08	9.17	9.00	9.38	5.08	5.11	5.22
Sm	2.23	2.15	1.73	1.80	2.70	2.73	2.64	2.80	1.62	1.64	1.63
Eu	0.85	0.82	0.69	0.75	0.97	0.98	0.97	1.01	0.64	0.65	0.67
Gd	3.11	3.11	2.54	2.63	3.76	3.81	3.69	3.91	2.55	2.60	2.58
Tb	0.58	0.55	0.46	0.47	0.65	0.66	0.65	0.67	0.48	0.48	0.46
Dy	3.85	3.69	3.07	3.17	4.32	4.34	4.26	4.53	3.38	3.42	3.26
Ho	0.82	0.79	0.66	0.67	0.92	0.94	0.91	0.96	0.77	0.77	0.74
Er	2.33	2.28	1.87	1.93	2.60	2.64	2.58	2.69	2.32	2.34	2.18
Yb	2.37	2.21	1.85	1.92	2.53	2.55	2.51	2.64	2.43	2.41	2.34
Lu	0.38	0.34	0.29	0.29	0.39	0.40	0.39	0.41	0.39	0.38	0.36
Hf	1.45	1.47	1.17	1.20	1.89	1.90	1.85	1.93	1.07	1.07	1.06
Ta	0.40	0.36	0.23	0.25	0.54	0.53	0.52	0.53	0.26	0.26	0.27
W					0.11		0.09			0.04	
Tl		0.006			0.008	0.009	0.009		0.003	0.003	
Pb	0.32	0.26		0.30	0.38	0.39	0.38	0.41	0.18	0.19	0.27
Th	0.44	0.38	0.26	0.27	0.55	0.56	0.54	0.59	0.28	0.28	0.28
U	0.14	0.13	0.10	0.09	0.19	0.19	0.18	0.18	0.09	0.09	0.10

Table B2 (Continued)

	ALV 519-3-2	ALV 519-3-3	ALV 519-4-1	ALV 519-4-2	ALV 519-5-1	ALV 520-1a	ALV 520-1b	ALV 520-2	ALV 521-1	ALV 522-1-2	ALV 522-2
	PO-3	PO-3	PO-3	PO-3	PO-3	PO-3	PO-3	PO-3	PO-3	PO-3	PO-3
	HiAl-LoSi	HiAl-LoSi	HiAl-LoSi	HiAl-LoSi	HiAl-LoSi	HiAl-LoSi	HiAl-LoSi	HiAl-LoSi	Main	HiAl-LoSi	HiAl-LoSi
	36.817	36.817	36.815	36.815	36.813	36.820	36.820	36.820	36.820	36.813	36.807
	-33.263	-33.263	-33.265	-33.265	-33.265	-33.260	-33.260	-33.270	-33.273	-33.270	-33.270
				-2690	-2700		-2689				
	solution	solution	solution	laser	laser	solution	laser	solution	solution	solution	solution
Li	4.2	4.2	4.2	3.9	3.9	4.0	4.0	4.3	5.4	4.1	4.4
Be	0.22	0.26	0.20			0.21		0.22	0.41	0.16	0.25
Sc	42.5	42.3	43.0	43.3	43.2	41.8	42.9	43.7	40.7	43.1	40.3
Ti	0.78	0.73	0.72	0.74	0.75	0.72	0.74	0.75	1.09	0.75	0.80
V	216	212	210	207	213	203	206	217	283	214	217
Cr	538	482	526	414	428	546	408	458	178	447	516
Mn	0.17	0.17	0.16	0.16	0.16	0.17	0.16	0.17	0.17	0.17	0.16
Co	49.0	49.5	48.7	46.6	46.8	55.0	45.7	49.3	44.2	49.0	52.2
Ni	183	193	178	169	161	286	166	174	82	175	241
Cu	97	97	98	95	97	96	92	100	73	98	89
Zn	62.1	62.4	61.6	54.0	55.9	62.6	54.7	63.3	77.9	62.5	64.4
Ga	13.9	13.8	14.0	11.8	12.3	13.5	11.8	14.1	15.6	14.0	13.8
Rb	2.12	2.13	2.01	2.06	2.11	2.04	2.11	2.18	4.62	2.12	2.36
Sr	70	67	71	65	66	70	66	68	112	68	75
Y	22.4	22.6	22.3	22.5	22.2	21.5	22.9	23.1	24.7	22.8	22.1
Zr	41.0	41.2	39.9	40.2	39.8	39.0	41.2	41.8	60.4	41.0	46.5
Nb	4.70	4.75	4.49	4.51	4.56	4.43	4.61	4.83	9.98	4.66	5.50
Mo	0.25	0.22	0.25			0.22		0.25	0.46	0.22	0.29
Sn	0.36	0.37	0.34			0.35		0.36	0.56	0.33	0.42
Cs	0.02	0.02	0.02			0.02		0.02	0.05	0.02	0.02
Ba	24.9	25.5	24.3	23.9	24.2	23.6	24.8	25.9	56.5	25.1	26.6
La	2.86	2.89	2.81	2.82	2.86	2.71	2.95	2.91	5.83	2.84	3.30
Ce	7.02	7.13	6.90	6.66	6.85	6.59	6.92	7.19	13.07	6.99	8.14
Pr	1.05	1.08	1.02	1.01	1.03	0.99	1.06	1.09	1.82	1.04	1.18
Nd	5.28	5.41	5.17	5.08	5.18	4.92	5.32	5.50	8.55	5.24	5.88
Sm	1.68	1.72	1.66	1.65	1.66	1.58	1.72	1.74	2.44	1.70	1.83
Eu	0.66	0.67	0.65	0.65	0.67	0.62	0.67	0.68	0.88	0.66	0.69
Gd	2.63	2.68	2.58	2.63	2.58	2.50	2.74	2.71	3.39	2.67	2.77
Tb	0.49	0.49	0.48	0.48	0.48	0.47	0.51	0.50	0.60	0.49	0.50
Dy	3.47	3.50	3.44	3.44	3.47	3.31	3.61	3.56	4.00	3.50	3.48
Ho	0.79	0.80	0.79	0.78	0.78	0.76	0.81	0.81	0.88	0.80	0.78
Er	2.35	2.39	2.33	2.33	2.29	2.25	2.43	2.45	2.52	2.38	2.31
Yb	2.47	2.48	2.43	2.47	2.40	2.36	2.59	2.54	2.51	2.50	2.36
Lu	0.39	0.39	0.39	0.39	0.38	0.38	0.41	0.40	0.40	0.40	0.37
Hf	1.14	1.12	1.11	1.09	1.07	1.08	1.17	1.14	1.65	1.13	1.25
Ta	0.28	0.28	0.27	0.26	0.26	0.26	0.29	0.29	0.58	0.27	0.32
W	0.05									0.06	0.06
Tl	0.006	0.004	0.004			0.004		0.003	0.011	0.002	0.004
Pb	0.21	0.19	0.27	0.23	0.24	0.19	0.25	0.19	0.40	0.21	0.23
Th	0.29	0.29	0.28	0.28	0.28	0.28	0.29	0.30	0.61	0.29	0.34
U	0.10	0.10	0.09	0.08	0.08	0.09	0.08	0.10	0.21	0.09	0.11

Table B2 (Continued)

	ALV 523-1	ALV 523-2	ALV 523-3	ALV 523-3a	ALV 523-4	ALV 524-2	ALV 525-2	ALV 525-4b	ALV 525-5-2	ALV 526-1b	ALV 526-2a
	PO-3	PO-3	PO-3	PO-3	PO-3	PO-3	PO-3	PO-3	PO-3	PO-3	PO-3
	Main	HiTi	HiTi	HiTi	HiTi	Main	Main	HiAl-LoSi	HiAl-LoSi	HiAl-LoSi	Main
	36.827	36.827	36.824	36.824	36.825	36.821	36.813	36.810	36.810	36.819	36.819
	-33.253	-33.252	-33.244	-33.244	-33.241	-33.279	-33.273	-33.268	-33.267	-33.254	-33.254
	-2726	-2743	-2540		-2532		-2715	-2750	-2625	-2694	
	laser	solution	laser	solution	laser	solution	laser	laser	laser	laser	solution
Li	4.6	6.1	5.8	6.3	5.9	6.2	5.7	4.2	4.0	3.8	5.1
Be		0.66		0.50		0.57					0.38
Sc	38.4	38.7	41.0	38.7	40.5	40.6	44.0	43.1	42.1	43.1	34.5
Ti	1.18	1.32	1.44	1.31	1.42	1.45	1.20	0.88	0.84	0.79	0.96
V	248	288	284	284	283	308	308	229	215	221	223
Cr	461	300	280	281	275	173	194	493	491	377	442
Mn	0.16	0.17	0.17	0.18	0.17	0.18	0.18	0.16	0.16	0.15	0.16
Co	41.9	44.4	44.2	45.2	43.5	43.1	42.5	45.6	46.4	40.1	48.0
Ni	131	120	112	115	111	68	64	148	173	133	200
Cu	62	69	58	72	56	65	68	90	86	83	83
Zn	73.4	86.5	83.1	87.6	83.7	89.1	84.5	65.2	58.9	53.8	75.2
Ga	13.6	16.7	14.5	16.7	14.4	16.7	14.3	13.1	12.4	11.5	15.5
Rb	5.62	8.25	5.99	5.79	5.89	5.66	5.31	2.79	2.58	2.91	3.16
Sr	128	141	116	118	115	118	105	85	81	89	104
Y	25.5	28.6	32.4	30.9	32.1	31.5	27.8	23.4	22.3	23.4	23.6
Zr	72.3	92.6	89.5	87.5	88.1	87.8	68.9	51.7	48.7	50.1	59.6
Nb	11.41	16.92	12.38	12.35	12.36	13.04	11.11	6.59	6.15	6.38	7.08
Mo				0.63		0.60					
Sn						0.82					
Cs		0.09		0.06		0.06					0.03
Ba	67.5	97.2	68.4	66.3	68.0	67.8	62.9	33.1	30.7	36.5	36.9
La	6.71	9.70	7.51	7.26	7.41	7.56	6.61	4.05	3.70	4.09	4.39
Ce	14.81	20.83	16.76	16.24	16.65	17.32	14.76	9.46	8.70	9.12	10.48
Pr	2.12	2.82	2.45	2.32	2.41	2.45	2.08	1.40	1.29	1.36	1.55
Nd	9.74	12.70	11.49	11.17	11.36	11.58	9.59	6.81	6.26	6.59	7.57
Sm	2.71	3.33	3.42	3.22	3.26	3.30	2.74	2.04	1.92	2.01	2.30
Eu	0.97	1.15	1.15	1.11	1.13	1.12	0.99	0.78	0.74	0.75	0.85
Gd	3.73	4.28	4.61	4.43	4.55	4.50	3.82	3.00	2.83	2.99	3.26
Tb	0.64	0.73	0.79	0.76	0.78	0.78	0.67	0.54	0.51	0.53	0.58
Dy	4.21	4.75	5.27	5.04	5.21	5.12	4.48	3.74	3.52	3.82	3.90
Ho	0.90	1.01	1.13	1.09	1.12	1.11	0.97	0.82	0.79	0.86	0.84
Er	2.56	2.85	3.26	3.07	3.24	3.17	2.84	2.42	2.28	2.55	2.38
Yb	2.47	2.81	3.19	3.02	3.15	3.14	2.80	2.51	2.38	2.64	2.33
Lu	0.39	0.44	0.50	0.47	0.49	0.49	0.44	0.39	0.37	0.43	0.37
Hf	1.90	2.35	2.43	2.32	2.40	2.35	1.88	1.38	1.27	1.43	1.60
Ta	0.65	0.96	0.72	0.70	0.71	0.75	0.64	0.39	0.36	0.40	0.42
W				0.17							
Tl											
Pb	0.44		0.48		0.49	0.53	0.46				
Th	0.73	1.06	0.79	0.78	0.81	0.79	0.71	0.41	0.37	0.45	0.46
U	0.21	0.33	0.24	0.24	0.23	0.25	0.22	0.13	0.12	0.13	0.15

Table B2 (Continued)

	ALV 526-3	ALV 526-4	ALV 526-5	ALV 526-6	ALV 527-1	ALV 527-4	ALV 527-5	ALV 527-6	ALV 527-6-3	ALV 528-1	ALV 528-1-2
	PO-3	PO-3	PO-3	PO-3	PO-3	PO-3	PO-3	PO-3	PO-3	PO-3	PO-3
	HiAl-LoSi	HiTi	HiTi	Main	HiAl-LoSi	HiTi	HiTi	HiTi	HiTi	HiAl-LoSi	HiAl-LoSi
	36.818	36.818	36.818	36.818	36.810	36.810	36.809	36.810	36.810	36.813	36.813
	-33.252	-33.251	-33.248	-33.244	-33.262	-33.252	-33.251	-33.247	-33.247	-33.267	-33.267
	-2663	-2585	-2550	-2604		-2584	-2512	-2565		-2680	
	laser	laser	laser	laser	solution	laser	laser	laser	solution	laser	solution
Li	4.9	5.9	6.1	4.9	3.8	6.3	6.1	5.8	6.2	4.2	6.5
Be					0.16				0.49		0.24
Sc	40.1	42.0	41.5	43.7	44.1	41.0	40.5	41.6	38.4	44.5	42.5
Ti	1.03	1.43	1.50	0.98	0.65	1.46	1.45	1.46	1.30	0.81	0.76
V	253	281	292	276	198	291	287	287	284	219	213
Cr	377	302	280	296	479	290	284	257	267	425	510
Mn	0.17	0.17	0.18	0.17	0.16	0.18	0.18	0.17	0.17	0.17	0.17
Co	44.3	44.4	45.4	43.4	49.9	45.5	44.4	43.4	44.6	47.7	49.1
Ni	119	116	113	78	196	114	110	99	111	167	191
Cu	69	60	60	80	98	59	61	64	71	107	96
Zn	72.8	82.2	87.7	73.6	57.9	79.9	87.9	80.5	87.7	62.9	62.9
Ga	14.0	14.2	14.9	12.9	13.7	14.6	14.8	14.1	16.9	12.5	14.1
Rb	4.00	5.65	6.30	3.45	1.51	6.15	6.02	6.22	5.81	2.46	2.30
Sr	96	113	112	98	68	111	111	118	114	69	74
Y	24.1	34.1	32.7	22.2	20.8	31.9	31.2	32.2	31.5	24.0	22.8
Zr	56.1	91.0	91.2	53.9	32.5	88.1	86.0	92.6	87.2	44.9	43.1
Nb	8.87	11.70	12.83	6.72	3.19	12.16	12.15	13.01	12.27	5.23	5.05
Mo					0.17				0.61		0.34
Sn					0.29						
Cs		0.06	0.06	0.03	0.02	0.07	0.06	0.07	0.06	0.02	0.02
Ba	49.0	63.1	69.1	42.2	18.2	66.8	66.5	70.4	66.7	27.8	26.6
La	5.20	7.25	7.58	4.40	2.05	7.16	7.13	7.83	7.18	3.27	3.08
Ce	12.32	15.80	16.98	10.57	5.22	16.52	16.39	17.14	16.30	7.71	7.50
Pr	1.74	2.34	2.47	1.56	0.81	2.35	2.36	2.49	2.33	1.15	1.11
Nd	7.96	11.26	11.50	7.62	4.10	11.32	11.20	11.77	11.22	5.82	5.48
Sm	2.30	3.42	3.51	2.33	1.41	3.30	3.21	3.45	3.28	1.82	1.74
Eu	0.86	1.16	1.16	0.86	0.58	1.11	1.14	1.14	1.11	0.70	0.66
Gd	3.23	4.83	4.61	3.08	2.30	4.43	4.39	4.64	4.47	2.91	2.69
Tb	0.58	0.84	0.81	0.55	0.44	0.78	0.78	0.80	0.78	0.52	0.50
Dy	3.98	5.72	5.48	3.52	3.18	5.23	5.14	5.31	5.16	3.72	3.52
Ho	0.87	1.24	1.16	0.78	0.74	1.14	1.10	1.13	1.11	0.85	0.80
Er	2.51	3.43	3.33	2.19	2.19	3.22	3.12	3.24	3.15	2.47	2.36
Yb	2.61	3.43	3.28	2.20	2.34	3.18	3.06	3.16	3.09	2.60	2.47
Lu	0.41	0.52	0.50	0.34	0.38	0.46	0.47	0.48	0.48	0.42	0.40
Hf	1.55	2.58	2.45	1.47	0.92	2.35	2.31	2.47	2.33	1.25	1.18
Ta	0.51	0.70	0.74	0.38	0.19	0.70	0.68	0.76	0.70	0.31	0.31
W		0.13	0.14	0.08		0.14	0.13	0.16	0.16	0.06	0.07
Tl					0.002						
Pb		0.46	0.48	0.34	0.15	0.47	0.48	0.48		0.25	
Th	0.55	0.78	0.81	0.42	0.20	0.76	0.74	0.82	0.77	0.32	0.31
U	0.18	0.21	0.24	0.13	0.07	0.23	0.23	0.26	0.24	0.11	0.10

Table B2 (Continued)

	ALV 528-2	ALV 528-3-1	ALV 528-3-2	ALV 528-4	ALV 528-4-1	ALV 529-3-1	ALV 529-3-2	ALV 529-4	ALV 530-2-1	ALV 530-3	ALV 534-2-1b
	PO-3	PO-3	PO-3	PO-3	PO-3	PO-3	PO-3	PO-3	PO-3	PO-3	PO-3
	HiAl-LoSi	HiAl-LoSi	HiAl-LoSi	HiAl-LoSi	HiAl-LoSi	HiBa, Main	HiBa, Main	Main	Main	HiAl-LoSi	HiAl-LoSi
	36.812	36.808	36.808	36.804	36.804	36.818	36.818	36.818	36.806	36.805	36.797
	-33.265	-33.264	-33.264	-33.265	-33.265	-33.265	-33.265	-33.261	-33.273	-33.268	-33.265
	-2625			-2526		-2705			-2663		
	laser	solution	solution	laser	solution	laser	solution	solution	laser	solution	solution
Li	3.8	4.2	4.2	3.5	3.7	3.6	3.9	5.0	5.4	3.9	4.3
Be		0.25	0.24		0.21		0.32	0.39		0.23	0.30
Sc	42.9	40.5	41.0	43.9	38.5	37.2	33.7	36.9	43.5	39.6	40.6
Ti	0.82	0.78	0.77	0.74	0.66	0.92	0.84	1.09	1.24	0.70	0.80
V	213	217	217	199	195	206	202	242	298	204	218
Cr	867	521	516	422	557	454	618	434	297	585	501
Mn	0.16	0.16	0.16	0.15	0.16	0.14	0.15	0.17	0.17	0.16	0.16
Co	47.4	49.7	50.3	43.7	49.9	40.8	47.7	48.5	42.2	50.7	50.1
Ni	184	208	216	156	231	147	247	189	81	239	211
Cu	103	91	92	102	96	83	78	76	76	96	91
Zn	58.7	62.4	63.2	51.7	57.3	61.3	66.6	85.6	78.9	59.8	63.8
Ga	12.2	13.9	13.8	11.2	13.7	12.2	13.8	15.7	13.7	14.0	13.9
Rb	2.41	2.15	2.16	1.53	1.62	4.19	3.95	3.67	4.13	1.97	2.39
Sr	81	74	74	70	71	124	119	102	101	81	77
Y	21.8	21.9	22.0	22.3	19.3	20.1	18.9	25.5	27.6	20.3	22.0
Zr	45.9	44.7	44.8	41.1	36.8	53.5	50.4	66.0	72.2	42.1	47.1
Nb	5.67	5.11	5.08	3.90	3.68	8.29	7.94	8.15	9.36	4.88	5.69
Mo		0.27	0.26		0.23		0.38	0.43		0.31	0.28
Sn		0.39	0.41				0.46	0.64			0.42
Cs	0.02	0.02	0.02	0.01		0.05	0.04	0.04	0.04	0.02	0.02
Ba	28.5	25.1	25.1	18.4	18.2	52.6	49.3	42.1	48.2	24.4	27.7
La	3.44	3.09	3.08	2.55	2.34	4.92	4.57	4.92	5.79	2.97	3.39
Ce	8.07	7.60	7.65	5.87	5.94	10.74	10.46	11.73	13.48	7.20	8.39
Pr	1.22	1.15	1.14	0.94	0.90	1.54	1.43	1.70	2.00	1.07	1.20
Nd	5.91	5.75	5.70	4.94	4.64	7.26	6.79	8.37	9.57	5.37	5.97
Sm	1.87	1.81	1.79	1.67	1.50	2.11	1.95	2.53	2.79	1.66	1.82
Eu	0.72	0.69	0.69	0.66	0.58	0.81	0.74	0.91	1.01	0.65	0.69
Gd	2.66	2.76	2.71	2.59	2.32	2.97	2.72	3.56	3.88	2.50	2.73
Tb	0.49	0.50	0.50	0.49	0.43	0.51	0.47	0.63	0.68	0.46	0.50
Dy	3.43	3.50	3.44	3.45	3.02	3.36	3.12	4.17	4.55	3.19	3.42
Ho	0.75	0.78	0.77	0.77	0.68	0.72	0.67	0.90	0.98	0.71	0.77
Er	2.30	2.33	2.27	2.31	2.00	2.00	1.88	2.60	2.86	2.09	2.26
Yb	2.30	2.36	2.33	2.36	2.05	1.95	1.83	2.53	2.72	2.16	2.32
Lu	0.37	0.37	0.37	0.37	0.33	0.29	0.28	0.40	0.42	0.34	0.37
Hf	1.24	1.23	1.21	1.16	1.00	1.42	1.34	1.76	1.93	1.12	1.26
Ta	0.33	0.30	0.30	0.24	0.22	0.50	0.46	0.48	0.55	0.29	0.34
W	0.05	0.05	0.06	0.03	0.06	0.09	0.09	0.10	0.11	0.08	0.07
Tl		0.007	0.005				0.005	0.006			0.006
Pb	0.25	0.20	0.20	0.19		0.34	0.30	0.35	0.40		0.22
Th	0.33	0.31	0.31	0.25	0.25	0.54	0.51	0.50	0.55	0.30	0.35
U	0.11	0.12	0.11	0.07	0.09	0.17	0.16	0.16	0.19	0.12	0.12

Table B2 (Continued)

	ALV 534-2-3a	ALV 818-12	ALV 820-3	ALV 820-5	ALV 821-1	ALV 821-2	ALV 821-8	ALV 821-9	ALV 822-1	ALV 822-3	ALV 824-4
	PO-3	PO-3	PO-3	PO-3	PO-3	PO-3	PO-3	PO-3	PO-3	PO-3	PO-3
	HiAl-LoSi	HiBa, Main	Main	Main	Main	Main	Main	Main	Main	Main	Main
	36.797	36.782	36.753	36.752	36.755	36.755	36.755	36.755	36.756	36.755	36.753
	-33.265	-33.303	-33.293	-33.287	-33.291	-33.288	-33.282	-33.282	-33.280	-33.276	-33.300
	solution	laser	laser	laser	laser	laser	solution	laser	laser	laser	solution
Li	4.3	4.5	5.7	5.1	5.0	4.7	5.4	4.5	4.5	4.6	5.3
Be	0.27						0.49				0.47
Sc	40.8	42.0	44.1	45.6	43.4	44.1	39.9	40.6	43.8	43.0	40.1
Ti	0.80	1.04	1.22	1.17	1.16	1.00	1.24	1.06	0.95	1.02	1.13
V	221	262	292	283	273	264	281	250	262	271	276
Cr	513	146	366	339	356	413	369	255	404	406	429
Mn	0.16	0.16	0.17	0.16	0.16	0.16	0.17	0.16	0.16	0.16	0.17
Co	49.7	44.3	42.3	40.2	40.2	40.2	45.7	42.7	42.0	40.9	43.9
Ni	203	80	91	81	94	96	127	79	101	97	112
Cu	99	99	69	69	65	72	70	86	84	74	73
Zn	64.5	70.6	76.5	72.1	71.1	67.0	80.0	70.5	67.8	70.8	77.1
Ga	14.1	13.3	14.1	13.6	13.5	13.0	15.5	13.2	12.8	13.5	15.3
Rb	2.43	6.05	4.17	4.08	3.89	3.24	6.30	4.36	4.68	3.31	4.40
Sr	77	127	99	96	98	94	116	117	98	94	107
Y	22.3	21.3	29.5	30.4	28.4	25.2	25.9	23.0	22.8	24.1	25.5
Zr	47.5	59.8	71.4	73.1	68.4	57.2	73.8	60.6	56.0	54.7	67.4
Nb	5.78	11.77	8.98	8.83	8.52	6.95	13.62	9.28	9.63	7.02	9.92
Mo	0.29						0.60				0.48
Sn							0.67				0.63
Cs	0.03						0.07				0.05
Ba	28.2	75.6	48.8	49.3	46.4	39.2	75.2	53.1	56.6	39.9	52.7
La	3.43	6.74	5.62	5.84	5.42	4.52	7.65	5.50	5.68	4.47	5.86
Ce	8.42	15.07	12.85	12.91	12.18	10.35	16.78	12.66	12.31	10.51	13.37
Pr	1.22	2.03	1.88	1.92	1.81	1.53	2.27	1.81	1.73	1.53	1.90
Nd	6.09	8.97	9.08	9.44	8.75	7.51	10.36	8.40	8.02	7.36	9.13
Sm	1.88	2.42	2.77	2.93	2.68	2.33	2.80	2.49	2.28	2.28	2.63
Eu	0.71	0.88	0.97	1.00	0.95	0.86	0.96	0.90	0.83	0.85	0.92
Gd	2.79	3.11	4.03	4.28	3.87	3.46	3.71	3.35	3.12	3.28	3.59
Tb	0.51	0.54	0.70	0.76	0.68	0.61	0.65	0.58	0.55	0.57	0.63
Dy	3.50	3.50	4.72	5.13	4.54	4.08	4.24	3.79	3.68	4.01	4.17
Ho	0.78	0.75	1.04	1.13	0.99	0.90	0.92	0.82	0.81	0.86	0.91
Er	2.31	2.12	2.93	3.19	2.81	2.52	2.59	2.26	2.31	2.47	2.57
Yb	2.37	2.09	2.89	3.14	2.80	2.53	2.56	2.21	2.31	2.47	2.53
Lu	0.37	0.33	0.45	0.51	0.43	0.40	0.40	0.35	0.37	0.38	0.40
Hf	1.28	1.53	1.91	2.11	1.83	1.60	1.96	1.66	1.51	1.52	1.81
Ta	0.34	0.63	0.52	0.56	0.50	0.41	0.78	0.52	0.56	0.41	0.58
W											
Tl							0.009				0.008
Pb		0.45	0.42	0.46	0.41	0.37	0.43	0.40	0.39	0.40	0.37
Th	0.35	0.75	0.58	0.64	0.56	0.46	0.81	0.58	0.64	0.45	0.58
U	0.12	0.23	0.20	0.19	0.16	0.14	0.25	0.18	0.19	0.13	0.20

Table B2 (Continued)

	ALV 830-6	ALV 832-2	ARP 73-10-02	ARP 73-13-004	ARP 73-7-001	ARP 74-10-14	ARP 74-11-17	ARP 74-11-18	ARP 74-12-19	ARP 74-13-24*	ARP 74-14-31
	PO-3	PO-3	PO-3	PO-3	PO-3	PO-3	PO-3	PO-3	PO-3	PO-3	PO-3
	Main	Main	Main	HiBa, Main	HiBa, Main	HiBa, Main	Main	Main	Main	Main	HiBa, HiAl-LoSi
	36.724	36.728	36.836	36.828	36.828	36.830	36.850	36.850	36.858	36.950	36.950
	-33.307	-33.301	-33.248	-33.267	-33.262	-33.270	-33.250	-33.250	-33.258	-33.161	-33.167
	solution	laser	solution	solution	solution	solution	solution	solution	solution	solution	solution
Li	5.3	5.8	6.9	4.2	4.1	3.9	5.0	5.0	5.2	4.1	3.5
Be	0.42		0.64	0.36	0.35	0.34	0.44	0.42	0.36	0.44	0.11
Sc	39.2	42.9	41.1	33.9	33.6	34.5	35.1	36.7	41.5	41.8	43.0
Ti	1.06	1.39	1.61	0.83	0.83	0.86	1.08	1.08	0.99	1.08	0.51
V	267	307	338	205	205	203	241	247	268	275	184
Cr	352	325	120	690	635	605	487	396	420	153	418
Mn	0.16	0.18	0.19	0.15	0.15	0.14	0.16	0.16	0.17	0.17	0.16
Co	41.2	43.3	45.2	46.6	46.2	46.0	45.3	43.3	45.2	44.7	50.8
Ni	101	89	65	233	227	217	182	123	133	62	169
Cu	70	75	59	75	73	75	70	69	75	76	104
Zn	72.6	85.7	101.0	66.4	67.6	66.8	77.1	79.1	73.4	74.4	52.5
Ga	15.4	15.3	17.7	13.8	13.9	14.2	15.0	15.5	14.8	15.6	13.4
Rb	3.78	4.69	6.86	4.08	3.70	3.90	4.82	4.01	2.97	4.03	1.34
Sr	106	101	114	123	112	120	113	116	90	123	72
Y	25.3	31.8	34.7	18.5	19.0	18.8	24.8	24.3	25.5	24.1	16.7
Zr	62.8	81.1	98.2	49.7	49.2	48.8	69.6	65.1	57.4	61.3	22.9
Nb	8.36	10.23	15.39	8.32	7.69	7.51	10.58	8.93	6.55	9.80	2.54
Mo	0.42		0.71	0.41	0.37	0.36	0.52	0.41	0.34	0.50	0.14
Sn	0.59		0.89	0.46	0.46		0.63	0.60	0.54	0.61	0.21
Cs	0.04		0.08	0.04	0.04	0.04	0.05	0.04	0.03		0.01
Ba	44.8	51.7	77.6	53.6	47.5	48.2	56.4	48.9	34.6	56.8	16.4
La	5.05	6.12	8.95	4.65	4.30	4.42	5.96	5.20	4.01	5.81	1.57
Ce	11.74	14.54	20.03	10.42	9.82	9.96	13.55	12.13	9.73	13.26	3.90
Pr	1.70	2.14	2.79	1.48	1.41	1.41	1.94	1.79	1.48	1.84	0.59
Nd	8.27	10.43	13.00	6.97	6.73	6.69	9.17	8.54	7.36	8.61	3.01
Sm	2.46	3.16	3.62	1.99	1.96	1.96	2.61	2.51	2.33	2.48	1.08
Eu	0.87	1.12	1.20	0.77	0.77	0.75	0.93	0.93	0.85	0.89	0.48
Gd	3.44	4.44	4.91	2.74	2.76	2.70	3.60	3.52	3.43	3.39	1.85
Tb	0.61	0.77	0.85	0.48	0.49	0.48	0.63	0.61	0.61	0.59	0.35
Dy	4.09	5.17	5.65	3.12	3.19	3.13	4.12	4.06	4.14	3.94	2.58
Ho	0.90	1.12	1.22	0.67	0.69	0.67	0.89	0.87	0.91	0.85	0.59
Er	2.57	3.14	3.50	1.89	1.93	1.88	2.52	2.47	2.63	2.42	1.77
Yb	2.54	3.12	3.49	1.82	1.87	1.81	2.46	2.40	2.59	2.40	1.88
Lu	0.40	0.49	0.54	0.27	0.28	0.29	0.38	0.37	0.40	0.38	0.30
Hf	1.73	2.20	2.55	1.34	1.35	1.34	1.86	1.75	1.60	1.65	0.66
Ta	0.49	0.58	0.89	0.48	0.43	0.44	0.61	0.52	0.38	0.60	0.15
W											0.04
Tl	0.012		0.012	0.007	0.008		0.008	0.008	0.006		0.004
Pb	0.35	0.46	0.52	0.37	0.33		0.40	0.37	0.33	0.39	0.12
Th	0.51	0.64	0.95	0.52	0.47	0.48	0.64	0.54	0.41	0.61	0.17
U	0.18	0.20	0.32	0.16	0.15	0.15	0.21	0.18	0.13	0.20	0.06

Table B2 (Continued)

	ARP 74-14-32*	ARP 74-14-33	ARP 74-16-36	ARP 74-16-37	ARP 74-7-5	ARP 74-7-6	ARP 74-8-10*	ARP 74-9-12	CH 31-D1-112	CH 31-D11-315
	PO-3	PO-3	PO-3	PO-3	PO-3	PO-3	PO-3	PO-3	PO-3	PO-3
	HiBa, HiAl-LoSi	HiBa, HiAl-LoSi	Main	Main	HiTi	HiTi	Main	HiBa, Main	HiBa, Main	HiTi
	36.930	36.950	36.900	36.900	36.830	36.830	36.850	36.830	36.833	36.825
	-33.167	-33.167	-33.200	-33.200	-33.250	-33.250	-33.250	-33.270	-33.267	-33.258
	solution	solution	solution	solution	solution	solution	solution	solution	solution	solution
Li	3.0	3.3	5.2	5.1	5.9	5.9	5.2	3.9	4.2	6.1
Be	0.11	0.16	0.46	0.47	0.56	0.60	0.44	0.37	0.33	0.55
Sc	40.0	42.8	38.5	39.8	38.8	39.0	41.5	33.6	34.2	38.9
Ti	0.49	0.51	1.06	1.08	1.43	1.40	1.14	0.84	0.86	1.38
V	173	184	258	264	285	289	294	203	210	287
Cr	476	522	458	241	279	278	181	617	595	280
Mn	0.15	0.15	0.16	0.16	0.18	0.18	0.18	0.15	0.15	0.18
Co	48.4	49.9	43.2	42.4	45.3	45.5	45.2	46.5	45.0	45.3
Ni	166	163	147	84	114	112	80	238	202	113
Cu	88	105	72	80	68	67	63	76	74	67
Zn	49.8	51.5	70.8	74.2	87.6	88.9	83.6	66.4	67.6	88.7
Ga	13.2	13.5	14.9	14.7	16.6	16.7	16.2	13.9	14.1	16.7
Rb	1.17	1.31	5.42	5.38	5.97	5.95	4.27	3.85	3.84	5.87
Sr	72	72	122	126	118	118	110	116	114	116
Y	15.7	16.8	24.7	24.6	30.9	31.1	25.4	18.8	19.6	31.0
Zr	21.3	22.7	67.8	71.1	87.6	88.4	62.4	49.5	51.6	87.5
Nb	2.36	2.52	11.81	11.75	12.59	12.57	9.76	7.76	7.87	12.52
Mo	0.12	0.14	0.47	0.50	0.60	0.60		0.37	0.42	0.71
Sn		0.20	0.61	0.65	0.86	0.83	0.60	0.45	0.48	0.82
Cs	0.01	0.01	0.06	0.06	0.06	0.07	0.04	0.04	0.04	0.07
Ba	15.1	16.3	67.2	65.2	69.3	68.3	53.2	48.8	48.4	67.1
La	1.46	1.57	6.82	6.82	7.39	7.42	5.69	4.40	4.48	7.31
Ce	3.68	3.89	14.97	14.99	16.76	16.84	12.89	9.97	10.24	16.69
Pr	0.55	0.59	2.08	2.10	2.39	2.40	1.83	1.43	1.48	2.37
Nd	2.84	3.06	9.58	9.63	11.30	11.30	8.59	6.77	7.00	11.29
Sm	1.02	1.10	2.63	2.67	3.28	3.26	2.49	1.96	2.04	3.26
Eu	0.46	0.48	0.95	0.95	1.10	1.11	0.89	0.76	0.79	1.10
Gd	1.73	1.85	3.58	3.60	4.46	4.48	3.46	2.75	2.85	4.43
Tb	0.33	0.36	0.62	0.61	0.77	0.77	0.61	0.48	0.49	0.77
Dy	2.42	2.58	4.09	4.07	5.09	5.10	4.13	3.16	3.29	5.07
Ho	0.55	0.59	0.88	0.88	1.09	1.10	0.90	0.68	0.70	1.09
Er	1.67	1.77	2.53	2.50	3.12	3.09	2.58	1.89	1.99	3.09
Yb	1.75	1.87	2.48	2.45	3.05	3.03	2.56	1.84	1.92	3.03
Lu	0.28	0.31	0.38	0.38	0.47	0.47	0.40	0.28	0.29	0.47
Hf	0.62	0.66	1.80	1.83	2.35	2.33	1.70	1.34	1.40	2.32
Ta	0.14	0.15	0.67	0.67	0.72	0.72	0.57	0.46	0.46	0.71
W		0.04			0.16					
Tl			0.008	0.010	0.010	0.009	0.012	0.009	0.009	0.009
Pb		0.12	0.45		0.47	0.48	0.36	0.32	0.39	0.48
Th	0.15	0.17	0.77	0.77	0.79	0.79	0.59	0.48	0.49	0.78
U	0.06	0.07	0.24	0.25	0.25	0.25	0.20	0.15	0.15	0.24

Table B2 (Continued)

	CH 31-D12	CH 31-D3-346	CH 31-D4	CH 31-D5-304	CH 31-D8	CH 31-D8-136	CH 31-D9-344	CYA 74-29-31C	CYA 74-30-32	CYA 74-30-33
	PO-3	PO-3	PO-3	PO-3	PO-3	PO-3	PO-3	PO-3	PO-3	PO-3
	HiBa, HiAl-LoSi	HiTi	HiBa, Main	Main	HiAl-LoSi	HiAl-LoSi	Main	Main	HiBa, HiAl-LoSi	Main
	36.867	36.792	36.829	36.767	36.838	36.838	36.873	36.900	36.850	36.853
	-33.248	-33.233	-33.265	-33.275	-33.244	-33.244	-33.252	-33.100	-33.250	-33.252
	solution	solution	solution	solution	solution	solution	solution	solution	solution	solution
Li	4.3	6.0	4.0	4.9	4.7	4.3	5.0	5.4	4.2	5.3
Be	0.22	0.60	0.32	0.44	0.25	0.23	0.40	0.45	0.21	0.49
Sc	43.0	39.0	33.8	35.0	41.7	41.1	39.2	39.0	41.8	37.9
Ti	0.66	1.35	0.84	1.02	0.75	0.75	0.99	1.10	0.65	1.21
V	221	287	203	231	230	226	253	267	214	261
Cr	1153	248	632	525	1045	812	478	437	898	395
Mn	0.16	0.17	0.15	0.15	0.16	0.16	0.16	0.17	0.16	0.17
Co	47.1	44.1	46.7	45.4	47.8	48.5	43.9	46.2	50.2	44.6
Ni	211	98	232	190	205	265	156	141	241	126
Cu	121	67	75	71	99	133	72	72	99	70
Zn	56.9	85.7	67.1	74.4	61.8	61.2	69.9	81.5	56.4	84.2
Ga	13.2	16.3	13.9	14.7	13.5	13.3	14.6	15.5	12.8	16.0
Rb	2.36	5.88	3.95	4.30	2.70	2.71	3.42	4.64	2.29	4.56
Sr	85	118	120	107	86	84	104	108	83	118
Y	20.6	29.7	18.7	23.5	22.2	21.6	24.4	26.8	20.0	26.5
Zr	36.7	84.9	50.0	64.1	43.3	43.5	60.4	66.6	35.8	71.8
Nb	4.86	12.65	8.19	9.34	5.90	5.90	7.58	9.39	4.76	9.92
Mo	0.25	0.57	0.43	0.45	0.29	0.29	0.35	0.44	0.24	0.47
Sn	0.32	0.77	0.46	0.60	0.38	0.38	0.57	0.64	0.31	0.67
Cs	0.02	0.07	0.04	0.05	0.03	0.03	0.04	0.05	0.02	0.05
Ba	31.6	69.5	51.8	50.4	34.5	34.2	41.5	51.5	30.6	53.3
La	2.92	7.37	4.57	5.32	3.47	3.47	4.61	5.78	2.85	5.82
Ce	7.02	16.67	10.21	12.23	8.28	8.24	10.93	13.08	6.83	13.45
Pr	1.04	2.37	1.46	1.77	1.21	1.20	1.62	1.86	1.01	1.95
Nd	5.16	11.11	6.88	8.44	5.96	5.89	7.87	8.86	5.01	9.34
Sm	1.58	3.17	1.98	2.45	1.81	1.78	2.39	2.59	1.52	2.74
Eu	0.64	1.08	0.77	0.88	0.69	0.67	0.87	0.92	0.62	0.97
Gd	2.40	4.33	2.76	3.37	2.68	2.63	3.40	3.66	2.33	3.79
Tb	0.45	0.74	0.48	0.59	0.50	0.48	0.59	0.65	0.44	0.66
Dy	3.14	4.89	3.16	3.92	3.43	3.36	3.99	4.32	3.04	4.36
Ho	0.73	1.05	0.67	0.84	0.78	0.77	0.87	0.94	0.71	0.93
Er	2.20	3.00	1.90	2.39	2.36	2.29	2.49	2.71	2.14	2.66
Yb	2.36	2.94	1.83	2.34	2.47	2.42	2.46	2.67	2.29	2.60
Lu	0.37	0.45	0.28	0.36	0.39	0.38	0.38	0.42	0.36	0.41
Hf	1.03	2.26	1.35	1.73	1.20	1.18	1.63	1.82	1.00	1.94
Ta	0.28	0.73	0.47	0.54	0.34	0.35	0.44	0.54	0.27	0.57
W										0.12
Tl	0.005	0.010	0.006	0.007	0.007	0.005	0.006	0.008	0.008	0.008
Pb	0.32	0.47	0.36	0.38	0.27	0.32	0.45	0.40	0.28	0.40
Th	0.30	0.79	0.51	0.58	0.36	0.36	0.47	0.61	0.30	0.61
U	0.11	0.25	0.16	0.18	0.12	0.12	0.16	0.19		0.20

Table B2 (Continued)

	CYA 74-30-34	GIL 103-16-2	GIL 103-20-6	GIL 103-21-1	GIL 103-24-19	GIL 103-32-13	GIL 103-35-3	KN 42-28-D4	KN 42-86-D12	KN 42-86-D12-78
	PO-3	PO-3	PO-3	PO-3	PO-3	PO-3	PO-3	PO-3	PO-3	PO-3
	HiBa, HiAl-LoSi	Main	Main	Main	Main	Main	Main	Main	Main	Main
	36.850	36.780	36.773	36.775	36.793	36.730	36.797	36.915	36.640	36.640
	-33.250	-33.278	-33.288	-33.277	-33.290	-33.292	-33.282	-33.163	-33.325	-33.325
								-2889 to -2608	-2901 to -2740	
	solution	solution	solution	solution	solution	solution	solution	laser	laser	solution
Li	3.8	4.7	5.9	5.0	5.1	4.9	5.7	5.8	5.6	5.2
Be	0.21	0.38	0.49	0.48	0.46	0.45	0.46			0.41
Sc	44.2	39.0	41.5	41.4	41.8	44.1	41.3	44.2	43.7	40.7
Ti	0.68	1.04	1.24	1.14	1.13	1.16	1.25	1.36	1.46	1.15
V	220	253	300	266	276	280	293	304	294	270
Cr	574	337	309	289	103	227	300	92	202	207
Mn	0.16	0.16	0.17	0.16	0.17	0.17	0.17	0.19	0.17	0.17
Co	46.3	42.5	43.1	41.9	45.3	44.3	44.5	45.5	41.4	45.2
Ni	205	98	88	86	68	77	95	44	65	92
Cu	134	75	70	83	82	83	69	73	66	78
Zn	56.3	72.7	84.8	72.7	76.1	76.1	81.7	80.6	77.7	76.5
Ga	13.4	15.2	16.1	15.0	15.3	15.5	15.9	15.0	14.3	15.2
Rb	2.42	3.99	4.30	4.87	6.10	4.60	3.95	5.99	5.65	4.12
Sr	89	105	102	123	127	104	103	122	108	110
Y	20.8	23.8	29.0	24.5	24.3	27.8	27.1	28.2	32.0	25.7
Zr	37.7	57.5	77.5	68.4	65.5	72.4	70.9	78.8	90.4	65.6
Nb	4.75	8.18	10.11	10.37	12.67	10.43	9.31	12.54	12.55	8.75
Mo	0.23	0.42	0.48	0.50	0.53	0.51	0.45			0.44
Sn	0.32	0.54	0.73	0.63	0.60	0.65	0.65			0.62
Cs	0.03	0.04	0.05	0.05	0.07	0.05	0.04	0.06	0.06	0.04
Ba	31.4	49.1	50.8	60.2	76.3	52.6	47.6	72.2	65.1	50.4
La	3.02	4.90	6.09	6.20	7.23	6.06	5.69	7.52	7.47	5.31
Ce	7.22	11.31	14.34	14.07	15.72	13.97	13.37	17.19	16.82	12.47
Pr	1.06	1.62	2.11	1.98	2.12	1.98	1.93	2.41	2.43	1.80
Nd	5.21	7.86	10.12	9.36	9.63	9.48	9.30	10.92	11.55	8.68
Sm	1.62	2.38	2.96	2.64	2.64	2.72	2.73	3.03	3.38	2.59
Eu	0.64	0.86	1.03	0.94	0.94	0.95	0.97	1.07	1.13	0.93
Gd	2.42	3.31	4.12	3.55	3.50	3.79	3.80	3.99	4.54	3.59
Tb	0.45	0.58	0.72	0.62	0.61	0.67	0.67	0.70	0.80	0.63
Dy	3.21	3.91	4.78	4.03	3.99	4.47	4.39	4.65	5.27	4.17
Ho	0.74	0.85	1.03	0.87	0.87	0.99	0.96	1.00	1.13	0.91
Er	2.19	2.40	2.96	2.45	2.47	2.84	2.72	2.85	3.16	2.58
Yb	2.33	2.35	2.89	2.40	2.43	2.85	2.70	2.85	3.16	2.55
Lu	0.38	0.37	0.45	0.37	0.38	0.45	0.42	0.45	0.49	0.40
Hf	1.05	1.61	2.05	1.81	1.76	1.93	1.91	2.05	2.40	1.80
Ta	0.28	0.48	0.60	0.60	0.72	0.61	0.55	0.70	0.73	0.51
W			0.09					0.14	0.14	
Tl	0.006	0.012	0.008		0.011		0.007			0.007
Pb	0.21	0.35	0.47	0.42	0.50	0.38	0.41	0.52	0.50	0.45
Th	0.30	0.51	0.62	0.64	0.80	0.64	0.55	0.79	0.81	0.54
U	0.10	0.16	0.22	0.22	0.24	0.21	0.19	0.25	0.24	0.17

Table B2 (Continued)

	KN 42-D23	KN 42-ST88-3	NR DR 3-4	NR DR 3-7	TR 119-4D-3A
	PO-3	PO-3	PO-3	PO-3	PO-3
	Main	Main	HiBa, Main	HiBa, Main	HiBa, Main
	36.810	36.850	36.847	36.847	36.850
	-33.280	-33.320	-33.222	-33.222	-33.230
	-2250 to -2221	-2271 to -1720			
	laser	laser	solution	solution	solution
Li	5.0	5.0	5.1	4.9	4.1
Be			0.51	0.49	0.42
Sc	44.5	43.2	38.7	39.5	37.4
Ti	1.09	1.18	1.07	1.12	0.98
V	277	272	261	262	252
Cr	153	107	496	504	562
Mn	0.17	0.18	0.16	0.16	0.16
Co	41.9	44.4	46.3	46.4	46.5
Ni	64	56	167	162	197
Cu	75	84	76	76	81
Zn	70.5	73.9	72.7	74.0	68.0
Ga	13.4	13.9	14.6	14.7	13.9
Rb	4.47	4.39	8.36	8.54	6.88
Sr	103	114	143	146	132
Y	25.2	25.0	22.9	23.1	21.7
Zr	59.5	64.9	70.5	70.8	61.0
Nb	9.44	8.79	16.07	15.95	12.25
Mo			0.62	0.66	0.56
Sn			0.62	0.64	
Cs	0.05	0.05	0.09	0.09	0.08
Ba	54.9	52.3	105.3	105.3	88.3
La	5.65	5.44	8.94	8.99	7.21
Ce	12.54	13.02	18.64	18.67	15.43
Pr	1.77	1.85	2.47	2.45	2.04
Nd	8.29	8.77	10.86	10.73	9.15
Sm	2.41	2.64	2.74	2.75	2.43
Eu	0.86	0.95	0.96	0.94	0.84
Gd	3.40	3.57	3.48	3.47	3.21
Tb	0.60	0.62	0.59	0.59	0.54
Dy	4.01	4.12	3.82	3.85	3.56
Ho	0.89	0.89	0.82	0.82	0.78
Er	2.54	2.51	2.35	2.33	2.15
Yb	2.54	2.50	2.30	2.29	2.13
Lu	0.40	0.37	0.35	0.36	0.34
Hf	1.61	1.73	1.82	1.84	1.61
Ta	0.55	0.48	0.90	0.90	0.72
W	0.13	0.12			0.16
Tl			0.010	0.011	
Pb	0.41	0.46		0.54	
Th	0.61	0.55	1.05	1.06	0.82
U	0.19	0.17	0.31	0.31	0.27

[a]Concentrations are in ppm except for Ti and Mn which are in wt. %

Table B3: Sr, Nd, and Pb Isotope Ratios of Samples from Segments PO-2 and -3

Detrick Segment	Sample Name	Sample Group	Latitude	Longitude	Sr Iso. Method	$^{87}Sr/^{86}Sr$	Nd Iso. Method	$^{143}Nd/^{144}Nd$	Pb Iso. Method	$^{206}Pb/^{204}Pb$	$^{207}Pb/^{204}Pb$	$^{208}Pb/^{204}Pb$
PO-3	A127 RC 119	HiTi	36.912	-33.235	TIMS	0.702960	MC-ICP-MS	0.513112	MC-ICP-MS	18.900	15.535	38.446
PO-3	A127 RC 27	Main	36.600	-33.347	TIMS	0.702903	MC-ICP-MS	0.513109	MC-ICP-MS	18.808	15.535	38.383
PO-3	A127 RC 28	Main	36.660	-33.331	TIMS	0.702930	MC-ICP-MS	0.513120	MC-ICP-MS	18.781	15.528	38.354
PO-3	A127 RC 30	HiBa, Main	36.716	-33.308	TIMS	0.702935	MC-ICP-MS	0.513104	MC-ICP-MS	18.852	15.534	38.405
PO-3	A127 RC 31	Main	36.855	-33.254	TIMS	0.702858	MC-ICP-MS	0.513126	MC-ICP-MS	18.764	15.524	38.315
PO-3	A127 RC 32	Main	36.875	-33.239	TIMS	0.702985	MC-ICP-MS	0.513089	MC-ICP-MS	18.991	15.555	38.537
PO-3	AII 73-10-DR2-1	Main	36.745	-33.253	TIMS	0.702940	MC-ICP-MS	0.513124	MC-ICP-MS	18.834	15.539	38.412
PO-3	AII 73-12-DR3-1	Main	36.740	-33.279	TIMS	0.702925	MC-ICP-MS	0.513123	MC-ICP-MS	18.730	15.526	38.325
PO-3	AII 73-16-DR5-1	Main	36.700	-33.290	TIMS	0.702891	MC-ICP-MS	0.513125	MC-ICP-MS	18.749	15.532	38.343
PO-3	ALV 518-1-1	Main	36.819	-33.255	TIMS	0.702869	MC-ICP-MS	0.513120	MC-ICP-MS	18.848	15.534	38.386
PO-3	ALV 518-2-2	Main	36.820	-33.257	TIMS	0.702832	MC-ICP-MS	0.513118	MC-ICP-MS			
PO-3	ALV 518-3-1	Main	36.821	-33.261	TIMS	0.702867	MC-ICP-MS	0.513127	MC-ICP-MS	18.785	15.522	38.323
PO-3	ALV 519-2-3	HiAl-LoSi	36.818	-33.263	TIMS	0.702865	MC-ICP-MS	0.513103	MC-ICP-MS	18.929	15.541	38.453
PO-3	ALV 523-2	HiTi	36.827	-33.252	TIMS	0.702995	MC-ICP-MS	0.513075	MC-ICP-MS			
PO-3	ALV 524-2	Main	36.821	-33.279	TIMS	0.702940	MC-ICP-MS	0.513128	MC-ICP-MS	18.745	15.525	38.323
PO-3	ALV 527-1	HiAl-LoSi	36.810	-33.262	TIMS	0.702885	MC-ICP-MS	0.513110	MC-ICP-MS	18.942	15.548	38.471
PO-3	ALV 528-3-1	HiAl-LoSi	36.808	-33.264	TIMS	0.702885	MC-ICP-MS	0.513113	MC-ICP-MS	18.857	15.537	38.403
PO-3	ALV 529-3-2	HiBa, Main	36.818	-33.265	TIMS	0.702902	MC-ICP-MS	0.513114	MC-ICP-MS	18.862	15.534	38.391
PO-3	ALV 534-2-1b	HiAl-LoSi	36.797	-33.265	TIMS	0.702916	MC-ICP-MS	0.513114	MC-ICP-MS	18.894	15.534	38.424
PO-3	ALV 821-8	Main	36.755	-33.282	TIMS	0.702959	MC-ICP-MS	0.513087	MC-ICP-MS	18.997	15.543	38.518
PO-3	ARP 74-13-24*	Main	36.950	-33.161	TIMS	0.702950	MC-ICP-MS	0.513114	MC-ICP-MS	18.749	15.534	38.337
PO-3	ARP 74-14-31	HiBa, HiAl-LoSi	36.950	-33.167	TIMS	0.702934	MC-ICP-MS	0.513128	MC-ICP-MS	18.871	15.544	38.416
PO-3	ARP 74-16-37	Main	36.900	-33.200	TIMS	0.703002	MC-ICP-MS	0.513111	MC-ICP-MS	18.795	15.528	38.351
PO-3	ARP 74-7-5	HiTi	36.830	-33.250	TIMS	0.702988	MC-ICP-MS	0.513123	MC-ICP-MS	18.869	15.538	38.445
PO-3	ARP73-7-1	HiBa, Main	36.828	-33.262			MC-ICP-MS	0.513116	MC-ICP-MS	18.852	15.540	38.403
PO-3	CH 31-D1-112	HiBa, Main	36.833	-33.267	TIMS	0.702877	MC-ICP-MS	0.513117	MC-ICP-MS	18.840	15.539	38.394
PO-3	CH 31-D11-315	HiTi	36.825	-33.258	TIMS	0.702963	MC-ICP-MS	0.513123	MC-ICP-MS	18.872	15.538	38.450
PO-3	CH 31-D8	HiAl-LoSi	36.838	-33.244	TIMS	0.702952	MC-ICP-MS	0.513109	MC-ICP-MS	18.875	15.535	38.422
PO-3	CYA 74-30-34	HiBa, HiAl-LoSi	36.850	-33.250	TIMS	0.702952	MC-ICP-MS	0.513077	MC-ICP-MS	19.016	15.550	38.531

Table B3 (Continued)

PO-3	GIL 103-16-2	Main	36.780	-33.278	TIMS	0.702900	MC-ICP-MS	0.513121	MC-ICP-MS	18.840	15.533	38.397
PO-3	GIL 103-24-19	Main	36.793	-33.290	TIMS	0.702958	MC-ICP-MS	0.513085	MC-ICP-MS	18.936	15.551	38.492
PO-3	KN 42-86-D12-78	Main	36.640	-33.325	TIMS	0.702921	MC-ICP-MS	0.513133	MC-ICP-MS	18.707	15.527	38.297
PO-3	NR DR 3-4	HiBa, Main	36.847	-33.222	TIMS	0.702989	MC-ICP-MS	0.513064	MC-ICP-MS	19.126	15.560	38.633
PO-3	TR 119-4D-3A	HiBa, Main	36.850	-33.230	TIMS	0.702956	MC-ICP-MS	0.513085	MC-ICP-MS			
PO-2	A127 DR13-1 avg.	N. Famous	36.998	-32.936	MC-ICP-MS	0.702873	MC-ICP-MS	0.513191	MC-ICP-MS	18.478	15.499	38.132
PO-2	A127 DR13-4	N. Famous	36.998	-32.936	MC-ICP-MS	0.702916	MC-ICP-MS	0.513158	MC-ICP-MS	18.665	15.521	38.292
PO-2	A127 DR13-8 avg.	N. Famous	36.998	-32.936	MC-ICP-MS	0.702915	MC-ICP-MS	0.513158	MC-ICP-MS	18.687	15.517	38.302
PO-2	A127 DR14-2	N. Famous	37.053	-32.908	MC-ICP-MS	0.702941	MC-ICP-MS	0.513148	MC-ICP-MS	18.686	15.519	38.294
PO-2	A127 RC 34	N. Famous	36.940	-32.988	MC-ICP-MS	0.702987	MC-ICP-MS	0.513154	MC-ICP-MS	18.764	15.531	38.388
PO-2	A127 RC 35 avg.	N. Famous	36.950	-32.967	MC-ICP-MS	0.702923	MC-ICP-MS	0.513148	MC-ICP-MS	18.691	15.522	38.311
PO-2	A127 RC 36	N. Famous	36.974	-32.950	MC-ICP-MS	0.702965	MC-ICP-MS	0.513133	MC-ICP-MS	18.801	15.534	38.408
PO-2	A127 RC 37	N. Famous	37.020	-32.927	MC-ICP-MS	0.702941	MC-ICP-MS	0.513132	MC-ICP-MS	18.780	15.531	38.375
PO-2	A127 RC 38	N. Famous	37.033	-32.913	MC-ICP-MS	0.702824	MC-ICP-MS	0.513183	MC-ICP-MS	18.472	15.501	38.107

Table B4: Modeling of the HiAl-LoSi Lavas

Sample	Average Main lava	Average HiAl-LoSi lava	Representative HiAl melt inclusion (Laubier et al., 2012)	Model Melt (Mix of Average Main lava + Representative MI)	Element fit (relative %)
SiO_2	51.03	49.18	47.49	49.26	0.2%
TiO_2	1.23	0.83	0.40	0.81	2.3%
Al_2O_3	14.89	16.22	17.50	16.19	0.2%
FeO_T	9.79	9.16	8.30	9.05	1.2%
MnO	0.19	0.17	0.16	0.17	1.3%
MgO	7.98	9.67	11.70	9.84	1.8%
CaO	12.23	12.41	12.54	12.39	0.2%
Na_2O	2.23	2.06	1.74	1.98	3.7%
K_2O	0.18	0.10	0.01	0.10	3.7%
P_2O_5	0.15	0.10	0.02	0.08	12.3%
Rb	4.53	2.29	0.07	2.30	0.4%
Ba	53.2	27.0	1.3	27.3	1.0%
Th	0.602	0.320	0.018	0.310	3.0%
U	0.193	0.104	0.007	0.100	4.2%
Nb	9.71	5.12	0.47	5.09	0.6%
Ta	0.56	0.30	0.03	0.29	3.2%
La	5.79	3.14	0.59	3.19	1.6%
Ce	13.39	7.55	1.57	7.48	0.9%
Pb	0.41	0.22	0.05	0.23	2.3%
Pr	1.92	1.12	0.37	1.14	2.0%
Sr	108	74	48	78	5.7%
Nd	9.17	5.57	2.11	5.64	1.2%
Zr	68.7	43.1	17.5	43.1	0.1%
Hf	1.84	1.17	0.44	1.14	2.6%
Sm	2.68	1.75	0.82	1.75	0.0%
Eu	0.96	0.68	0.41	0.68	0.3%
Gd	3.72	2.68	1.77	2.74	2.5%
Tb	0.65	0.49	0.39	0.52	6.0%
Dy	4.34	3.46	2.41	3.38	2.4%
Ho	0.94	0.78	0.70	0.82	5.0%
Er	2.68	2.31	1.68	2.18	5.8%
Yb	2.64	2.41	1.92	2.28	5.2%
Y	26.6	22.1	17.0	21.8	1.6%
Lu	0.41	0.38	0.35	0.38	0.4%
Tb	0.45	0.58	0.72	0.62	0.61
Dy	3.21	3.91	4.78	4.03	3.99
Ho	0.74	0.85	1.03	0.87	0.87
Er	2.19	2.40	2.96	2.45	2.47
Yb	2.33	2.35	2.89	2.40	2.43
Lu	0.38	0.37	0.45	0.37	0.38

Table B5: Kds, Mantle Source Compositions and Melting Reactions Used in the Modeling

	K_d Olivine/Melt	K_d Opx/Melt	K_d Cpx/Melt	K_d Spl/melt	Metasomatized Source (MetaM) (Gale et al., 2011)	DM (S&S, 2004)
Rb	0.000045	0.00045	0.0006	0.000005	0.685	0.088
Sr	0.008	0.009	0.096	0.0003	15.189	9.800
Y	0.007	0.025	0.421	0.003	1.881	3.67*
Zr	0.0013	0.013	0.128	0.0003	5.483	6.789*
Nb	0.000041	0.0001	0.007	0.000005	1.240*	0.284*
Ba	0.000043	0.00004	0.00068	0.000005	8.072*	1.200
La	0.00005	0.00005	0.042	0.00002	0.706	0.234
Ce	0.00006	0.003	0.09	0.00003	1.473	0.772
Nd	0.0002	0.007	0.19	0.0002	0.851	0.713
Sm	0.0006	0.01	0.28	0.0004	0.223	0.270
Eu	0.00015	0.013	0.355	0.0006	0.084	0.107
Gd	0.00099	0.016	0.37	0.0009	0.288	0.395
Tb	0.002	0.021	0.382	0.0012	0.049	0.075
Dy	0.004	0.025	0.402	0.0015	0.326	0.531
Ho	0.006	0.029	0.41	0.0023	0.069	0.122
Er	0.0087	0.041	0.422	0.003	0.205	0.371
Yb	0.017	0.047	0.432	0.0045	0.212	0.401
Lu	0.02	0.052	0.439	0.0053	0.034	0.063
Hf	0.005	0.013	0.23	0.0003	0.155	0.199
Pb	0.0003	0.0021	0.086	0.000005	0.049*	0.025*
Th	0.00005	0.00005	0.003	0.000005	0.082*	0.014
U	0.00005	0.00005	0.0052	0.000005	0.024	0.005
$^{143}Nd/^{144}Nd$					0.513039 (FAMOUS)/ 0.513081 (N. Fam.)	0.513210
$^{206}Pb/^{204}Pb$					19.241 (FAMOUS)/ 19.243 (N. Fam.)	18.000
$^{207}Pb/^{204}Pb$					15.571 (FAMOUS)/ 15.574 (N. Fam.)	15.462
$^{208}Pb/^{204}Pb$					38.748 (FAMOUS)/ 38.785 (N. Fam.)	37.700

	Source mineralogy	*Melting reaction, cpx residual*	* = slightly modified value	
Ol	0.565	-0.33		
Opx	0.285	0.57		
Cpx	0.125	0.72		
Spl	0.025	0.04		

Appendix C

Supplementary Material for Chapter 4

Table C1: Regional D-MORB; E-MORB average trace element compositions

	n	**Pacific D-MORB Mean[1]**	± (95% conf)	n	**Atlantic D-MORB Mean[1]**	± (95% conf)	n	**E-MORB[2]**	± (95% conf)	n	**E-MORB[3]**	± (95% conf)
Ba	55	13.9	1.9	93	13.0	1.8	38	125.5	18.8	19	56.2	26.2
Be	25	0.77	0.06	39	0.55	0.04	8	0.56	0.23	7	0.74	0.10
Ce	59	12.96	1.26	102	9.23	0.59	37	25.52	3.73	19	17.16	4.23
Co	47	44.0	1.0	89	44.0	0.7	34	41.7	1.6	19	45.8	3.4
Cr	52	231	20	93	304	14	34	216	33	19	226	47
Cs	37	0.017	0.003	76	0.022	0.004	28	0.124	0.024	19	0.053	0.024
Cu	45	72	3	92	77	3	34	74	8	19	83	13
Dy	59	6.46	0.39	102	5.18	0.17	37	4.62	0.21	19	4.50	0.54
Er	58	4.08	0.24	102	3.29	0.11	37	2.75	0.12	19	2.74	0.37
Eu	59	1.40	0.09	102	1.13	0.04	37	1.29	0.08	19	1.17	0.13
Ga	42	17.7	0.4	96	16.6	0.3	27	17.3	0.7	18	17.4	1.1
Gd	59	5.21	0.32	102	4.08	0.15	37	4.26	0.26	19	3.99	0.49
Hf	54	2.90	0.30	101	2.08	0.15	37	2.54	0.26	19	2.44	0.37
Ho	58	1.38	0.09	100	1.14	0.04	35	0.96	0.05	19	0.96	0.13
La	59	4.03	0.39	102	2.84	0.20	38	12.02	1.66	19	7.07	2.12
Li	34	6.8	0.6	86	5.7	0.2	22	5.3	0.6	12	5.2	1.3
Lu	59	0.58	0.04	102	0.47	0.01	37	0.38	0.02	19	0.39	0.06
Mn	6	0.21	0.01	18	0.18	0.01	6	0.18	0.02	2	0.19	0.05
Mo	17	0.38	0.08	71	0.31	0.03	21	0.76	0.21	16	0.67	0.20
Nb	56	3.44	0.49	98	2.38	0.27	38	17.07	2.83	19	8.49	3.33
Nd	59	11.56	0.89	102	8.76	0.47	38	14.86	1.33	19	11.46	1.96
Ni	49	82	10	93	119	7	34	97	10	19	97	22
Pb	52	0.50	0.04	95	0.40	0.03	35	0.98	0.14	19	0.66	0.17
Pr	54	2.12	0.19	100	1.61	0.10	35	3.28	0.42	19	2.45	0.48
Rb	44	1.50	0.38	92	1.14	0.14	38	10.56	1.47	19	4.87	1.98
Sc	38	42.0	1.3	90	39.5	0.9	35	35.7	1.2	18	40.0	1.9
Sm	59	3.95	0.27	102	3.09	0.14	38	3.72	0.28	19	3.28	0.42
Sn	19	0.93	0.12	65	0.75	0.08	24	0.87	0.14	13	0.83	0.29
Sr	59	113	4	100	109	5	37	207	22	19	151	29
Ta	51	0.23	0.03	94	0.17	0.02	32	1.09	0.18	18	0.60	0.20
Tb	54	0.97	0.07	100	0.77	0.03	35	0.73	0.04	19	0.72	0.09
Th	53	0.236	0.035	99	0.149	0.018	36	1.367	0.232	19	0.643	0.250
Ti	23	1.57	0.14	88	1.36	0.06	27	1.50	0.11	14	1.47	0.21
Tl	17	0.018	0.002	76	0.017	0.001	21	0.031	0.005	12	0.022	0.013
U	51	0.084	0.013	97	0.049	0.005	36	0.386	0.061	19	0.202	0.069
V	43	348	22	97	284	7	35	265	10	18	297	20
W	22	0.08	0.01	79	0.09	0.01	23	0.31	0.07	13	0.17	0.11
Y	59	39.3	2.7	101	31.0	1.0	37	26.6	1.1	19	26.1	3.2
Yb	59	3.88	0.24	102	3.13	0.11	37	2.59	0.10	19	2.61	0.39
Zn	47	97.5	6.5	90	86.2	2.1	29	82.4	6.1	19	82.3	9.8
Zr	59	117.4	10.0	101	84.7	4.9	37	110.1	12.0	19	89.0	14.9

1= mean weighted by spreading rate and length
2= E-MORB calculated as the log-normal mean of segments with $La/Sm_N>1.5$, excluding back-arcs, weighted by length
3= E-MORB calculated as the log-normal mean of segments within 200 km of a hotspot, excluding back-arcs, weighted by length

Table C2: Global Catalog of Ridge Segments

Segment Name	Lat1	Lat2	Lon1	Lon2	Length	Spr. Rate	Spr. Azimuth	Mean Depth	Stdev. Depth	Min - Max Depth	Polygon Width	Min Depth	Max Depth	Plate Boundary
AARR1	-55.776	-56.304	-4.709	-4.658	58.7855	17.37	86.48	-3706	343	1068	10	-4328	-3260	AntaSoam
AARR10	-60.796	-60.332	-19.468	-19.419	51.7427	15.67	87.59	-3980	601	1986	10	-5193	-3208	AntaSoam
AARR2	-56.320	-56.569	-4.538	-4.538	27.6431	17.20	86.43	-3301	259	801	10	-3668	-2867	AntaSoam
AARR3	-56.579	-57.266	-6.091	-6.100	76.4485	17.03	86.53	-3334	369	1304	10	-3734	-2430	AntaSoam
AARR4	-57.330	-57.980	-6.988	-6.979	72.2454	16.74	86.55	-4100	431	1397	10	-4942	-3546	AntaSoam
AARR5	-58.464	-59.069	-16.067	-16.284	68.4618	16.39	87.37	-4517	223	823	10	-5123	-4301	AntaSoam
AARR6	-59.633	-59.134	-18.441	-17.865	64.2821	16.15	87.53	-4422	465	1387	10	-5350	-3963	AntaSoam
AARR7	-59.926	-59.637	-18.687	-18.457	34.6938	15.99	87.55	-3744	243	783	10	-4127	-3344	AntaSoam
AARR8	-59.955	-60.210	-18.749	-18.818	28.5692	15.87	87.55	-4068	86	242	10	-4197	-3955	AntaSoam
AARR9	-60.311	-60.222	-19.362	-18.827	31.1171	15.79	87.57	-3982	74	303	10	-4191	-3888	AntaSoam
AFAR1	13.042	12.717	57.598	58.264	80.7760	24.85	24.22	-3814	448	1668	10	-4720	-3051	AfriArab
AFAR10	13.369	13.136	50.611	51.242	73.0289	20.64	27.03	-3260	332	1252	10	-4047	-2795	AfriArab
AFAR11	13.342	13.206	50.255	50.566	36.8943	20.33	27.31	-3056	142	518	10	-3239	-2720	AfriArab
AFAR12	13.408	13.176	49.696	50.210	61.3179	20.05	27.58	-3055	144	545	10	-3246	-2701	AfriArab
AFAR13	13.127	13.066	49.344	49.525	20.6898	19.80	28.28	-2921	220	668	10	-3272	-2604	AfriArab
AFAR14	13.004	12.864	48.836	49.208	43.2224	19.61	28.87	-2403	172	575	10	-2753	-2179	AfriArab
AFAR15	12.780	12.543	48.087	48.569	58.6118	19.29	29.88	-2329	139	550	10	-2653	-2103	AfriArab
AFAR16	12.593	12.453	47.583	47.866	34.4837	18.98	30.62	-2408	240	761	10	-2767	-2006	AfriArab
AFAR17	12.364	12.181	46.969	47.294	40.7996	18.73	31.59	-2105	208	539	10	-2454	-1914	AfriArab
AFAR18	12.351	12.179	46.525	46.822	37.5242	18.46	32.02	-2026	145	430	10	-2206	-1777	AfriArab
AFAR19	12.138	12.019	46.081	46.388	35.8576	18.27	32.79	-1779	214	701	10	-2198	-1498	AfriArab
AFAR2	13.778	13.466	57.104	57.867	89.3905	24.40	23.36	-3355	408	1456	10	-3858	-2403	AfriArab
AFAR20	11.926	12.108	43.433	46.002	280.0938	17.42	34.46	-1192	176	974	10	-1840	-865	AfriArab
AFAR21	11.767	11.842	42.003	43.254	136.3800	16.32	37.38	367	560	2463	10	-1003	1460	AfriArab
AFAR22	11.211	11.841	41.672	41.248	83.8953	15.80	39.54	407	142	659	10	254	913	AfriArab
AFAR23	11.892	12.543	41.226	40.734	89.9387	15.21	38.80	562	160	473	10	372	845	AfriArab
AFAR24	12.558	12.919	40.681	40.424	48.9371	14.74	38.29	476	80	230	10	350	580	AfriArab
AFAR25	13.148	14.323	40.938	40.303	147.6519	14.34	35.89	-1	154	489	10	-126	363	AfriArab
AFAR26	14.353	15.559	40.280	39.592	153.1307	13.42	33.83	27	165	722	10	-121	601	AfriArab
AFAR27	16.621	16.194	40.834	41.296	68.4395	13.55	28.46	-1007	209	678	10	-1389	-711	AfriArab
AFAR28	16.621	17.600	40.897	40.318	125.0551	13.02	26.99	-1109	191	750	10	-1438	-688	AfriArab
AFAR29	17.503	18.099	40.350	39.951	78.5507	12.50	25.43	-1224	139	485	10	-1500	-1015	AfriArab
AFAR3	14.449	14.033	56.335	57.072	91.9305	23.79	22.75	-3374	203	940	10	-3805	-2864	AfriArab
AFAR30	18.099	19.092	39.943	39.309	129.0601	11.92	23.45	-1346	75	322	10	-1522	-1200	AfriArab

Table C2 (Continued)

AFAR31	19.041	19.683	39.348	38.785	92.6588	11.34	21.40	-1767	328	1363	10	-2602	-1238	AfriArab
AFAR32	19.764	20.769	38.621	38.081	125.1497	10.63	18.73	-1915	186	831	10	-2389	-1558	AfriArab
AFAR33	22.487	20.777	37.815	38.158	193.3340	10.09	13.52	-1810	286	1474	10	-2324	-850	AfriArab
AFAR34	23.896	22.474	36.572	37.844	204.7365	9.35	6.96	-1598	308	1341	10	-2461	-1120	AfriArab
AFAR35	25.338	23.937	36.147	36.535	160.6473	8.68	0.17	-1337	197	994	10	-2092	-1099	AfriArab
AFAR36	25.354	27.445	36.129	34.399	289.4264	8.06	10.27	-1224	178	1206	10	-2232	-1026	AfriArab
AFAR4	14.759	14.519	55.801	56.190	49.5808	23.27	22.41	-2959	148	503	10	-3222	-2719	AfriArab
AFAR5	14.857	14.560	55.175	55.566	53.5156	22.88	22.52	-2761	196	694	10	-3122	-2428	AfriArab
AFAR6	14.431	14.718	54.943	54.450	61.9180	22.51	22.99	-2579	282	983	10	-3102	-2118	AfriArab
AFAR7	14.649	14.483	53.954	54.311	42.6735	22.18	23.23	-2805	90	344	10	-2994	-2650	AfriArab
AFAR8	14.457	14.276	53.425	53.777	42.9746	21.91	23.77	-3390	118	395	10	-3595	-3199	AfriArab
AFAR9	14.765	14.288	52.240	53.252	121.1436	21.36	23.90	-2238	656	2347	10	-3695	-1348	AfriArab
CHIL1	-33.135	-34.552	-109.170	-109.246	157.7195	55.94	100.42	-3074	189	726	10	-3479	-2753	NazcAnta
CHIL10	-38.960	-39.831	-91.597	-91.505	97.1292	56.94	86.64	-3450	182	672	10	-3793	-3121	NazcAnta
CHIL11	-39.923	-40.178	-91.604	-91.576	28.4458	57.05	86.68	-3753	80	255	10	-3899	-3644	NazcAnta
CHIL12	-40.275	-41.049	-91.881	-91.838	86.1284	57.15	86.89	-3689	268	1041	10	-4358	-3318	NazcAnta
CHIL13	-41.076	-41.225	-91.300	-91.271	16.7807	57.22	86.46	-4131	74	292	10	-4310	-4018	NazcAnta
CHIL14	-41.183	-41.305	-90.336	-90.315	13.7362	57.24	85.72	-4301	131	575	10	-4461	-3886	NazcAnta
CHIL15	-41.284	-41.406	-89.153	-89.124	13.8138	57.27	84.81	-4637	454	1295	10	-5193	-3899	NazcAnta
CHIL16	-41.305	-41.454	-87.750	-87.707	16.9324	57.29	83.74	-4582	252	1135	10	-5283	-4148	NazcAnta
CHIL17	-41.316	-41.518	-85.653	-85.589	23.0720	57.32	82.13	-4488	110	440	10	-4713	-4273	NazcAnta
CHIL18	-41.449	-41.565	-84.682	-84.654	13.1887	57.34	81.41	-4470	460	1315	10	-5228	-3913	NazcAnta
CHIL19	-41.565	-41.782	-84.342	-84.285	24.5846	57.37	81.15	-3789	251	854	10	-4380	-3526	NazcAnta
CHIL2	-35.311	-35.741	-105.586	-105.678	48.4785	56.24	97.59	-3612	286	1215	10	-4582	-3366	NazcAnta
CHIL20	-41.698	-41.978	-84.030	-83.945	31.8993	57.40	80.90	-3898	160	589	10	-4235	-3646	NazcAnta
CHIL21	-42.004	-43.002	-83.718	-83.435	113.3455	57.48	80.60	-3606	263	1116	10	-4157	-3041	NazcAnta
CHIL22	-42.986	-43.846	-82.762	-82.464	98.5375	57.58	79.89	-3399	281	1046	10	-3800	-2754	NazcAnta
CHIL23	-43.815	-44.698	-82.457	-82.067	102.9731	57.65	79.64	-3384	197	740	10	-3772	-3032	NazcAnta
CHIL24	-44.707	-44.984	-81.972	-81.894	31.3761	57.70	79.40	-3594	97	439	10	-3857	-3418	NazcAnta
CHIL25	-44.395	-45.781	-78.404	-77.859	159.9137	57.75	76.56	-3222	334	1474	10	-3923	-2448	NazcAnta
CHIL26	-45.632	-45.933	-76.888	-76.725	35.8185	57.78	75.59	-3700	243	804	10	-4139	-3335	NazcAnta
CHIL27	-45.825	-46.292	-75.981	-75.804	53.7087	57.80	74.91	-3182	121	566	10	-3342	-2776	NazcAnta
CHIL3	-36.386	-36.989	-97.081	-97.074	66.9756	56.38	90.92	-3939	286	1124	10	-4586	-3462	NazcAnta
CHIL4	-36.994	-37.090	-96.203	-96.189	10.7699	56.46	90.23	-4147	201	529	10	-4419	-3891	NazcAnta
CHIL5	-37.056	-37.322	-95.338	-95.331	29.5067	56.49	89.56	-3974	262	844	10	-4353	-3509	NazcAnta

Table C2 (Continued)

CHIL6	-37.310	-38.123	-94.120	-94.077	90.4454	56.61	88.60	-3370	263	949	10	-3924	-2975	NazcAnta
CHIL7	-38.073	-38.301	-93.858	-93.850	25.3934	56.70	88.41	-3634	138	466	10	-3898	-3431	NazcAnta
CHIL8	-38.287	-38.397	-92.946	-92.940	12.2652	56.74	87.71	-3325	179	556	10	-3694	-3138	NazcAnta
CHIL9	-38.418	-38.949	-92.582	-92.540	59.1596	56.81	87.42	-3797	141	490	10	-4036	-3546	NazcAnta
CIRR1	-25.227	-25.481	69.914	70.017	30.1219	47.38	60.15	-4161	76	344	10	-4265	-3921	AfriAust
CIRR10	-20.766	-21.041	68.561	68.747	36.2226	43.24	59.24	-3219	101	307	10	-3417	-3110	AfriAust
CIRR11	-20.303	-20.836	68.039	68.383	69.2565	42.75	59.64	-2856	119	509	10	-3173	-2664	AfriAust
CIRR12	-20.103	-20.406	67.545	67.737	39.1876	42.23	60.24	-3368	146	407	10	-3581	-3175	AfriAust
CIRR13	-19.992	-20.366	66.737	67.003	50.0091	41.82	61.30	-3445	264	841	10	-4036	-3195	AfriAust
CIRR14	-19.346	-20.258	65.716	66.394	123.7548	41.13	62.25	-2900	296	1016	10	-3465	-2449	AfriAust
CIRR15	-19.065	-19.337	65.537	65.710	35.3591	40.42	62.51	-2841	59	177	10	-2947	-2771	AfriAust
CIRR16	-18.763	-18.998	65.424	65.567	30.2245	40.08	62.50	-2978	104	302	10	-3103	-2801	AfriAust
CIRR17	-17.953	-18.715	65.038	65.499	97.7766	39.49	62.48	-3119	268	701	10	-3468	-2767	AfriAust
CIRR18	-16.558	-16.956	66.481	66.850	59.2538	38.75	59.19	-3540	436	1452	10	-4371	-2919	AfriAust
CIRR19	-15.581	-16.008	67.091	67.446	60.6965	38.22	57.50	-3560	256	1093	10	-4123	-3031	AfriAust
CIRR2	-24.711	-25.140	69.851	70.112	54.4423	47.05	59.89	-3654	164	766	10	-3895	-3129	AfriAust
CIRR20	-14.792	-15.442	66.730	67.256	91.6583	37.49	57.35	-3248	184	745	10	-3696	-2951	AfriAust
CIRR21	-13.948	-14.867	65.859	66.577	128.1012	36.45	57.96	-2882	312	1387	10	-3869	-2482	AfriAust
CIRR22	-12.720	-13.307	66.307	66.724	79.3472	35.39	56.21	-3540	398	1648	10	-4782	-3135	AfriAust
CIRR23	-12.075	-12.751	65.673	66.198	94.3670	34.53	56.58	-3542	362	1408	10	-4234	-2825	AfriAust
CIRR24	-11.196	-11.587	66.126	66.453	56.2591	33.83	54.97	-3619	361	1256	10	-4408	-3152	AfriAust
CIRR25	-10.325	-10.857	66.267	66.693	75.1582	33.25	53.80	-3633	400	1247	10	-4254	-3007	AfriAust
CIRR26	-9.654	-9.907	66.595	66.834	38.4662	32.70	52.50	-3894	297	865	10	-4365	-3500	AfriAust
CIRR27	-7.824	-8.280	67.880	68.278	67.0707	34.91	40.31	-3656	553	1884	10	-4724	-2840	AfriIndi
CIRR28	-7.103	-7.455	67.915	68.270	55.2795	34.66	39.80	-3482	195	693	10	-3833	-3140	AfriIndi
CIRR29	-6.056	-6.549	68.013	68.535	79.6491	34.41	39.03	-3462	466	1588	10	-4448	-2859	AfriIndi
CIRR3	-23.771	-24.641	69.454	69.886	106.2739	46.36	59.89	-3373	353	1231	10	-3856	-2624	AfriAust
CIRR30	-5.217	-5.383	68.525	68.704	27.1095	34.22	38.13	-4250	356	1061	10	-4787	-3726	AfriIndi
CIRR31	-4.885	-5.102	68.390	68.589	32.6585	34.07	37.99	-3785	127	547	10	-3979	-3432	AfriIndi
CIRR32	-4.088	-4.530	68.278	68.774	73.7443	33.86	37.48	-3773	213	706	10	-4272	-3566	AfriIndi
CIRR33	-3.248	-3.717	68.004	68.633	87.1183	33.50	37.01	-3080	349	1237	10	-3876	-2639	AfriIndi
CIRR34	-2.656	-2.850	67.977	68.190	32.0339	33.16	36.61	-3668	74	235	10	-3764	-3529	AfriIndi
CIRR35	-2.000	-2.248	67.951	68.278	45.6786	32.97	36.11	-3644	274	809	10	-4098	-3289	AfriIndi
CIRR36	-1.389	-1.841	67.419	68.048	86.0812	32.64	35.94	-3566	331	1022	10	-3979	-2957	AfriIndi
CIRR37	-0.778	-1.035	67.251	67.605	48.6672	32.27	35.56	-3053	296	1289	10	-3639	-2350	AfriIndi

Table C2 (Continued)

CIRR38	-0.424	-0.654	67.038	67.392	46.9975	32.05	35.38	-3522	171	563	10	-3714	-3151	AfriIndi
CIRR39	0.001	-0.132	67.074	67.206	20.90	31.86	35.03	-3761	154	445	10	-3987	-3542	AfriIndi
CIRR4	-23.153	-23.720	69.145	69.488	72.1274	45.59	59.91	-3428	341	1212	10	-4005	-2793	AfriAust
CIRR40	0.258	0.134	66.958	67.118	22.4666	31.73	34.87	-3497	44	169	10	-3564	-3395	AfriIndi
CIRR41	0.595	0.356	66.737	67.056	44.3251	31.57	34.72	-3371	195	624	10	-3755	-3131	AfriIndi
CIRR42	0.819	1.095	66.871	66.551	46.9941	31.32	34.41	-2899	475	1346	10	-3484	-2137	AfriIndi
CIRR43	1.492	1.825	66.929	66.596	52.3795	31.12	33.76	-3342	314	959	10	-3717	-2758	AfriIndi
CIRR44	2.325	3.093	66.750	65.590	154.5852	30.49	33.14	-3369	269	978	10	-3864	-2886	AfriIndi
CIRR45	3.074	2.946	65.288	65.468	24.4830	30.00	33.31	-3864	109	399	10	-4005	-3606	AfriIndi
CIRR46	3.675	2.915	64.115	65.178	145.1930	29.54	33.46	-3825	268	967	10	-4265	-3298	AfriIndi
CIRR47	3.746	3.675	63.610	64.079	52.6867	28.99	33.52	-4078	186	617	10	-4385	-3768	AfriIndi
CIRR48	3.932	3.737	63.255	63.548	38.9871	28.72	33.66	-3962	143	545	10	-4310	-3765	AfriIndi
CIRR49	4.231	3.841	62.680	63.154	68.1763	28.40	33.76	-3353	171	675	10	-3868	-3194	AfriIndi
CIRR5	-22.883	-23.076	69.165	69.283	24.6750	45.19	59.77	-3504	96	304	10	-3667	-3364	AfriAust
CIRR50	4.934	4.321	62.039	62.699	100.0197	27.91	33.47	-3297	500	1605	10	-3783	-2178	AfriIndi
CIRR51	5.559	5.094	61.616	62.199	82.7776	27.43	33.00	-3338	327	1272	10	-3901	-2629	AfriIndi
CIRR52	6.059	5.600	60.863	61.607	96.8198	26.89	32.85	-3750	357	1147	10	-4335	-3188	AfriIndi
CIRR53	6.437	6.147	60.394	60.837	58.6543	26.40	32.71	-3706	298	830	10	-4182	-3351	AfriIndi
CIRR54	6.710	6.428	60.119	60.429	46.4130	26.11	32.60	-3385	287	785	10	-3728	-2943	AfriIndi
CIRR55	7.323	6.821	59.610	60.200	85.7581	25.73	32.23	-3345	404	1790	10	-4357	-2567	AfriIndi
CIRR56	8.067	7.605	59.027	59.764	96.0629	25.18	31.59	-3175	602	2041	10	-4011	-1970	AfriIndi
CIRR57	8.522	8.011	58.341	59.053	96.7874	24.64	31.49	-3426	211	751	10	-3827	-3075	AfriIndi
CIRR58	8.922	8.777	58.213	58.444	30.0796	24.23	30.95	-4102	193	601	10	-4355	-3754	AfriIndi
CIRR59	9.390	9.131	57.950	58.360	53.4527	23.99	30.49	-3830	158	434	10	-4055	-3621	AfriIndi
CIRR6	-22.191	-22.657	69.040	69.404	63.9427	44.74	59.43	-3544	224	867	10	-4097	-3230	AfriAust
CIRR60	9.970	9.722	57.509	58.032	63.5822	23.57	29.91	-3820	164	636	10	-4152	-3516	AfriIndi
CIRR61	10.119	9.834	56.722	57.200	61.2906	23.05	30.25	-3969	259	681	10	-4254	-3573	AfriIndi
CIRR7	-21.748	-22.102	68.985	69.198	45.0108	44.27	59.30	-3290	113	403	10	-3504	-3101	AfriAust
CIRR8	-21.409	-21.733	68.702	68.936	43.4138	43.86	59.45	-3104	126	418	10	-3367	-2950	AfriAust
CIRR9	-21.166	-21.389	68.523	68.686	30.0378	43.52	59.55	-2746	130	390	10	-2970	-2580	AfriAust
EPRR1	31.076	31.376	-114.465	-114.092	48.6822	44.52	136.73	-56	30	153	10	-176	-23	PaciNoam
EPRR10	23.609	23.247	-108.380	-108.646	48.5470	47.55	125.75	-2367	49	259	10	-2464	-2205	PaciNoam
EPRR11	22.894	22.250	-108.081	-108.551	86.3525	54.67	89.07	-3005	180	663	10	-3260	-2597	PaciCoco
EPRR12	22.222	21.938	-108.485	-108.706	38.9695	56.51	89.99	-2998	92	363	10	-3180	-2817	PaciCoco
EPRR13	21.904	21.304	-108.589	-109.009	79.6115	58.30	90.61	-2731	170	694	10	-3105	-2411	PaciCoco

Table C2 (Continued)

EPRR14	21.252	20.532	-108.784	-109.353	99.5885	60.98	91.37	-2745	153	665	10	-3208	-2543	PaciCoco
EPRR15	20.427	20.004	-109.185	-109.492	56.9538	63.52	92.07	-2713	67	371	10	-2882	-2510	PaciCoco
EPRR16	18.512	17.860	-106.236	-106.334	73.1355	71.39	84.22	-2754	80	461	10	-2981	-2520	PaciCoco
EPRR17	18.040	17.698	-105.699	-105.480	44.5728	72.83	82.62	-3047	56	281	10	-3177	-2896	PaciCoco
EPRR18	17.693	16.274	-105.471	-105.289	159.0565	76.13	82.45	-2744	63	251	8	-2884	-2633	PaciCoco
EPRR19	16.382	15.993	-105.397	-105.443	43.4887	78.99	82.82	-2620	189	544	8	-2862	-2318	PaciCoco
EPRR2	30.120	30.313	-114.051	-113.800	32.2688	45.11	135.44	-331	27	88	10	-376	-288	PaciNoam
EPRR20	15.966	15.416	-105.446	-105.356	61.8675	80.78	82.93	-2356	49	198	10	-2495	-2297	PaciCoco
EPRR21	15.420	15.192	-104.907	-104.822	26.9312	82.40	81.91	-3461	109	361	10	-3599	-3238	PaciCoco
EPRR22	15.210	14.411	-104.449	-104.315	89.9720	84.42	81.07	-2972	110	413	10	-3196	-2784	PaciCoco
EPRR23	14.392	13.670	-104.274	-104.139	81.6367	87.27	81.01	-2803	66	278	10	-2980	-2703	PaciCoco
EPRR24	13.671	12.899	-104.155	-103.979	87.9301	89.97	81.00	-2656	71	384	10	-2960	-2576	PaciCoco
EPRR25	12.899	12.657	-103.967	-103.905	27.7364	91.81	80.93	-2635	14	60	10	-2669	-2610	PaciCoco
EPRR26	12.639	11.721	-103.930	-103.781	103.4195	93.94	80.98	-2728	54	191	5	-2807	-2617	PaciCoco
EPRR27	11.822	11.128	-103.863	-103.742	78.2109	96.41	81.11	-2575	43	334	5	-2845	-2510	PaciCoco
EPRR28	11.131	10.301	-103.726	-103.579	93.6240	99.10	81.09	-2744	145	602	10	-3145	-2543	PaciCoco
EPRR29	10.167	9.108	-104.351	-104.191	119.0436	102.50	82.46	-2590	20	88	10	-2634	-2546	PaciCoco
EPRR3	29.634	29.848	-113.978	-113.746	32.6392	45.47	134.89	-702	105	356	10	-802	-446	PaciNoam
EPRR30	9.059	8.393	-104.271	-104.171	74.8747	105.62	82.60	-2598	27	116	10	-2657	-2541	PaciCoco
EPRR31	8.410	8.336	-103.944	-103.923	8.4952	106.94	82.21	-3624	119	365	10	-3811	-3447	PaciCoco
EPRR32	8.396	8.338	-103.526	-103.511	6.6032	107.16	81.54	-3121	17	56	10	-3145	-3089	PaciCoco
EPRR33	8.426	8.012	-102.900	-102.823	46.8049	108.00	80.51	-2757	38	161	10	-2858	-2698	PaciCoco
EPRR34	8.012	7.393	-102.836	-102.691	70.6793	109.77	80.50	-2746	35	130	10	-2808	-2677	PaciCoco
EPRR35	7.488	5.564	-102.797	-102.410	218.1448	113.76	80.59	-2823	64	331	10	-3014	-2684	PaciCoco
EPRR36	5.610	4.906	-102.497	-102.358	79.8301	118.00	80.66	-2800	110	457	10	-3128	-2672	PaciCoco
EPRR37	4.988	3.428	-102.456	-102.157	176.6438	121.45	80.75	-3060	75	357	10	-3218	-2861	PaciCoco
EPRR38	3.495	2.180	-102.265	-102.033	148.4871	125.89	80.86	-3079	145	573	10	-3406	-2833	PaciCoco
EPRR39	2.187	1.828	-102.070	-102.137	40.6216	128.53	80.98	-3323	166	681	10	-3686	-3005	PaciCoco
EPRR4	27.532	27.160	-111.327	-111.594	49.0182	45.85	131.18	-1994	83	337	10	-2069	-1733	PaciNoam
EPRR40	1.784	1.216	-102.274	-102.212	63.4971	130.04	81.28	-3052	71	282	10	-3172	-2889	PaciCoco
EPRR41	0.715	-1.219	-102.168	-102.576	219.8061	126.46	98.26	-3040	86	352	10	-3256	-2904	NazcPaci
EPRR42	-1.472	-2.717	-102.537	-102.723	139.9577	129.08	98.26	-3020	66	269	10	-3201	-2932	NazcPaci
EPRR43	-2.820	-3.739	-102.502	-102.682	104.1158	130.66	98.13	-3061	78	432	10	-3366	-2934	NazcPaci
EPRR44	-3.666	-4.038	-103.979	-104.059	42.3658	131.68	98.98	-3203	152	566	10	-3498	-2932	NazcPaci
EPRR45	-4.016	-4.595	-104.530	-104.640	65.6024	132.37	99.29	-2779	61	240	10	-2948	-2708	NazcPaci

Table C2 (Continued)

EPRR46	-4.552	-5.305	-106.315	-106.485	85.7674	133.53	100.35	-2651	65	237	10	-2768	-2531	NazcPaci
EPRR47	-5.256	-6.340	-106.615	-106.965	126.6108	134.66	100.50	-2795	117	427	10	-3046	-2619	NazcPaci
EPRR48	-6.250	-6.984	-107.411	-107.590	83.9906	135.77	100.85	-2850	108	480	10	-3086	-2606	NazcPaci
EPRR49	-6.990	-7.242	-107.631	-107.710	29.3891	136.37	100.90	-2813	49	224	10	-2957	-2733	NazcPaci
EPRR5	27.099	26.952	-111.352	-111.470	20.1490	46.11	130.83	-2003	38	148	10	-2039	-1890	PaciNoam
EPRR50	-7.268	-9.135	-107.774	-108.171	212.1562	137.62	100.98	-2914	92	626	10	-3377	-2751	NazcPaci
EPRR51	-8.898	-9.073	-109.670	-109.729	20.4833	138.81	101.92	-3056	117	443	10	-3340	-2897	NazcPaci
EPRR52	-9.053	-9.657	-109.894	-110.025	68.6607	139.24	102.03	-2714	86	320	10	-2926	-2607	NazcPaci
EPRR53	-9.656	-10.835	-110.071	-110.357	134.8297	140.17	102.10	-2733	49	204	10	-2843	-2639	NazcPaci
EPRR54	-10.832	-11.655	-110.377	-110.603	94.7208	141.17	102.17	-2916	66	347	10	-3133	-2786	NazcPaci
EPRR55	-11.671	-12.518	-110.686	-110.891	96.7836	142.00	102.27	-2681	66	343	10	-2925	-2582	NazcPaci
EPRR56	-12.550	-13.398	-110.853	-111.002	95.6655	142.79	102.28	-2771	165	644	10	-3087	-2443	NazcPaci
EPRR57	-13.279	-13.499	-111.156	-111.224	25.5875	143.19	102.40	-3230	85	405	10	-3399	-2993	NazcPaci
EPRR58	-13.385	-13.455	-111.931	-111.978	9.3339	143.35	102.82	-3645	68	255	10	-3781	-3526	NazcPaci
EPRR59	-13.361	-15.027	-112.318	-112.749	190.9987	144.07	103.08	-2673	87	376	10	-2971	-2596	NazcPaci
EPRR6	26.286	26.158	-110.514	-110.609	17.0991	46.26	129.56	-2254	107	508	10	-2474	-1966	PaciNoam
EPRR60	-14.982	-15.552	-112.784	-112.885	64.3224	144.94	103.17	-2746	133	427	10	-3028	-2601	NazcPaci
EPRR61	-15.533	-15.953	-112.912	-112.982	47.2111	145.30	103.20	-2742	85	281	10	-2926	-2644	NazcPaci
EPRR62	-15.941	-19.283	-112.974	-113.497	375.7560	146.60	103.24	-2809	109	562	10	-3154	-2592	NazcPaci
EPRR63	-19.324	-20.685	-113.514	-113.855	155.4629	148.04	103.35	-2910	110	490	10	-3258	-2768	NazcPaci
EPRR64	-20.610	-23.046	-114.131	-114.535	274.0615	148.99	103.61	-2997	105	440	10	-3249	-2809	NazcPaci
EPRR65	-22.925	-24.314	-115.461	-115.461	154.3942	149.80	104.14	-2988	234	1000	10	-3632	-2632	NazcPaci
EPRR66	-24.229	-24.533	-115.641	-116.254	70.6952	150.09	104.37	-3528	374	1408	10	-4131	-2723	NazcPaci
EPRR67	-24.869	-26.700	-116.544	-115.034	253.5241	150.47	104.25	-2695	273	1330	10	-3369	-2039	NazcPaci
EPRR68	-22.996	-25.017	-111.869	-112.067	225.6673	149.67	102.28	-3227	536	2522	10	-5140	-2619	NazcPaci
EPRR69	-24.753	-25.552	-112.410	-112.384	88.9611	150.09	102.47	-3035	159	538	10	-3307	-2769	NazcPaci
EPRR7	25.563	25.327	-109.768	-109.963	32.7504	46.51	128.41	-3204	79	495	10	-3321	-2826	PaciNoam
EPRR70	-27.364	-25.390	-112.779	-112.564	220.6185	150.46	102.59	-2643	89	403	10	-2844	-2442	NazcPaci
EPRR71	-27.364	-28.493	-112.942	-112.924	125.5626	150.82	102.70	-2378	169	598	10	-2760	-2162	NazcPaci
EPRR72	-28.463	-29.304	-113.010	-112.950	93.7194	150.98	102.71	-2548	212	712	10	-3035	-2323	NazcPaci
EPRR73	-29.346	-30.495	-111.725	-111.782	127.7921	151.08	102.04	-2607	125	514	10	-2823	-2309	NazcPaci
EPRR74	-30.626	-32.293	-111.868	-112.125	186.9246	151.20	102.17	-2394	41	263	10	-2599	-2337	NazcPaci
EPRR75	-32.309	-34.008	-112.411	-112.544	189.3808	151.21	102.42	-2448	74	344	10	-2654	-2310	NazcPaci
EPRR76	-34.047	-34.837	-112.737	-111.946	113.8692	151.13	102.36	-2707	285	1129	10	-3473	-2345	NazcPaci
EPRR8	24.668	24.443	-109.107	-109.278	30.3963	46.91	127.17	-3041	245	834	10	-3534	-2700	PaciNoam

Table C2 (Continued)

EPRR9	23.966	23.866	-108.689	-108.755	12.9770	47.22	126.30	-3039	482	1431	10	-4099	-2668	PaciNoam
GAKK1	79.945	78.468	123.226	125.697	171.9852	6.88	108.01	-3192	261	945	10	-3524	-2579	NoamEura
GAKK10	86.652	87.010	45.666	59.007	90.9047	10.75	179.54	-4681	424	1597	10	-5141	-3545	NoamEura
GAKK11	85.990	86.650	29.529	45.366	134.0998	11.09	164.86	-4356	477	1586	10	-5114	-3528	NoamEura
GAKK12	85.928	85.984	22.418	29.437	55.3593	11.39	153.25	-4634	151	477	10	-4921	-4444	NoamEura
GAKK13	85.199	85.925	11.686	22.317	121.6672	11.67	144.36	-4544	369	1474	10	-4986	-3512	NoamEura
GAKK14	84.607	85.199	2.843	11.551	108.1347	12.03	134.64	-4663	265	1037	10	-5183	-4147	NoamEura
GAKK15	84.126	84.506	0.043	2.829	52.2315	12.31	128.92	-3856	235	758	10	-4182	-3425	NoamEura
GAKK16	83.583	84.115	-3.669	-0.037	73.2378	12.51	125.63	-3593	317	1088	10	-4115	-3027	NoamEura
GAKK17	83.222	83.577	-5.501	-3.740	45.4284	12.70	122.88	-3586	370	1260	10	-4250	-2990	NoamEura
GAKK18	83.209	82.934	-5.513	-6.731	34.6706	12.82	121.35	-3977	182	671	10	-4311	-3640	NoamEura
GAKK2	81.498	79.958	120.340	123.253	178.9208	7.50	110.44	-3849	580	2106	10	-5216	-3111	NoamEura
GAKK3	82.238	81.517	118.628	120.113	83.5226	7.96	112.61	-4521	609	2098	10	-5197	-3098	NoamEura
GAKK4	83.365	82.309	116.062	118.443	122.0247	8.34	114.37	-4253	52	247	10	-4376	-4129	NoamEura
GAKK5	83.374	84.888	115.960	101.831	231.5243	8.94	123.20	-4140	108	463	10	-4381	-3918	NoamEura
GAKK6	85.351	84.891	89.776	101.814	124.4890	9.52	136.95	-4178	151	576	10	-4421	-3844	NoamEura
GAKK7	85.982	85.359	77.364	89.708	124.2424	9.93	149.50	-4090	90	337	10	-4272	-3935	NoamEura
GAKK8	86.743	85.994	65.955	77.082	113.9511	10.31	160.90	-3936	423	1873	10	-4799	-2926	NoamEura
GAKK9	87.044	86.851	60.123	65.923	40.4368	10.54	168.53	-4338	201	647	10	-4635	-3988	NoamEura
GALA1	1.116	0.708	-102.177	-102.239	45.9175	38.56	10.43	-2919	41	172	10	-3034	-2862	CocoNazc
GALA10	2.371	2.097	-93.246	-92.198	120.3807	53.05	5.53	-2022	147	560	10	-2376	-1816	CocoNazc
GALA11	2.153	1.851	-92.137	-90.823	149.7320	54.93	5.75	-1882	142	744	10	-2367	-1624	CocoNazc
GALA12	1.034	0.759	-90.793	-89.222	177.2680	57.26	7.19	-1792	82	414	10	-1945	-1531	CocoNazc
GALA13	0.827	0.719	-89.160	-87.831	148.2527	59.45	7.11	-1966	102	340	10	-2139	-1799	CocoNazc
GALA14	0.677	0.751	-87.770	-87.045	81.0902	60.99	7.03	-2244	104	413	10	-2422	-2010	CocoNazc
GALA15	0.890	0.697	-87.109	-85.331	198.9446	62.62	6.76	-2471	122	533	10	-2744	-2211	CocoNazc
GALA16	1.755	1.720	-85.246	-84.690	61.9722	64.20	5.45	-3105	144	480	10	-3355	-2875	CocoNazc
GALA17	3.343	3.264	-84.257	-82.945	145.8903	65.88	3.52	-3254	321	1194	10	-4082	-2889	CocoNazc
GALA2	1.203	1.478	-102.163	-101.494	80.4098	39.05	9.26	-2791	298	1089	10	-3384	-2295	CocoNazc
GALA3	2.276	2.153	-101.551	-100.315	138.0237	40.29	6.96	-3679	328	1399	10	-4626	-3227	CocoNazc
GALA4	2.248	2.181	-100.292	-98.973	146.7775	42.37	6.67	-3155	306	1337	10	-3801	-2464	CocoNazc
GALA5	2.202	2.286	-98.965	-97.857	123.4778	44.30	6.36	-3026	318	1375	10	-3769	-2394	CocoNazc
GALA6	2.178	2.105	-97.809	-96.499	145.7903	46.29	6.34	-3223	165	787	10	-3752	-2965	CocoNazc
GALA7	2.350	2.305	-96.470	-95.631	93.4022	47.97	5.81	-2865	140	604	10	-3270	-2666	CocoNazc
GALA8	2.308	2.362	-95.618	-95.351	30.2771	48.84	5.71	-2952	126	401	10	-3174	-2773	CocoNazc

Table C2 (Continued)

GALA9	2.649	2.480	-95.412	-93.261	239.7319	50.57	5.16	-2584	279	1124	10	-3351	-2228	CocoNazc
JUAN1	51.535	51.367	-130.754	-131.085	29.5815	54.60		-2074	176	564	10	-2459	-1895	JFPA
JUAN10	46.246	45.546	-129.896	-130.123	79.7941	50.40		-1904	224	806	9	-2310	-1504	JFPA
JUAN11	45.556	45.061	-129.931	-130.223	59.6724	50.00		-2431	30	155	6	-2520	-2365	JFPA
JUAN12	45.084	44.525	-130.164	-130.456	66.2688	49.50		-2190	58	242	10	-2339	-2097	JFPA
JUAN13	43.840	43.702	-128.696	-128.729	15.5063	49.00		-3452	56	203	10	-3509	-3305	JFPA
JUAN14	43.402	43.288	-127.719	-127.794	14.0925	48.80		-2812	214	891	10	-3044	-2154	JFPA
JUAN15	42.998	42.433	-126.585	-126.925	68.7427	48.60		-3365	259	938	10	-3974	-3036	JFPA
JUAN16	42.427	41.610	-127.019	-127.262	93.0485	47.90		-3370	174	614	10	-3714	-3100	JFPA
JUAN17	41.543	40.455	-127.453	-127.496	121.0117	47.00		-3243	100	461	10	-3452	-2991	JFPA
JUAN2	50.914	50.746	-130.306	-130.583	26.9714	54.20		-2327	104	291	10	-2476	-2185	JFPA
JUAN3	50.347	50.114	-130.051	-130.381	34.9524	53.80		-2225	123	435	10	-2453	-2018	JFPA
JUAN4	49.982	49.249	-130.071	-130.668	92.1378	53.30		-2334	316	1125	10	-2895	-1769	JFPA
JUAN5	48.740	48.324	-128.904	-129.125	48.9835	52.70		-2929	98	462	10	-3057	-2594	JFPA
JUAN6	48.252	48.110	-128.951	-129.046	17.3809	52.40		-2684	54	239	10	-2773	-2534	JFPA
JUAN7	48.100	47.645	-129.011	-129.315	55.4423	52.10		-2368	215	655	10	-2717	-2062	JFPA
JUAN8	47.515	46.534	-128.876	-129.492	118.5932	51.50		-2516	119	426	10	-2691	-2265	JFPA
JUAN9	46.551	46.051	-129.565	-129.870	60.2918	50.80		-2260	102	371	6	-2476	-2105	JFPA
MARR1	81.911	82.325	-5.049	-3.663	50.6041	13.06	122.06	-3851	198	688	10	-4043	-3355	NoamEura
MARR10	75.327	74.698	7.743	8.412	72.5198	14.53	126.08	-3233	171	627	10	-3473	-2847	NoamEura
MARR100	32.319	32.657	-40.139	-40.064	38.2584	22.11	103.28	-3063	217	762	10	-3465	-2702	AfriNoam
MARR101	32.165	32.303	-40.361	-40.139	25.8759	22.18	103.24	-3470	167	586	10	-3706	-3120	AfriNoam
MARR102	32.162	31.813	-40.377	-40.540	41.6789	22.26	103.20	-2926	238	813	10	-3407	-2594	AfriNoam
MARR103	31.522	31.816	-41.036	-40.537	57.4261	22.35	103.16	-3527	306	1099	8	-3932	-2834	AfriNoam
MARR104	31.478	31.143	-41.052	-41.228	40.7496	22.46	103.12	-3481	124	503	10	-3721	-3218	AfriNoam
MARR105	31.177	30.805	-41.362	-41.600	47.1481	22.55	103.07	-3406	181	751	10	-3810	-3059	AfriNoam
MARR106	30.830	30.587	-41.701	-41.825	29.5842	22.63	103.04	-3401	57	275	10	-3529	-3254	AfriNoam
MARR107	30.022	30.589	-42.013	-41.863	64.7125	22.74	102.98	-3727	633	2504	10	-4979	-2475	AfriNoam
MARR108	30.125	29.369	-42.657	-42.904	87.4282	22.91	102.92	-3630	591	2896	10	-4958	-2062	AfriNoam
MARR109	29.362	28.905	-43.107	-43.247	52.6129	23.07	102.84	-3290	141	534	10	-3641	-3108	AfriNoam
MARR11	74.688	73.648	8.890	8.494	116.2097	14.72	125.89	-2905	139	554	10	-3121	-2566	NoamEura
MARR110	28.889	28.648	-43.254	-43.610	43.7932	23.16	102.79	-3581	133	618	10	-3893	-3275	AfriNoam
MARR111	28.646	28.159	-43.612	-43.865	59.5522	23.26	102.75	-3459	208	829	10	-3962	-3133	AfriNoam
MARR112	28.159	27.736	-43.913	-44.051	48.9925	23.37	102.70	-3477	228	782	10	-3841	-3059	AfriNoam
MARR113	27.681	27.117	-44.128	-44.346	66.3025	23.50	102.63	-3656	300	1024	10	-4120	-3096	AfriNoam

Table C2 (Continued)

MARR114	26.593	27.111	-44.589	-44.451	59.2229	23.63	102.57	-3658	192	658	10	-3996	-3338	AfriNoam
MARR115	26.579	26.370	-44.593	-44.661	24.2132	23.71	102.53	-3811	139	576	10	-4201	-3625	AfriNoam
MARR116	26.359	26.009	-44.665	-44.881	44.5172	23.78	102.50	-3926	360	1300	10	-4395	-3095	AfriNoam
MARR117	26.013	25.634	-44.881	-45.225	54.4498	23.87	102.46	-3829	331	1252	10	-4400	-3148	AfriNoam
MARR118	25.588	24.909	-45.256	-45.503	79.4070	23.99	102.40	-3740	416	1370	10	-4393	-3023	AfriNoam
MARR119	24.587	24.891	-46.129	-45.667	57.5945	24.11	102.35	-4272	196	923	10	-4684	-3761	AfriNoam
MARR12	73.316	73.621	7.010	8.405	55.6734	14.95	124.72	-2733	179	588	10	-2999	-2411	NoamEura
MARR120	24.594	23.852	-46.199	-46.345	83.7733	24.23	102.30	-4371	275	1109	10	-5010	-3901	AfriNoam
MARR121	23.641	23.123	-44.905	-44.988	58.1921	24.34	102.21	-3957	544	1818	10	-5216	-3398	AfriNoam
MARR122	23.127	22.725	-44.937	-44.972	44.7765	24.42	102.17	-3668	218	765	10	-4092	-3328	AfriNoam
MARR123	22.693	22.093	-45.001	-45.138	68.1679	24.52	102.12	-3952	199	970	10	-4327	-3357	AfriNoam
MARR124	22.072	21.437	-45.190	-45.316	71.8709	24.64	102.07	-3226	326	1056	10	-3760	-2703	AfriNoam
MARR125	21.408	21.006	-45.722	-45.791	45.3135	24.75	102.02	-3918	191	848	10	-4324	-3476	AfriNoam
MARR126	20.913	20.685	-45.674	-45.718	25.8220	24.82	101.99	-3494	132	551	10	-3731	-3180	AfriNoam
MARR127	20.668	20.341	-45.595	-45.687	37.5458	24.87	101.96	-2770	481	1508	10	-3440	-1932	AfriNoam
MARR128	20.370	19.789	-45.648	-45.730	65.2135	24.94	101.93	-4029	199	876	10	-4339	-3464	AfriNoam
MARR129	19.814	18.901	-45.911	-46.067	102.7877	23.68	94.42	-3551	233	1155	10	-4071	-2916	AfriSoam
MARR13	72.585	73.287	3.186	6.881	143.5407	15.22	122.57	-2960	231	1201	10	-3353	-2152	NoamEura
MARR130	18.909	18.496	-46.240	-46.349	47.3234	23.97	94.57	-3820	169	707	10	-4206	-3499	AfriSoam
MARR131	18.525	17.908	-46.606	-46.746	70.1607	24.19	94.78	-3907	300	1026	10	-4513	-3487	AfriSoam
MARR132	17.879	17.622	-46.733	-46.410	44.5614	24.39	94.67	-4208	291	946	10	-4712	-3766	AfriSoam
MARR133	17.651	16.997	-46.384	-46.502	73.6993	24.56	94.56	-3714	378	1801	10	-4356	-2555	AfriSoam
MARR134	16.910	16.262	-46.423	-46.628	75.2264	24.87	94.55	-3925	527	1684	10	-4780	-3096	AfriSoam
MARR135	16.237	15.399	-46.641	-46.611	93.3163	25.19	94.56	-3796	556	2085	10	-5114	-3030	AfriSoam
MARR136	15.196	14.751	-44.800	-45.078	57.8271	25.49	93.46	-4075	430	1435	10	-5065	-3630	AfriSoam
MARR137	14.734	13.693	-45.072	-45.000	115.9748	25.80	93.47	-3297	310	1116	10	-4033	-2917	AfriSoam
MARR138	13.630	12.736	-44.884	-44.865	99.4416	26.20	93.32	-3367	431	1562	10	-4091	-2529	AfriSoam
MARR139	12.603	12.136	-44.050	-44.050	51.9836	26.50	92.79	-4339	182	594	10	-4637	-4043	AfriSoam
MARR14	72.139	72.574	0.189	3.225	113.1431	15.53	120.02	-2879	246	939	10	-3340	-2401	NoamEura
MARR140	12.168	11.858	-43.966	-43.733	42.7700	26.63	92.66	-3621	734	2102	10	-4732	-2629	AfriSoam
MARR141	11.883	10.849	-43.733	-43.700	114.9742	26.87	92.56	-4416	449	1662	10	-5302	-3641	AfriSoam
MARR142	10.760	10.124	-40.887	-40.932	70.8933	27.19	90.88	-4261	291	1117	10	-4904	-3787	AfriSoam
MARR143	10.135	9.992	-40.928	-40.730	26.8721	27.33	90.83	-4284	93	528	10	-4516	-3988	AfriSoam
MARR144	9.978	9.481	-40.719	-40.680	55.4516	27.45	90.75	-3805	395	1454	10	-4664	-3209	AfriSoam
MARR145	9.474	9.382	-40.673	-40.522	19.4705	27.56	90.69	-3922	68	208	10	-4074	-3866	AfriSoam

Table C2 (Continued)

MARR146	9.372	8.874	-40.499	-40.499	55.3862	27.67	90.63	-4348	145	738	10	-4811	-4073	AfriSoam
MARR147	8.817	8.247	-39.632	-39.658	63.3618	27.88	90.14	-3495	947	3157	10	-5216	-2059	AfriSoam
MARR148	8.119	7.748	-38.054	-38.067	41.3367	28.09	89.24	-4349	348	1215	10	-5135	-3920	AfriSoam
MARR149	7.741	7.498	-36.793	-36.793	27.0871	28.21	88.53	-4642	125	381	10	-4848	-4467	AfriSoam
MARR15	71.860	72.119	-1.543	0.098	63.3638	15.74	118.23	-2720	130	445	10	-2936	-2492	NoamEura
MARR150	7.427	7.203	-34.639	-34.639	24.9655	28.34	87.33	-4596	151	617	10	-4920	-4302	AfriSoam
MARR151	7.164	6.882	-33.889	-33.999	33.6705	28.45	86.95	-3992	143	469	10	-4259	-3790	AfriSoam
MARR152	6.810	6.207	-33.835	-33.747	67.7732	28.63	86.88	-4238	105	363	10	-4438	-4075	AfriSoam
MARR153	6.188	5.853	-33.320	-33.262	37.7441	28.80	86.63	-3726	192	593	10	-4066	-3474	AfriSoam
MARR154	5.783	5.268	-33.022	-32.815	61.6793	28.97	86.44	-3289	264	779	10	-3696	-2917	AfriSoam
MARR155	5.306	3.933	-32.803	-32.550	155.2201	29.26	86.35	-3895	313	1552	10	-5023	-3471	AfriSoam
MARR156	3.977	3.559	-31.530	-31.534	46.4950	29.55	85.77	-3884	287	1013	10	-4400	-3387	AfriSoam
MARR157	3.555	3.438	-31.526	-31.450	15.4999	29.64	85.76	-3874	117	405	10	-4023	-3618	AfriSoam
MARR158	3.436	3.152	-31.406	-31.341	32.3978	29.70	85.71	-3727	198	694	10	-3981	-3287	AfriSoam
MARR159	3.191	2.655	-31.347	-31.283	60.0441	29.82	85.69	-3600	162	596	10	-3900	-3304	AfriSoam
MARR16	71.730	71.880	-2.679	-1.853	33.1626	15.85	117.13	-2364	172	592	10	-2718	-2127	NoamEura
MARR160	2.654	2.565	-31.264	-30.805	51.9603	29.92	85.56	-3500	222	870	10	-4145	-3275	AfriSoam
MARR161	2.563	1.573	-30.776	-30.671	110.6958	30.08	85.42	-3069	393	1441	10	-3734	-2293	AfriSoam
MARR162	1.523	1.293	-30.686	-30.540	30.3209	30.28	85.39	-3363	274	1149	10	-4086	-2936	AfriSoam
MARR163	1.282	0.783	-30.497	-30.397	56.6562	30.39	85.32	-3300	430	1675	10	-4268	-2593	AfriSoam
MARR164	1.052	0.825	-27.691	-27.676	25.2542	30.49	83.91	-4413	162	516	10	-4654	-4137	AfriSoam
MARR165	0.904	0.683	-26.371	-26.358	24.6449	30.57	83.26	-4756	115	370	10	-4973	-4603	AfriSoam
MARR166	0.787	0.530	-25.489	-25.462	28.7095	30.64	82.82	-4585	194	565	10	-4966	-4401	AfriSoam
MARR167	0.570	-1.149	-25.065	-24.527	200.3271	30.91	82.54	-3798	298	1797	10	-4943	-3146	AfriSoam
MARR168	-0.229	0.202	-16.280	-16.837	78.3176	31.20	78.58	-3950	381	1674	10	-5057	-3383	AfriSoam
MARR169	-0.223	-0.643	-16.239	-16.015	52.8670	31.32	78.42	-3731	368	1254	10	-4332	-3078	AfriSoam
MARR17	71.556	71.718	-3.778	-2.744	40.4782	15.94	116.41	-2206	176	629	10	-2639	-2010	NoamEura
MARR170	-0.689	-1.544	-16.073	-15.855	98.1983	31.50	78.41	-4054	392	1665	10	-5231	-3566	AfriSoam
MARR171	-0.890	-1.562	-13.155	-12.971	77.4579	31.67	77.12	-4055	284	1307	10	-4954	-3646	AfriSoam
MARR172	-1.556	-2.021	-12.994	-12.919	52.3728	31.81	77.12	-3913	157	704	10	-4143	-3439	AfriSoam
MARR173	-1.998	-2.296	-12.695	-12.575	35.7948	31.90	77.02	-3970	124	417	10	-4212	-3795	AfriSoam
MARR174	-2.337	-3.008	-12.305	-12.040	80.2115	32.04	76.86	-3597	243	1047	10	-4261	-3214	AfriSoam
MARR175	-3.111	-3.891	-12.299	-12.058	90.7471	32.22	76.94	-3595	171	529	10	-3768	-3239	AfriSoam
MARR176	-3.898	-4.042	-12.082	-12.239	23.6546	32.31	76.97	-4073	137	434	10	-4231	-3797	AfriSoam
MARR177	-4.069	-4.567	-12.264	-12.374	56.7192	32.38	77.07	-3199	298	1253	10	-4016	-2763	AfriSoam

Table C2 (Continued)

MARR178	-4.613	-5.111	-12.483	-12.282	59.6843	32.48	77.14	-3088	314	963	10	-3635	-2672	AfriSoam
MARR179	-4.933	-5.860	-11.564	-11.512	103.1743	32.62	76.82	-3366	381	1324	10	-4104	-2780	AfriSoam
MARR18	71.564	71.367	-3.907	-4.979	43.7875	16.03	115.56	-2329	266	878	10	-2665	-1787	NoamEura
MARR180	-5.865	-6.659	-11.518	-11.282	92.0150	32.79	76.83	-3297	417	1544	10	-4249	-2705	AfriSoam
MARR181	-7.110	-7.315	-13.023	-13.005	22.8924	32.89	77.58	-4486	166	567	10	-4763	-4196	AfriSoam
MARR182	-7.440	-8.191	-13.482	-13.407	83.9340	32.98	77.81	-3786	360	1717	10	-5026	-3309	AfriSoam
MARR183	-8.237	-9.311	-13.569	-13.308	122.808	33.14	77.86	-2654	378	1638	10	-3664	-2025	AfriSoam
MARR184	-9.307	-10.100	-13.312	-13.117	90.7293	33.29	77.82	-2162	337	1211	10	-2754	-1543	AfriSoam
MARR185	-11.526	-10.155	-12.894	-13.225	156.6878	33.47	77.82	-3248	215	1061	10	-3980	-2920	AfriSoam
MARR186	-11.828	-12.148	-14.418	-14.309	37.5301	33.59	78.43	-3507	169	511	10	-3766	-3256	AfriSoam
MARR187	-12.345	-13.493	-14.798	-14.424	133.8885	33.70	78.58	-3219	489	1877	10	-4249	-2373	AfriSoam
MARR188	-13.588	-14.123	-14.620	-14.424	63.1571	33.81	78.58	-3805	162	622	10	-4158	-3536	AfriSoam
MARR189	-13.992	-16.037	-13.665	-13.165	233.6607	33.96	78.15	-2885	317	1688	10	-3779	-2091	AfriSoam
MARR19	71.368	70.908	-5.144	-6.334	66.6793	16.17	114.59	-1768	537	1745	10	-2747	-1001	NoamEura
MARR190	-16.384	-17.960	-14.314	-14.091	176.8113	34.14	78.55	-3448	433	2074	10	-4564	-2490	AfriSoam
MARR191	-17.676	-18.768	-12.974	-12.772	123.2338	34.24	78.02	-3750	419	1608	10	-4769	-3161	AfriSoam
MARR192	-18.725	-19.247	-12.181	-12.108	58.5022	34.30	77.73	-2820	308	999	10	-3375	-2377	AfriSoam
MARR193	-19.168	-20.041	-11.931	-11.900	97.0837	34.34	77.65	-3525	375	1398	10	-4116	-2717	AfriSoam
MARR194	-20.089	-21.158	-11.861	-11.495	124.7656	34.39	77.57	-3618	424	1537	10	-4329	-2792	AfriSoam
MARR195	-21.280	-22.111	-11.944	-11.670	96.6467	34.42	77.63	-3684	248	864	10	-4185	-3321	AfriSoam
MARR196	-22.363	-22.668	-12.819	-12.740	34.8694	34.44	78.05	-4209	236	697	10	-4554	-3857	AfriSoam
MARR197	-22.923	-23.632	-13.676	-13.421	82.9958	34.45	78.38	-3875	261	1071	10	-4560	-3488	AfriSoam
MARR198	-23.687	-24.437	-13.505	-13.263	86.9925	34.47	78.31	-3424	191	614	10	-3669	-3056	AfriSoam
MARR199	-24.511	-24.806	-13.453	-13.330	35.0571	34.47	78.32	-3755	290	811	10	-4234	-3424	AfriSoam
MARR2	81.421	81.770	-4.502	-3.291	43.4690	13.19	122.03	-3468	363	1205	10	-3994	-2789	NoamEura
MARR20	70.656	71.657	-14.001	-12.252	127.8024	16.43	109.87	-1303	527	1611	10	-2273	-662	NoamEura
MARR200	-24.936	-25.600	-13.761	-13.570	76.2950	34.47	78.43	-3392	444	1829	10	-4326	-2498	AfriSoam
MARR201	-25.696	-26.603	-13.947	-13.724	103.3349	34.47	78.50	-3588	372	1664	10	-4178	-2514	AfriSoam
MARR202	-26.603	-27.362	-13.628	-13.437	86.4626	34.45	78.37	-3559	82	396	10	-3786	-3389	AfriSoam
MARR203	-27.343	-28.298	-13.490	-13.176	110.5975	34.43	78.28	-3611	245	1080	10	-4173	-3094	AfriSoam
MARR204	-28.186	-28.798	-12.676	-12.463	71.2218	34.41	77.95	-3629	243	909	10	-4059	-3150	AfriSoam
MARR205	-28.919	-29.129	-13.117	-13.080	23.5635	34.39	78.17	-3728	334	1112	10	-4476	-3364	AfriSoam
MARR206	-29.254	-29.745	-13.761	-13.655	55.5374	34.37	78.42	-3577	137	458	10	-3812	-3354	AfriSoam
MARR207	-29.828	-30.646	-13.883	-13.703	92.6136	34.34	78.44	-3230	248	1064	10	-3603	-2539	AfriSoam
MARR208	-30.633	-31.239	-13.548	-13.410	68.7631	34.30	78.30	-3487	141	844	10	-3914	-3070	AfriSoam

Table C2 (Continued)

MARR209	-31.236	-31.354	-13.409	-13.486	15.0812	34.28	78.27	-3549	249	750	10	-3935	-3185	AfriSoam
MARR21	69.996	70.704	-15.578	-14.633	86.2400	16.71	108.35	-1385	338	1263	10	-2245	-982	NoamEura
MARR210	-31.353	-32.082	-13.500	-13.298	83.2435	34.25	78.24	-3448	255	987	10	-3895	-2908	AfriSoam
MARR211	-32.329	-32.473	-14.304	-14.298	15.9865	34.21	78.62	-3805	82	338	10	-3984	-3646	AfriSoam
MARR212	-32.536	-33.411	-14.543	-14.320	99.4696	34.17	78.66	-3146	436	1458	10	-3927	-2469	AfriSoam
MARR213	-33.420	-33.663	-14.329	-14.591	36.4126	34.13	78.66	-4115	188	756	10	-4587	-3831	AfriSoam
MARR214	-33.646	-34.101	-14.570	-14.495	51.0578	34.10	78.68	-3772	237	829	10	-4307	-3478	AfriSoam
MARR215	-34.246	-34.461	-15.214	-15.182	24.1077	34.07	78.96	-3772	179	485	10	-3975	-3490	AfriSoam
MARR216	-34.474	-34.702	-15.123	-15.086	25.5471	34.04	78.91	-3246	169	768	10	-3769	-3001	AfriSoam
MARR217	-34.785	-35.199	-15.219	-15.112	47.0549	34.01	78.92	-3495	350	1088	10	-4190	-3102	AfriSoam
MARR218	-35.648	-36.323	-17.818	-17.548	78.8638	33.94	80.01	-3655	368	1268	10	-4221	-2953	AfriSoam
MARR219	-36.362	-37.334	-17.451	-17.250	109.5930	33.85	79.83	-3204	414	1508	10	-3758	-2250	AfriSoam
MARR22	69.968	68.887	-15.363	-16.707	131.1053	16.99	107.50	-1066	192	806	10	-1593	-787	NoamEura
MARR220	-37.418	-38.056	-17.515	-17.380	71.8644	33.74	79.84	-3520	334	1153	10	-4228	-3075	AfriSoam
MARR221	-38.122	-38.407	-17.086	-17.110	31.7891	33.67	79.67	-3382	218	660	10	-3800	-3140	AfriSoam
MARR222	-38.312	-38.549	-16.425	-16.383	26.6280	33.64	79.35	-3614	552	1479	10	-4520	-3041	AfriSoam
MARR223	-38.586	-39.148	-16.132	-15.847	67.1817	33.57	79.14	-3564	113	405	10	-3806	-3401	AfriSoam
MARR224	-39.133	-39.339	-15.805	-16.006	28.6489	33.52	79.09	-3754	35	98	10	-3802	-3704	AfriSoam
MARR225	-39.299	-39.702	-16.001	-15.913	45.3955	33.49	79.10	-3773	130	453	10	-4057	-3604	AfriSoam
MARR226	-39.816	-40.308	-16.553	-16.437	55.5398	33.42	79.32	-3357	249	753	10	-3669	-2916	AfriSoam
MARR227	-40.365	-41.159	-16.765	-16.793	88.2980	33.32	79.41	-3306	170	814	10	-3687	-2873	AfriSoam
MARR228	-41.152	-41.547	-16.728	-16.602	45.1814	33.23	79.33	-3744	222	1402	10	-4735	-3333	AfriSoam
MARR229	-41.523	-41.798	-16.639	-16.229	45.7590	33.17	79.21	-3276	245	1689	10	-3965	-2276	AfriSoam
MARR23	68.880	67.880	-17.588	-18.404	116.1281	17.32	106.01	-827	233	841	10	-1386	-546	NoamEura
MARR230	-41.794	-42.437	-16.234	-15.996	74.1141	33.09	79.04	-3321	209	780	10	-3755	-2974	AfriSoam
MARR231	-43.300	-42.513	-16.161	-16.124	87.5626	32.96	79.01	-3493	352	1445	10	-4366	-2921	AfriSoam
MARR232	-43.315	-44.456	-16.211	-15.955	128.5787	32.78	78.92	-3759	216	1001	10	-4199	-3198	AfriSoam
MARR233	-44.459	-44.688	-15.917	-15.456	44.5237	32.64	78.69	-3953	142	545	10	-4207	-3662	AfriSoam
MARR234	-44.705	-45.317	-15.386	-15.069	72.5249	32.55	78.45	-3520	220	1042	10	-4032	-2990	AfriSoam
MARR235	-45.331	-45.907	-14.906	-14.487	71.9377	32.41	78.16	-3338	338	1454	10	-4205	-2751	AfriSoam
MARR236	-45.839	-46.053	-14.208	-14.045	26.9110	32.33	77.87	-3627	97	432	10	-3835	-3403	AfriSoam
MARR237	-46.072	-46.205	-13.993	-13.565	36.1562	32.28	77.69	-3549	256	880	10	-3919	-3039	AfriSoam
MARR238	-46.156	-46.625	-13.607	-13.369	55.2529	32.22	77.53	-3015	216	772	10	-3315	-2543	AfriSoam
MARR239	-46.623	-46.811	-13.368	-13.486	22.7630	32.14	77.48	-3729	232	765	10	-3950	-3185	AfriSoam
MARR24	67.841	66.982	-18.494	-18.786	96.2305	17.59	105.39	-326	73	321	10	-523	-203	NoamEura

Table C2 (Continued)

MARR240	-46.820	-47.296	-13.518	-13.350	54.4319	32.07	77.45	-3313	139	634	10	-3597	-2963	AfriSoam
MARR241	-47.351	-47.576	-13.420	-13.353	25.5600	31.98	77.39	-3356	159	576	10	-3646	-3070	AfriSoam
MARR242	-46.982	-48.278	-10.551	-9.926	151.4900	31.83	75.90	-2491	535	2041	10	-3766	-1724	AfriSoam
MARR243	-48.256	-48.502	-9.937	-10.144	31.3525	31.66	75.73	-3682	237	794	5	-3978	-3184	AfriSoam
MARR244	-48.465	-49.236	-10.223	-9.863	89.7303	31.55	75.68	-3368	446	1474	10	-4176	-2702	AfriSoam
MARR245	-48.970	-49.511	-8.409	-7.909	70.2578	31.38	74.75	-3690	215	972	10	-3994	-3022	AfriSoam
MARR246	-49.513	-49.701	-7.899	-8.062	23.9111	31.28	74.62	-4134	280	1158	10	-4755	-3597	AfriSoam
MARR247	-49.696	-50.192	-8.099	-7.669	63.1378	31.19	74.53	-3800	264	1471	10	-4662	-3191	AfriSoam
MARR248	-50.066	-50.434	-7.103	-6.944	42.4211	31.08	74.08	-3531	190	800	10	-3847	-3046	AfriSoam
MARR249	-50.419	-51.253	-6.516	-6.063	98.0745	30.90	73.66	-2493	431	1390	10	-3040	-1650	AfriSoam
MARR25	66.956	66.775	-18.077	-18.270	21.9134	17.72	105.54	-302	40	142	10	-389	-248	NoamEura
MARR250	-51.245	-52.312	-5.855	-5.243	125.8958	30.61	73.17	-2067	390	1423	10	-2973	-1550	AfriSoam
MARR251	-52.223	-53.599	-4.830	-3.704	170.6200	30.24	72.37	-2336	464	1893	10	-3600	-1708	AfriSoam
MARR252	-53.398	-54.195	-3.120	-2.393	100.5910	29.91	71.48	-2415	361	1266	10	-3030	-1764	AfriSoam
MARR253	-53.973	-54.609	-1.615	-1.104	78.0903	29.69	70.71	-2387	196	734	10	-2833	-2100	AfriSoam
MARR254	-54.559	-54.914	-0.992	-0.741	42.5806	29.53	70.38	-2333	354	1235	10	-2964	-1729	AfriSoam
MARR255	-54.914	-55.491	-0.758	-0.698	64.3299	29.39	70.22	-2988	276	1073	10	-3675	-2601	AfriSoam
MARR26	66.646	66.352	-17.453	-17.722	34.7902	17.79	105.80	-259	36	128	10	-327	-199	NoamEura
MARR27	66.259	65.297	-16.495	-17.035	109.7607	17.95	106.12	289	189	585	10	-35	550	NoamEura
MARR28	64.403	65.265	-18.029	-16.649	115.9143	18.20	105.58	1025	252	891	10	551	1442	NoamEura
MARR29	64.394	63.847	-18.061	-19.289	85.1086	18.42	104.66	696	112	477	10	549	1025	NoamEura
MARR3	81.240	80.986	-1.930	-2.891	32.6795	13.29	122.85	-3542	233	712	10	-3925	-3213	NoamEura
MARR30	64.099	63.822	-21.196	-19.371	94.2576	18.50	103.72	238	212	608	10	42	650	NoamEura
MARR31	63.903	64.152	-21.908	-21.175	45.2164	18.51	103.01	385	126	424	10	101	524	NoamEura
MARR32	63.656	63.975	-23.057	-22.207	54.7490	18.59	102.35	-45	121	363	10	-233	129	NoamEura
MARR33	63.019	63.707	-24.678	-23.240	104.8138	18.73	101.53	-203	84	349	10	-414	-65	NoamEura
MARR34	62.669	62.997	-25.389	-24.745	48.9859	18.88	100.83	-543	81	367	10	-692	-324	NoamEura
MARR35	62.117	62.662	-26.280	-25.382	76.2833	19.00	100.34	-663	86	333	10	-798	-465	NoamEura
MARR36	62.110	61.839	-26.300	-26.793	39.6639	19.11	99.89	-769	128	584	10	-1045	-462	NoamEura
MARR37	61.493	61.832	-27.200	-26.802	43.1627	19.19	99.60	-811	84	442	10	-1025	-583	NoamEura
MARR38	60.813	61.513	-28.308	-27.349	93.3541	19.32	99.08	-892	84	426	10	-1102	-676	NoamEura
MARR39	60.432	60.799	-28.754	-28.394	45.2798	19.45	98.62	-738	97	567	10	-973	-406	NoamEura
MARR4	80.855	80.368	-0.868	-2.388	60.7356	13.41	123.08	-3534	508	1605	10	-4256	-2651	NoamEura
MARR40	60.123	60.493	-29.214	-28.840	46.0606	19.53	98.34	-886	109	461	10	-1103	-642	NoamEura
MARR41	59.700	60.127	-29.928	-29.305	58.9062	19.62	97.98	-965	118	584	10	-1222	-638	NoamEura

Table C2 (Continued)

MARR42	59.084	59.649	-30.791	-29.919	79.8869	19.75	97.53	-1209	110	667	10	-1459	-791	NoamEura
MARR43	58.810	59.052	-31.022	-30.859	28.5410	19.85	97.18	-1294	92	388	10	-1526	-1137	NoamEura
MARR44	58.807	58.606	-31.204	-31.458	26.8030	19.91	96.95	-1618	181	689	10	-1916	-1227	NoamEura
MARR45	58.599	58.390	-31.485	-31.644	24.9177	19.96	96.81	-1441	90	398	8	-1651	-1253	NoamEura
MARR46	58.435	57.645	-31.706	-32.805	109.0847	20.06	96.41	-1848	148	646	10	-2240	-1594	NoamEura
MARR47	57.637	56.845	-32.828	-33.956	111.1633	20.24	95.75	-2238	221	937	10	-2745	-1808	NoamEura
MARR48	56.768	55.824	-34.313	-34.565	106.0627	20.44	95.15	-1962	285	1084	10	-2627	-1543	NoamEura
MARR49	55.778	55.083	-34.936	-35.278	80.2507	20.61	94.76	-2406	135	618	10	-2749	-2130	NoamEura
MARR5	80.475	80.181	1.841	0.361	42.7676	13.40	125.01	-2692	164	501	10	-3038	-2537	NoamEura
MARR50	55.066	54.406	-35.189	-35.278	73.6334	20.74	94.66	-2239	168	582	10	-2516	-1934	NoamEura
MARR51	54.315	53.484	-35.115	-35.367	93.8939	20.90	94.62	-2500	158	528	10	-2724	-2196	NoamEura
MARR52	53.480	53.160	-35.389	-35.077	41.1163	21.00	94.61	-2389	373	1113	10	-2869	-1756	NoamEura
MARR53	53.174	52.668	-35.092	-34.944	57.1277	21.07	94.70	-3081	234	731	10	-3547	-2816	NoamEura
MARR54	52.573	52.179	-31.743	-31.773	43.8905	21.13	96.33	-3518	389	1064	10	-4157	-3093	NoamEura
MARR55	52.051	51.578	-29.991	-29.932	52.7313	21.20	97.21	-3503	278	1083	10	-4026	-2943	NoamEura
MARR56	51.310	51.620	-29.969	-29.932	34.5661	21.26	97.20	-3516	238	678	10	-3836	-3159	NoamEura
MARR57	51.310	51.072	-29.976	-29.984	26.3917	21.31	97.16	-3309	156	492	10	-3598	-3106	NoamEura
MARR58	50.632	51.049	-29.746	-29.939	48.3527	21.36	97.21	-3476	88	296	10	-3621	-3325	NoamEura
MARR59	50.608	50.391	-29.627	-29.442	27.4984	21.41	97.35	-3479	94	312	10	-3670	-3358	NoamEura
MARR6	79.585	79.089	4.083	2.543	63.6124	13.60	125.93	-3851	1005	3253	10	-5554	-2301	NoamEura
MARR60	50.353	50.168	-29.308	-28.974	31.4276	21.45	97.53	-3615	277	736	10	-3907	-3171	NoamEura
MARR61	49.815	50.192	-28.810	-28.989	43.8231	21.49	97.64	-3613	280	812	10	-3995	-3182	NoamEura
MARR62	49.805	49.699	-28.773	-28.439	26.7159	21.52	97.77	-3789	122	355	10	-3956	-3601	NoamEura
MARR63	49.680	49.173	-28.454	-28.395	56.5504	21.57	97.84	-3456	124	391	10	-3647	-3256	NoamEura
MARR64	49.212	48.773	-28.395	-27.927	59.5176	21.63	97.94	-3569	170	537	10	-3861	-3323	NoamEura
MARR65	48.798	48.118	-27.986	-27.815	76.6104	21.71	98.04	-2912	569	1662	10	-3618	-1956	NoamEura
MARR66	48.118	47.994	-27.815	-27.504	26.9712	21.76	98.14	-3165	147	454	10	-3486	-3031	NoamEura
MARR67	48.009	47.600	-27.548	-27.555	45.4710	21.80	98.17	-3270	127	433	10	-3507	-3074	NoamEura
MARR68	47.550	47.198	-27.325	-27.318	39.1446	21.86	98.26	-3336	142	522	10	-3630	-3108	NoamEura
MARR69	47.173	46.528	-27.281	-27.370	72.0401	21.93	98.23	-3289	210	845	10	-3853	-3008	NoamEura
MARR7	78.451	76.879	7.516	7.629	174.8302	13.87	127.79	-3123	242	1070	10	-3556	-2486	NoamEura
MARR70	46.525	45.993	-27.380	-27.567	60.9243	22.01	98.13	-2969	140	478	10	-3291	-2813	NoamEura
MARR71	45.930	45.594	-27.735	-27.819	37.9076	22.08	97.96	-3129	223	782	10	-3457	-2675	NoamEura
MARR72	45.590	45.307	-27.819	-27.934	32.6856	22.13	97.90	-2965	132	469	10	-3156	-2687	NoamEura
MARR73	44.600	45.314	-28.164	-27.971	80.8980	22.19	97.79	-2769	215	782	10	-3123	-2341	NoamEura

Table C2 (Continued)

MARR74	44.594	43.731	-28.202	-28.521	99.2707	22.29	97.61	-2950	174	976	10	-3306	-2330	NoamEura
MARR75	43.667	43.225	-28.899	-28.996	49.7740	22.38	97.30	-2937	267	720	10	-3301	-2580	NoamEura
MARR76	43.149	42.780	-29.300	-29.330	41.1575	22.44	97.11	-2701	236	665	10	-3008	-2342	NoamEura
MARR77	42.778	42.308	-29.324	-29.390	52.5312	22.49	97.08	-2858	132	498	10	-3084	-2586	NoamEura
MARR78	42.238	41.962	-29.211	-29.241	30.7320	22.53	97.13	-2574	237	729	10	-2993	-2264	NoamEura
MARR79	41.951	41.413	-29.248	-29.271	59.8404	22.58	97.10	-2463	152	703	10	-2972	-2270	NoamEura
MARR8	76.805	76.480	7.606	7.039	38.9731	14.15	126.78	-2979	212	722	10	-3311	-2589	NoamEura
MARR80	41.436	40.640	-29.338	-29.278	88.5846	22.64	97.05	-2390	130	440	10	-2632	-2192	NoamEura
MARR81	40.596	39.994	-29.483	-29.669	68.7346	22.72	96.91	-2605	152	538	10	-2956	-2418	NoamEura
MARR82	39.966	39.492	-29.679	-29.753	53.0880	22.77	96.82	-2030	138	499	10	-2387	-1888	NoamEura
MARR83	39.458	38.430	-29.887	-30.273	119.0876	19.76	104.12	-1560	446	1708	10	-2822	-1115	AfriNoam
MARR84	38.564	38.045	-30.548	-30.704	59.2485	19.98	104.01	-1561	436	1452	10	-2292	-840	AfriNoam
MARR85	38.139	37.582	-31.394	-31.610	64.7448	20.17	103.96	-1617	419	1335	10	-2221	-886	AfriNoam
MARR86	37.554	37.038	-32.208	-32.328	58.3708	20.38	103.88	-2585	474	1759	10	-3357	-1599	AfriNoam
MARR87	37.097	36.928	-32.863	-32.957	20.6040	20.49	103.85	-2885	136	425	10	-3152	-2727	AfriNoam
MARR88	36.939	36.560	-33.218	-33.342	43.5432	20.59	103.82	-2675	269	922	10	-3167	-2245	AfriNoam
MARR89	36.659	36.245	-33.603	-33.763	48.2316	20.70	103.78	-2700	197	809	10	-3031	-2222	AfriNoam
MARR9	76.446	75.386	6.978	7.456	118.5848	14.34	126.14	-3172	106	430	10	-3422	-2992	NoamEura
MARR90	36.095	36.253	-34.082	-33.792	31.4057	20.79	103.73	-2714	338	1159	10	-3172	-2013	AfriNoam
MARR91	36.074	35.664	-34.118	-34.268	47.4980	20.89	103.69	-2526	137	734	10	-3067	-2333	AfriNoam
MARR92	35.625	35.021	-34.776	-34.962	69.2254	21.08	103.61	-3083	502	2027	10	-4130	-2102	AfriNoam
MARR93	35.280	34.493	-36.325	-36.534	89.4808	21.29	103.59	-2804	475	1672	10	-3881	-2209	AfriNoam
MARR94	34.509	34.078	-37.026	-37.205	50.6765	21.49	103.50	-3133	134	548	10	-3465	-2916	AfriNoam
MARR95	34.111	33.700	-37.632	-37.760	47.2170	21.62	103.45	-3377	260	865	10	-3796	-2931	AfriNoam
MARR96	33.694	33.591	-38.183	-38.239	12.5590	21.72	103.42	-4166	250	638	10	-4535	-3897	AfriNoam
MARR97	33.713	33.145	-39.103	-39.256	64.8062	21.82	103.41	-2638	305	1042	10	-3185	-2143	AfriNoam
MARR98	32.857	33.155	-39.804	-39.256	60.8801	21.95	103.35	-3265	345	1660	10	-3980	-2320	AfriNoam
MARR99	32.846	32.676	-39.807	-39.875	19.9589	22.03	103.31	-3026	131	530	10	-3416	-2886	AfriNoam
PARR1	-35.104	-36.374	-110.815	-111.014	142.3109	94.53	101.59	-2719	205	694	10	-3139	-2445	PaciAnta
PARR10	-48.492	-49.783	-113.297	-113.821	148.4946	87.12	103.74	-2359	66	398	10	-2678	-2281	PaciAnta
PARR11	-49.363	-50.980	-116.700	-117.358	185.8713	85.94	105.43	-2455	209	787	10	-2957	-2171	PaciAnta
PARR12	-50.967	-52.932	-117.486	-118.544	230.2932	84.44	106.14	-2562	149	578	10	-2934	-2356	PaciAnta
PARR13	-53.095	-54.560	-117.681	-118.475	171.0188	82.90	106.47	-2629	203	830	10	-3210	-2380	PaciAnta
PARR14	-54.379	-54.455	-119.409	-119.474	9.4594	82.20	107.21	-2866	53	183	10	-2958	-2775	PaciAnta
PARR15	-54.211	-54.603	-120.718	-120.983	46.8927	81.99	107.87	-2464	66	305	10	-2619	-2314	PaciAnta

Table C2 (Continued)

PARR16	-54.632	-56.037	-120.819	-121.679	165.4440	81.12	108.24	-2389	90	387	10	-2633	-2247	PaciAnta
PARR17	-54.850	-55.344	-127.461	-127.753	57.9342	80.19	111.15	-2626	138	819	10	-3293	-2475	PaciAnta
PARR18	-53.788	-54.666	-134.469	-135.200	108.5868	79.42	114.18	-2399	57	364	10	-2651	-2287	PaciAnta
PARR19	-54.158	-54.545	-137.024	-137.347	47.8432	78.75	115.24	-2265	60	287	10	-2465	-2177	PaciAnta
PARR2	-36.424	-38.872	-110.498	-111.194	279.0902	93.82	101.65	-2403	151	724	10	-2898	-2174	PaciAnta
PARR20	-54.491	-55.709	-137.384	-138.383	149.5825	77.91	115.78	-2096	57	245	10	-2265	-2019	PaciAnta
PARR21	-55.788	-56.318	-138.342	-138.944	69.8351	76.85	116.44	-2562	143	627	10	-2963	-2336	PaciAnta
PARR22	-56.215	-56.618	-139.252	-139.644	50.9253	76.31	116.92	-2769	80	307	10	-2917	-2610	PaciAnta
PARR23	-56.628	-57.118	-139.600	-140.129	63.3283	75.78	117.27	-3444	197	1092	10	-4138	-3046	PaciAnta
PARR24	-55.694	-56.243	-144.760	-145.271	68.8906	75.19	119.21	-2719	182	846	10	-3295	-2449	PaciAnta
PARR25	-56.222	-56.864	-145.402	-146.096	83.1500	74.44	119.76	-2684	95	414	10	-2896	-2482	PaciAnta
PARR26	-56.917	-57.847	-146.060	-146.991	117.4942	73.42	120.46	-2577	83	374	10	-2852	-2478	PaciAnta
PARR27	-58.310	-57.475	-148.977	-147.942	111.2025	72.35	121.55	-2428	157	533	10	-2798	-2265	PaciAnta
PARR28	-58.505	-59.709	-148.654	-150.329	164.5318	70.85	122.60	-2449	113	433	10	-2728	-2296	PaciAnta
PARR29	-59.385	-61.112	-151.310	-153.426	224.7270	68.80	124.53	-2438	92	352	10	-2624	-2272	PaciAnta
PARR3	-38.882	-40.161	-111.200	-111.486	144.3402	92.97	101.96	-2339	123	590	10	-2656	-2066	PaciAnta
PARR30	-61.172	-62.129	-153.363	-154.804	130.8550	66.85	126.16	-2510	138	471	10	-2769	-2298	PaciAnta
PARR31	-63.174	-61.995	-157.526	-155.477	167.9064	65.09	127.93	-2347	216	1330	10	-3099	-1769	PaciAnta
PARR32	-62.850	-62.458	-159.792	-159.203	52.9811	63.93	129.44	-2920	153	438	10	-3166	-2727	PaciAnta
PARR33	-63.012	-62.758	-160.476	-160.072	34.9473	63.42	129.99	-2722	230	643	10	-3009	-2367	PaciAnta
PARR34	-63.272	-62.508	-163.409	-161.950	112.6121	62.50	131.16	-2473	83	340	10	-2653	-2313	PaciAnta
PARR35	-62.748	-63.582	-164.723	-166.188	118.3577	61.14	132.73	-2473	176	838	10	-2813	-1975	PaciAnta
PARR36	-63.364	-64.049	-166.877	-168.121	97.7091	59.79	134.19	-2550	110	478	10	-2780	-2302	PaciAnta
PARR37	-64.781	-63.957	-170.188	-168.302	128.8944	58.45	135.67	-2400	120	428	10	-2686	-2258	PaciAnta
PARR38	-65.121	-64.365	-173.158	-171.254	123.3586	56.85	137.53	-2774	180	790	10	-3254	-2464	PaciAnta
PARR39	-65.655	-64.999	-175.173	-173.380	110.6672	55.41	139.21	-2960	183	873	10	-3558	-2685	PaciAnta
PARR4	-40.226	-41.252	-111.430	-111.564	114.6321	92.39	102.10	-2460	113	648	10	-2807	-2159	PaciAnta
PARR40	-66.221	-65.189	-179.146	-176.112	180.1056	53.59	141.38	-2576	212	1023	10	-3284	-2261	PaciAnta
PARR41	-64.610	-64.351	175.654	176.597	53.6028	51.70	143.07	-2780	523	1889	10	-3733	-1844	PaciAnta
PARR42	-63.440	-63.940	173.480	172.014	91.1019	50.68	143.68	-2061	506	1765	10	-2746	-981	PaciAnta
PARR43	-63.122	-63.557	170.442	169.290	75.1050	49.47	144.55	-2059	352	1182	10	-2849	-1667	PaciAnta
PARR44	-62.411	-62.702	167.402	165.977	79.9129	48.41	144.86	-2904	140	455	10	-3138	-2683	PaciAnta
PARR45	-61.967	-62.245	164.789	163.522	72.7932	47.38	145.28	-2608	343	1214	10	-3330	-2116	PaciAnta
PARR46	-61.799	-62.023	162.770	161.859	53.7915	46.49	145.73	-2431	102	378	10	-2615	-2237	PaciAnta
PARR5	-41.259	-42.085	-111.305	-111.277	91.8653	91.94	102.08	-2591	104	424	10	-2800	-2376	PaciAnta

Table C2 (Continued)

PARR6	-42.120	-44.089	-111.248	-111.877	224.8277	91.15	102.30	-2669	106	445	10	-2948	-2502	PaciAnta
PARR7	-44.103	-45.523	-111.982	-112.401	161.3075	90.11	102.71	-2544	106	486	10	-2840	-2354	PaciAnta
PARR8	-45.530	-47.716	-112.535	-113.240	248.9603	88.91	103.18	-2589	97	438	10	-2811	-2373	PaciAnta
PARR9	-47.709	-48.473	-113.173	-113.383	86.3618	87.89	103.50	-2555	80	456	10	-2871	-2415	PaciAnta
SEIR1	-25.636	-26.173	70.051	70.539	77.1259	55.41	47.56	-3665	148	724	10	-4063	-3340	AntaAust
SEIR10	-29.334	-29.723	74.982	75.380	57.9265	59.68	44.82	-3211	232	803	10	-3712	-2909	AntaAust
SEIR11	-29.907	-30.691	75.225	76.179	126.4867	60.28	44.71	-3280	294	1205	10	-4084	-2879	AntaAust
SEIR12	-30.792	-31.452	76.080	76.753	97.3535	60.98	44.45	-3085	219	841	10	-3520	-2680	AntaAust
SEIR13	-31.676	-33.119	76.527	78.138	220.5350	61.94	44.20	-2925	199	1045	10	-3635	-2590	AntaAust
SEIR14	-33.713	-34.616	77.384	78.278	129.8376	62.92	44.49	-3261	150	661	10	-3611	-2950	AntaAust
SEIR15	-34.625	-35.074	78.294	78.749	65.0236	63.46	44.15	-3178	245	905	10	-3595	-2690	AntaAust
SEIR16	-35.273	-35.328	78.547	78.604	7.9956	63.67	44.28	-3184	25	79	10	-3220	-3141	AntaAust
SEIR17	-35.551	-36.359	78.346	79.168	116.4051	64.00	44.37	-2856	237	1057	10	-3397	-2340	AntaAust
SEIR18	-37.048	-37.262	78.232	78.439	30.0760	64.35	45.18	-1983	103	341	10	-2149	-1808	AntaAust
SEIR19	-38.435	-37.712	78.562	77.855	101.4285	64.68	45.62	-1870	252	1526	10	-2422	-895	AntaAust
SEIR2	-26.059	-26.217	70.743	70.872	21.7825	55.80	47.19	-4099	107	319	10	-4282	-3964	AntaAust
SEIR20	-38.864	-39.215	78.019	78.254	43.9792	65.05	46.02	-2057	76	279	10	-2184	-1906	AntaAust
SEIR21	-39.331	-40.083	77.979	78.591	98.6000	65.35	46.10	-2483	347	1169	10	-3241	-2072	AntaAust
SEIR22	-40.332	-40.869	77.889	78.422	74.7066	65.66	46.51	-3088	161	772	10	-3599	-2827	AntaAust
SEIR23	-40.816	-41.831	78.613	79.813	150.9263	66.21	45.78	-2723	152	714	10	-3173	-2458	AntaAust
SEIR24	-41.278	-41.065	81.209	80.943	32.5661	66.65	44.08	-2675	39	286	10	-2846	-2560	AntaAust
SEIR25	-41.566	-41.275	81.618	81.214	46.7414	66.83	43.86	-2671	114	425	10	-2919	-2494	AntaAust
SEIR26	-41.560	-41.814	81.590	81.925	39.6540	67.00	43.64	-2684	124	499	10	-3016	-2517	AntaAust
SEIR27	-42.174	-41.808	82.322	81.901	53.5809	67.19	43.42	-2693	91	315	10	-2848	-2533	AntaAust
SEIR28	-42.216	-42.889	82.350	83.381	112.8624	67.55	42.92	-2709	157	680	10	-3165	-2484	AntaAust
SEIR29	-40.850	-42.103	85.896	88.149	233.7638	68.25	39.11	-2610	264	1546	10	-3828	-2281	AntaAust
SEIR3	-26.045	-26.393	71.358	71.606	45.9388	56.17	46.57	-3680	128	411	10	-3916	-3505	AntaAust
SEIR30	-41.707	-42.345	88.686	89.734	111.9401	68.90	37.46	-2473	99	393	10	-2729	-2336	AntaAust
SEIR31	-42.349	-42.742	89.763	90.588	80.4313	69.23	36.80	-2594	54	287	10	-2745	-2458	AntaAust
SEIR32	-42.775	-43.473	90.528	91.894	135.3338	69.56	36.10	-2660	190	730	10	-3074	-2343	AntaAust
SEIR33	-43.328	-44.432	91.990	94.334	224.3701	70.08	34.70	-2754	148	598	10	-3077	-2478	AntaAust
SEIR34	-44.504	-45.175	94.176	95.601	134.8762	70.54	33.52	-2848	146	566	10	-3242	-2676	AntaAust
SEIR35	-44.982	-45.265	95.705	96.444	65.9819	70.76	32.63	-2903	134	481	10	-3142	-2662	AntaAust
SEIR36	-45.976	-46.276	95.702	96.249	53.7563	70.89	32.88	-3245	140	519	10	-3504	-2984	AntaAust
SEIR37	-47.100	-46.619	96.925	95.869	96.4856	71.04	32.67	-2712	76	331	10	-2923	-2592	AntaAust

Table C2 (Continued)

SEIR38	-47.156	-47.369	96.870	97.403	46.6852	71.18	32.14	-2718	104	353	10	-2922	-2569	AntaAust
SEIR39	-47.417	-48.255	97.326	99.300	174.3417	71.39	31.28	-2738	69	350	10	-2921	-2570	AntaAust
SEIR4	-26.345	-27.033	71.784	72.342	94.5228	56.72	46.27	-3588	204	675	10	-3930	-3255	AntaAust
SEIR40	-47.260	-47.637	100.242	101.391	96.0313	71.62	29.26	-2828	136	582	10	-3186	-2604	AntaAust
SEIR41	-47.607	-48.045	101.408	102.534	97.1826	71.76	28.40	-2972	180	615	10	-3343	-2728	AntaAust
SEIR42	-47.755	-48.233	102.878	104.247	114.9366	71.90	27.18	-3067	239	1007	10	-3736	-2729	AntaAust
SEIR43	-48.128	-48.398	104.326	105.176	69.7152	72.00	26.28	-3139	155	540	10	-3484	-2944	AntaAust
SEIR44	-48.644	-48.741	105.024	105.277	21.4584	72.04	26.01	-3721	156	560	10	-4071	-3511	AntaAust
SEIR45	-48.975	-49.306	105.097	106.105	82.0793	72.09	25.69	-3531	166	667	10	-3805	-3138	AntaAust
SEIR46	-48.841	-48.871	106.483	106.601	9.2391	72.13	24.94	-4445	73	250	10	-4522	-4272	AntaAust
SEIR47	-48.327	-48.812	107.052	108.499	119.3205	72.17	23.98	-3086	212	910	10	-3711	-2800	AntaAust
SEIR48	-49.019	-49.096	108.443	108.719	21.8796	72.21	23.39	-3924	70	295	10	-4023	-3728	AntaAust
SEIR49	-49.273	-49.948	108.612	110.842	177.3416	72.25	22.52	-3571	303	1149	10	-4319	-3169	AntaAust
SEIR5	-26.985	-27.467	72.439	72.868	68.4472	57.31	46.00	-3727	176	629	10	-3975	-3346	AntaAust
SEIR50	-49.716	-49.861	110.876	111.389	40.2201	72.27	21.45	-3722	128	462	10	-3992	-3530	AntaAust
SEIR51	-50.021	-50.331	111.327	112.628	98.8628	72.28	20.80	-3384	282	1080	10	-3953	-2874	AntaAust
SEIR52	-50.173	-50.399	112.808	113.895	81.2390	72.27	19.75	-3435	275	851	10	-3894	-3043	AntaAust
SEIR53	-49.842	-50.076	114.367	115.534	87.4457	72.24	18.54	-4302	114	611	10	-4632	-4021	AntaAust
SEIR54	-49.935	-49.983	115.610	115.850	17.9990	72.22	17.94	-4500	99	333	10	-4664	-4331	AntaAust
SEIR55	-49.401	-49.442	116.166	116.427	19.4004	72.21	17.54	-3600	318	858	10	-3967	-3110	AntaAust
SEIR56	-49.245	-49.366	116.564	117.093	40.6415	72.19	17.14	-4622	207	735	10	-4942	-4208	AntaAust
SEIR57	-49.468	-49.553	117.093	117.429	26.0231	72.17	16.81	-4504	302	900	10	-4945	-4045	AntaAust
SEIR58	-49.678	-49.921	117.429	118.569	86.1901	72.13	16.24	-4016	482	1566	10	-4759	-3193	AntaAust
SEIR59	-49.820	-50.102	118.707	120.039	100.3350	72.05	15.19	-3643	231	964	10	-4322	-3359	AntaAust
SEIR6	-27.353	-27.486	73.137	73.282	20.5814	57.68	45.58	-3668	156	487	10	-3943	-3456	AntaAust
SEIR60	-49.802	-49.868	120.265	120.567	22.8868	71.99	14.42	-4149	98	316	10	-4310	-3994	AntaAust
SEIR61	-48.849	-48.952	121.000	121.597	45.1388	71.95	13.85	-4697	296	815	10	-5055	-4240	AntaAust
SEIR62	-49.682	-49.890	121.426	122.538	83.1271	71.87	13.25	-4289	196	828	10	-4726	-3898	AntaAust
SEIR63	-49.554	-49.500	123.317	122.938	27.9963	71.77	12.43	-4372	193	536	10	-4648	-4112	AntaAust
SEIR64	-49.007	-49.047	123.576	123.856	20.9131	71.73	12.05	-4303	93	422	10	-4422	-4000	AntaAust
SEIR65	-49.102	-48.848	125.090	123.969	86.5733	71.65	11.46	-4190	484	2870	10	-4949	-2079	AntaAust
SEIR66	-49.730	-49.570	125.981	125.206	58.5696	71.51	10.58	-4182	565	2168	10	-5448	-3281	AntaAust
SEIR67	-48.837	-48.663	127.515	126.328	89.1524	71.38	9.73	-4319	369	1058	10	-4756	-3698	AntaAust
SEIR68	-50.149	-50.170	128.175	126.963	86.3703	71.24	9.02	-3410	94	410	10	-3587	-3177	AntaAust
SEIR69	-50.160	-50.444	128.257	131.210	212.0935	70.93	7.37	-3160	149	633	10	-3539	-2906	AntaAust

Table C2 (Continued)

SEIR7	-27.863	-27.404	73.916	73.474	67.0923	58.02	45.24	-3391	196	688	10	-3799	-3111	AntaAust
SEIR70	-50.415	-50.152	135.091	131.528	254.8236	70.32	4.67	-2873	118	568	10	-3198	-2630	AntaAust
SEIR71	-50.170	-50.200	135.105	137.617	178.8745	69.71	2.38	-2800	126	511	10	-3115	-2603	AntaAust
SEIR72	-50.238	-50.231	139.717	137.696	143.7433	69.19	0.57	-2742	170	803	10	-3340	-2537	AntaAust
SEIR73	-52.378	-52.326	139.632	140.883	85.1587	68.83	1.30	-2835	297	1307	10	-3633	-2325	AntaAust
SEIR74	-54.087	-54.206	140.883	143.975	201.7944	68.35	3.65	-2754	117	625	10	-3115	-2490	AntaAust
SEIR75	-54.818	-54.840	143.965	146.424	157.5114	67.69	6.20	-2538	170	792	10	-3018	-2226	AntaAust
SEIR76	-55.572	-55.522	146.557	147.250	43.9540	67.29	7.92	-2476	289	984	10	-3217	-2234	AntaAust
SEIR77	-57.551	-57.458	147.745	148.795	63.5562	67.09	9.87	-2888	153	859	10	-3477	-2618	AntaAust
SEIR78	-59.910	-60.403	153.505	150.773	160.7727	66.41	14.43	-2813	147	835	10	-3434	-2599	AntaAust
SEIR79	-61.536	-62.874	161.186	156.276	294.7780	65.16	21.54	-2140	174	1129	10	-2901	-1771	AntaAust
SEIR8	-28.227	-27.840	74.419	73.967	61.8235	58.46	44.98	-3676	219	880	10	-4234	-3354	AntaAust
SEIR9	-28.500	-29.292	74.177	75.025	120.7544	59.10	45.04	-3630	279	1089	10	-4076	-2988	AntaAust
SWIR1	-53.645	-54.285	3.001	4.543	123.4658	13.54	43.61	-2739	589	2275	10	-4195	-1920	AfriAnta
SWIR10	-52.208	-52.257	15.606	14.898	48.5155	13.89	32.57	-4135	111	566	10	-4352	-3786	AfriAnta
SWIR11	-52.309	-52.197	16.297	15.634	46.7591	13.92	31.94	-3979	177	628	10	-4200	-3572	AfriAnta
SWIR12	-52.347	-52.288	16.725	16.388	23.8235	13.94	31.43	-3692	186	680	10	-4006	-3326	AfriAnta
SWIR13	-52.528	-52.299	17.815	16.828	71.6949	13.97	30.79	-3657	309	1145	10	-4154	-3009	AfriAnta
SWIR14	-52.712	-52.515	18.757	17.901	61.8445	14.01	29.95	-3813	246	959	10	-4141	-3182	AfriAnta
SWIR15	-52.857	-52.677	19.927	18.826	76.7730	14.05	29.07	-3754	450	1398	10	-4410	-3012	AfriAnta
SWIR16	-52.936	-52.847	20.675	20.047	43.2924	14.08	28.25	-3849	291	992	10	-4294	-3301	AfriAnta
SWIR17	-53.029	-52.898	21.446	20.738	49.5888	14.10	27.63	-4119	201	823	10	-4395	-3572	AfriAnta
SWIR18	-52.944	-53.078	21.563	22.211	45.7808	14.13	26.96	-4145	80	311	10	-4301	-3990	AfriAnta
SWIR19	-53.245	-52.991	23.164	22.314	63.3782	14.15	26.25	-3662	164	632	10	-3976	-3344	AfriAnta
SWIR2	-54.225	-54.575	4.732	5.520	64.1131	13.62	42.43	-3566	477	1544	10	-4338	-2794	AfriAnta
SWIR20	-53.429	-53.228	24.169	23.307	61.4605	14.19	25.43	-3897	350	1253	10	-4600	-3348	AfriAnta
SWIR21	-53.558	-53.385	25.042	24.306	52.4103	14.21	24.66	-4078	248	915	10	-4597	-3682	AfriAnta
SWIR22	-52.574	-52.927	25.930	27.628	120.7933	14.25	22.77	-3851	1319	4449	10	-5929	-1480	AfriAnta
SWIR23	-51.135	-51.226	28.868	29.384	37.3635	14.28	20.60	-5228	545	2172	10	-6543	-4371	AfriAnta
SWIR24	-47.074	-47.260	32.126	33.448	102.0950	14.32	17.15	-3672	690	2537	10	-4819	-2282	AfriAnta
SWIR25	-45.999	-46.119	33.866	34.874	78.9115	14.34	15.82	-3325	940	3030	10	-4758	-1728	AfriAnta
SWIR26	-44.616	-44.837	35.407	36.956	124.8281	14.37	14.34	-2400	851	3413	10	-4456	-1043	AfriAnta
SWIR27	-44.657	-44.499	37.915	37.062	69.7504	14.39	13.38	-2584	260	923	10	-2924	-2001	AfriAnta
SWIR28	-44.037	-44.176	38.286	39.141	69.9677	14.41	12.46	-2237	588	2196	10	-3610	-1413	AfriAnta
SWIR29	-43.906	-43.850	41.511	40.424	87.3458	14.43	10.86	-2802	501	1994	10	-4023	-2029	AfriAnta

Table C2 (Continued)

SWIR3	-53.869	-54.182	6.641	8.022	96.7002	13.68	40.25	-3796	709	2837	10	-5031	-2194	AfriAnta
SWIR30	-43.415	-43.352	40.393	39.336	85.7117	14.42	11.60	-3097	521	1793	10	-4413	-2619	AfriAnta
SWIR31	-42.720	-42.767	41.873	42.416	44.6962	14.44	9.99	-3654	598	2120	10	-4821	-2701	AfriAnta
SWIR32	-40.917	-40.991	42.865	44.340	124.1666	14.45	8.95	-3306	217	1065	10	-3992	-2927	AfriAnta
SWIR33	-40.650	-40.650	44.373	44.783	34.5722	14.45	8.30	-3403	168	673	10	-3602	-2929	AfriAnta
SWIR34	-40.414	-40.407	44.791	45.094	25.6800	14.45	8.06	-3487	227	639	10	-3753	-3114	AfriAnta
SWIR35	-40.120	-40.120	45.094	46.062	82.2415	14.46	7.64	-3162	332	1204	10	-3740	-2536	AfriAnta
SWIR36	-38.797	-38.778	46.217	47.602	120.0694	14.45	6.80	-3242	362	1543	10	-3850	-2308	AfriAnta
SWIR37	-38.233	-38.772	48.266	47.635	81.2732	14.45	6.15	-3360	229	867	10	-3820	-2954	AfriAnta
SWIR38	-38.072	-38.072	48.274	48.865	51.6556	14.45	5.78	-2982	176	522	10	-3298	-2776	AfriAnta
SWIR39	-37.904	-37.897	48.947	49.438	43.1572	14.44	5.41	-3245	259	927	10	-3685	-2758	AfriAnta
SWIR4	-52.854	-52.902	10.896	9.949	63.8207	13.74	37.08	-3797	409	1316	10	-4543	-3227	AfriAnta
SWIR40	-37.755	-37.761	49.488	49.824	29.5470	14.44	5.13	-3188	323	904	10	-3657	-2752	AfriAnta
SWIR41	-37.658	-37.638	49.848	50.856	88.7812	14.43	4.71	-2260	308	1070	10	-2888	-1818	AfriAnta
SWIR42	-37.450	-37.404	50.864	51.610	66.0593	14.42	4.19	-2959	152	507	10	-3223	-2715	AfriAnta
SWIR43	-37.254	-37.241	51.643	52.430	69.6669	14.41	3.72	-3592	463	1646	10	-4653	-3006	AfriAnta
SWIR44	-36.170	-36.157	52.307	53.381	96.3987	14.40	3.33	-4281	811	2661	10	-5908	-3247	AfriAnta
SWIR45	-35.392	-35.359	53.422	54.127	64.0180	14.38	2.86	-3784	581	2209	10	-5282	-3074	AfriAnta
SWIR46	-34.721	-34.728	54.135	54.856	65.9155	14.37	2.52	-3824	398	1460	10	-4745	-3285	AfriAnta
SWIR47	-34.357	-34.384	54.954	55.577	57.2498	14.35	2.12	-3673	112	384	10	-3805	-3422	AfriAnta
SWIR48	-33.691	-33.718	55.766	57.061	119.8307	14.32	1.57	-3663	549	2259	10	-5139	-2880	AfriAnta
SWIR49	-31.788	-31.785	57.044	57.593	51.9010	14.30	1.36	-3892	376	1215	10	-4537	-3322	AfriAnta
SWIR5	-52.923	-52.760	11.678	10.936	53.0077	13.77	36.26	-2458	461	1674	10	-3320	-1646	AfriAnta
SWIR50	-31.722	-31.687	57.598	58.376	73.7673	14.28	1.02	-4292	541	1662	10	-5455	-3793	AfriAnta
SWIR51	-31.102	-31.082	58.426	58.985	53.2289	14.25	0.75	-4166	564	1882	10	-5326	-3444	AfriAnta
SWIR52	-30.643	-31.031	59.603	59.020	70.3511	14.23	0.48	-4360	178	759	10	-4687	-3928	AfriAnta
SWIR53	-30.244	-30.633	60.756	59.615	117.6312	14.19	0.11	-4697	327	1589	10	-5776	-4186	AfriAnta
SWIR54	-29.346	-29.336	60.672	61.029	34.5747	14.17	0.00	-5006	254	1101	10	-5518	-4417	AfriAnta
SWIR55	-29.025	-28.994	61.005	61.683	65.9647	14.14	0.17	-3845	644	2026	10	-4535	-2509	AfriAnta
SWIR56	-28.806	-28.817	61.730	62.087	34.7628	14.12	0.41	-4703	336	1144	10	-5115	-3971	AfriAnta
SWIR57	-28.201	-28.567	63.014	62.122	96.2187	14.08	0.63	-4709	342	1164	10	-5248	-4084	AfriAnta
SWIR58	-28.054	-28.064	63.049	63.632	57.1503	14.04	0.92	-4380	203	771	10	-4684	-3914	AfriAnta
SWIR59	-27.875	-27.875	64.368	63.655	70.0923	14.01	1.19	-4205	722	2128	10	-4987	-2858	AfriAnta
SWIR6	-52.518	-52.785	12.706	11.735	71.8647	13.79	35.38	-4295	255	1344	10	-4669	-3325	AfriAnta
SWIR60	-27.928	-27.928	65.331	64.345	96.9085	13.96	1.59	-4599	264	1044	10	-4959	-3915	AfriAnta

Table C2 (Continued)

SWIR61	-27.686	-27.686	65.307	65.664	35.1122	13.92	1.83	-4258	742	2038	10	-5343	-3305	AfriAnta
SWIR62	-27.570	-27.581	66.424	65.676	73.8035	13.89	2.07	-4602	314	1102	10	-5069	-3968	AfriAnta
SWIR63	-27.338	-27.338	67.066	66.472	58.6924	13.84	2.34	-4410	285	1122	10	-5007	-3885	AfriAnta
SWIR64	-27.127	-27.127	67.244	66.983	25.8789	13.82	2.44	-4120	465	1406	10	-4932	-3526	AfriAnta
SWIR65	-26.852	-26.852	67.518	67.185	33.0058	13.80	2.46	-4903	329	1196	10	-5378	-4182	AfriAnta
SWIR66	-26.565	-26.576	68.053	67.482	56.7392	13.77	2.56	-4308	355	1255	10	-5002	-3747	AfriAnta
SWIR67	-25.604	-26.416	69.895	68.029	207.1520	13.69	2.93	-4301	381	1736	10	-5079	-3343	AfriAnta
SWIR7	-52.521	-52.504	12.917	12.723	13.2768	13.81	34.81	-3988	266	877	10	-4370	-3493	AfriAnta
SWIR8	-52.166	-52.504	14.321	12.934	101.4808	13.83	34.04	-3904	340	1192	10	-4543	-3351	AfriAnta
SWIR9	-52.253	-52.155	14.858	14.356	35.9254	13.86	33.13	-3600	368	1303	10	-4053	-2750	AfriAnta
BLAU1	-15.236	-15.724	-176.095	-176.730	86.9923	108.30		-1876	192	798	10	-2244	-1445	FTNI
BLAU10	-21.495	-22.175	-176.403	-176.619	78.8309	54.50		-2064	138	631	10	-2300	-1669	AUTO
BLAU11	-22.191	-22.689	-176.607	-176.765	57.6962	44.40		-2063	157	765	10	-2592	-1827	AUTO
BLAU12	-14.748	-15.160	-173.949	-174.129	49.7877	116.90		-2923	244	891	10	-3438	-2547	NITO
BLAU13	-15.176	-15.577	-174.123	-174.381	52.4723	106.20		-2325	291	908	10	-2675	-1768	NITO
BLAU14	-15.155	-15.597	-174.499	-174.795	58.5131	104.80		-2267	148	535	10	-2575	-2039	NITO
BLAU15	-15.610	-16.161	-174.831	-174.820	61.3131	92.50		-2358	154	684	10	-2703	-2019	NITO
BLAU16	-17.002	-16.073	-174.545	-174.509	103.4047	78.40		-2079	179	715	10	-2458	-1744	NITO
BLAU17	-17.258	-16.915	-174.529	-174.482	38.4877	66.00		-2146	424	1296	10	-2950	-1654	NITO
BLAU18	-17.665	-17.269	-174.585	-174.533	44.3552	57.00		-2511	428	1383	10	-3038	-1655	NITO
BLAU2	-16.092	-15.536	-177.653	-177.054	89.0455	75.80		-2230	83	298	10	-2385	-2087	AUNI
BLAU3	-18.214	-16.844	-176.297	-176.917	165.9973	82.20		-2327	200	1007	10	-2927	-1920	AUNI
BLAU4	-18.281	-18.845	-176.286	-176.571	69.5681	87.90		-2279	17	76	10	-2316	-2240	AUNI
BLAU5	-18.856	-19.218	-176.584	-176.545	40.3723	91.30		-2323	69	323	10	-2570	-2246	AUNI
BLAU6	-19.149	-19.377	-176.112	-176.208	27.2921	96.20		-2961	134	546	10	-3177	-2631	AUTO
BLAU7	-19.334	-20.091	-175.893	-176.152	88.3800	89.70		-2692	148	753	5	-3103	-2350	AUTO
BLAU8	-20.080	-20.676	-176.078	-176.253	68.6617	78.70		-2666	66	343	5	-2754	-2411	AUTO
BLAU9	-21.493	-20.586	-176.393	-176.125	104.6722	68.00		-2211	118	582	10	-2463	-1881	AUTO
BMNS1	-3.668	-3.246	149.740	150.159	66.0515	71.20		-2241	98	333	10	-2445	-2112	MNNB
BMNS2	-3.243	-3.026	150.166	150.499	44.1557	22.10		-2483	76	261	10	-2586	-2325	MNNB
BMNS3	-3.909	-3.705	150.229	150.999	88.4065	81.40		-2383	146	604	10	-2561	-1957	MNSB
BMNS4	-3.829	-3.668	151.076	151.301	30.7181	146.10		-2585	35	135	10	-2671	-2536	MNSB
BMNS5	-3.788	-3.641	151.654	152.031	44.9344	142.00		-2075	51	198	10	-2179	-1981	NBSB
BMRN1	14.153	13.417	144.228	144.135	82.5196	48.40		-3789	341	1522	10	-4298	-2776	MAPS
BMRN10	19.967	18.974	144.253	144.649	117.9630	26.80		-4230	368	1742	10	-4813	-3071	MAPS
BMRN11	20.607	19.903	143.823	144.068	82.2949	23.10		-4704	463	1615	10	-5669	-4055	MAPS

Table C2 (Continued)

BMRN12	21.454	20.563	143.223	143.767	114.0564	19.60		-3593	319	1240	10	-4168	-2928	MAPS
BMRN13	22.164	21.489	142.730	143.286	94.4756	15.80		-3211	265	1225	10	-3850	-2624	MAPS
BMRN14	22.876	22.284	142.380	142.841	81.1402	12.40		-3119	570	2712	10	-4188	-1475	MAPS
BMRN2	14.896	14.129	144.312	144.270	85.3952	45.70		-4234	172	761	10	-4677	-3916	MAPS
BMRN3	15.676	14.944	144.599	144.455	82.7922	42.80		-4138	347	1172	10	-4756	-3585	MAPS
BMRN4	16.257	15.704	144.785	144.766	61.5354	40.50		-3770	244	888	10	-4264	-3376	MAPS
BMRN5	16.615	16.267	144.809	144.852	38.9114	38.80		-3913	280	949	10	-4572	-3623	MAPS
BMRN6	17.570	16.664	144.702	144.880	102.5249	36.20		-3982	431	1624	10	-4682	-3057	MAPS
BMRN7	17.958	17.621	144.826	144.944	39.5005	33.80		-4286	180	600	10	-4634	-4033	MAPS
BMRN8	18.467	17.951	144.623	144.785	59.8738	31.90		-3957	212	875	10	-4423	-3549	MAPS
BMRN9	18.989	18.495	144.557	144.708	57.2600	29.80		-4434	392	1482	10	-5086	-3605	MAPS
BSCO1	-55.679	-56.465	-30.325	-30.372	87.3588	59.40		-3257	221	823	10	-3728	-2904	SCSW
BSCO2	-56.413	-56.911	-30.747	-30.747	55.4084	60.90		-3558	84	339	10	-3736	-3397	SCSW
BSCO3	-56.920	-57.227	-30.472	-30.494	34.2634	61.80		-3550	321	953	10	-4118	-3165	SCSW
BSCO4	-57.237	-57.681	-30.171	-30.180	49.3402	62.80		-3903	121	369	10	-4117	-3748	SCSW
BSCO5	-57.690	-58.319	-29.827	-29.782	69.9925	64.10		-3508	199	663	10	-3852	-3190	SCSW
BSCO6	-58.319	-58.872	-29.954	-29.945	61.4374	65.50		-3632	94	296	10	-3772	-3476	SCSW
BSCO7	-58.830	-59.641	-29.537	-29.537	90.2124	67.00		-3260	209	676	10	-3572	-2896	SCSW
BSCO8	-59.462	-60.388	-29.954	-29.800	103.3793	68.60		-2982	225	738	10	-3263	-2525	SCSW
BWDL1	-10.000	-10.182	151.995	154.212	243.5463	28.10		-3059	288	1750	10	-4289	-2538	WLAU
BWDL2	-9.706	-9.874	155.193	154.226	107.5950	33.80		-3515	350	1262	10	-4151	-2889	WLAU
BWDL3	-9.577	-9.565	155.199	156.135	102.6381	37.20		-3857	193	884	10	-4205	-3321	WLAU
BWDL4	-9.244	-9.230	156.060	156.472	45.2452	39.50		-4105	215	848	10	-4479	-3631	WLAU
CAYM1	18.232	17.764	-81.732	-81.732	51.9947	19.30		-5382	367	1273	10	-5926	-4652	CANA
CAYM2	18.716	18.255	-81.726	-81.695	51.3075	19.20		-5079	483	1874	10	-6449	-4575	CANA
FIJI1	-13.630	-15.590	172.709	173.500	233.9800	26.90		-3271	304	1371	10	-3979	-2608	NHBR
FIJI10	-19.344	-19.821	175.817	175.548	60.0814	29.30		-2889	231	872	10	-3155	-2284	CRAU
FIJI11	-19.872	-20.829	175.502	175.917	114.8519	22.70		-3017	207	809	10	-3470	-2660	CRAU
FIJI2	-15.605	-16.769	173.300	173.745	137.9096	35.30		-3279	207	797	10	-3681	-2884	NHBR
FIJI3	-16.883	-18.094	173.966	173.546	141.7905	62.60		-2528	250	871	10	-2826	-1955	NHCR
FIJI4	-18.326	-19.738	173.538	173.402	157.6456	79.30		-2758	73	333	10	-2998	-2665	NHCR
FIJI5	-19.761	-21.265	173.390	173.384	167.2606	96.50		-2910	167	595	10	-3310	-2716	NHCR
FIJI6	-20.685	-21.751	174.167	174.160	118.5027	106.90		-2766	151	628	10	-3177	-2549	NHCR
FIJI7	-16.637	-17.751	176.178	175.955	126.1266	49.50		-3294	287	932	10	-3741	-2809	CRAU
FIJI8	-17.817	-18.422	176.339	176.178	69.4128	41.70		-3472	468	1345	10	-4238	-2892	CRAU
FIJI9	-18.481	-19.286	176.316	175.886	100.3741	35.10		-3791	453	1694	10	-4349	-2655	CRAU

Table C3: Interlaboratory Bias Correction Factors

Method-Institution	SiO_2	Al_2O_3	MgO	CaO	Na_2O	TiO_2	FeO_t	Interlab Bias Factor Code
DCP-LAMONT-DOHERTY EARTH OBSERVATORY OF COLUMBIA UNIVERSITY	1.005	0.971	1.000	1.000	1.000	1.036	1.000	Method 1
WET-UNIVERSITY OF RHODE ISLAND	1.005	0.971	1.000	1.000	1.010	1.036	1.000	Method 2
EMP-SMITHSONIAN INSTITUTION OF WASHINGTON	0.995	0.996	1.036	0.989	1.044	1.028	1.012	Method 3
EMP-LAMONT-DOHERTY EARTH OBSERVATORY OF COLUMBIA UNIVERSITY	1.000	1.000	1.000	1.000	1.000	1.000	1.000	Method 4
EMP-UNIVERSITY OF HAWAII	0.994	0.985	1.089	1.015	1.001	1.002	0.963	Method 5
EMP-UNIVERSITY OF CAPE TOWN	0.998	0.962	1.035	0.996	0.981	1.007	1.033	Method 6
EMP-UNIVERSITY OF RHODE ISLAND	0.985	0.978	1.038	1.005	0.949	0.967	1.088	Method 7
EMP-INSTITUT FRANCAIS POUR L'EXPLOITATION DE LA MER	1.002	0.952	1.039	1.007	0.985	0.997	1.040	Method 8
XRF-UNIVERSITY OF CAPE TOWN	1.002	0.939	1.057	0.981	0.998	1.107	1.060	Method 9
EMP-MASSACHUSETTS INSTITUTE OF TECHNOLOGY	0.995	0.987	1.032	1.018	0.978	1.006	0.983	Method 10
XRF-UNIVERSITY OF HAWAII	0.992	0.974	1.045	1.010	1.045	0.999	1.017	Method 11
XRF-UNIVERSITAET KARLSRUHE	1.005	0.993	0.967	1.024	0.991	1.020	0.971	Method 12
XRF-MASSACHUSETTS INSTITUTE OF TECHNOLOGY	0.999	0.983	1.042	0.991	1.058	1.010	0.986	Method 13
XRF-R/V JEAN CHARCOT	1.007	1.009	0.937	1.018	1.030	1.041	0.966	Method 14
EMP-SUNY AT STONY BROOK	1.003	0.954	1.016	1.003	0.973	1.058	1.008	Method 15
EMP-UNIVERSITY OF TASMANIA	0.988	0.973	1.075	0.998	1.048	1.036	1.022	Method 16
ICPAES-UNIVERSITY OF HOUSTON	0.998	1.013	0.972	1.026	0.995	1.037	0.961	Method 17
XRF-UNIVERSITY OF BRITISH COLUMBIA	1.011	0.992	0.957	0.996	0.973	1.018	0.987	Method 18
EMP-UNIVERSITY OF HOUSTON	0.997	0.979	1.092	1.007	0.987	1.047	0.974	Method 19
EMP-RUSSIAN NATIONAL ACADEMY OF SCIENCES	1.001	0.983	1.103	1.013	0.988	0.935	0.933	Method 20
AAS-UNIV OF NEWCASTLE-UPON-TYNE	0.993	0.969	1.033	1.014	1.025	0.999	1.023	Method 21
EMP-UNIVERSITY OF BRITISH COLUMBIA	0.996	0.980	1.088	1.000	1.001	0.998	0.981	Method 22
EMP-AUSTRALIAN NATIONAL UNIVERSITY	0.993	0.977	1.031	0.998	0.969	0.990	1.065	Method 23
EMP-UNIVERSITY OF TULSA	1.000	1.000	1.000	1.013	1.034	1.032	1.000	Method 24

Note: All factors except for the EMP-Smithsonian factors are from Su, 2002 and are published with permission in Gale et al., submitted.

Table C4: Estimated H_2O/K_2O Ratios for Back-Arc Basin Segments in this study

Back-Arc Basin:	Scotia			Manus	Lau		Marianas
	BSCO1	BSCO2,3,4,5,6,7	BSCO8	All BMNS segments	BLAU7,8,9,10,11	Other BLAU segments	All BMRN segments
H_2O/K_2O Ratio	4.0	2.0	1.1	4.8	14.1	1.5	4.0

Appendix D

Supplementary Material for Chapter 5

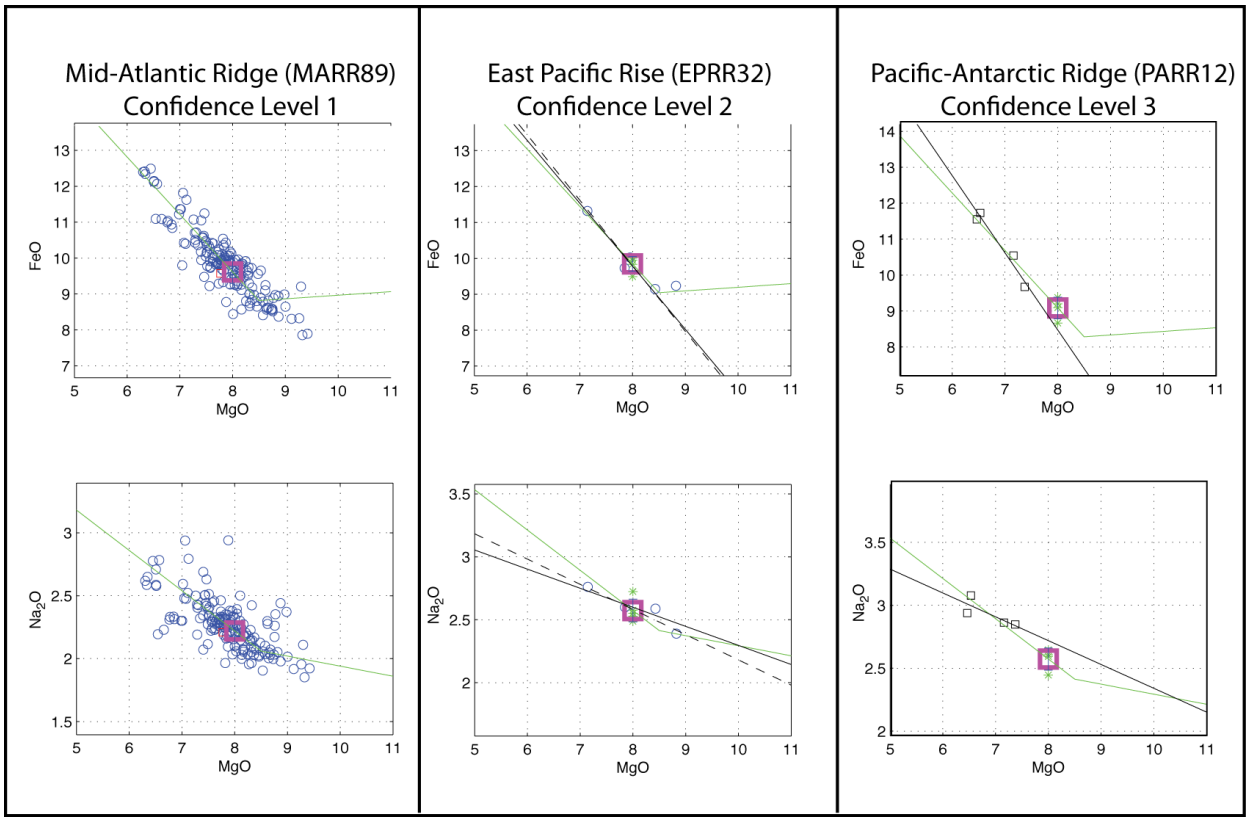

Figure D1. Sample variation diagrams (FeO and Na_2O versus MgO) of three segments from our ridge catalog with different 8-value "confidence levels". Confidence levels were assigned qualitatively to give some indication of how well the segment 8-value is known. Note that the Confidence 1 segment has well-defined liquid lines of descent and many samples around 8 wt. % MgO. Confidence 2 is far less well-constrained, but still has samples with ~8 wt.% MgO. Confidence 3 is the poorest case where the liquid lines of descent are unclear, and there are no samples near 8 wt. % MgO.

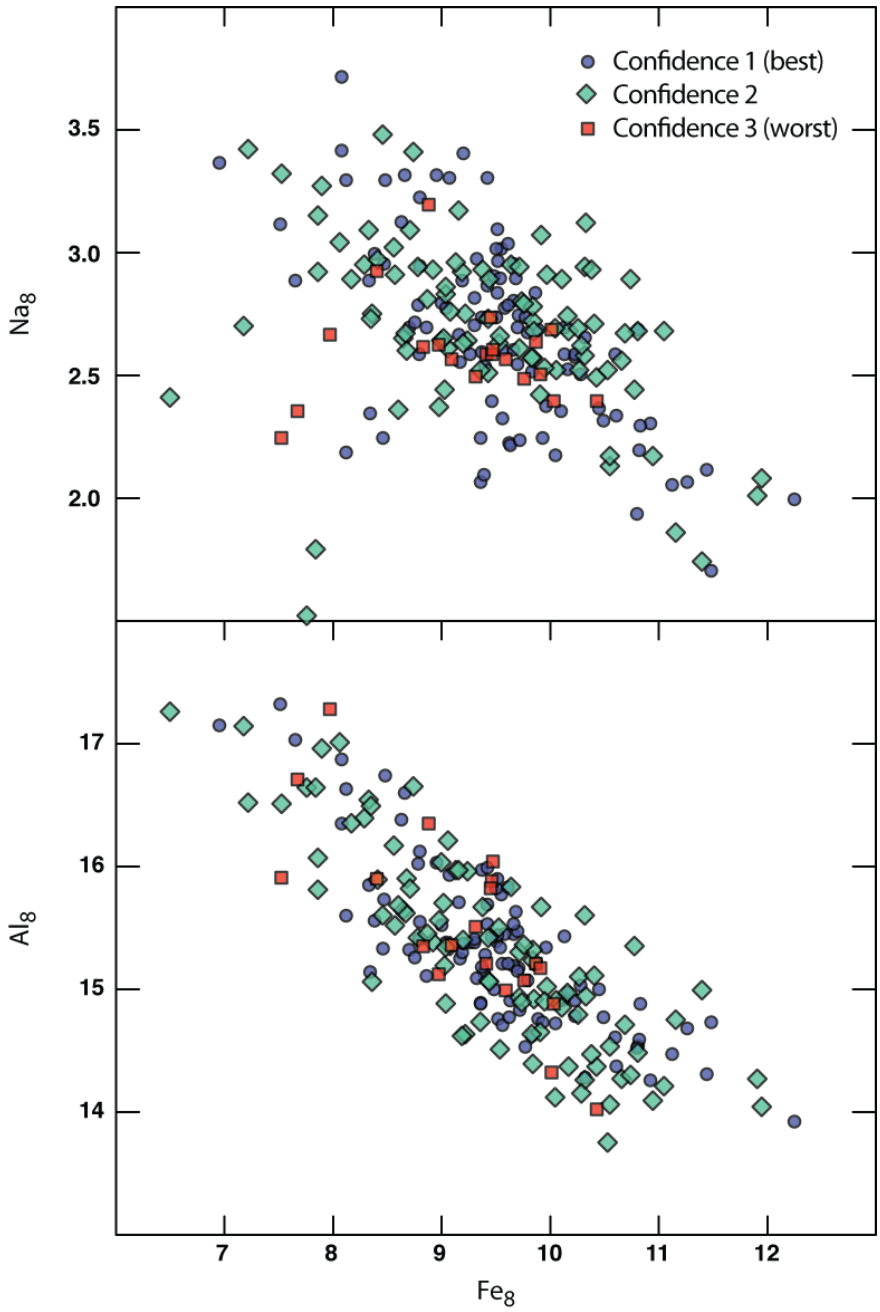

Figure D2. Na_8 and Al_8 versus Fe_8 in the global segments, color coded by Confidence Level. Note that the trends in the dataset do not depend on Confidence Level. Indeed, the highest-confidence segments span the full chemical range.

Table D1: Summary table of the method codes and customization options used for fractionation correction

Seg Name	Si*	Fe*	Al*	Ca*	Na*	Ti*	Mg Min	Mg Max	Si Min	K Max	HiAl (1= present)	Notes	Special	Confidence (1=best, 3= worst)
AARR1	1	1	1	1	1	1		8.5			0		Normal	2
AARR3	3	3	3	3	3	3		8.5			1		Normal	1
AFAR33	3	3	3	3	3	3					0		Normal	2
BLAU10	3	3	3	3	3	3							Normal	2
BLAU15	1	1	1	1	1	1		8.5			0		Normal	2
BLAU4	3	3	3	3	3	3							Normal	2
BLAU5	1	1	3	3	1	1	6	8					Normal	3
BLAU7	2	1	1	1	1	1							Normal	1
BLAU8	1	2	2	1	1	3		8.5			1		Normal	1
BLAU9	3	3	3	3	3	3							Normal	2
BMNS1	3	3	3	3	3	3		8.5			0		Normal	2
BMNS2	1	1	1	1	1	1							Normal	2
BMRN12	3	3	3	3	3	3					0		Normal	2
BMRN3	1	1	1	1	1	1					0		Normal	2
BMRN4	3	3	3	3	3	3					0		Normal	2
BMRN5	1	1	1	3	3	1					0		Normal	3
CAYM1	1	1	1	1	1	1							Normal	1
CAYM2	1	1	1	1	1	1					0		Normal	2
CHIL25	3	3	3	3	3	3		9					Normal	2
CHIL27	1	1	1	1	1	1		8.5					Normal	1
CIRR23CIRR22	4	4	4	4	4	4	7.5	8.49					Normal	1
CIRR27	4	4	4	4	4	4	7.5	8.49					Normal	1
CIRR30	3	3	3	3	3	3							Normal	2
CIRR36	3	3	3	3	3	3							Normal	1
EPRR10	1	1	1	1	1	1							Normal	1
EPRR11	2	2	2	2	2	2							Normal	1
EPRR14	4	4	4	4	4	4	7.5	8.49					Normal	1
EPRR16	3	3	3	3	3	3							Normal	2
EPRR17	1	1	1	1	1	1							Normal	2
EPRR18	2	2	2	2	2	2							Normal	1
EPRR19	3	3	3	3	3	3							Normal	1
EPRR20	3	1	1	3	3	1							Normal	2
EPRR22	4	4	4	4	4	4	7.5	8.49					Normal	2

Table D1 (Continued)

EPRR23	1	1	1	1	1	1							Normal	1
EPRR24	3	3	3	3	3	3							Normal	1
EPRR25	3	3	3	3	3	3							Normal	1
EPRR26	1	1	1	1	1	1							Normal	1
EPRR27	1	1	1	1	1	1							Normal	1
EPRR28	1	1	1	1	3	1							Normal	
EPRR29	1	1	1	1	1	1							Normal	1
EPRR30	3	3	3	3	3	3							Normal	1
EPRR32	3	3	3	3	3	3							Normal	2
EPRR34EPRR33	3	3	3	3	3	3							Normal	1
EPRR35	3	3	3	3	3	3							Normal	2
EPRR50	1	1	1	1	1	1							Normal	2
EPRR56	4	4	4	4	4	4	7.5	8.49					Normal	2
EPRR59	2	2	2	2	2	2							Normal	1
EPRR60	3	3	3	3	3	3							Normal	2
EPRR61	3	3	3	3	3	3							Normal	2
EPRR62	1	1	1	1	1	1							Normal	1
EPRR63	1	1	1	1	1	1							Normal	2
EPRR64	1	1	1	1	1	1							Normal	1
EPRR65	3	3	3	3	3	3							Normal	3
EPRR67	3	3	3	3	3	3							Normal	3
EPRR70	3	3	3	3	3	3							Normal	2
EPRR71	3	3	3	3	3	3	7.5	8.5					Normal	2
FIJI2	3	3	3	3	3	3							Normal	2
FIJI4	3	3	3	3	3	3							Normal	1
GAKK10	3	3	3	3	3	3	6	8.5			1		Normal	2
GAKK11	1	1	1	1	1	1							Normal	1
GAKK13	3	3	3	3	3	3	5.5	8.2			1		Normal	1
GAKK15	3	3	3	3	3	3	6.5	8.4					Normal	2
GAKK16	1	1	1	1	1	1							Normal	1
GAKK17	3	3	3	3	3	3							Normal	2
GAKK18	3	3	3	3	3	3							Normal	2
GAKK7	1	1	1	1	1	1	6	8.5					Normal	1
GAKK8	3	3	3	3	3	3	7	8.5					Normal	1
GALA10	1	3	3	3	3	3		9					Normal	1

Table D1 (Continued)

GALA11	1	1	1	1	1	1		8.5			1		Normal	1
GALA14GALA13	3	1	1	1	1	1							Normal	2
GALA15	3	3	1	1	1	3	6						Normal	1
GALA3	2	2	2	2	2	2		8.5			1		Normal	1
GALA5GALA4	3	3	3	3	3	3							Normal	3
GALA7	3	1	1	1	1	3		9.2			1		Normal	2
GALA9	1	1	1	1	1	1		8.5					Normal	1
JUAN10	3	3	3	3	3	3		8			1		Normal	1
JUAN11	4	4	4	4	4	4	7.5	8.49					Normal	1
JUAN12	1	1	1	1	3	3	6						Normal	1
JUAN15	4	4	4	4	4	4	7.5	8.49					Normal	1
JUAN16	2	2	2	4	2	2							Normal	
JUAN17	1	1	1	1	1	1							Normal	1
JUAN3	3	3	3	3	3	3		8.5			1		Normal	2
JUAN4	1	1	1	1	1	1		8.8			1		Normal	1
JUAN7	3	3	3	3	3	3							Normal	2
JUAN9	3	3	3	3	3	3		8.2			1		Normal	1
MARR101MARR100	3	3	3	3	3	3							Normal	2
MARR104	1	1	1	1	1	1							Normal	2
MARR105	3	3	3	3	3	3		8.5					Normal	2
MARR107	3	3	3	3	3	3		8.5					Normal	2
MARR108	3	3	3	3	3	3		8.5			1		Normal	2
MARR115MARR114	1	3	3	3	3	3							Normal	3
MARR116	3	3	3	3	3	3							Normal	1
MARR117	1	1	1	1	1	1							Normal	1
MARR120	2	1	1	1	3	1							Normal	1
MARR121	1	1	1	1	1	1							Normal	1
MARR122	1	1	1	1	1	1							Normal	1
MARR123	3	3	3	3	3	3							Normal	1
MARR129	3	1	1	1	1	3							Normal	2
MARR134	1	1	1	1	1	1							Normal	2
MARR135	1	1	1	1	1	1							Normal	1
MARR136	4	4	4	4	4	4	7.5	8.49					Normal	1
MARR137	1	1	1	1	1	1							Normal	1
MARR138	1	1	1	1	1	1							Normal	2

Table D1 (Continued)

MARR141	1	1	1	1	1	1							Normal	1
MARR155	4	4	4	4	4	4	7.5	8.49					Normal	2
MARR156	3	3	3	3	3	3		9			1		Normal	2
MARR161	1	1	1	1	1	1							Normal	2
MARR166	3	3	3	1	3	3		9			1		Normal	1
MARR167	3	3	3	3	3	3		9			1		Normal	1
MARR170	1	1	1	1	1	1							Normal	1
MARR172MARR173	1	1	1	1	1	1							Normal	2
MARR18MARR17	3	3	3	3	3	3							Normal	2
MARR201	3	3	3	3	3	3							Normal	1
MARR210	1	1	1	1	1	1							Normal	1
MARR212	2	2	2	2	2	2							Normal	1
MARR214	1	1	1	1	1	1		8.5					Normal	1
MARR227MARR228	4	4	4	4	4	4	7.5	8.49					Normal	2
MARR22MARR21	1	1	1	1	1	1							Normal	1
MARR235MARR234	3	3	3	3	3	3							Normal	2
MARR24	3	1	1	1	1	1							Normal	1
MARR240MARR241	3	3	3	3	3	3		9			1		Normal	2
MARR242	4	4	4	4	4	4	7.5	8.49					Normal	2
MARR245MARR248	4	4	4	4	4	4	7.5	8.49					Normal	2
MARR249	3	3	3	3	3	3							Normal	2
MARR250	3	3	3	3	3	3							Normal	2
MARR253MARR254	3	3	3	3	3	3		9			1		Normal	3
MARR29	3	1	1	1	1	1							Normal	1
MARR33	3	3	3	3	3	3							Normal	2
MARR35	3	3	3	3	3	3							Normal	2
MARR36	1	1	1	3	1	3							Normal	2
MARR41	1	1	1	1	1	1							Normal	1
MARR53	4	4	4	4	4	4	7.5	8.49					Normal	1
MARR56MARR55	3	3	3	3	3	3							Normal	2
MARR62MARR61	3	3	3	3	3	3							Normal	2
MARR70MARR69	1	1	1	1	1	1							Normal	2
MARR74MARR73	4	4	4	4	4	4	7.5	8.49					Normal	2
MARR77MARR76	1	1	1	1	1	1							Normal	1
MARR79MARR80	3	3	3	3	3	3							Normal	3

Table D1 (Continued)

MARR81	1	3	1	1	3	1		9			1		Normal	1
MARR83	1	1	1	1	1	1							Normal	1
MARR84	1	1	1	1	1	1							Normal	3
MARR85	1	1	1	1	1	1							Normal	1
MARR86	1	1	1	1	1	1							Normal	1
MARR87	3	1	1	1	1	1							Normal	1
MARR88	4	4	4	4	4	4	7.5	8.49			1		Normal	1
MARR89	4	4	4	4	4	4	7.5	8.49					Normal	1
MARR91	1	1	1	1	1	1							Normal	1
MARR94	3	3	3	3	3	3		9					Normal	1
MARR95	3	3	3	3	3	3		9			1		Normal	1
PARR13	1	1	1	1	1	1							Normal	1
PARR15PARR16	3	3	3	3	3	3							Normal	2
PARR17	3	3	3	3	3	3							Normal	2
PARR2	3	3	3	3	3	3							Normal	2
PARR20PAR-R23PARR21	3	3	3	3	3	3	6	8					Normal	2
PARR24	3	3	3	3	3	3							Normal	2
PARR25PARR26	3	3	3	3	3	3							Normal	2
PARR27PARR28	3	3	3	3	3	3							Normal	3
PARR29PARR30	3	3	3	3	3	3							Normal	2
PARR39PAR-R38PARR35	3	3	3	3	3	3							Normal	2
SEIR30SEIR31	3	3	3	3	3	3		9			1		Normal	1
SEIR32	1	1	1	1	3	1							Normal	2
SEIR33	3	3	3	3	3	3							Normal	2
SEIR34	1	1	1	1	1	1							Normal	1
SEIR35	4	4	4	4	4	4	7.5	8.49					Normal	1
SEIR39	3	1	1	1	1	3							Normal	3
SEIR40	3	1	1	1	1	1							Normal	1
SEIR41	1	1	1	1	1	1							Normal	1
SEIR42	3	3	3	3	3	3							Normal	1
SEIR43SEIR44	3	3	3	3	3	3							Normal	2
SEIR47	1	1	1	1	1	3							Normal	1
SEIR49	3	3	3	3	3	3		9					Normal	2
SEIR51	3	3	3	3	3	3							Normal	2

Table D1 (Continued)

SEIR52	3	3	3	3	3	3							Normal	2
SEIR53	1	1	1	1	1	1							Normal	2
SEIR56SEIR57	3	1	3	1	3	1							Normal	2
SEIR65	3	3	3	3	3	3							Normal	2
SEIR67	3	1	1	1	3	1							Normal	2
SEIR68	3	3	1	1	3	3					1		Normal	2
SEIR69	3	3	3	3	3	3		8					Normal	2
SEIR71SEIR70	3	3	3	3	3	3		8					Normal	2
SWIR11	3	3	3	3	3	3							Normal	2
SWIR13	1	1	1	1	1	1							Normal	1
SWIR15	1	1	1	1	1	1							Normal	1
SWIR16	3	3	3	3	3	3							Normal	2
SWIR17	3	3	3	3	3	3							Normal	1
SWIR18	1	1	1	1	1	1							Normal	1
SWIR19	1	1	1	1	1	1							Normal	1
SWIR1SWIR2	3	3	3	3	3	3		8.5			1		Normal	3
SWIR21SWIR20	3	3	3	3	3	3							Normal	3
SWIR5	1	1	1	1	3	3	6						Normal	2
SWIR67SWIR66	3	3	3	3	3	3							Normal	1
SWIR7SWIR6	3	3	3	3	3	3		8			1		Normal	2
BMRN10	1	-1	1	1	1	2	6	8.5			1		Special1	1
BMRN6	3	-1	1	1	4	1	6						Special1	3
MARR102	3	3	3	3	3	3		9	49		1		Special1	
MARR111MARR110	3	-1	3	1	3	3		9	49		1		Special1	
MARR168MARR169	3	3	3	3	3	3				0.5			Special1	2
MARR171	4	4	4	4	4	4	7.5	8.49	49				Special1	1
MARR40MAR-R38MARR37	1	3	0.6	1	1	1							Special1	1
MARR82	3	3	3	3	3	3			49		1		Special1	
MARR92	3	3	1	1	3	3			49		1		Special1	1
MARR93	4	4	4	4	4	4	7.5	8.49	49		1		Special1	1
SEIR36	3	3	3	3	3	3				0.5			Special1	3
FIJI3	3	3	3	3	3	3	6	8.5				Use WR, no requirement of interlab bias factors	Special2	3

Table D1 (Continued)

MARR23	3	3	3	3	3	3						Use WR, no requirement of interlab bias factors	Special2	1
MARR34	3	3	3	3	3	3						Use WR, no requirement of interlab bias factors	Special2	2
PARR11	3	3	3	3	3	3						Use WR, no requirement of interlab bias factors	Special2	3
PARR12	3	3	3	3	3	3						Use WR, no requirement of interlab bias factors	Special2	3
PARR6	1	1	1	1	1	1						Use WR, no requirement of interlab bias factors	Special2	3
PARR8	1	1	1	1	1	1						Use WR, no requirement of interlab bias factors	Special2	3
BMRN8	3	1	1	1	1	1						Exclude samples with TiO2<0.8	Special3	1
MARR238	4	4	4	4	4	4	7	9					Special3	2
MARR97	4	4	4	4	4	4	7.4	8.6			1		Special3	1
MARR244	3	3	3	3	3	3		9				Hinge Point at 7.5	Special4	
SWIR4	1	1	1	2	1	1						Hinge Point at 7.5	Special4	
AFAR30AFAR29	3	-1.2	1	3	3	3							Special5	
SWIR8	3	3	3	3	3	3		9				Custom slopes	Special6	
SWIR9	3	3	3	3	3	3			49		1	Custom slopes	Special6	
GALA6	3	3	1	1	3	3		9.2	49				Special7	
GALA8	3	1	1	1	1	1		9.2					Special7	
JUAN5	3	3	3	3	3	3		8.5	49				Special7	
MARR103	3	3	3	3	3	3		9	49				Special7	
MARR118	1	3	3	1	3	3		8.5					Special7	
MARR159	3	3	3	3	3	3							Special7	
MARR28	1	1	1	1	1	1							Special7	
SWIR26SWIR27	3	3	3	3	3	3							Special7	
SWIR29	3	3	3	3	3	3							Special7	
SWIR30	3	3	3	3	3	3							Special7	
SWIR47SWIR48	3	3	3	3	3	3							Special7	

Table D1 (Continued)

SWIR52SWIR53	3	3	3	3	3	3							Special7	
GALA12	1	1	1	1	1	1						Use WR, no requirement of interlab bias factors	Special8	
JUAN8	1	1	1	1	1	1						Use WR, no requirement of interlab bias factors	Special8	
MARR14	4	4	4	4	4	4	7.5	8.49				Use WR, no requirement of interlab bias factors	Special8	
MARR31	4	4	4	4	4	4	7.5	8.49				Use WR, no requirement of interlab bias factors	Special8	
MARR32	3	3	3	3	3	3						Use WR, no requirement of interlab bias factors	Special8	
MARR42	1	1	1	1	1	1						Use WR, no requirement of interlab bias factors	Special8	
MARR43	4	4	4	4	4	4	7.5	8.49				Use WR, no requirement of interlab bias factors	Special8	
MARR44	2	2	2	2	2	2						Use WR, no requirement of interlab bias factors	Special8	
MARR46	1	1	1	1	1	1						Use WR, no requirement of interlab bias factors	Special8	
MARR47	1	1	1	1	1	1						Use WR, no requirement of interlab bias factors	Special8	
SWIR59	4	4	4	4	4	4	7.5	8.49				Use WR, no requirement of interlab bias factors	Special8	

* = Metod Code. Any number not 1,2,3,4 is a custom slope value

Table D2: “Olivine-only” slopes used for fractionation correction in this study

	SiO_2	FeO	Al_2O_3	CaO	Na_2O	TiO_2
Slope (versus MgO)	-0.27	0.1	-0.4	-0.3	-0.08	-0.05